MARTIAN METEORITES AS WINDOWS INTO PLANETARY VOLCANISM: INSIGHTS FROM OLIVINE-PHYRIC SHERGOTTITE METEORITES

By

Chad Jordan Peel

Supervised by

Doctor Geoffrey Howarth

A dissertation submitted in fulfilment of

the requirements for the degree of

DOCTOR OF PHILOSOPHY

UNIVERSITY OF CAPE TOWN

Department of Geological Sciences

LIST OF TABLES

LIST OF FIGURES

TABLE OF CONTENTS

Abstract

Martian meteorites are the only samples currently available from the surface of Mars to study in terrestrial laboratories and can provide valuable insight into magmatic processes and the planet's geological evolution. With more meteorites being found every year, researchers no longer need to look only at single meteorites but rather groups, paired based on their crystallisation ages, ejection ages, and geochemistry. This allows for the development of models of volcanism using suites of meteorites, rather than relying solely on single meteorites. One group of shergottite meteorites, comprising approximately 20 samples with crystallisation ages from 2.4 to 0.35 Ga, share similar geochemical characteristics and ejection ages of 1.1 Ma, and are suggested to have originated from a common long-lived volcanic system. Thus, by studying these 1.1 Ma ejection paired meteorites, it is now possible to evaluate martian magma plumbing systems through time.

In chapter 2, I present a comprehensive investigation of two 1.1 Ma ejection-paired olivine-phyric shergottites, Northwest Africa (NWA) 2046 and NWA 4925. I show that Mg-rich olivine megacrysts in both samples represent phenocrysts and evidence of early olivine fractionation in staging chambers prior to ascent to surface. Distinct patterns of terrestrial alteration, notably in NWA 4925, have been identified through Ca and K elemental mapping, manifesting in the preferential alteration of olivine megacryst cores and LREE enrichment of bulk-rock and pyroxene. Analysis of $^{87}Sr/^{86}Sr$ in maskelynite and low fO_2 crystallisation conditions suggest a shared mantle source region with other 1.1 Ma ejection-paired samples, particularly the ~470 Ma DaG 476, SaU 005, and Yamato 980459, while pressure estimates using pyroxene Ti/Ai ratios, indicate common or multiple staging chambers near the base of the crust. In this chapter, I combine my data with literature data for other 1.1 Ma shergottites (e.g., DaG 476, SaU 005, and Yamato 980459) to present a model for volcanism at this site.

One of the other major unanswered questions in the study of martian meteorites is the origin of the enriched geochemical reservoir on Mars, as either a distinct mantle source or crust. Olivine-phyric shergottites, the most primitive type of martian meteorite, are commonly interpreted to represent primary mantle derived melts, and can be categorised into three distinct geochemical groups, incompatible-trace element depleted, intermediate, and enriched, reflecting distinct source reservoirs. The primary focus of remaining chapters (3 and 4) of this dissertation is to track the evolution of REEs in these rocks from the start of crystallisation to the end. This was carried out using a newly developed laser ablation ICP-MS technique with enhanced sensitivity to analyse REEs in olivine as a proxy for the initial parent melt. The REEs of olivine-hosted melt inclusion glass and late-stage merrillite from the same samples were then measured for comparison against olivine. By comparing these, I can robustly constrain the REE evolution of shergottite parent melts and evaluate the possibility of crustal assimilation or open system processes during evolution. To do this, in chapter 3 I present the first full REE dataset for Mg-rich

olivine in shergottites in a comprehensive suite of depleted, intermediate, and enriched olivine-phyric shergottites (11 samples) including: Dar Al Gani (DaG) 1037, NWA 2046, 4925, 6234, 10170, 1068, 1183, Dhofar (Dho) 019, Sayh al Uhaymir (SaU) 005, Tissint, and Larkman Nunatak (LAR) 12011. In chapter 4, I combine the olivine REE findings of chapter 3 with melt inclusion glass and merrillite data to fully evaluate the REE evolution of shergottite melts.

In chapter 3, my analysis of early formed olivine megacryst trace element and ultra-trace element compositions in depleted shergottites indicates closed-system crystallisation behaviour, supporting interpretations that these meteorites represent partial melting of a LREE depleted mantle source. Olivine in the enriched shergottite LAR 12011 are LREE-depleted and identical to the REE pattens of olivine in depleted shergottites. This suggests open-system behaviour, potentially involving assimilation of xenocrystic LREE-depleted olivine or mixing with a LREE-enriched melt. Olivines in the enriched shergottite NWA 1183 are LREE enriched compared to NWA 1068 and LAR 06319 and points towards open system processes such as magma mixing and/or crustal assimilation.

In chapter 4, I evaluate the use of olivine-hosted melt inclusion glass in constraining primary REE patterns for shergottites. My findings show that the REE patterns of melt inclusion glass parallel that of bulk-rock, which indicates that glass is useful in constraining REE contents of early melts trapped in olivine. The REE patterns for melt inclusion glass in the depleted shergottites also parallel REE patterns for Mg-rich olivine and later-crystallising merrillite, indicating closed-system behaviour during crystallisation and consistent with my findings of chapter 3. Intermediate shergottites NWA 6234 and NWA 10170 also exhibit closed-system behaviour, indicating partial melting from distinct mantle source regions. For LAR 12011, distinct LREE-depleted and LREE-enriched melt inclusion glass populations were observed in LREE-depleted olivine megacrysts previously analysed in chapter 3, with depleted glasses hosted in olivine megacryst core regions (Fo_{68} to Fo_{75}) and LREE-enriched glasses in olivine core-mantle regions (Fo_{69} to Fo_{73}). These findings suggest that olivine megacryst cores from LAR 12011 appear to have crystallised from a depleted melt rather than an enriched melt. Melt inclusion glass of NWA 1183 shows LREE enrichment attributed to assimilation of an enriched crustal component, akin to processes observed in NWA 7034, before any crystallisation had occurred.

Acknowledgements

Looking back on the past four years, I am filled with gratitude for the incredible individuals who have stood by me and carried me through my academic journey.

First and foremost, I would like to express my deepest appreciation to my supervisor, Dr. Geoffrey Howarth. I am profoundly indebted to him for his brilliance as an academic and his wisdom as a supervisor. His guidance has transformed my PhD studies into the most exhilarating adventure I could have hoped for. I am truly grateful for his unwavering patience, invaluable advice, and constant support. But above all, I want to thank him for giving me the opportunity to pursue my dream of exploring the worlds beyond our own.

I would also like to extend my heartfelt thanks to Dr. James Day from the Scripps Institution of Oceanography, Dr. Petrus le Roux from the University of Cape Town, Gabi Costin from Rice University, and Dr. Olivier Alard from Macquarie University. Their assistance with various analytical techniques and their expertise extending beyond analytical questions have greatly enriched my research. I am sincerely grateful for their contributions, which have enhanced the quality and depth of my work.

Moreover, I want to express my immense gratitude to my close friends who have become my family during this journey. Akhil Rampersadh, Guy Salomon, Phillip Ruhesi, Dr. Saif Khan, Dr. Farhaan Dobah, Wanye de Jager, Natasha Wood, Dr. Miengah "senpai" Abrahams, and Dr. Vuyo Mlaza - each of you has left an indelible mark on my heart. Your impact and the unforgettable moments we have shared have significantly influenced my life. Without your constant support I would not have reached this milestone. I am genuinely thankful to every one of you.

To my mom, Audrey Peel, my sister, Kia Peel, and better half, Vhutali Brian Gadisi, words cannot express how deeply thankful I am for your unconditional love and unwavering support. You have been my pillars of strength throughout the ups and downs of this journey. Your belief in me and the constant motivation you provided have been instrumental in reaching the finish line. Above all, I am forever grateful for your presence in my life – I love you too much! To my dad, Ellery Peel, whom I lost along the way, I dedicate this PhD to you. I am grateful for your unwavering support throughout my studies and the immense sacrifices and tireless hours you dedicated, which granted me the opportunities I have been fortunate to have had. Your guidance and support have shaped me into the person I am today.

To everyone mentioned here and to all those who have played a part in my academic and personal growth, my heartfelt gratitude goes out to you. Without your support, this accomplishment would not have been possible. I consider myself truly blessed to have had you by my side.

Author's declaration

I, **Chad Jordan Peel**, declare that this work has not previously been submitted for a degree or diploma in any university or institution of learning. To the best of my knowledge and belief, all content in this thesis is original and does not contain any previously published or written material by another person unless properly referenced within the thesis itself.

Signature: Signed by candidate **Date**: 08/04/2024

Declaration on the Inclusion of Publication in the PhD Thesis

I confirm that I have been granted permission by the University of Cape Town's Doctoral Degrees Board to include the following publication, with the approval of my co-authors, in my PhD thesis:

1. **Peel, C.J.**, Howarth, G.H., Day, J.M., le Roux, P. and Alard, O., 2023. Constraints on martian depleted shergottite volcanism from the petrogenesis of olivine-phyric shergottites NWA 2046 and NWA 4925. Journal of African Earth Sciences, 202, 104901.

Signature: Signed by candidate **Date**: 08/04/2024

Student Name: Chad Jordan Peel **Student Number**: PLXCHA003 (1474554)

1 Chapter 1

1.1 General Introduction

For decades, researchers have unravelled the geology of Mars through two primary approaches: missions to Mars (i.e., orbiting satellites, ground-based landers, and rovers etc.) and studies of martian meteorites – fragments of crustal rock ejected from the martian surface due to impacts by celestial bodies like asteroids or comets. Martian meteorites serve as valuable physical samples from Mars, and as such, provide an opportunity to study the geochemistry and petrology, and by extension, the geological history of Mars from hand-sample to the atomic scale. A key advantage to studying meteorites is the ability to analyse these samples in high-precision laboratories on Earth; however, the disadvantage being that their exact origin on Mars is not well-constrained. Recent studies suggest that the source of martian meteorites is most likely the Tharsis plateau, which represents a geological young volcanic terrane on Mars (e.g., Werner, 2009; Robbins et al., 2011; Lagain et a., 2021).

To-date, the martian meteorite collection includes ~370 known samples, based on the meteorite list last updated in February 2024 and compiled by A.J. Irving (https://imca.cc/mars/martian-meteorites-list.htm). The collection of known martian meteorites can be broadly categorised into three major groups commonly abbreviated to SNC (Shergottites, Nakhlites and Chassignites), named after the Shergotty (India, 1865), Nakhla (Egypt, 1911), and Chassigny (France, 1815) meteorites. In addition to these groups, the martian meteorite collection includes several outlier specimens such as the orthopyroxenite Allan Hills (ALH) 84001 and the polymict breccia Northwest Africa (NWA) 7034 and its 16 paired meteorites. Excluding NWA 7034 and its paired stones, all other martian meteorites are igneous in origin and range from mafic to ultramafic compositions. The meteorites Shergotty and Zagami were the first proposed to be martian in origin when their crystallisation ages and chemistry pointed to them having been derived from a planetary object sufficient in size to have had active volcanism in the last 500 million years (Stolper and McSween, 1979; McSween and Stolper, 1980). These findings were later confirmed by other studies that successfully linked the composition of shock-related glass and trapped gases in Elephant Moraine (EETA) 79001 to measured gas compositions and isotope concentrations from the martian atmosphere recorded by the Viking Landers (e.g., McSween, 1984; Bogard and Johnson, 1983). Moreover, several other studies including Clayton and Mayeda (1996), Romanek et al. (1998), Franchi et al. (1999), and Ali et al. (2016), showed that many of the meteorites suspected to be from Mars exhibited remarkably similar bulk-rock $\Delta^{17}O$ values that are on average 0.3‰ higher than samples from Earth and the moon.

Shergottites are the most geochemically diverse of the SNC meteorites and can be classified based on rare earth element (REE) and radiogenic isotope (i.e. Sr, Nd, Hf and Pb) compositions into LREE depleted, enriched and intermediate shergottites (e.g. Debaille et al., 2008; McSween, 2015). The

classification of shergottites in these geochemical groups has prompted much debate regarding why shergottites exhibit such a broad incompatible trace element range with competing models; crustal assimilation vs distinct mantle reservoirs (e.g., Brandon et al., 2000; Herd et al., 2002; Brandon et al., 2012; Ferdous et al., 2017; Armytage et al., 2018; Tait & Day, 2018). Importantly, as many new meteorites are being found every year it is now possible to study suites of meteorites rather than individual samples to build more robust models of volcanism on Mars. In previous studies of shergottites, it was shown that these meteorites can be separated into suites based on the timing of their ejection from the martian surface (e.g., Nyquist et al., 2001; Misawa, 2004; Nishiizumi et al., 2011; Lapen et al., 2017). One of these ejection-paired suites at ~1.1 Ma, includes ~20 depleted meteorites (e.g., Borg et al., 2003; Shih et al., 2005, 2007; Symes et al., 2008; Lindsay et al., 2012; Brennecka et al., 2014; Lapen et al., 2017; Herd et al., 2017) that were suggested to represent a long-lived volcanic system that was active for at least 2 billion years (Lapen et al., 2017).

1.2 Research objectives and thesis structure

This dissertation focuses on two major objectives (1) constraining the petrogenesis of the long-lived volcanic plumbing system associated with 1.1 Ma ejection paired shergottite meteorites and (2) constraining the REE evolution in shergottite melts from early to late stages of crystallisation, to assess the timing of LREE enrichment and evaluate open vs closed system behaviour during evolution. This dissertation is structured into three chapters to further investigate these topics.

Chapter 2 of the dissertation presents a comprehensive petrogenetic study of two depleted olivine-phyric shergottites, NWA 2046 and NWA 4925, that form part of the 1.1 Ma ejection paired group of shergottite meteorites, exploring their characteristics and terrestrial alteration histories. These meteorites contain Mg-rich olivine (Mg# 83 for NWA 2046 and 81 for NWA 4925; Ramsey et al., 2021) that are among the most primitive reported for shergottite meteorites. This chapter examines and presents bulk-rock major and trace element geochemistry, mineral major and trace element concentrations, and in-situ maskelynite and pyroxene $^{87}Sr/^{86}Sr$ data for NWA 2046 and NWA 4925. The primary aims are: 1) to assess if NWA 2046 and NWA 4925 represent primary mantle-derived magmas, 2) to put them into context with the 1.1 Ma site and, 3) to further develop a magmatic history for the Tharsis plateau. The findings presented in this chapter and the appendix of the thesis have already been published, and are attached at the end of the thesis, in a special issue of the Journal of African Earth Sciences intended to showcase planetary geology done in Africa (Peel et al., 2023).

Shergottites are typically classified based using bulk-rock data where the REE concentrations are primarily controlled by late-stage merrillite. Olivine is, however, the first mineral to crystallise in shergottites, and as such, would best represent the original parent magma. Unfortunately, olivine has

very low concentrations of REEs that are below the detection limit of conventional LA-ICP-MS techniques. Thus, in Chapter 3, I make use of a newly developed LA-ICP-MS technique by Veter et al. (2019), with higher sensitivity (1.5-fold) than conventional techniques, to acquire ultra-trace elements in olivine for the first time. This chapter presents the first complete set of rare earth elements (REE) and other ultra-trace elements (e.g., Y, Zr, Nb, and Hf) in olivine from shergottites, down to ~0.1 ppb. The REEs were used to evaluate the nature and origin of megacrysts in shergottites and the changes in LREE patterns during the earlier stages of evolution in shergottites, to constrain open vs closed system processes. In this chapter, I also present the first full suite of olivine-melt REE partition coefficients for shergottites, calculated using Tissint olivine REE data collected in this study and the Tissint literature bulk-rock REE data of Balta et al. (2015). Additionally, V concentrations in olivine, in conjunction with literature parent melt major element compositions, V concentrations, and liquidus temperatures, were utilised for a V-in-olivine oxybarometer (e.g., Shearer et al. 2006; Wang et al., 2019; Nicklas et al., 2021) to determine the oxygen fugacity of their parent magmas and mantle sources.

Chapter 4 seeks to evaluate the use of glass in olivine hosted melt inclusions to again constrain the early stages of REE melt evolution and evaluate the REE patterns for melts in equilibrium with olivine from chapter 3. Melt inclusions preserve the composition of shergottite parent melts at the time of entrapment, providing notable insights into shergottite mantle source regions, and are also used to evaluate open vs closed system processes during evolution at the earliest stages. In this chapter, melt inclusion glass from a suite of depleted, intermediate, and enriched olivine-phyric shergottites was used to address questions such as (1) does the REE composition of olivine-hosted melt inclusion glass represent bulk rock or (2) has the melt inclusion glass been modified by post-entrapment processes, and (3) how does the melt inclusion glass compare with REE in olivine from the previous chapter. Groundmass merrillite, the primary carrier of REEs in these meteorites, was also analysed from the suite of samples to aid in understanding later stage evolution of shergottite parent magmas

By addressing these research objectives, this thesis aims to provide crucial information into the composition and evolution of martian mantle sources. Ultimately, this work seeks to contribute to a deeper understanding of the geological processes that have influenced the surface of Mars, advance current knowledge of martian geology, and shed light on the formation and evolution of the Red Planet.

1.3 Background

1.3.1 1.1 Ma ejection paired shergottites and a long-lived volcanic system on Mars

The ejection ages of martian meteorites are assessed through the analysis of their cosmic ray exposure (or CRE) ages, which indicate how long the samples were exposed to cosmic radiation in space. Meteorites with the same CRE ages are interpreted to have been ejected from the martian surface from

a single impact event, and thus, likely origin from the same location. This allows volcanic systems to be studied using suites of meteorites rather than with individual meteorites. Previous studies of cosmogenic nuclides in depleted shergottites indicate that these meteorites can be separated into three distinct ejection events at 18 Ma, 3 Ma, and 1.1 Ma (**Figure 1.1** e.g., Eugster et al., 1997; Shukolyukov et al., 2002; Nyquist et al., 2001; Misawa, 2004; Nishiizumi et al., 2011; Nishiizumi et al., 2012; Brennecka et al., 2014; Wieler et al., 2016; Lapen et al., 2017; Herd et al., 2017).

Depleted shergottites around the 1.1 Ma ejection event are represented by at least 20 samples including: DaG 476 (paired with DaG 489/670/735/975/1037; Aucamp et al., 2023), NWA 1195, NWA 2046, NWA 2626, NWA 4925, NWA 5789, NWA 6162, NWA 7635, NWA 8159, SaU 005 (possibly paired with SaU 008/051/060/094/150), Tissint, and Yamato 980459 (i.e., Nishiizumi et al., 2011; Nishiizumi et al., 2012; Lapen et al., 2017; Herd et al., 2017). These 1.1 Ma ejection-paired shergottites have crystallisation ages that range between 347 Ma and 2.4 Ga (e.g., Borg et al., 2003; Shih et al., 2005, 2007; Symes et al., 2008; Lindsay et al., 2012; Brennecka et al., 2014; Lapen et al., 2017; Herd et al., 2017), and are suggested to represent a long-lived volcanic system that has been volcanically active for at least 2 billion years. Crater-counting chronology, using high-resolution imaging of impact craters on the martian surface, indicate that the Tharsis volcanic province, is the most likely source for the 1.1 Ma ejection-paired depleted shergottites (e.g., Werner, 2009; Robbins et al., 2011; Lagain et a., 2021). The crater-counting studies of Werner (2009) and Robbins et al. (2011) also showed ages for some volcanoes of the Tharsis province that indicate active volcanism spanning more than 3 billion years, with the oldest volcanoes having formed before 3.5 Ga.

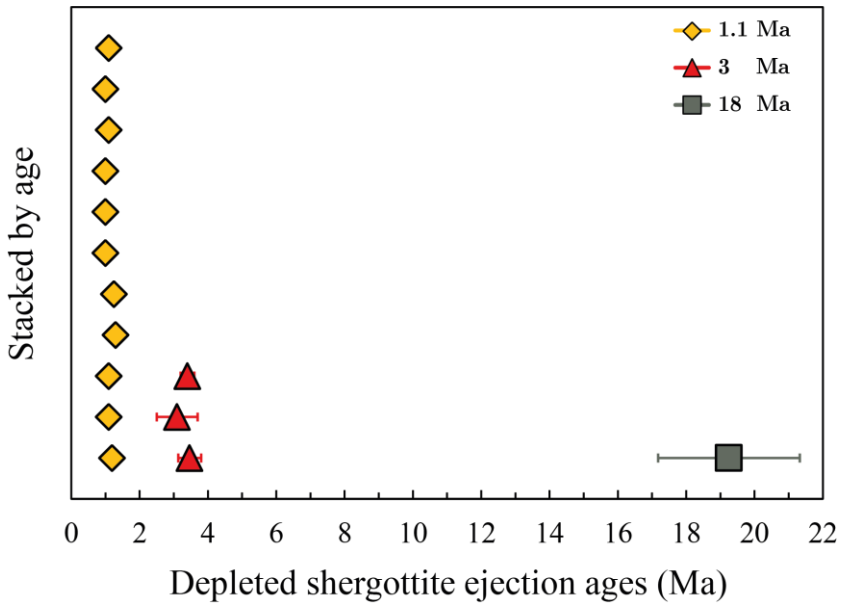

Figure 1.1: Summary of ejection ages for depleted shergottites at ~1.1 Ma, ~3 Ma, and ~18 Ma. Literature data for these samples was taken from Shukolyukov et al. (2002), Nishiizumi et al. (2011), Wieler et al. (2016), Lapen et al. (2017), and Herd et al. (2017).

Within the 1.1 ejection-paired suite, Yamato 980459 and NWA 5789 (possibly paired with Yamato 980459), are the most primitive and interpreted to represent primary mantle-derived melts (e.g., Greshake et al., 2004; Gross et al., 2011; Musselwhite et al., 2006; Usui et al., 2008). Experimental modelling of Yamato 980459 and NWA 5789 indicate source melting conditions of 12±0.5 kbar and 1540±20°C or a depth of ~100 km (e.g., Musselwhite et al., 2006; Gross et al., 2011). Yamato 980459, along with several other 1.1 Ma ejection-paired shergottites including DaG 476 (and paired meteorites) and SaU 005 (and paired meteorites), show similar crystallisation ages between 440-470 Ma (e.g., Borg et al., 2003; Shih et al., 2005, 2007). Aucamp et al. (2023) also noted strong similarities in the REE and $^{87}Sr/^{86}Sr$ compositions and redox conditions of these samples and subsequently interpreted Yamato 980459, DaG 476, and SaU 005 to represent a co-magmatic suite from a single volcanic event at ~470 Ma (**Figure 1.2**). Other shergottites within the 1.1 Ma ejection-paired suite including NWA 1195, Tissint, NWA 7635, and NWA 8159, are isotopically dissimilar from one another and the co-magmatic suite at ~470 Ma and are interpreted to have been derived from several separate eruption events (e.g., Symes et al., 2008; Brennecka et al., 2014; Lapen et al., 2017; Herd et al., 2017).

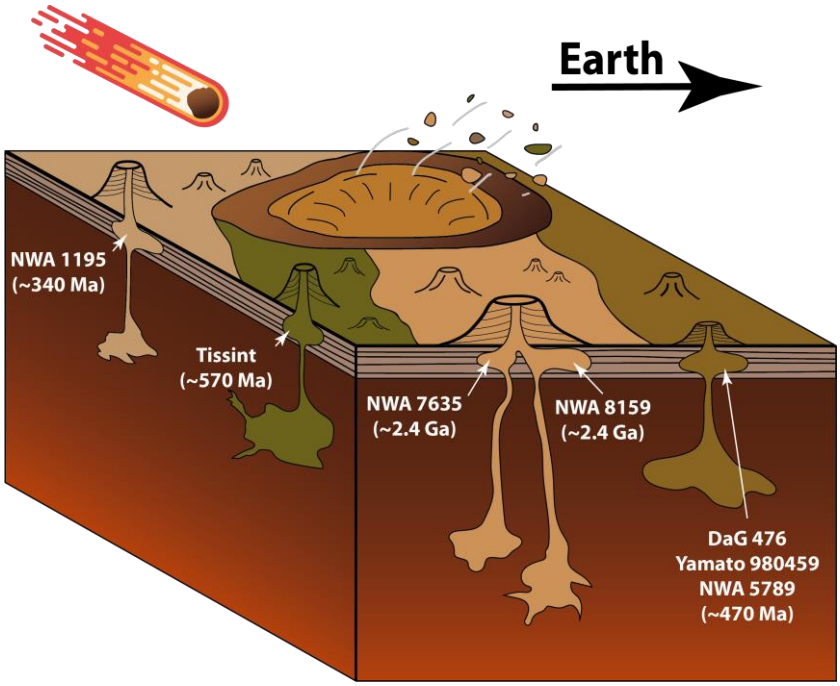

Figure 1.2: Sketch illustrating the proposed ejection crater on Mars for 1.1 Ma ejection-paired depleted shergottites. Figure modified from Brennecka et al. (2014) and depicts the possible source regions for each meteorite.

Based on the crystallisation ages of these samples there are at least 5 possible eruption events for the 1.1 Ma ejection-paired suite (**Figure 1.2**). These include: 1) at ~2.4 Ga represented by NWA 7635, 2) at ~2.4 Ga represented by NWA 8159, 3) at ~570 Ma represented by Tissint, 4) at ~470 Ma represented by DaG 476 (and DaG 489/670/735/975/1037), SaU 005 (and SaU 008/051/060/094/150), and Yamato 980459 (and NWA 5789), and 5) at ~340 Ma represented by NWA 1195. The petrology of other 1.1 Ma ejection-paired samples such as NWA 2046 and NWA 4925 has not yet been constrained, thus

leaving gaps in our knowledge of the suite. Investigating the relationship between NWA 2046 and NWA 4925 and the other 1.1 ejection-paired samples is a major focus of chapter 2.

1.3.2 Mantle source or crustal assimilation: the origin of the LREE enriched shergottites

The geochemical diversity of shergottite meteorites has previously been suggested to reflect the existence of at least three distinct magma sources: incompatible-trace element depleted, intermediate, and enriched reservoirs (Nyquist et al., 2001; Borg et al., 2002, 2003, 2008, 2016; Debaille et al., 2008; Lapen et al., 2008, 2017; Symes et al., 2008; Peslier et al., 2010; Gross et al., 2013; Brennecka et al., 2014; Kiefer and Jones, 2015; McSween, 2015; Combs et al., 2019). The depleted reservoir is characterised by low initial $^{87}Sr/^{86}Sr$, $^{207,206,208}Pb/^{204}Pb$, and $^{187}Os/^{188}Os$ ratios, relatively high initial $^{142,143}Nd/^{144}Nd$ and $^{176}Hf/^{177}Hf$ ratios and REE compositions with $(La/Yb)_{CI}$ <0.3 (**Figure 1.3**). In contrast, the enriched reservoir shows higher initial $^{87}Sr/^{86}Sr$, $^{207,206,208}Pb/^{204}Pb$, and $^{187}Os/^{188}Os$ ratios, lower initial $^{142,143}Nd/^{144}Nd$ and $^{176}Hf/^{177}Hf$ ratios and bulk REE compositions with $(La/Yb)_{CI}$ >0.8 (**Figure 1.3**). Intermediate shergottites, show compositions that fall between the enriched and depleted shergottites and represented by bulk REE compositions with $(La/Yb)_{CI}$ values between 0.3 and 0.8 (**Figure 1.3**).

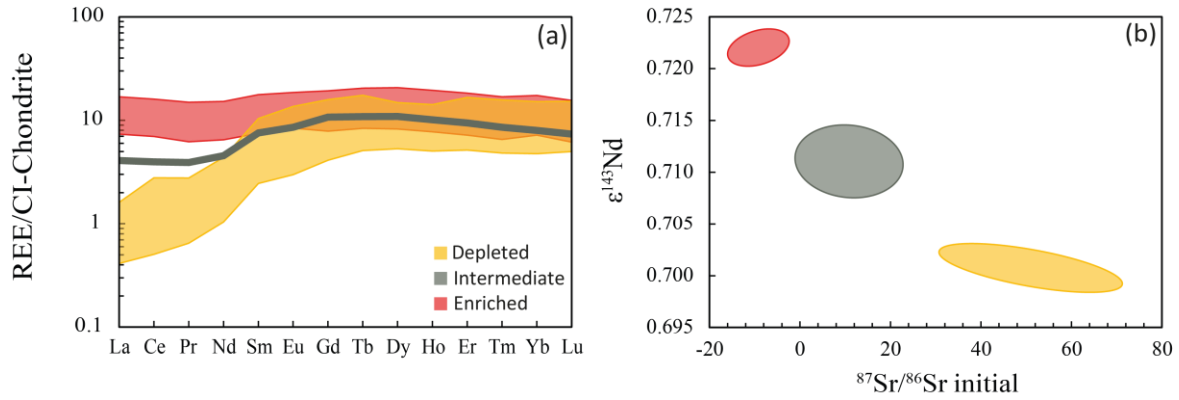

Figure 1.3: Different shergottite source reservoirs based on (a) CI-chondrite normalised (McDonough and Sun, 1995) bulk-rock REE patterns and (b) bulk-rock initial epsilon ^{143}Nd and $^{87}Sr/^{86}Sr$ compositions, for shergottites across geochemical groups. (Fig. 2b modified after Shearer et al. (2008, 2015), and Symes et al. (2008). Literature bulk-rock REE data sourced from: Lodders (1998), Dreibus et al. (2000), Taylor et al. (2002), Greshake et al. (2004), Misawa (2004); Shirai and Ebihara (2004), Sarbadhikari et al. (2009), Filiberto et al. (2010, 2012), Irving et al. (2012), Treiman and Filiberto (2015), Day et al. (2018), and Nicklas et al. (2022). Literature bulk-rock initial epsilon ^{143}Nd and $^{87}Sr/^{86}Sr$ data sourced from: Wooden et al. (1982), Shih et al. (1982, 2003, 2005, 2007, 2009, 2011), Jagoutz and Wänke (1986), Borg et al. (2001, 2002, 2003, 2008), Nyquist et al. (2001b, 2009), Symes et al. (2008), Brennecka et al. (2014), Ferdous et al. (2017), and Lapen et al. (2017).

It is generally accepted that incompatible-trace intermediate and enriched reservoirs represent distinct mantle sources, despite some authors having proposed that REE enrichment may be related to crustal assimilation. One prominent model argues in favour of a homogeneous depleted mantle and suggests that the incompatible-element and isotopic systematics of intermediate-enriched shergottites were inherited through varying degrees of interaction with crustal material during ascent to surface (**Figure 1.4a**) (e.g., Jones, 1989; Longhi, 1991; Borg et al., 1997; Herd et al., 2002). Unfortunately, this model is not supported by numerous other studies of shergottite radiogenic isotopic systematics (e.g., Rb–Sr, Sm–Nd, Lu–Hf, Re–Os) including Brandon et al., (2000, 2012), Ferdous et al. (2017), Armytage et al. (2018), and Tait & Day (2018). In these studies, the radiogenic isotope compositional array of shergottites could not be modelled by mixing depleted mantle-derived melts with an ancient martian crust.

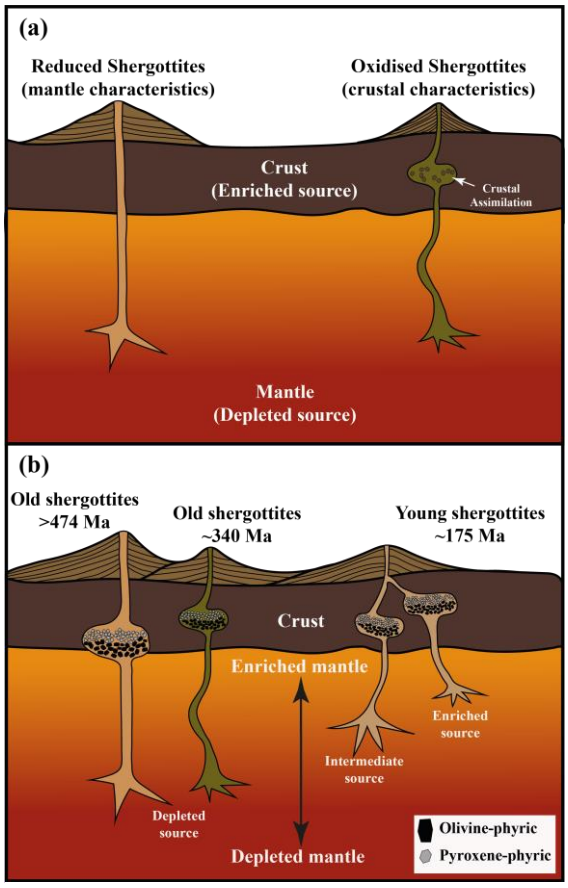

Figure 1.4: Sketches illustrating the two primary models of shergottite magmatism. (a) Crustal assimilation model modified from Herd et al. (2002) and (b) Multiple mantle source model modified from Symes et al. (2008).

The second prominent model argues in favour of a heterogenous martian mantle that potentially formed early in Mars' history, at ~4.5 Ga, during planetary differentiation and crystallisation after a magma ocean phase (e.g., Blichert-Toft et al., 1999; Borg et al., 2002; Borg and Draper, 2003; Elkins-Tanton et al., 2003; Debaille et al. 2007; Debaille et al. 2008; Borg et al., 2016). In this model, the heterogeneity

of the martian mantle has been suggested to reflect poor convection not efficiently mixing the mantle (Kiefer, 2003), thus, preserving early-formed and geochemically distinct mantle reservoirs (**Figure 1.4b**). Shergottites derived from the intermediate (150–346 Ma) and enriched (150–225 Ma) reservoirs also show younger crystallisation ages than their depleted counterparts (<327 Ma) (e.g., Nyquist et al., 2001; Borg et al., 2002; Shih et al., 2003; Bouvier et al., 2005; Borg et al., 2008; Bouvier et al., 2008; Lapen et al., 2008; Nyquist et al., 2009; Shih et al., 2009; Ferdous et al., 2017; Combs et al., 2019). This indicates that the shergottite source reservoirs were likely isolated from one another, with any potential mixing between shergottite reservoirs only having occurred at the time of magma formation to produce the current collection of shergottite meteorites available for study (e.g., Borg and Drapper, 2003; Symes et al., 2008). The work of Combs et al. (2019) also showed that modelled source $^{176}Lu/^{177}Hf$ compositions for enriched shergottites, including NWA 4468, NWA 10169, Larkman Nunatuk (LAR) 06319, Robert Massif (RBT) 04262, Shergotty, Zagami, Los Angeles, NWA 856, and NWA 7320, suggest these samples were derived from two distinct enriched reservoirs rather than just one.

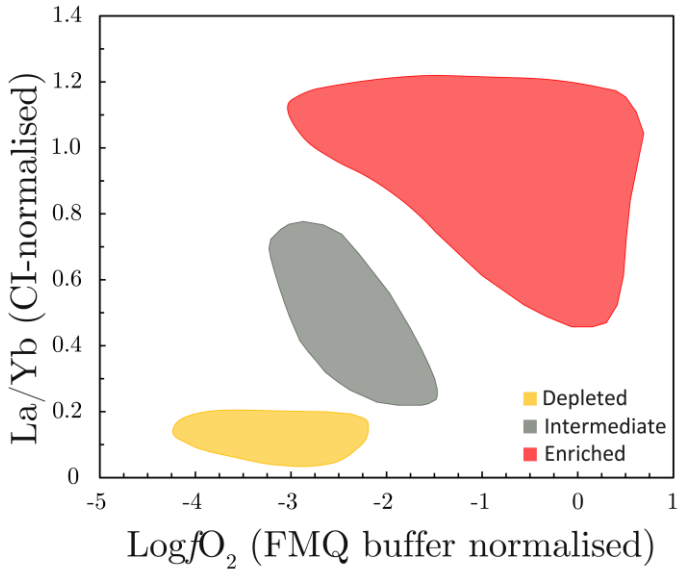

Figure 1.5: Shergottite bulk-rock $(La/Yb)_{cl}$ ratios plotted against fO_2 showing general fields for depleted, intermediate, and enriched shergottites. Shergottite fields constructed using literature fO_2 data from: Herd (2003), Herd (2006), Shearer et al. (2006), Sarbadhikari et al. (2009), Peslier et al. (2010), Usui et al. (2008, 2010), Gross et al. (2011), Walton et al. (2012), Gross et al. (2013), Balta et al. (2015), Howarth and Udry (2017), and Combs et al. (2018). Modified after Combs et al. (2019).

Previous studies of shergottite oxygen fugacity such as Herd et al. (2002) and Herd (2003), have also shown differences in oxygen fugacity for the distinct source reservoirs, with depleted shergottites typically more reduced, increasing by as much as 3 log units (relative to the ΔQFM, quartz-fayalite-magnetite buffer) towards enriched shergottites (**Figure 1.5**). These differences in fO_2 values for shergottites, calculated using a multi-phase (olivine, pyroxene, and chromite) oxybarometer, were interpreted to suggest that the depleted shergottite reservoir is relatively reduced and the enriched shergottite reservoir more oxidised (**Figure 1.4a**). These multi-phase oxybarometer fO_2 values are, however, fraught with uncertainty relating to equilibrium between early crystallising phases and potential degassing during early-stage cooling. This proposed relation between shergottite geochemical reservoir and oxygen fugacity was later challenged in a study by Nicklas et al. (2021) which, utilising a

V-in-olivine oxybarometer and Mg-rich olivine in a suite of depleted, intermediate, and enriched shergottites, showed no correlation between trace element enrichment and fO_2.

Much uncertainty remains about REE evolution in shergottite parent melts as the classification of shergottites is generally done using bulk-rock REEs, where the REEs are primarily hosted in late-stage merrillite or by direct measurement of the merrillite REE. There is also a gap in knowledge of the REE contents of the earliest crystallised phase olivine as a result of analytical difficulties, which have been overcome in this work.

2 Chapter 2

2.1 Introduction

At least 20 of the depleted shergottites have ejection ages that are within error of 1.1 Ma, suggesting that these samples were ejected in a single impact event (i.e., Nishiizumi et al., 2011; Udry et al., 2020). Most of these meteorites have crystallisation ages that range between 347 Ma and 575 Ma (e.g., Brennecka et al., 2014; Lapen et al., 2017; Nyquist et al., 2001 etc.), with two exceptions, Northwest Africa (NWA) 7635 (2403 ± 140 Ma; Lapen et al., 2017) and NWA 8159 (2370 ± 250 Ma; Herd et al., 2017). These ejection-paired depleted shergottites are therefore likely to represent a long-lived volcanic system on Mars. High-resolution imaging of impact craters on the martian surface has been used to identify the Tharsis volcanic province as the most likely source of these depleted shergottites (Lagain et a., 2021).

The ejection paired depleted shergottites are predominantly olivine-phyric textured, meaning that they are composed of olivine megacrysts and pyroxene phenocrysts set in a groundmass (typically) of Fe-rich olivine, orthopyroxene, pigeonite, augite, maskelynite (shock modified plagioclase), accessory oxides (including spinel, ulvöspinel, chromite and ilmenite), phosphates (merrillite and apatite) and Cu-Ni-Fe sulphides. Initial descriptions of the olivine-phyric shergottites noted that their megacryst and groundmass components resembled that of the poikilitic and basaltic shergottites respectively, which subsequently led to the idea that olivine-phyric shergottites were the product of mixing between basaltic and poikilitic components (e.g., Steele and Smith 1982; McSween and Jarosewich 1983). Later studies, however, showed that this was not the case as these olivine-phyric samples were distinct from both basaltic and poikilitic shergottites. In particular, their relatively high bulk-rock and olivine megacryst magnesium numbers (Mg#) could only have been the result of these meteorites having crystallised from olivine saturated primitive melts (Barrat et al., 2002; Goodrich, 2003). Only three of the olivine-phyric shergottites (e.g., Yamato 980459, NWA 5789, and NWA 6234) have been shown to represent primary mantle-derived melt compositions (Musselwhite et al., 2006; Gross et al., 2011, 2013). Most olivine-phyric shergottites are not primary melt compositions owing to an excess amount of olivine that results in bulk-rock Mg# that are not representative of primary melt compositions (e.g., Taylor et al. 2002; Papike et al. 2009; Filiberto et al. 2010).

In this study, two depleted olivine-phyric shergottites with ejection ages of ~1.1 Ma, NWA 2046 and NWA 4925, which have previously been shown to contain Mg-rich olivine (Mg# 83 and 81, respectively; Ramsey et al., 2021), are analysed in-depth. The main objectives of this investigation are to assess whether NWA 2046 and NWA 4925 represent primary mantle-derived melt compositions, and further, to constrain the origin of the long-lived volcanic system associated with the 1.1 Ma ejection paired meteorites. Furthermore, sample NWA 4925 has a distinct terrestrial weathering rind, which is

used here to constrain the chemical effects of terrestrial alteration on primary martian geochemical signatures. Presented are major- and trace-element data for olivine, pyroxene, maskelynite, merrillite and spinel, in situ $^{87}Sr/^{86}Sr$ data for maskelynite and pyroxene, along with bulk-rock major and trace element geochemistry for both NWA 2046 and NWA 4925, to evaluate their petrogenetic histories on Mars and their relationship to other depleted shergottites.

2.2 Samples and analytical techniques

2.2.1 Samples

Thin slices of two olivine-phyric shergottites, NWA 2046, a 63 g stone found in Lakhbi, Algeria (2003), and NWA 4925, a 282.3 g stone found in Erfoud, Morocco (2007), were obtained for this study. A polished thin section of each sample was prepared and used for *in situ* analyses as well as to calculate mineral modal abundances, based on the areas exposed in the section. Small chips of ~ 1.0 g were analysed for bulk major and trace element chemistry at Scripps Institution of Oceanography (SIO).

2.2.2 Micro XRF mapping

High-resolution elemental distribution maps were acquired for samples NWA 2046 and NWA 4925 using a Bruker M4 Tornado Micro X-ray fluorescence (μXRF) spectrometer equipped with a Rh-anode X-ray source, at the Department of Earth and Planetary Sciences (Macquarie University, Australia). This non-destructive mapping method, in conjunction with petrographic microscopy observations, was used for phase identification, and to visualise the element abundance distribution in NWA 2046 and NWA 4925 (**Figure 2.1**-**Figure 2.2**). Analyses were performed at 50 kV and 200 μA, under low vacuum conditions of 18 mbar, using spot and step sizes of 20 μm and scanning time to 10 ms per spot, which allowed sensitive imaging of twelve elements (Na, Mg, Al, P, S, Si, K, Ca, Ti, Cr, Mn, Fe) in each sample.

2.2.3 Electron probe microanalysis (EPMA)

The major and minor element compositions of minerals in both samples were obtained using a Cameca SX-100 Microprobe analyser housed at the University of Johannesburg (UJ, Johannesburg, South Africa). Analyses on all major phases (i.e., pyroxene, olivine, maskelynite, oxides and phosphates) in both samples were determined using an accelerating potential of 15 kV, beam current of 20 nA (6 nA on phosphates), beam diameters of between 1-5 μm (5-10 μm on maskelynite) and counting times of 30 seconds (s) on peaks and 15 s on backgrounds. Standard ZAF correction procedures were applied. Natural and synthetic standards which include fluorite (F), jadeite (Na), olivine (Mg), almandine (Al), diopside (Si), NaCl (Cl), orthoclase (K), wollastonite (Ca), TiO_2 (Ti), Cr_2O_3 (Cr), rhodonite (Mn), hematite (Fe), NiO (Ni), and barite (Ba) were periodically analysed within analytical sessions, to account

for instrumental drift. Detection limits were <0.02 wt. % for all elements, excluding Fe (~0.04 wt. %) and Mn (~0.03 wt%).

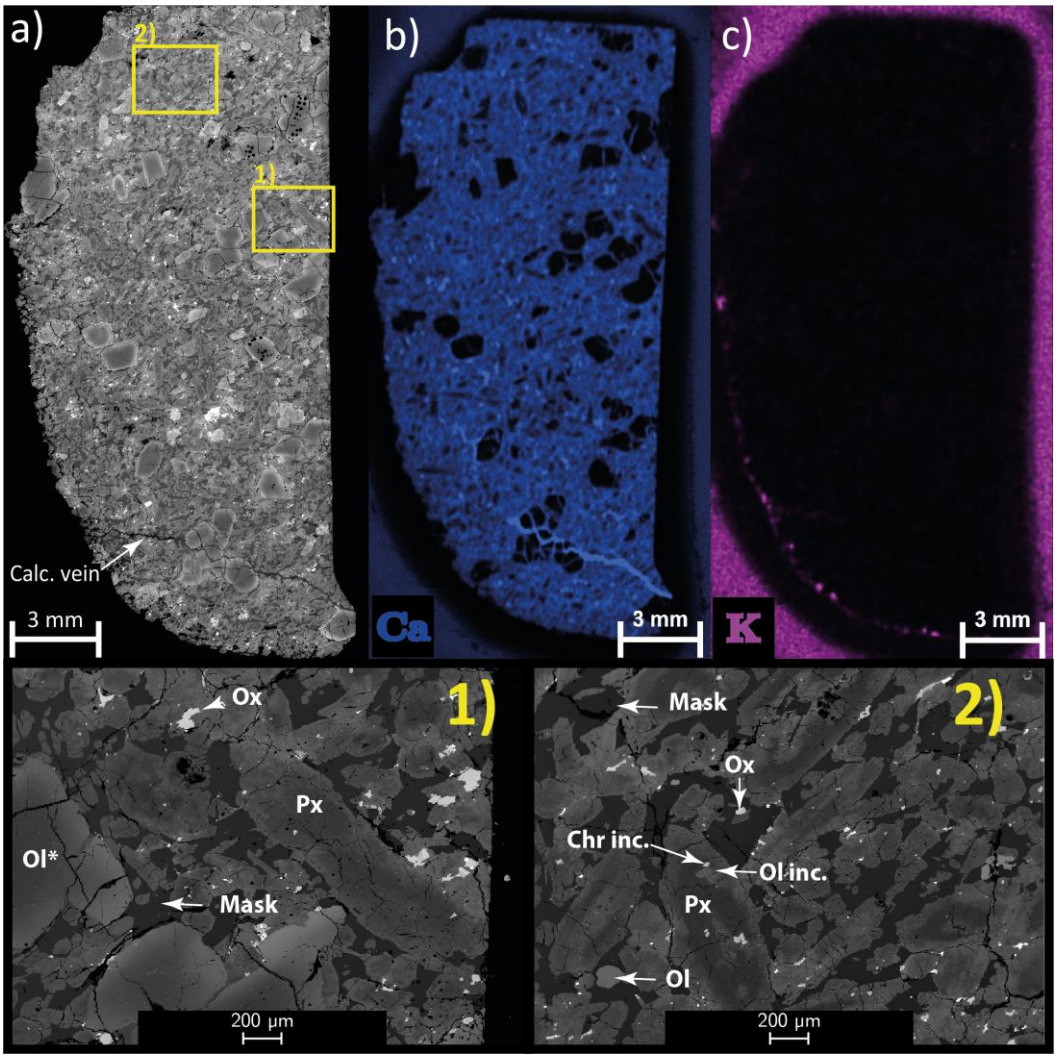

Figure 2.1: (a) Back-scattered electron image of the NWA 2046 thin section analysed in this study. (b) calcium compositional map showing secondary carbonate (blue) veining and (c) potassium compositional map showing no apparent enrichment in the sample, the latter highlighting differences in the degree of alteration between NWA 2046 and NWA 4925. Laser ablation pits (black circles) are visible in olivine megacrysts and pyroxene and maskelynite grains selected for trace element analyses. The overall texture of NWA 2046 can be seen in the close-up BSE images 1) and 2), which show olivine megacrysts (Ol*) and pyroxene (px) phenocrysts, in a groundmass of finer grained Fe-rich olivine (ol), pyroxene, maskelynite (mask) and oxide (ox) phases. Rare olivine and chromite inclusions have also been observed in coarse pyroxene phenocrysts in NWA 2046 (2).

2.2.4 Scanning electron microscope (SEM)

A FEI Nova NanoSEM 230 scanning electron microscope (SEM) equipped with an Oxford X- max detector and INCA software was used for back-scattered electron (BSE) imaging and for the analysis of the major element composition of mineral phases in both NWA 2046 and NWA 4925 by energy

dispersive x-ray spectroscopy (EDS) analysis. The SEM, which is housed at the Electron Microscope Unit (EMU) of the University of Cape Town, South Africa, was operated at a working distance of 5 millimetres, with an accelerating voltage of 20 kV and a spot size of 4 µm.

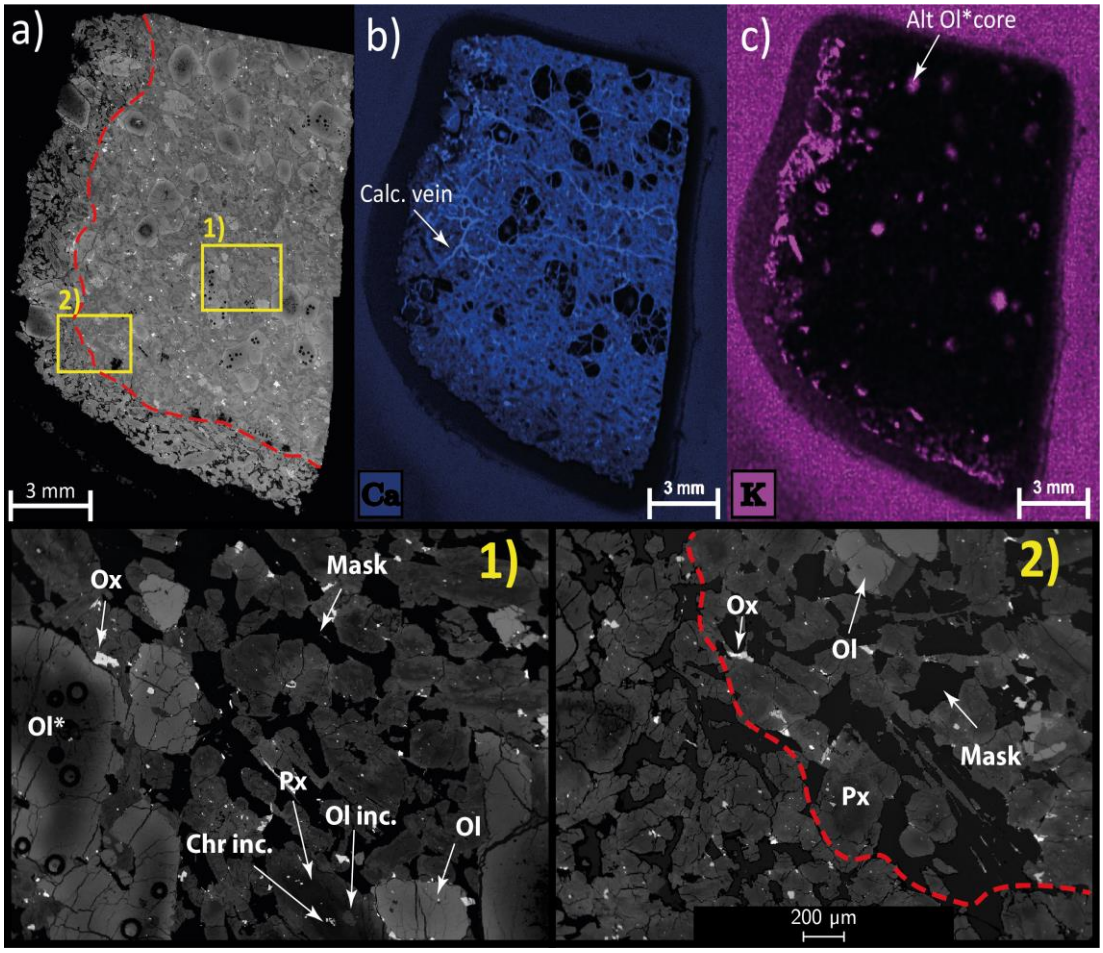

Figure 2.2: (a) Back-scattered electron image of the NWA 4925 thin section showing the weathering rind (red dashed line) of the sample as well as laser ablation pits (black circles) in olivine megacrysts, pyroxene and maskelynite grains selected for trace element analyses. (b) Calcium compositional map showing secondary carbonate (blue) veining, and (c) potassium compositional map showing enrichment (pink) towards the weathering rind of the sample as well as in the cores of several olivine megacrysts from the interior of the sample. The overall texture of NWA 4925 can be seen in the close-up BSE images 1) and 2), which show olivine megacrysts (Ol*) and pyroxene (px) phenocrysts, in a groundmass of finer grained Fe-rich olivine (ol), pyroxene, maskelynite (mask) and oxide (ox) phases. Rare olivine and chromite inclusions have also been observed in coarse pyroxene phenocrysts in NWA 4925 (2).

2.2.5 Laser Ablation Inductively Coupled Plasma Mass Spectrometry (LA-ICP-MS)

Trace element concentrations were determined at the University of Stellenbosch (SU, Stellenbosch, South Africa), using a Resolution M-50-LR Excimer laser ablation system coupled to an Agilent 7500 quadrupole ICP-MS (inductively coupled plasma-mass spectrometer). Beam sizes of 40-55 µm were used on olivine and pyroxene, 40 µm for maskelynite and 15 µm and phosphate. The laser was routinely run with a repetition rate of 8 Hz and fluence of ~3.5 J/cm^2. Helium (He) was used as the primary carrier

gas, which connects to an Argon (Ar) gas line downstream of the laser cell. Reference standard NIST (National Institute of Standards and Technology) 610 was used as an external standard and run after every 15 unknown spot analyses, with BCR-2G & BHVO-2G (values from GeoReM: Jochum et al., 2005) also run as an unknown after each standard check, as a means of assessing instrument precession. Reproducibility of the BCR-2G & BHVO-2G glass standards for minor- and trace-elements, using spots sizes of 40-55um, was generally better than 7% (relative standard deviation or RSD), with the exception of Ho, Er, Tm and Lu; reproducibility for these elements was better than 14%. ^{29}Si and ^{44}Ca was used as internal standards for the silicate and phosphate minerals respectively. The data were subsequently reduced using the LADR software package from Norris Scientific (Norris and Danyushevsky, 2018).

2.2.6 LA-MC-ICP-MS in situ ^{87}Sr/^{86}Sr analysis

In situ analysis of Sr isotope compositions in grains of pyroxene and plagioclase were measured by laser ablation in both NWA 2046 and NWA 4925. Spots were measured using an ASI RESOlution SE 193 nm Excimer laser ablation unit with double-volume sample chamber coupled to a Nu Instruments NuPlasma HR MC-ICP-MS instrument housed at the University of Cape Town (UCT, Cape Town, South Africa). Each analysis was performed in raster mode along a line in a He atmosphere, after which the ablated material and He sweep gas are mixed with argon before transport to the plasma. Laser ablation transverses were made at a scan speed of 2.5 µm.sec^{-1} using a beam with a diameter of 50 µm, yielding transverse lengths of 150-200 µm. The ablation was performed with a repetition rate of 8 Hz, an energy density of about 8.1 J.cm^{-2} and sample run times of 3 min, with 60 s of background measurement followed by c. 110 s of sample ablation. To reduce the risk of any potential surface contamination, each transverse was pre-ablated with a 64 µm spot at 50 µm.sec^{-1}. After the data had been acquired, the signal stability of each analysis was visually assessed, and if necessary, the data reduction intervals adjusted accordingly. In some instances, the first and last few seconds of laser firing were discarded owing to weak or declining signals. Grains or regions of grains with cracks or fractures were also avoided to eliminate secondary alteration effects i.e., Sr enrichment through terrestrial calcite in hot desert environments (Crozaz and Wadhwa, 2001). All ^{87}Sr/^{86}Sr data were corrected for isobaric krypton interference using on-peak background measurements, while the interference of ^{87}Rb on ^{87}Sr was corrected using the measured signal of ^{85}Rb and the natural Rb isotope abundances. Total Sr voltage for laser ablation analyses ranged between 3V and 0.10V for JJG1424, NWA 2046 and NWA 4925, and the Rb/Sr ratio monitored to ensure no significant isobaric Rb interference occurred which could not be accurately corrected. The effect of instrumental mass fractionation was corrected using the measured ^{86}Sr/^{88}Sr ratio, an accepted value for this ratio of 0.1194 and the exponential law. The potential interferences of argides, calcium dimers and double-charged ytterbium and erbium were monitored, but no significant effects were observed, and no corrections applied. At the start of each analytical session, an in-house clinopyroxene strontium isotope reference standard JJG1424 (from a garnet websterite) was analysed, and results compared to accepted ratios for ^{87}Sr/^{86}Sr to ensure data quality. Results for ^{87}Sr/^{86}Sr

measured on JJG1424 from the sessions for this project (0.70484±0.00004, 0.70496±0.00002, 0.70489±0.00004, 0.70483±0.00004) compared well with published ratios for this reference material (i.e., le Roux et al., 2014: solution $^{87}Sr/^{86}Sr$ 0.70495±0.00003, laser ablation 0.70483±0.0003; Zhao et al., 2020: laser ablation $^{87}Sr/^{86}Sr$ 0.70494±0.00031). Through the solution data for JJG1424, all laser ablation values reported here are referenced to an $^{87}Sr/^{86}Sr$ value of 0.710255 for the international isotope reference standard NIST SRM987.

2.2.7 Bulk-rock major- and trace-element chemistry

Bulk-rock major and trace element analyses for NWA 2046 and NWA 4925 were performed following the procedure of Day et al. (2018), with 50 mg powder aliquots taken from larger homogenised sample powder of ~ 1.0 g for each sample. Both samples were initially embedded in epoxy. To minimise any potential chemical modification, the samples were crushed using an agate pestle and mortar and the epoxy then handpicked and separated out, resulting in an estimated purity of > 95 %. The samples were subsequently homogenised and digested at 150 °C in concentrated HF (4 mL) and HNO_3 (1 mL) for > 72 hrs on a hotplate, then dried and taken up in concentrated HNO_3 to remove fluorides, before dilution and doping with indium, used to observe any instrumental drift (e.g., Day et al., 2018; Udry and Day, 2018). A *ThermoScientific* iCAP Qc quadrupole inductively coupled plasma mass spectrometer in normal mode was then used to analyse the major- and trace-element abundances of NWA 2046 and NWA 4925. BHVO-2 was used as a reference standard to monitor any potential instrument drift, with repeat analyses generally with 5% (RSD) for both major and trace elements.

2.3 Results

Shergottites NWA 2046 and NWA 4925 have similar petrographic features (Figure -Figure 2.2). Both samples are comprised of coarse-grained olivine (0.6–2.4 mm in NWA 2046; 0.6–1.8 mm in NWA 4925) and pyroxene (0.5–1.8 mm in both samples) megacrysts in a groundmass of finer grained Fe-rich olivine, pyroxene, maskelynite (<0.5 mm in length), with minor amounts of oxides, phosphates, and sulphides (**Figure 2.1**-**Figure 2.2**). The coarse-grained or megacrystic olivine in both samples are subhedral to euhedral in shape and occur either as single grains or as clusters of olivine (i.e., **Figure 2.1**-**Figure 2.2**). The modal abundances for NWA 2046 and NWA 4925 were estimated using BSE image mosaics of both samples and optical imagery to determine phases. The estimated modal abundances for these samples are 60 (±2%) pyroxene, 21 (±1%) maskelynite, 17 (±1%) olivine, and 1-2% accessory phases (including oxides and phosphates) in NWA 2046, and 60 (±2%) pyroxene, 22 (±1%) maskelynite, 16 (±1%) olivine, and 1-2% accessory phases in NWA 4925.

Both samples contain several melt pockets and veins that were likely formed by shock during ejection from the martian surface as well as secondary carbonate-filled veins cross-cutting the sample (**Figure 2.1b**-**Figure 2.2b**). The intensity of carbonate veining is noticeable higher in NWA 4925 than in NWA

2046. Additionally, NWA 4925 is partly covered by a 1 to 4 mm thick weathering rind along the terrestrially exposed edge of the rock (Figure 2.2). Overall, grains within or near the rind of NWA 4925 show a more reddish-brown to black appearance in plane polarised light (Sup. Fig. 1), a consequence of iron in the mineral phases here having oxidised in the hot desert terrestrial environment. The core regions of olivine (and pyroxene) grains here also show clear evidence of being strongly enrichment in Ca and K (**Figure 2.2b-c**).

Table 2.1: Bulk-rock major and trace element abundances for depleted olivine-phyric shergottites NWA 2046 and NWA 4925 (oxides in wt%, trace elements in ppm).

	NWA 2046	NWA 4925	BHVO-2 (*n = 4*)	
			Average	±1SD
SiO_2	49.9	49.2	49.53	0.86
TiO_2	0.48	0.46	2.73	0.07
Al_2O_3	5.66	5.23	13.53	0.19
FeO	18.5	20.0	12.34	0.24
MnO	0.53	0.56	0.2	0.00
MgO	16.4	15.50	7.23	0.12
CaO	7.41	8.07	11.43	0.21
Na_2O	0.75	0.58	2.22	0.04
K_2O	0.02	0.11	0.52	0.02
P_2O_5	0.34	0.34	0.27	0.01
Total	100.00	100.00	100.00	
S	77	82	68.5	3.04
Li	2.34	9.71	4.80	0.03
Be	0.04	0.11	1.07	0.11
B	0.05	3.63	2.95	0.66
Sc	34.90	35.61	32.00	0.46
Ti	3005	3045	16300	306
V	176	177	317	6
Cr	4911	5233	280	5
Mn	3308	3477	1270	11
Co	46.8	52.8	45.0	0.6
Ni	148	160	119	2
Cu	29	15	127	4
Zn	48	51	103	11
Ga	12	11	22	0.22
Ge	1.49	1.59	1.60	0.02
Rb	0.45	1.24	9.11	0.17
Sr	32	80*	396	5

Y	12	13	26	0.28
Zr	13	13	172	2
Nb	0.24	0.25	18.10	0.32
Mo	0.11	0.12	4.00	0.19
Sn	2.05	0.58	1.70	0.07
Cs	0.02	0.04	0.10	0.00
Ba	87*	700*	131	8
La	0.58*	2.07*	15.20	0.13
Ce	1.30*	1.63*	37.50	0.23
Pr	0.22*	0.47*	5.35	0.05
Nd	1.18	2.40*	24.50	0.27
Sm	0.67	0.92*	6.07	0.05
Eu	0.34	0.49*	2.07	0.02
Gd	1.31	1.61	6.24	0.09
Tb	0.28	0.31	0.92	0.01
Dy	2.08	2.25	5.31	0.05
Ho	0.44	0.48	0.98	0.00
Er	1.26	1.32	2.54	0.02
Tm	0.18	0.18	0.33	0.00
Yb	1.16	1.20	2.00	0.03
Lu	0.17	0.17	0.27	0.00
Hf	0.60	0.58	4.36	0.05
Ta	0.02	0.02	1.14	0.03
W	0.04	0.04	0.21	0.00
Tl	0.05	0.02	0.02	0.00
Pb	0.41	0.46	1.60	0.14
Th	0.05	0.05	1.22	0.01
U	0.03	0.06	0.40	0.00

* Indicates the abundances significantly modified by terrestrial weathering or anomalous values. 50 mg powdered aliquots of each sample were analysed for each sample. The major and trace element abundances were determined on the same solutions, using a ThermoScientific iCAP Qc quadrupole ICP-MS, and dilution factors of 5000× and 50000×, respectively. The major elements, which including SiO_2, TiO_2, Al_2O_3, FeO, MnO, MgO, CaO, Na_2O, K_2O, and P2O, were normalised to 100 wt. %.

2.3.1 Major and trace element mineral compositions

2.3.1.1 Olivine

Olivine megacrysts from both samples show core to rim zonation from cores of Fo_{83} to rims of Fo_{50} in NWA 2046 and from cores of Fo_{81} to rims of Fo_{48} in NWA 4925. The core regions of olivine megacrysts in both NWA 2046 and NWA 4925 have melt inclusions, as well as numerous micro-inclusions (<5 μm)

of a bright (white in BSE images) oxide phase too small for reliable electron microprobe measurement. Coarser grained chromite inclusions (30–100 μm) are typically found closer to the rim of megacrysts and in association with olivine up to Fo_{70} in both samples. Finer grained groundmass olivine (<0.5 mm) grains are more Fe-rich than the olivine megacryst cores, and display ranges in composition of Fo_{66-32} in NWA 2046 and Fo_{71-31} in NWA 4925.

Olivine megacrysts in the weathering rind of NWA 4925 have darkened core zones with mottled textures (**Figure 2.2a**; Sup Fig. 1-2), surrounded by pristine Fe-rich rims that lack alteration features. Elemental X-ray maps show that the altered interiors of olivine megacrysts from the weathering rind are strongly enriched in CaO and K_2O (Figure 2.2b-c). SEM-EDS analysis of the altered megacryst cores show depletion in MgO (> 2 wt. % vs 24-30 wt. % for MgO) and SiO_2 (20-30 wt. % vs 38-40 wt. % for SiO_2) and enrichment in Al_2O_3 (6-12 wt. % vs >1 wt. %), CaO (3-10 wt. % vs >1 wt. %) and FeO (> 50 wt. % vs 29-35 wt. % FeO) relative to their corresponding unaltered rims. A handful of olivine megacryst cores from the interior of NWA 4925 also show CaO and K_2O enrichment, but the degree of alteration observed here is significantly less intense and extensive relative to weathering rind olivine megacrysts (**Figure 2.2b-c**). The calcium enrichment observed appears to have infiltrated the cores of these olivine megacrysts through distinct calcite filled cracks cutting across the sample (**Figure 2.2b**) and is therefore likely due to terrestrial alteration.

The trace element concentrations for the olivine megacrysts in NWA 2046 and NWA 4925 are presented in the supporting information. Olivine grains from NWA 2046 are characterised by Mn, Ni, Co, and V abundances of 2493–4949 ppm, 152–705 ppm, 88–100 ppm and 13–68 ppm, respectively, while unaltered olivine grains from the interior of NWA 4925 have concentrations of 3091–4722 ppm Mn, 205–543 ppm Ni, 91–107 ppm Co and 14–34 ppm V. When plotted against Ni, the abundances of Mn and Co in olivine megacryst from both samples correlate negatively, while V shows the inverse.

2.3.1.2 Pyroxene

The pyroxene in both samples occur as prismatic subhedral to anhedral grains. Pyroxene grains from both NWA 2046 and NWA 4925 are chemically zoned and can be separated into two distinct groups, the majority of which belong to the first (type-I), which display zoning profiles that extend from low-Ca orthopyroxene cores (i.e., $En_{77}Fs_{19}Wo_4$ in NWA 2046 and $En_{77}Fs_{20}Wo_3$ in NWA 4925) to rims of augite (i.e., $En_{46-53}Fs_{19-27}Wo_{21-35}$ in NWA 2046 and $En_{49-63}Fs_{28-37}Wo_{9-14}$ in NWA 4925) – transect 1, Sup Fig. 3a,c and 4a. The second group of zoned pyroxene grains have cores of either pigeonite or augite, intermediate zones of orthopyroxene and low-Ca (relative to core) pigeonite rims – transect 2, Sup Fig. 3b and 4a. Rare inclusions of finer grained olivine (Fo_{66} in NWA 2046 and Fo_{71} in NWA 4925) and chromite (**Figure 2.1** and **Figure 2.2**.) have also been observed in at least one large pyroxene grain from each sample, both of which are comparable to textures described for poikilitic shergottites (i.e.,

Rahib et al., 2019). Pyroxene analysed next to the olivine inclusions have Mg# of 80 (NWA 2046) and 79 (NWA 4925) and are orthopyroxenes with compositions of $En_{78}Fs_{19\text{-}37}Wo_3$ in NWA 2046 and $En_{77}Fs_{20}Wo_3$ in NWA 4925.

The REE abundances were measured across 23 pyroxenes (22 low-Ca and 1 high-Ca) in NWA 2046 and 24 pyroxene (14 low-Ca from the 'fresh' interior and 10 low-Ca from the weathering rind) in NWA 4925. The REE patterns for pyroxene grains in NWA 2046 (La/Yb_{CI} <0.2), as well as most of the fresh pyroxene grains in NWA 4925 (La/Yb_{CI} <0.1), are LREE-depleted (**Figure 2.3a-b**). A few pyroxene grains in NWA 2046 are characterised by a positive La anomaly, while large positive La anomalies have been observed in three grains from the interior (La/Yb_{CI} of 0.32–2.7) of NWA4925 and in all grains analysed from the weathering rind (La/Yb_{CI} = 0.32–7.0). Pyroxene grains analysed across both samples (20 of the 23 in NWA 2046 and 13 of the 24 in NWA 4925) show minor negative Eu anomaly, with Eu/Eu* values ranging between 0.5 – 0.1. The rims of pyroxene grains in both samples are more REE- and LREE-enriched relative to corresponding pyroxene cores.

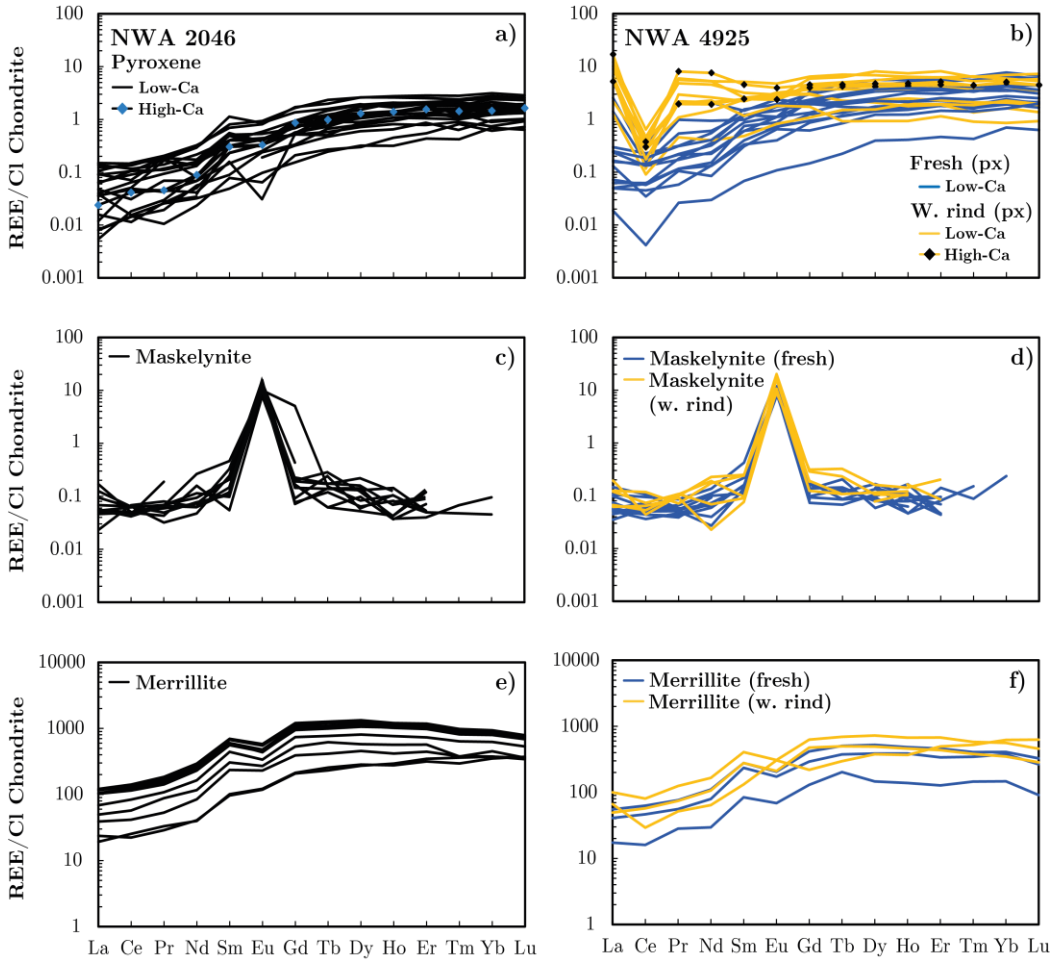

Figure 2.3: REE compositions for pyroxene, maskelynite, and merrillite grains in NWA 2046 and NWA 4925, normalised to CI chondrites (McDonough and Sun, 1995).

2.3.1.3 Maskelynite (shocked plagioclase)

Maskelynite in both samples occurs as groundmass material. These grains have retained their plagioclase composition, and as per convention in the literature, are reported as plagioclase end members. Maskelynite grains in NWA 2046 show a range in composition of An_{75-62} and low K_2O (wt. %) contents ($Or_{<3}$). Maskelynite in NWA 4925 have very low K_2O (wt. %) contents ($Or_{<0.02}$) and an anorthite range of An_{77-66}.

The REE abundances were measured in 13 grains from NWA 2046 and in 15 (10 fresh and 5 weathering rind) from NWA 4925. Maskelynite grains across both samples are compositionally similar and exhibit relatively flat LREE patterns, with $(La/Sm)_{CI}$ ratios of between 0.2–1.2 for NWA 2046 and 0.3–0.8 for NWA 4925. Large positive Eu anomalies are observed for maskelynite from NWA 2046 and NWA 4925, respectively (**Figure 2.3c-d**). CI chondrite-normalised Eu/Eu* (where Eu* is the interpolated value between CI-normalised Gd and Sm abundances) values range from ~55 to ~165 for maskelynite grains in NWA 2046 and from ~32 to ~129 for grains in NWA 4925. Minor positive La anomalies have also been observed in a handful of grains (4/13 in NWA 2046 and 12/15 in NWA 4925). Additionally, no differences have been observed between the REE patterns of maskelynite from the interior and weathering rind of NWA 4925.

2.3.1.4 Oxide minerals

Oxide minerals present in both NWA 2046 and NWA 4925 include Cr-rich spinel (chromite), ulvöspinel and ilmenite. Chromite grains in NWA 2046 and NWA 4925 show ranges in composition of $Chr_{78-85}Sp_{11-16}Usp_{1-6}Mt_{1-5}$ and $Chr_{70-85}Sp_{13-22}Usp_{1-6}Mt_{<3,}$ respectively, and are typically found partially to completely enclosed in olivine and pyroxene megacrysts and in finer grained Fe-rich olivine as well as discrete chromite grains in the groundmass. Ulvöspinel in NWA 2046 ($Chr_{2-50}Sp_{5-14}Usp_{36-81}Mt_{<14}$) and NWA 4925 ($Chr_{20-58}Sp_{8-15}Usp_{24-67}Mt_{2-7}$) is found either as inclusions in pyroxene megacrysts or as discrete groundmass grains. Ilmenite grains from both samples have comparable compositions with 6–12 % geikielite ($MgTiO_3$), 0% hematite (Fe_2O_3), and approximately 1.5 % pyrophanite ($MnTiO_3$) components, and have been observed either partially enclosed within finer grained olivine grains or as discrete groundmass grains. Rare chromite-ulvöspinel intergrowths have also been observed in both samples (Sup Fig. 5).

2.3.1.5 Merrillite and rare apatites

Two types of fine-grained phosphate laths (<100 μm length), found in close association with Fe-rich pyroxene and maskelynite, have been observed in NWA 2046 and NWA 4925. All the analysed phosphate grains in this study are merrillite in composition, but occasional grains of apatite have been measured. Merrillite grains in both samples show extensive fracturing and are commonly found near or in direct contact with shock melt (Sup Fig. 6). Grains of merrillite in NWA 2046 display Mg# of 70-83

and Na_2O contents of 0.9 – 1.4 wt. % while those in NWA 4925 show corresponding ranges of 71-81 (Mg#) and 1.1 – 1.6 wt. % Na_2O.

A total of 11 merrillite grains in NWA 2046 and 6 (3 fresh and 3 weathering rind) in NWA 4925 were analysed for their REE abundances (**Figure 2.3e-f**). Merrillite grains from both NWA 2046 and NWA 4925 yield LREE-depleted patterns, with $(La/Yb)_{Cl}$ ratios of <0.13 and <0.18 respectively. Nine of the eleven merrillite grains analysed in NWA 2046 show higher LREE and REE abundances, while grains from the weathering rind of NWA 4925 partially overlap with fresh grain data from NWA 4925 but towards higher REE concentrations. Negative Eu anomalies have been noted for most of the merrillite grains analysed in this study including all 11 grains in NWA 2046 and in 5 of 6 grains in NWA 4925. In contrast, the last merrillite grain analysed in NWA 4925 displays a positive Eu anomaly as well as evidence of LREE enrichment as exemplified by a positive La anomaly.

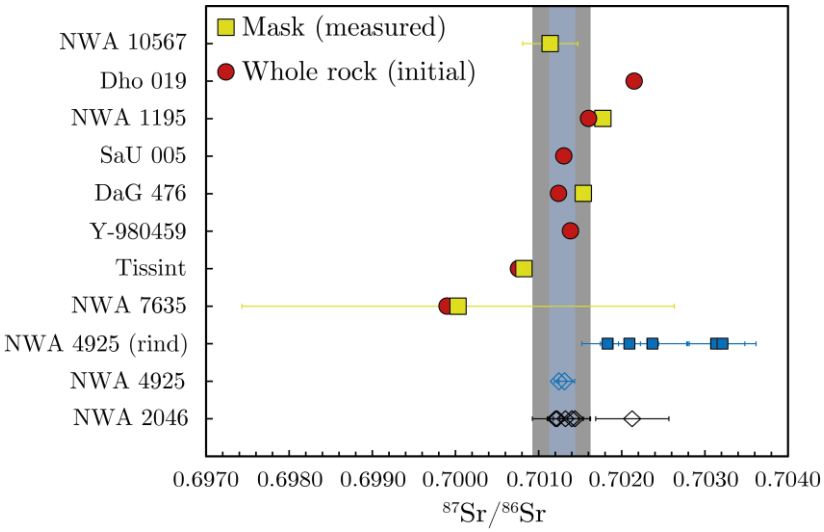

Figure 2.4: Measured $^{87}Sr/^{86}Sr$ ratios in NWA 2046 and NWA 4925, in comparison to (i) measured $^{87}Sr/^{86}Sr$ ratios in maskelynite from other depleted ol-phyric shergottites as well as (ii) age-corrected initial bulk-rock $^{87}Sr/^{86}Sr$ values. Isotope data for the depleted shergottites was taken from Borg et al. (2003); Shih et al. (2005); Shih et al. (2007); Symes et al. (2008); Shih et al. (2011); Brennecka et al. (2014); Lapen et al. (2017); Burgin et al. (2022). In-situ analysis of maskelynite grains in NWA 2046 and NWA 4925 was done by LA-MC-ICP-MS.

2.3.2 *In situ* $^{87}Sr/^{86}Sr$ isotope analyses of maskelynite and pyroxene

Seven maskelynite grains from sample NWA 2046 and nine (three fresh and six weathering rind) maskelynite grains from NWA 4925 were selected for $^{87}Sr/^{86}Sr$ isotope analyses, the full results are presented in the supporting information. Six of seven maskelynite grains analysed in NWA 2046 have measured $^{87}Sr/^{86}Sr$ of 0.70130 $\pm$ 7, while the last recorded a higher $^{87}Sr/^{86}Sr$ value of 0.70213 $\pm$ 44 (**Figure 2.4**). Fresh grains analysed from the interior of NWA 4925 yield measured $^{87}Sr/^{86}Sr$ ratios of

0.70128 ± 10, while maskelynite grains analysed from the weathering rind of NWA 4925 recorded more radiogenic ratios of 0.70244 ± 29. One pyroxene grain from NWA 2046 and three from NWA 4925 were also analysed for $^{87}Sr/^{86}Sr$. Measured $^{87}Sr/^{86}Sr$ ratios for pyroxene grains from both NWA 2046 (0.70458 ± 62) and NWA 4925 (0.71024 ± 36) are substantially more radiogenic than weathered rind maskelynite from NWA 4925. It is worth noting that pyroxene grains in both samples are full of cracks and therefore the measured regions inevitably incorporated cracked regions.

2.3.3 Bulk-rock geochemistry

The measured major- and trace-element bulk-rock compositions for NWA 2046 and NWA 4925 are presented in **Table 2.1** and illustrated in **Figure 2.5**, **Figure 2.6**, **Figure 2.7**, **Figure 2.8**. Samples NWA 2046 and NWA 4925 have Al_2O_3 contents of 5.66 and 5.23 wt% respectively, CaO of 7.41 and 8.07 wt%, MgO of 16.4 and 15.5 wt%, and SiO_2 contents of 49.9 and 49.2 wt%. The calculated Mg# for NWA 2046 of 61 is marginally higher than that of NWA 4925 with a Mg# of 58. The total alkalis (Na_2O+K_2O) and TiO_2 contents of NWA 2046 (0.77 and 0.48 wt% respectively) are comparable to those measured in NWA 4925 (0.69 and 0.46 wt%).

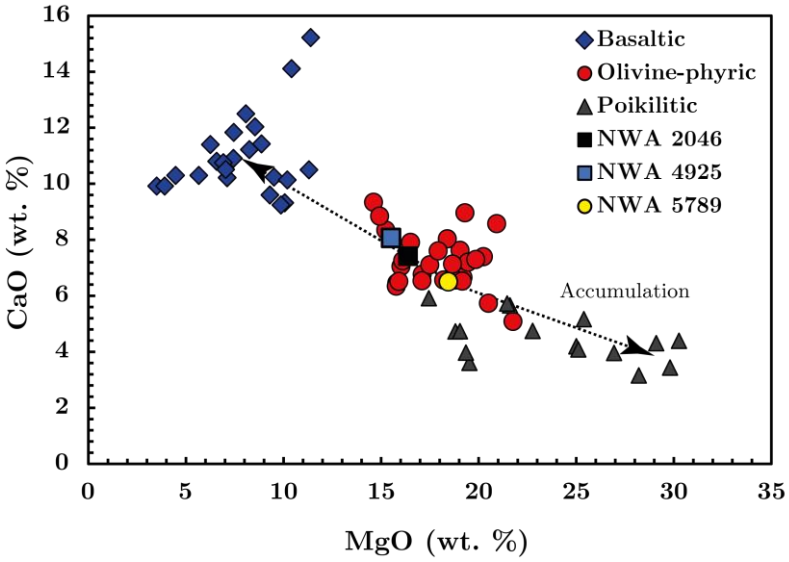

Figure 2.5: Bulk-rock CaO (wt. %) plotted against MgO (wt. %) for basaltic, olivine-phyric, and poikilitic shergottites. Data compiled from Lodders (1998); Dreibus et al. (2000); Taylor et al. (2002); Greshake et al. (2004); Misawa (2004); Shirai and Ebihara (2004); Sarbadhikari et al. (2009); Filiberto et al. (2010, 2012); Irving et al. (2012), Treiman and Filiberto (2015); Day et al. (2018); Nicklas et al. (2022). The yellow dot represents the primary melt composition (i.e., NWA 5789) while the arrows indicate fractionation and accumulation towards the basaltic and poikilitic shergottites, respectively.

The chondrite-normalised REE and incompatible trace element (ITE) plots for NWA 2046 and NWA 4925 show considerable overlap with other depleted olivine-phyric shergottites (**Figure 2.6a-b**). The

REE plot for NWA 2046 is characterised by low abundances of LREE (La/Sm = 0.54) and a flat-HREE pattern (Lu/Gd = 0.96), while the REE plot for NWA 4925 is characterised by much higher LREE abundances (La/Sm = 1.40) and a relatively flat-HREE pattern (Lu/Gd = 0.81). NWA 2046 does show evidence of La enrichment relative to other depleted olivine-phyric shergottites, while NWA 4925 is enriched in Ba, Rb, K and La relative to NWA 2046 and other depleted olivine-phyric shergottites (Figure 2.8b).

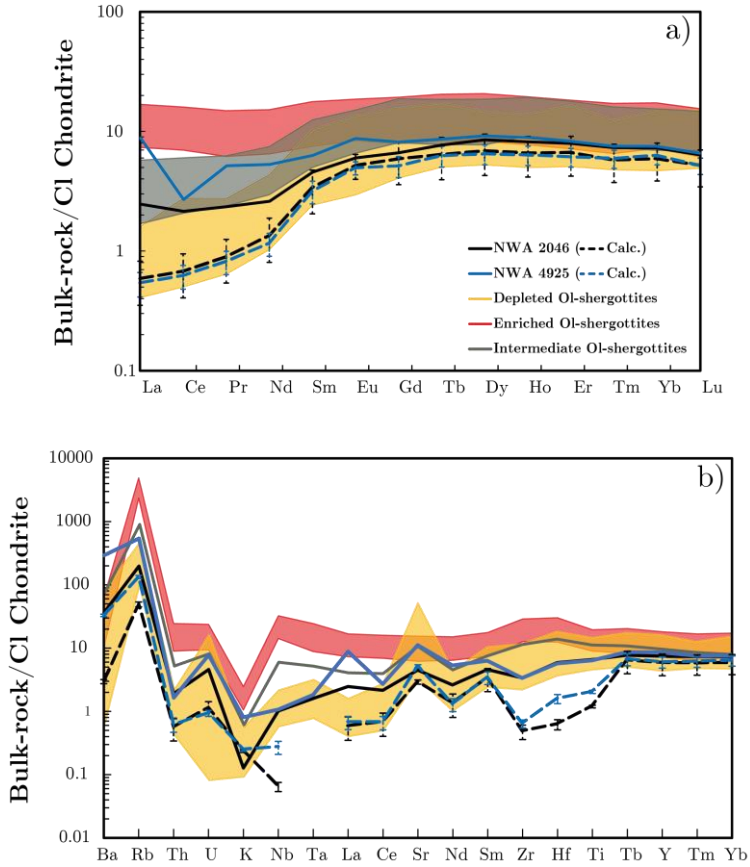

Figure 2.6: Comparison of the CI chondrite normalised (McDonough and Sun, 1995) REE (a) and ITE (incompatible trace element (b)compositions for NWA 2046 and NWA 4925, relative to other olivine-phyric shergottites across geochemical groups (see **Figure 2.5** for olivine-phyric shergottite data references). Melts calculated in equilibrium with pyroxene, merrillite and maskelynite grains from NWA 2046 (black dotted lines) and NWA 4925 (blue dotted lines), using the partition coefficients of Lundberg et al. (1990), have also been included for comparison.

High field strength elements (HFSE) such as Nb, Ta, Hf, Zr, and Y plotted against MgO (wt. %), shows clear distinctions between the olivine-phyric shergottites geochemical groups (depleted, enriched, and intermediate). In plots of MgO (wt. %) against Ce/Pb, Nb/Y, Zr/Ti, and Zr/Nb respectively, NWA 2046 and NWA 4925 plot consistently with the other depleted olivine-phyric samples (**Figure 2.8a-b, e-f**). In plots of MgO (wt. %) against $(La/Yb)_{CI}$ and Ba/Nb, NWA 2046 and NWA 4925 both show elevated

ratios and plot away from other depleted olivine-phyric shergottites (**Figure 2.8c-d**). The calculated $(La/Yb)_{CI}$ and Ba/Nb ratios for NWA 4925 are significantly higher than those for NWA 2046.

2.4 Discussion

2.4.1 Terrestrial weathering effects and constraining primary martian geochemical signatures

2.4.1.1 The effects of terrestrial alteration on olivine

Back-scattered electron images and elemental X-ray maps of olivine from the weathering rind of NWA 4925 show that the Mg-rich core zones have been preferentially affected by alteration, and replaced by minerals rich in K and Ca and depleted in Mg (**Figure 2.2b-c**), whereas the surrounding Fe-rich rims remain fresh. Similar findings, most notable in the K map, have been observed in a handful of Mg-rich olivine megacryst cores towards the interior of NWA 4925 (**Figure 2.2b-c**), although the alteration in these grains is less extensive than in olivine from the weathering rind as they still preserve primary textures and compositions. Calcite-rich veins can also be tracked from the edge of the meteorite to the altered olivine cores, implying that Ca-K-rich terrestrial fluid infiltrated along cracks and preferential altered Mg-rich olivine megacryst cores. The intensity of Ca-rich veining in the weathering rind olivine is also noticeably higher than in olivine from the interior of the sample and consistent with weathering rind olivine being more extensively altered (**Figure 2.2a**). In the absence of a terrestrial weathering rind, alteration in NWA 4925 would not be as obvious, but can be effectively constrained using Ca and K compositional maps to track the occurrence of cross-cutting veins filled with terrestrial alteration material and show the alteration of olivine cores. Elemental X-ray maps for NWA 2046 (**Figure 2.1b-c**) show no K alteration present in the sample and although Ca-rich veins are observed, they have not significantly altered the olivine megacrysts. These findings, along with the younger terrestrial exposure age for NWA 2046 (90±50 Ka) relative to NWA 4925 (400-500 Ka; Nishiizumi et al., 2011), suggest a link between severity of terrestrial alteration and duration of residence in a hot terrestrial desert environment.

2.4.1.2 Effects on REE compositions and implications for use of bulk-rock geochemistry

Terrestrial alteration of martian meteorites in hot terrestrial desert environments can result in the enrichment of fluid mobile phases like Ba, Sr, U and LREE (i.e., La, Pr-Sm) in minerals that are typically depleted in these elements such as olivine and pyroxene (Barrat et al., 2001; Crozaz and Wadhwa, 2001; Crozaz et al., 2003; Burgin et al., 2022; Orr et al., 2022). The presence of CI-normalised Ce anomalies, which can also be indicative of terrestrial alteration is caused by the oxidation of Ce^{3+} to Ce^{4+}, which is less mobile than trivalent LREE (Crozaz et al., 2003), while the type of Ce anomaly, either positive or negative, is dependent on whether Ce^{4+} has been added or lost during alteration.

Sample NWA 4925 has a distinct terrestrial weathering rind relative to other depleted olivine-phyric shergottites. Pyroxene grains analysed from the weathering rind of NWA 4925 show elevated La and Ba abundances, as well as elevated Pr, Nd, Sm and Eu abundances consistent with extensive terrestrial alteration. Several (3/14) pyroxene grains from the interior of NWA 4925 show the same pattern as those from the weathering rind, whereas the remaining grains appear largely unaffected by secondary enrichment processes display LREE-depleted patterns. Maskelynite and merrillite grains from the weathering rind and interior of NWA 4925 are generally indistinguishable from each other and largely unaffected by terrestrial alteration, though several grains of both phases display minor positive La anomalies. Bulk-rock REE and ITE plots for NWA 4925 show elevated LREE (La-Pr), Ba, Rb and K abundances relative to other depleted olivine-phyric. These bulk-rock trends for NWA 4925 mirror those discussed for pyroxene grains from the weathering rind, which suggests that pyroxene grains from the weathering rind of the sample are the main contributors to the terrestrial alteration features observed for the NWA 4925 bulk-rock.

An estimate of the primary bulk-rock REE composition of NWA 4925 can be assessed using the REE concentrations and relative modal abundances of unaltered pyroxene (60±2%), maskelynite (22±1%) and merrillite (~1±0.3%) in the sample. The contribution of the REE from olivine grains in this calculation are taken to be zero owing to very low concentrations. The calculated bulk-rock REE pattern for NWA 4925 (La/Yb_{Cl} 0.09) is significantly more LREE depleted than the measured bulk-rock REE pattern (La/Yb_{Cl} 1.17) and more comparable with other depleted olivine-phyric shergottites (**Figure 2.6a**).

The REE plots for pyroxene and maskelynite grains from NWA 2046 generally do not show evidence for terrestrial alteration, despite several grains of each phase show positive La anomalies that are in line with the sample having undergone minor terrestrial alteration. Rare earth element and ITE plots for bulk-rock NWA 2046 also shows some evidence of terrestrial alteration, primarily as a positive CI-normalised La anomaly; however, the degree of enrichment observed in this sample is substantially less pronounced than in NWA 4925. An estimate of the primary bulk-rock REE composition of NWA 2046 using only unaltered grains, calculated using modal abundances of 60(±2) % pyroxene, 21(±1) % maskelynite and ~1(±0.3) % merrillite, yields a calculated REE pattern (La/Yb_{Cl} 0.10) that is significantly more LREE depleted than the measured bulk-rock REE pattern of NWA 2046 (La/Yb_{Cl} 0.34) and in line with other depleted shergottites (Figure 2.6a). Bulk-rock LREE enrichment can occur during terrestrial alteration and must be carefully assessed before using bulk-rock La/Yb to classify or constrain source characteristics of shergottites. This is particularly evident in NWA2046 which does not display obvious signs of terrestrial alteration, only subtle indications observed in some pyroxene REE patterns.

2.4.1.3 Effects on $^{87}Sr/^{86}Sr$ in shergottites

Radiogenic isotope compositions of meteorites recovered from hot desert environments can also be affected by terrestrial alteration. For example, olivine and pyroxene mineral fractions and leachates from the depleted olivine-phyric shergottite DaG 476 have more radiogenic $^{87}Sr/^{86}Sr$ than expected, which was interpreted to result from the presence of terrestrial calcite in cross-cutting veins (Borg et al., 2000; Crozaz and Wadhwa, 2001).

Measured $^{87}Sr/^{86}Sr$ ratios for maskelynite (and pyroxene) grains from the weathering rind of NWA 4925 are consistently higher and more variable than in the interior of the sample (Figure 2.4). The weathering rind of NWA 4925 clearly represents terrestrial alteration with more radiogenic $^{87}Sr/^{86}Sr$, while the fresh maskelynite grains from the interior of the sample are interpreted to reflect primary signatures. Measured $^{87}Sr/^{86}Sr$ ratios for pyroxene and one maskelynite grain in NWA 2046 are more radiogenic than fresh maskelynite in NWA 4925 but comparable to $^{87}Sr/^{86}Sr$ for grains analysed from the weathering rind of NWA 4925 and are therefore interpreted to reflect terrestrial alteration in NWA 2046. The more radiogenic nature of pyroxene in both samples is consistent with these grains being significantly more cracked than corresponding maskelynite, and therefore more susceptible to secondary processes. Measured $^{87}Sr/^{86}Sr$ for the remaining maskelynite grains analysed in NWA 2046 (0.70130 $\pm$ 7; *n=6*) are indistinguishable from fresh maskelynite in NWA 4925 (0.70128 $\pm$ 10; *n=3*) and are therefore interpreted to reflect primary martian signatures, in line with the results of Burgin et al. (2022).

2.4.2 Petrogenesis of NWA2046 and NWA4925

2.4.2.1 Do NWA4925 and NWA2046 represent melt compositions or cumulates?

Debate surrounding the origin of olivine megacrysts in olivine-phyric shergottites concerns whether they represent phenocrysts, crystals with a genetic relationship to their host magma (i.e., Musselwhite et al., 2006; Sarbadhikari et al., 2009; Gross et al., 2011), antecrysts, accumulated crystals that may show some evidence of a genetic relationship to their host magma (i.e., Barrat et el., 2002; Balta et al., 2015; Nicklas et al., 2022), or xenocrysts, crystals with no genetic relationship to their host magma (i.e., Wadhwa et al., 2001; Shearer et al., 2006; Filiberto et al., 2010; Nicklas et al., 2022). Equilibrium between olivine megacrysts and the bulk-rock composition of a meteorite can be assessed using the experimentally determined Fe-Mg partition coefficient (or $K_D^{Ol-melt}_{Mg-Fe}$) value of 0.35 ± 0.01 (Filiberto and Dasgupta, 2011), calculated for specific use on martian basalts (**Figure 2.7**). Using this K_D value, olivine in equilibrium with the bulk-rock composition of NWA 2046 (Mg# = 61) would have $Fo_{83\pm1}$, while olivine in NWA 4925 (Mg# = 58) would have $Fo_{81\pm1}$. In comparison, the most Mg-rich olivine measured in NWA 2046 and NWA 4925 have Fo_{83} and $Fo_{80,}$ respectively. These findings highlight that the most primitive olivine megacryst cores from samples NWA 2046 and NWA 4925 have Fo contents consistent with them being in Fe-Mg equilibrium with their respective bulk-rock composition and

suggests that both samples represent melt compositions. The Mg# of NWA 2046 (61) and NWA 4925 (59) are, however, lower than those recorded for the most primitive olivine-phyric shergottites, NWA 5789 (Mg# - 66; Gross et al., 2011) and Yamato 980459 (Mg# - 67; Greshake et al., 2004), which suggests that while NWA 2046 and NWA 4925 do represent melt compositions, they are not primary mantle-derived melts and must therefore have undergone some degree of olivine fractionation in a staging chamber prior to intrusion/extrusion at the martian surface.

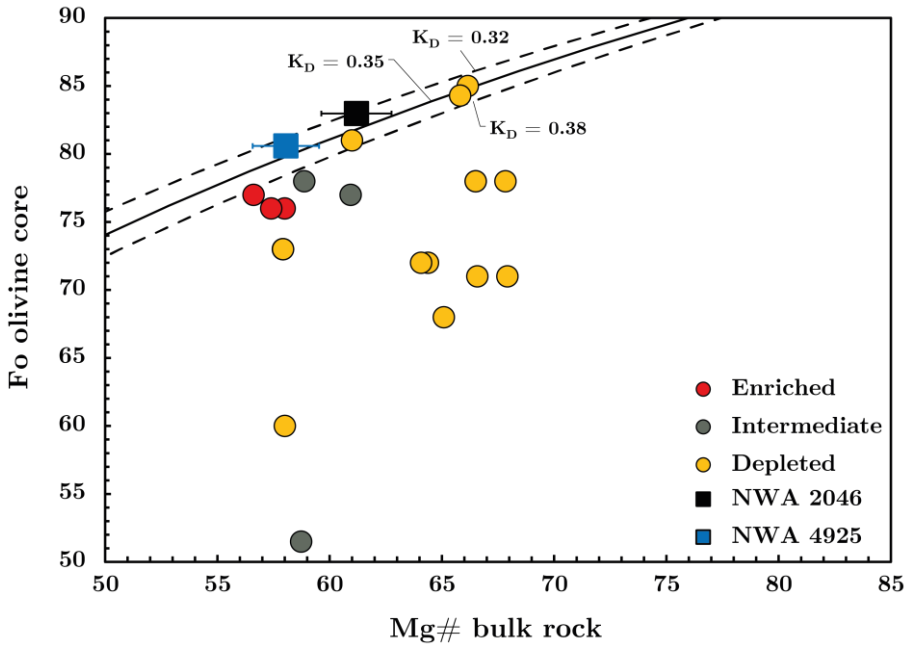

Figure 2.7: Mg# of bulk-rock versus Forsterite content in olivine cores of olivine-phyric shergottites. Solid line represents the calculated Mg# of melt in equilibrium with the olivine cores using a Fe-Mg melt-mineral partition coefficient of 0.35, while the dotted lines (i.e., K_D of 0.32 and 0.38) represent the uncertainty of the solid line. (see **Figure 2.5** for olivine-phyric shergottite data references).

The amount of olivine fractionation can be assessed using the Ni olivine-melt partition coefficient calculated from the model outlined by Jones et al. (1995), which has previously been shown to be consistent with experimental work performed on martian Gusev Adirondack-class basalts (Filiberto et al., 2009). Using this method yields $D_{NiO}^{Ol-Melt}$ values of 5.2 ± 2.0 (1σ) for NWA 2046 (at $D_{MgO}^{Ol-Melt}$ = 2.6) and 5.5 ± 2.0 (1σ) for NWA 4925 (at $D_{MgO}^{Ol-Melt}$ = 2.7). These partition coefficients were then used to calculate the amount of Ni present in a melt in-equilibrium with the most primitive olivine megacryst composition in NWA 2046 (Fo_{83}) and NWA4925 (Fo_{81}), which have Ni contents of 705 ppm and 630 ppm, respectively. The melts in equilibrium with these primitive olivine megacrysts in each sample have Ni contents of 137 ppm in NWA 2046 and 115 ppm in NWA 4925, both of which are lower than the measured bulk-rock Ni contents of each sample (i.e., 148 ppm for NWA 2046 and 160 ppm for NWA 4925). In contrast, Yamato 980459, one of the most primitive olivine-phyric shergottites reported to-date has a bulk-rock Ni abundance of 203 ppm (Shirai and Ebihara, 2004) and is interpreted to

represent a mantle-derived melt. Using the bulk-rock Yamato 980459 as the composition of primary martian mantle melts and the Ni partition coefficients calculated above, Rayleigh fractionation can be applied to estimate the degree of fractionation required to produce melts with Ni concentrations of 135 ppm (NWA 2046) and 115 ppm (NWA 4925). These findings show that an initial melt with a composition of Yamato 980459 requires 8-10% and 10-13% fractionation to produce a melt in equilibrium with the most primitive olivine megacrysts in NWA 2046 and NWA 4925, respectively.

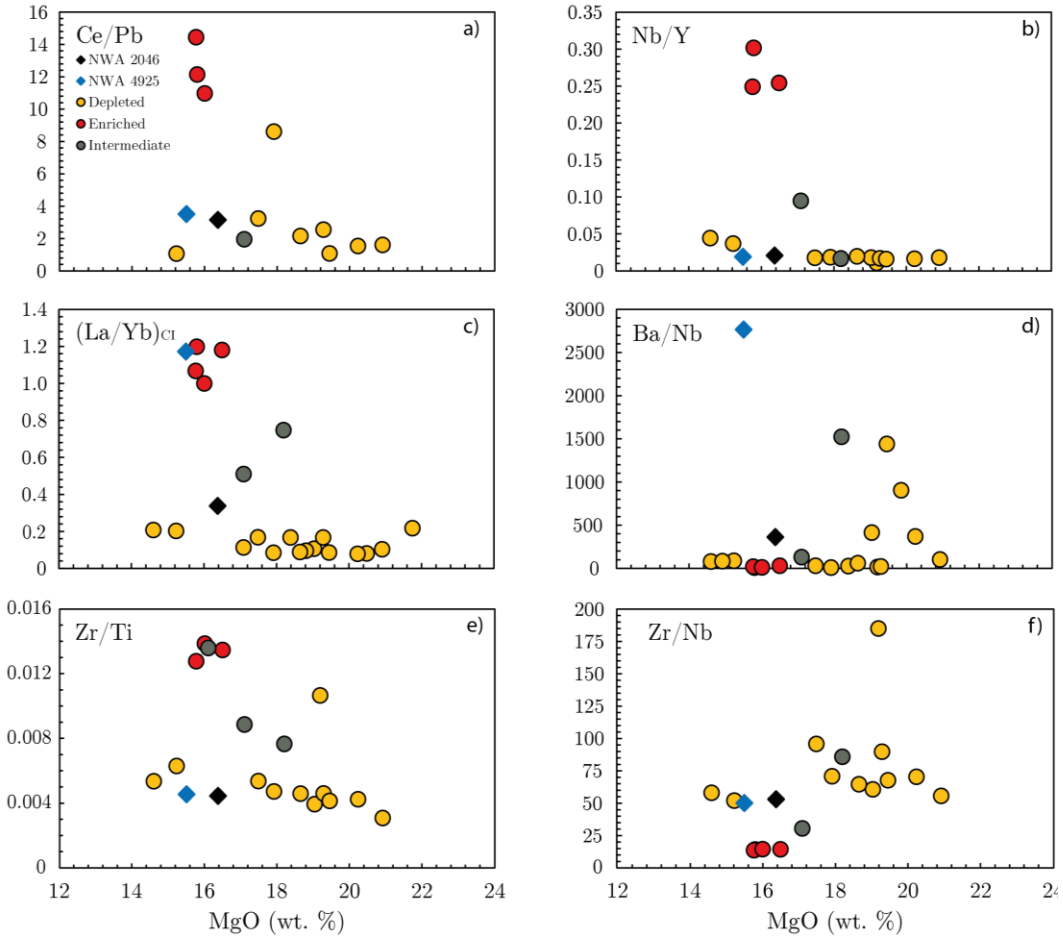

Figure 2.8: Bulk rock trace element concentrations from NWA 2046 and NWA 4925, in comparison to other olivine-phyric shergottites across geochemical subgroups. (see **Figure 2.5** for olivine-phyric shergottite data references.)

2.4.2.2 Crystallisation sequence

Petrography and mineral compositions allow for constraints to be placed on the order in which minerals crystallised in NWA 2046 and NWA 4925. Chromite is often one of the earliest phases to crystallise in olivine-phyric shergottites and is typically found as inclusions associated with the most Mg-rich regions of olivine megacrysts (Goodrich, 2003). Inclusions of chromite have also been observed in olivine megacrysts from NWA 2046 and NWA 4925, but not near the Mg-rich core zones. Chromite inclusions in both samples are instead found closer to the rims of the olivine megacrysts, where the most Mg-rich olivine measured next to a chromite inclusion had Fo_{70}. Rare chromite inclusions have also been

observed in the core regions of pyroxene megacrysts from both samples, with pyroxene measured near the inclusions having Mg# of 80 in NWA 2046 and 79 in NWA 4925. In contrast, the most Mg-rich pyroxenes measured in NWA 2046 and NWA 4925 have Mg# of 81 and 80, respectively, which suggests that chromite grains from both samples began crystallising at a similar time to pyroxene.

Equilibrium between olivine and pyroxene has previously been evaluated using an exchange coefficient ($K_{D,Fe-Mg}^{Ol-Px}$) value of 1.2 (Longhi and Pan, 1989). The most primitive orthopyroxene and olivine core in NWA 2046 have compositions of $En_{68}Fs_{28}Wo_4$ and Fo_{83} respectively, and a calculated $K_{D,Fe-Mg}^{Ol-Px}$ value of 0.91, while those in NWA 4925 have compositions of $En_{67}Fs_{30}Wo_3$ and $Fo_{80,}$ and a corresponding $K_{D,Fe-Mg}^{Ol-Px}$ value of 0.99. In both cases, these findings are inconsistent with the exchange coefficient of Longhi and Pan (1989) and indicate that the most magnesian olivine in each sample crystallised prior to orthopyroxene joining the crystallisation sequence. The $K_{D,Fe-Mg}^{Ol-Px}$ value of 1.2 instead suggests that olivine with compositions of Fo_{78} and Fo_{77}, are in equilibrium with the most Mg-rich pyroxene grains in NWA 2046 and NWA 4925, respectively. These findings are consistent with numerous other depleted olivine-phyric shergottites (e.g., Larkman Nunatak (LAR) 12095/12240, NWA 5789, SaU 005, Tissint, Yamato 980459), where olivine was shown to have entered the crystallising assemblage before orthopyroxene (Goodrich, 2003; Usui et al., 2008; Gross et al., 2011; Balta et al., 2015; Dunham et al., 2019). Additionally, the rare olivine (Fo_{66} in NWA 2046 and Fo_{71} in NWA 4925) (and chromite) inclusions observed in low-Ca pyroxene phenocrysts from both NWA 2046 and NWA 4925 have not been reported in any of the other ejection-paired depleted shergottites, and are dissimilar to the poikilitic lithologies (composed of coarse-grained pyroxene oikocrysts enclosing olivine and chromite chadacrysts) described for poikilitic shergottites (i.e., Walton et al., 2012; Howarth et al., 2014; Combs et al., 2019; Rahib et al., 2019).

The ratio of Ti/Al in pyroxenes can be used to determine the onset of plagioclase crystallisation, which causes Al depletion in residual liquids that results in abrupt changes to the Ti/Al in pyroxene. In **Figure 2.9a**, the Ti/Al ratios for pyroxenes from NWA 2046 and NWA 4925 decrease relatively slowly before beginning to rapidly decrease around Mg# 69 (equivalent to olivine with Fo_{65}) and around Mg# 68 (equivalent to olivine with Fo_{64}), respectively, thus indicating the onset of plagioclase at this point in the magma evolution.

The behaviour and concentration of major and minor elements (i.e., Mg, Fe^{2+} and Na) in merrillite can also be used to place constraints on the crystallisation sequence, specifically between merrillite and plagioclase. Previous studies looking at merrillite have shown that grains with high-Na (>1 wt. %) likely began crystallising before the onset of plagioclase while those with low-Na concentrations would have begun crystallising afterwards (i.e., Burgers et al., 2012; Shearer et al., 2015). Most merrillite grains in

both NWA 2046 and NWA 4925 have Na_2O contents that exceed 1.0 wt. %, and thus likely crystallised prior to plagioclase joining the assemblage, similar to merrillite grains in DaG 476, LAR 12095/12240 and NWA 1195 (Wadhwa et al., 2001; Shearer et al., 2015; Dunham et al., 2019). Merrillite grains from other depleted olivine-phyric shergottites including NWA 5789 and Tissint have <1.0 wt. % Na_2O and therefore began crystallising after plagioclase (Balta et al., 2015; Shearer et al., 2015).

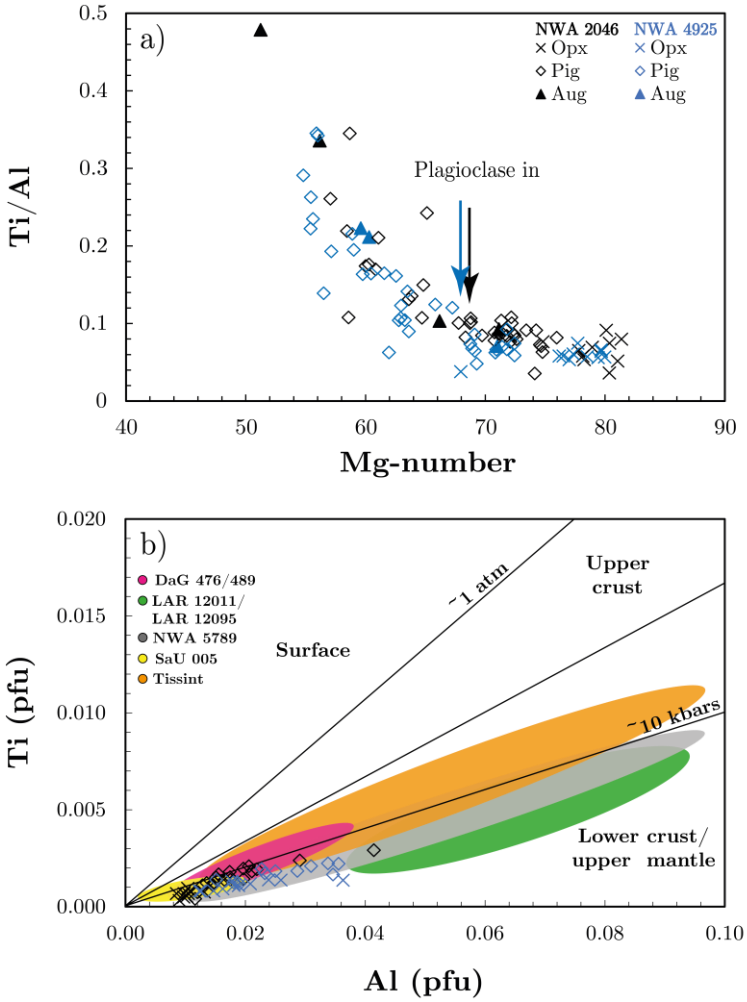

Figure 2.9: (a) Plot of the Ti/Al ratio vs Mg# for pyroxene phenocrysts in NWA 2046 and 4925. Black (NWA 2046) and blue (NWA 4925) arrows indicate the onset of plagioclase crystallisation in each sample. (b) Plot of Al versus Ti (afu) for pyroxene grains in NWA 2046 and NWA 4925. Included for comparison is pyroxene data from other depleted olivine-phyric shergottites (Wadwha et al., 2001; Goodrich, 2003; Musselwhite et al., 2006; Gross et al., 2011; Balta et al., 2015; Dunham et al., 2019).

2.4.2.3 Oxygen fugacity

Oxygen fugacity constraints on the source of the depleted olivine-phyric shergottites can be estimated using two approaches: the olivine–pyroxene–chromite oxybarometer (Ol-Px-Chr; Mattioli and Wood, 1988 and Wood and Virgo, 1989) and the V-in-olivine oxybarometer (i.e., Nicklas et al., 2021). Since

olivine is generally the first phase to crystallise in basaltic assemblages, fO_2 values collected with the V-in-olivine oxybarometer are the closest possible to the liquidus. Additionally, this method works independently of other mineral phases such as pyroxene and spinel (chromite) and is therefore unaffected by uncertainties regarding equilibrium between olivine and these other early crystallising phases.

Olivine-Px-Chr oxybarometry calculations for each sample were performed at 10 ± 1 kbars pressure for six olivine, low-Ca pyroxene, and Cr-rich spinel assemblages, using spinel grains at the rims of olivine megacrysts where all three phases are in contact with each other. These calculations, which yield average fO_2 estimates of -2.8 (± 0.5) and -2.7 (± 0.2) log units below the Quartz-Fayalite-Magnetite (QFM) buffer for NWA 2046 and NWA 4925, respectively (**Figure 2.10a**), overlap entirely with recorded fO_2 for other depleted olivine-phyric shergottites (i.e., -2 to -4 QFM e.g., Herd et al., 2013; Balta et al., 2015). Oxygen fugacity estimates by V-in-olivine (**Figure 2.10b**) for NWA 2046 (QFM -2.7 ± 0.7) and NWA 4925 (QFM -2.9 ± 0.6) are comparable to estimates of the Ol-Px-Chr oxybarometer outlined above and previous estimates by Nicklas et al. 2021 for depleted olivine-phyric shergottites (-2.2 ± 1.8 QFM; 2SD). These findings suggest that NWA 2046 and NWA 4925 crystallised from mantle sources with similar redox conditions that remained relatively constant during the early stages of crystallisation.

2.4.2.4 Parent magma REE evolution

The evolution of the parent melts of NWA 2046 and NWA 4925 can be tracked using the REE compositions for calculated melts in equilibrium with pyroxene, maskelynite and merrillite, respectively. The REE compositions are calculated using the equation $C_l = C_x/D_{REE}$, where C_l and C_x are the concentrations of a particular REE in the melt and in each mineral phase, respectively, while D_{REE} is the mineral/melt partition coefficient calculated in Lundberg et al. (1990). Low-Ca pyroxene is the earliest REE-bearing phase to crystallise and as such, should broadly reflect the REE composition of the parent melts of each sample, while the REE compositions of melt in equilibrium with later crystallising merrillite and maskelynite reflect evolution of the melt. The melts in equilibrium with pyroxene, merrillite and maskelynite yield $(La/Yb)_{CI}$ ratios of 0.10, 0.04 and 0.05 respectively in NWA 2046 and 0.31, 0.04 and 0.11 respectively in NWA 4925. These REE plots for melts in equilibrium with each phase from NWA 2046 and NWA 4925 broadly mirror each other and their respective calculated bulk-rock REE patterns. These findings suggest that NWA 2046 and NWA 4925 crystallised from fractionating melts that experienced little to no addition or loss of incompatible trace elements.

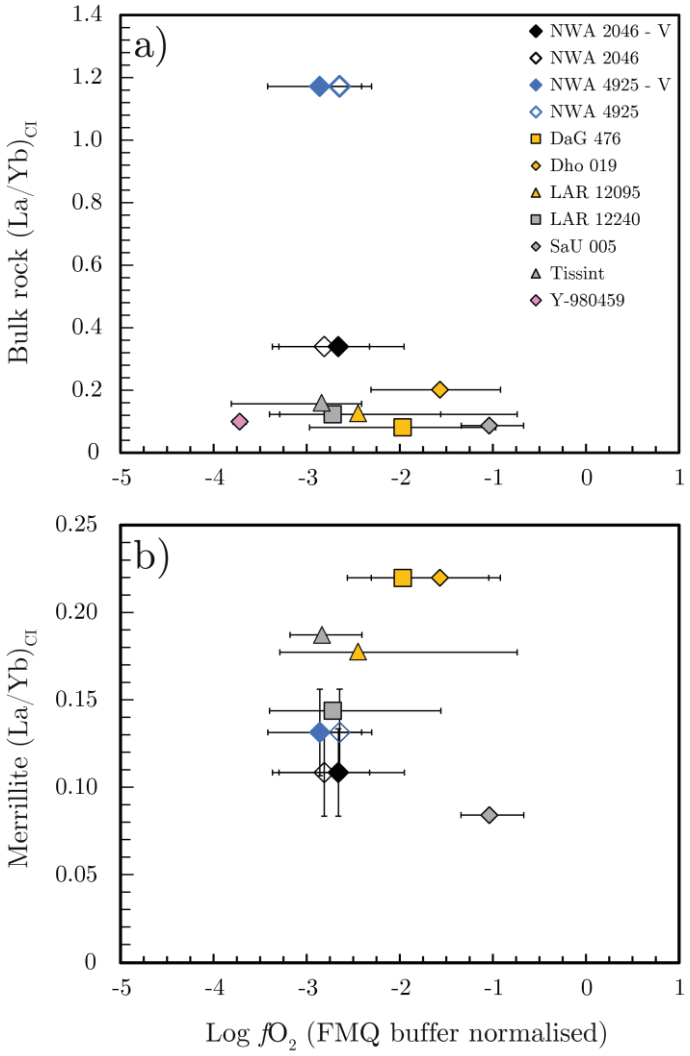

Figure 2.10: Oxygen fugacities (FMQ buffer normalised) versus CI chondrite-normalised (McDonough and Sun, 1995) bulk-rock La/Yb ratio for NWA 2046 and NWA 4925. Oxygen fugacities were calculated using a) ol-py-sp oxybarometer (open diamonds) and b) Vanadium-in-olivine oxybarometer (filled diamonds). Literature bulk-rock and merrillite collected from Balta et al., 2015; Shearer et al., 2015; Howarth and Udry, 2017; Dunham et al., 2019; Nicklas et al., 2021 and references within.

2.4.3 Implications for volcanism at the 1.1 Ma ejection site at the Tharsis plateau

2.4.3.1 NWA2046 and NWA4925 in context with depleted shergottites

Northwest Africa 2046 and NWA 4925 along with numerous other LREE-depleted shergottites including DaG 476 (possibly paired with DaG 489/670/735/975/1037), NWA 1195, NWA 2626, NWA 6162, NWA 7635, NWA 8159, SaU 005 (possibly paired with SaU 008/051/060/094/150), Tissint, NWA5789, and Yamato 980459, are 1.1 Myr ejection-paired meteorites likely from the Tharsis plateau (Nishiizumi et al., 2011; Brennecka et al., 2014; Herd et al., 2017; Lapen et al., 2017). These depleted

shergottites show a broad range of crystallisation ages from 347 Ma to 2.4 Ga, indicating that they formed part of a long-lived volcanic centre (Lapen et al., 2017).

Many of the mineralogical, petrographic, and geochemical characteristics reported in this study for NWA 2046 and NWA 4925 are comparable to other ejection-paired samples including DaG 476, LAR 12095/12240, SaU 005 and Yamato 980459. Major element compositions of minerals present in NWA 2046 and NWA 4925 are generally similar to those in other depleted shergottites, but some differences have been observed. The compositional range of olivine in NWA 2046 and NWA 4925 resembles many of ejection paired olivine-phyric shergottites (i.e., **Table 2.2**); however, the most primitive olivine megacrysts in DaG 476, NWA 6162 and SaU 005 are more Fe-rich than in the samples here and would therefore have crystallised from more evolved melts. Pyroxene grains in NWA 2046 and NWA 4925, as well as in DaG 476, NWA 1195, NWA 2626, NWA 5789, Tissint and Yamato 980459, are compositionally zoned from orthopyroxene cores to rims of augite or pigeonite, suggesting cooling rates quick enough for zoning to be preserved. These trends from low-Ca cores to higher-Ca rims for pyroxene phenocrysts are the result of delayed plagioclase nucleation, which would have increased the activity of Ca in the melt, thus driving pyroxene to crystallise with higher CaO (wt. %) contents (Papike et al., 2009). Maskelynite major element compositions in NWA 2046 (i.e., An_{75-62}) and NWA 4925 (i.e., An_{77-64}) resemble those in DaG 476 (An_{72-52}; Zipfel et al., 2000), but also partially overlap with maskelynite in NWA 5789 (An_{65-58}; Gross et al., 2011) and LAR 12095/12240 (An_{67-53}; Dunham et al., 2019), although grains from these samples are generally more Na-rich. The Mg#, and Na and Mn concentrations of merrillite grains in NWA 2046 and NWA 4925 overlap with those in Dho 019 (Shearer et al., 2015), and partially with merrillite in LAR 12095/12240 (Dunham et al., 2019), NWA 1195, and DaG 476 (Shearer et al., 2015), but are more Mg- and Na-rich and Mn-depleted relative to merrillite in NWA 5789 and Tissint (Liu et al., 2016) (Sup fig. 9).

The REE abundances and patterns of pyroxene, maskelynite and merrillite in NWA 2046 and NWA 4925 are most comparable to DaG 476/489 (Wadhwa et al. 2001), although the positive Eu anomaly for maskelynite in NWA 2046 (Eu/Eu* ~55–165) and NWA 4925 (~32–129) extend to higher values than observed for the DaG samples (~61–67). The REE patterns for individual phases in NWA 2046 and NWA 4925 also show overlap with pyroxenes in Tissint (Balta et al., 2015) and Yamato 980459 (Usui et al., 2008), as well as merrillite grains in Tissint and NWA 1195 (Shearer et al., 2015).

The calculated fO_2 for NWA 2046 (QFM -2.7) and NWA 4925 (QFM -2.9), are within error of redox estimated for Tissint, LAR 12095/12240, DaG 476 and Dho 019 (Nicklas et al., 2021). Finally, the measured $^{87}Sr/^{86}Sr$ for the fresh maskelynite grains in NWA 2046 and NWA 4925 overlap with measured ratios for maskelynite mineral separates from DaG 476, as well as with age-corrected initial bulk-rock ratios for DaG 476, SaU 005 and Yamato 980459 (Figure 2.4), suggesting that these meteorites originate from isotopically similar sources.

Overall, the major and trace element (including REE) compositions and isotopic characteristics of mineral phases in NWA 2046 and NWA 4925 most strongly resemble DaG 476, implying a similar mantle source and petrogenesis for NWA 2046, NWA 4925, and DaG 476. In summary I present **Figure 2.11**, a schematic model modified after Brennecka et al. (2014), illustrating the proposed source location for NWA 2046 and NWA 4925 in relation to the other 1.1 Ma ejection-paired olivine-phyric shergottite meteorites.

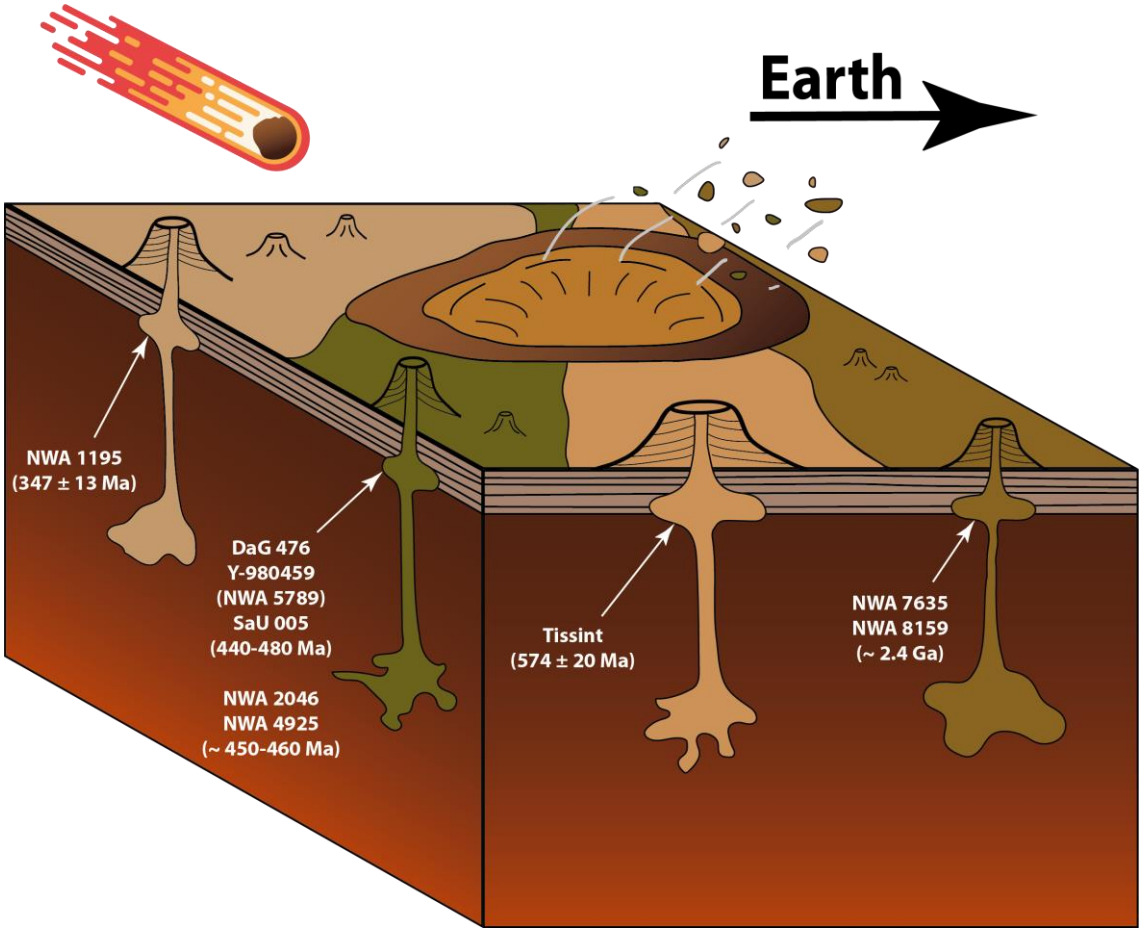

Figure 2.11: Schematic illustration showing the proposed emplacement scenario on Mars for NWA 2046 and NWA 4925, in relation to other 1.1 Ma ejection-paired depleted olivine-phyric shergottites. On this diagram samples are grouped together by their crystallisation ages.

2.4.3.2 Crustal staging chambers

The Ti/Al ratio in pyroxenes from shergottites can be used to constrain the crystallisation pressures at which they formed (Filiberto et al., 2010). It is worth noting that because this model is not calibrated for the exact composition of pyroxene in martian meteorites, the values calculated are only approximations for the crystallising depths. Additionally, the Ti/Al ratio of a melt is affected by the onset of plagioclase crystallisation (McSween et al., 1996), and as such, the Ti/Al barometer provides best estimates when applied to pyroxene that crystallised prior to plagioclase entering the crystallising assemblage (i.e., Mg#

> 68 for both NWA 2046 and NWA 4925; **Figure 2.9a**). These selected pyroxene compositions for NWA 2046 and NWA 4925 are plotted in **Figure 2.9b**, along with experimentally derived pressure fields for the martian crust and mantle and literature data for other depleted olivine-phyric shergottites. The Ti/Al ratios for pyroxene grains from both samples suggest crystallising pressure of ~10 kbars (or 85 km depth), equivalent to the crust-mantle boundary. Moreover, this indicates that the Mg-rich olivine megacryst cores (± Cr-rich oxides), which crystallised prior to pyroxene in NWA 2046 and NWA 4925, would likely have crystallised at similar depths.

The Ti/Al ratios for pyroxenes in NWA 2046 and NWA 4925 are also consistent with pyroxenes in DaG 476/489, LAR 12095/12240, NWA 5789, SaU 005, and Tissint (i.e., **Figure 2.9b**), indicating similar crystallising depths. These findings along with the spatial association of depleted olivine-phyric shergottites from the 1.1 Ma ejection event are consistent with the development of either a common long-lived staging chamber for all 1.1 Ma ejection paired shergottites or multiple staging chambers near the base of the martian crust (e.g., Usui et al., 2008; Sarbadhikari et al., 2009; Filiberto et al., 2010; Peslier et al., 2010). The development of a staging chamber/s is accompanied by the co-crystallisation of Mg-rich olivine megacrysts, orthopyroxene cores, low-Ca pyroxene phenocrysts (± chromite), after which the residual melts would have continued their ascent, entraining olivine and low-Ca pyroxene (± chromite) crystals in the process. The most Mg-rich olivine megacrysts in many of depleted olivine-phyric shergottites, with the exception of NWA 2046, NWA 4925, NWA 5789 and Y98, show varying degrees of disequilibrium with their bulk-rock compositions (i.e., **Figure 2.7**), which in addition to the substantial variation in the modal abundance of olivine megacrysts in these samples (from 5 to 31%; **Table 2.2**), indicates that many of them accumulated/entrained olivine megacrysts, either in the staging chamber at depth or during ascent to surface.

The crystal-bearing magmas of the depleted shergottites would have been emplaced at or near the surface cooling fast enough to produce either fine-grained groundmass assemblages or quenched groundmass textures (i.e., **Table 2.2**), as well as to prevent settling of the coarse-grained phases. In rare instances such as in Yamato 980459 (i.e., Usui et al., 2008) and NWA 5789 (i.e., Gross et al., 2011), quenched groundmass textures have been observed, which in comparison to the crystalline and mineralogically comparable groundmasses of NWA 2046 and NWA 4925 along with DaG 476, NWA 1195, NWA 2626, NWA 6162, SaU 005 and Tissint suggests more rapid cooling, further highlighting the variation in the emplacement scenarios of depleted olivine-phyric shergottites.

2.4.3.3 Source characteristics with time

The crystallisation age and incompatible trace element compositions of depleted shergottites, used in tandem, can provide crucial information on the origin and evolution of their mantle sources over time. Measured $^{87}Sr/^{86}Sr$ for maskelynite grains in NWA 2046 (0. 70130 ± 0.00007) and NWA 4925 (0.70128 ± 0.00010), are within uncertainty of the modelled source value (0.70127 ± 0.00004) for ejection-paired olivine-phyric shergottites DaG 476, NWA 1195, SaU 005, Tissint and Yamato 980459 (i.e., Borg et

al., 2003; Shih et al., 2005, 2007; Symes et al., 2008; Brennecka et al., 2014). Age-corrected initial bulk-rock $^{87}Sr/^{86}Sr$ and εNd ratios for these ejection-paired meteorites, along with other depleted shergottites including Dho 019, NWA 5590 and QUE 94201 (Borg et al., 1997; Borg et al., 2001; Shih et al., 2011; Yang et al., 2013; Day et al., 2018), increase with decreasing crystallisation ages (**Figure 2.12a, c**), reflecting evolution from a long-lived common source. The negative correlation between age-corrected initial $^{87}Sr/^{86}Sr$ versus age, further constrained between outliers NWA 1195 and Tissint (**Figure 2.12a**), can be used to approximate crystallisation ages for NWA 2046 (i.e., 452 Ma) and NWA 4925 (i.e., 460 Ma).

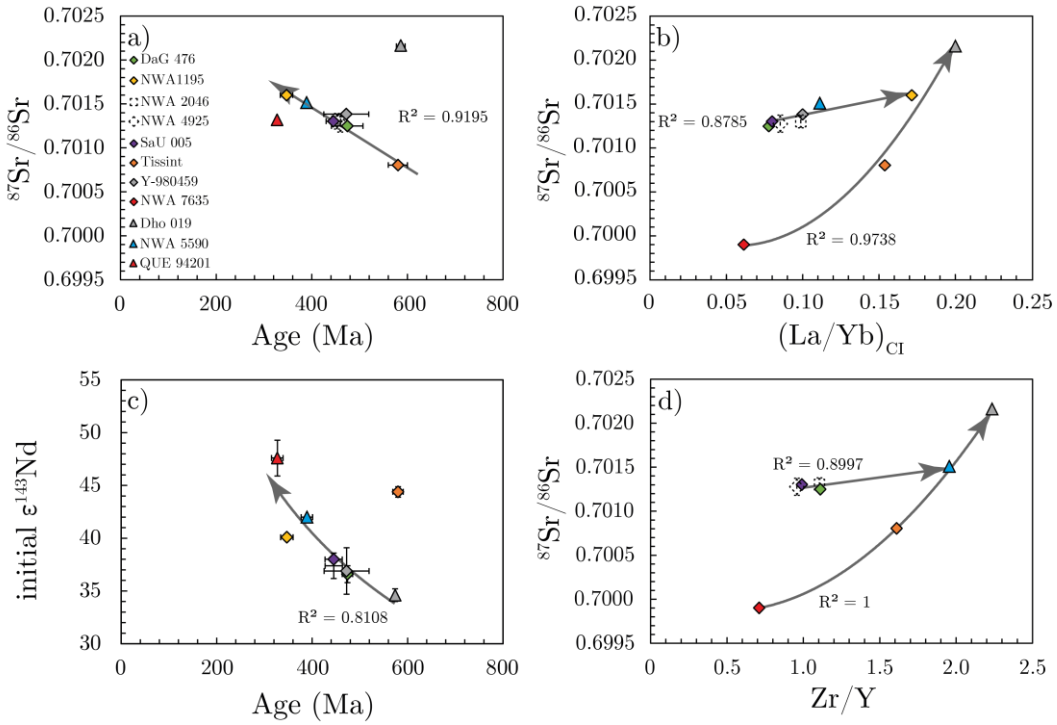

Figure 2.12: (a) Age vs $^{87}Sr/^{86}Sr$, (b) $^{87}Sr/^{86}Sr$ vs REE ratios, (c) Age vs Nd-isotope systematics and (d) $^{87}Sr/^{86}Sr$ vs HSFE ratios for NWA 2046 and NWA 4925 in comparison to other 1.1 Ma ejection-paired depleted shergottites, as well as Dho 019, NWA 5990, and QUE 94201 (3 Ma ejection-paired depleted shergottites). Age-corrected initial bulk-rock ratios for the depleted shergottites was taken from Borg et al. (1997), Borg et al. (2001), Borg et al. (2003), Shih et al. (2005), Shih et al. (2007), Symes et al. (2008), Shih et al. (2011), Brennecka et al. (2014), Lapen et al. (2017) and Herd et al. (2017).

Positive correlations have also been observed when age-corrected initial bulk-rock $^{87}Sr/^{86}Sr$ are plotted against $(La/Yb)_{CI}$ and Zr/Y respectively (**Figure 2.12b, d**). In both plots, SaU 005, NWA 2046, NWA 4925, DaG 476, and Yamato 980459 define one set of compositional trends, while Dho 019, Tissint and NWA 7635 define another. These trends are interpreted to reflect at least two distinct source evolution paths for depleted shergottites, while their intersection in **Figure 2.12b, d** highlights their shared source reservoir. Additionally, $^{87}Sr/^{86}Sr$ isotope systematics and age estimates as well as the degrees of REE and HFSE enrichment for the depleted shergottites, all show no correlation against bulk fO_2. These

finding are consistent with those of Nicklas et al. (2021), where the recorded variation in fO_2 for shergottites was interpreted to reflect variation in the redox state of the upper mantle, possibly related to ineffective mixing of a martian magma ocean by mantle convection (i.e., Kiefer, 2003).

2.5 Summary of findings

In this chapter I conducted a comprehensive study of two LREE depleted olivine-phyric shergottites, NWA 2046 and NWA 4925, both of which are low fO_2 rocks with olivine megacrysts, among the most Mg-rich observed in martian meteorites.

NWA 4925 with its distinctly older terrestrial age, relative to other ejection-paired shergottites, has undergone significant terrestrial alteration, tracked using Ca and K elemental maps of the sample. Terrestrial alteration of NWA 4925 also resulted in the preferential alteration of olivine megacryst cores relative to rims, and the LREE enrichment of bulk-rock and pyroxene.

Primitive olivine megacryst cores from both samples are in equilibrium with their respective bulk-rock compositions and interpreted to be phenocrysts with the bulk-rock compositions of NWA 2046 and NWA 4925 representing melt compositions. Both samples also show evidence of olivine fractionation in the staging chamber prior to ascent, as indicated by their lower Fo contents and low Ni-contents relative to the primitive mantle-derived sample Yamato 980459, with estimates suggesting 8-10% and 10-13% fractionation to produce NWA 2046 and NWA 4925, respectively. The location of the staging chamber in which these and other depleted shergottites crystallised, constrained using Ti/Ai ratios in pyroxene grains of depleted olivine-phyric shergottites, is at pressures that are consistent with the martian crust-mantle boundary (10 kbars).

Additionally, maskelynite grains in olivine-phyric shergottites proves useful in assessing the primary $^{87}Sr/^{86}Sr$ compositions of olivine-phyric shergottites. Maskelynite grains analysed from NWA 2046 and NWA 4925 yield $^{87}Sr/^{86}Sr$ comparable to age-corrected initial bulk-rock values for several 1.1 Ma ejection-paired olivine-phyric shergottites, including Dag 476, SaU 005 and Yamato 980459, and are therefore believed to have been derived from similar sources during similar timed eruption events. Other ejection-paired samples such as Dho 019 and Tissint, while isotopically different, appear to represent partial melts that evolved from the common long-lived depleted source along a separate trend to that of DaG 476, NWA 2046, NWA 4925, SaU 005 and Yamato 980459.

Table 2.2. Summary table of bulk-rock properties for depleted olivine-phyric shergottites, as well as the modal abundance and composition of olivine in each sample.

	Textures[1]	Crystallisation age (Myr)	Ejection age (Myr)	Bulk-rock Mg#	% Ol, Fo range	$(La/Yb)_{CI}$	$(^{87}Sr/^{86}Sr)_i$
DaG 476	porphyritic; ol + opx megacrysts in mask + px + ol + ox + phos + sf groundmass[2]	474 ± 20[3]	1.0 ± 0.1[4]	67[5]	10-24, 76-58[6]	0.08[5]	0.7012 ± 33
NWA 1195	See DaG 476, minus larger opx megacrysts[7]	347 ± 13[8]	1.2 ± 0.2[4]	59[9]	22, 81-60[7]	0.17[10]	> 0.7016
NWA 2046	See DaG 476	-	1.2 ± 0.2[4]	61	17, 83-32	0.1*	0.7013 ± 7
NWA 2626	See DaG 476[11]	514 ± 24[12]	1.3 ± 0.2[4]	-	15, 83-53[6]	-	-
NWA 4925	See DaG 476	-	1.1 ± 0.1[4]	58	16, 81-31	0.09*	0.7013 ± 10
NWA 5789	porphyritic; ol megacrysts in px + ol + ox + mesostatis (mask + px + ox + phos + sf) groundmass[13-14]	-	1.0 ± 0.2[4]	66[13-14]	19, 84-30[14]	0.08[10]	-
NWA 6162	See NWA 1195[10]	-	1.1	68[10]	26, 72-65[10]	0.23[10]	-
SaU 005	See NWA 1195[15]	445 ± 18[16]	1.0 ± 0.1[4]	67[17]	22-31, 72-65[6]	0.08[17]	0.7013 ± 15
Tissint	See NWA 1195[18-19]	574 ± 20[20]	1.1 ± 0.15[21]	61[5]	21-28, 81-28[18-19]	0.17[5]	0.7008 ± 11
Yamato 980459	See NWA 5798, minus mesostatis phos[22-23]	472 ± 42[24]	1.1 ± 0.2[4]	66[22-23]	9-26, 86-32[6]	0.10[22]	0.7014 ± 21[24]

NWA 7635[25]	porphyritic; mask + px + ol + mt phenocrysts in mask + px + sf groundmass	2403 ± 140	1.1	25	61-56	0.06	0.6999 ± 25
NWA 8159[26]	aphanitic; ol + mt phenocrysts with rims replaced by opx + mt in mask + px groundmass	2370 ± 250	1.2 ± 0.1	25	5, 20-41	0.08	-

Mineral abbreviations: mask = maskelynite; ol = olivine; opx = orthopyroxene; ox = oxides; phos = phosphates; px = pyroxene; sf=sulfide.

[2] Wadhwa et al., 2001; [3] Borg et al., 2003; [4] Nishiizumi et al., 2011; [5] Day et al., 2018 ; [6] Shearer et al., 2008; [7] Irving et al., 2002; [8] Symes et al., 2008; [9] Irving et al., 2004; [10] Kuehner et al., 2011; [11] Irving et al., 2005; [12] Lindsay et al., 2012; [13] Irving et al., 2010; [14] Gross et al., 2011; [15] Goodrich, 2003; [16] Shih et al., 2007; [17] Dreibus et al., 2000; [18] Balta et al., 2015; [19] Sarbadhikari et al., 2016; [20] Brennecka et al., 2014; [21] Nishiizumi et al., 2012; [22] Greshake et al., 2004; [23] Misawa, 2003; [24] Shih et al., 2005; [25] Lapen et al., 2017; [26] Herd et al., 2017

3 Chapter 3

3.1 Introduction

Olivine is one of the major constituent minerals in basaltic rocks from Earth and Mars and is typically the earliest silicate mineral to crystallise. As such, olivine is the best representation of parent magmas, and thus, can be used to understand mantle sources. The mantle of planets can be studied in three ways: 1) using mantle xenoliths, 2) using primitive magma compositions, which can be constrained using olivine, and 3) employing geophysical techniques. In the case of Mars, where mantle xenoliths are absent from among martian meteorites, researchers rely heavily on the analysis of primitive magma compositions alongside geophysical methods, such as seismology, magnetometry, geodesy, and geothermal studies, to investigate the composition and structure of the martian mantle. Unfortunately, there are currently no available mantle-derived rocks that were directly sampled from the martian surface, and instead is primarily inferred from the analysis of olivine and meteorite bulk-rock compositions (i.e., Sr-Nd-Hf isotope studies), specifically shergottites (e.g., Barret et al., 2002; Herd, 2003; Filiberto and Dasgupta, 2011; Shearer et al., 2006, 2008). Recent geophysical investigations, particularly those employing seismic data from NASA's InSight (Interior Exploration using Seismic Investigations, Geodesy and Heat Transport) Mission (Lognonné, et al., 2019; Banerdt et al., 2020), have provided valuable constraints into the structure and composition of the martian mantle (i.e., Khan et al., 2021; Drilleau et al., 2022; Huang et al., 2022). For instance, the findings of these studies revealed mantle potential temperatures of between 1770–2070 ℃ and suggested that the martian mantle contains 10–20 times lower abundances heat-producing elements than the crust (Khan et al., 2021; Drilleau et al., 2022; Huang et al., 2022). Thus, by integrating findings from both meteorite studies and geophysical methods, researchers can establish important connections between observed geophysical properties and the martian mantle's mineralogical composition, as exemplified by the trace element chemistry of olivine in this study. This not only enhances researchers understanding of Mars' internal structure but also elucidates on mantle processes and the planet's thermal evolution, thereby providing a more holistic view of its geological history. Such integrated analyses are crucial for deciphering the complex relationships between composition, structure, and thermal state in planetary mantles, with implications that extend to other terrestrial bodies in the solar system.

The most primitive of the shergottites are the geochemically diverse olivine–phyric shergottites, which are divided into three geochemical groups thought to represent at least three distinct mantle sources. Olivine–phyric shergottites are porphyritic rocks with olivine (± orthopyroxene) megacrysts (up to 3 mm in length) set in a fine–grained groundmass of more Fe-rich olivine, clinopyroxene, maskelynite (shock-altered plagioclase). The olivine megacrysts in these rocks host small (µm-sized) inclusions of Cr-spinel that give the grains a speckled appearance and show extensive networks of shock-induced fractures, cracks and melt veins that are associated with their host meteorites ejection from the martian

surface. These megacrysts are typically the earliest phase to have crystallised, with forsterite contents ($\text{Fo} = \text{molar}\ \frac{\text{MgO}}{\text{MgO+FeO}} \times 100$) as high as Fo_{86} (Yamato 980459; Musselwhite et al., 2006), and as such, can preserve information useful in constraining the composition of their parent melts (e.g., Shearer et al., 2008; Howarth and Udry, 2017). There is much discussion on the origin of olivine in shergottites (i.e., phenocrystic, antecrystic or xenocrystic), as textural and compositional disequilibrium between megacryst and groundmass phases in most of these meteorites is consistent with olivine sorting and accumulation, either in the staging chamber at depth or during ascent to surface (i.e., NWA 1068, Filiberto et al., 2010; LAR 06319, Balta et al., 2013; Tissint, Balta et al., 2015). Olivine megacrysts that represent xenocrysts cannot be used to assess parent melt compositions, while those that represent antecrysts can only be used if they are co–genetic with groundmass material. To date, only a handful of olivine–phyric shergottites have been shown to represent magma compositions where olivine is in equilibrium with bulk-rock compositions. These include Northwest Africa (NWA) 2046 and NWA 4925, as presented in chapter 2 (and Peel et al., 2023), and NWA 5789, NWA 6234 and Yamato 980459 (Y980459) (Musselwhite et al., 2006; Gross et al., 2011, 2013). Of these meteorites, NWA 5789, NWA 6234, and Y980459 are primary mantle derived melts whereas NWA 2046 and NWA 4925 represent more evolved melt compositions.

Constraining the trace element characteristics of martian mantle sources using olivine in olivine-phyric shergottites is not without its issues as very low concentrations of trace element in martian olivine are difficult to accurately measure by conventional laser ablation inductively coupled plasma mass spectrometry (LA–ICP–MS) (e.g., Shearer et al., 2008; Sarbadhikari et al. 2009; Balta et al. 2013; Balta et al. 2015; Howarth and Udry, 2017). The exposure of these meteorites to terrestrial environments during their residence on Earth can also result in these rocks becoming weathered, as terrestrial fluids percolate through cracks, shock melt veins, and mineral fractures. The effects of terrestrial alteration on martian meteorites does vary significantly across the various meteorite landing sites. Meteorites collected from hot desert regions (e.g., Sahara) are typically more altered than those from cold deserts (e.g., Antarctica) as the presence of ice in the latter environments limits the amount interaction these rocks have with liquid water (Sharp et al., 2019). Cold desert weathering is known to affect LREE concentrations and is often accompanied by Ce anomalies, owing to the oxidation of Ce^{3+} to its tetravalent state which is more fluid immobile than trivalent REEs and therefore preferentially retained (Crozaz et al., 2003). Hot desert weathering is also accompanied by LREE enrichment and Ce anomalies, along with Sr, Ba, and U enrichment attributed to secondary carbonates (Barrat et al., 2001; Crozaz and Wadhwa, 2001; Crozaz et al., 2003; Pourkhorsandi et al., 2017; Burgin et al., 2022; Orr et al., 2022).

As one of the earliest liquidus phases and the first silicate mineral to have crystallized from shergottite basaltic melts, olivine megacrysts in olivine-phyric shergottites provide valuable information about the composition and geochemical characteristics of their parent melts and by extension primary martian basaltic magmas. Unfortunately, olivine has a limited set of trace elements that are detectable by conventional LA-ICP-MS techniques (i.e., Ni, Mn, Ca, Co, Cr, Zn, Ti, Cr, V, Sc, Li) whereas highly incompatible elements such as the REEs are generally below detection of such techniques. Using a newly developed LA-ICP-MS technique by Veter et al. (2019), with much higher sensitivity (1.5-fold) than usual techniques, it is now possible to analyse REEs for the first time in olivine (down to ~0.1 ppb) to give insight into the REE evolution of their parent magmas throughout their crystallisation histories. Presented here is the first complete set of REE and other ultra-trace (e.g., Y, Zr, Nb, Yb – see SOM for full list) elements in olivine from shergottites and chassignite and nakhlite examples. The data are first used to assess and look through the effects of terrestrial alteration and Cr-spinel contamination on olivine trace element compositions. Following this, olivine trace element data are used to evaluate the nature and origin of early–formed olivine, assess REE during evolution of their parent magmas by using olivine as a proxy for primary REE of magma prior to any significant magma evolution, and place constraints on the locations of intermediate and enriched shergottite source regions i.e., mantle vs. crust. Additionally, vanadium concentrations measured for olivine in these meteorites were applied to a V-in-olivine oxybarometry (e.g., Shearer et al. 2006; Wang et al., 2019; Nicklas et al., 2021) to determine if fO_2 and La/Yb_{CI} show any variation in olivine specifically rather than previous studies which rely on correlating fO_2 estimates with merrillite or bulk rock REE.

3.2 Samples and analytical techniques

Olivines from 13 martian meteorites, including 11 olivine–phyric shergottites, one nakhlite (NWA 11013), and one chassignite (Chassigny), were analysed for this study. The 11 olivine–phyric shergottites studied were selected to represent all three geochemical groups and include six depleted: Dar al Gani (DaG) 1037, Dhofar (Dho) 019, NWA 2046, NWA 4925, Sayh al Uhaymir (SaU) 005 and Tissint, two intermediate: NWA 6234 and NWA 10170, and three enriched: Larkman Nunatak (LAR) 12011, NWA 1068, and NWA 1183 samples. These meteorites originally collected from several different countries including Algeria (NWA 2046), Antarctica (LAR 12011), Libya (DaG 1037), Mali (NWA 6234), Morocco (NWA 4925, Tissint, NWA 10170, NWA 1068, NWA 1183, and NWA 11013), Oman (Dho 019 and SaU 005), and France (Chassigny) (**Figure 3.1**). The bulk-rock major and trace element concentrations for most of the meteorites analysed in this study are presented in previous studies, including: Dreibus et al. (2000) – SaU 005, Barrat et al. (2002) – NWA 1068, Filiberto et al. (2012) – NWA 6234, Day et al. (2018) – DaG 476/1037, Dho 019, Tissint, LAR 12011, NWA 11013, and Chassigny, and Peel et al. (2023) (chapter 2) – NWA 2046 and NWA 4925. No bulk-rock data are available for NWA 10170 and NWA 1183. The meteorites can be separated into either "falls" or "finds",

based on how they were recovered, with "falls" referring to samples recovered after witnessed landing events and "finds" to those with relatively long residence times on Earth and typically in hot and cold desert environments. Most of these meteorites are hot desert finds, excluding LAR 12011 (Antarctica), which is a cold desert find, and Chassigny (France) and Tissint (Morocco) that are observed falls. Of the meteorites studied here, NWA 1183 is the only sample that has not officially been named but is thought to be paired with NWA 1068 and has been worked on in previous studies (e.g., Shearer et at., 2013; Shearer et at., 2015; Ramsey et al., 2021).

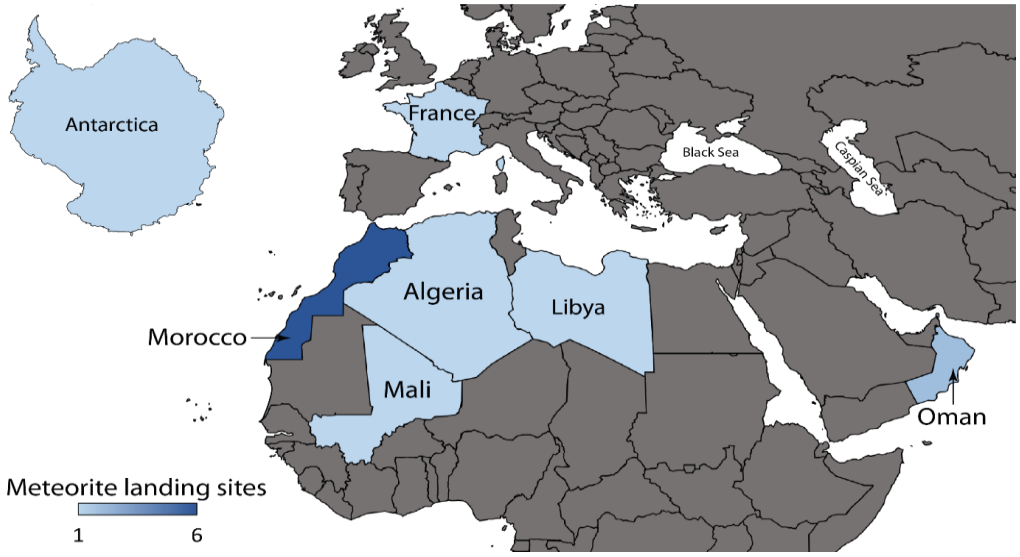

Figure 3.1: Map showing the various countries the shergottite meteorites analysed in this study were collected from.

The olivine-phyric samples analysed here follow on from the study of Ramsey et al. (2021) who presented high-precision EPMA major element data for olivine-chromite pairs with the focus on Al-in-olivine thermometry to constrain crystallisation temperatures. I analysed the same grains and use the EMPA data collected in the Ramsey et al. (2021) study to calculate Fo contents presented here. Most of the olivine grains analysed across the olivine-phyric shergottites represent megacrysts with sizes ranging from 520 μm to 2900 μm, excluding one medium-grained olivine crystal (~360 μm in length) from NWA 10170. This medium-grained olivine does not show the core-to-rim zoning observed in olivine megacrysts but have trace element concentrations that are identical to the megacrysts analysed from the sample. The Fo contents of the olivine megacryst cores and rims analysed in this study are presented in **Table 3.1** and range between 33–83. The least Mg-rich megacryst cores were recorded in Dho 019 (Fo_{44}) and the most Mg-rich in Tissint (Fo_{80}), NWA 4925 (Fo_{81}), and NWA 2046 (Fo_{83}), respectively. The crystallisation and terrestrial ages for each meteorite are also summarised in **Table 3.1**.

Table 3.1: Martian meteorites analysed in this study.

Meteorite		Olivine Fo contents	Crystallisation Age (Ma)	Terrestrial Age (Ka)
Shergottites	*Depleted*			
	DaG 1037	75-61	474±11	60±20
	Dho 019	58-33	586±9	320±70
	NWA 2046	83-47	452*	90±50
	NWA 4925	81-48	460*	420-490
	SaU 005	72-65	445±18	11±1
	Tissint	80-54	574±20	-
	Intermediate			
	NWA 6234	75-56	224±42^{+}	-
	NWA 10170	78-51	-	-
	Enriched			
	LAR 12011	75-52	183±12	-
	NWA 1068	74-52	185±11	>40
	NWA 1183	75-45	185±11^{+}	>40^{+}
Nakhlites	NWA 11013	40-14	1380±40	-
Chassignites	Chassigny	69-68	1380±40	-

* Denotes estimated crystallisation ages

$^{+}$ Denotes data from paired samples

Note: Crystallisation age data taken from the following: DaG 1037/476: Borg et al. (2003); Dho 019: Borg et al (2001); NWA 2046 and NWA 4925: Peel et al. (2023); SaU 005: Shih et al. (2007); Tissint: Brennecka et al. (2014); NWA 6234/2990: Lapen et al. (2013); NWA 1068/1183: Shih et al. (2003); LAR 12011: Righter et al. (2015); NWA 11013 and Chassigny: Udry and Day (2018). Terrestrial ages data taken from the following: DaG 1037/476, NWA 2046, NWA 4925, SaU 005: Nishiizumi et al. (2011); Dho 019: Nishiizumi et al. (2002); NWA 1068/1183/1110: Nishiizumi et al. (2004). Olivine forsterite (Fo) contents are from the following sources: DaG 1037, Dho 019, NWA 2046, NWA 4925, SaU 005, Tissint, NWA 6234, NWA 10170, LAR 12011, NWA 1068, and NWA 1183: Ramsey et at (2021); NWA 11013 and Chassigny: Udry and Day (2018).

The Chassigny and NWA 11013 meteorites analysed here are the same samples analysed in the study Udry and Day (2018) and are on-loan from Arya Udry at the University of Nevada Las Vegas, Las Vegas, USA. The olivine EMPA data collected in the Udry and Day (2018) study was used to calculate Fo contents presented here. Olivine grains analysed from Chassigny are generally medium-grained (~480 μm in length), with Fo contents that range between 68–69 (Udry and Day, 2018). The single olivine grain observed in NWA 11013 (~4 mm in length) has Fo contents that range between 40–14 (Udry and Day, 2018) and is significantly more Fe–rich in comparison to olivine from shergottites and

chassignites but has been included to highlight any differences/similarities between olivine from the different meteorite types.

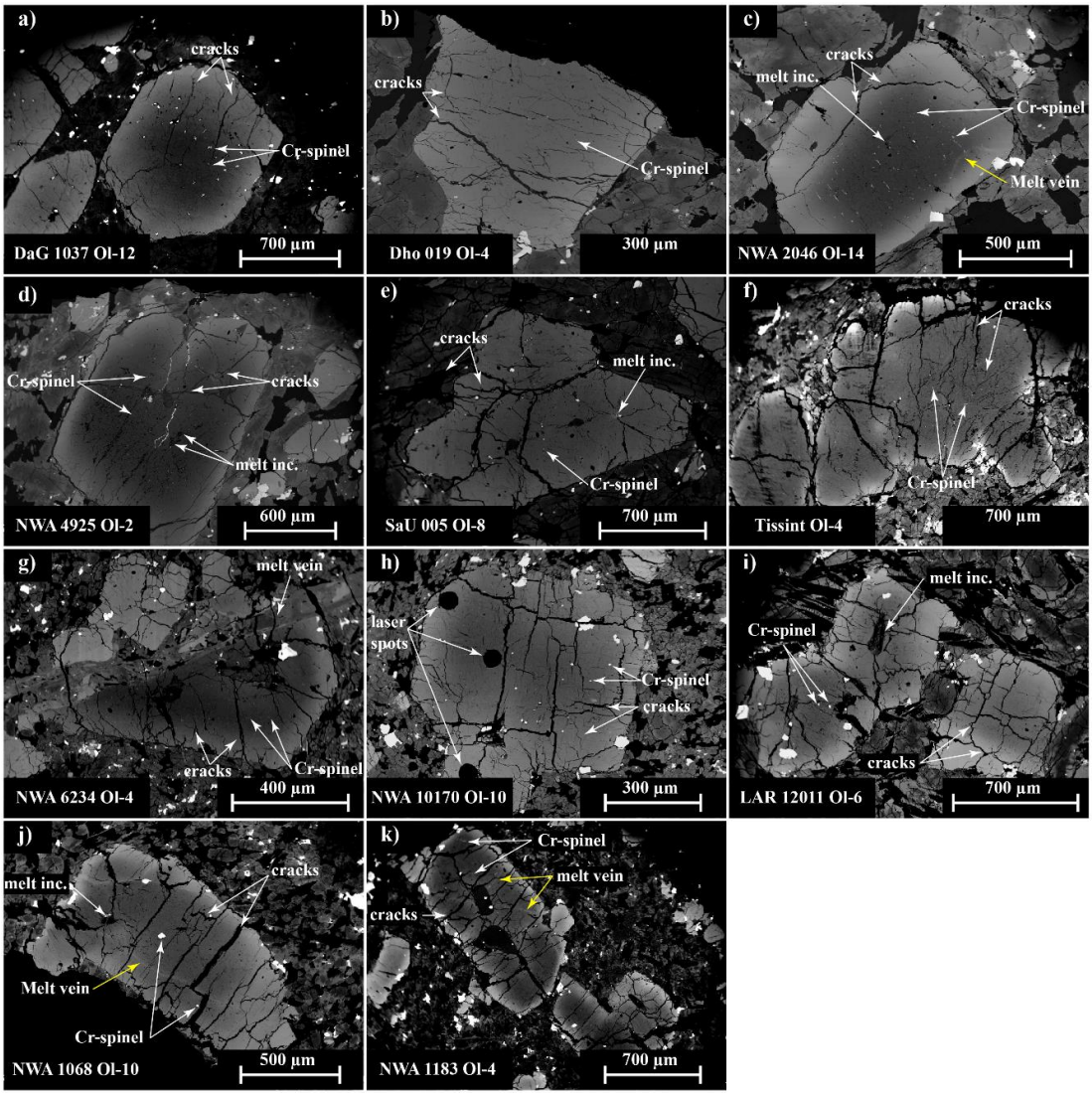

Figure 3.2: Backscattered electron (BSE) images of olivine megacrysts from the various shergottites analysed in this study showing the micron sized Cr-spinel inclusions and networks of shock-induced fractures and cracks within the grains. These BSE images for (a) DaG 1037, (b) Dho 019, (c) NWA 2046, (d) NWA 4925, (e) SaU 005, (f) Tissint, (g) NWA 6234, (h) NWA 10170, (i) LAR 12011, (j) NWA 1068, and (k) NWA 1183, were taken from the study of Ramsey et al., (2021) using a CAMECA SX100 electron probe microanalyzer (EPMA) at the University of Tennessee at Knoxville (UT) and a JEOL JXA-8600 Superprobe at the University of Georgia.

3.2.1 Micro XRF mapping

High–resolution elemental distribution maps were acquired for most of the shergottite meteorites, excluding LAR 12011, using a Bruker M4 Tornado Micro X–ray fluorescence (µXRF) equipped with a Rh–anode X–ray source and housed at the Macquarie University's Department of Earth and Planetary Sciences (Australia). This non–destructive mapping method, in conjunction with petrographic

microscopy observations, was used for phase identification and to visualise element abundance distribution in these meteorites. Analyses were performed at 50 kV and 200 μA, under low vacuum conditions of 18 mbar, using spot sizes of 20 μm and scanning time to 10 ms per spot, which allowed the sensitive imaging of twelve elements (Na, Mg, Al, P, S, Si, K, Ca, Ti, Cr, Mn, Fe) in olivine from each sample.

3.2.2 Laser Ablation Inductively Coupled Plasma – Mass Spectrometry (LA–ICP–MS)

The trace (0.1–1000 ppm) and ultra–trace (<0.1 ppm) element concentrations of olivine megacrysts from the samples in this study were analysed by laser ablation inductively coupled plasma mass spectrometry (LA–ICP–MS), using an Agilent 7700cs quadrupole ICP–MS coupled with a Photon Analyte G2 193nm ArF Excimer laser system equipped with a HelEx II Cell, and housed at Macquarie GeoAnalytical (Department of Earth and Planetary Sciences, Macquarie University, Australia). Analyses were performed using the "hydrogen mode" where a few mL min^{-1} of H_2 are added to the traditionally used Argon (Ar) carrier gas, which has been shown to increase the sensitivity of most elements measured by at least two–fold (e.g., Demouchy and Alard, 2021). The operating parameters were set at a frequency of 10 Hz, an energy density of 7.2 J cm^{-2}, spot size of 100 μm, and counting times of 60 and 220 s for peaks and background, respectively. Plasma torch conditions were optimised to keep the ThO/Th ratio (oxide levels) to a minimum (below 1%).

A total of 82 masses were acquired and separated into two separate analysis programs, each with a list of elements, (i) the "standard" silicates which include REEs and lithophile elements (^{7}Li, ^{23}Na, ^{24}Mg, ^{25}Mg, ^{27}Al, ^{28}Si, ^{29}Si, ^{31}P, ^{39}K, ^{43}Ca, ^{44}Ca, ^{45}Sc, ^{47}Ti, ^{51}V, ^{52}Cr, ^{53}Cr, ^{55}Mn, ^{56}Fe, ^{59}Co, ^{60}Ni, ^{62}Ni, ^{63}Cu, ^{66}Zn, ^{69}Ga, ^{71}Ga, ^{85}Rb, ^{86}Sr, ^{88}Sr, ^{89}Y, ^{90}Zr, ^{93}Nb, ^{133}Cs, ^{137}Ba, ^{138}Ba, ^{139}La, ^{140}Ce, ^{141}Pr, ^{146}Nd, ^{147}Sm, ^{153}Eu, ^{157}Gd, ^{159}Tb, ^{163}Dy, ^{165}Ho, ^{166}Er, ^{169}Tm, ^{172}Yb, ^{175}Lu, ^{178}Hf, ^{181}Ta, ^{208}Pb, ^{232}Th, ^{238}U), and (ii) the "transitional" silicates which include volatile chalcophile and siderophile elements (^{12}C, ^{19}F, ^{25}Mg, ^{27}Al, ^{29}Si, ^{35}Cl, ^{43}Ca, ^{44}Ca, ^{51}V, ^{63}Cu, ^{65}Cu, ^{69}Ga, ^{71}Ga, ^{72}Ge, ^{73}Ge, ^{74}Ge, ^{75}As, ^{79}Br, ^{89}Y, ^{93}Nb, ^{95}Mo, ^{98}Mo, ^{107}Ag, ^{109}Ag, ^{111}Cd, ^{112}Cd, ^{114}Cd, ^{115}In, ^{118}Sn, ^{120}Sn, ^{121}Sb, ^{123}Sb, ^{127}I, ^{140}Ce, ^{153}Eu, ^{172}Yb, ^{178}Hf, ^{182}W, ^{183}W, ^{184}W, ^{185}Re, ^{187}Re, ^{205}Tl, ^{208}Pb, ^{209}Bi, ^{238}U). The data were then reduced using GLITTER software (Griffin et al., 2008), which allows for the careful inspection of the time–resolved analyses and subsequent removal of heterogeneity present in the analysed volume. These heterogeneities might be the product of mixed analyses or inclusions present in the sample and should therefore be excluded. Reference glasses BCR2–G and NIST (National Institute of Standards and Technology) 612 and several natural olivine standards including SCOL-1 (San Carlos olivine; Köhler and Brey, 1990), 355OL (Bussweiler et at., 2019), ALM-1 (Almklovdalen, Norway), MongOL and Sh11–2 (Batanova et al., 2019), were used for quality control (as a means of confirming the accuracy of the analyses). The synthetic silicate reference glass NIST 610 was used as the external standard for the calibration of measurements and ^{29}Si as the internal standard, with the silica content (SiO_2 wt%.) previously

determined by EPMA. For minor- and trace-elements, reproducibility of the reference glass standards was generally better than 10% (relative standard deviation or RSD).

3.3 Summary of olivine in martian meteorites

3.3.1 Olivine-phyric shergottites

Olivine megacrysts (between 520–2900 μm in length) in the olivine-phyric shergottites are subhedral to euhedral in shape with modal abundances ranging from 7 to 29 vol. %. These megacrysts are found either as discrete crystals or clusters of grains (glomerocrysts), with those from the depleted shergottites sometimes showing parallel alignment along crystallographic directions (**Figure 3.3**). Olivine megacrysts across these meteorites are zoned from Mg-rich cores to Fe-rich rims. Megacryst cores from several of these samples including Dho 019, Tissint, NWA 6234, NWA 1068, and NWA 1183, are nearly homogeneous in composition and suggest slower cooling rates during the initial growth of olivine crystals (e.g., Barrat et al., 2002; Taylor et al., 2002; Gross et al., 2013; Shearer et al., 2013; Balta et al., 2015; Sarbadhikari et al. 2016). Megacrysts in these rocks host melt inclusions with varying degrees of crystallization (see Chapter 4), along with micron-sized Cr-spinel inclusions predominantly in the core regions of megacrysts, and coarser grained oxides (between 10 and 150 μm) that are present in rims and absent in cores (**Figure 3.2**). Extensive networks of shock-induced fractures, cracks and melt veins, are observed cross-cutting olivine megacrysts in all cases (Fig. 2). In some cases, megacrysts have embayed or irregular boundaries (e.g., DaG 1037, SaU 005, NWA 1068, and NWA 1183).

X-ray elemental maps for several of these samples including DaG 1037, NWA 2046, NWA 4925, SaU 005, and NWA 1068, show that fractures and cracks cross-cutting olivine megacrysts have been infilled by secondary Ca-rich (likely calcite) material (**Figure 3.3**). Olivine megacrysts from NWA 4925 are the most pervasively altered by these secondary carbonate-filled veins, where more severely altered megacrysts from the interior of the sample have Ca-rich zones towards their cores (**Figure 3.3b**). Calcium-rich regions towards megacryst cores have also been observed in NWA 6234, NWA 10170, and NWA 1183, along with a pronounced Ca-rich melt vein in NWA 6234 that cuts as a straight line through the sample. Megacryst cores enriched in Ca also appear to be enriched in K and depleted in Mg. These features were previously observed in the weathering rind of NWA 4925 in chapter 2 and reflect the effects of more severe olivine alteration.

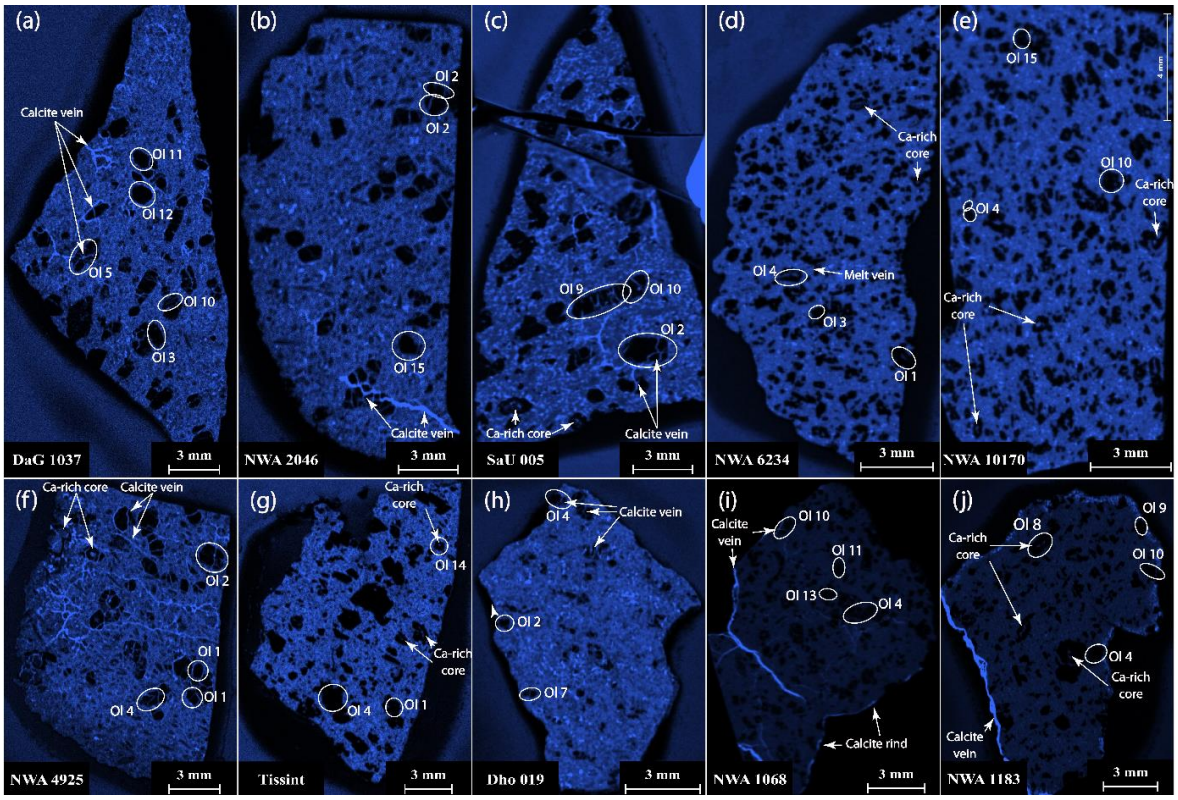

Figure 3.3: Calcium X-ray elemental maps for the shergottite meteorites analysed in this study, excluding LAR 12011, showing Ca-enriched in shock-induced fractures present in olivine megacrysts from (a) DaG 1037, (b) NWA 4925, (c) NWA 2046, (d) Tissint, (e) SaU 005, (f) NWA 6234, (g) NWA 1068, (h) NWA 10170, (i) NWA 1183.

3.3.2 Nakhlite and Chassignite meteorites

The nakhlite, NWA 11013, is a cumulate textured clinopyroxenite, composed primarily of subhedral and acicular clinopyroxene grains and a single large olivine grain (~4 mm in length), set in a fine-grained interstitial mesostasis. The single olivine grain in NWA 11013 accounts for ~12 vol. % of the sample, shows an elongated and rectangular prism like appearance, and poikilitically encloses finer grained clinopyroxene grains equidistantly from its core (Udry and Day, 2018).

Chassigny is a cumulate textured dunite composed of anhedral to subhedral olivine grains with chromite inclusions and interstitial material. Olivine grains in Chassigny range between 0.1 and 2.4 mm in length and account for ~91 vol. %. These olivine grains host melt inclusions exhibiting varying degrees of crystallisation and are crosscut by shock-induced planar fractures that are likely related to its ejection from Mars.

3.4 Results: Trace and ultra-trace elements in olivine

Trace elements measured in olivine from these meteorites were studied in-depth and plotted: (1) Ni and Mn as proxies for melt evolution; (2) Cr and Al as a proxy for spot contamination by Cr-spinel during

laser analyses; (3) V to evaluate the effects of oxidation-induced exsolution of Cr-spinel during olivine evolution, and subsequently, constrain the fO_2 of their parental melts; (4) Sr and Ba to track and assess the effects of terrestrial alteration related to the carbonate-rich veins cross-cutting olivine; (5) REE, multi-incompatible trace-elements, and high field strength element (HFSE i.e., Zr/Y, Nb/Y, Hf/Y) ratios to evaluate their primary melt ratios and possibly constrain their mantle sources.

3.4.1 Depleted olivine–phyric shergottites

The results for the depleted shergottites have been divided into three subgroups based on bulk-rock trace element and isotopic data previously collected for these samples that suggest distinct parental magma sources (i.e., Brennecka et al., 2014; Ramsey et al., 2021; Peel et al., 2023; Aucamp et al., 2023). Samples DaG 1037, NWA 2046, NWA 4925, and SaU 005, with crystallisation ages between 440–470 Ma, are thought to represent a co-magmatic suite (Aucamp et al., 2023) and are presented together below, while the considerably older (570–590 Ma) but isotopically dissimilar meteorites, Tissint and Dho 019, are discussed separately.

3.4.1.1 DaG 1037, NWA 4925, NWA 2046, and SaU 005

Trace element concentrations were measured across twelve (7 cores and 5 rims; $Fo_{75–62}$) olivine in DaG 1037, eleven (9 cores and 2 rims; $Fo_{80–53}$) in NWA 4925, seven (4 cores and 3 rims; $Fo_{83–50}$) in NWA 2046, and five (3 cores and 2 rims; $Fo_{72–66}$) in SaU 005. The cores of olivine megacrysts in these samples have higher Ni (430–727 ppm), V (21–52 ppm), and Cr (514–2993 ppm) and lower Co (83–121 ppm) and Mn (2667–4294 ppm) concentrations relative to rims (i.e., 210–409 ppm Ni, 16–33 ppm V, 270–950 ppm Cr, 106–163 ppm Co, and 3714–5946 ppm Mn). Megacryst cores from NWA 2046 and NWA 4925 also have higher concentrations of Ca (1716–4990 ppm) relative to rims (1518–1845 ppm). Similarly, megacryst cores from SaU 005 show more variable concentrations of Ca (2026–2412 ppm) that extend to higher values than those of megacryst rims (2126–2247 ppm). In contrast, megacryst cores from DaG 1037 show lower concentrations of Ca for (1367–1612 ppm) relative to rims (1615–2289 ppm). Olivine across these samples plot along common trends and yield strong (R^2 of 0.78–0.94) positive correlations between Mn–Co and moderate to strong (R^2 of 0.63–0.97) negative correlations between Mn–Ni and Ni–Co, excluding NWA 4925 from the latter which does overlap with the other samples but shows more scatter (**Figure 3.4a, e-f**). Weak to moderate (R^2 of 0.39–0.25) positive correlations between Ni–Ca were observed for NWA 2046 and NWA 4925, a strong negative (R^2 of 0.77) correlation for DaG 1037, and no correlation for SaU 005 (**Figure 3.4b**). Strong (R^2 of 0.86–0.94) positive correlations between Cr–V, along with positive correlations (R^2 of 0.37–0.83) between Ni–V and Cr–Al, and negative correlations (R^2 of 0.49–0.64) between V–Mn were also observed for olivine across these samples, excluding those of SaU 005, which show no correlations against V **Figure 3.4d, g-h**). One of the SaU 005 megacryst cores shows higher concentrations of Al, V, and Cr, relative to the other grains analysed from this sample.

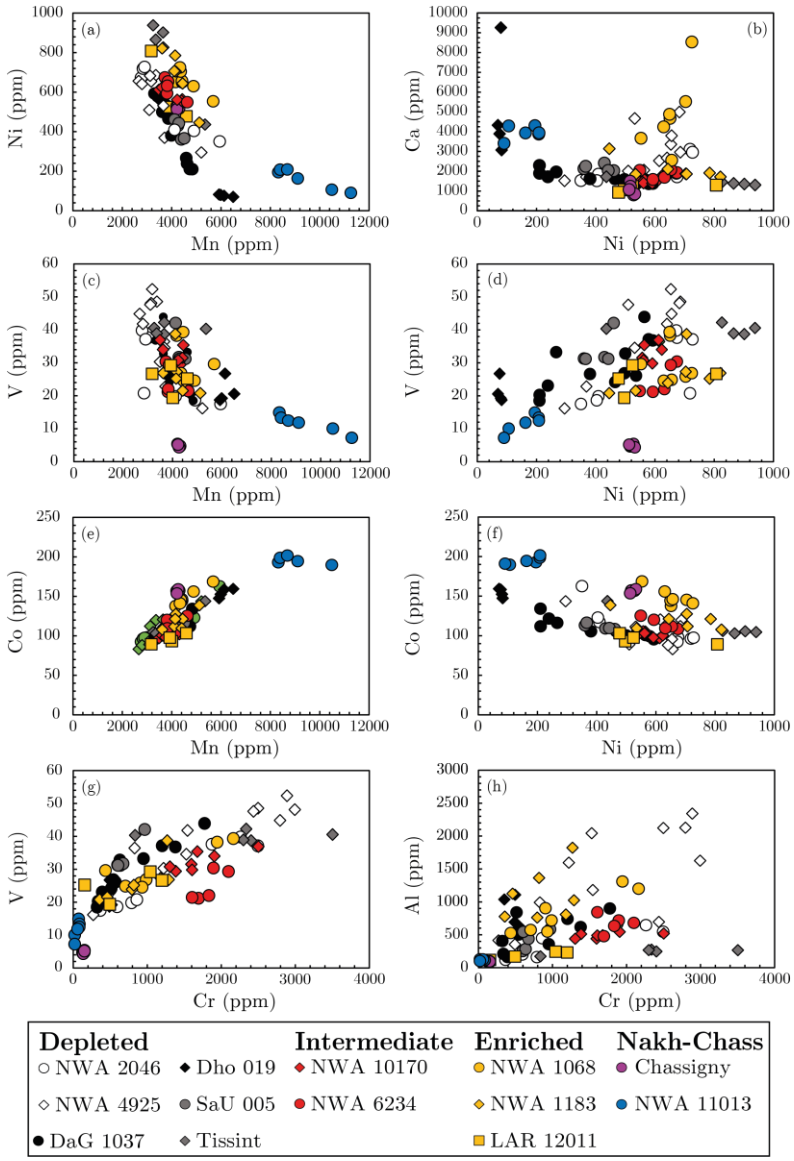

Figure 3.4: Olivine trace elements trends using Ni and Mn as proxies for melt evolution against (a) each other, (b) Ca, (c-d) V, and (e-f) Co. Olivine Cr concentrations were also plotted against (g) V and (h) Al to test for Cr-spinel contamination.

The concentrations of LREE (La–Eu), Ba and Sr for NWA 4925 (0.0005–0.03 ppm, 23–204 ppm, and 3–31 ppm) and NWA 2046 cores (0.0004–0.08 ppm, 42–94 ppm, 7–13 ppm) are generally higher and vary considerably in comparison to NWA 2046 rims (<0.001 ppm, 0.1–4.6 ppm, 0.1–1.5 ppm), DaG 1037 (<0.003 ppm, 1.8–5.8 ppm Ba, 4.2–10.2 ppm Sr), and SaU 005 (<0.001 ppm, 4.0–9.0 ppm, 13–21 ppm). Olivine megacrysts from NWA 2046 and NWA 4925 also show similar concentrations of HFSEs (i.e., Y, Zr, Nb, and Hf) that range between 0.075–0.350 ppm Y, 0.02–0.62 ppm Zr, 0.0003–0.010 ppm Nb, and 0.0002–0.008 Hf. The concentrations of Nb in megacrysts from DaG 1037 and SaU 005 extend to lower values than those of NWA 2046 and NWA 4925, while the concentrations of Zr and Hf in NWA 4925 megacrysts are generally higher and more variable than those of DaG 1037, NWA 2046, and SaU 005. For NWA 2046 and DaG 1037, strong negative and positive correlations were observed

between Ni–Y (R^2 of 0.81–0.94) and Ni–Nb (R^2 of 0.84–0.95), and no correlations between Ni–Zr and Ni–Hf owing to elevated concentrations of Zr and Hf in megacryst cores relative to rims (**Figure 3.5a-d**). For NWA 4925, a strong positive correlation was observed between Ni–Y (R^2 of 0.77) and no correlations between Ni–Zr, and Ni–Nb, Ni–Hf, with elevated concentrations of Y, Zr, and Hf, for megacryst cores to rims. For SaU 005, strong positive correlations were observed between Ni–Hf, Ni–Zr, and Ni–Nb (R^2 of 0.82–0.93), and a strong negative correlation between Ni–Y (R^2 of 0.74).

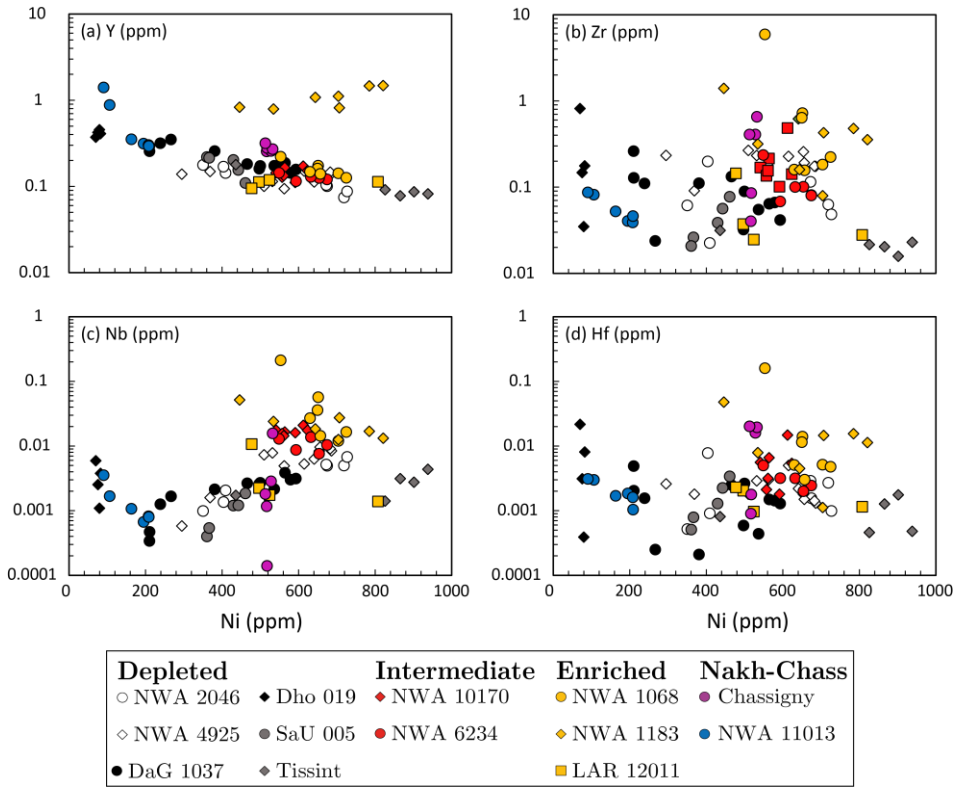

Figure 3.5: Olivine trace elements trends for Ni against HFSEs (ppm) including (a) Y, (b) Zr, (c) Nb, and (d) Hf.

The CI–chondrite normalised REE patterns (**Figure 3.6c-d**) for NWA 4925 and NWA 2046 megacryst cores are LREE–depleted, with $(La/Yb)_{CI}$ ratios of 0.01–0.29 (*n=11*; NWA 4925) and 0.05–0.08 (*n=4*; NWA 2046), but display upward inflections of LREEs (La–Sm) that produce concave-up to flat LREE patterns and positive Eu anomalies (i.e., Eu_{CI} /$[Sm_{CI}*Gd_{CI}]^{0.5}$) of 2.7–7.8 (NWA 4925) and 2.9–4.3 (NWA 2046). The REE patterns for NWA 2046 rims, DaG 1037, and SaU 005 are significantly more LREE-depleted, with $(La/Yb)_{CI}$ ratios of ~0.0004 (*n=1*; NWA 2046), 0.0004–0.02 (*n=12*; DaG 1037), and 0.001–0.006 (*n=4*; SaU 005), respectively (**Figure 3.6a, c, e**). Several grains from DaG 1037 (6 cores and 3 rims) show positive La anomalies and more concave-up LREE patterns between La–Sm, while one SaU 005 core shows an upward inflection from Pr to Ce, and one NWA 2046 rim a positive La anomaly. Additionally, the concentrations of HREEs (Ho–Lu) in NWA 2046 and DaG 1037 cluster into two distinct groups with higher $(Ho/Lu)_{CI}$ ratios for cores (i.e., 0.30–0.40, NWA 2046; 0.39–0.62 DaG 1037) relative to rims (i.e., 0.15–0.29, NWA 2046; 0.16–0.28, DaG 1037). The olivine CI–Chondrite normalised incompatible trace element (ITE) patterns across these samples (**Figure 3.7a, c-**

e) show positive Ba, U, and Sr anomalies, moderate positive Zr–Hf and Ti anomalies, and minor positive Y anomalies, with notably lower concentrations of Rb, Ba, Th, Sr and LREEs (La–Eu) for DaG 1037, SaU 005, and NWA 2046 rims relative to those of NWA 4925 and NWA 2046 cores. Olivine grains in NWA 2046 and DaG 1037 also cluster into two distinct groups based on their Ti concentrations, with lower values for cores (i.e., 24–39 ppm, NWA 2046; 24–46 ppm, DaG 1037) relative to rims (i.e., 62–106 ppm, NWA 2046; 31–133 ppm, DaG 1037).

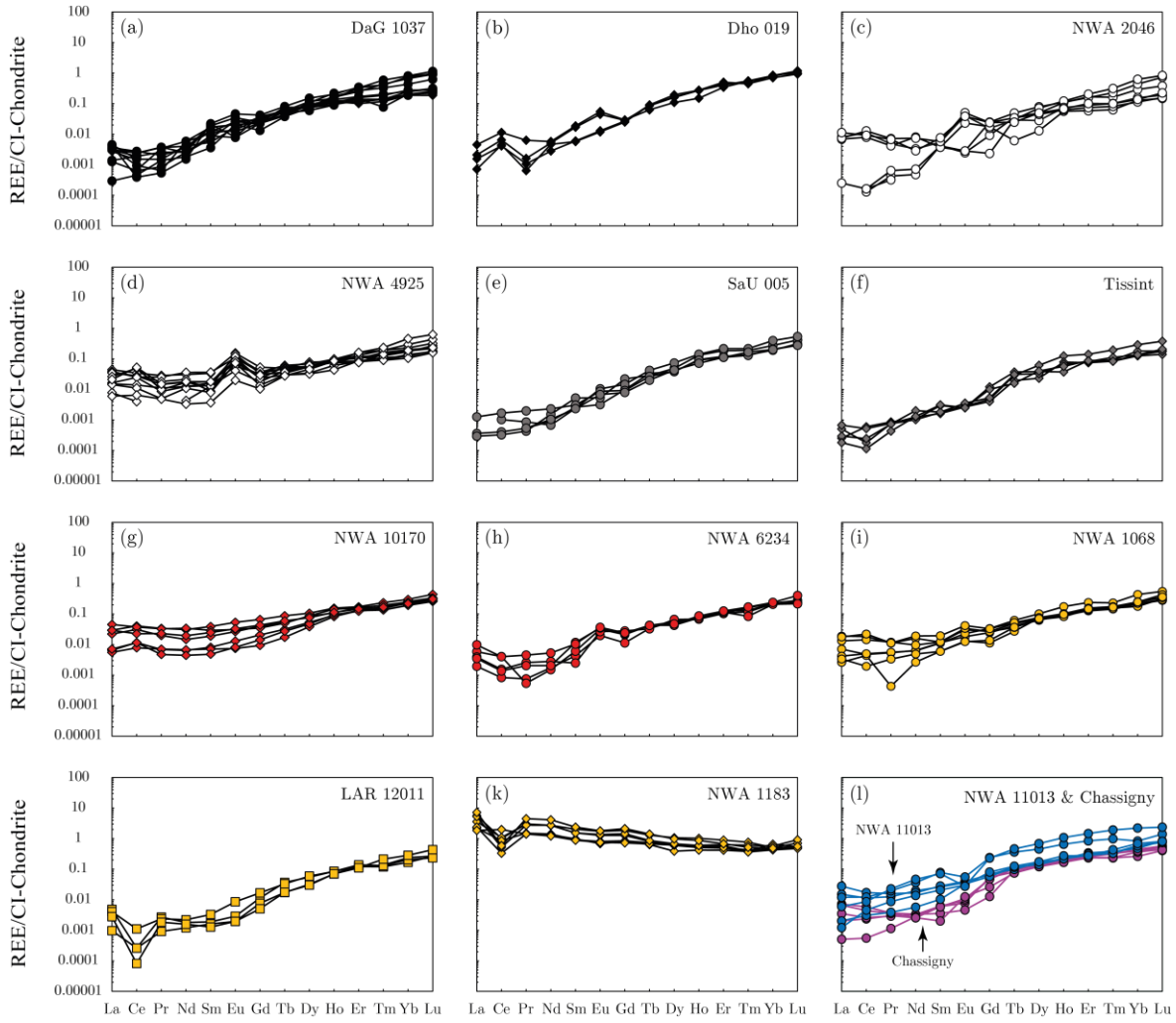

Figure 3.6: CI-chondrite normalised rare earth element (REE) patterns for olivine grains analysed across the martian meteorites. Chondrite normalisation values taken from McDonough and Sun (1995).

For NWA 2046 and NWA 4925, moderate to strong positive correlations were observed for Ba against Sr, as well as for each against V, Nb, Eu/Eu*, and $(La/Yb)_{CI}$ (R^2 of 0.59–0.99; Figure 9a-h), and no correlations against Y, Zr, and Hf. For DaG 1037, moderate positive correlations were observed for Sr against Ba and La/Yb_{CI} and for V against $(La/Yb)_{CI}$ (R^2 of 0.50–0.58), and no correlations for Ba and Sr against Y, Zr, Nb, and Hf (Figure 9a-h). For SaU 005, no clear correlations were observed for Sr against Ba, as well as for each against La/Yb_{CI}, V, Y, Zr, Nb, and Hf, with higher concentrations of HFSEs in megacryst cores relative to rims.

3.4.1.2 Tissint

Five olivine, 4 cores and 1 rim ($Fo_{80–55}$), were analysed from Tissint. Olivine cores from this sample have higher Ni (826–938 ppm) and Cr (2299–3503 ppm), and lower Mn (3252–3662 ppm) and Co (103–106 ppm) concentrations relative to the rim (i.e., 436 ppm Ni, 836 ppm Cr, 5353 ppm Mn, and 144 ppm Co), but show similar concentrations of V (39–42 ppm for cores vs 40 ppm for rims). Megacryst cores have lower concentrations of Ca (1305–1450 ppm) relative to megacryst rims (~1722 ppm). A strong positive correlation that overlaps with the main depleted shergottite trend has been observed between Mn–Co (R^2 of 0.97), strong negative correlations that plots above the main trends for Mn–Ni and Ni–Co (R^2 of 0.96), and a strong negative correlation (R^2 of 0.98) that partially overlaps with DaG 1037 between Ni–Ca (**Figure 3.4a-b, e-f**). No clear correlations were observed for V against Cr, Mn, and Ni, and for Cr against Al. Two of the megacryst cores analysed from this sample show distinctly higher V concentrations (i.e., 41–42 ppm vs 38–39 ppm).

The concentrations of LREE (La–Eu, <0.0005 ppm), Ba (<0.01 ppm) and Sr (<0.07 ppm) in these grains are low compared to olivine in other samples, while their Y (0.078–0.179 ppm), Zr (0.02–0.03 ppm), Nb (0.001–0.004 ppm), and Hf (0.0005–0.002), concentrations overlap consistently with the other depleted meteorites. Strong negative correlations were observed between Ni–Y and Ni–Zr (R^2 of 0.75–0.97), and weak positive to no correlations between Ni–Nb and Ni–Hf (R^2 of <0.37; **Figure 3.5a-d**).

The olivine CI–normalised REE patterns for Tissint are LREE–depleted, with $(La/Yb)_{CI}$ ratios of 0.001–0.01. Four olivines (3 cores and 1 rim) show minor positive La anomalies, with two of the cores also showing negative Eu anomalies between 0.42–0.45 (**Figure 3.6f**). Olivine CI–normalised ITE patterns are characterised by positive U, Pb, Sr, Zr–Hf and Ti anomalies, and minor positive Y anomalies (**Figure 3.7f**). Two olivine cores with the highest $(La/Yb)_{CI}$ values have significantly higher Pb concentrations (i.e., 0.12–0.17 vs 0.002–0.005, *n=3*) that result in more pronounced positive anomalies. A moderate (R^2 of 0.60) positive correlation has been observed between Ba and $(La/Yb)_{CI}$ (**Figure 3.8c**), and no correlations for Ba against Sr or for each against V, Y, Zr, Nb, and Hf (Figure 9a-b). Three of the olivine cores appear to be enriched in Nb relative to the megacryst rim, with two also showing elevated Hf and Pb concentrations.

3.4.1.3 Dho 019

The four olivine ($Fo_{53–39}$) analysed from Dho 019 include 3 megacryst cores and 1 rim. Olivine cores have higher Ni (76–82 ppm) and Cr (489–519 ppm) and lower Mn (5920–6124 ppm) concentrations relative to the rim (i.e., 70 ppm Ni, 382 ppm Cr, and 6494 ppm Mn). Megacryst cores also show more variable concentrations of V (19–27 ppm) and Ca (3072–9464 ppm) overlap with and extend to higher values that those of the megacryst rim (21 ppm V and 4328 ppm Ca). Strong negative correlations were observed between Mn–Ni and Ni–Co (R^2 of 0.84–0.96) and a moderate positive correlation between

Mn–Co (R^2 of 0.68) (**Figure 3.4**a, e-f). A strong positive correlation between Mn–V (R^2 of 0.97) and strong negative correlations between Ni–V and Cr–Al (R^2 of 0.99) were observed for most of the grains (*n=3*), excluding one megacryst core with anomalously high Al and V concentrations, and no correlation between Cr–V (**Figure 3.4c-d, g-h**). A strong (R^2 of 0.99) negative correlation was also observed between Ni–Ca for most of the grains (*n=3*), excluding one megacryst core with anomalously high Ca (**Figure 3.4b**).

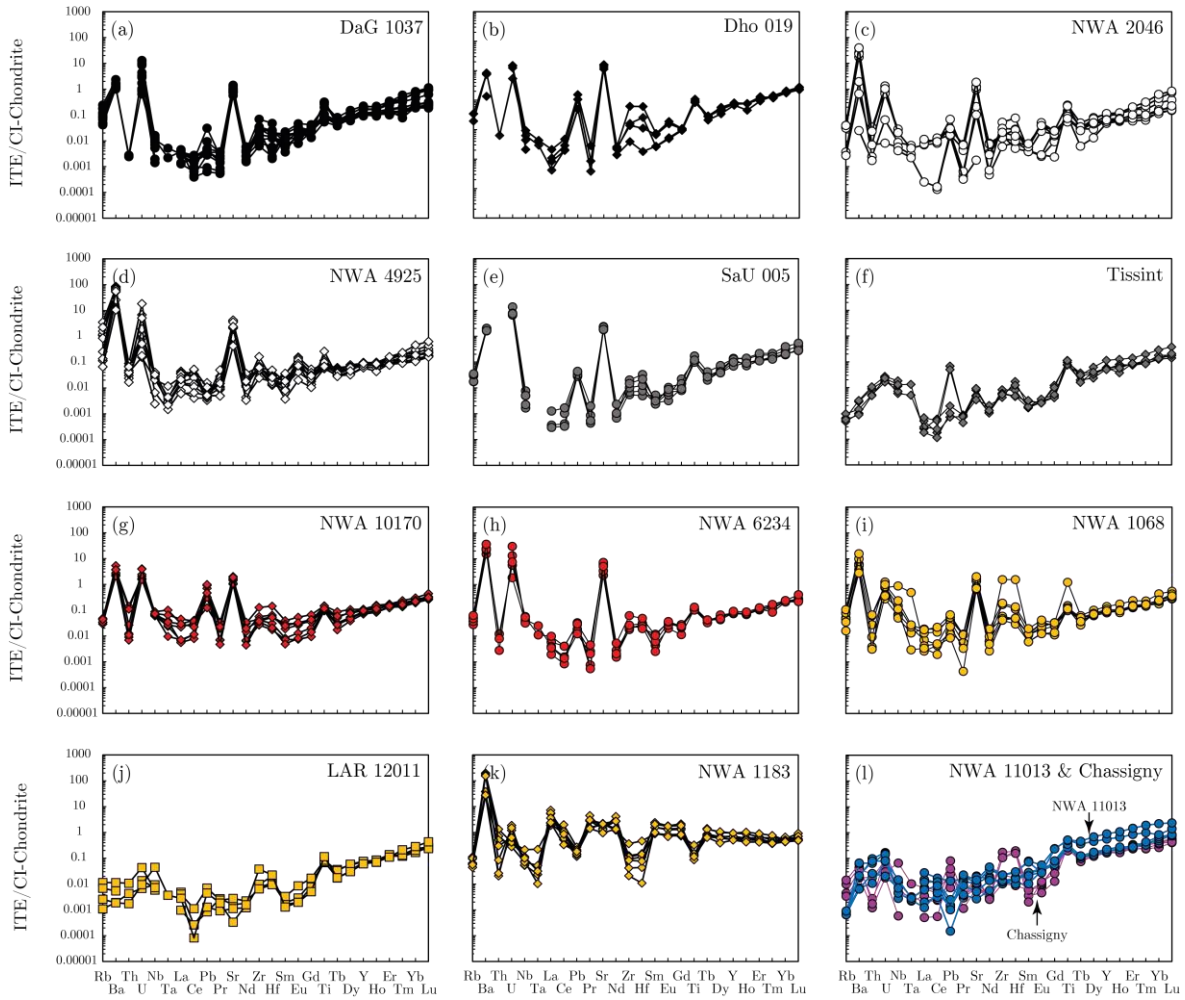

Figure 3.7: CI-chondrite normalised incompatible trace element (ITE) patterns for olivine grains analysed across the martian meteorites. Chondrite normalisation values taken from McDonough and Sun (1995).

The concentrations of LREEs, Ba, Sr, Y, Zr, Nb, and Hf in these grains range between 0.0001–0.007 ppm, 1.2–10.3 ppm, 43–64 ppm, 0.372–0.455 ppm, 0.03–0.82 ppm, 0.001–0.006 ppm, and 0.0004–0.02, respectively. Strong negative correlations between Ni–Hf, Ni–Zr, and Ni–Nb (R^2 of 0.90–0.98), and a strong positive correlation between Ni–Y (R^2 of 0.99), were also observed for most of the grains (*n=3*) excluding the more Ni-rich megacryst core analysed from this sample (**Figure 3.5**a-d). Olivine CI–normalised REE patterns for Dho 019 are LREE-depleted and characterised by $(La/Yb)_{CI}$ ratios of 0.0008–0.006 (**Figure 3.6b**) but show elevated La–Pr concentrations and positive Ce anomalies between 2.1–6.5, two of which also display positive Eu anomalies (2.0–2.3). The ITE patterns for these grains

are consistent with DaG 1037 rims, but show more pronounced Ba, Pb, Sr, Zr–Hf, and Ti anomalies (**Figure 3.7b**). Strong (R^2 of 0.84–0.97) positive correlation were observed for Ba against Sr (**Figure 3.8a**), and for each against Ce/Ce*, along with strong negative and positive correlations for Sr against Y and Nb (R^2 of 0.73–0.75), and weak to moderate positive correlations Sr against Zr and Hf.

3.4.2 Intermediate olivine–phyric shergottites

3.4.2.1 NWA 6234 and NWA 10170

Five olivines ($Fo_{75–60}$) were analysed from NWA 6234 and seven ($Fo_{75–62}$) from NWA 10170. These include four megacryst cores and one rim for NWA 6234, and five megacrysts cores, one megacryst rim and one medium-grained olivine from NWA 10170. Olivine in these samples have Mn, Cr, Ni, Co, and V concentrations of 3729–4634 ppm Mn, 1607–2098 ppm Cr, 549–674 ppm Ni, 109–125 Co ppm and 21–30 ppm V, in NWA 6234, and 3487–4433 ppm Mn, 1306–2502 ppm Cr, 541–623 ppm Ni, 97–106 Co ppm, 29–37 ppm V, in NWA 10170. The concentrations of Ca in megacryst from NWA 6234 (1580–2075 ppm) and NWA 10170 (1392–1761 ppm) are more variable and extend to higher values than rims from each sample (~2044 and 1457–1761 ppm).

Olivine in both samples yield moderate to strong negative correlations that plot above the main depleted trend between Mn–Ni (R^2 of 0.68–0.85), as well as moderate to strong positive correlations that overlap with the main trend between Mn–Co (R^2 of 0.64–0.82), and weak negative correlations between Mn–V (**Figure 3.4a, c, e**). The concentrations of Co in olivine from NWA 10170 also plot consistently with the depleted shergottites against Ni, while those of NWA 6234 plot above the main trend and partially overlap with Tissint (**Figure 3.4f**). No correlations were observed for NWA 6234 in plots of Ni–V, Cr–V, and Cr–Al (**Figure 3.4d, g-h**). Two of megacryst cores analysed from NWA 6234 show higher concentrations of Cr (1895–2095 ppm), Al (681–717 ppm), V (29–31 ppm), relative to other cores analysed from this sample (i.e., 1694–1834 ppm Cr, 478–634 ppm Al, 21–22 ppm V). Olivine grains from NWA 10170 yield a moderate (R^2 of 0.69) positive correlation between Cr–V, a weak (R^2 of 0.32) positive correlation between Cr–Al, and no clear correlation between Ni–V and Mn–V (**Figure 3.4c-d, g-h**). Grains with >4000 ppm Mn appear to be enriched in V relative to those with <4000 ppm Mn. A weak (R^2 of 0.28) negative correlation was also observed for NWA 10170 between Ni–Ca and no clear correlation for NWA 6234 (**Figure 3.4b**).

Olivine grains from NWA 6234 are characterised by LREE, Ba, Sr, and Pb concentrations that range between <0.003 ppm, 37–88 ppm, and 17–52 ppm, and 0.03–0.08 ppm, respectively, while those of NWA 10170 are generally more enriched in LREEs (0.0001–0.02 ppm) and Pb (0.31–2.44 ppm) and more depleted in Ba (5.2–14 ppm) and Sr (7.6–15 ppm). The concentrations of HREEs (Gd–Lu) and HFSEs in olivine from both samples overlap consistently with each other and range between 0.001–0.05

ppm, 0.111–0.172 ppm Y, 0.07–0.24 ppm Zr, 0.008–0.021 ppm Nb, and 0.002–0.005 ppm Hf, excluding one NWA 10170 megacryst core with much higher Zr (0.49 ppm) and Hf Zr (0.015 ppm) concentrations. The concentrations Y in olivine from NWA 6234 are also generally lower and less variable than those of NWA 10170. For NWA 6234, a strong (R^2 of 0.84) negative correlation was observed between Ni–Hf, and no correlations for Ni–Y, Ni–Nb, and Ni–Zr (**Figure 3.5a-d**). For NWA 10170, no clear correlations were observed between Ni–Y, Ni–Zr, Ni–Nb, and Ni–Hf. The olivine CI–normalised REE patterns for both samples are LREE–depleted, with $(La/Yb)_{CI}$ ratios of 0.01–0.04 for NWA 6234 and 0.03–0.19 for NWA 10170 (**Figure 3.6g-h**). Flat to concave up LREE patterns have been observed for both samples, along with positive Eu* (2.2–2.8; *n=4*) anomalies for NWA 6234 and positive Ce (1.2–2.0; *n=5*) anomalies for NWA 10170. Olivine CI–normalised ITE patterns for both samples are comparable to the depleted shergottites and to each other, although megacrysts from NWA 6234 show more pronounced Ba, U, and Sr and less pronounced Pb anomalies relative to those of NWA 10170 (**Figure 3.7g-h**).

For NWA 6234, strong positive correlations were observed for Ba against Y and Zr, as well as for Sr against U (R^2 of 0.89–0.97), and strong positive correlations along two distinct trends for Sr against Ba (**Figure 3.8a**) and Zr, for Ba against U (R^2 of 0.79–0.99). A moderate positive correlation was also observed for Ba and Eu* (R^2 of 0.60; **Figure 3.8e**) and no correlations for Ba and Sr against $(La/Yb)_{CI}$, V, Nb, and Hf (**Figure 3.8b-d, g-h**). The two olivine grains with the highest Ba concentrations show elevated Hf concentrations that correlate directly with Ba enrichment, as well as significantly higher $(La/Yb)_{CI}$ ratios. For NWA 10170, strong positive correlations were observed for Sr against Ba (**Figure 3.8a**) and U (R^2 of 0.81–0.86), and no correlations for each against $(La/Yb)_{CI}$, V, Y, Nb, and Hf (**Figure 3.8b-d, g-h**). Grains with >7 ppm Ba (or 10.5 ppm Sr; *n=4)* are generally more enriched in LREEs, Y, Zr, Nb, and Hf, relative to those with <7 ppm Ba.

3.4.3 Enriched olivine–phyric shergottites

3.4.3.1 NWA 1068, LAR 12011, and NWA 1183

Four olivine megacrysts (2 core and 2 rims; $Fo_{75–52}$) were analysed from LAR 12011, seven (6 core and 1 rim; $Fo_{74–69}$) from NWA 1068 and seven (5 cores and 2 rims; $Fo_{75–45}$) from NWA 1183. As with the depleted shergottites, the cores of olivine megacrysts in these samples have higher Ni (524–821 ppm), Cr (705–2163 ppm), and V (24–39 ppm) and lower Mn (3175–4888 ppm) and Co (89–156 ppm) concentrations, relative to rims (i.e., 446–553 ppm Ni, 155–494 ppm Cr, 21–30 ppm V, 4007–5684 ppm Mn, and 93–169 ppm Co). Megacryst cores from NWA 1068 and LAR 12011 have higher concentrations of Ca (1230–1293 and 2553–8533 ppm, respectively) relative to megacryst rims (937–1057 and ~3668 ppm, respectively). In contrast, concentrations of Ca in megacryst cores from NWA 1183 (1718–2110 ppm) are generally lower than values for megacryst rims (1848–2110 ppm).

For LAR 12011, moderate negative and strong positive correlations that overlap with the main depleted trends were observed between Ni–Co (R^2 of 0.58) and Mn–Co (R^2 of 0.84), and a strong (R^2 of 0.82) negative correlation that plots above but partially overlaps with the main depleted trend between Mn–Ni (**Figure 3.4a, e-f**). A strong positive correlation was also observed between Cr–Al (R^2 of 0.95), no correlations for V against Cr, Mn, and Ni, and a moderate (R^2 of 0.57) positive correlation between Ni–Ca (**Figure 3.4b-d, g-h**). The two megacrysts cores analysed from this sample are significantly more enriched in Al, V, and Cr, relative to the rims. For NWA 1068, moderate to strong correlations parallel to but above the main depleted trends were observed between Mn–Ni, Mn–Co, and Ni–Co (R^2 of 0.67-0.97), strong positive correlations between Cr–V and Cr–Al (R^2 of 0.76–0.85), and a weak (R^2 of 0.46) positive correlation Ni–Ca (**Figure 3.4a-b, e-h**). Two seemingly distinct moderate to strong positive and negative correlations have also been observed between Ni–V and Mn–V (R^2 of 0.51–0.99; **Figure 3.4c-d**). For NWA 1183, a moderate positive correlation that overlaps with the main trend is observed between Mn–Co (R^2 of 0.58), weak and strong negative correlations that overlap with Tissint between Ni–Co (R^2 of 0.26) and Ni–Mn (R^2 of 0.84), and a moderate negative correlation that plots above Tissint and DaG 1037 between Ni–Ca (**Figure 3.4a-b, e-f**). A moderate positive correlation was also observed between Cr–V (R^2 of 0.59), along with moderate negative and strong positive correlations between Mn–V (R^2 of 0.69) and Ni–V (R^2 of 0.80) for most of the grains, excluding one megacryst core with anomalously high V (i.e., <30 ppm V) (**Figure 3.4c-d, g**). Two seemingly distinct weak and strong positive correlations were also observed between Cr–Al (R^2 of 0.46 and 0.95) (**Figure 3.4f**).

The concentrations of LREEs, Ba and Sr for olivine in these samples range between <0.001 ppm, <0.02 ppm Ba, and <0.02 ppm Sr, for LAR 12011, <0.01 ppm, 6.8–37 ppm Ba, and 4.8–15 ppm Sr, for NWA 1068, and 0.04–1.89 ppm, 42–94 ppm Ba, and 7–13 ppm Sr, for NWA 1183. The concentrations of HFSEs in megacrysts from LAR 12011 range between 0.095–0.119 ppm Y, 0.02–0.04 ppm Zr, 0.001–0.002 ppm Nb, and 0.001–0.002 ppm Hf, while those of NWA 1068 range between 0.126–0.221 ppm Y, 0.16–0.72 ppm Zr, 0.001–0.057 ppm Nb, and 0.003–0.014 ppm Hf, excluding one grain with anomalously high Zr (5.93 ppm), Nb (0.212 ppm), and Hf (0.160 ppm) values. Concentrations of HFSEs for NWA 1183 range 0.791–1.477 ppm Y, 0.08–0.48 ppm Zr, 0.013–0.032 ppm Nb, and 0.011–0.016 ppm Hf, excluding one rim with anomalously high Zr (1.40 ppm), Nb (0.052 ppm), and Hf (0.048 ppm) values. For LAR 12011, a weak negative correlation was observed between Ni–Nb (R^2 of 0.23), and strong positive correlations between Ni–Zr, Ni–Y, and Ni–Hf (R^2 of 0.74–0.95), for most of the grains analysed from this sample (*n=3*), excluding the most Ni-rich megacryst core (**Figure 3.5a-d**). For NWA 1068, a strong negative correlation was observed between Ni–Y (R^2 of 0.79) and no correlations between Ni–Zr, Ni–Nb, and Ni–Hf (**Figure 3.5a-d**). For NWA 1183, strong negative correlations along two seemingly parallel trends were observed between Ni–Nb, Ni–Zr, and Ni–Hf (R^2 of 0.93–0.99), and a broad moderate positive correlation between Ni–Y (R^2 of 0.65; **Figure 3.5a-d**). Four of the megacryst

cores show much higher concentrations of Y (i.e., 1.1–1.5 ppm) relative to other grains analysed from the sample (i.e., 0.79–0.83 ppm Y; *n=3*).

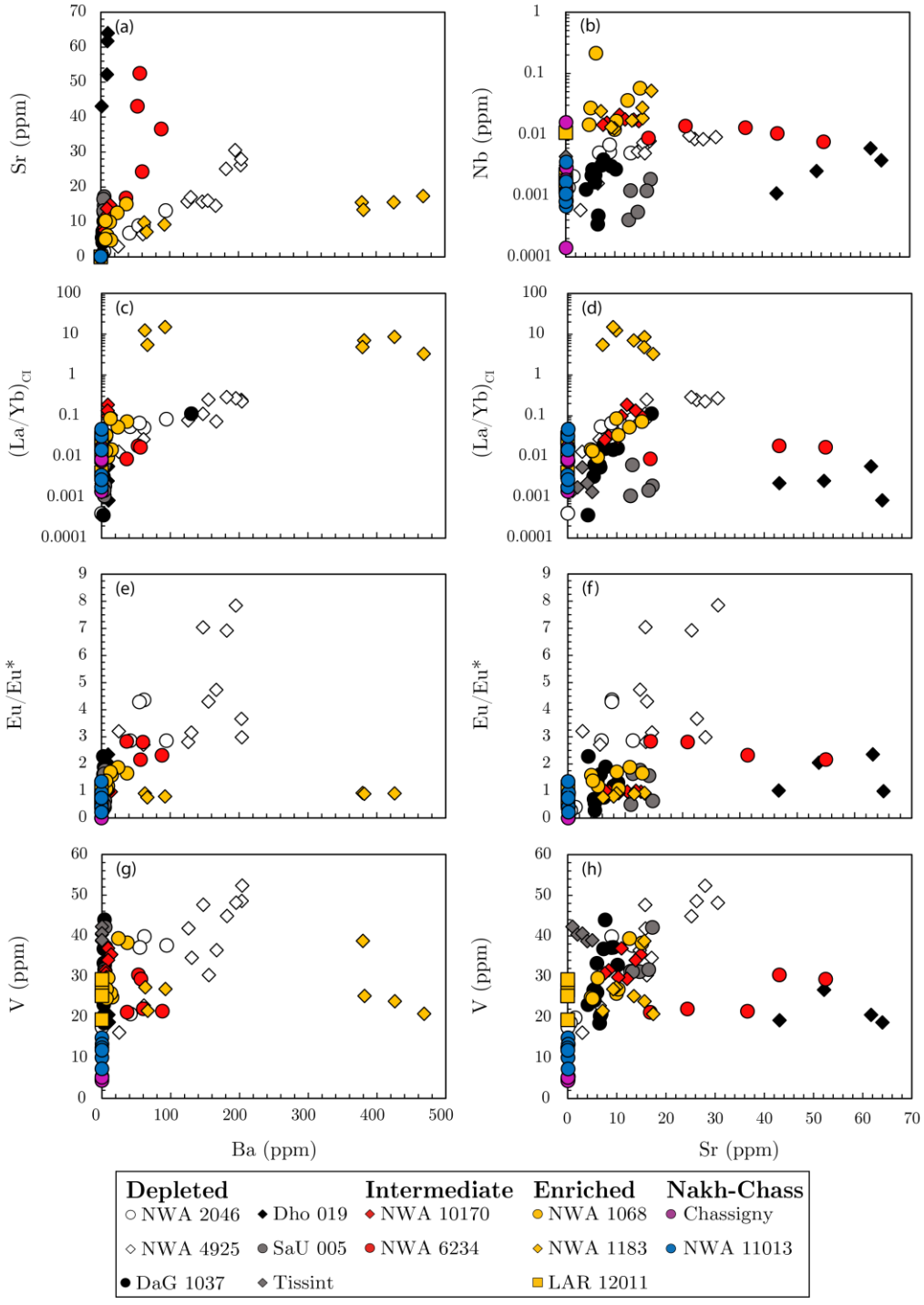

Figure 3.8: Terrestrial alteration trends for olivine grains analysed across the martian meteorites. Trace elements typically associated with terrestrial alteration, Ba and Sr, are plotted against (a) each other and for each against (b–c) LREE enrichment, (d–e) Eu anomalies, and (f–g) V concentrations.

The olivine CI–Chondrite normalised REE patterns for NWA 1068 and LAR 12011 are LREE–depleted and characterised by $(La/Yb)_{CI}$ ratios of 0.01–0.08 and 0.004–0.03, respectively (**Figure 3.6**i-j). Upwards

inflections of LREE that produce relatively flat to concave-up LREE patterns have been observed for both samples (i.e., *n=6;* NWA 1068 and *n=4;* LAR 12011), along with some positive Eu/Eu* (1.6–1.9; *n=4*) anomalies for NWA 1068 and pronounced negative Ce/Ce* (0.04–0.28; *n=4*) anomalies for LAR 12011. Olivine from NWA 1183 are significantly more LREE-enriched, with $(La/Yb)_{CI}$ ratios of 3.3–15.0. Most of the grains (*n=7*) analysed from this sample display negative Ce (0.10–0.47) and Eu (0.76–0.93) anomalies, excluding one grain with positive Ce (i.e., 1.22) and no Eu anomalies (**Figure 3.6k**). The olivine CI–normalised ITE patterns for the NWA 1068 olivine overlap with those from NWA 10170 but are generally more enriched in Ba and depleted in U and Pb, while those of LAR 12011 best resemble the Tissint olivines but extend to higher Rb, U, and LREE concentrations (**Figure 3.7i-j**). Northwest Africa 1183 olivines, on the other hand, display more pronounced Ba anomalies and significantly higher REE concentrations that has resulted in negative Zr–Hf anomalies (**Figure 3.7k**).

For LAR 12011, strong positive correlation was observed for Sr against Ce/Ce* and Y (R^2 of 0.79–0.80), and moderate to strong negative correlations for Sr against Nb (Figure 9b), Zr, and Hf (R^2 of 0.58–0.83). No clear correlations were observed for Ba and Sr against V and $(La/Yb)_{CI}$ (**Figure 3.8a, c-d, g-h**). Megacryst cores analysed from this sample are enriched in Ba, Sr, V, and LREEs, relative to megacrysts rims. For NWA 1068, moderate to strong positive correlations were observed for Ba against Sr, as well as for each against V and Eu/Eu* (R^2 of 0.60–0.71; **Figure 3.8a, e-h**). Strong positive correlations have also been observed for Sr against Zr and Hf (R^2 of 0.73–0.84), for most of the megacrysts analysed from this sample, excluding the grain with anomalously high Zr and Hf concentrations. The concentrations of Nb in megacrysts cores analysed from this sample also appear to correlate directly with Ba and Sr enrichment (**Figure 3.8b**). For NWA 1183, a strong (R^2 of 0.87–0.93) positive correlation was observed for Ba against Sr (**Figure 3.8a**), weak negative (R^2 of 0.28–0.39) correlations for La/Yb_{CI} against Ba and Sr, respectively, and no clear correlations for each against Ce/Ce*. Four of the grains are significantly more enriched in Ba (>100 ppm) and Sr (>10 ppm) and are characterised by less pronounced negative Ce anomalies, with the most Ba–Sr enriched grain showing a positive Ce anomaly. A moderate (R^2 of 0.65) positive correlation was observed for Eu/Eu* against Ni, with less pronounced negative Eu anomalies for megacryst cores relative to rims, and a strong (R^2 of 0.89) positive correlation for Eu/Eu* against Y. A strong negative correlation was also observed between Sr and Nb for grains with <10 ppm Sr (or 100 ppm Ba; *n=3*) and a positive correlation for grains with >10 ppm Sr (*n=4*). No correlations were observed for Ba and Sr against V, Zr, Nb, and Hf. Four of these grains, three megacryst cores with <705 ppm Ni and the anomalous megacryst rim, appear to be enriched in Zr and Hf relative to the other megacryst rim analysed from this sample.

3.4.4 Nakhlites and Chassignites

3.4.4.1 NWA 11013 and Chassigny

Six olivines were analysed from NWA 11013 and five from Chassigny. These olivines are characterised by Mn, Ca, Ni, Co, Cr, and V concentrations of 8324–11262 ppm, 3407–4302 ppm, 91–209 ppm, 190–202 ppm, 20–84 ppm, and 7.2–14.9 ppm, for NWA 11013 and 4204–4301 ppm, 800–1490 ppm, 513–532 ppm, 154–159 ppm, 125–152 ppm, and 4.4–5.4 ppm, for Chassigny. For NWA 11013, strong negative correlations that are shallower and at higher Mn concentrations than the depleted shergottites were observed between Mn–Ni and Mn–V (R^2 of 0.93–0.95), along with strong positive correlations between Cr–V and Ni–V (R^2 of 0.78–0.80), and no correlation between Ni–Ca and Cr–Al (**Figure 3.4a-b, c-d, h-g**). In contrast to the other samples analysed in this study, the concentrations of Co in olivine from NWA 11013 appears to increase with increasing Ni and decreasing Mn, respectively (**Figure 3.4e-f**). Chassigny olivines on the other hand show little compositional variation and yield no trends in plots in various plots of Ni and Mn against Ca, Co, and V, and for Cr against V and Al (**Figure 3.4**).

The concentrations of LREEs and HREEs in olivine from Chassigny range between 0.0001–0.004 ppm and 0.003–0.07 ppm, respectively, and overlap with but are generally lower and less variable than those of NWA 11013 (0.0003–0.02 ppm and 0.003–0.4 ppm). The concentrations of Ba and Sr in both samples are consistently low and well restricted, with values ranging between 0.003–0.16 ppm and 0.09–0.24 ppm, respectively, for NWA 11013, and 0.03–0.16 ppm and 0.05–0.15 ppm, respectively, for Chassigny. Olivine in these samples show differences in Pb concentrations, with those of NWA 11013 characterised by lower and less variable values (0.0004–0.033 ppm) relative to Chassigny (0.018–0.198 ppm). The concentrations of HFSEs in olivine from Chassigny range between 0.255–0.317 ppm Y, 0.04–0.66 ppm Zr, 0.0001–0.003 ppm Nb, 0.001–0.020 ppm Hf, excluding one grain with anomalously high Nb (i.e., 0.02 ppm), while those of NWA 11013 range between 0.294–1.406 ppm Y, 0.04–0.09 ppm Zr, 0.0007–0.004 ppm Nb, 0.001–0.003 ppm Hf. For Chassigny, no clear correlations were observed between Ni–Y and Ni–Nb (**Figure 3.5a, c**). Two of the olivine grains analysed from this sample show higher concentrations of Nb that appear to increase with increasing Ni concentrations. No clear correlations were also observed between Ni–Zr and Ni–Hf (**Figure 3.5b, d**). The concentrations of Zr and Hf in grains with >516 ppm Ni (*n=4*) appear to increase with increasing Ni concentrations. For NWA 11013, strong negative correlations were observed between Ni–Nb, Ni–Y, Ni–Hf, and Ni–Zr (R^2 of 0.86–0.96; **Figure 3.5a-d**).

The olivine CI–chondrite normalised REE patterns for NWA 11013 and Chassigny are LREE–depleted and characterised by $(La/Yb)_{CI}$ ratios of 0.002–0.05 (n=6) and 0.001–0.02 (n=5), respectively (**Figure 3.6l-m**). Two NWA 11013 olivine grains show upward inflections between La–Pr, while three from Chassigny show upwards inflections between La–Sm. Another two NWA 11013 olivine are notably

more REE- and HREE-enriched relative to other the grains from this sample (i.e., Dy/Lu_{CI} of 0.29–0.32 vs 0.18–0.21, *n=4*), and show pronounced negative Eu* anomalies between 0.08–0.15. The ITE patterns for most NWA 11013 olivine are characterised by positive Ba–U and negative Pb, Sr, and Zr–Hf anomalies, excluding one olivine with a less pronounced negative Pb and positive Sr anomaly, while those of Chassigny display positive Ba, U, Pb, Sr, and Zr–Hf anomalies (**Figure 3.7l-m**).

For NWA 11013, a strong positive correlation was observed for Ba against Sr (R^2 of 0.72; Figure 9a), and no correlations for Ba and Sr against V (**Figure 3.8g-h**), Y, Zr, Nb, and Hf. Olivine showing negative Eu anomalies (*n=2*) are characterised by higher concentrations of Y (i.e., 0.88–1.41 ppm), Zr (i.e., 0.08–0.09 ppm), Nb (i.e., 0.002–0.004 ppm), and Hf (i.e., 0.0030–0.0031 ppm), relative to the other grains analysed from this sample (i.e., 0.29–0.35 ppm Y, 0.04–0.005 ppm Zr, 0.0007–0.001 ppm Nb, and 0.0010–0.0019 ppm Hf; *n=4*). Three of the NWA 11013 grains show elevated $(La/Yb)_{CI}$ ratios that correlate positively with Ba enrichment and elevated concentrations of Pb (0.0038–0.0327 vs 0.0004 – 0.0032 ppm, *n=3*), two of which also show higher concentrations of V. For Chassigny, strong positive correlations were observed for Ba against Sr (R^2 of 0.69–0.74; **Figure 3.8a**), along with strong (R^2 of 0.83–0.99) positive correlations along two distinct trends for Ba and Sr against $(La/Yb)_{CI}$ (**Figure 3.8c-d**) and Nb, and no correlations for Ba and Sr against Y, Zr, and Hf. The three olivine grains with the highest $(La/Yb)_{CI}$ values are significantly more enriched in Zr (i.e., 0.41–0.66 ppm) and Hf (i.e., 0.016–0.020 ppm), relative to the other grains analysed from this sample (i.e., 0.04–0.09 ppm Zr and 0.001–0.002 ppm Hf; *n=2*).

3.5 Discussion

3.5.1 Contamination of LA-ICP-MS spot analyses during ablation

3.5.1.1 Terrestrial alteration of martian meteorites

Shock melt veins and cracks are common in martian meteorites and abundant within olivine grains from the studied sections (**Figure 3.2-Figure 3.3**). In chapter 2, these shock-induced veins and cracks were shown to have acted as pathways along which terrestrial fluids infiltrated, and in several instances, preferentially altered core regions of megacrysts from NWA 4925, the terrestrially oldest (420-490 Ka; Nishiizumi et al., 2011) and most extensively altered meteorite analysed in this study. The preferential alteration of megacryst cores has also been observed in the Ca elemental maps (**Figure 3.3**) and trace element data for most of the shergottites analysed in this chapter. The extent to which olivine has been altered does, however, vary significantly across the meteorites analysed. Tissint and Chassigny, as the only "fall" meteorites analysed in this study have the shortest residences time on Earth, and as such, can be assumed to have been least affected by terrestrial alteration processes. These meteorites are used here to evaluate the effects of terrestrial alteration on other martian meteorites.

Alteration of martian meteorites in terrestrial environments is typically associated with enrichment of fluid mobile phases such as Ba, Sr, U, and LREEs, which alter fractures and/or micron sized shock veins within the olivine megacrysts that are occasionally impossible to avoid with laser spots (Barrat et al., 2001; Crozaz and Wadhwa, 2001; Crozaz et al., 2003; Burgin et al., 2022; Orr et al., 2022). To assess the effects of terrestrial alteration on olivine trace element compositions in these meteorites, alteration proxies, Ba and Sr, were plotted against each other and against REE ratios including $(La/Yb)_{CI}$, Ce/Ce*, and Eu/Eu*. The data show clear distinctions between hot and cold desert meteorites (i.e., NWA vs Antarctica) and between different hot desert regions (i.e., Sahara vs Oman; **Figure 3.8a**).

Olivine from Tissint and Chassigny have very low concentrations of Ba (<0.02 and <0.2 ppm, respectively) and Sr (<0.07 and <0.2 ppm, respectively) that are consistent with their short terrestrial residence times and the general absence of significant calcite veining. Several grains analysed from both samples (4/5 from Tissint and 3/5 from Chassigny) show positive La anomalies and elevated concentrations of HFSE that correlate positively with Ba enrichment, with two from Tissint and all three from Chassigny also showing elevated Pb concentrations. These trends are comparable to those observed for hot desert meteorite finds and are consistent with the Ca elemental map of Tissint, which shows minor amounts of Ca-rich alteration towards the core regions of megacrysts (**Figure 3.3g**). These findings suggest that olivine from Tissint and Chassigny likely experienced minor amounts of terrestrial alteration, the effects of which are considerably less pronounced than in the other meteorites analysed and that regardless of residence time on Earth shergottites have likely undergone some degree of terrestrial alteration.

In previous studies of Sahara Desert meteorites, minor weathering was shown to enrich samples in Sr relative to Ba, and that through more extensive weathering the meteorites becoming increasingly more enriched in Ba relative to Sr (Folco et al., 2007; Pourkhorsandi et al., 2017). Similar findings are observed in nakhlite and shergottite meteorites here, with olivine analyses from NWA 11013, DaG 1037, and NWA 10170, characterised by marginally higher concentrations of Sr relative to Ba, while those of NWA 2046, NWA 4925, NWA 6234, NWA 1068, and NWA 1183, have significantly higher concentrations of Ba relative to Sr (**Figure 3.8a**). Olivine from the Sahara 'find' shergottites also display several distinct Ba–Sr trends, but interestingly, meteorites collected from different regions such as NWA 2046 (Algeria) and NWA 4925 (Morocco), NWA 6234 (Mali) and NWA 1068 (Morocco), and DaG 1037 (Libya) and NWA 10170 (Morocco–Algeria), overlap consistently with each other. These findings may reflect the homogeneity of the terrestrial components altering the meteorites across the Sahara landing sites. In the case of NWA 6234, where multiple Ba-Sr trends were observed, olivine cores (*n=2*) with higher concentrations of Sr relative to Ba that define one trend are cut by a melt vein running through the section (**Figure 3.2g**). The Ba-Sr trend defined by these is therefore interpreted as an extreme case, and as such, does not reflect of the overall terrestrial alteration trend for olivine in this

sample. In line with these observations, I suggest that the distinct Ba–Sr trends observed for the various Sahara meteorites may reflect changes in Ba–Sr enrichment as a function of the severity of terrestrial alteration, possibly related to the severity of shock-induced fracturing and veining during their ejection from the martian surface. As not all these shergottite meteorites have calculated terrestrial ages, it remains unclear as to how strongly linked the severity of alteration is to residence time on Earth.

Positive correlations observed between Sr, Ba and $(La/Yb)_{CI}$ across the Sahara find meteorites, excluding NWA 1183, illustrate that the LREE compositions of olivine in these samples have also been affected by terrestrial alteration products (**Figure 3.8c-d**). Positive Eu anomalies observed in REE patterns of megacrysts from most of these samples, excluding NWA 1183, were also shown to correlate directly with Ba and Sr (**Figure 3.8e-f**), and thus, interpreted to reflect the more severe effects of terrestrial alteration on martian olivine REE concentrations. Terrestrial alteration in these more severely altered samples has also affected the HFSEs of olivine, resulting in positive correlations for Ba (and Sr) against Nb in NWA 2046 and NWA 4925, as well as against Y and Zr in NWA 6234, and Zr and Hf in NWA 1068. Megacryst cores from NWA 2046 and NWA 4925, also appear to be enriched in Y, Zr, and Hf, relative to rims. Similar findings were observed for some of the other shergottites, which have megacryst cores with elevated concentrations of Hf for NWA 6234 (>60 ppm Ba; *n=2*), Zr, Nb, and Hf for DaG 1037 (>7 ppm Sr; *n=4*), and Y and Hf for NWA 10170 (>7 ppm; Ba *n=4*), relative to rims.

These findings contrast those of NWA 1183 where broad negative (R^2 of 0.28–0.39) correlations were observed for Ba and Sr against $(La/Yb)_{CI}$ (**Figure 3.8b-c**), despite REE patterns for these megacrysts being distinctly more LREE-enriched than those of NWA 1068. Excluding the Ce anomalies, REE patterns for megacrysts from NWA 1183 mirror and largely overlap with those of chassignite bulk-rock compositions. Similarities between NWA 1183 megacrysts and chassignite bulk-rocks are further highlighted in their ITE patterns, which partially overlap and show negative Zr–Hf anomalies that contrast positive anomalies of shergottites. In the case of chassignites, their highly fractionated and LREE-enriched bulk-rock REE patterns were previously interpreted to reflect metasomatism of their mantle source region by LREE-enriched fluids and is suggested to also have enriched these samples in K (Goodrich et al., 2013; McCubbin et al., 2013; Ostwald et al., 2020). Unfortunately, this model of LREE enrichment via mixing with an enriched crustal component is unlikely to account for the negative Ce anomalies observed in the megacryst REE patterns which suggest alteration in oxidising conditions, possibly during its hosts residence on earth. These negative Ce anomalies show no clear correlations against alteration proxies but are less pronounced (Ce enriched) in megacryst cores and one rim, analysed next to a melt vein, with higher concentrations of Ba and Sr (>100 and >10 ppm, respectively; *n=4*). These findings are consistent with the observations made in chapter 2, which showed that Mg-rich megacrysts cores are more heavily fractured and, by extension, preferentially altered over megacryst rims. Based on these findings, enrichment of LREEs in the NWA 1183 megacrysts is suggested to reflect

either magma mixing or crustal assimilation shortly after melt segregation from source as well as some later alteration in a terrestrial environment during its residence on Earth to produce pronounced Ce anomalies. This later terrestrial alteration appears to also have influenced HFSEs, as megacrysts with >100 ppm Ba all show elevated concentrations of Nb, Zr, and Hf. Yttrium, on the other hand does not appear to have been affected by terrestrial alteration but does correlate directly with enrichment in Eu.

Olivine in Oman Desert 'find' meteorites Dho 019 and SaU 005 are significantly more enriched in Sr at a given Ba concentration, relative to Sahara meteorites. These observations are consistent with the findings of Pourkhorsandi et al. (2017) and highlight compositional differences in the terrestrial components altering Sahara and Oman Desert meteorites. Megacrysts from these samples also show distinct Ba–Sr trends, with a steeper trend towards higher Sr and Ba concentrations observed for Dho 019 relative to SaU 005 (**Figure 3.8a**). Additionally, previous studies of meteorites from the Oman Desert have shown that soils over the entire region have a high degree of homogeneity (Al-Kathiri et al., 2005), from which I infer that the distinct Ba–Sr trends for these samples may reflect differences in the severity of terrestrial alteration. These findings correlate with the terrestrial ages of these Oman meteorites, with more pronounced alteration features observed in the terrestrially older Dho 019 (586±9; Borg et al., 2001) meteorite relative to SaU 005 (445±18; Shih et al., 2007). Terrestrial alteration in both meteorites is also accompanied by LREE-enrichment that has resulted in positive Ce anomalies, most notably in Dho 019. Elevated concentrations of Zr, Nb, and Hf in megacryst cores from SaU 005 relative to megacryst rims and positive correlations for Sr against Nb, Zr, and Hf in Dho 019, show that the concentrations of HFSEs in olivine from both samples have also been affected by terrestrial alteration.

The concentrations of Ba (<0.02 ppm) and Sr (<0.02 ppm) in olivine from the Antarctica 'find' shergottite LAR 12011 despite being consistently low, correlate positively against each other, as well as for Ba against $(La/Yb)_{CI}$ and Sr and Ce/Ce*, and thereby, illustrate that terrestrial alteration of olivine here is also accompanied by some LREE-enrichment.

The results presented above show that the effects of terrestrial alteration and associated enrichment of LREEs (i.e., La) and HFSEs are visible in olivine from most of the samples analysed in this study. These alteration effects are more pronounced in megacryst cores relative to rims, consistent with the findings of chapter 2, and must therefore be filtered, where possible, before attempting to constrain primary trace element characteristics. For DaG 1037, NWA 2046, and NWA 4925, all megacryst core data collected from these samples show evidence of LREE- and HFSE-enrichment and have subsequently been filtered out. These include eight olivine from DaG 1037, four from NWA 2064, and nine from NWA 4925. For the remaining Sahara Desert find shergottites, and in order of increasing severity of alteration, olivine with >7 ppm Ba were removed from NWA 10170 (*n=4*), >10 ppm Ba for NWA 1068 (*n=3*), >60 ppm

Ba for NWA 6234 (*n=2*), and >100 ppm Ba for NWA 1183 (*n=4*). For the Oman find meteorites, SaU 005 and Dho 019, olivine with >15 (*n=1*) and >60 (*n=2*) ppm Sr, respectively, were filtered out. For the cold desert find LAR 12011, terrestrial alteration has affected the LREE concentrations of both olivine megacrysts cores, and hence have been filtered out, but not their HFSE concentrations, which are used in later HFSE ratio calculations. For Chassigny, three olivine with evidence of LREE-enrichment and elevated concentrations of HFSEs (i.e., 0.41–0.66 ppm Y vs <0.09 ppm, *n=2*) were filtered out, three from NWA 11013 with positive Ba and Sr anomalies and elevated Pb concentrations, and two olivine cores from Tissint with elevated concentrations of Ba, Sr, Pb, and Zr-Hf. The average $(La/Yb)_{CI}$ and HFSE ratios for unaltered or least altered olivine grains from each sample following the filtering are presented in **Table 3.2** and **Table 3.5**, respectively.

Table 3.2:Average trace element compositions and fO_2 estimates for olivine in martian meteorites.

Meteorite		**$(La/Yb)_{CI}$**	**2σ**	***N***	**V (ppm)**	**2σ**	**Bulk-rock fO_2**	**Parent melt fO_2**	**2σ**	***N***
Shergottites	*Depleted*									
	DaG 1037	0.004	0.003	4	23.6	6.5	-2.84	-1.46	0.48	7
	Dho 019	0.002	0.0003	2	19.5	1.9	-1.93	-1.07	0.16	3
	NWA 2046	0.0004	-	1	19.2	2.8	-2.03	-1.92	0.25	4
	NWA 4925	0.020	0.013	2	19.5	9.4	-2.11	-1.85	0.82	2
	SaU 005	0.003	0.002	4	31.3	0.5	-3.60	-2.16	0.03	4
	Tissint	0.002	0.0003	2	39.3	1.8	-3.26	-2.90	0.07	3
	Intermediate									
	NWA 6234	0.015	0.006	3	21.6	0.8	-2.46	-1.58	0.07	3
	NWA 10170	0.029	0.003	3	30.4	1.9	-2.95	-2.20	0.11	4
	Enriched									
	LAR 12011	0.007	0.006	2	22.8	8.3	-1.64	-0.88	0.63	2
	NWA 1068	0.013	0.003	3	26.3	4.1	-2.45	-1.54	0.25	5
	NWA 1183	10.9	5.6	3	23.0	6.2	-1.94	-1.11	0.45	6
Nakhlites	NWA 11013	0.003	0.001	3	11.6	5.4	0.24	0.13	0.86	6
Chassignites	Chassigny	0.005	0.006	2	4.9	0.8	-3.70	2.65	0.14	5

3.5.1.2 Contamination by Cr-spinel exsolutions (Cr and V correlations)

The speckled appearance observed in BSE images of olivine megacrysts is the result of micron sized Cr-spinel inclusions (**Figure 3.2**). These Cr-spinel inclusions could not be entirely avoided during olivine analyses, and as such, need to be evaluated to account for any consequences in the olivine data i.e., elevated concentrations of these elements compatible in Cr-spinel such as Cr, Al, and V. Following

the method of Nicklas et al. (2021), olivine data were first filtered using Cr and Al concentrations, with grains showing Cr and Al values 2SD above the mean olivine concentration for a given meteorite rejected. Most of the olivine grains from the various meteorites analysed in this study pass this filtering, excluding one olivine megacryst core from DaG 1037.

Olivine data were further filtered by plotting Cr concentrations against V and Al (**Figure 3.4g-h**). For SaU 005, Dho 019, Tissint, NWA 6234, NWA 11013, and Chassigny, no clear correlations were observed for Cr against V and Al, respectively, and thus, suggests that megacrysts analysed from these samples are largely unaffected by Cr-spinel contamination. One megacryst core from SaU 005 and two from Tissint and NWA 6234 appear to be enriched in V and Al at a given Cr concentration and are interpreted to have been affected by Cr-spinel contamination. In contrast, positive correlations in plots of Cr against Al and V for olivine from DaG 1037, NWA 2046, NWA 4925 NWA 10170, LAR 12011, NWA 1068, and NWA 1183 suggests that some olivine analyses from these samples have been affected by Cr-spinel contamination (**Figure 3.4g-h**).

Based on these findings, olivine V data that appears to have been affected by Cr-spinel contamination has subsequently been filtered out, where possible. For most of the depleted shergottites, excluding Tissint and SaU 005, olivine with >30 ppm V were filtered out and includes four grains from DaG 1037, three from NWA 2046, and eight from NWA 4925. For the remaining depleted shergottites, SaU 005 and Tissint, olivine with >40 ppm V were filtered out and includes one grain from SaU 005 and two from Tissint. For the intermediate shergottites, olivine with >29 ppm V were filtered from NWA 6234 (*n=2*) and >32 ppm V from NWA 10170 (*n=3*). For the enriched shergottites, olivine with >27 ppm V were filtered out from NWA 1183 (*n=3*) and LAR 12011 (*n=2*), respectively, and >30 ppm V for NWA 1068 (*n=2*). The average V concentrations for olivine from each of the martian meteorites, following attempts to filter for Cr-spinel contamination, are presented in **Table 3.2**.

3.5.2 V-in-olivine oxybarometry

Oxygen fugacity estimates were calculated using the V-in-olivine oxybarometer outlined by Wang et al. (2019) and previously applied to martian meteorites by Nicklas et al. (2021) and listed below as Equation (1). As olivine is typically the earliest phase in to crystallise in basaltic assemblages, fO_2 estimates using this oxybarometer provide the closest possible to the liquidus. Additionally, this technique which only requires olivine and parent melt V concentrations, is unaffected by uncertainties relating to equilibrium between minerals such as with the olivine-orthopyroxene-spinel (i.e., Mattioli and Wood, 1988; Wood, 1991) or Fe-Ti oxide (i.e., Ghiorso and Sack 1991; Herd et al., 2001) oxybarometers.

$$\mathrm{Log}_{10}\left(\mathrm{D}_{\mathrm{V}}^{\mathrm{ol-melt}}\right) = -2.30 - 0.258(\Delta\mathrm{QFM}) + \frac{1871}{\mathrm{T}} - 0.24\left(\frac{\mathrm{NBO}}{\mathrm{Totl}}\right) \quad (1)$$

Where, $D_V^{ol-melt}$ is the partitioning of V between olivine and parent melt, T (in Kelvin) is the liquidus temperatures taken from literature sources, NBO/Tot is the ratio of non-bonding oxygen to total oxygen calculated from parental melt compositions, and ΔQFM is the oxygen fugacity relative to the QFM (quartz-fayalite-magnetite) buffer.

To calculate fO_2 for these samples, two different approaches were adopted. For the first approach, the bulk-rock major element compositions and V concentrations of each sample (**Table 3.3**) were assumed to equal those of the olivine megacryst parental melts. As discussed in detail in chapter 2, olivine in many of these meteorites including DaG 1037, Dho 019, SaU 005, NWA 10170, NWA 1068, NWA 1183, LAR 12011, and NWA 11013, contain accumulated olivine (e.g., Taylor et al. 2002; Papike et al. 2009; Filiberto et al. 2010). As such, estimates calculated from this approach are likely to be less accurate. For samples NWA 10170 and NWA 1183, no literature bulk-rock data were available. Northwest Africa 1183 is thought to be paired with NWA 1068 and should therefore have the same bulk-rock geochemistry, and in the case of NWA 10170 the bulk-rock composition of the other intermediate olivine-phyric shergottite NWA 6234, which may also be paired to NWA 10170, was used as a proxy.

For the second approach and following the approach of Nicklas et al. (2021), melts in equilibrium with olivine, previously estimated using bulk-rock Mg#, olivine Fo contents and the equilibrium $K_D^{FeO-MgO}$ (0.35 ± 0.01; Filiberto and Dasgupta, 2011), were assumed to equal the parent magma compositions of the meteorites. These literature parent magma compositions were taken from Filiberto and Dasgupta (2011) (DaG 1037/476, Dho 019, SaU 005, NWA 1068/1183, and LAR 12011/06319), Herd et al. (2013) (Tissint), and Filiberto (2008) (Chassigny) and estimated for the remaining samples using the same approach. Following this, parent magma V concentrations were then estimated by linear regression using the average megacryst core compositions and available bulk-rock MgO (wt. %) contents for each meteorite. Liquidus temperatures required for these calculations are presented in **Table 3.3**, with values for most of the shergottites taken from Ramsey et al. (2021) and calculated using Al-in-olivine thermometry. Shergottites with no literature liquidus temperature estimates including Dho 019, NWA 4925, and SaU 005, were assumed to have crystallised at temperatures close to those of other depleted shergottites (~1300 °C). A crystallisation temperature of ~1140 °C (Johnson et al., 1991), calculated on melt inclusion pyroxenes using a two-pyroxene geothermometer, was used for Chassigny, while NWA 11013 was assumed to have crystallised at the same temperature as other meteorites paired to it (i.e., NWA 10720 at ~1050 °C; Cao et al., 2022).

Table 3.3: Crystallisation temperatures and bulk-rock and parent melt compositions for the martian meteorites.

Meteorites	**Bulk-rock**	**Parent melt**

		Temperatures (ºC)	V (ppm)	NBO/Tot	V (ppm)	NBO/Tot
Shergottites	*Depleted*					
	DaG 1037	1416	188	1.86	293	1.17
	Dho 019	1300	198	1.64	245	1.11
	NWA 2046	1291	176	1.60	181	1.52
	NWA 4925	1300	177	1.66	190	1.51
	SaU 005	1300	136	1.90	206	1.10
	Tissint	1377	249	1.99	272	1.75
	Intermediate					
	NWA 6234	1438	228	1.88	296	1.41
	NWA 10170	1405	228	1.88	276	1.41
	Enriched					
	LAR 12011	1147	213	1.77	265	1.35
	NWA 1068	1468	280	1.81	378	1.37
	NWA 1183	1363	280	1.81	361	1.37
Nakhlites	NWA 11013	1050	191	1.32	177	1.15
Chassignites	Chassigny	1190	39.1	3.69	441	1.24

*Note: Liquidus temperatures are from the following: DaG 1037, NWA 2046, SaU 005, Tissint, NWA 6234, NWA 10170, NWA 1068, NWA 1183, and LAR 12011: Ramsey et al. (2021), NWA 11013/10720: Cao et al. (2022), Chassigny: Wadhwa and Crozaz (1995). Bulk-rock V concentrations and NBO/T ratios are from the following: DaG 1037/476, Dho 019, Tissint, LAR 12011, NWA 11013 and Chassigny: Day et al. (2018); NWA 2046 and NWA 4925: Peel et al. (2023); SaU 005: Dreibus et al. (2000); NWA 6234 and 10170: Filiberto et al. (2012); NWA 1068 and NWA 1183: Barret et al. (2002). Parental magma major element data (for NBO/Tot calculations) taken from the following: DaG 1037/476, Dho 019, SaU 005, NWA 1068 (and NWA 1183), and LAR 12011/06319: Filiberto and Dasgupta (2011), Tissint: Herd et al. (2013), Chassigny: Filiberto (2008).

3.5.2.1 Olivine-phyric shergottites

Oxygen fugacity estimates calculated from the average V concentrations for olivine from each sample using the two approaches are reported in **Table 3.3**. Calculated fO_2 for shergottites using bulk-rock data range from −3.6 to −1.4 ΔQFM (log units relative to the quartz-fayalite-magnetite buffer), while those calculated with estimated parent melt compositions range from −2.9 to −0.7 ΔQFM (**Figure 3.9**). Estimates using both approaches plot within 2SD of literature fO_2 determined using the same method (i.e., −2.1 ± 1.8 ΔQFM; Nicklas et al., 2021), with values calculated using bulk-rock data generally more reduced than those using estimated parent melt data. The depleted meteorites show the broadest range of fO_2 (i.e., −2.9 to −1.0 ΔQFM using approach 2) for all three groups and have the most reduced

values (i.e., Tissint) but do overlap consistently with fO_2 estimates for both the intermediate (−2.3 to −1.6 ΔQFM) and enriched (−1.7 to −0.7 ΔQFM) shergottite groups.

The V-in-olivine fO_2 estimates for most of the depleted shergottites, excluding Tissint and SaU 005, overlap with literature estimates for later-stage oxides using the Fe-Ti oxide oxybarometer of Ghiorso and Sack (1991) (i.e., −1.5±0.4 for DaG 1037/476 Herd et al., 2001). These findings suggest that the fO_2 for DaG 1037, Dho 019, NWA 2046, and NWA 4925 remained relatively constant during the crystallisation of early and later stage phases. In the case of Tissint, measured differences in fO_2 estimates between early and later stage were previously interpreted to reflect additional oxidisation via possible degassing (Castle and Herd, 2017). For the intermediate and enriched shergottites, V-in-olivine fO_2 estimates partially overlap with but are generally lower than Fe-Ti oxide estimates (i.e., −1.0 to 0.3 ΔQFM, Goodrich et al., 2003; Herd, 2006; Peslier et a., 2010; Howarth and Udry, 2017). Higher fO_2 estimates for later-stage crystallising phases in intermediate and enriched shergottites may reflect auto-oxidation during evolution as late-stage melts (and crystallising phases) become increasing more enriched in Fe^{3+} and has previously been modelled to increase fO_2 by ∼1 log unit (relative to QFM) (Castle and Herd, 2017). The modelled increase in fO_2 is consistent with differences in fO_2 estimates for early and later-stage crystallising phases in the intermediate and enriched shergottites, and hence, suggests that auto-oxidation during magma evolution is the likely cause of more oxidised fO_2 estimates for late-stage oxides in these meteorites.

3.5.2.2 Nakhlite and Chassignite meteorites

Oxygen fugacity estimates for NWA 11013 using the two approaches overlap considerably with each other but are notably different to the results collected for shergottites. Estimates using bulk-rock data (−0.2 to 1.0 ΔQFM) are marginally more oxidised than those using estimated parent melt compositions (−0.3 to 0.9 ΔQFM) (**Figure 3.9**), but both fall within the range previous calculated for late-stage Fe-Ti oxides in Nakhlites using Fe-Ti oxybarometry (−0.8 to 1.6 ΔQFM; Syzmanski et al., 2010, Wang et al., 2021). These findings suggest that fO_2 for nakhlites remained relatively constant during the crystallisation of early and later stage phases and are consistent with the results of numerous previous studies which showed that nakhlite meteorites crystallised from more oxidised melts than shergottites (Makishima et al., 2007; Righter et al., 2008; Syzmanski et al., 2010; McCubbin et al., 2013). For Chassigny, calculated fO_2 using the estimated parental melt composition range from 2.6 to 2.7 ΔQFM and overlap with the results of Nicklas et al. (2021) using the same method (i.e., 1.7 to 2.9 ΔQFM), but are significantly higher than values using bulk-rock data (−3.8 to −3.6 ΔQFM) and previous estimates using early-formed oxides (i.e., −1.3 ΔQFM; Beck et al., 2006) (**Figure 3.9**). These more reduced fO_2 using bulk-rock data and V/(Al +Cr) ratios in oxide grains were calculated under the assumption that bulk-rock was in equilibrium with olivine and spinel, respectively, but owing to the cumulate nature of chassignites are likely to not be as accurate as those using estimated parent melt compositions.

Additionally, the higher calculated parent melt fO_2 estimate for Chassigny suggests that chassignite meteorites crystallised from more oxidised melts than shergottites, and thus, support previous interpretations that chassignite (and nakhlite) meteorites represent low degree partial melts of metasomatized lithosphere mantle sources (Udry and Day, 2018; Nicklas et al. 2021). Discrepancies in nakhlite (NWA 11013) and chassignite (Chassigny) parent melt fO_2 estimates may reflect variations in their degrees of partial melting or metasomatism or both.

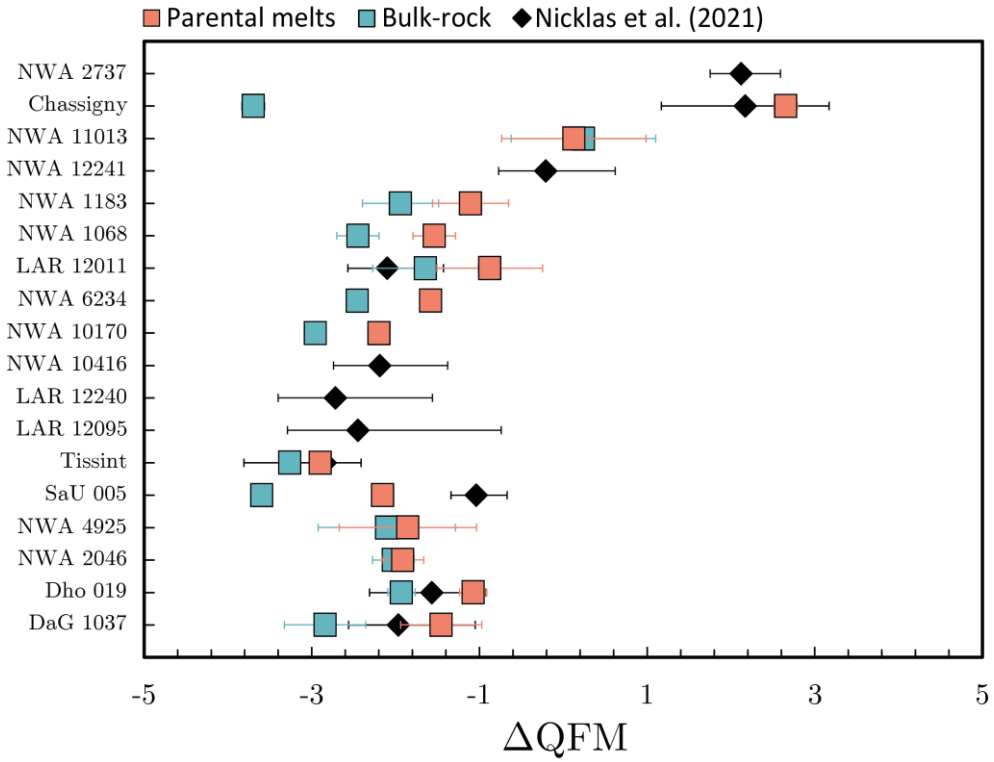

Figure 3.9: Calculated V-in-olivine oxygen fugacity estimates for olivine in the martian meteorites using olivine parental melt (blue) and bulk-rock (red) data, in comparison to the results of Nicklas et al. (2021) using the same method.

3.5.3 Olivine parental melt REE modelling

Melt compositions in equilibrium with megacrysts from these meteorites can be estimated using appropriate olivine-melt REE partition coefficients for basaltic compositions. There are, however, limited olivine-melt REE partition coefficients with the only complete set of olivine-melt REE partition coefficients available having been experimentally derived and calculated for terrestrial basalts (Nielsen et al., 1992). Olivine-melt partition coefficients for martian basalts can be estimated from this current data set using the Tissint meteorite, the most primitive sample analysed in this study with the least effects of terrestrial contamination that have also previously been shown to be in Mg-Fe equilibrium with bulk-rock (e.g., Liu et al., 2016). The olivine-melt partition coefficients ($\pm$ 2SD) used in this study and subsequent models are presented in **Table 3.4** were estimated using the bulk-rock composition of Tissint taken from Day et al., (2018) and the average REE concentrations of the least altered megacrysts analysed from this sample.

Overall, the estimated olivine-melt partition coefficients using Tissint are comparable to those experimentally derived for terrestrial systems but show some differences such as marginally higher La–Nd, Tb–Dy, Er–Tm, and Yb and lower Sm–Gd, Ho, and Lu values. The Tissint and terrestrial basalt olivine-melt partition coefficients, plotted as a function of effective cationic radii (Onuma et al., 1968) and assuming all REEs are in eightfold coordination (Shannon, 1976), show a negative correlation that overlaps consistently (**Figure 3.10**). Regrettably, the minor amounts of terrestrial alteration and subsequent LREE-enrichment observed in the more LREE-depleted olivine megacryst cores analysed from Tissint have resulted in an elevated $\mathbf{K_D^{ol\text{-}melt}}$ for La.

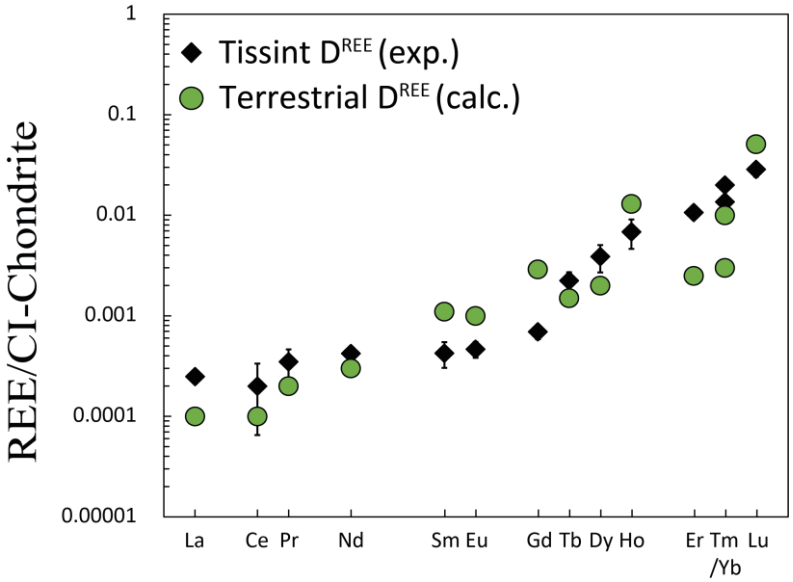

Figure 3.10: Olivine-melt partition coefficients for the Tissint meteorite, calculated using olivine and bulk-rock REE data (Balta et al., 2015; Day et al., 2018), and experimental olivine-melt partition coefficients for terrestrial basalts, plotted against cationic radii in 8-fold coordination (Onuma et al., 1968; Shannon, 1976). Experimental olivine-melt partition coefficients for terrestrial basalts taken from Lundberg et al. (1990).

3.5.3.1 Olivine-phyric shergottites

The average REE composition of unaltered (or least altered) megacrysts from the meteorites, filtered as per *section **3.5.1.1***, are presented in **Table 3.6** and the Cl-normalised REE patterns for the equilibrium melts in **Figure 3.11**. Equilibrium melts for DaG 1037, Dho 019, NWA 2046, and SaU 005, are characteristically LREE depleted and parallel those of their bulk-rocks although at significantly higher absolute concentrations (**Figure 3.11a-c, e**), and thus, suggest a genetic link between the olivine megacrysts and bulk-rock compositions. For NWA 2046, the REE pattern for the equilibrium melt overlaps considerably with that of its bulk-rock (**Figure 3.11c**). These findings suggest that NWA 2046 megacrysts are in REE equilibrium with bulk-rock. This interpretation is consistent with the findings

presented in chapter 2 and Peel et al. (2023), which showed that the high-Fo megacryst cores are in Mg-Fe equilibrium with bulk-rock Mg#. Equilibrium melt REE patterns for DaG 1037, Dho 019, and SaU 005 plot above their bulk-rock patterns, with SaU 005 plotting closest to bulk-rock values and Dho 019 the furthest away (**Figure 3.11a-b, e**). It is important to note that the incompatible nature of REE in olivine means that any addition or subtraction of olivine grains would affect the absolute concentrations of these elements in the host-rock (Shafer et al., 2010). Discrepancies in equilibrium melt and bulk-rock REE compositions reflect variable amounts of olivine accumulation, with previous studies of olivine and bulk-rock Mg-Fe partitioning showing between 30–34, 18–22, and 32–38 wt.% olivine accumulation for DaG 476/1037, Dho 019, and SaU 005, respectively (Filiberto and Dasgupta, 2011). The amount of olivine accumulation was estimated using the olivine and bulk-rock REE compositions for each sample and suggests 70±6, 78±7, and 57±4 wt.% (2SD) olivine accumulation for DaG 1037, Dho 019, and SaU 005, respectively. These calculated accumulation percentages are significantly higher than the amount of olivine present in these samples and may suggest accumulation of other mineral phases such as orthopyroxene and/or clinopyroxene in addition to olivine, which for DaG and SaU are consistent with previous interpretations for these meteorites (e.g., Zipfel et al., 2000; Goodrich, 2003; Filiberto and Dasgupta, 2011; Aucamp et al., 2023). Alternatively, these discrepancies may suggest that fractional crystallisation has occurred and that the REE concentrations have increased in the residual melt relative to the original parent melt. Olivine accumulation for NWA 2046 and NWA 4925 was estimated using the (1) measured bulk-rock HREE (Dy–Lu) compositions, which are largely unaffected by terrestrial alteration, and (2) calculated bulk-rock REE compositions, both presented in chapter 2. For NWA 2046, discrepancies in equilibrium melt and measured bulk-rock HREE compositions suggest the loss of 10±7 (2SD) wt.% olivine, while discrepancies in equilibrium melt and calculated bulk-rock REE compositions suggest 13±5 (2SD) wt.% olivine accumulation. For NWA 4925, discrepancies in equilibrium melt and measured bulk-rock HREE (Dy–Lu) compositions suggest the loss of 12±6 (2SD) wt.% olivine, while discrepancies in equilibrium melt and calculated bulk-rock HREE compositions suggest 14±7 (2SD) wt.% olivine accumulation.

The CI-normalised REE pattern for the equilibrium melt of NWA 6234 strongly mirrors and partially overlaps with that of its bulk-rock (**Figure 3.11f**). These results, which suggest that the megacrysts are in REE equilibrium with bulk-rock, and further, that NWA 6234 likely crystallised as a closed-system, are consistent with the findings of Gross et al. (2013) who showed that the megacrysts are in Mg-Fe equilibrium with bulk-rock. Discrepancies in equilibrium melt and bulk-rock REE compositions may suggest some olivine accumulation, with estimates showing 16±10 wt.% (2SD) olivine accumulation. The REE pattern for the olivine equilibrium melt of NWA 10170 largely mirrors but plots above that of bulk-rock NWA 6234 between Sm and Lu (**Figure 3.11g**). These findings are consistent with similarities in bulk-rock and modelled bulk-rock REE patterns for NWA 6234 and NWA 10170 (Howarth and Udry,

2017), and further shows that these meteorites originate from a similar mantle source. Estimates for olivine accumulation using bulk-rock NWA 6234 as a proxy for NWA 10170, show differences in megacryst and bulk-rock REE compositions (between Sm–Lu) that are consistent with 30±12 wt.% (2SD) olivine accumulation. Furthermore, the NWA 10170 equilibrium melt is notably more LREE-enriched (La–Nd) than NWA 6234 bulk-rock and shows a distinct positive Ce anomaly. Decoupling of Ce relative to other REEs, has previously been reported in REE patterns of pyroxene grains from shergottite meteorites and was suggested to reflect alteration in oxidising conditions such as during its hosts residence on Earth (e.g., Crozaz and Wadhwa, 2001; Crozaz et al., 2003). This interpretation is, however, inconsistent with lack of correlations between NWA 10170 megacryst La/Yb_{CI} ratios and terrestrial alteration proxies, and as such, may indicate post-magmatic alteration on or near the martian surface rather than alteration during its hosts residence on Earth. A similar model was proposed by Aoudjehane et al. (2012) to explain the LREE enrichment in impact glass from Tissint but was later challenged by subsequent studies that found no exotic LREE components in Tissint impact glass (Barrat et al., 2014, Peters et al., 2015, Suarez et al., 2022). Further research on olivine-host melt inclusion glass and radiogenic isotopes is necessary to support or refute this interpretation. Overall, the LREE enrichment in NWA 10170 olivine megacrysts does not reflect the primary trace element characteristics of its parent melt and is likely a result of post-magmatic processes.

The REE pattern for the melt in equilibrium with megacrysts from LAR 12011 overlaps with the HREE pattern of its bulk-rock but shows a more LREE-depleted pattern that resembles those of melts calculated for depleted shergottites (**Figure 3.11h**). These findings suggest that the megacrysts are not in REE equilibrium with bulk-rock. This is consistent with high-Fo megacryst cores not being in Mg-Fe equilibrium with the Mg# of bulk-rock LAR 12011, in line with olivine accumulation, but only a handful of olivine were analysed it is entirely possible that these LREE-depleted megacrysts form part of a mixed population. This interpretation of mixed olivine populations has previously been suggested for LAR 06319, an enriched olivine-phyric shergottite paired to LAR 12011, that hosts phenocrystic olivine megacrysts and accumulated olivine (i.e., Sarbadhikari et al., 2009; Balta et al., 2013). For NWA 1068, the REE pattern for the melt in equilibrium with olivine strongly mirrors and plots above that of its bulk-rock (**Figure 3.11i**). These findings, which suggest that the megacrysts and bulk-rock NWA 1068 are genetically linked, and further, that NWA 1068 likely crystallised as a closed-system, are consistent with previous studies of olivine-hosted melt inclusions from NWA 1068/1110 which show LREE-enriched REE patterns that mirror bulk-rock (Shearer et al., 2013). Differences in megacryst and bulk-rock REE compositions suggest between 27±5 wt.% (2SD) olivine accumulation, consistent with the findings of Filiberto and Dasgupta (2011), which estimated between 21–26 wt.% olivine accumulation. The REE pattern for the NWA 1068 equilibrium melt does deviate from that of bulk-rock towards La and Eu but reflect the terrestrial alteration effects that could not be removed. For NWA 1183, the REE pattern for the equilibrium melt is significantly more LREE- and REE-enriched than the bulk-rock

pattern of its suggested pair NWA 1068 (**Figure 3.11j**), and as discussed above, likely reflect a more complex set of processes.

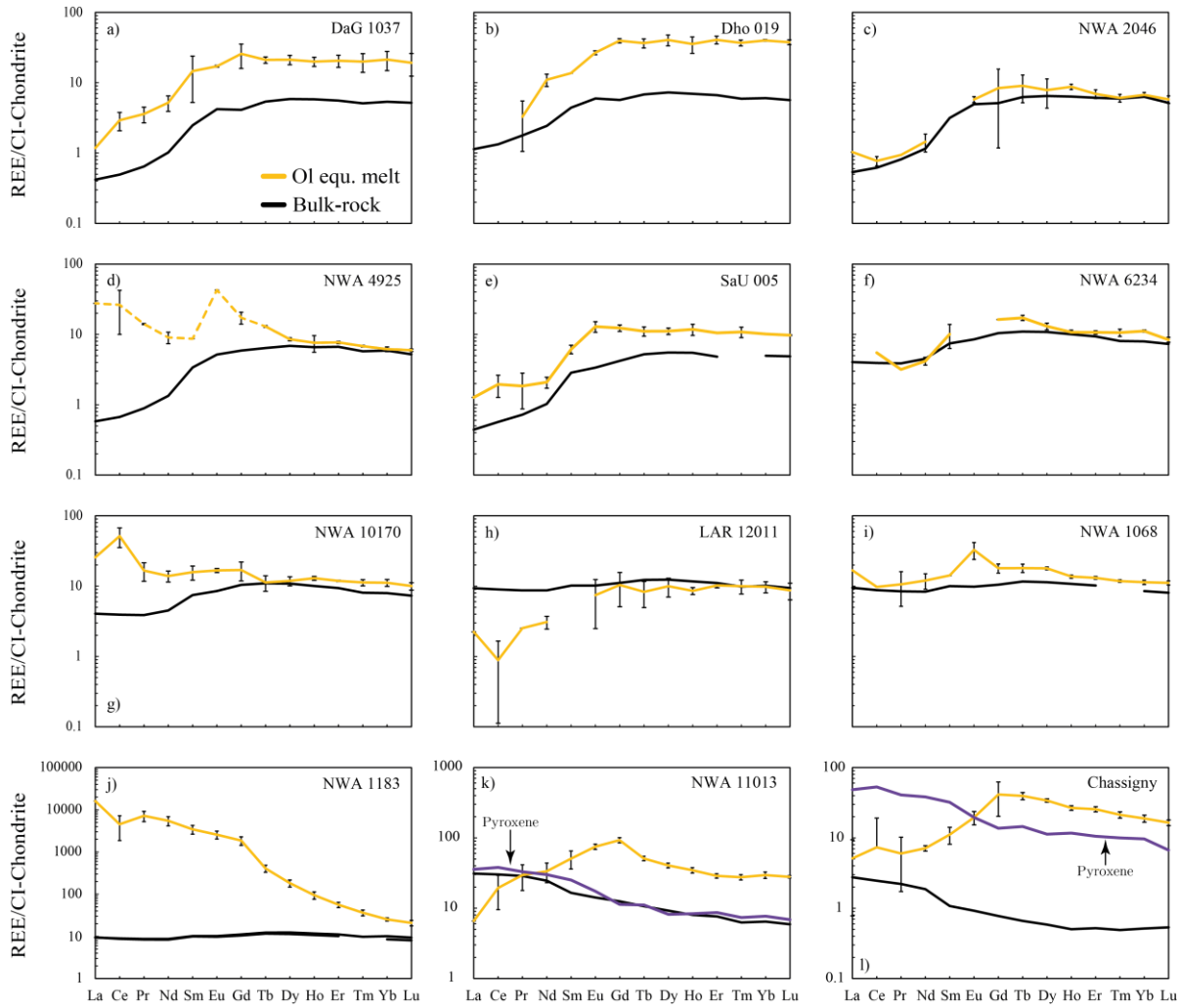

Figure 3.11: Calculated Cl-normalised REE patterns for melts in equilibrium with olivine from the various meteorites analysed in this study, in comparison to the bulk-rock REE patterns for each meteorite. Olivine-melt REE partitioning coefficients used in this study were calculated from Tissint. Pyroxene equilibrium melt REE patterns for NWA 11013 and Chassigny, taken and calculated from the study of Udry and Day (2018) using the experimental partition coefficients of Oe et al. (2001). Olivine REE data presented used was filtered as outlined in *section 3.5.1.1*.

3.5.3.2 Nakhlite and Chassignite meteorites

The REE patterns for melts in equilibrium with olivine from Chassigny and NWA 11013 broadly parallel each other, with that of NWA 11013 plotting at higher REE- and LREE concentrations (**Figure 3.11k–l**). These variations in REE concentrations are consistent with differences in nakhlite and chassignite bulk-rock and pyroxene equilibrium melt REE compositions reported by Udry and Day (2018). The LREE-depleted REE patterns for Chassigny and NWA 11013 olivine equilibrium melts are, however, inconsistent with the LREE-enriched patterns of nakhlite-chassignite bulk-rock and pyroxene

equilibrium melts (**Figure 3.11k–l**). These findings may imply open-system behaviour during crystallisation, possibly through assimilation of a LREE-enriched component or mixing with a LREE-enriched melt. This interpretation of open-system crystallisation was also previously suggested by Udry and Day (2018) to account for discrepancies in nakhlite-chassignite bulk-rock and pyroxene equilibrium melt $(La/Lu)_{CI}$ ratios, where pyroxene equilibrium melts were shown to yield lower $(La/Lu)_{CI}$ ratios than bulk-rock compositions.

Table 3.4: Calculated olivine-melt partitioning coefficients using bulk-rock and olivine data from Tissint

	$K_D^{ol\text{-}melt}$	2SD	$(K_D^{ol\text{-}melt})^{exp}$
La	0.0002	-	0.0001
Ce	0.0002	0.0001	0.0001
Pr	0.0003	0.0001	0.0002
Nd	0.0004	0.0001	0.0003
Sm	0.0004	0.0001	0.0011
Eu	0.0005	0.0001	0.0010
Gd	0.0007	0.0001	0.0029
Tb	0.0022	0.0005	0.0015
Dy	0.0039	0.0012	0.0020
Ho	0.0069	0.0022	0.0130
Er	0.0107	0.0009	0.0025
Tm	0.0136	0.0008	0.0030
Yb	0.0200	0.0010	0.0100
Lu	0.0287	0.0045	0.0510

3.5.4 Olivine HFSE element characteristics

High field strength elements (HFSEs) such as Nb, Hf, Zr, or Y have been shown to be useful in classifying shergottite, nakhlite and chassignite meteorites into distinct groups, with ratios of Nb/Y and Zr/Y generally increasing from the depleted to the enriched shergottites, and nakhlites/chassignites characterised by higher Nb/Y values at a given Zr/Y relative to all shergottites (Day et al., 2018). As discussed earlier terrestrial alteration has influenced the concentrations of HFSEs in olivine megacrysts from most of the shergottite meteorites but was subsequently filtered out, where possible (*see section **3.5.1.1***). The average ($\pm$ 2SD) HFSEs ratios (i.e., Nb/Y, Zr/Y, and Hf/Y) for olivine following these filtering efforts are presented in **Table 3.5** and **Figure 3.12**.

3.5.4.1 Olivine-phyric shergottites

Olivine from the depleted shergottites have similar average ratios of Nb/Y, Zr/Y, and Hf/Y, with olivine from DaG 1037, Dho 019, NWA 2064, SaU 005 and Tissint, overlapping consistently in plots of Zr/Y, Nb/Y, and Hf/Y, against each other (**Figure 3.12**). These observations are consistent with the similarities

in REE patterns for melts in equilibrium with olivine and further attest to megacrysts from DaG 1037, Dho 019, NWA 2064, SaU 005 and Tissint, having crystallised from parent melts with similar trace element characteristics (e.g., Aucamp et al., 2023). Olivine megacrysts from NWA 4925 also overlap consistently with Nb/Y ratios for megacrysts from the other depleted shergottites but have higher average Zr/Y and Hf/Y ratios.

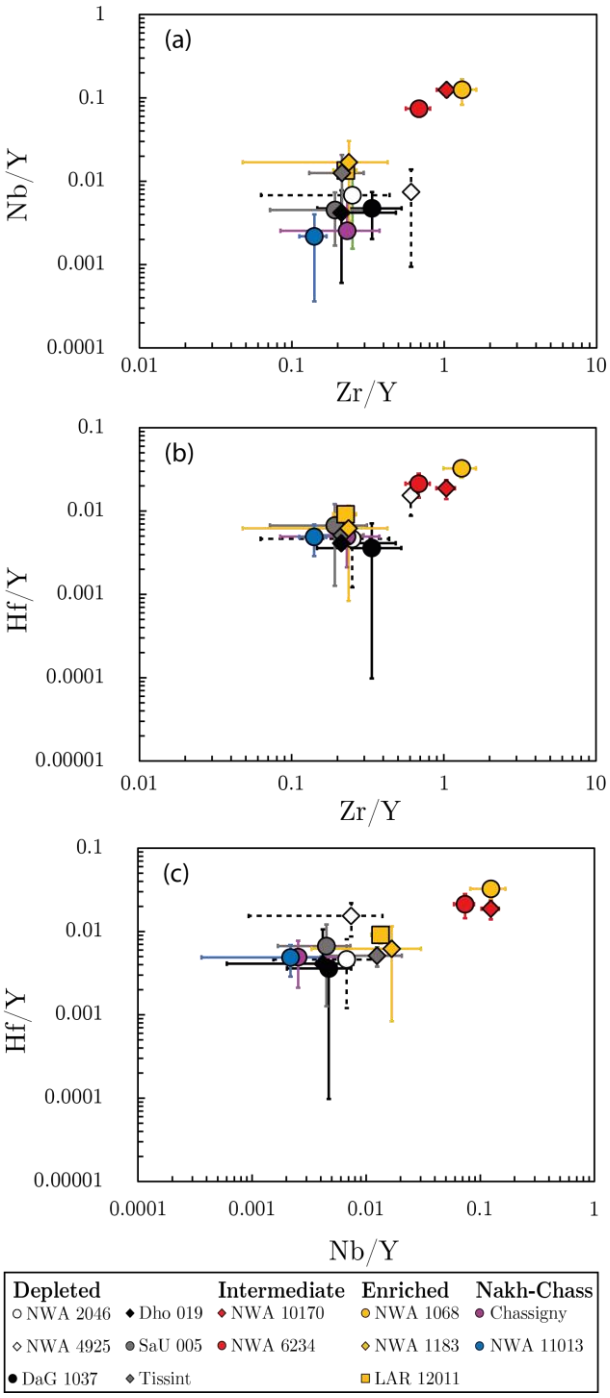

Figure 3.12: Average HFSE (Zr/Y, Hf/Y, and Nb/Y) ratios for olivine in martian meteorites analysed in this study. Olivine HFSE data were filtered as outlined in *section **3.5.1.1.***

Megacrysts from NWA 6234 and NWA 10170, have similar average ratios of Nb/Y, Zr/Y, and Hf/Y that plot at higher values than those for depleted shergottites (**Figure 3.12**). These observations are consistent with the depleted-intermediate shergottite bulk-rock findings of Day et al. (2018).

For the enriched shergottites NWA 1183 and LAR 12011, the average HFSE ratios for olivine megacrysts from both samples overlap with those for depleted shergottites (**Figure 3.12**). For LAR 12011, the average ITE pattern for olivine analysed from this sample also mirrors that of Tissint (**Figure 3.13**). This finding, in addition to the LREE-depleted REE pattern for the LAR 12011 olivine equilibrium melt, further supports the earlier interpretation that these megacrysts were derived from a LREE-depleted source and are not in equilibrium with the enriched parent melt interpreted from bulk-rock geochemistry. For NWA 1183, the similarities in HFSE ratios with the depleted shergottites are the result of very high concentrations of Y (0.8–1.5 ppm) for olivine from this sample relative to other shergottite meteorites (i.e., <0.5 ppm Y). These high Y concentrations correlate directly with the Eu negative anomalies and were likely inherited from their parent melt. The average ITE pattern for NWA 1183 olivine is different from the shergottites in general, including NWA 1068 (paired to NWA 1183), which may indicate more open-system behaviour during crystallisation. For NWA 1068, the average HFSE ratios for olivine overlap with but are generally higher than values for intermediate shergottites. Additionally, the average ITE pattern for NWA 1068 olivine also shows higher concentrations of U-La than olivine from Tissint as well as LAR 12011 (**Figure 3.13**). These findings are consistent with those previously reported for shergottite depleted and enriched bulk-rock compositions (Day et al., 2018) and further highlight differences in the ITE characteristics of martian mantle sources.

3.5.4.2 Nakhlite and Chassignite meteorites

The HFSEs (Zr/Y, Nb/Y, and Hf/Y) ratios for olivine from Chassigny and NWA 11013 plot within uncertainty of values for megacrysts from the depleted shergottites but show some differences, with lower average ratios for NWA 11013 olivine relative to that of Chassigny. In contrast, nakhlite-chassignite bulk-rock compositions have previously been shown to plot at higher Nb/Y and Zr/Y values than the depleted shergottites, and at higher Nb/Y (at a given Zr/Y value) than intermediate-enriched shergottites (Day et al., 2018). The HFSE characteristics for olivine from NWA 11013 and Chassigny are instead, consistent with the REE patterns for grains from both samples and further suggest that olivine in these meteorites likely crystallised from a LREE-depleted mantle source. This interpretation for Chassigny olivine is further highlighted in the strong similarities in ITE patterns for Chassigny and Tissint olivine (**Figure 3.13**).

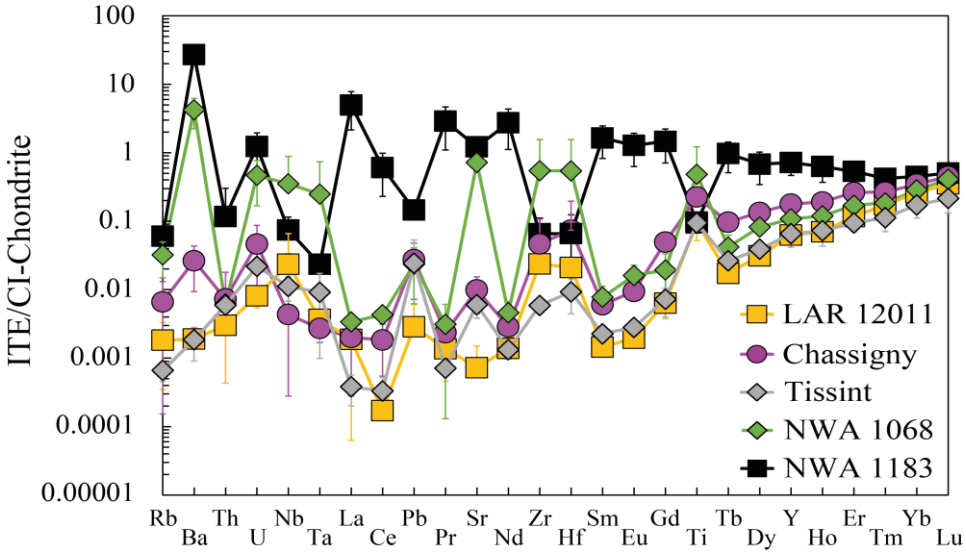

Figure 3.13: Comparison of the average Cl-normalised ITE patterns for olivine from LAR 12011, Tissint, Chassigny, NWA 1068, and NWA 1183. Chondrite normalisation values taken from McDonough and Sun (1995). Olivine data were filtered as outlined in *section **3.5.1.1***.

3.5.5 Ultra-trace elements in depleted and intermediate shergottite olivine consistent with closed system evolution

As shown in *section **3.5.3***, calculated REE patterns for melt in equilibrium with olivine from most of the shergottite meteorites including DaG 1037, Dho 019, NWA 2046, SaU 005, NWA 6234, and NWA 1068, parallel those of their respective bulk-rocks. These findings, in addition to their HFSE characteristics, suggest that the megacrysts analysed from these samples were derived from parent melts that are compositionally similar to their bulk-rock compositions, and further, that their parent magmas crystallised as closed (or near-closed) systems; i.e., no change in REE and other incompatible element ratios with evolution.

The $(La/Yb)_{CI}$ ratios for megacrysts from DaG 1037, Dho 019, NWA 2046, SaU 005, and Tissint, are consistent with these samples having crystallised from parent magmas that represent partial melting of the depleted martian mantle. Despite their similarity in crystallisation ages, Dho 019 and Tissint show significant differences in redox conditions (-1.1±0.2 and -2.9±0.1 ΔQFM, respectively) that are consistent with isotopic dissimilarities previously reported for these meteorites (i.e., ε^{143}Nd of 34.8±0.4 and 42.2±0.5, respectively, Borg et al., 2001; Brennecka et al., 2014). These findings support interpretations that Dho 019 and Tissint were derived from distinct mantle source regions and are also consistent with their differences in ejection ages, ~18 Ma for Dho 019 (Shukolyukov et al., 2002) and ~1.1 Ma for Tissint (Brennecka et al., 2014). Depleted shergottites with crystallisation ages between 440–470 Ma (DaG 1037, NWA 2046, NWA 4925, and SaU 005), show remarkable overlap in redox conditions and incompatible trace element ratios (i.e., La/Yb_{CI} and HFSEs) (**Figure 3.12**, **Figure 3.14**),

that are consistent with their similarities in radiogenic isotopes presented in chapter 2. These findings further support their co-magmatic relationship and suggest that DaG 1037, NWA 2046, NWA 4925, and SaU 005 were likely derived from a common depleted mantle source, with redox conditions of ~-2 ΔQFM and $^{87}Sr/^{86}Sr$ of 0.7013, and little to no variation in degree of partial melting.

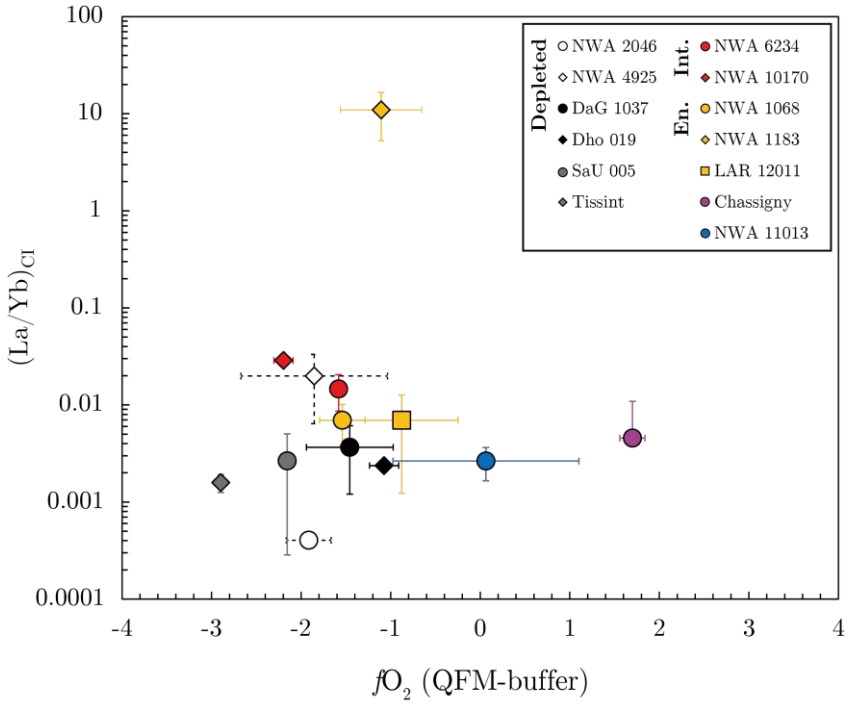

Figure 3.14: V-in-olivine fO_2 estimates, using parental melt data, plotted against olivine chondrite-normalised La/Yb ratios as a proxy for geochemical enrichment. Olivine REE data were filtered as outlined in *section **3.5.1.1.***

The $(La/Yb)_{CI}$ ratios for megacrysts from the intermediate shergottite NWA 6234 are consistent with bulk-rock, indicating closed (or near-closed) system behaviour, and further, that the parent melt of the sample was derived from a distinct mantle source region. This interpretation of closed-system behaviour for NWA 6234, is consistent with the findings of Gross et al. (2013) who demonstrated that NWA 6234 represents a primary mantle-derived melt composition. For NWA 10170, the REE pattern for the olivine equilibrium melt is distinctly more LREE-enriched than that of NWA 6234 bulk-rock indicating post-magmatic alteration processes, however, further research on olivine-host melt inclusion glass and radiogenic isotopes are necessary to confirm this interpretation. Despite the differences in LREE patterns, the MREE-HREE pattern for the NWA 10170 equilibrium melt broadly parallels that of NWA 6234 bulk-rock. Additionally, average HFSE (i.e., Nb/Y, Zr/Y, and Hf/Y) ratios for NWA 10170 megacrysts plot consistently with those NWA 6234. These findings suggest that olivine from NWA 10170 and NWA 6234 were likely derived from parent melts with similar geochemical characteristics.

3.5.6 Olivine ultra-trace elements in enriched shergottite olivine reveal complex evolution processes

The $(La/Yb)_{CI}$ ratios for megacrysts from the enriched shergottite NWA 1068 are consistent with bulk-rock. These findings, which indicate closed (or near-closed) system behaviour, suggest that the parent melt of NWA 1068 was derived from a mantle source region with enriched incompatible-element characteristics. For NWA 1183, the REE pattern for the olivine equilibrium melt is inconsistent with that of bulk-rock and distinctly more LREE-enriched. Similarly, the average ITE pattern for NWA 1183 olivine is different from that of NWA 1068, while average Nb/Y, Zr/Y, and Hf/Y ratios for NWA 1183 megacrysts consistently plot away from NWA 1068 megacrysts. These observations are inconsistent with previous suggestions that NWA 1183 and NWA 1068 are paired and indicate a complex petrogenetic history for NWA 1183. Overall, these findings show that REE and ITE compositions of NWA 1183 olivine megacrysts do not reflect the primary trace element characteristics of olivine that crystallised from a LREE-enriched shergottite parent magma. Instead, the compositions of NWA 1183 megacrysts may be the result of open system processes, such as magma mixing and crustal assimilation, but further research on olivine-host melt inclusion glass in the next chapter are necessary to confirm this interpretation.

For LAR 12011, the LREE-depleted REE pattern for the equilibrium melt is inconsistent with that of bulk-rock. Furthermore, the modelled source $^{176}Lu/^{177}Hf$ composition for LAR 12011 (0.02726; Righter et al., 2015), calculated using bulk-rock and pyroxene and maskelynite mineral separates, overlaps within uncertainty with other enriched shergottites (0.02735±0.00013 to 0.02789±0.00017; Bouvier et al., 2005, 2008; Lapen et al., 2008, 2009; Shafer et al., 2010; Combs et al., 2019). These previous findings indicate that parent melt of LAR 12011 during the crystallisation of pyroxene had LREE-enriched characteristics. This may suggest that LREE-depleted LAR 12011 megacrysts represent xenocrysts that were entrained in the LAR 12011 parent magma during its ascent to surface, or alternatively, that the parent melt of LAR 12011 was derived from a LREE-depleted mantle source that subsequently mixed with a LREE-enriched melt composition after olivine had started to crystallise. If the LAR 12011 olivine are xenocrysts they may not be related to the same plumbing system and if they formed from a depleted melt with subsequent assimilation, then they could represent partial melting of a depleted source at a younger age. The model of assimilation, coupled with differences in crystallisation ages for depleted (2403-327 Ma) and enriched (i.e., 183±12 for LAR 12011) shergottites, may also suggest that partial melting of depleted martian mantle sources persisted for a longer period of martian geologic history than previously suggested. Distinguishing between these scenarios, xenocrystic olivine and magma mixing, is one of the key objectives for the next chapter where olivine-hosted melt inclusion REE concentrations are analysed to answer this question.

Table 3.5: Average HFSE ratios for olivine in martian meteorites analysed in this study.

Meteorite		Zr/Y	2σ	*N*	Hf/Y	2σ	*N*	Nb/Y	2σ	*N*
Shergottites	*Depleted*									
	DaG 1037	0.338	0.190	4	0.004	0.004	4	0.005	0.003	4
	Dho 019	0.213	0.272	2	0.004	0.007	2	0.004	0.004	2
	NWA 2046	0.251	0.189	2	0.005	0.005	2	0.007	0.004	3
	NWA 4925	0.610	-	1	0.015	0.007	2	0.007	0.006	2
	SaU 005	0.193	0.121	4	0.007	0.005	4	0.005	0.003	4
	Tissint	0.206	0.060	2	0.005	0.001	2	0.013	0.006	2
	Intermediate									
	NWA 6234	0.688	0.125	3	0.021	0.007	3	0.074	0.015	3
	NWA 10170	1.045	0.146	3	0.019	0.005	3	0.125	0.022	3
	Enriched									
	LAR 12011	0.227	0.039	2	0.009	0.002	2	0.013	0.002	2
	NWA 1068	1.318	0.319	4	0.033	0.007	4	0.125	0.043	4
	NWA 1183	0.238	0.190	3	0.006	0.005	3	0.017	0.014	3
Nakhlites	NWA 11013	0.115	0.046	4	0.003	0.001	4	0.003	0.0005	4
Chassignites	Chassigny	0.231	0.147	2	0.005	0.003	2	0.003	0.004	2

3.6 Summary of findings

The results presented in this chapter demonstrate that the trace element compositions of early-formed olivine megacrysts in olivine-phyric shergottites offer significant insight into their parent melt compositions and mantle source regions. The CI-normalised REE patterns for melts in equilibrium with megacrysts in DaG 1037, Dho 019, NWA 2046, SaU 005, Tissint, NWA 6234, and NWA 1068, are consistent with these meteorites having crystallised with closed-system behaviour, which supports previous interpretations that shergottites result from partial melting of distinct mantle source regions. Some meteorites, including LAR 12011 and NWA 1183, also preserve evidence of more open-system behaviour. For LAR 12011, the presence of LREE-depleted olivine megacrysts may indicate shared enriched/depleted volcanic plumbing systems or magma mixing processes for some shergottites derived from distinct mantle source reservoirs. For NWA 1183, the enrichment of LREEs in megacrysts relative to those from other enriched shergottites, is inconsistent with post-magmatic alteration alone and may reflect open system processes, such as magma mixing and crustal assimilation, shortly after melt segregated from source. Olivine megacrysts in these shergottite meteorites also preserve evidence of post-magmatic alteration associated with their hosts residence in terrestrial environments, the effects of which vary across their terrestrial landing sites and are more pronounced in megacryst cores relative to rims.

The V-in-olivine oxygen fugacity estimates for depleted, intermediate, and enriched shergottite meteorites show that the fO_2 of shergottite mantle sources remained relatively constant over a prolonged period of martian volcanic history (590–180 Ma), consistent with the findings of Nicklas et al. (2021). These V-in-olivine fO_2 estimates for intermediate and enriched shergottites are more reduced than fO_2 estimates for later-stage crystallising phases and is suggested to reflect auto-oxidation during magma evolution.

Table 3.6: Average REE concentrations (ppm) for olivine used to calculate the equilibrium melts.

Meteorite			La	Ce	Pr	Nd	Sm	Eu	Gd	Tb	Dy	Ho	Er	Tm	Yb	Lu
Shergottites	*Depleted*															
	DaG 1037		0.00007	0.00036	0.00014	0.00135	0.00054	0.00045	0.00270	0.00153	0.01843	0.00612	0.02513	0.00506	0.03943	0.00663
		2SD	-	0.00008	0.00005	0.00039	-	0.00002	-	0.00020	0.00470	0.00144	0.00220	0.00045	0.00674	0.00139
	Dho 019		0.00035	0.00309	0.00011	0.00211	0.00086	0.00070	0.00560	0.00291	0.03868	0.01328	0.06938	0.01303	0.12825	0.02653
		2SD	0.00019	0.00091	0.00009	0.00058	-	0.00006	0.00039	0.00046	0.00874	0.00336	0.01149	0.00154	0.01039	0.00308
	NWA 2046		0.00006	0.00009	0.00003	0.00028	0.00056	0.00015	0.00118	0.00071	0.00743	0.00325	0.01173	0.00213	0.02147	0.00405
		2SD	-	0.00001	-	0.00011	0.00000	0.00001	0.00140	0.00050	0.00522	0.00032	0.00266	0.00057	0.00417	0.00057
	NWA 4925		0.00142	0.00322	0.00046	0.00175	0.00055	0.00112	0.00213	0.00099	0.00815	0.00285	0.01310	0.00240	0.01983	0.00421
		2SD	-	0.00153	0.00001	0.00045	-	-	-	-	0.00050	0.00096	0.00071	0.00010	0.00218	0.00024
	SaU 005		0.00007	0.00022	0.00005	0.00040	0.00039	0.00029	0.00183	0.00096	0.01034	0.00468	0.01837	0.00373	0.03207	0.00715
		2SD	-	0.00007	0.00001	0.00010	0.00005	0.00012	0.00022	0.00019	0.00123	0.00077	0.00093	0.00058	0.00131	0.00054
	Tissint		0.00241	0.00010	0.00011	0.00007	0.00061	0.00026	0.00017	0.00143	0.00078	0.00906	0.00397	0.01323	0.00241	0.02305
		2SD	-	0.00005	0.00005	0.00001	0.00016	0.00002	0.00003	0.00122	0.00032	0.00110	0.00063	0.00134	0.00049	0.00384
	Intermediate															
	NWA 6234		-	0.00068	0.00010	0.00081	0.00064	-	0.00231	0.00134	0.01277	0.00387	0.01778	0.00353	0.03533	0.00594
		2SD	-	0.00033	0.00009	0.00014	0.00031	-	-	0.00019	0.00234	0.00018	0.00146	0.00065	0.00159	0.00066
	NWA 10170		0.00152	0.00633	0.00058	0.00269	0.00100	0.00054	0.00300	0.00090	0.01137	0.00487	0.02030	0.00399	0.03607	0.00707
		2SD	0.00022	0.00152	0.00014	0.00067	0.00029	0.00019	0.00133	0.00030	0.00215	0.00040	0.00070	0.00057	0.00585	0.00118
	Enriched															
	LAR 12011		0.0010	0.0002	0.0009	0.0014	0.0020	0.0038	0.0102	0.0261	0.0439	0.0772	0.1231	0.1492	0.2228	0.3000

		2SD	-	0.0001	-	0.0004	0.0009	0.0032	0.0051	0.0102	0.0149	0.0085	0.0116	0.0426	0.0498	0.0907
	NWA 1068		0.00099	0.00119	0.00034	0.00231	0.00090	0.00082	0.00254	0.00144	0.01705	0.00511	0.02225	0.00416	0.03638	0.00781
		2SD	-	-	0.00022	0.00080	0.00001	0.00020	0.00052	0.00026	0.00108	0.00035	0.00144	0.00026	0.00372	0.00073
	NWA 1183		0.95600	0.55844	0.23329	1.06186	0.21854	0.06767	0.26486	0.03256	0.17483	0.03560	0.09596	0.01288	0.08140	0.01474
		2SD	0.36929	0.25273	0.08068	0.36702	0.06612	0.01976	0.08383	0.00838	0.04348	0.00887	0.01904	0.00286	0.01000	0.00299
Nakhlites	NWA 11013		0.00039	0.00237	0.00095	0.00640	0.00319	0.00196	0.01310	0.00404	0.03850	0.01287	0.04868	0.00968	0.09445	0.01958
		2SD	0.00019	0.00093	0.00048	0.00276	0.00119	0.00023	0.00156	0.00040	0.00388	0.00146	0.00487	0.00118	0.01398	0.00102
Chassignites	Chassigny		0.00030	0.00090	0.00019	0.00122	0.00070	0.00051	0.00587	0.00315	0.03246	0.00998	0.04342	0.00748	0.06056	0.01157
		2SD	0.00036	0.00111	0.00017	0.00010	0.00025	0.00015	0.00414	0.00050	0.00234	0.00094	0.00517	0.00110	0.00999	0.00150

1

4 Chapter 4

4.1 Introduction

The main objective of this chapter is the unanswered question on the timing of REE enrichment during shergottite magma evolution. In particular, do olivine with REE depleted patterns, such as those reported for the enriched shergottite LAR 12011 in chapter 3, represent a mixed magma plumbing system (i.e., xenocrysts) or do they represent early depleted magmas that then become enriched by assimilation of crust. Another way to investigate the REE contents of early melts in equilibrium with olivine megacrysts is the use of olivine-hosted glass-bearing melt inclusions. Glass-bearing melt inclusions preserve a snapshot of the melt composition at the time of entrapment and have been utilized in numerous studies on SNC-type meteorites (e.g., Goodrich, 2003; Peslier et al., 2010; Varela and Zinner, 2015; Sarbadhikari et al., 2011; Sautter et al., 2012; Goodrich et al., 2013). Ideal glass-bearing melt inclusions are those entirely quenched to glass, with minimal post-entrapment modification. Unfortunately, the occurrence of ideal glass-bearing melt inclusions is rare in olivine-phyric shergottites due to post-entrapment processes. These post-entrapment processes include (i) the crystallisation of daughter crystals within the melt inclusions, (ii) the crystallisation of host olivine onto walls of the melt inclusions, and (iii) Fe-Mg re-equilibration with host olivine resulting in higher MgO (wt. %) contents (Danyushevsky et al., 2000, Gaetani and Watson, 2000; Goodrich et al., 2013). As a result, the multi-phase nature of these melt inclusions exhibit variations in texture and mineral assemblages, which have been interpreted to reflect the cooling rates of the host rocks (Ikeda, 2005). Despite their complexities, these multi-phase melt inclusions typically preserve some quenched glass, which has previously been shown to be valuable in constraining shergottite parent melt compositions (i.e., Sarbadhikari et al., 2011; Peters et al., 2015). This chapter evaluates if the REE compositions of glasses in multi-phase olivine-hosted melt inclusions preserve the composition of early melts or if the glasses have been affected by post-entrapment processes. If the former, the REE compositions of the melt inclusion glasses can then be compared to olivine REEs from the previous chapter to robustly assess the composition of early melts during olivine crystallisation.

The late-stage REE composition of melts can be constrained from merrillite, the major host of REEs in the groundmass. Merrillite, a calcium-rich phosphate, is present in low abundances (<2 vol. %) as relatively fine-grained (<70 µm), subhedral to anhedral grains in olivine-phyric shergottites. Despite its low abundance, merrillite bears significant importance as it is the principal control on shergottite bulk-rock REE compositions, and owing to its elevated REE concentrations, is rarely affected by secondary enrichment processes such as terrestrial alteration or interaction with enriched martian crustal fluids. Importantly, the concentrations of REEs for merrillite in depleted, intermediate, and enriched shergottites vary across these meteorites, as evidenced in previous studies such as that of Shearer et al. (2015) and mirror the bulk-rock compositions of these shergottites. Consequently, the REE

concentrations of merrillite serve as a direct reflection of the REE composition of the late-stage melts, and as such, offer key perspectives to unravelling the evolutionary trajectory of these melts as they underwent processes of crystallisation and cooling. Analysing the variations in REE concentrations in merrillite across different olivine-phyric shergottites also provides a means to decipher the complexities of magmatic processes that shaped these meteorites. Furthermore, by combining the olivine REEs from the previous chapter with melt inclusion glass and merrillite REEs, I can robustly track the evolution of shergottite parent melts and evaluate the timing of LREE changes.

In this chapter, the major and trace element compositions of glass in olivine-hosted melt inclusions and late-stage groundmass merrillite from eight shergottites across the depleted, intermediate, and enriched olivine-phyric shergottite geochemical groups are presented. A key objective of this study is to evaluate the use of glass in melt inclusions as representative of the REE of the melt at the time of entrapment i.e., not affected by crystallisation of other phases like pyroxene and phosphate in the melt inclusions. Another key objective of this chapter, aligned with the earlier investigation of chapter 3 into olivine megacryst trace element chemistry, is to robustly constrain the timing of LREE-enrichment in these meteorites, most notably LAR12011 (i.e., distinct mantle source regions vs assimilation of LREE-enriched crustal material), offering fresh perspectives into the geological complexities of shergottite petrogenesis. By combining the olivine REEs from the previous chapter with the comprehensive analysis of the trace element compositions for melt inclusion glass in olivine-hosted melt inclusions and late-stage merrillite from a range of depleted to enriched shergottite meteorites, this study serves as a cornerstone in advancing knowledge of shergottite REE evolution of the parent melts.

Table 4.1: Magnesium numbers (Mg#) and sizes (in µm) of olivine-hosted melt inclusions and phosphate (merrillite) grains analysed in this study.

Meteorites	**Olivine Mg#**	**Melt inclusion**		**Merrillite**	
		size (µm) (*n*)	Glass Mg# (2SD)	size (µm) (*n*)	Mg# (2SD)
Depleted					
DaG 1037	60–71	20–40 (*3*)	30.6 (1.1)	25–60 (*3-4*)	82.5 (0.8)
Dho 019	34–45	25–80 (*3*)	56.5 (0.9)	10–45 (*3*)	69.0 (2.9)
SaU 005	65–71	25–100 (*3*)	47.8 (6.5)	30–65 (*3*)	84.3 (0.3)
Intermediate					
NWA 6234	58–74	80–150 (*2*)	21.3 (1.3)	20–35 (*3*)	80.0 (0.04)
NWA 10170	51–68	26–100 (*2*)	11.3 (1.3)	15–45 (*6*)	79.0 (1.1)
Enriched					
NWA 1068	53–72	30–125 (*2*)	13.9 (6.5)	15–40 (*3*)	68.7 (2.4)
NWA 1183	52–73	35–210 (*2*)	28.6 (2.4)	25–40 (*2*)	62.0 (4.6)

LAR 12011	55–75	51–250 (5)	41 (28)	27–58 (3)*	57.9 (1.8)*

Note: Values given in brackets for size reflect the number of grains analysed from each sample, while those for reflect 2SD. *Merrillite data for LAR 12011 taken from Caseres, J.R. (2015).

4.2 Samples and analytical techniques

Eight martian meteorites were analysed in this study; all have been analysed for olivine REEs in the previous chapter. Shergottites analysed in this chapter include three depleted olivine-phyric shergottites: Dar al Gani (DaG) 1037, Dhofar (Dho) 019, Sayh al Uhaymir (SaU) 005, two intermediate olivine-phyric shergottites: NWA 6234 and NWA 10170, and three enriched olivine-phyric shergottites: Larkman Nunatak (LAR) 12011, NWA 1068, and NWA 1183. These shergottite meteorites display porphyritic textures, with olivine (± orthopyroxene) megacrysts set among a fine-grained groundmass and are characterised by MgO and total alkalis (i.e., $Na_2O + K_2O$) contents between 14.9–20.5 and 0.57–1.30 wt. %, respectively (i.e., Barrat et al., 2002; Filiberto et al., 2010; Filiberto et al. 2012; Howarth and Udry, 2017; Day et al. 2018; Peel et al., 2023). Olivine megacrysts in these samples are typically the earliest phase to have crystallised, with forsterite contents ($\text{Fo} = \text{molar}\ \frac{\text{MgO}}{\text{MgO+FeO}} \times 100$) as high as Fo_{78} (NWA 10170; Ramsey et al., 2021). These megacrysts also host melt inclusions (between 10 and 100 s of μm in length) and show extensive networks of shock-induced fractures, cracks, and melt veins that are associated with their host meteorites ejection from the martian surface. Most of the melt inclusions analysed in this study are <100 μm in diameter, excluding a few larger melt inclusions between 100–250 μm in SaU 005 (*n=1*), NWA 1068 (*n=1*), NWA 1183 (*n=1*), and LAR 12011 (*n=2*), respectively, and are variably intersected by cracks and fractures cross-cutting their host megacrysts. The Mg# for the host olivine megacrysts in which the melt inclusions were found are presented in **Table *4.1*** and range between 71–34, 74–51, and 75–52, for the depleted, intermediate, and enriched meteorites, respectively. In this study, glass in two olivine-hosted melt inclusion from NWA 6234, NWA 10170, NWA 1068, and NWA 1183, three from Dho 019 and SaU 005, four from DaG 1037, and five from LAR 12011, were analysed for their major-, minor- and trace-element compositions. Phosphate grains in this study are generally fine-grained, ranging between 10–80 μm in length, and are all merrillite in composition; however, occasional grains of chlorapatite have been measured. In this study, two merrillite grains from Dho 019 and NWA 1183, three from SaU 005, NWA 6234, and NWA 1068, and four from DaG 1037 and NWA 10170 were analysed for their major-, minor- and trace-element compositions. No merrillite grains from LAR 12011 were analysed in this study. Literature data for LAR 12011 merrillite is available from the study of Caseres J.R. (2015) and used for comparison in this study.

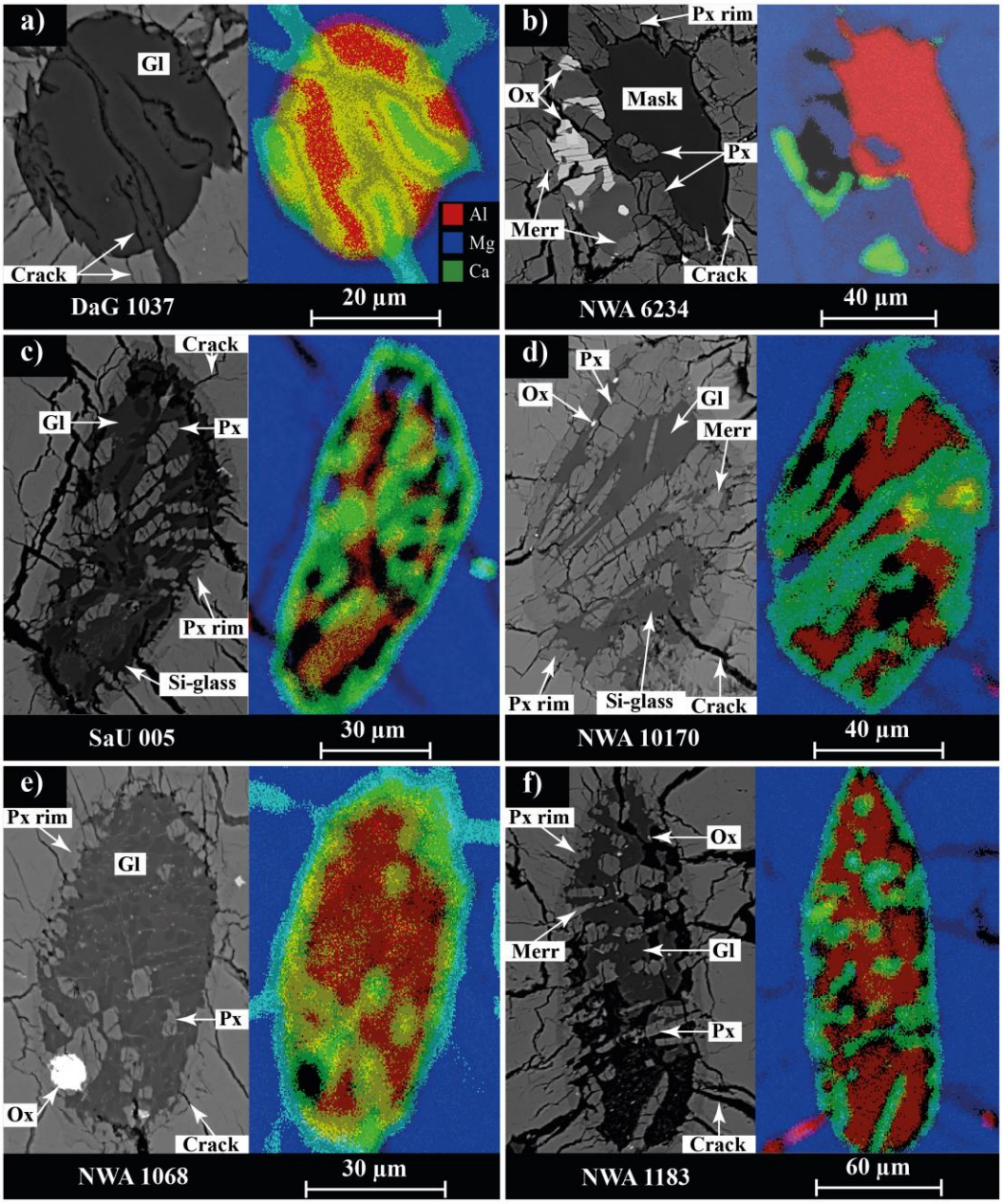

Figure 4.1: Back-scattered electron (BSE, grey) images and Mg-Ca-Al composite X-ray (coloured) maps of olivine-hosted melt inclusions in (a) DaG 1037, (b) NWA 6234, (c) SaU 005, (d) NWA 10170, (e) NWA 1068, and (f) NWA 1183. These melt inclusions occur as glassy (i.e., a) or multi-phase inclusions composed of Gl (glass) + Px (pyroxene) + Merr (merrillite) ± Mask (maskelynite) ± Ox (Fe-rich oxide) daughter crystals and rimmed by pyroxene (i.e., b-f), with some also showing Si-glass (Si-rich glass) (i.e., c-d). Many of the melt inclusions are intersected by cracks and fractures, some of which have altered the melt inclusions (i.e., a). X-ray map colours are Blue = Mg, Green = Ca, Red = Al.

4.2.1 Electron probe microanalysis (EPMA)

The major and minor element compositions of melt inclusion glass and daughter crystals hosted in olivine megacrysts and merrillite grains from the shergottite meteorites were obtained using a JEOL JXA 8530F Hyperprobe field emission Electron Probe MicroAnalyser (EPMA), housed in the Department of Earth, Environmental and Planetary Sciences at Rice University (Houston, Texas). Analyses were determined using an accelerating potential of 15 kV, beam current of 50 nA, beam diameters of between 2–10 μm and counting times of 10 seconds (s) on peaks and 5s on backgrounds for most elements, excluding S and P in the melt inclusions (40 s peak and 30 s background) and Nd, Ce, and Sr, in the phosphates (30 s peak and 20 s background). Standard ZAF correction procedures were applied. Natural and synthetic standards were periodically analysed within analytical sessions to account for instrumental drift and include: plagioclase (Na, Al, Si, Ca), olivine (Fe), glass (Mg, P, K, S), Rutile (Ti), Chromite (Cr), and rhodonite (Mn), for the melt inclusions and plagioclase (Na), olivine (Si, Mg, Fe), apatite (Ca, F), monazite (La, Nd, Ce), celestite (Sr), anhydrite (S), and Tugtupite (Cl), for the phosphates. Backscattered electron (BSE) and X-ray elemental mapping were acquired throughout the electron microprobe sessions. Element maps for the major elements were acquired for the melt inclusions with an accelerating potential and beam current of 15 kV and 40 nA respectively, while maps for minor elements (P, Ca, Ni, S, Cr and Al) required a 400 nA beam and a dwell time of 800 ms on each point. Detection limits were <0.01 wt. % for all elements.

4.2.2 Scanning electron microscope (SEM)

A FEI Nova NanoSEM 230 scanning electron microscope (SEM) with an energy dispersive spectrometer (EDS), housed at the Electron Microscope Unit (EMU) of the University of Cape Town (South Africa), was used for the qualitative analysis of LAR 12011 MI glass major element contents (not available at time of EPMA analyses of glass in the other meteorites). Analyses were performed at a working distance of 5 millimetres with an accelerating voltage of 20 kV and a spot size of 4 μm. This technique is less sensitive than the electron microprobe, and thus, less accurate at measuring the elemental composition of MI glass but can provide useful estimates of LAR 12011 MI glass calcium contents (CaO wt. %) for internal calibration during trace element analysis. The SEM is also equipped with an Oxford X- max detector and INCA software and was used for back-scattered electron (BSE) imaging of the olivine-hosted MIs observed and analysed from LAR 12011.

4.2.3 Laser Ablation Inductively Coupled Plasma – Mass Spectrometry (LA–ICP–MS)

Trace element concentrations were determined at the University of Stellenbosch (SU, Stellenbosch, South Africa), using a Resolution M-50-LR Excimer laser ablation system coupled to an Agilent 7500 quadrupole ICP-MS (inductively coupled plasma-mass spectrometer). Beam sizes of 11-15 μm were used for both the olivine megacryst-hosted melt inclusions (i.e., on glasses and daughter mineral phases)

and phosphates analysed from each sample. The laser was routinely run with a repetition rate of 8 Hz and fluence of ~3.5 J/cm^2. Helium (He) was used as the primary carrier gas, which connects to an Argon (Ar) gas line downstream of the laser cell. Reference standard NIST (National Institute of Standards and Technology) 610 was used as an external standard and run after every 15 unknown spot analyses, with BCR-2G and BHVO-2G (values from GeoReM: Jochum et al., 2005) also run as an unknown after each standard check, as a means of assessing instrument precession. Each melt inclusion glass and phosphate LA-ICP-MS analysis was normalised to CaO (wt%), previously measured by the electron microprobe and scanning electron microscope, as an internal standard to account for variable ablation yield. The data were subsequently reduced using the LADR software package from Norris Scientific (Norris et al., 2018). For minor- and trace-elements, reproducibility of the reference glass standards was generally better than 10% (relative standard deviation or RSD), excluding REEs (Sm–Lu) and U in both BCR-2G and BHVO-2G, as well as Cr and Ni in BCR-2G and Si and Zn in BHVO-2G; reproducibility for these elements was better than 30%.

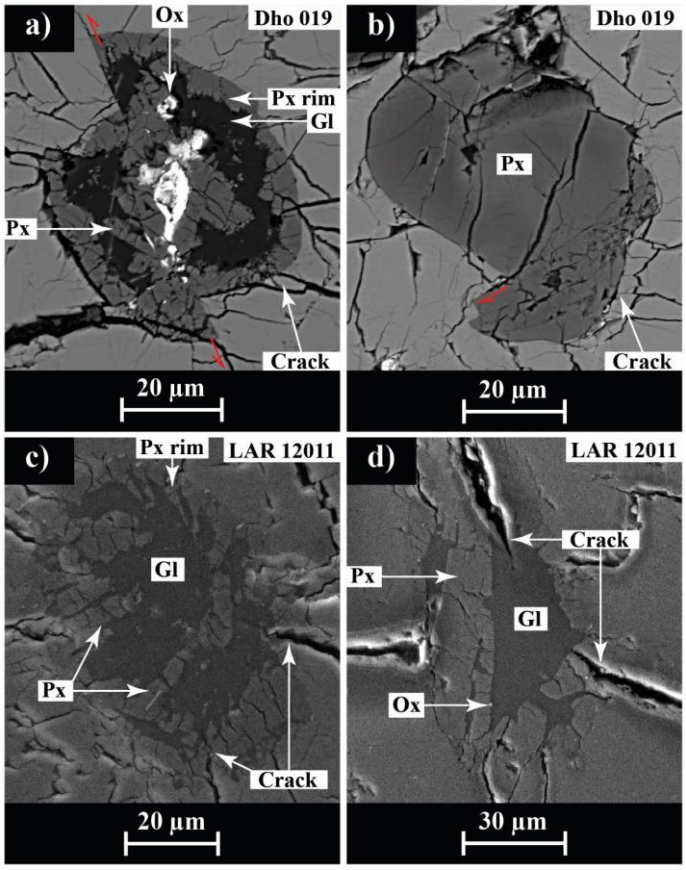

Figure 4.2: BSE images of melts inclusions observed in Dho 019, with (a) showing a poly-phase melt inclusion composed of glass + rim and blocky clinopyroxene + Fe-rich oxides and (b) a melt inclusion that has entirely crystallised to a pyroxene daughter crystal. Both melt inclusions also showing evidence of shearing as a result of shock. BSE images of melts inclusions observed in LAR 12011 are also presented in (c) and (d).

4.3 Results: Major and trace element compositions

4.3.1 Melt inclusions

Olivine-hosted melt inclusions in the olivine-phyric shergottites analysed in this study are circular to elliptical in shape and typically on the order of 20–100, 15–150, and 20–210 μm in diameter in depleted, intermediate, and enriched shergottites, respectively. Larger melt inclusions between 300–600 μm have also observed in megacrysts from NWA 10170. Melt inclusions in these meteorites show variable degrees of crystallisation (**Figure 4.1**-**Figure 4.2**, **Table 4.2**) and can be separated into several distinct types: 1) entirely silicate glass, 2) glass + skeletal clinopyroxene 3) glass + skeletal clinopyroxene + clinopyroxene rims surrounding the melt inclusion, 4) glass + skeletal and rim clinopyroxene + Fe-rich oxides (± phosphates), 5) glass + blocky and rim clinopyroxene + Fe-rich oxides + phosphates, 6) entirely crystallised to daughter crystals. Silica-rich glass has also been observed in some multi-phase inclusions such as in SaU 005 and NWA 10170 (**Figure 4.1c-d**). Many of the melt inclusions from these samples are intersected by cracks and fractures from their host olivine megacrysts (**Figure 4.1**-**Figure 4.2**), which in rare instances have infiltrated and altered the melt inclusions, such as in the BSE and X-ray map of the DaG 1037 glass-rich melt inclusion (**Figure 4.1a**). Some melt inclusions from Dho 019 show evidence of shearing along micro-fractures and shock-melt veins cutting through the host olivine megacrysts (**Figure 4.2a-b**). Additionally, all multi-phase melt inclusions containing glass observed in Dho 019 megacrysts were either heavily altered by shock-melt veins or too small to analyse. As such, only melt inclusions that had entirely crystallised to pyroxene daughter crystals were analysed from this sample.

Table 4.2: Types of melt inclusions (based on degree of crystallisation) observed in the shergottite meteorites analysed in this study.

Meteorites	Melt inclusion types
Depleted	
DaG 1037	Types 1 (entirely glass), 2 (glass + skeletal cpx), 3 (glass + skeletal and rim cpx), 4 (glass + skeletal and rim cpx + Fe-rich oxides)
Dho 019	Type 3, 4, 5 (glass + skeletal and blocky cpx + Fe-rich oxides), 6 (entirely crystallised to daughter crystals)
SaU 005	Types 1–*5*
Intermediate	
NWA 6234	Types 1–6
NWA 10170	Types 2–5

Enriched	
NWA 1068	Types 2–5
NWA 1183	Types 1–5
LAR 12011	Types 2–5

4.3.1.1 Depleted shergottites

Glasses in MIs from DaG 1037 and SaU 005 are characterised by similar SiO_2 (62–69 wt. %), Al_2O_3 (15–21 wt. %), FeO (1.8–4.3 wt. %), Na_2O (0.5–2.5 wt. %), and P_2O_5 (0.7–2.2 wt. %), but show differences in CaO, TiO_2, and MgO (wt. %) contents. Glasses in MIs from DaG 1037 are characterised by higher CaO (11-14 wt.%) and TiO_2 (0.8–1.2 wt. %) and lower MgO (0.7-1.0 wt. %) contents relative to SaU 005 (4–10, 0.3–0.6, and 0.9–3.2 wt. %, respectively). The Mg# for MI glasses from DaG 1037 range between 28–33 and show negative correlations when plotted against Al_2O_3 and TiO_2, respectively, and a broad positive correlation against CaO (**Figure 4.3a-c**). The Mg# for MI glasses from SaU 005 range between 42–57 and broadly parallel DaG 1037 MI glasses when plotted against Al_2O_3 and CaO, respectively, but at higher Al_2O_3 and lower CaO (wt. %) contents at a given Mg# (**Figure 4.3a-b**). In contrast to DaG 1037, the TiO_2 (wt. %) contents of SaU 005 MI glasses show a positive correlation against Mg# (**Figure 4.3c**). When plotted on a CaO–Na_2O–K_2O ternary diagram, MI glasses from both samples overlap consistently with each other (**Figure 4.4**).

Melt inclusions analysed from Dho 019 have entirely crystallised to daughter crystals that are compositionally comparable to groundmass pyroxene previously analysed from this sample (i.e., Taylor et al., 2002). These low-Ca pyroxene daughter crystals are pigeonite in composition, $En_{51-52}Fs_{39-41}Wo_{8-10}$, and have Mg# between 55–58.

Trace elements compositions were measured for glasses in two MIs from DaG 1037 and three from SaU 005, and for pyroxene daughter crystals in three MIs from Dho 019. The MI glasses from DaG 1037 and SaU 005 show similar concentrations of REEs, Sr, Ba, and Zr that range between 0.04–6.6 ppm, 25–174 ppm, 1.1–35 ppm, and 19–23 ppm, respectively. Glasses from DaG 1037 are more enriched in Y (33–42 ppm) and Nb (0.37–0.49 ppm) relative to that of SaU 005 (19–27 ppm Y and 0.12–0.36 ppm Nb). Pyroxene daughter crystals in MIs from Dho 019 are characterised by REEs, Sr, Ba, Y, Zr, and Nb that range between 0.02–6.3, 227–425, 17–37, 15–35, 26–28, 0.36–0.83 ppm, respectively.

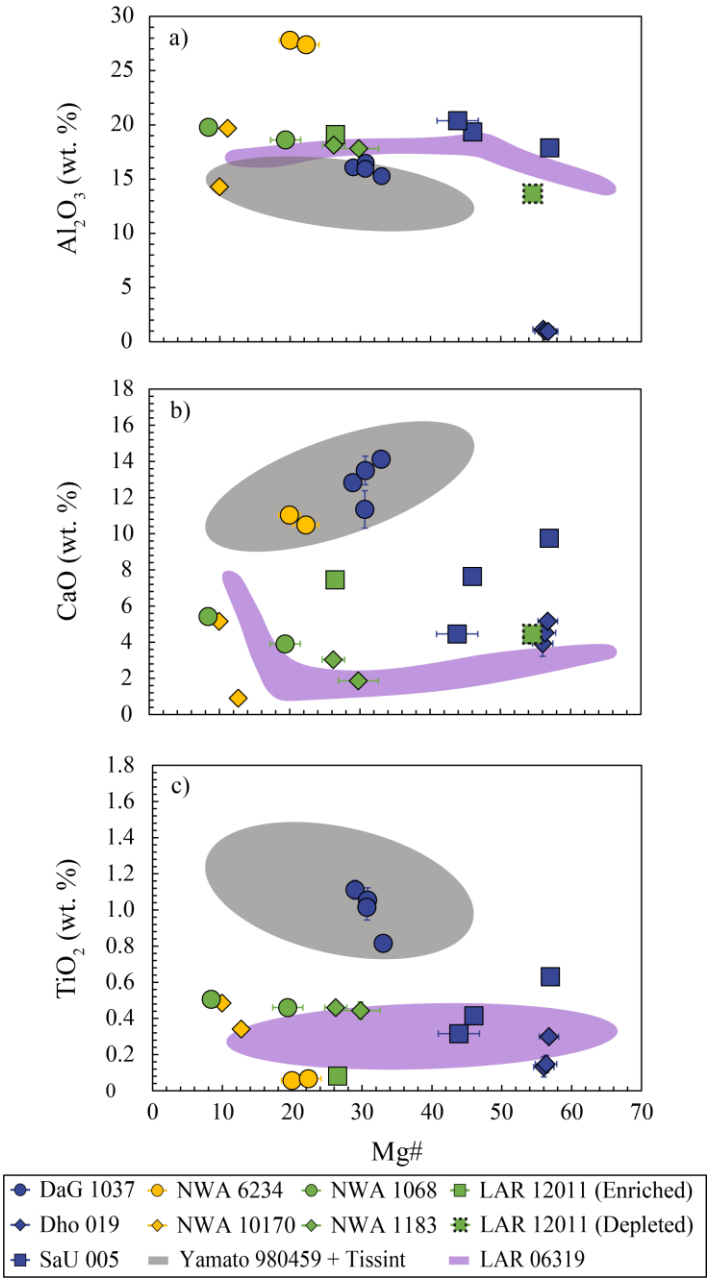

Figure 4.3: Melt inclusion glass major element data and Mg# comparison. Literature MI glass data for the depleted olivine-phyric shergottites, Yamato 980459 and Tissint (Peters et al., 2015), and the enriched olivine-phyric shergottite, LAR 06319 (Peslier et al., 2010; Sarbadhikari et al., 2011), were included for comparison.

The chondrite-normalised REE patterns for MI glasses from DaG 1037 and SaU 005, using the values of McDonough and Sun (1995), are LREE-depleted and characterised by $(La/Yb)_{CI}$ values between 0.02–0.11 (**Figure 4.5a-c**). Clear flattening and upward inflections of La (and Ce) have been observed for glass in one MI from DaG 1037, which also shows a positive Eu ($Eu/Eu^* = Eu_{CI}/[Sm_{CI}*Gd_{CI}]^{0.5}$ ~4.6, n=1) anomaly (~2.1), and for glasses in two MIs from SaU 005 (Fig. 5a-b). Chondrite-normalised

incompatible trace element (ITE) patterns for DaG 1037 and SaU 005 MI glasses show positive Ba, U, Sr, and Zr–Hf, and negative Pb anomalies (**Figure 4.6a-b**). Ratios of Zr/Y, Nb/Y, Zr/Nb, and Y/Nb for DaG 1037 and SaU 005 MI glasses range between 0.45–1.2, 0.005–0.014, 39–176, and 72–219, respectively, with those of SaU 005 extending to significantly higher Zr/Nb and Y/Nb values than that of DaG 1037. In plots of Zr/Nb against Y/Nb and La/Yb_{CI}, respectively, and Zr/Y against Nb/Y, values for DaG 1037 and SaU 005 MI glasses plot within 2SD of each other (**Figure 4.7**).

Chondrite-normalised REE patterns for pyroxene daughter crystals in MIs from Dho 019 show LREE-depleted patterns, with $(La/Yb)_{CI}$ values between 0.05–0.10. Two negative Eu anomalies between 0.7–0.9 were observed in the REE patterns of Dho 019 pyroxene daughter crystals, one of which also shows an upwards inflection of La, and a positive Eu anomaly of ~1.3 for pyroxene daughter crystal in the third MI (**Figure 4.5c**). Chondrite-normalised ITE patterns for Dho 019 pyroxene daughter crystals show positive Ba, U, Sr, and Zr–Hf, and negative Pb anomalies (**Figure 4.6a-c**). Ratios of Zr/Y, Nb/Y, Zr/Nb, and Y/Nb for Dho 019 pyroxene daughter crystals range between 0.82–1.7, 0.014–0.036, 34–75, and 28–72, respectively. In plots of Zr/Nb against Y/Nb and La/Yb_{CI}, respectively, Dho 019 pyroxene daughter crystals plot within 2SD of MI glasses from DaG 1037 and SaU 005 (**Figure 4.7**).

4.3.1.2 Intermediate shergottites

Glasses in MIs from NWA 10170 (*n=2*) are characterised by Na_2O, TiO_2, and P_2O_5 contents of 0.57–1.4, 0.3–0.5, and 0.2–0.3 wt. %, respectively, but show some compositional differences. Glass in one MI is characterised by SiO_2, Al_2O_3, CaO, and K_2O contents that range between 77.0–77.5 wt. %, 14.2–14.4 wt. %, 5.1–5.3 wt. %, and 0.15–0.18 wt. %, respectively, while glass in the second MI is characterised by lower SiO_2 (72.5–73.0 wt. %) and CaO (0.91–0.93 wt. %) and higher Al_2O_3 (19.3–20.1 wt. %) and K_2O (2.7–4.8 wt. %) contents. Glasses in both MIs show relatively narrow ranges in FeO and MgO contents (1.1–1.5 and 0.08–0.10 wt. %, respectively) that correspond to Mg# between 9.4–11 and 12–14, respectively. The Mg# for LAR 12011 MI glasses show a negative correlation against CaO that plots parallel to NWA 1068 and NWA 1183 MI glasses but at higher CaO (wt. %) contents at a given Mg#, and a positive correlation against Al_2O_3 that partially overlaps with NWA 1068 and NWA 1183 MI glasses towards lower Mg# (**Figure 4.3a-c**). The CaO, Na_2O, and K_2O (wt. %) contents for NWA 10170 MI glasses show two distinct groupings that trend from high-CaO (low-K_2O) values for the lower-Mg# glass, which overlap with those of MI glasses from the depleted shergottites, to low-CaO and high-K_2O and Na_2O values for the higher-Mg# glass (**Figure 4.4**).

For NWA 6234, MIs analysed from this sample have entirely crystallised to daughter crystals that are compositionally comparable to maskelynite previously analysed from NWA 10170 (i.e., Howarth and Udry, 2017), which may be paired to NWA 6234. These maskelynite daughter crystals are characterised by SiO_2, Al_2O_3, CaO, Na_2O, TiO_2 and contents that range between 57–59 wt. %, 27–28 wt. %, 10–11

wt. %, 4.8–5.4 wt. %, and 0.03–0.08 wt. %, respectively. The FeO and MgO contents for NWA 6234 maskelynite daughter crystals range between 1.0–1.5 and 0.16–0.22 wt. %, respectively, and correspond to Mg# between 18–25.

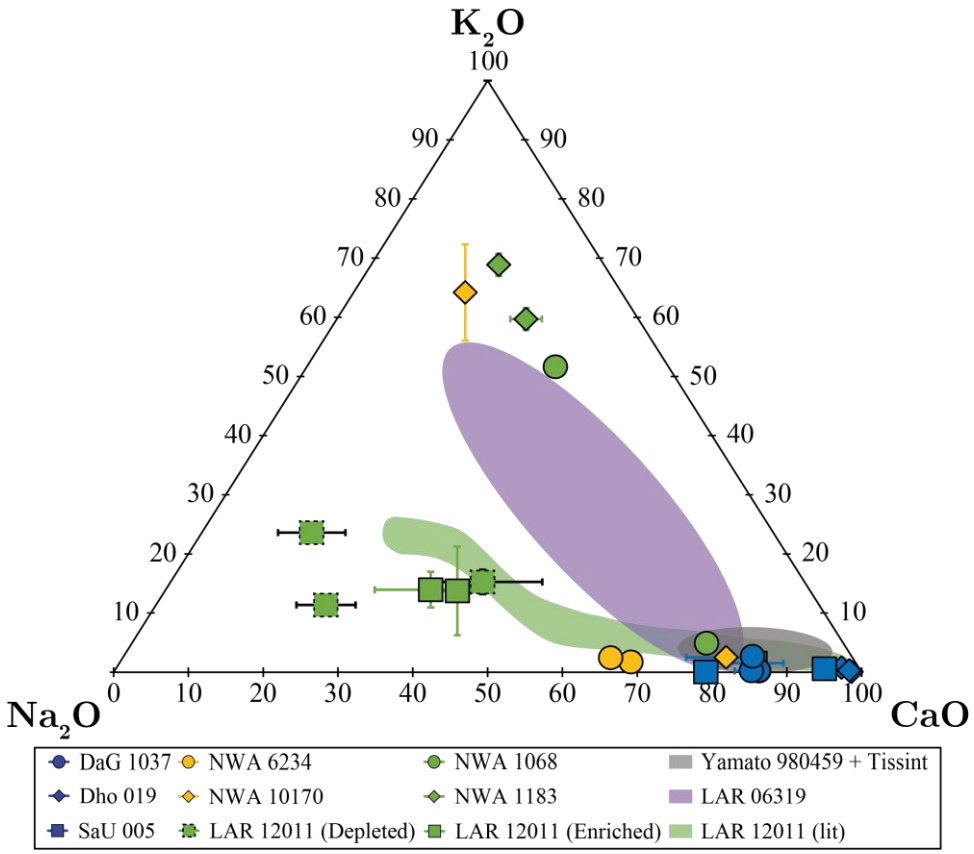

Figure 4.4: CaO-K_2O-Na_2O ternary diagram for MI glass from the shergottite meteorites analysed in this study. (See **Figure 4.3** for Yamato 980459, Tissint, and LAR 06319 MI glass literature sources).

Trace elements compositions were measured for glasses in two MIs from NWA 10170, and for maskelynite daughter crystals in two MIs from NWA 6234. Glasses in the NWA 10170 MIs also show compositional differences in their trace element compositions, with the lower-Mg# glasses characterised by REEs, Sr, Ba, Y, Zr, and Nb concentrations of 0.17–4.4 ppm, ~94 ppm, ~43 ppm, ~11 ppm, ~78 ppm, and ~ 2.3 ppm, respectively. The higher-Mg# MI glasses are characterised by higher concentrations of REEs (0.83–14 ppm), Sr (~151 ppm), Ba (~50 ppm), Y (~62 ppm), and Nb (~4.3 ppm), respectively, and lower Zr (~61 ppm). Chondrite-normalised REE patterns for glasses in both MIs are LREE-enriched (**Figure 4.5e**), with $(La/Yb)_{CI}$ values of 0.5–0.6, and show upward inflections of La–Ce. The lower-Mg# MI glasses analysed also show a distinct positive Ce ($Ce/Ce^* = Ce_{CI}/[La_{CI}*Pr_{CI}]^{0.5}$) anomaly of ~1.5, while the higher-Mg# MI glasses show a negative Ce anomaly of ~0.8 and a positive Eu anomaly of ~1.5. The CI-normalised ITE pattern for lower-Mg# MI glasses are characterised by negative Pb and positive Ba, Sr, and Zr–Hf anomalies, while that of the higher-Mg# MI glasses show negative Pb, Sr, and Zr–Hf and positive Rb and U anomalies (**Figure 4.6e**). Ratios of

Zr/Nb, Y/Nb, Zr/Y, and Nb/Y average ~34, ~4.9, ~6.9, and ~0.20, respectively for the lower-Mg# MI glass and ~14, ~15, ~1.0, and ~0.07, respectively, for the higher-Mg# glass. In plots of Zr/Nb against Y/Nb and La/Yb_{CI}, respectively, values for glasses from the NWA 10170 MIs plot at lower values than MI glasses from the depleted shergottites (**Figure 4.7a-b**). In the plot of Zr/Y against Nb/Y, values for glasses from the NWA 10170 MIs plot at higher values and parallel the broad positive correlation for MI glasses from the depleted shergottites (**Figure 4.7c**).

Maskelynite daughter crystals in MIs from NWA 6234 are characterised by REEs, Sr, Ba, Y, Zr, and Nb that range between 0.02–0.37 ppm, 84–97 ppm, 12–15 ppm, 0.15–0.27 ppm, 0.50–1.04 ppm, and <0.03 ppm, respectively. Chondrite-normalised REE patterns for maskelynite daughter crystals in the NWA 6234 MIs are relatively flat (i.e., REE of ~0.1–6.5x chondrite), with $(La/Yb)_{CI}$ of 0.74 (*n=1*), and show pronounced positive Eu anomalies ($Eu/Eu^* = Eu_{CI}/[Sm_{CI}*Gd_{CI}]^{0.5}$ ~4.6, n=1) (**Figure 4.5d**). The CI-normalised ITE patterns for these NWA 6234 maskelynite daughter crystals show positive Ba, U, Pb, and Sr and negative Zr–Hf anomalies (**Figure 4.6d**). Ratios of Zr/Nb, Y/Nb, and Zr/Y for maskelynite daughter crystals range between 20–41, 6.0–11, and 3.1–3.9, respectively.

4.3.1.3 Enriched shergottites

Glasses in MIs from NWA 1068 MIs (*n=2*) show compositional differences yet are both characterised by similar SiO_2 (67–71 wt. %), Al_2O_3 (19–20 wt. %), CaO (3.8–5.6 wt. %), Na_2O (1.3–1.8 wt. %), P_2O_5 (0.6–1.6 wt. %), and TiO_2 (0.5–0.8 wt. %) contents. Glasses in these MIs have two populations - low K_2O (0.3–0.4 wt. %) and high K_2O (5.9–6.3 wt. %). Glasses from NWA 1183 MIs (*n=2*) are characterised by similar SiO_2 (65–67 wt. %), Na_2O (1.4–1.9 wt. %), and P_2O_5 (0.9–1.4 wt. %) contents to that of NWA 1068 MI glass but shows higher K_2O (7.1–8.4 wt. %) and lower Al_2O_3 (17–18 wt. %), CaO (1.6–3.2 wt. %), and TiO_2 (0.4–0.5 wt. %) contents. Glasses from both samples show relatively narrow ranges in FeO and MgO contents (0.9–2.0 and 0.1–0.4 wt. %, respectively) that correspond to Mg# between 8–25 (NWA 1068) and 19–38 (NWA 1183). In plots of Mg# against Al_2O_3, CaO, and TiO_2, respectively, MI glasses from NWA 1068 and NWA 1183 show continuous negative trends that extend from the higher-Mg# glasses of NWA 1183 to lower-Mg# glasses of NWA 1068 (**Figure 4.3 a-c**). The CaO, Na_2O, and K_2O (wt. %) contents for NWA 1068 MI glasses show two distinct groupings that trends from high-CaO (low-K_2O) values, which overlap with those of MI glasses from the depleted shergottites, to low-CaO (high-K_2O) at relatively constant Na_2O, which plots close to the higher-Mg# MI glass from NWA 10170. Glasses in NWA 1183 MIs plot along the CaO–K_2O (at relative constant Na_2O) trend defined by NWA 1068 but at even higher K_2O (and lower CaO) (wt. %) contents (**Figure 4.4**).

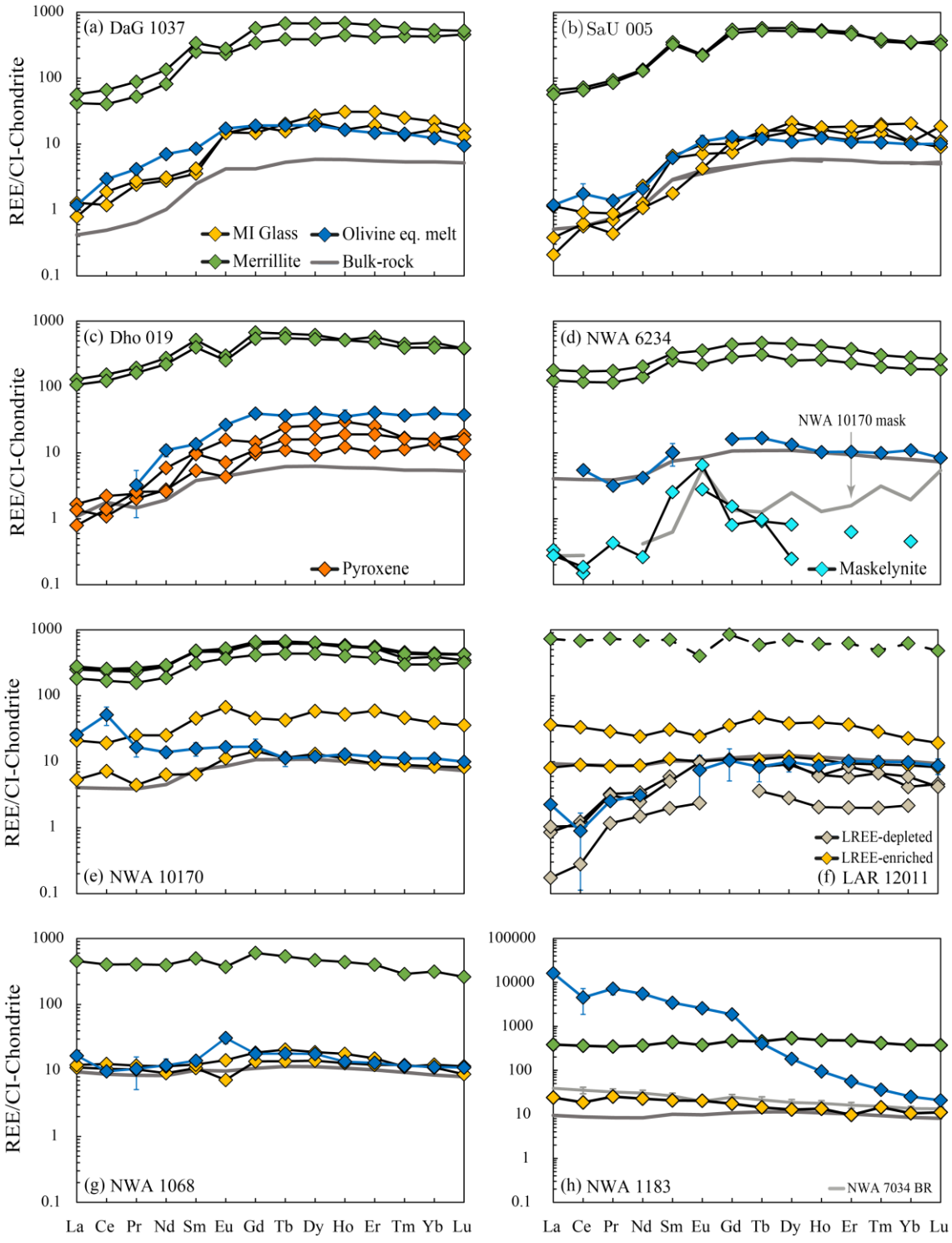

Figure 4.5: CI–normalised (McDonough and Sun, 1995) REE plots for MI glass and late-stage merrillite from the shergottite meteorites analysed in this study. The REE patterns for melts in equilibrium with olivine (from chapter 3) and bulk-rock for each sample were included for comparison. Bulk-rock REE data were sourced from the following: DaG 1037/476, Dho 019, SaU 005/051, LAR 12011: Day et al. (2018); Dho 019: Taylor et al. (2002); SaU 005: Dreibus et al. (2000); NWA 6234 and 10170: Filiberto et al. (2012); NWA 1068 and NWA 1183: Barret et al. (2002) and Filiberto et al. (2010). REE data for NWA 7034 bulk-rock (Nyquist et al., 2016; Armytage et al., 2018) was also included for comparison. Literature merrillite REE data for LAR 12011 was taken from Caseres, J.R. (2015).

Glasses in LAR 12011 MIs (*n=5*) are characterised by FeO contents that range between 1.2–2.0 wt. % but show some compositional differences. Glasses from three MIs show SiO_2, Al_2O_3, Na_2O, and CaO that range between 70–72, 14–16, 6.0–7.4, and 1.9–4.4 wt. %, respectively, while glass in the remaining MIs (*n=2*) show lower SiO_2 (59–66 wt. %) and Na_2O (5.3–5.8 wt. %) and higher Al_2O_3 (17–19 wt. %) and CaO (7.0–7.4 wt. %) contents. The K_2O contents for glass in these MIs range between 1.3–2.7 wt. %, excluding one MI glass with an anomalously high K_2O content of 7.6 wt. %. The CaO, Na_2O, and K_2O (wt. %) contents for LAR 12011 MI glasses plot at similar CaO contents to MI glasses from NWA 1068 and NWA 1183 but at significantly lower K_2O (higher Na_2O) contents (**Figure 4.4**).

The trace element concentrations of glasses were measured in two MIs from NWA 1068, one from NWA 1183, and five from LAR 12011. The concentrations of REEs in MI glasses range between 0.21–7.6 ppm for NWA 1068, 0.27–11 ppm for NWA 1183, and 0.04–20 ppm for LAR 12011. The MI glasses of NWA 1068 are also characterised by lower concentrations of Sr (123–148 ppm), Ba (45–88 ppm), Y (19–22 ppm), Zr (62–83 ppm), and Nb (4.2–5.2 ppm) relative to that of NWA 1183 (177 ppm Sr, 390 ppm Ba, 17 ppm Y, 133 ppm Zr, and 10 ppm Nb). Glasses in MIs from LAR 12011 are compositionally more variable and characterised by Sr, Ba, Y, Zr, and Nb concentrations that range between 80–280 ppm, 111–240 ppm, 0.57–50 ppm, 55–247 ppm, and 2.4–20 ppm, respectively.

Glasses in NWA 1068 MIs are characterised by LREE and HREE concentrations of 7.1–18x and 8.6–20x chondrite, respectively. The REE patterns for these glasses are LREE-enriched, with $(La/Yb)_{CI}$ values of ~1.0, and show concave MREE-HREE profiles that peak between Gd–Tb–Dy and negative Eu anomalies between 0.6–0.8 (**Figure 4.5g**). Glasses from the NWA 1183 MI are characterised by similar concentrations of HREEs (10–15x chondrite) but are more LREE-enriched (17–25x chondrite). The REE pattern for NWA 1183 MI glass is characterised by a $(La/Yb)_{CI}$ ~2.3 and shows a minor negative Ce anomaly of ~0.8 (**Figure 4.5h**).

Glass in one MI from LAR 12011 is characterised by similar concentrations of LREE (8.1–11x chondrite) and HREE (8.2–12x chondrite) to those of NWA 1068 MI glasses, and show a LREE-enriched REE pattern with $(La/Yb)_{CI}$ value of ~0.9. Glasses from a second LAR 12011 MI are characterised by significantly higher concentrations of LREE (24–36x chondrite) and HREE (19–47x chondrite) and show a LREE-enriched REE pattern, with a $(La/Yb)_{CI}$ value of ~1.6. Glasses from the remaining three MIs show consistently lower concentrations of LREE (0.17–9.8x chondrite) and HREE (2.0–9.5x chondrite) and display LREE-depleted REE patterns with $(La/Yb)_{CI}$ values ranging between 0.08–0.21. Olivine megacrysts hosting LREE-depleted MI glasses have Fo contents between Fo_{68} and Fo_{75}, while those hosting LREE-enriched MI glass have values between Fo_{69} and Fo_{73}. One of the LREE-enriched MI glasses analysed from LAR 12011 was found towards the rim of its host olivine megacryst

and the other towards the core of its host. In contrast, all the LREE-depleted MI glasses were found towards the cores of their host olivine.

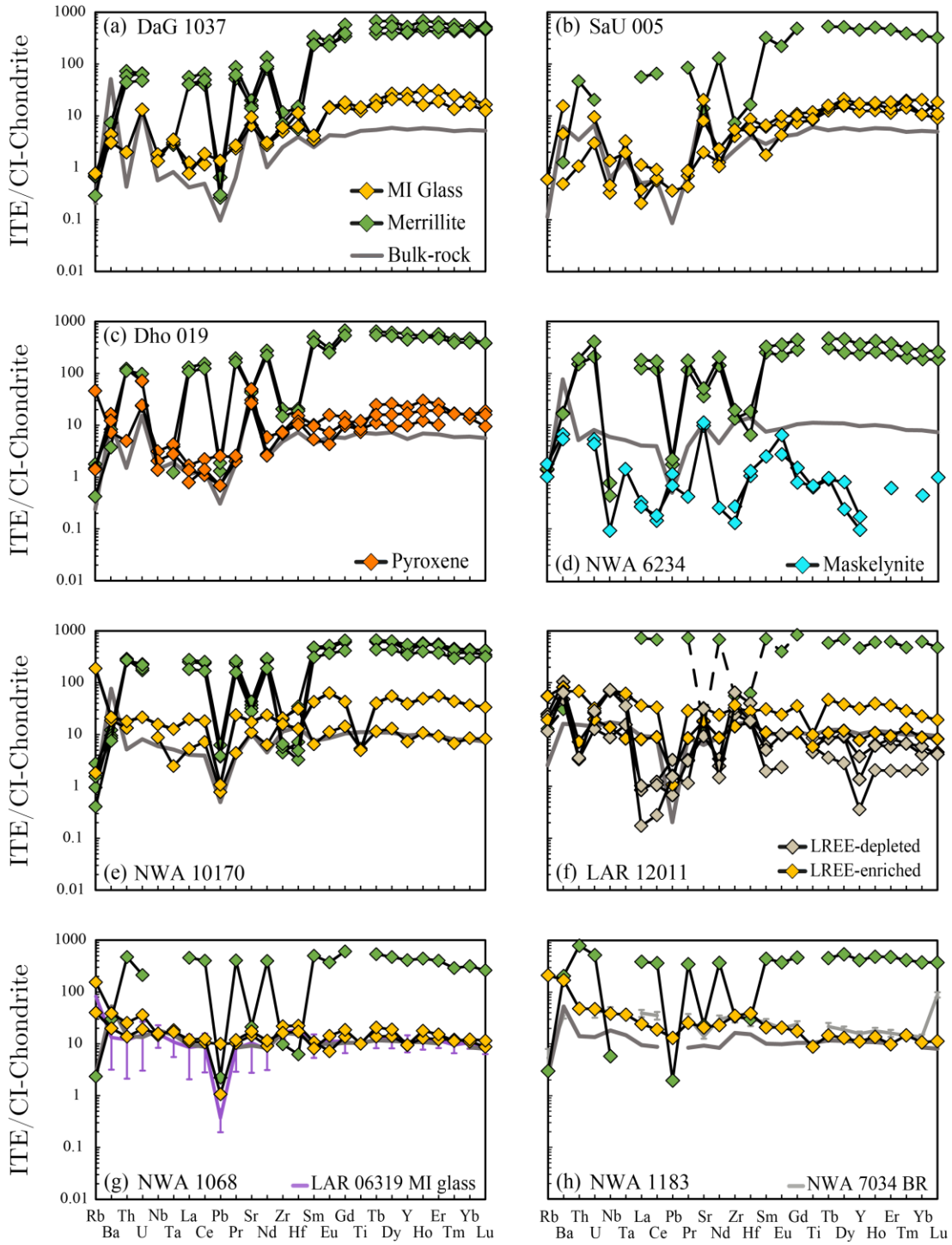

Figure 4.6: CI–Chondrite normalised (McDonough and Sun, 1995) ITE plots for MI glass and late-stage merrillite from the shergottite meteorites analysed in this study. Bulk-rock ITE data for NWA 7034 was also included for comparison (See Fig. 1 for bulk-rock ITE data references). (See **Figure 4.5** for Yamato 980459, Tissint, and LAR 06319 MI glass and NWA 7034 bulk-rock literature sources). Literature merrillite ITE data for LAR 12011 was taken from Caseres, J.R. (2015).

Chondrite-normalised ITE patterns for MI glasses across these samples show positive Zr–Hf and Sr and negative Pb anomalies, with those of LAR 12011 also showing distinct negative Y anomalies that are more pronounced in MI glasses with lower concentrations of LREEs (**Figure 4.6f-h**). The Zr/Nb, Y/Nb, Zr/Y, and Nb/Y values for NWA 1068 MI glasses range between 15–16, 3.7–5.2, 2.8–4.3, and 0.19–0.27, respectively, and plot consistently within 2SD of enriched shergottite bulk-rock compositions (**Figure 4.7**). In contrast, NWA 1183 MI glasses shows lower Zr/Nb (~13) and Y/Nb (~1.7) and higher Zr/Y (~7.7) and Nb/Y (~0.60) values than NWA 1068 MI glasses. The NWA 1183 MI glasses partially overlap with enriched shergottite bulk-rock Zr/Nb and Y/Nb values and away from bulk-rock Zr/Y and Nb/Y values (**Figure 4.7a-b**). For LAR 12011, MIs glasses with LREE-enriched characteristics (*n=2*) show Zr/Nb, Y/Nb, Zr/Y, and Nb/Y values that range between 6.2–15, 2.5–3.3, 2.5–4.5, and 0.30–0.40, respectively, while those with LREE-depleted characteristics show values between 7.2–39, 0.03–2.5, 15–250, and 0.40–35, respectively (*n=3*). When plotted against Y/Nb, the Zr/Nb values for LREE-depleted and LREE-enriched MI glasses show two distinct negative trends, with LREE-depleted glass plotting at higher Zr/Nb values at a given Y/Nb (**Figure 4.7a**). When plotted against $(La/Yb)_{CI}$, the Zr/Nb values for LREE-depleted MI glasses plot towards MI glasses from the depleted shergottites, while values for the LREE-enriched MI glasses plot towards enriched bulk-rock compositions (**Figure 4.7b**). In the plot of Zr/Y against Nb/Y, values for glasses from the LREE-enriched MI glasses plot towards and partially overlap with enriched bulk-rock compositions, while values for the LREE-depleted MI glasses plot at higher Zr/Y and Nb/Y values and away from depleted shergottite MI glasses (**Figure 4.7c**).

4.3.2 Merrillite

4.3.2.1 Depleted shergottites

Major element compositions were measured for four merrillite from DaG 1037, two from Dho 019, and three from SaU 005. Merrillite from DaG 1037 and SaU 005 are characterised by Na_2O and FeO contents of 1.3–1.7 and 1.1–1.4 wt. %, respectively, but show differences in MgO content (i.e., 3.1–3.4 vs 3.4–3.6 wt. % for DaG 1037 and SaU 005 respectively). Merrillites in both samples are characterised by high Mg# values (81–85) that overlap consistently with each other and show no clear correlations when plotted against Na_2O (**Figure 4.8**). Merrillite from Dho 019 is characterised by MgO contents of 3.0–3.4 wt. % and FeO (2.1–3.2 wt. %) contents that are higher than those of DaG 1037 and SaU 005. The Mg# for these merrillite grains range between 66–73 and plot at lower Na_2O (1.0–1.1 wt. %) contents than DaG 1037 and SaU 005.

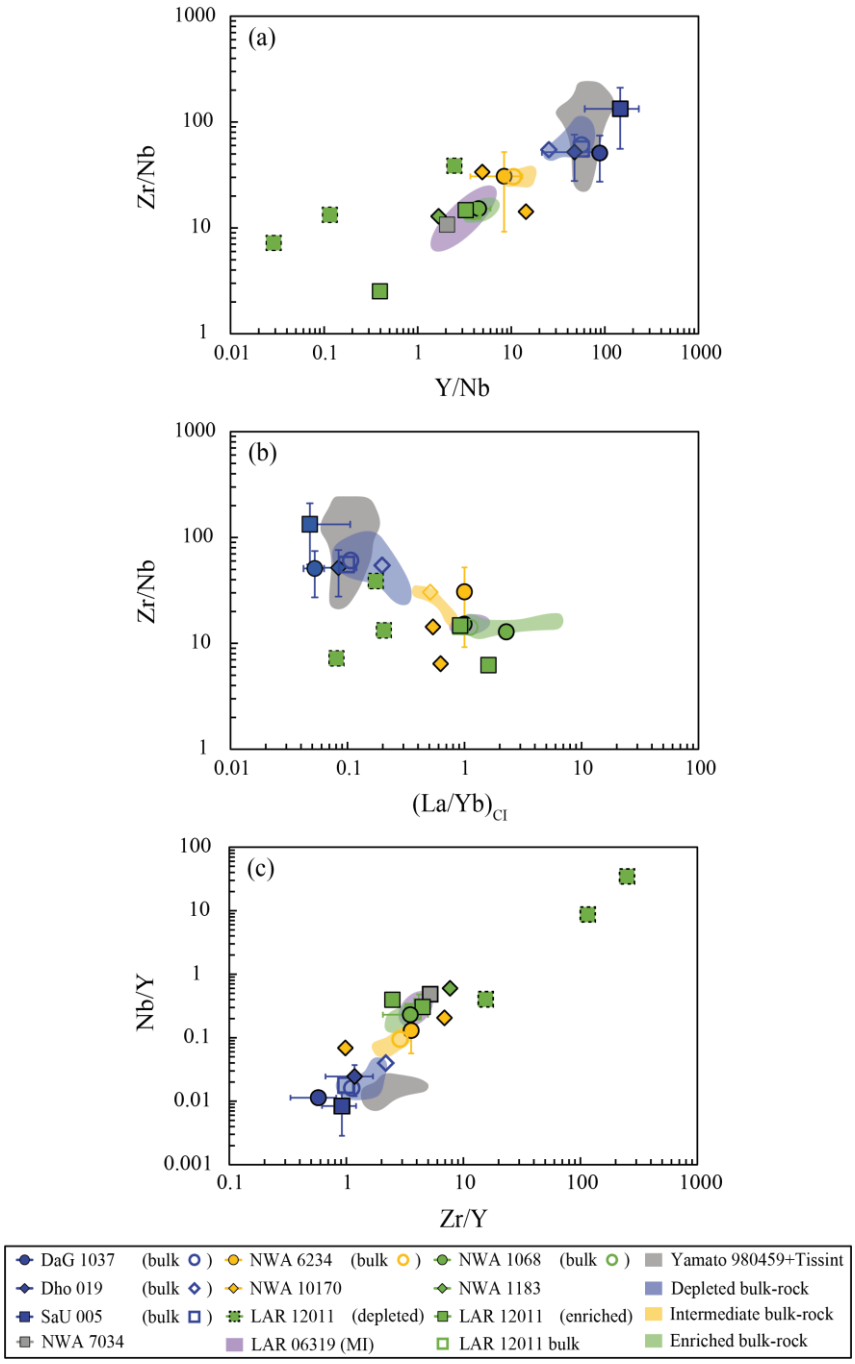

Figure 4.7: HFSEs ratios for MI glass from the shergottite meteorites in comparison to values for shergottite bulk-rock compositions. Shergottite fields constructed using bulk-rock data from Day et al. (2018). HFSE data for MIs from Yamato 980459 and Tissint (Peters et al., 2015), LAR 06319 (Sarbadhikari et al., 2011), and bulk-rock NWA 7034 (Nyquist et al., 2016; Armytage et al., 2018) has also been included for comparison.

Trace element concentrations of merrillite were measured for three grains from DaG 1037 and two from Dho 019 and SaU 005, respectively. The concentrations of REEs and Y for merrillite across these samples range between 4.8–166 ppm and 626–922 ppm, respectively. Merrillite from DaG 1037 and SaU 005 record similar concentrations of Sr (119–172 ppm) and Zr (5.5–45 ppm) but show differences

in Ba concentrations, with higher values for DaG 1037 (7.0–17 ppm) relative to SaU 005 (2.9–6.8 ppm). Merrillite from Dho 019 is characterised by significantly higher concentrations of Sr (367–391ppm) and Zr (56–78 ppm) but shows similar concentrations of Ba (8.5–18.9 ppm) to merrillite from DaG 1037. The CI-normalised REE patterns for merrillite from DaG 1037, Dho 019, and SaU 005 are LREE-depleted and characterised by $(La/Yb)_{CI}$ values between 0.09–0.10, 0.27–0.28, and 0.16–0.19, respectively (**Figure 4.5a-c**). These merrillite REE patterns show negative Eu anomalies, between 0.5 and 0.8 that are generally more pronounced for Dho 019 and SaU 005 relative to DaG 1037. A minor positive La anomaly has also been observed for one merrillite grain from DaG 1037. Chondrite-normalised ITE patterns for merrillite across these meteorites overlap consistently with each other and show positive Th–U, La–Ce and negative Nb, Sr, Zr–Hf anomalies (**Figure 4.6a-c**).

4.3.2.2 Intermediate shergottites

Major element compositions were measured for three merrillite from NWA 6234 and four from NWA 10170. Merrillite in these samples are compositionally similar and are characterised by Na_2O, FeO, and MgO contents that range between 1.0–1.3, 1.4–2.2, and 2.9–3.6 wt. %, respectively, with those of NWA 6234 showing marginally higher FeO and lower MgO contents. The Mg# for merrillite from NWA 6234 and NWA 10170 range between 76–82 and broadly plot along the Mg#-Na_2O trend for merrillite from the depleted shergottites (**Figure 4.8**).

Merrillite trace element compositions were measured for two grains from NWA 6234 and four from NWA 10170. Merrillite from both samples show similar concentrations of REEs (4.5–157 ppm), Sr (234–441 ppm), Y (371–848 ppm), and Zr (22–75 ppm), with those of NWA 10170 extending to lower Sr and Zr and higher REE and Y concentrations. Merrillite from these samples show differences in Ba contents, with lower concentrations recorded for NWA 10170 (17–28 ppm) relative to NWA 6234 (38–39 ppm). Chondrite-normalised REE patterns for merrillite from both samples are more LREE-enriched than those from depleted shergottites and characterised by $(La/Yb)_{CI}$ values between 0.6–0.7 (**Figure 4.5d-e**). The REE patterns for most merrillites from NWA 6234 and NWA 10170 show no Eu anomalies, excluding one NWA 6234 grain with a minor negative Eu anomaly of ~0.8. The CI-normalised ITE patterns for merrillite from NWA 6234 and NWA 10170 show positive Th–U, La–Ce and negative Nb, Sr, and Zr–Hf anomalies, and strongly resemble those of merrillite from the depleted shergottites (**Figure 4.6d-e**).

4.3.2.3 Enriched shergottites

Major element compositions were measured for three merrillites from NWA 1068 and two from NWA 1183. Merrillite from both samples are characterised by similar Na_2O and MgO contents that range between 1.1–1.6 and 2.2–2.9 wt. %, respectively, but show differences in FeO contents, with lower values for NWA 1068 (1.9–2.2 wt. %) relative to NWA 1183 (2.5–3.1 wt. %). The Mg# for merrillite

range between 64–71 and 58–66 for NWA 1068 and NWA 1183, respectively, and show no clear correlation against Na_2O (**Figure 4.8**).

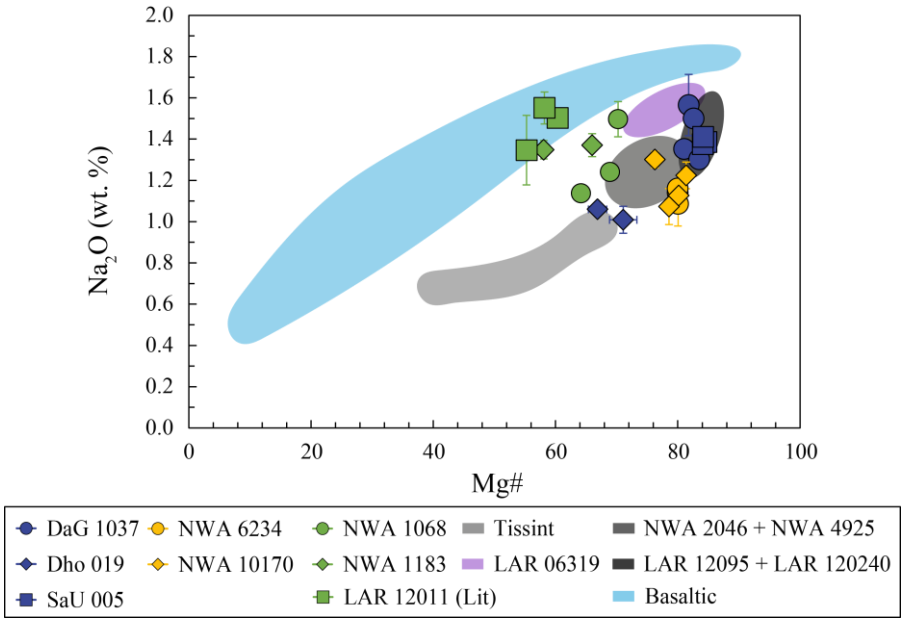

Figure 4.8: Merrillite Na_2O contents vs Mg#. Merrillite data for NWA 2046 and NWA 4925 was taken from the first chapter of this thesis, while those of Tissint, LAR 12095-LAR 12240, LAR 06319, LAR 12011, and basaltic shergottites were taken from the following literature sources: Peslier et al. (2010), Balta et al. (2013), Balta et al. (2015), Caseres (2015), Shearer et al. (2015), and Dunham et al. (2019). Literature merrillite data for LAR 12011 was taken from Caseres, J.R. (2015).

Merrillites from NWA 1068 and NWA 1183 are fine-grained and difficult to analyse, and as a result, trace element compositions were only measured for one grain from each sample. The merrillites analysed from NWA 1068 and NWA 1183 both show similar concentrations of REE (6.4–247 and 9.2–223 ppm, respectively), Sr (180 and 193 ppm, respectively), and Y (645 and 655 ppm, respectively). Merrillite from NWA 1183 is distinctly more enriched in Ba (471 ppm) and Zr (129 ppm) relative to that of NWA 1068 (69 ppm Ba and 37 ppm Zr). Chondrite-normalised REE patterns for merrillite from NWA 1068 and NWA 1183 are LREE-enriched, with $(La/Yb)_{CI}$ values of 1.5 and 1.0, respectively, and show negative Eu anomalies of ~0.7 (NWA 1068) and ~0.8 (NWA 1183) (**Figure 4.5g-h**). Chondrite-normalised ITE patterns for merrillite from both samples also show positive Th–U, La–Ce and negative Nb, Sr, and Zr–Hf anomalies and strongly resemble those of merrillite from the depleted and intermediate shergottites (**Figure 4.6g-h**).

4.4 Discussion

4.4.1 The influence of post-magmatic alteration on melt inclusion glass REE compositions

The impact of post-magmatic alteration on martian meteorites was explored in-depth in chapters 2 and 3, where enrichment of LREEs was observed in olivine megacrysts from DaG 1037, Dho 019, SaU 005, NWA 6234, NWA 10170, NWA 1068, NWA 1183, and LAR 12011. For most of these samples, LREE-enrichment was accompanied by enrichment of other fluid mobile elements, including Ba, Sr, and U, indicating alteration processes during their host meteorites residence on Earth as terrestrial fluids percolated through shock-induced melt veins and cracks (e.g., Barrat et al., 2001; Crozaz and Wadhwa, 2001; Crozaz et al., 2003; Burgin et al., 2022; Orr et al., 2022). These melt veins and cracks were shown to intersect some MIs from their host olivine megacrysts (**Figure 4.1** and **Figure 4.2**) and may have sub-surface areas that could not be avoided during laser analyses. As such, the trace element data for MI glasses and daughter crystals must first be assessed for terrestrial alteration effects prior to interpreting primary signatures.

The MI pyroxene daughter crystal showing a positive La anomaly in Dho 019 (*n=1*) is characterised by significantly higher concentrations of Sr (>400 ppm) and Ba (>37 ppm) relative to other MI pyroxene daughter crystals analysed (<270 ppm Sr and <27 ppm Ba; *n=2*). Similarly, MI glasses with minor positive La anomalies from SaU 005 (*n=2*) also show higher concentrations of Sr (>100 ppm) and Ba (>20 ppm) relative to other MI glasses (<70 and <11 ppm, respectively; *n=1*). These observations for Dho 019 pyroxene daughter crystals and SaU 005 MI glasses are consistent with the enrichment of LREEs, Ba, and Sr observed in the olivine and bulk-rock trace element findings of chapters 2 and 3, which were interpreted to reflect the effects of terrestrial alteration. This suggests that the minor positive La and Ce anomalies observed in SaU 005 MI glasses and Dho 019 pyroxene daughter crystals were likely inherited during their hosts residence on Earth. For DaG 1037, the concentrations of Sr and Ba for MI glass with a minor positive La anomaly (<60 and <8 ppm, respectively, *n=1*) are lower than in glass from the other MI (>80 and >10 ppm, respectively, *n=1*), and therefore, inconsistent with terrestrial alteration.

For NWA 10170, enrichment of LREEs in MI glasses has resulted in a distinct positive Ce anomaly in one MI. Positive Ce anomalies have also been observed in the REE patterns of olivine megacrysts analysed in chapter 3 and were interpreted to reflect alteration in an oxidising environment, possibly through terrestrial alteration on Earth. This interpretation does require more work on NWA 10170 MI glass trace elements.

For NWA 1183, the REE pattern for NWA 1183 MI glass shows upward inflections of LREE-MREEs (La–Gd) and a distinct Ce anomaly, relative to NWA 1068 MI glass and bulk-rock. The REE pattern for NWA 1183 MI glass does, however, broadly mirror those of olivine megacrysts analysed in chapter 3, which were suggested to have inherited their LREE characteristics through a complex set of processes. The NWA 1183 MI glass also shows higher concentrations of Sr (>170 ppm) and Ba (>390 ppm) relative to MI glasses from NWA 1068 (<150 ppm Sr and <90 ppm Ba; *n=2*), which coupled with the upward inflections of LREE-MREEs for NWA 1183 MI glass are consistent with the effects of terrestrial alteration. Nevertheless, terrestrial alteration alone is unlikely to account for the K_2O-rich contents of NWA 1183 MI glass relative to NWA 1068 and LAR 12011 (**Figure 4.4**), which may allude to more open-system processes, such as magma mixing and crustal assimilation, likely soon after its parent melt segregated from source.

For LAR 12011, depleted MI glasses (*n=3*) show similar concentrations of Sr (80 – 270 ppm) and Ba (111 – 240 ppm) to values for enriched MI glasses (157 – 280 ppm Sr and 157 – 189 ppm Ba; *n=2*). This suggests that there are minimal effects of terrestrial alteration on the REE patterns of depleted and enriched MI glasses analysed from LAR 12011.

4.4.2 Evaluating the use of MI glass to constrain shergottite parent melt REE contents

4.4.2.1 Depleted shergottites

The CI-normalised REE and ITE patterns for glass in MIs from DaG 1037 and SaU 005 parallel those of their bulk-rocks although at higher absolute concentrations (**Figure 4.5a-b, Figure 4.6a-b**), with those of SaU 005 showing some overlap with bulk-rock LREE profiles. Discrepancies in the REE concentrations for DaG 1037 and SaU 005 MI glass and bulk-rock could possibly reflect REE changes through (i) post-entrapment crystallisation of wall olivine and daughter pyroxene crystals within the melt inclusions, or (ii) olivine fractionation in the parent melt affecting the absolute concentrations of these elements in bulk-rock (Shafer et al., 2010; Filiberto and Dasgupta, 2011). In a study of MIs in the depleted shergottites Yamato 980459 and Tissint, Peters et al. (2015) demonstrated through post-entrapment re-equilibration modelling that the crystallisation of wall olivine and daughter crystals alters the absolute concentrations of REEs in MI glasses, owing to reduction in melt volume, with no significant changes in REE patterns. These findings, coupled with strong similarities in MI glass and bulk-rock REE and ITE patterns for DaG 1037 and SaU 005, indicate that the REE patterns for MI glasses from these samples were not significantly affected by post-entrapment crystallisation. As such, the trace element compositions for DaG 1037 and SaU 005 MI glasses reliably reflect the trapped melt compositions. This interpretation is also supported by plots of REE and HFSE ratios, which show DaG 1037 and SaU 005 MI glasses consistently plotting within 2SD of MIs from Yamato 980459 and Tissint and depleted shergottite bulk-rock compositions (**Figure 4.7a-b**).

The CI-normalised REE pattern for the melt in equilibrium with pyroxene daughter crystals in Dho 019 MIs can be estimated with pyroxene-melt partition coefficients for martian basalts calculated using Tissint, the most primitive sample analysed in this study and previously shown to be in Mg-Fe equilibrium with bulk-rock (e.g., Liu et al., 2016). Tissint pyroxene and bulk-rock REE used to estimate pyroxene-melt partition coefficients were taken from Balta et al. (2015) and Day et al. (2018). The calculated melt in equilibrium with pyroxene daughter crystals in MIs from Dho 019 plots parallel to that of Dho 019 bulk-rock and the calculated melt in equilibrium with Dho 019 olivine megacrysts from chapter 3, although at higher absolute concentrations (**Figure 4.11**).

4.4.2.2 Intermediate shergottites

The CI-normalised REE and ITE patterns for glass from the two NWA 10170 MIs strongly mirror those of bulk-rock NWA 6234, which may be paired to NWA 10170, and as such, can be used as a possible bulk-rock equivalent. (**Figure 4.5 d-e, Figure 4.6d-e**). One MI glass is near-identical to that of NWA 6234 bulk-rock but shows a distinct positive Ce anomaly that was also observed for the melt in equilibrium with NWA 10170 megacrysts analysed in the previous chapter (**Figure 4.5e**). The near-identical REE and ITE patterns for this NWA 10170 MI glass and NWA 6234 bulk-rock indicate that the trace element composition of the MI glass is largely unaffected by pre- and post-entrapment crystallisation, and thus, likely represents the parent melt composition of NWA 10170. This MI glass also shows similar Zr/Nb and La/Yb_{CI} ratios to those of intermediate bulk-rock compositions (**Figure 4.7a-b**). The second MI glass is at significantly higher REE concentrations than bulk-rock, which may reflect possible analysis of merrillite daughter crystals, which have been observed in some NWA 10170 MIs (**Figure 4.1d**), but shows similar Y/Nb and La/Yb_{CI} ratios to intermediate bulk-rock compositions and lower Zr/Nb and Zr/Y (**Figure 4.7a-b**).

4.4.2.3 Enriched shergottites

The REE and ITE patterns for NWA 1068 MI glass strongly mirror and plot above the REE and ITE patterns of bulk-rock NWA 1068 (**Figure 4.5g, Figure 4.6g**). The MIs analysed from this sample all show wall olivine and daughter pyroxene crystals (**Figure 4.1e**), which likely resulted in the disparity in MI glass and bulk-rock REE and ITE concentrations. Nevertheless, REE and HFSE ratios for NWA 1068 MI glasses overlap consistently with bulk-rock values (**Figure 4.7**), indicating that the trace element concentrations for the MI glasses are largely unaffected by post-entrapment crystallisation. This suggests that the trace element concentrations for NWA 1068 MI glasses are a good proxy for NWA 1068 parent melt, consistent with earlier interpretations for MI glasses from DaG 1037, SaU 005, and NWA 10170. These findings further highlight that the trace element compositions of MI glasses in these meteorites can aid in understanding the evolution REE and other trace element in shergottites.

In contrast to MI glasses from NWA 1068, NWA 1183 MI glass is significantly more enriched in LREE (La–Gd) than enriched shergottite bulk-rock REE compositions (no bulk-rock data available for this meteorite) and shows upward inflections of LREE-MREEs (La–Gd) with distinct negative Ce anomaly (**Figure 4.5h**). The REE pattern of this MI glass does mirror that of the melt in equilibrium with NWA 1183 olivine presented in chapter 3 (**Figure 4.5h**) and bulk-rock NWA 7034, a polymict regolith breccia with $^{147}Sm/^{144}Nd$ and $^{176}Lu/^{177}Hf$ characteristics that are consistent with a LREE-enriched crust (Nyquist et al., 2016; Armytage et al., 2018).

For LAR 12011, REE and ITE patterns for glass from the two LREE-enriched MIs parallel that of enriched shergottite bulk-rock compositions. One MI glass is identical to that of bulk-rock, and as such, is a good proxy for the parent melt composition of LAR 12011, while the second is at higher REE concentrations than bulk-rock (**Figure 4.5f, Figure 4.6f**). The significantly higher REE concentrations of the second MI glass may reflect post-entrapment crystallisation of wall olivine and daughter pyroxene crystals (**Figure 4.2**). Glass from the other three LAR 12011 MIs show LREE-depleted patterns that mirror and partially overlap with the REE patterns of the calculated melt in equilibrium with early-formed olivine megacrysts in this meteorite from chapter 3 (**Figure 4.5f**) and MI glasses in the depleted shergottites.

Ratios of HFSEs, Zr/Nb, Y/Nb, and Zr/Y, for NWA 1068 MI glasses overlap consistently with bulk-rock values (**Figure 4.7a-b**), while those of NWA 1183 MI glasses partially overlap with enriched shergottite bulk-rock compositions and bulk-rock NWA 7034 (**Figure 4.7a-b**). For LAR 12011, HFSE ratios for the LREE-enriched MI glass identical to bulk-rock also overlap with values for bulk-rock LAR 12011, while MI glass with higher REE concentrations than bulk-rock plot at lower Zr/Nb and Y/Nb values and towards NWA 1183 MI glass and bulk-rock NWA 7034 (**Figure 4.7a-b**). Ratios of Zr/Nb for LREE-depleted MI glasses in LAR 12011 plot at higher values at a given Y/Nb relative to LAR 12011 bulk-rock and LREE-enriched glasses, and parallel the negative Zr/Nb-Y/Nb trend observed for LREE-enriched glasses.

4.4.3 Merrillite parental melt REE modelling

4.4.3.1 Evaluation of merrillite-melt partition coefficients for shergottites

Merrillite is a late-stage crystallising phase in shergottites and the principal control on shergottite bulk-rock REE compositions, and thus, is a valuable tool for tracking late-stage REE evolution of shergottite melts. The REE composition of melts in equilibrium with the late-stage groundmass merrillite from shergottite meteorites can be estimated using appropriate merrillite-melt REE partition coefficients calibrated for martian basaltic compositions, such as those experimentally derived by Lundberg et al. (1990). Merrillite-melt REE partition coefficients can also be estimated using the Tissint meteorite, a LREE-depleted and Mg-rich olivine-phyric shergottite previously interpreted to represent a magma

composition that crystallised in a closed system (Balta et al., 2015). Furthermore, Tissint's classification as a "fall" meteorite indicates that it has undergone minimal alteration from terrestrial sources, consistent with the olivine trace element findings presented in chapter 3.

The REE compositions for merrillite and bulk-rock Tissint used to estimate the merrillite-melt partition coefficients were taken from Balta et al. (2015) and Day et al. (2018). The REE partition coefficients for merrillite estimated using Tissint as well as those of Lundberg et al. (1990) are presented in **Table 4.3** and **Figure 4.9** and show some differences, with those of Tissint being larger by a factor of ~3 for LREE (La–Gd) and between 3 and 8 for HREEs (Tb–Yb). As a result of these differences in partition coefficients, the estimated merrillite equilibrium melt REE concentrations using Tissint are lower by factors of between 0.1 and 0.4. The Tissint and Lundberg et al. (1990) merrillite-melt partition coefficients were plotted as a function of effective cationic radii (Onuma et al., 1968) assuming all REEs are in eightfold coordination (Shannon, 1976), with both sets of coefficients showing negative correlations between Gd and Lu and relatively flat trends between La and Sm (**Figure 4.9**). The REE compositions for melts in equilibrium with merrillite from each sample using the two sets of partition coefficients are presented in **Table 4.4**.

Table 4.3: Calculated merrillite-melt partitioning coefficients using bulk-rock and merrillite data from Tissint

	Tissint		**Lundberg**
	$K_D^{merr\text{-}melt}$	2SD	$(K_D^{merr\text{-}melt})_{exp}$
La	76	1.5	26
Ce	71	0.9	26
Pr	74	1.8	26
Nd	73	1.3	26
Sm	76	2.1	26
Eu	52	1.4	23
Gd	86	1.3	26
Tb	77	1.5	25
Dy	84	1.3	22
Ho	78	1.4	19
Er	75	1.5	15
Tm	68	2.1	11
Yb	63	1.3	8
Lu	54	1.8	–

4.4.3.2 Applicability of Tissint vs. Lundberg K_d

The results presented in **Figure 4.9** show the merrillite-melt REE partition coefficients of Lundberg et al. (1990) and Tissint plotted against cationic radii in 8-fold coordination (Onuma et al., 1968; Shannon,

1976). Overall, the estimated olivine-melt partition coefficients using Tissint parallel those of Lundberg et al. (1990) but show some differences towards HREEs, with those of Lundberg et al. (1990) showing a more abrupt change from Ho–Yb compared to the values calculated using Tissint. Estimated La/Yb_{CI} values for melts in equilibrium with merrillite from intermediate and enriched shergottites using the Lundberg et al. (1990) partition coefficients are inconsistent those of bulk-rock, which suggests that these partition coefficients do not properly model the HREE patterns of melts in equilibrium with merrillite. Based on these findings, which highlight the limitations of using the Lundberg et al. (1990) merrillite-melt partition coefficients for predicting HREE patterns, it is recommended to utilise the merrillite-melt REE partition coefficients determined using Tissint for more accurate estimates. By prioritising the use of Tissint-derived merrillite-melt REE partition coefficients, it is possible to obtain better estimates of the HREEs for melts that are in equilibrium with merrillite.

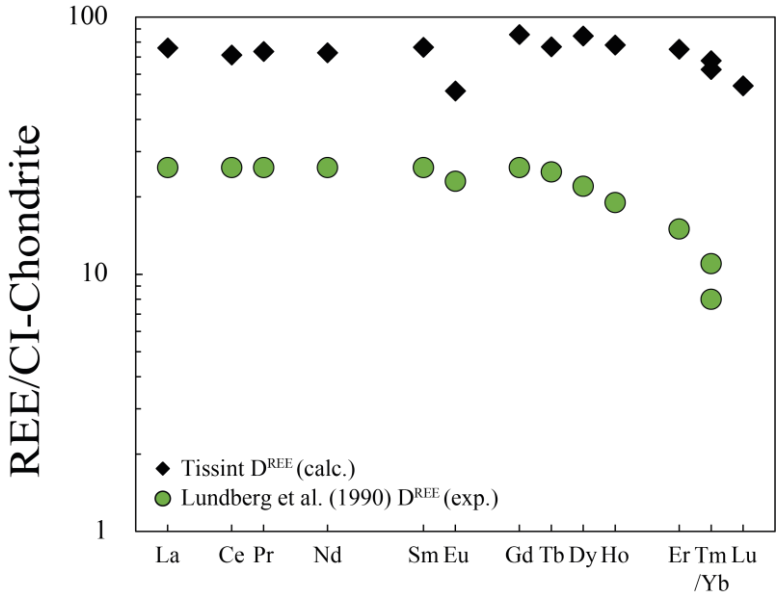

Figure 4.9: Merrillite-melt partition coefficients calculated using merrillite and bulk-rock REE data for the Tissint meteorite (Balta et al., 2015; Day et al., 2018) and terrestrial basalts plotted against cationic radii in 8-fold coordination (Onuma et al., 1968; Shannon, 1976). Experimental merrillite-melt partition coefficients for terrestrial basalts taken from Lundberg et al. (1990).

4.4.3.3 Merrillite as a tool for tracking late-stage REE evolution in shergottites

The CI-normalised REE patterns for melts in equilibrium with the average merrillite composition from DaG 1037, Dho 019, and SaU 005, are characteristically LREE-depleted, with that of DaG 1037 plotting within 2SD of its bulk-rock between Ce–Er (**Figure 4.10a-c**). The La/Yb_{CI} ratios for melts in equilibrium with merrillite from DaG 1037 (0.08±0.01, 2SD, *n=3*), Dho 019 (0.23±0.01, 2SD, *n=2*), and SaU 005 (0.14±0.03, 2SD, *n=2*) are consistent with depleted shergottite bulk-rock compositions (<0.3, Udry et al., 2020). The REE patterns for melt in equilibrium with merrillite from Dho 019 and SaU 005 also show distinct negative Eu anomalies that are consistent with late-stage crystallisation of merrillite after

plagioclase (e.g., Wadhwa et al., 1994; Sarbadhikari et al., 2009; Hui et al., 2011; Shearer et al., 2011; Shearer et al., 2015; Ferdous et al., 2017; Udry et al., 2017) (**Figure 4.10b-c**).

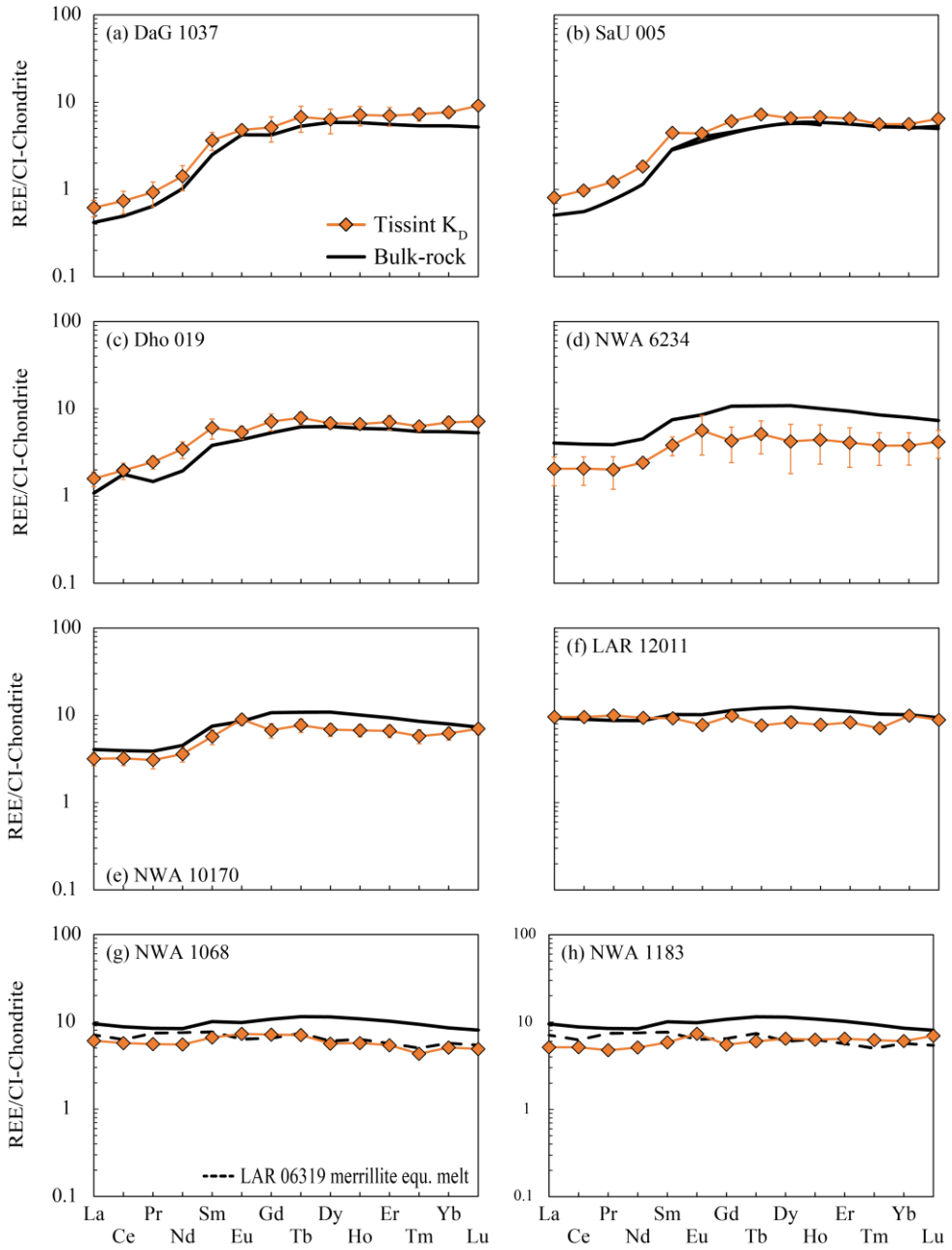

Figure 4.10: REE patterns for melts in equilibrium with merrillite from the shergottite meteorites, calculated using the estimated Tissint merrillite-melt partition coefficients. Literature bulk-rock REE data for Tissint REE taken from Balta et al. (2015) and Day et al (2018). Literature merrillite REE data for LAR 12011 was taken from Caseres, J.R. (2015).

The REE patterns for melts in equilibrium with NWA 6234 and NWA 10170 merrillite parallel and overlap with each other and are more enriched in LREE relative to merrillite equilibrium melts for the depleted shergottites (**Figure 4.10d-e**). The La/Yb_{CI} ratios for melts in equilibrium with merrillite from NWA 6234 (0.54 ± 0.02, 2SD, *n=2*) and NWA 10170 (0.51 ± 0.03, 2SD, *n=4*) overlap consistently with

intermediate shergottite bulk-rock compositions (0.3–0.8, Udry et al., 2020), with REE patterns for both samples also showing positive Eu anomalies.

For the enriched shergottites NWA 1068, NWA 1183, and LAR 12011, Cl-normalised REE patterns for equilibrium melts from each sample parallel and partially overlap with each other and are more enriched in LREE relative to merrillite equilibrium melts for intermediate shergottites (**Figure 4.10f-h**). The La/Yb_{CI} ratios for melts in equilibrium with merrillite from NWA 1068 (~1.20, *n=1*), NWA 1183 (~0.85, *n=1*), and LAR 12011 (0.95±0.12, 2SD, *n=3*) also overlap consistent with enriched shergottite bulk-rock compositions (>0.8, Udry et al., 2020). Furthermore, merrillite REE equilibrium melts for all three samples strongly mirror that of the melt in equilibrium with merrillite from the enriched shergottite LAR 06319 (i.e., Sarbadhikari et al., 2009).

4.4.4 Closed-system evolution of depleted and intermediate shergottites

The CI-normalised REE patterns for MI glass, melts in equilibrium with early-formed olivine, and melts in equilibrium with merrillite from DaG 1037 and SaU 005 parallel their respective bulk-rock compositions (**Figure 4.11a-b**). Similarly, the CI-normalised REE patterns for melt in equilibrium with pyroxene daughter crystals in MIs and with olivine megacrysts and late-stage merrillite from Dho 019 also parallel bulk-rock (**Figure 4.11c**). These findings show that the REE patterns remained constant during evolution with no evidence for open-system processes. Previous studies of these meteorites and other olivine-phyric shergottites have shown that their parent magmas formed staging chambers near the base of the martian crust (~10 kbars or 85 km depth, e.g., Usui et al., 2008; Sarbadhikari et al., 2009; Filiberto et al., 2010; Peslier et al., 2010; Gross et al., 2011; Dunham et al., 2019; Aucamp et al., 2023; Peel et al., 2023). This indicates that DaG 1037, SaU 005, and Dho 019 crystallised with closed-system behaviour with no discernible geochemical evidence for assimilation of an enriched crustal component. Additionally, the strong similarities in DaG 1037 and SaU 005 MI glass REE and HFSE patterns and ratios also support previous interpretations that these 1.1 Ma ejection-paired meteorites, along with Yamato 980459, NWA 5789, NWA 2046, and NWA 4925, form a co-magmatic suite between 440–470 Ma (i.e., Aucamp et al., 2023; Peel et al., 2023).

The CI-normalised REE patterns for melts in equilibrium with merrillite from intermediate shergottites NWA 6234 and NWA 10170, as well as the melt in equilibrium with olivine megacrysts from NWA 6234 and MI glass from NWA 10170, parallel the bulk-rock composition of NWA 6234. These results are consistent with both NWA 6234 and NWA 10170 having crystallised with closed-system behaviour, and further, suggest that the parent melt compositions of these meteorites were likely derived from a common or similar source region that had moderately enriched incompatible-element characteristics. This interpretation for NWA 6234 is supported by previous findings by Gross et al. (2013), who demonstrated that most Mg-rich olivine megacryst cores in NWA 6234 are in Mg-Fe equilibrium with

the bulk rock, indicating a primary mantle-derived melt composition. The presence of multiple shergottite meteorites, such as NWA 6234 and NWA 10170, that appear to have undergone closed-system crystallisation from an intermediate LREE source further supports the notion of distinct martian magma sources contributing to the diversity of shergottite meteorites.

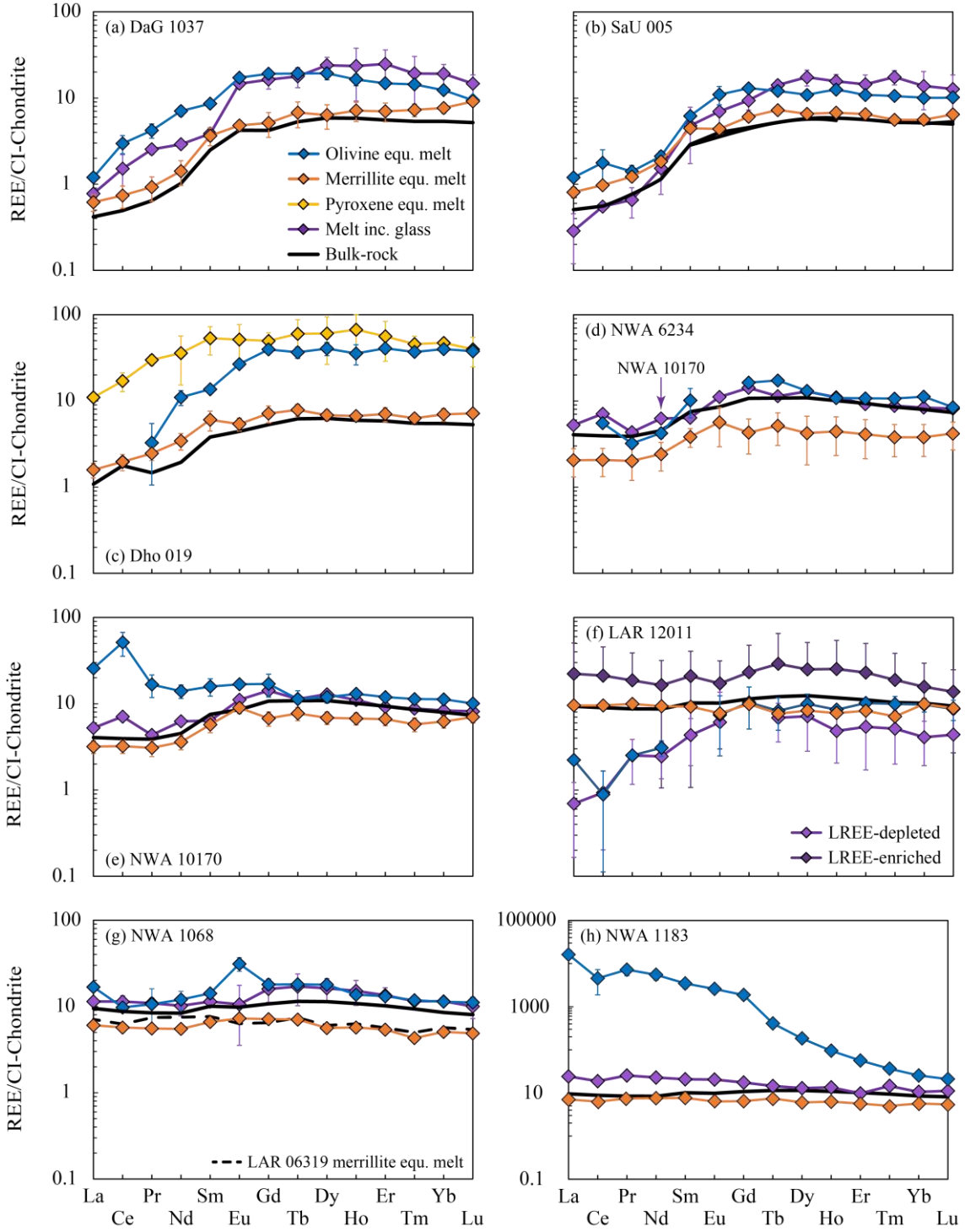

Figure 4.11: REE patterns for MI glass, melts in equilibrium with olivine, and melts in equilibrium with merrillite from the shergottite meteorites analysed in this study. Literature merrillite REE data for LAR 12011 was taken from Caseres, J.R. (2015).

4.4.5 Open-system evolution of enriched shergottites

The CI-normalised REE patterns for MI glasses analysed from LAR 12011 show mixed populations with LREE-enriched and LREE-depleted patterns. One of the LREE-enriched MI glasses was found towards the rim of its host olivine megacryst (with Fo_{69}) and the other towards the core of its host (with Fo_{73}) (**Figure 4.12a**). Both LREE-enriched glasses show REE patterns that mirror LAR 12011 bulk-rock and MIs hosted in Mg-rich olivine (up to Fo_{77}) from LAR 06319 (Sarbadhikari et al., 2011), paired to LAR 12011 (**Figure 4.11f**). The LREE-depleted MI glasses were found closer to the cores of their host olivine (**Figure 4.12b**), with Fo contents between Fo_{68} and Fo_{75}, and show REE patterns that mirror LAR 12011 megacrysts and MI glasses from depleted shergottites such as Tissint and Yamato 980459. Importantly, one LREE-depleted MI glass and one LREE-enriched MI glass are hosted in LREE-depleted olivines analysed in chapter 3, with the LREE-depleted glass located next to olivine with Fo_{75} and LREE-enriched glass next to olivine with Fo_{73}. The La/Yb_{CI} ratios of the depleted and enriched LAR 12011 MI glasses also show distinct populations against host-olivine Fo contents. The La/Yb_{CI} ratios for LREE-depleted MI glasses correlate negatively against host-olivine Fo contents and overlap consistently with MI glass data for Yamato 980459 and Tissint (Peters et al., 2015) (**Figure 4.13**). Conversely, LREE-enriched glasses plot at higher La/Yb_{CI} values at a given Fo content, relative to the LREE-depleted glasses, and overlap with MI glass data from NWA 1068 (this study) and LAR 06319 (Sarbadhikari et al., 2011). The REE pattern of LREE-enriched glass also plots parallel to that of the melt in equilibrium with LAR 12011 merrillite. The presence of LREE-depleted MI glass in LREE-depleted olivine provides robust evidence that the olivines crystallised from a depleted mantle parent magma and represent a depleted mantle source. These findings suggest that the parent melt of LAR 12011 may have been derived from a LREE-depleted mantle source that was subsequently enriched, possibly through mixing with a melt derived from an enriched mantle source, either during or shortly after the formation of Mg-rich olivine megacryst cores. Overall, these findings highlight the complex magmatic evolution of LAR 12011 and emphasise the importance of considering various factors, including olivine chemistry and REE patterns in MI glasses, to unravel the intricate history of martian meteorites.

The CI-normalised REE patterns for NWA 1068 MI glasses, hosted in olivine with Fo_{72}, plot parallel to NWA 1068 bulk-rock and the NWA 1068 olivine equilibrium melt (**Figure 4.11g**), indicating closed-system behaviour during crystallisation. It is important to note that while NWA 1068 MI glasses and olivine are both enriched, the forsterite content of NWA 1068 olivine (Fo_{72}) measured in this study is on the lower range of olivine analysed in LAR12011 ($Fo_{75\text{-}68}$). As no olivine with higher forsterite content ($Fo_{>74\text{-}75}$) were analysed from NWA 1068, it is not possible to completely rule out an early depleted component in more primitive olivine megacrysts similar to that of LAR 12011 megacrysts.

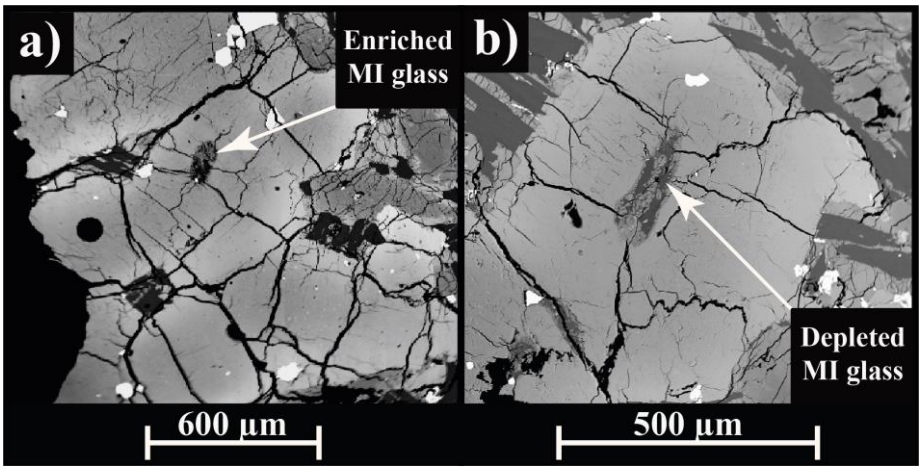

Figure 4.12: BSE images of olivine megacrysts from LAR 12011 showing the relative positions of LREE-enriched and LREE-depleted glasses.

For NWA 1183, the CI-normalised REE patterns for MI glass and the olivine equilibrium melt both show enrichment of LREEs relative to HREEs and do not mirror the REE patterns of NWA 1068 bulk-rock and NWA 1183 merrillite equilibrium melt (**Figure 4.11h**). The LREE-enriched REE patterns for NWA 1183 olivine and MI glasses do resemble that of bulk-rock NWA 7034, a regolith breccia with radiogenic isotope characteristics indicating a LREE-enriched crust (Nyquist et al., 2016; Armytage et al., 2018). Similarities between NWA 1183 MI glass and NWA 7034 bulk-rock are further highlighted in their ITE patterns, which parallel and overlap significantly with each other (**Figure 4.6h)**, and HFSE ratios which consistently plot together (**Figure 4.7**). Furthermore, the K_2O-rich contents of NWA 1183 MI glass relative to the other enriched shergottites, such as NWA 1068, resembles the K_2O enriched compositions previously observed in MIs from poikilitic shergottites (Combs et al., 2019) and nakhlites (Goodrich et al., 2013) and interpreted to indicate mixing with a K-rich melt. These findings reveal a complex magmatic history for NWA 1183, indicating that the enrichment of incompatible elements in MI glasses and olivine megacrysts may be attributed to a combination of mixing with an enriched crustal component and terrestrial alteration. This scenario posits that NWA 1183 megacrysts may have originated from earlier batches of enriched shergottite melt that mixed with a crustal component. Following this, the megacrysts were likely entrained by a new pulse of enriched melt, either during its residency in the magma chamber or while ascending to the surface, implying a continuously replenished magma chamber.

This interpretation of incompatible element enrichment through mixing with a K-rich melt is not without flaws. Notably, NWA 1068 MI glasses exhibit vastly different K_2O contents (0.3–0.4 wt.% and 5.9–6.3 wt. %) yet display nearly identical rare earth element (REE) patterns. Moreover, findings presented in *section 4.4.3* suggest that the parent melt of NWA 1183, at the time of merrillite crystallization, possessed a REE composition consistent with that of NWA 1068. Taken together, these observations

imply that the enrichment of incompatible elements in the NWA 1183 MI glasses and host-olivine megacrysts may primarily be the result of post-magmatic alteration within a terrestrial environment.

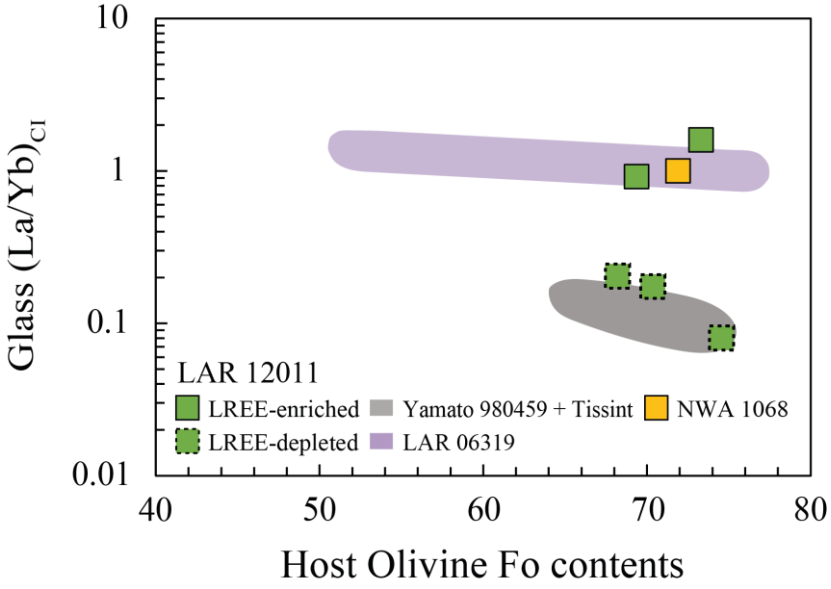

Figure 4.13: Comparison of host-olivine Fo contents and MI glass La/Yb_{CI} ratios for LREE-depleted and LREE-enriched LAR 12011 glass. Literature MI glass data for Yamato 980459, Tissint, and LAR 06319 taken from Peslier et al. (2010), Sarbadhikari et al. (2011), Peters et al. (2015).

4.4.6 Origin of LREE enrichment in LAR 12011

In a recent study by Eckley et al. (2024), X-ray computed tomography (CT) scanning was used to examine the morphology of olivine in shergottite meteorites. The study revealed that LAR 12011 olivines display several morphological types indicative of multiple stages of olivine growth including: (1) mantled dendritic olivine, characterised by primary branches of olivine in the shape of an "X" along the central plane of the olivine crystal, (2) olivine with elongated melt inclusions, and (3) polyhedral olivine (Eckley et al., 2024). Eckley et al. (2024) suggested that olivine with mantled dendritic morphologies likely experienced high degrees of early undercooling, >70℃ lower than olivine liquidus temperature, which facilitated the rapid formation and cooling of the primary "X" branches at the start of olivine crystallisation window. During the period of initial olivine growth, the parent melt of LAR 12011 approached thermal equilibrium due to the introduction of new melts into the system, resulting in crystal infilling of dendritic olivine and growth of polyhedral and elongated melt inclusions in olivine crystals (Eckley et al., 2024). Although several possible scenarios were proposed to account for the early growth rate of olivine including conductive heat loss, magma mixing, vigorous convection, and volatile exsolution, the study favoured a model of conductive heat loss over other mechanisms. It should be noted that this interpretation was made using literature melt inclusion and bulk-rock REE findings for LAR 06319 (Sarbadhikari et al., 2009) as a proxy for LAR 12011, which are inconsistent with LAR 12011 olivine and melt inclusion glass REE findings presented in this study.

In terrestrial studies of olivine-hosted melt inclusions in Icelandic lava flows (e.g., Maclennan et al., 2003; Maclennan, 2008), it was shown that melt inclusion REEs within single lavas can be more variable than bulk-rock and range from LREE depleted CI-normalised patterns (La/Yb – 0.06 to 0.28) to LREE-enriched patterns (La/Yb – 0.34 to 1.24). The studies also found that, despite the compositionally variability of the melt inclusions, the average REE composition of melt inclusions within a single lava flow were comparable to that of bulk-rock and that melt inclusion REE variability decreased with decreasing host-olivine forsterite contents. Maclennan (2008) interpreted these findings to indicate concurrent mixing and crystallisation of compositionally distinct melts, with olivine having formed from the melts that mixed and progressively homogenised to form the melt that retained (or re-entrained) the olivines and carried them to surface. Using these findings for melt inclusions in terrestrial lavas as a comparison for martian meteorites could explain the preservation of mixed populations of MIs in LREE-depleted LAR 12011 megacrysts as well as the compositional disequilibrium between the LAR 12011 olivine equilibrium melt and bulk-rock REE patterns.

Previous studies of enriched shergottites have also shown that their radiogenic isotope compositions and crystallisation and cosmic ray exposure ages reflect sampling of two distinct enriched mantle sources (Combs et al. 2019). One of these enriched shergottite groups, with crystallisation ages ranging from ~225 Ma to ~150 Ma (Borg et al., 2008; Lapen et al., 2008), includes LAR 12011 as well as NWA 1068, and LAR 06319. For LAR 12011, initial $^{176}Hf/^{177}Hf$ and $^{206}Pb/^{204}Pb$ ratios for the sample were calculated as 0.282134 (Righter et al., 2015) and 13.81±0.10 (Bellucci et al., 2015), respectively. These calculated values for LAR 12011 overlap consistently with modelled source $^{176}Hf/^{177}Hf$ (0.282141±10 to 0.291349±38) and $^{206}Pb/^{204}Pb$ (12.22±1.17 to 13.87±0.22) values for LAR 06319, Roberts Massif (RBT) 04262, NWA 4468, NWA 10169, Shergotty, and Zagami (e.g., Borg et al., 2005; Bouvier et al., 2005, 2008; Lapen et al., 2008, 2009; Shafer et al., 2010; Combs et al., 2019; Wu et al., 2021). These findings, which were calculated by analysing radiogenic isotopes on bulk-rock and mineral separates (i.e., olivine, pyroxene, maskelynite), are indicative of a shared mantle source region for LAR 12011 with the other enriched shergottites. Furthermore, initial $^{176}Hf/^{177}Hf$ for LAR 12011 are also distinct from source $^{176}Hf/^{177}Hf$ ratios modelled for NWA 7034 (0.02–0.04 or 0.012–0.014 at 150 Ma; Armytage et al., 2018), and thus, inconsistent with a model of crustal assimilation.

Based on the possible scenarios suggested by Eckley et al. (2024), the model for terrestrial systems by Maclennan (2008), and the LAR 12011 olivine and melt inclusion glass REE findings presented in this study, the petrogenetic history of LAR 12011 may involve mixing between a cooler, crystal-bearing depleted melt and a hotter, crystal-poor enriched melt. This model aligns with the interpretation that olivine in LAR 12011 likely represents crystallisation from an initial LREE-depleted parent magma that was later enriched through mixing with a melt derived from a LREE-enriched mantle source or through

assimilation of LREE-enriched crust shortly after or during the formation of Mg-rich olivine megacryst cores. These findings, coupled with the younger crystallisation age of LAR 12011 (~200 Ma; Righter et al., 2015) relative to depleted shergottites (327 Ma to 2403 Ma, Nyquist et al., 2001; Brennecka et al., 2014; Herd et al., 2017; Lapen et al., 2017), suggests that depleted magmatism continued at younger times in Mars evolution. This indicates that the processes leading to the formation of depleted shergottites were more complex and may have occurred intermittently over a longer period of martian geologic history than previously suggested.

4.5 Summary of findings

The results presented in this study demonstrate parallelisms in the REE patterns of melt inclusion glass, bulk-rock compositions, melt in equilibrium with host olivine, and melts in equilibrium with merrillite, indicating closed-system behaviour during crystallisation. These observations are particularly evident in the depleted shergottites DaG 1037, Dho 019, and SaU 005, aligning with previous interpretations that these meteorites originate from partial melts of a depleted martian mantle source. The intermediate shergottites NWA 6234 and NWA 10170, and the enriched shergottite NWA 1068, also exhibit closed-system behaviour suggestive of melting from distinct mantle source regions.

In contrast, the presence of LREE-depleted MI glass within LREE-depleted LAR 12011 olivine megacrysts suggest open-system behaviour during crystallisation, and further, shows that the olivine crystallised from a depleted melt source. The preservation of LREE-enriched MI glass within LREE-depleted olivine megacrysts resembles the compositional variability of olivine-hosted melts inclusions within single lava flows from terrestrial studies. This suggests that LAR 12011 likely formed through similar processes involving mixing of distinct LREE-depleted and LREE-enriched melt compositions, with the mixing having occurred during the crystallisation of olivine megacryst cores. For NWA 1183, the observed enrichment of LREEs in MI glass and host-olivine equilibrium melt REE patterns is attributed primarily to terrestrial alteration during their host residence on Earth. Consequently, the trace element compositions of NWA 1183 MI glass and host-olivine cannot be used to constrain the primary trace element characteristics of the parent melt from which they were derived. In contrast, the melt in equilibrium with NWA 1183 merrillite, which is largely unaffected by terrestrial alteration, shows a parent melt REE composition consistent with other melts derived from an enriched shergottite mantle source, in particularly NWA 1068. This similarity in late-stage parent melt REE compositions for NWA 1183 and NWA 1068, aligns with previous suggestions that these samples are likely paired to one another.

The findings presented in this chapter provide key information into the origins and evolutionary histories of the studied shergottite meteorites, shedding light on the complexities of mantle melting processes and

the interactions between different source regions during magmatic evolution on Mars. The interpretations drawn from the examination of MI-glass compositions, as well as bulk-rock and crystalline phase characteristics, offer a nuanced understanding of the geological processes that have shaped these shergottite meteorites and contributes to the broader understanding of martian geology and magmatism. Finally, I present summary **Figure 4.14**, illustrating the petrogenetic model(s), from source to emplacement at surface, for the depleted, intermediate, and enriched, shergottites analysed in this study.

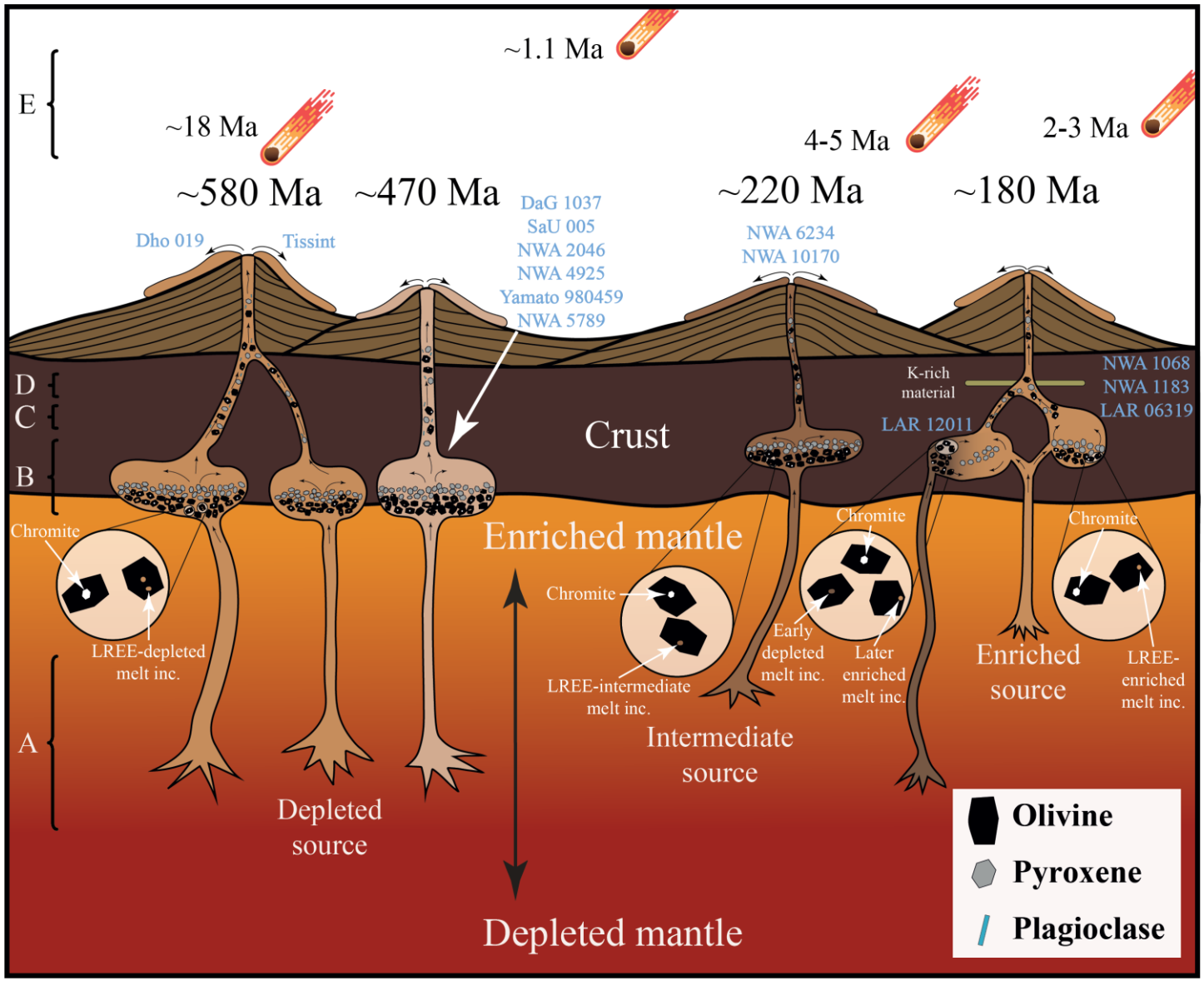

Figure 4.14: Sketch illustrating the petrogenetic model(s) of emplacement for the depleted, intermediate, and enriched olivine-phyric shergottites analysed in this study. (A) Partial melting of distinct shergottite mantle sources with LREE-depleted, LREE-intermediate, and LREE-enriched, REE characteristics. (B) Ponding of shergottite parent magmas near the base of the martian crust (~ 10 kbar), followed by the crystallisation of olivine megacrysts, entrapment of melt inclusions and chromite grains, and crystallisation of pyroxene phenocrysts. (C) Ascent of shergottite parent magmas, and transport of entrained olivine and pyroxene crystals, to surface, during which plagioclase begins to crystallise. (D) Assimilation of K-rich crustal material for the enriched shergottites. (E) Ejection of shergottites from the martian surface based on CRE ages i.e., ~18 Ma (Dho 019); 4-5 Ma (intermediate shergottites); 2-3 Ma (enriched shergottites); ~1.1 Ma (remaining depleted shergottites) (Nyquist et al., 2001; Shukolyukov et al., 2002; Walton et al., 2007; Nishiizumi et al., 2011; Park et al., 2013; Wieler et al., 2016; Lapen et al., 2017, and Herd et al., 2017; Combs et al., 2018).

Table 4.4: REE compositions for melts in equilibrium with merrillite using the two sets of partition coefficients

		La	Ce	Pr	Nd	Sm	Eu	Gd	Tb	Dy	Ho	Er	Tm	Yb	Lu	La/Yb	Eu*
DaG 1037																	
	Tissint	0.61	0.73	0.91	1.40	3.61	4.76	5.09	6.71	6.28	7.09	6.95	7.23	7.61	9.06	0.08	-
	2SD	0.13	0.21	0.29	0.45	0.85	0.66	1.63	2.23	1.98	1.80	1.70	1.23	1.02	0.69		
	Lund	1.77	1.99	2.58	3.91	10.58	10.68	16.73	20.55	24.11	29.04	34.73	44.45	59.43	-	0.03	-
	2SD	0.66	1.00	1.41	2.17	4.32	2.56	9.30	11.84	13.14	12.74	14.73	13.04	13.81	-		
Dho 019																	
	Tissint	1.56	1.94	2.43	3.40	5.99	5.34	7.09	7.81	6.78	6.63	6.99	6.23	6.92	7.11	0.23	0.82
	2SD	0.30	0.42	0.42	0.74	1.55	0.91	1.56	1.25	1.00	0.08	1.31	0.84	1.17	0.08		
	Lund	4.56	5.32	6.87	9.50	17.57	11.99	23.32	23.92	26.00	27.15	34.97	38.33	54.08	-	0.08	0.59
	2SD	1.24	1.63	1.67	2.93	6.43	2.89	7.26	5.40	5.43	0.44	9.25	7.27	12.97	-		
SaU 005																	
	Tissint	0.80	0.96	1.21	1.81	4.42	4.34	6.02	7.23	6.51	6.71	6.46	5.55	5.56	6.41	0.14	0.84
	2SD	0.12	0.09	0.11	0.09	0.37	0.14	0.74	0.63	0.72	0.31	0.55	0.46	0.20	0.89		
	Lund	2.33	2.63	3.41	5.07	12.95	9.75	19.78	22.16	24.99	27.48	32.32	34.15	43.43	-	0.05	0.61
	2SD	0.48	0.36	0.44	0.35	1.55	0.44	3.43	2.74	3.89	1.80	3.85	3.96	2.16	-		
NWA 6234																	
	Tissint	2.03	2.05	1.99	2.40	3.80	5.62	4.26	5.11	4.19	4.39	4.07	3.75	3.76	4.15	0.54	1.40
	2SD	0.73	0.74	0.81	0.88	0.93	2.70	1.87	2.10	2.40	2.09	1.95	1.53	1.51	1.48		
	Lund	5.91	5.60	5.63	6.70	11.15	12.61	14.02	15.67	16.09	17.99	20.33	23.08	29.39	-	0.20	1.04
	2SD	3.01	2.86	3.24	3.47	3.86	8.55	8.68	9.08	13.04	12.12	13.79	13.26	16.71	-		
NWA 10170																	

	Tissint	3.16	3.19	3.05	3.57	5.67	8.92	6.72	7.67	6.83	6.70	6.59	5.73	6.18	6.98	0.51	1.45
	2SD	0.54	0.57	0.64	0.68	1.09	1.27	1.27	1.35	1.13	1.06	1.07	1.05	1.01	1.02		
	Lund	9.21	8.74	8.63	9.99	16.63	20.02	22.10	23.50	26.19	27.43	32.97	35.27	48.27	-	0.19	0.76
	2SD	3.14	3.10	3.59	3.78	6.40	5.69	8.37	8.29	8.66	8.71	10.72	12.94	15.75	-		
NWA 1068																	
	Tissint	6.02	5.65	5.51	5.45	6.56	7.22	7.08	7.01	5.58	5.65	5.35	4.26	5.03	4.84	1.20	1.06
	2SD	0.12	0.07	0.13	0.10	0.18	0.20	0.11	0.14	0.09	0.11	0.11	0.13	0.10	0.17		
	Lund	17.55	15.48	15.59	15.24	19.24	16.20	23.29	21.47	21.39	23.16	26.73	26.23	39.29	-	0.45	0.76
NWA 1183																	
	Tissint	5.09	5.10	4.72	5.06	5.79	7.29	5.47	5.96	6.39	6.23	6.39	6.16	6.01	6.90	0.8	1.29
	2SD	0.10	0.06	0.12	0.09	0.16	0.20	0.09	0.12	0.10	0.12	0.13	0.19	0.12	0.24		
	Lund	14.84	13.97	13.35	14.15	16.99	16.35	17.98	18.25	24.53	25.51	31.93	37.88	46.94	-	0.32	0.94

5 Summary Chapter

This chapter details the key findings and interpretations presented in previous chapters and demonstrates the significance of martian meteorites in understanding the geological history of Mars.

The primary aims of chapter 2 were to 1) assess if NWA 2046 and NWA 4925 represent primary mantle-derived magmas, 2) put them into context with the 1.1 Ma site and, 3) further develop a magmatic history for the Tharsis plateau. These aims were accomplished by studying NWA 2046 and NWA 4925 for their petrology, bulk-rock major and trace element geochemistry, mineral major and trace element concentrations, and in-situ maskelynite and pyroxene $^{87}Sr/^{86}Sr$ data. The findings presented here show that primitive olivine megacryst cores from both samples are in Mg-Fe equilibrium with their respective bulk-rock compositions, and thus, were interpreted to be phenocrysts with the NWA 2046 and NWA 4925 bulk-rock compositions representing melt compositions. Both samples do show evidence of early olivine fractionation in staging chambers prior to ascent to surface. Northwest Africa 4925 also shows distinct terrestrial weathering pattens, indicative of significant terrestrial alteration and consistent with its older terrestrial age, that can be tracked using Ca and K elemental maps. In-situ maskelynite $^{87}Sr/^{86}Sr$ data for both samples were shown to overlap consistently with age-corrected initial bulk-rock values for other 1.1 Ma ejection-paired meteorites, including Dag 476, SaU 005 and Yamato 980459, and suggests a shared mantle source region. Ratios of Ti/Al in pyroxene grains from NWA 2046 and NWA 4925 were then used to constrain the location of the staging chamber in which these and other depleted shergottites crystallised, with my findings showing pressures consistent with the martian crust-mantle boundary (10 kbars). Finally, I combined my findings for NWA 2046 and NWA 4925 with literature data for other 1.1 Ma shergottites (e.g., DaG 476, SaU 005, and Yamato 980459) to present a model for volcanism at this site.

In chapter 3, the trace and ultra-trace element concentrations of olivine megacryst in a suite of olivine-phyric shergottites were analysed to evaluate the nature and origin of megacrysts in shergottites and constrain open vs closed system processes during the earlier stages of evolution in shergottites. This was carried out using a newly developed LA-ICP-MS technique by Veter et al. (2019), with higher sensitivity (1.5-fold) than conventional techniques, to acquire ultra-trace elements in olivine for the first time.
Olivines in shergottites require careful screening to remove secondary signatures, such as terrestrial alteration, before interpreting primary signatures. The study reveals that the effects of terrestrial alteration have been preserved in the olivine megacrysts of the shergottites, with significant variations observed across different meteorites landing sites. Notably, the cores of these megacrysts exhibit more pronounced signs of terrestrial alteration compared to their rims. Despite the secondary terrestrial alteration signatures, the analysis of olivine ultra-trace elements can be particularly valuable in constraining shergottite petrogenesis. This chapter presents the first REEs in olivine dataset for

shergottites and the first full suite of shergottite olivine-melt REE partition coefficients. The results presented here show that Cl-normalised REE patterns for melts in equilibrium with olivine from DaG 1037, Dho 019, NWA 2046, SaU 005, Tissint, NWA 6234, and NWA 1068 parallel those of their respective bulk-rock compositions. These findings are indicative of these meteorites having crystallised with closed-system behaviour and supports previous interpretations that shergottites were derived through partial melting of geochemically distinct mantle sources. Other meteorites, such as NWA 1183 and LAR 12011, preserve evidence of open-system processes. For NWA 1183, the Cl-normalised REE pattern for the melt equilibrium with megacrysts analysed from this sample is significantly more enriched in LREEs relative to enriched shergottite bulk-rock REE patterns, indicating possible open-system processes such as possible magma mixing or crustal assimilation shortly after melt segregated from source. For LAR 12011, the Cl-normalised REE for the olivine equilibrium melt is LREE-depleted and inconsistent with that of LAR 12011 bulk-rock but strongly resembles those of melts in equilibrium with olivine from the depleted shergottites. These findings indicate that early-formed LAR 12011 olivine megacrysts crystallised from a LREE-depleted parent magma.

Chapter 4 of this dissertation sought to evaluate the use of olivine-hosted melt inclusion glass in constraining primary REE patterns for shergottites and address the olivine LREE-depleted and LREE-enriched profiles seen in the previous chapter. The REE compositions of olivine-hosted melt inclusion glasses were analysed to determine if they represent bulk-rock or if they had been modified by post-entrapment processes, and how the melt inclusion glasses compare with olivine REEs from the previous chapter. The REE compositions of late-stage merrillite was also analysed from these samples to track the REE evolution of shergottite melts. The results presented in this chapter show that the REE patterns of melt inclusion glass mirror those of bulk-rock in most cases, indicating the usefulness of melt inclusion glass in constraining REE contents of early shergottite melts trapped in olivine. The REE patterns for melt inclusion glasses from depleted shergottites also mirror REE patterns for melts in equilibrium with olivine megacrysts and merrillite, indicating closed-system behaviour during crystallisation and consistent with findings presented in the previous chapter. These findings show that the approach presented in this chapter works and that olivine, MI glass, and merrillite can be effectively used to track REE and other trace element evolution throughout shergottite melt evolution. The intermediate shergottites NWA 6234 and NWA 10170 also exhibit closed-system behaviour, indicating partial melting of a distinct mantle source region. In contrast to the depleted and intermediate shergottites, LREE-depleted MI glass within LREE-depleted olivine megacrysts from LAR 12011 suggests more open-system behaviour during crystallisation and indicates that early-formed LAR 12011 megacryst cores likely crystallised from a depleted magma. For NWA 1183, REE patterns for melt inclusion glass and the melt in equilibrium with olivine are more enriched in LREEs relative to REE patterns for NWA 1068 bulk-rock and melt inclusions glasses. The enrichment of LREEs in melt inclusion glass and olivine megacrysts is suggested to largely reflect the effects of terrestrial alteration,

although possible assimilation of an enriched crustal component, akin to processes observed in NWA 7034, before any crystallisation had occurred cannot be ruled out entirely. These findings show that enriched shergottites appear to have a more complex petrogenesis than previously thought and that REE enrichment may not always be related to a REE enriched source.

In conclusion, this dissertation has made significant contributions to the composition and origin of shergottite parent melts and their mantle sources, providing deeper context into the geological processes that have shaped the martian mantle. Through the analysis of depleted olivine-phyric shergottites, olivine megacrysts, melt inclusion glass and merrillite, my research has gained valuable knowledge into the geological processes that have shaped the martian mantle. The findings presented here have implications not only for our understanding of martian geology but also for our understanding of the early solar system. Ultimately, this research has provided a more comprehensive picture of the martian mantle and its role in shaping the Red Planet's surface, advancing our knowledge of martian geology, and contributing to a deeper understanding of the geological history of Mars.

6 References

1. Ali, A., Jabeen, I., Gregory, D., Verish, R. and Banerjee, N.R., 2016. New triple oxygen isotope data of bulk and separated fractions from SNC meteorites: Evidence for mantle homogeneity of Mars. Meteoritics & Planetary Science, 51(5), 981-995.

2. Aoudjehane, H.C., Avice, G., Barrat, J.A., Boudouma, O., Chen, G., Duke, M.J.M., Franchi, I.A., Gattacceca, J., Grady, M.M., Greenwood, R.C. and Herd, C.D.K., 2012. Tissint Martian meteorite: A fresh look at the interior, surface, and atmosphere of Mars. Science, 338(6108), 785-788.

3. Armytage, R.M., Debaille, V., Brandon, A.D., and Agee, C.B., 2018. A complex history of silicate differentiation of Mars from Nd and Hf isotopes in crustal breccia NWA 7034. Earth and Planetary Science Letters, 502, 274-283.

4. Aucamp, T., Howarth, G.H., Peel, C.J., Costin, G., Day, J.M., le Roux, P., Scott, J.M., Greshake, A. and Bartoschewitz, R., 2023. Petrogenesis of the Dar al Gani (DaG) 1.1 Ma ejection-paired olivine-phyric shergottites and implications for~ 470 Ma Martian volcanism. Meteoritics & Planetary Science, 58(11), 1654-1676.

5. Balta, J.B., Sanborn, M., McSween Jr, H.Y. and Wadhwa, M., 2013. Magmatic history and parental melt composition of olivine-phyric shergottite LAR 06319: Importance of magmatic degassing and olivine antecrysts in Martian magmatism. Meteoritics & Planetary Science, 48(8), 1359-1382.

6. Balta, J.B., Sanborn, M.E., Udry, A., Wadhwa, M. and McSween Jr, H.Y., 2015. Petrology and trace element geochemistry of Tissint, the newest shergottite fall. Meteoritics & Planetary Science, 50(1), 63-85.

7. Banerdt, W.B., Smrekar, S.E., Banfield, D., Giardini, D., Golombek, M., Johnson, C.L., Lognonné, P., Spiga, A., Spohn, T., Perrin, C. and Stähler, S.C., 2020. Initial results from the InSight mission on Mars. Nature Geoscience, 13(3), 183-189.

8. Barrat, J.A., Blichert-Toft, J., Nesbitt, R.W. and Keller, F., 2001. Bulk chemistry of Saharan shergottite Dar al Gani 476. Meteoritics & Planetary Science, 36(1), 23–29.

9. Barrat, J.A., Jambon, A., Bohn, M., Gillet, P., Sautter, V., Göpel, C., Lesourd, M. and Keller, F., 2002. Petrology and chemistry of the picritic shergottite Northwest Africa 1068 (NWA 1068). Geochimica et Cosmochimica Acta, 66(19), 3505–3518.

10. Barrat, J.A., Jambon, A., Ferrière, L., Bollinger, C., Langlade, J.A., Liorzou, C., Boudouma, O. and Fialin, M., 2014. No Martian soil component in shergottite meteorites. Geochimica et Cosmochimica Acta, 125, 23-33.

11. Batanova, V.G., Thompson, J.M., Danyushevsky, L.V., Portnyagin, M.V., Garbe-Schönberg, D., Hauri, E., Kimura, J.I., Chang, Q., Senda, R., Goemann, K. and Chauvel, C., 2019. New olivine reference material for in situ microanalysis. Geostandards and Geoanalytical Research, 43(3), 453–473.

12. Beck, P., Barrat, J.A., Gillet, P., Wadhwa, M., Franchi, I.A., Greenwood, R.C., Bohn, M., Cotten, J., van de Moortèle, B. and Reynard, B., 2006. Petrography and geochemistry of the chassignite Northwest Africa 2737 (NWA 2737). Geochimica et Cosmochimica Acta, 70(8), 2127–2139.

13. Bellucci, J.J., Nemchin, A.A., Whitehouse, M.J., Snape, J.F., Bland, P. and Benedix, G.K., 2015. The Pb isotopic evolution of the Martian mantle constrained by initial Pb in Martian meteorites. Journal of Geophysical Research: Planets, 120(12), pp.2224-2240.

14. Bogard, D.D. and Johnson, P., 1983. Martian gases in an Antarctic meteorite?. Science, 221(4611), 651-654.

15. Borg, L.E. and Draper, D.S., 2003. A petrogenetic model for the origin and compositional variation of the Martian basaltic meteorites. Meteoritics & Planetary Science, 38(12), 1713-1731.

16. Borg, L.E., Brennecka, G.A. and Symes, S.J., 2016. Accretion timescale and impact history of Mars deduced from the isotopic systematics of martian meteorites. Geochimica et Cosmochimica Acta, 175, 150-167.

17. Borg, L.E., Gaffney, A.M. and DePaolo, D.J., 2008. Preliminary age of martian meteorite Northwest Africa 4468 and its relationship to the other incompatible-element-enriched shergottites (abstrast#1391). 39th Lunar and Planetary Science Conference.

18. Borg, L.E., Nyquist, L.E., Reese, Y., Wiesmann, H., Shih, C.Y., Taylor, L.A. and Ivanova, M., 2001. The age of Dhofar 019 and its relationship to the other Martian meteorites (abstract#1144). 32nd Lunar and Planetary Science Conference.

19. Borg, L.E., Nyquist, L.E., Taylor, L.A., Wiesmann, H. and Shih, C.Y., 1997. Constraints on Martian differentiation processes from Rb/Sr and Sm/Nd isotopic analyses of the basaltic shergottite QUE 94201. Geochimica et Cosmochimica Acta, 61(22), 4915-4931.

20. Borg, L.E., Nyquist, L.E., Wiesmann, H. and Reese, Y., 2002. Constraints on the petrogenesis of Martian meteorites from the Rb-Sr and Sm-Nd isotopic systematics of the lherzolitic shergottites ALH77005 and LEW88516. Geochimica et Cosmochimica Acta, 66(11), 2037–2053.

21. Borg, L.E., Nyquist, L.E., Wiesmann, H., Reese, Y. and Papike, J.J., 2000. Sr-Nd isotopic systematics of Martian meteorite DaG 476 (abstract#1036). 31st Lunar and Planetary Science Conference.

22. Borg, L.E., Nyquist, L.E., Wiesmann, H., Shih, C.Y. and Reese, Y., 2003. The age of Dar al Gani 476 and the differentiation history of the martian meteorites inferred from their radiogenic isotopic systematics. Geochimica et Cosmochimica Acta, 67(18), 3519-3536.

23. Bouvier, A., Blichert-Toft, J., Vervoort, J.D. and Albarede, F., 2005. The age of SNC meteorites and the antiquity of the Martian surface. Earth and Planetary Science Letters, 240(2), 221-233.

24. Bouvier, A., Vervoort, J.D. and Patchett, P.J., 2008. The Lu–Hf and Sm–Nd isotopic composition of CHUR: constraints from unequilibrated chondrites and implications for the bulk composition of terrestrial planets. Earth and Planetary Science Letters, 273(1-2), 48-57.

25. Brandon, A.D., Puchtel, I.S., Walker, R.J., Day, J.M., Irving, A.J. and Taylor, L.A., 2012. Evolution of the martian mantle inferred from the ^{187}Re–^{187}Os isotope and highly siderophile element abundance systematics of shergottite meteorites. Geochimica et Cosmochimica Acta, 76, 206-235.

26. Brandon, A.D., Walker, R.J., Morgan, J.W. and Goles, G.G., 2000. Re-Os isotopic evidence for early differentiation of the Martian mantle. Geochimica et Cosmochimica Acta, 64(23), 4083-4095.

27. Brennecka, G.A., Borg, L.E. and Wadhwa, M., 2014. Insights into the Martian mantle: The age and isotopics of the meteorite fall Tissint. Meteoritics & Planetary Science, 49(3), 412-418.

28. Burger, P.V., Shearer, C.K., Papike, J.J. and McCubbin, F.M., 2012, March. Crystal chemistry of merrillite in martian basalts and its significance to interpreting basalt petrogenesis (abstract#1178). 43rd Lunar and Planetary Science Conference.

29. Burgin, D.L., Scott, J.M., le Roux, P.J., Howarth, G., Palmer, M.C., Czertowicz, T.A., Negrini, M., Reid, M.R. and Stirling, C.H., 2022. Rapid characterisation of Mars' mantle reservoirs by in situ laser ablation $^{87}Sr/^{86}Sr$ analysis of shocked feldspar (maskelynite). Geochimica et Cosmochimica Acta, 341, 46-61.

30. Bussweiler, Y., Giuliani, A., Greig, A., Kjarsgaard, B.A., Petts, D., Jackson, S.E., Barrett, N., Luo, Y. and Pearson, D.G., 2019. Trace element analysis of high-Mg olivine by LA-ICP-MS–Characterization of natural olivine standards for matrix-matched calibration and application to mantle peridotites. Chemical Geology, 524, 136–157.

31. Cao, H., Chen, J., Fu, X., Xin, Y., Qi, X., Shi, E. and Ling, Z., 2022. Raman spectroscopic and geochemical studies of primary and secondary minerals in Martian meteorite Northwest Africa 10720. Journal of Raman Spectroscopy, 53(3), 420–434.

32. Caseres, J.R. (2015). The Mineralogy and Petrology of the New Martian Meteorite Larkman Nunatak 12011 (Unpublished undergraduate thesis). California Institute of Technology.

33. Castle, N. and Herd, C.D., 2017. Experimental petrology of the Tissint meteorite: Redox estimates, crystallization curves, and evaluation of petrogenetic models. Meteoritics & Planetary Science, 52(1), 125-146.

34. Clayton, R.N. and Mayeda, T.K., 1996. Oxygen isotope studies of achondrites. Geochimica et Cosmochimica Acta, 60(11), 1999-2017.

35. Cohen, B.E., Mark, D.F., Cassata, W.S., Lee, M.R., Tomkinson, T. and Smith, C.L., 2017. Taking the pulse of Mars via dating of a plume-fed volcano. Nature Communications, 8(1), 640.

36. Combs, L.M., Udry, A., Howarth, G.H., Righter, M., Lapen, T.J., Gross, J., Ross, D.K., Rahib, R.R. and Day, J.M.D., 2019. Petrology of the enriched poikilitic shergottite Northwest Africa 10169: Insight into the martian interior. Geochimica et Cosmochimica Acta, 266, 435-462.

37. Crozaz, G. and Wadhwa, M., 2001. The terrestrial alteration of Saharan shergottites Dar al Gani 476 and 489: A case study of weathering in a hot desert environment. Geochimica et Cosmochimica Acta, 65(6), 971-977.

38. Crozaz, G., Floss, C. and Wadhwa, M., 2003. Chemical alteration and REE mobilization in meteorites from hot and cold deserts. Geochimica et Cosmochimica Acta, 67(24), 4727-4741.

39. Danyushevsky, L.V., Della-Pasqua, F.N. and Sokolov, S., 2000. Re-equilibration of melt inclusions trapped by magnesian olivine phenocrysts from subduction-related magmas: petrological implications. Contributions to Mineralogy and Petrology, 138(1), 68-83.

40. Day, J., Tait, K.T., Udry, A., Moynier, F., Liu, Y. and Neal, C.R., 2018. Martian magmatism from plume metasomatized mantle. Nature communications, 9(1), 1–8.

41. Debaille, V., Brandon, A.D., Yin, Q.Z. and Jacobsen, B., 2007. Coupled ^{142}Nd–^{143}Nd evidence for a protracted magma ocean in Mars. Nature, 450(7169), 525-528.

42. Debaille, V., Yin, Q.Z., Brandon, A.D. and Jacobsen, B., 2008. Martian mantle mineralogy investigated by the ^{176}Lu–^{176}Hf and ^{147}Sm–^{143}Nd systematics of shergottites. Earth and Planetary Science Letters, 269(1-2), 186-199.

43. Demouchy, S. and Alard, O., 2021. Hydrogen, trace, and ultra-trace element distribution in natural olivines. Contributions to Mineralogy and Petrology, 176(4), 26.

44. Dreibus, G., Spettel, B., Haubold, R., Jochum, K.P., Palme, H., Wolf, D. and Zipfel, J., 2000. Chemistry of a new shergottite: Sayh al Uhaymir 005. Meteoritics & Planetary Science, 35 (S), A49.

45. Drilleau, M., Samuel, H., Garcia, R.F., Rivoldini, A., Perrin, C., Michaut, C., Wieczorek, M., Tauzin, B., Connolly, J.A., Meyer, P. and Lognonné, P., 2022. Marsquake locations and 1-D seismic models for Mars from InSight data. Journal of Geophysical Research: Planets, 127(9), 2021JE007067.

46. Dunham, E.T., Balta, J.B., Wadhwa, M., Sharp, T.G. and McSween Jr, H.Y., 2019. Petrology and geochemistry of olivine-phyric shergottites LAR 12095 and LAR 12240: Implications for their petrogenetic history on Mars. Meteoritics & Planetary science, 54(4), 811-835.

47. Elkins-Tanton, L.T., Parmentier, E.M. and Hess, P.C., 2003. Magma ocean fractional crystallization and cumulate overturn in terrestrial planets: Implications for Mars. Meteoritics & Planetary Science, 38(12), 1753-1771.

48. Eugster, O., Weigel, A. and Polnau, E., 1997. Ejection times of Martian meteorites. Geochimica et Cosmochimica Acta, 61(13), 2749-2757.

49. Ferdous, J., Brandon, A.D., Peslier, A.H. and Pirotte, Z., 2017. Evaluating crustal contributions to enriched shergottites from the petrology, trace elements, and Rb-Sr and Sm-Nd isotope systematics of Northwest Africa 856. Geochimica et Cosmochimica Acta, 211, 280-306.

50. Filiberto, J. and Dasgupta, R., 2011. Fe^{2+}–Mg partitioning between olivine and basaltic melts: Applications to genesis of olivine-phyric shergottites and conditions of melting in the Martian interior. Earth and Planetary Science Letters, 304(3-4), 527–537.

51. Filiberto, J., 2008. Experimental constraints on the parental liquid of the Chassigny meteorite: A possible link between the Chassigny meteorite and a Martian Gusev basalt. Geochimica et Cosmochimica Acta, 72(2), 690–701.

52. Filiberto, J., Chin, E., Day, J.M., Franchi, I.A., Greenwood, R.C., Gross, J., Penniston-Dorland, S.C., Schwenzer, S.P. and Treiman, A.H., 2012. Geochemistry of intermediate olivine-phyric shergottite Northwest Africa 6234, with similarities to basaltic shergottite Northwest Africa 480 and olivine-phyric shergottite Northwest Africa 2990. Meteoritics & Planetary Science, 47(8), 1256–1273.

53. Filiberto, J., Jackson, C., Le, L. and Treiman, A.H., 2009. Partitioning of Ni between olivine and an iron-rich basalt: Experiments, partition models, and planetary implications. American Mineralogist, 94(2-3), 256-261.

54. Filiberto, J., Musselwhite, D.S., Gross, J., Burgess, K., Le, L. and Treiman, A.H., 2010. Experimental petrology, crystallization history, and parental magma characteristics of olivine-phyric shergottite NWA 1068: Implications for the petrogenesis of “enriched” olivine-phyric shergottites. Meteoritics & Planetary Science, 45(8), 1258-1270.

55. Folco, L., D'Orazio, M. and Perchiazzi, N., 2007. Authenticating the recovery location of meteorites: The case of Castenaso. Meteoritics & Planetary Science, 42(3), 321–330.

56. Franchi, I.A., Wright, I.P., Sexton, A.S. and Pillinger, C.T., 1999. The oxygen-isotopic composition of Earth and Mars. Meteoritics & Planetary Science, 34(4), 657-661.

57. Gaetani, G.A. and Watson, E.B., 2000. Open system behavior of olivine-hosted melt inclusions. Earth and Planetary Science Letters, 183(1-2), 27-41.

58. Ghiorso M. S. and Sack R. O. (1991) Fe-Ti oxide geothermometry: Thermodynamic formulation and the estimation of intensive variables in silicic magmas. Contrib. Mineral. Petrol. 108, 485–510.

59. Goodrich, C.A., 2003. Petrogenesis of olivine-phyric shergottites Sayh al Uhaymir 005 and Elephant Moraine A79001 lithology A. Geochimica et Cosmochimica Acta, 67(19), 3735-3772.

60. Goodrich, C.A., Herd, C.D. and Taylor, L.A., 2003. Spinels and oxygen fugacity in olivine-phyric and lherzolitic shergottites. Meteoritics & Planetary Science, 38(12), 1773-1792.

61. Goodrich, C.A., Treiman, A.H., Filiberto, J., Gross, J. and Jercinovic, M., 2013. K_2O-rich trapped melt in olivine in the Nakhla meteorite: Implications for petrogenesis of nakhlites and evolution of the Martian mantle. Meteoritics & Planetary Science, 48(12), 2371-2405.

62. Greshake, A., Fritz, J. and Stöffler, D., 2004. Petrology and shock metamorphism of the olivine-phyric shergottite Yamato 980459: Evidence for a two-stage cooling and a single-stage ejection history. Geochimica et Cosmochimica Acta, 68(10), 2359-2377.

63. Griffin WL, Powell WJ, Pearson NJ, O'Reilly SY (2008) GLITTER: data reduction software for laser ablation ICP-MS. In Sylvester P (eds) Laser Ablation–ICP–MS in the Earth Sciences. Mineralogical Association of Canada Short Course Series 40, 204–207

64. Gross, J., Filiberto, J., Herd, C.D., Daswani, M.M., Schwenzer, S.P. and Treiman, A.H., 2013. Petrography, mineral chemistry, and crystallization history of olivine-phyric shergottite NWA 6234: A new melt composition. Meteoritics & Planetary Science, 48(5), 854-871.

65. Gross, J., Treiman, A.H., Filiberto, J. and Herd, C.D., 2011. Primitive olivine-phyric shergottite NWA 5789: Petrography, mineral chemistry, and cooling history imply a magma similar to Yamato-980459. Meteoritics & Planetary Science, 46(1), 116-133.

66. Harper Jr, C.L., Nyquist, L.E., Bansal, B., Wiesmann, H. and Shih, C.Y., 1995. Rapid accretion and early differentiation of Mars indicated by $^{142}Nd/^{144}Nd$ in SNC meteorites. Science, 267(5195), 213-217.

67. Herd C.D.K., Papike J.J., and Brearley A.J. 2001. Oxygen fugacity of Martian basalts from electron microprobe oxygen and TEM-EELS analyses of Fe-Ti oxides. American Minerologist, 86, 1015–1024.

68. Herd, C.D.K, 2003. The oxygen fugacity of olivine-phyric Martian basalts and the components within the mantle and crust of Mars. Meteoritics & Planetary Science, 38(12), 1793–1805.

69. Herd, C.D.K, 2006. Insights into the redox history of the NWA 1068/1110 Martian basalt from mineral equilibria and vanadium oxybarometry. American Mineralogist, 91(10), 1616-1627.

70. Herd, C.D.K, Borg, L. E., Jones, J. H., & Papike, J. J., 2002. Oxygen fugacity and geochemical variations in the martian basalts: implications for martian basalt petrogenesis and the oxidation state of the upper mantle of Mars. Geochimica et Cosmochimica Acta, 66(11), 2025–2036.

71. Herd, C.D.K, Walton, E.L., Agee, C.B., Muttik, N., Ziegler, K., Shearer, C.K., Bell, A.S., Santos, A.R., Burger, P.V., Simon, J.I. and Tappa, M.J., 2017. The Northwest Africa 8159 martian meteorite: Expanding the martian sample suite to the early Amazonian. Geochimica et Cosmochimica Acta, 218, 1–26.

72. Herd, C.D.K., Duke, M.J.M., Bryden, C.D. and Pearson, D.G., 2013. Tissint among the shergottites: Parental melt composition, redox state, La/Yb and V/Sc (abstract#2683). 44th Annual Lunar and Planetary Science Conference.

73. Howarth, G.H. and Udry, A., 2017. Trace elements in olivine and the petrogenesis of the intermediate, olivine-phyric shergottite NWA 10170. Meteoritics & Planetary Science, 52(2), 391–409.

74. Howarth, G.H., Pernet-Fisher, J.F., Balta, J.B., Barry, P.H., Bodnar, R.J. and Taylor, L.A., 2014. Two-stage polybaric formation of the new enriched, pyroxene-oikocrystic, lherzolitic shergottite, NWA 7397. Meteoritics & Planetary Science, 49(10), 1812-1830.

75. Huang, Q., Schmerr, N.C., King, S.D., Kim, D., Rivoldini, A., Plesa, A.C., Samuel, H., Maguire, R.R., Karakostas, F., Lekić, V. and Charalambous, C., 2022. Seismic detection of a deep mantle discontinuity within Mars by InSight. Proceedings of the National Academy of Sciences, 119(42), 2204474119.

76. Hui, H., Peslier, A.H., Lapen, T.J., Shafer, J.T., Brandon, A.D., and Irving, A.J., 2011. Petrogenesis of basaltic shergottite Northwest Africa 5298: Closed-system crystallization of an oxidized mafic melt. Meteoritics & Planetary Science, 46(9), 1313-1328.

77. Ikeda, Y., 2005. Magmatic inclusions in martian meteorites. Antarctic Meteorite Research, Vol. 18, p. 170, 18, 170.

78. Irving A. J., Kuehner S. M., Herd C. D. K., Gellissen M., Korotev R. L., Puchtel I., Walker R. J., Lapen T. J., and Rumble D. III. 2010. Petrologic, elemental and multi-isotopic characterization of permafic olivine-phyric shergottite Northwest Africa 5789: A primitive magma derived from depleted Martian mantle (abstract #1547). 41st Lunar and Planetary Science Conference.

79. Irving, A.J., Bunch, T.E., Kuehner, S.M., Wittke, J.H., 2004. Petrology of Primitive Olivine-Orthopyroxene-Phyric Shergottites NWA 2046 and NWA 1195: Analogies with Terrestrial Boninites and Implications for Partial Melting of Hydrous Martian Mantle (abstract #1444). 35th Lunar and Planetary Science Conference.

80. Irving, A.J., Bunch, T.E., Wittke, J.H., Kuehner, S.M., 2005. Olivine-Orthopyroxene-Phyric Shergottites NWA 2626 and DaG 476: The Tharsis Connection (abstract #1229). 36th Lunar and Planetary Science Conference.

81. Irving, A.J., Kuehner, S.M., Hupe, H.C., Hupe, G.M., 2002. Olivine-Orthopyroxene-Phyric Shergottites NWA 2626 and DaG 476: The Tharsis Connection (abstract #5229). 65th Annual Lunar and Planetary Science Conference.

82. Irving, A.J., Kuehner, S.M., Tanaka, R., Herd, C.D.K., Chen, G. and Lapen, T.J., 2012. The Tissint depleted permafic olivine-phyric Shergottite: Petrologic, elemental, and isotopic characterization of a recent Martian Fall in Morocco (abstract #2510). 43rd Lunar and Planetary Science Conference.

83. Jagoutz, E. and Wänke, H., 1986. Sr and Nd isotopic systematics of Shergotty meteorite. Geochimica et Cosmochimica Acta, 50(6), 939-953.

84. Jochum et al 2005. GeoReM: A New Geochemical Database for Reference Materials and Isotopic Standards. Geostandards and Geoanalytical Research 29, 333-338.

85. Johnson, K.T., 1998. Experimental determination of partition coefficients for rare earth and high-field-strength elements between clinopyroxene, garnet, and basaltic melt at high pressures. Contributions to Mineralogy and Petrology, 133(1-2), 60-68.

86. Johnson, M.C., Rutherford, M.J. and Hess, P.C., 1991. Chassigny petrogenesis: melt compositions, intensive parameters and water contents of Martian (?) magmas. Geochimica et Cosmochimica Acta, 55(1), 349–366.

87. Jones, J.H., 1995. Experimental trace element partitioning. Rock physics and phase relations: A handbook of physical constants, American Geophysical Union, 3, 73-104.

88. Khan, A., Ceylan, S., van Driel, M., Giardini, D., Lognonné, P., Samuel, H., Schmerr, N.C., Stähler, S.C., Duran, A.C., Huang, Q. and Kim, D., 2021. Upper mantle structure of Mars from InSight seismic data. Science, 373(6553), 434-438.

89. Kiefer, W.S. and Jones, J.S., 2015. Formation and Preservation of the Depleted and Enriched Shergottite Isotopic Reservoirs in a Convecting Martian Mantle (abstract #1197). 46th Lunar and Planetary Science Conference.

90. Kiefer, W.S., 2003. Melting in the Martian mantle: Shergottite formation and implications for present-day mantle convection on Mars. Meteoritics & Planetary Science, 38(12), 1815-1832.

91. Köhler, T.P. and Brey, G., 1990. Calcium exchange between olivine and clinopyroxene calibrated as a geothermobarometer for natural peridotites from 2 to 60 kb with applications. Geochimica et Cosmochimica Acta, 54(9), 2375–2388.

92. Kuehner S.M., Irving A.J., Herd C.D.K., Gellissen M., Lapen T.J. and Rumble D., 2011. Pristine olivine–phyric Shergottite NWA 6162: A primitive magma with accumulated crystals derived from depleted Martian mantle (Abstract# 1610). 42nd Lunar and Planetary Science Conference.

93. Lagain, A., Benedix, G.K., Servis, K., Baratoux, D., Doucet, L.S., Rajšic, A., Devillepoix, H.A.R., Bland, P.A., Towner, M.C., Sansom, E.K. and Miljković, K., 2021. The Tharsis mantle source of depleted shergottites revealed by 90 million impact craters. Nature communications, 12(1), 1-9.

94. Lapen T. J., Andreasen R., Righter M., Irving A. J., 2013. Lu-Hf Age and Isotope Systematics of Intermediate Permafic Olivine-Phyric Shergottite NWA 2990: Implications for the Diversity of Shergottite Sources (Abstract# 2686). 44th Lunar and Planetary Science Conference.

95. Lapen, T.J., Brandon, A.D., Beard, B.L., Peslier, A.H., Lee, C.T. and Dalton, H.A., 2008. Lu-Hf age and isotope systematics of the olivine-phyric shergottite RBT 04262 and implications for the sources of enriched shergottites (abstract#1391). 39th Lunar and Planetary Science Conference.

96. Lapen, T.J., Righter, M., Andreasen, R., Irving, A.J., Satkoski, A.M., Beard, B.L., Nishiizumi, K., Jull, A.T. and Caffee, M.W., 2017. Two billion years of magmatism recorded from a single Mars meteorite ejection site. Science advances, 3(2), e1600922.

97. Lapen, T.J., Righter, M., Brandon, A.D., Beard, B.L., Shafer, J., and Irving, A.J., 2009. Lu-Hf isotope systematics of NWA 4468 and NWA 2990: Implications for the sources of shergottites (abstrast#2376). 40th Lunar and Planetary Science Conference.

98. Le Roux, P.J., Lee-Thorp, J.A., Copeland, S.R., Sponheimer, M. and De Ruiter, D.J., 2014. Strontium isotope analysis of curved tooth enamel surfaces by laser-ablation multi-collector ICP-MS. Palaeogeography, Palaeoclimatology, Palaeoecology, 416, 142-149.

99. Lindsay, F., Turrin, B., Herzog, G.F., Swisher, C. and Emge, T., 2012, March. $^{39}Ar/^{40}Ar$ Ages of Single Grains from Shergottite NWA 2626: Pushing the Limits of Laser Step-Heating (abstract#2836). 43rd Lunar and Planetary Science Conference.

100. Liu, Y., Baziotis, I.P., Asimow, P.D., Bodnar, R.J. and Taylor, L.A., 2016. Mineral chemistry of the Tissint meteorite: Indications of two-stage crystallization in a closed system. Meteoritics & Planetary Science, 51(12), 2293-2315.

101. Lodders, K., 1998. A survey of shergottite, nakhlite and chassigny meteorites whole-rock compositions. Meteoritics & Planetary Science, 33(S4), A183–A190.

102. Lognonné, P., Banerdt, W.B., Giardini, D., Pike, W.T., Christensen, U., Laudet, P., De Raucourt, S., Zweifel, P., Calcutt, S., Bierwirth, M. and Hurst, K.J., 2019. SEIS: Insight's seismic experiment for internal structure of Mars. Space Science Reviews, 215, 1-170.

103. Longhi, J. and Pan, V., 1989. The parent magmas of the SNC meteorites. Proceedings, 19th Lunar and Planetary Science Conference, 451-464.

104. Longhi, J., 1991. Complex magmatic processes on Mars-Inferences from the SNC meteorites. Proceedings, 21st Lunar and Planetary Science Conference, 695-709.

105. Lundberg, L.L., Crozaz, G. and McSween Jr, H.Y., 1990. Rare earth elements in minerals of the ALHA77005 shergottite and implications for its parent magma and crystallization history. Geochimica et Cosmochimica Acta, 54(9), 2535-2547.

106. Makishima, J., McKay, G., Le, L., Miyamoto, M. and Mikouchi, T., 2007, January. Oxidation state of nakhlites as inferred from Fe-Ti oxide equilibria and augite/melt europium partitioning (abstract#1834). 38th Lunar and Planetary Science Conference.

107. Mattioli G. S. and Wood B. J. (1988) Magnetite activities across the $MgAl_2O_4$-Fe_3O_4 join, with application to thermobarometric estimates of upper mantle oxygen fugacity. Contrib. Mineral. Petrol. 98, 148–162.

108. McCubbin, F.M. and Nekvasil, H., 2008. Maskelynite-hosted apatite in the Chassigny meteorite: Insights into late-stage magmatic volatile evolution in martian magmas. American Mineralogist, 93(4), 676-684.

109. McCubbin, F.M., Elardo, S.M., Shearer Jr, C.K., Smirnov, A., Hauri, E.H. and Draper, D.S., 2013. A petrogenetic model for the comagmatic origin of chassignites and nakhlites: Inferences from chlorine-rich minerals, petrology, and geochemistry. Meteoritics & Planetary Science, 48(5), 819-853.

110. McDonough, W.F. and Sun, S.S., 1995. The composition of the Earth. Chemical geology, 120(3-4), 223-253.

111. McSween H. Y., Eisenhour D. D., Taylor L. A., Wadhwa M., and Crozaz G. 1996. QUE 94201 shergottite: Crystallization of a Martian basaltic magma. Geochimica et Cosmochimica Acta 60, 4563–4569.

112. McSween Jr, H.Y. and Jarosewich, E., 1983. Petrogenesis of the Elephant Moraine A79001 meteorite: Multiple magma pulses on the shergottite parent body. Geochimica et Cosmochimica Acta, 47(8), 1501-1513.

113. McSween Jr, H.Y., 1984. SNC meteorites: Are they Martian rocks?. Geology, 12(1), 3-6.

114. McSween Jr, H.Y., 2015. Petrology on mars. American Mineralogist, 100(11-12), 2380-2395.

115. McSween, H.Y. and Stolper, E.M., 1980. Basaltic meteorites. Scientific American, 242(6), 54-63.

116. Misawa, K., 2004. The Yamato 980459 olivine-phyric shergottite consortium. Antarctic Meteorite Research, 17, 1-12.

117. Musselwhite, D.S., Dalton, H.A., Kiefer, W.S. and Treiman, A.H., 2006. Experimental petrology of the basaltic shergottite Yamato-980459: Implications for the thermal structure of the Martian mantle. Meteoritics & Planetary Science, 41(9), 1271-1290.

118. Nicklas, R.W., Day, J.M., Vaci, Z. and Udry, A., 2022. Petrogenesis of Northwest Africa 8686: A ferroan olivine-phyric shergottite. Meteoritics & Planetary Science, 57(5), 947-964.

119. Nicklas, R.W., Day, J.M.D., Vaci, Z., Udry, A., Liu, Y. and Tait, K.T., 2021. Uniform oxygen fugacity of shergottite mantle sources and an oxidized martian lithosphere. Earth and Planetary Science Letters, 564, 116876.

120. Nielsen, R.L., Gallahan, W.E. and Newberger, F., 1992. Experimentally determined mineral-melt partition coefficients for Sc, Y and REE for olivine, orthopyroxene, pigeonite, magnetite and ilmenite. Contributions to Mineralogy and Petrology, 110, 488–499.

121. Nishiizumi, K., Caffee, M.W. and Irving, A.J., 2012. Exposure history of Tissint: Evidence for 1.1 million year launch pairing with other depleted olivine-phyric shergottites. Meteoritics and Planetary Science Supplement, 75, 5349.

122. Nishiizumi, K., Hillegonds, D.J., McHargue, L.R. and Jull, A.J.T., 2004. Exposure and terrestrial histories of new lunar and martian meteorites. (abstract#1130). 35th Lunar and Planetary Science Conference.

123. Nishiizumi, K., Nagao, K., Caffee, M.W., Jull, A.J.T. and Irving, A.J., 2011, March. Cosmic-ray exposure chronologies of depleted olivine-phyric shergottites (abstract#2371). 42nd Lunar and Planetary Science Conference.

124. Nishiizumi, K., Okazaki, R., Park, J., Nagao, K., Masarik, J. and Finkel, R.C., 2002, March. Exposure and terrestrial histories of Dhofar 019 Martian meteorite (abstract#1366). 33rd Lunar and Planetary Science Conference.

125. Norris, A. and Danyushevsky, L. (2018). Towards Estimating the Complete Uncertainty Budget of Quantified Results Measured by LA-ICP-MS (abstract#1894). Goldschmidt Conference, Boston, Massachusetts.

126. Nyquist, L.E., Bogard, D.D., Shih, C.Y., Greshake, A., Stöffler, D. and Eugster, O., 2001. Ages and geologic histories of Martian meteorites. In Chronology and evolution of Mars. Springer Netherlands, 105-165.

127. Nyquist, L.E., Bogard, D.D., Shih, C.Y., Park, J., Reese, Y.D. and Irving, A.J., 2009. Concordant Rb–Sr, Sm–Nd, and Ar–Ar ages for Northwest Africa 1460: a 346 Ma old basaltic shergottite related to "lherzolitic" shergottites. Geochimica et Cosmochimica Acta, 73(14), 4288–4309.

128. Nyquist, L.E., Reese, Y., Wiesmann, H., and Shih, C.Y., 2001b. Age of EET79001B and implications for shergottite origins(abstract#1407). 32nd Lunar and Planetary Science Conference.

129. Nyquist, L.E., Shih, C.Y., McCubbin, F.M., Santos, A.R., Shearer, C.K., Peng, Z.X., Burger, P.V. and Agee, C.B., 2016. Rb-Sr and Sm-Nd isotopic and REE studies of igneous components in the bulk matrix domain of Martian breccia Northwest Africa 7034. Meteoritics & Planetary Science, 51(3), 483-498.

130. Onuma, N., Higuchi, H., Wakita, H. and Nagasawa, H., 1968. Trace element partition between two pyroxenes and the host lava. Earth and Planetary Science Letters, 5, 47-51.

131. Orr, K.J., Forman, L.V., Rankenburg, K., Evans, N.J., McDonald, B.J., Godel, B. and Benedix, G.K., 2022. Geochemical and mineralogical classification of four new shergottites: NWA 10441, NWA 10818, NWA 11043, and NWA 12335. Meteoritics & Planetary Science, 57(6), 1194–1223.

132. Ostwald, A., Udry, A., Day, J.M. and Gross, J., 2024. Melt inclusion heterogeneity in nakhlite and chassignite meteorites and evidence for complicated, multigenerational magmas. Meteoritics & Planetary Science, 59(6), 1473-1497.

133. Ostwald, A.M., Udry, A., Gross, J. and Day, J.M.D., 2020, March. Chassignite and nakhlite parental melts determined from melt inclusion analysis (abstract#2213). 51st Lunar and Planetary Science Conference.

134. Park, J., Bogard, D.D., Nyquist, L.E., Garrison, D.H. and Mikouchi, T., 2013. Ar–Ar ages and trapped Ar components in Martian shergottites RBT 04262 and LAR 06319. Geochimica et Cosmochimica Acta, 121, 546-570.

135. Papike, J.J., Karner, J.M., Shearer, C.K. and Burger, P.V., 2009. Silicate mineralogy of martian meteorites. Geochimica et Cosmochimica Acta, 73(24), 7443-7485.

136. Peel, C.J., Howarth, G.H., Day, J.M., le Roux, P. and Alard, O., 2023. Constraints on martian depleted shergottite volcanism from the petrogenesis of olivine-phyric shergottites NWA 2046 and NWA 4925. Journal of African Earth Sciences, 202, 104901.

137. Peslier, A.H., Hnatyshin, D., Herd, C.D., Walton, E.L., Brandon, A.D., Lapen, T.J. and Shafer, J.T., 2010. Crystallization, melt inclusion, and redox history of a Martian meteorite: Olivine-phyric shergottite Larkman Nunatak 06319. Geochimica et Cosmochimica Acta, 74(15), 4543-4576.

138. Peters, T.J., Simon, J.I., Jones, J.H., Usui, T., Moriwaki, R., Economos, R.C., Schmitt, A.K. and McKeegan, K.D., 2015. Tracking the source of the enriched martian meteorites in olivine-hosted melt inclusions of two depleted shergottites, Yamato 980459 and Tissint. Earth and Planetary Science Letters, 418, 91-102.

139. Pourkhorsandi, H., D'Orazio, M., Rochette, P., Valenzuela, M., Gattacceca, J., Mirnejad, H., Sutter, B., Hutzler, A. and Aboulahris, M., 2017. Modification of REE distribution of ordinary chondrites from Atacama (Chile) and Lut (Iran) hot deserts: Insights into the chemical weathering of meteorites. Meteoritics & Planetary Science, 52(9), 1843-1858.

140. Rahib, R.R., Udry, A., Howarth, G.H., Gross, J., Paquet, M., Combs, L.M., Laczniak, D.L. and Day, J.M., 2019. Mantle source to near–surface emplacement of enriched and intermediate poikilitic shergottites in Mars. Geochimica et Cosmochimica Acta, 266, 463–496.

141. Ramsey, S.R., Howarth, G.H., Udry, A. and Gross, J., 2021. Nickel–manganese variability in olivine and Al-in-olivine thermometry for olivine-phyric shergottites. Meteoritics & Planetary Science, 56(8), 1597-1618.

142. Righter, K., Keller, L., Rahman, Z. and Christoffersen, R., 2014. Redox-driven exsolution of iron-titanium oxides in magnetite in Miller Range (MIL) 03346 nakhlite: Evidence for post crystallization oxidation in the nakhlite cumulate pile?. American Mineralogist, 99 (11-12), 2313-2319.

143. Righter, K., Yang, H., Costin, G. and Downs, R.T., 2008. Oxygen fugacity in the Martian mantle controlled by carbon: New constraints from the nakhlite MIL 03346. Meteoritics & Planetary Science, 43(10), 1709-1723.

144. Righter, M., Andreasen, R. and Lapen, T.J., 2015, March. Lu-Hf and Sm-Nd systematics of martian meteorites Larkman Nunatak 12011 and 12095 (abstract#1832). 46th Lunar and Planetary Science Conference.

145. Robbins, S.J., Di Achille, G. and Hynek, B.M., 2011. The volcanic history of Mars: High-resolution crater-based studies of the calderas of 20 volcanoes. Icarus, 211(2), 1179-1203.

146. Romanek, C.S., Perry, E.C., Treiman, A.H., Socki, R.A., Jones, J.H. and Gibson Jr, E.K., 1998. Oxygen isotopic record of silicate alteration in the Shergotty—Nakhla—Chassigny meteorite Lafayette. Meteoritics & Planetary Science, 33(4), 775-784.

147. Sarbadhikari, A.B., Babu, E., Kumar, T.V., and Aoudjehane, H.C., 2016. Martian meteorite Tissint records unique petrogenesis among the depleted shergottites. Meteoritics & Planetary Science, 51(9), 1588-1610.

148. Sarbadhikari, A.B., Day, J.M., Liu, Y., Rumble III, D. and Taylor, L.A., 2009. Petrogenesis of olivine–phyric shergottite Larkman Nunatak 06319: Implications for enriched components in martian basalts. Geochimica et Cosmochimica Acta, 73(7), 2190–2214.

149. Sarbadhikari, A.B., Goodrich, C.A., Liu, Y., Day, J.M. and Taylor, L.A., 2011. Evidence for heterogeneous enriched shergottite mantle sources in Mars from olivine-hosted melt inclusions in Larkman Nunatak 06319. Geochimica et Cosmochimica Acta, 75(22), 6803-6820.

150. Sautter, V., Toplis, M.J., Lorand, J.P. and Macri, M., 2012. Melt inclusions in augite from the nakhlite meteorites: A reassessment of nakhlite parental melt and implications for petrogenesis. Meteoritics & Planetary Science, 47(3), 330-344.

151. Shafer, J.T., Brandon, A.D., Lapen, T.J., Righter, M., Peslier, A.H. and Beard, B.L., 2010. Trace element systematics and ^{147}Sm–^{143}Nd and ^{176}Lu–^{176}Hf ages of Larkman Nunatak 06319: Closed-system fractional crystallization of an enriched shergottite magma. Geochimica et Cosmochimica Acta, 74(24), 7307–7328.

152. Shannon, R.D., 1976. Revised effective ionic radii and systematic studies of interatomic distances in halides and chalcogenides. Acta crystallographica section A: crystal physics, diffraction, theoretical and general crystallography, 32(5), 751-767.

153. Sharp, T.G., Walton, E.L., Hu, J. and Agee, C., 2019. Shock conditions recorded in NWA 8159 martian augite basalt with implications for the impact cratering history on Mars. Geochimica et Cosmochimica Acta, 246, 197–212.

154. Shearer, C.K., Aaron, P.M., Burger, P.V., Guan, Y., Bell, A.S. and Papike, J.J., 2013. Petrogenetic linkages among fO_2, isotopic enrichments-depletions and crystallization history in Martian basalts. Evidence from the distribution of phosphorus in olivine megacrysts. Geochimica et Cosmochimica Acta, 120, 17–38.

155. Shearer, C.K., Burger, P.V., Papdce, J.J., Borg, L.E., Irving, A.J. and Herd, C., 2008. Petrogenetic linkages among Martian basalts: Implications based on trace element chemistry of olivine. Meteoritics & Planetary Science, 43(7), 1241-1258.

156. Shearer, C.K., Burger, P.V., Papike, J.J., McCubbin, F.M. and Bell, A.S., 2015. Crystal chemistry of merrillite from Martian meteorites: Mineralogical recorders of magmatic processes and planetary differentiation. Meteoritics & Planetary Science, 50(4), 649-673.

157. Shearer, C.K., McKay, G., Papike, J.J. and Karner, J.M., 2006. Valence state partitioning of vanadium between olivine-liquid: Estimates of the oxygen fugacity of Y980459 and application to other olivine-phyric martian basalts. American Mineralogist, 91(10), 1657-1663.

158. Shearer, C.K., Papike, J.J., Burger, P.V., Sutton, S.R., McCubbin, F.M. and Newville, M., 2011. Direct determination of europium valence state by XANES in extraterrestrial merrillite: Implications for REE crystal chemistry and martian magmatism. American Mineralogist, 96(8-9), 1418-1421.

159. Shih, C.Y., Nyquist, L.E., Bogard, D.D., McKay, G.A., Wooden, J.L., Bansal, B.M. and Wiesmann, H., 1982. Chronology and petrogenesis of young achondrites, Shergotty, Zagami, and ALHA77005: Late magmatism on a geologically active planet. Geochimica et Cosmochimica Acta, 46(11), 2323-2344.

160. Shih, C.Y., Nyquist, L.E., Reese, Y., 2009. Rb-Sr and Sm-Nd Studies of Olivine-Phyric Shergottites RBT 04262 and LAR 06319: Isotopic Evidence for Relationship to Enriched Basaltic Shergottites (abstrast#1360). 40th Lunar and Planetary Science Conference.

161. Shih, C.Y., Nyquist, L.E., Wiesmann, H., Barrat, J. A., 2003. Age and Petrogenesis of Picritic Shergottite NWA1068: Sm-Nd and Rb-Sr Isotopic Studies (abstrast#1439). 34th Lunar and Planetary Science Conference.

162. Shih, C.Y., Nyquist, L.E., Reese. Y., 2007. Rb-Sr and Sm-Nd isotopic studies of martian depleted shergottites SaU 094/005 (abstract#1745). 38th Lunar and Planetary Science Conference.

163. Shih, C.Y., Nyquist, L.E., Reese. Y., Irving, A.J., 2011. Rb-Sr and Sm-Nd ages, and petrogenesis of depleted shergottite Northwest Africa 5990 (abstract#1846). 42nd Lunar and Planetary Science Conference.

164. Shih, C.Y., Nyquist, L.E., Wiesmann, H., Reese, Y. and Misawa, K., 2005. Rb-Sr and Sm-Nd dating of olivine-phyric shergottite Yamato 980459: Petrogenesis of depleted shergottites. Antarctic Meteorite Research, 18, 46-65.

165. Shirai, N. and Ebihara, M., 2004. Chemical characteristics of a Martian meteorite, Yamato 980459. Antarctic Meteorite Research, 17, 55.

166. Shukolyukov, Y.A., Nazarov, M.A. and Schultz, L., 2002. A new Martian meteorite: The Dhofar 019 shergottite with an exposure age of 20 million years. Solar System Research, 36, 125-135.

167. Steele, I.M. and Smith, J.V., 1982. Petrography and mineralogy of two basalts and olivine-pyroxene-spinel fragments in achondrite EETA79001. Journal of Geophysical Research: Solid Earth, 87(S01), A375-A384.

168. Stolper, E. and McSween Jr, H.Y., 1979. Petrology and origin of the shergottite meteorites. Geochimica et Cosmochimica Acta, 43(9), 1475-1498.

169. Suarez, S.E., Lapen, T.J., Righter, M., Beard, B.L. and Irving, A.J., 2022. Isotopic and trace element data of Tissint indicate a homogeneous strewn field, mobilization of Sr, REE, and Pb during shock metamorphism, and limits on the incorporation of martian surficial materials in impact melt glass. Geochimica et Cosmochimica Acta, 327, 137-157.

170. Symes, S.J., Borg, L.E., Shearer, C.K. and Irving, A.J., 2008. The age of the Martian meteorite Northwest Africa 1195 and the differentiation history of the shergottites. Geochimica et Cosmochimica Acta, 72(6), 1696-1710.

171. Tait, K.T. and Day, J.M., 2018. Chondritic late accretion to Mars and the nature of shergottite reservoirs. Earth and Planetary Science Letters, 494,99-108.

172. Taylor, L.A., Nazarov, M.A., Shearer, C.K., McSween Jr, H.Y., Cahill, J., Neal, C.R., Ivanova, M.A., Barsukova, L.D., Lentz, R.C., Clayton, R.N. and Mayeda, T.K., 2002. Martian meteorite Dhofar 019: A new shergottite. Meteoritics & Planetary Science, 37(8), 1107-1128.

173. Treiman, A.H. and Filiberto, J., 2015. Geochemical diversity of shergottite basalts: Mixing and fractionation, and their relation to Mars surface basalts. Meteoritics & Planetary Science, 50(4), 632-648.

174. Treiman, A.H., 2005. The nakhlite meteorites: Augite-rich igneous rocks from Mars. Geochemistry, 65(3), 203-270.

175. Udry, A. and Day, J.M., 2018. 1.34 billion–year–old magmatism on Mars evaluated from the co–genetic nakhlite and chassignite meteorites. Geochimica et Cosmochimica Acta, 238, 292–315.

176. Udry, A., Howarth, G.H., Herd, C.D.K., Day, J.M.D., Lapen, T.J. and Filiberto, J., 2020. What martian meteorites reveal about the interior and surface of Mars. Journal of Geophysical Research: Planets, 125(12), e2020JE006523.

177. Udry, A., Howarth, G.H., Lapen, T.J. and Righter, M., 2017. Petrogenesis of the NWA 7320 enriched martian gabbroic shergottite: Insight into the martian crust. Geochimica et Cosmochimica Acta, 204, 1–18.

178. Usui, T., McSween Jr, H.Y. and Floss, C., 2008. Petrogenesis of olivine-phyric shergottite Yamato 980459, revisited. Geochimica et Cosmochimica Acta, 72(6), 1711-1730.

179. Usui, T., Sanborn, M., Wadhwa, M. and McSween Jr, H.Y., 2010. Petrology and trace element geochemistry of Robert Massif 04261 and 04262 meteorites, the first examples of geochemically enriched lherzolitic shergottites. Geochimica et Cosmochimica Acta, 74(24), 7283-7306.

180. Varela, M.E. and Zinner, E., 2015. Glass-bearing inclusions in Shergotty and Chassigny: Consistent samples of a primary trapped melt?. Meteoritics & Planetary Science, 50(12), 2045-2066.

181. Veter, M., Foley, S.F. and Alard, O., 2019. Improved LA-ICP-MS analytical routine for low-concentration chalcophile and siderophile elements in olivine and orthopyroxene. Geochim. Cosmochim. Acta, 73, 1755-1778.

182. Wadhwa, M. and Crozaz, G., 1995. Trace and minor elements in minerals of nakhlites and Chassigny: Clues to their petrogenesis. Geochimica et Cosmochimica Acta, 59(17), 3629–3645.

183. Wadhwa, M., Lentz, R.C.F., McSween Jr, H.Y. and Crozaz, G., 2001. A petrologic and trace element study of Dar al Gani 476 and Dar al Gani 489: Twin meteorites with affinities to basaltic and lherzolitic shergottites. Meteoritics & Planetary Science, 36(2), 195-208.

184. Wadhwa, M., McSween Jr, H.Y. and Crozaz, G., 1994. Petrogenesis of shergottite meteorites inferred from minor and trace element microdistributions. Geochimica et Cosmochimica Acta, 58(19), 4213-4229.

185. Walton, E.L., Irving, A.J., Bunch, T.E. and Herd, C.D.K., 2012. Northwest Africa 4797: A strongly shocked ultramafic poikilitic shergottite related to compositionally intermediate Martian meteorites. Meteoritics & Planetary Science, 47(9), 1449-1474.

186. Walton, E.L., Kelley, S.P. and Spray, J.G., 2007. Shock implantation of Martian atmospheric argon in four basaltic shergottites: A laser probe 40Ar/39Ar investigation. Geochimica et Cosmochimica Acta, 71(2), 497-520.

187. Wang, J., Xiong, X., Takahashi, E., Zhang, L., Li, L., Liu, X., 2019. Oxidation state of arc mantle revealed by partitioning of V, Sc, and Ti between mantle minerals and basaltic melts. J. Geophys. Res., Solid Earth, 124, 4617–4638.

188. Wang, Z., Tian, W. and Di, Y., 2021. New temperature and oxygen fugacity data of Martian nakhlite from Northwest Africa (NWA) 5790 and implications for shallow sulphur degassing. Earth, Planets and Space, 73(1), 1–8.

189. Werner, S.C., 2009. The global martian volcanic evolutionary history. Icarus, 201(1), 44-68.

190. Wieler, R., Huber, L., Busemann, H., Seiler, S., Leya, I., Maden, C., Masarik, J., Meier, M.M.M., Nagao, K., Trappitsch, R. and Irving, A.J., 2016. Noble gases in 18 Martian meteorites and angrite Northwest Africa 7812—exposure ages, trapped gases, and a re-evaluation of the evidence for solar cosmic ray-produced neon in shergottites and other achondrites. Meteoritics & planetary science, 51(2), 407-428.

191. Wood B. J., 1991. Oxygen barometry of spinel peridotites. In Oxide Minerals: Petrologic and Magnetic Significance (ed. D. H. Lindsley), Reviews in Mineralogy 25. Mineralogical Society of America. 417–431.

192. Wood, B.J., and Virgo, D., 1989. Upper mantle oxidation state: Ferric iron contents of Iherzolite spinels by ^{57}Fe Mössbauer spectroscopy and resultant oxygen fugacities. Geochimica et Cosmochimica Acta, 53, 1277–1291.

193. Wooden, J., Shih, C.Y., Nyquist, L., Bansal, B., Wiesmann, H. and McKay, G., 1982. Rb-Sr and Sm-Nd isotopic constraints on the origin of EETA 79001: A second Antarctic shergottite (abstract#1450). 13th Lunar and Planetary Science Conference.

194. Wu, Y., Li, Q.L., Che, X. and Liao, S., 2021. Heterogeneous martian mantle: Evidence from petrology, mineral chemistry, and in situ U-Pb chronology of the basaltic shergottite Northwest Africa 8653. Geochimica et Cosmochimica Acta, 309, 352-365.

195. Yang, S., Humayun, M., Jefferson, G., Fields, D., Righter, K. and Irving, A.J., 2013, January. Chemical composition of four shergottites from Northwest Africa (NWA 2800, NWA, 5214, NWA 5990, NWA 6342) (abstract#1738). 44th Lunar and Planetary Science Conference.

196. Zhao, H., Zhao, X.M., Le Roux, P.J., Zhang, W., Wang, H., Xie, L.W., Huang, C., Wu, S.T., Yang, J.H., Wu, F.Y. and Yang, Y.H., 2020. Natural Clinopyroxene Reference Materials for in situ Sr Isotopic Analysis via LA-MC-ICP-MS. Frontiers in Chemistry, 8, 1131.

197. Zipfel, J., Scherer, P., Spettel, B., Dreibus, G. and Schultz, L., 2000. Petrology and chemistry of the new shergottite Dar al Gani 476. Meteoritics & Planetary Science, 35(1), 95-106.

7 Supplementary Figures

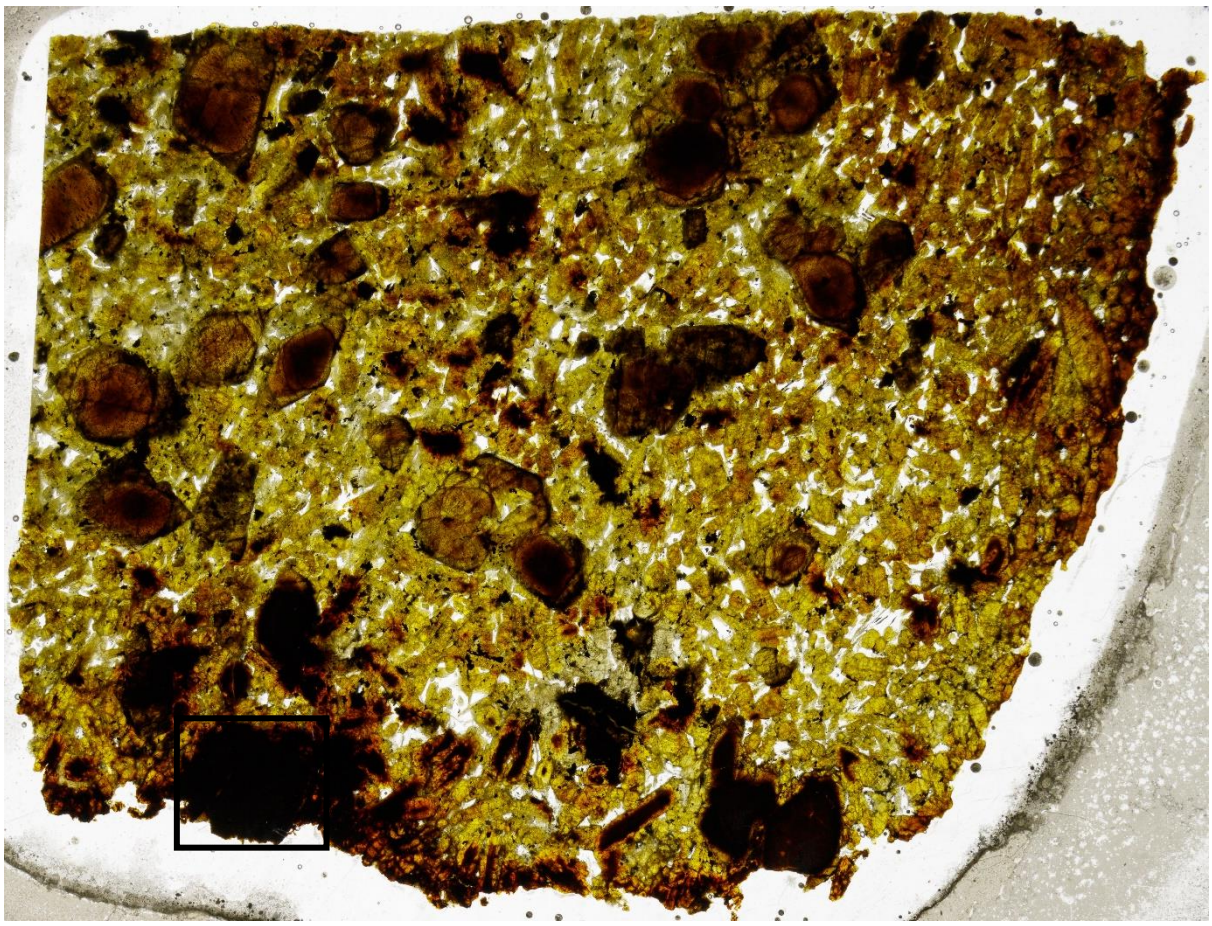

Supplementary Figure 1: Transmitted plane polarised light image of NWA 4925. The core and core margin regions of grains from the weathering rind of the sample are extensively altered, relative to olivine grains from the interior of NWA 4925. Black box outlines grains in Supplementary figure 2.

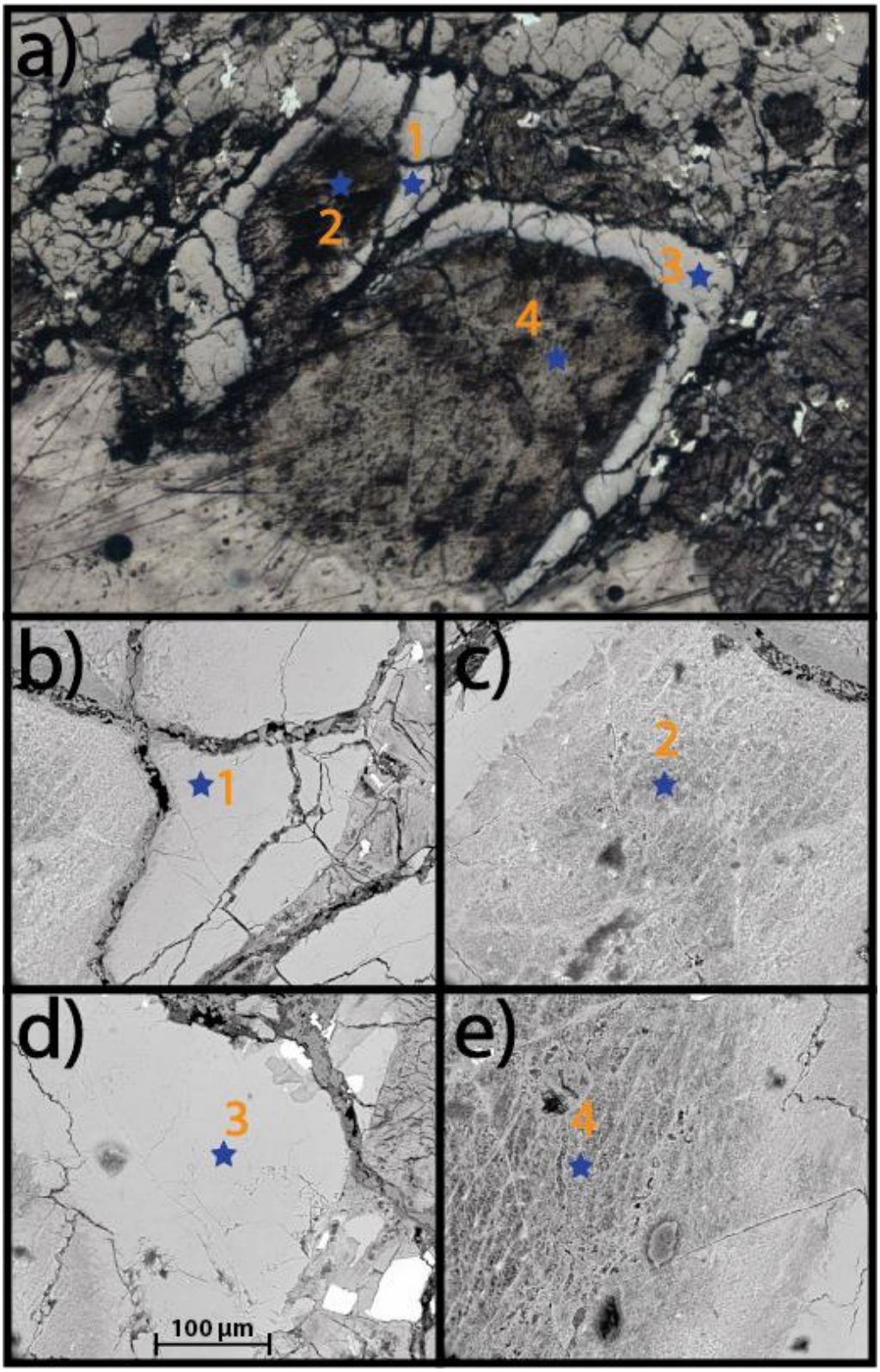

Supplementary Figure 2: BSE images of the core and rim zones of olivine megacrysts from the weathering rind of NWA 4925. The cores of these grains display mottled or mottled-like textures and are Al-, Ca- and Fe-rich and Mg- and Si-poor in comparison to their rims.

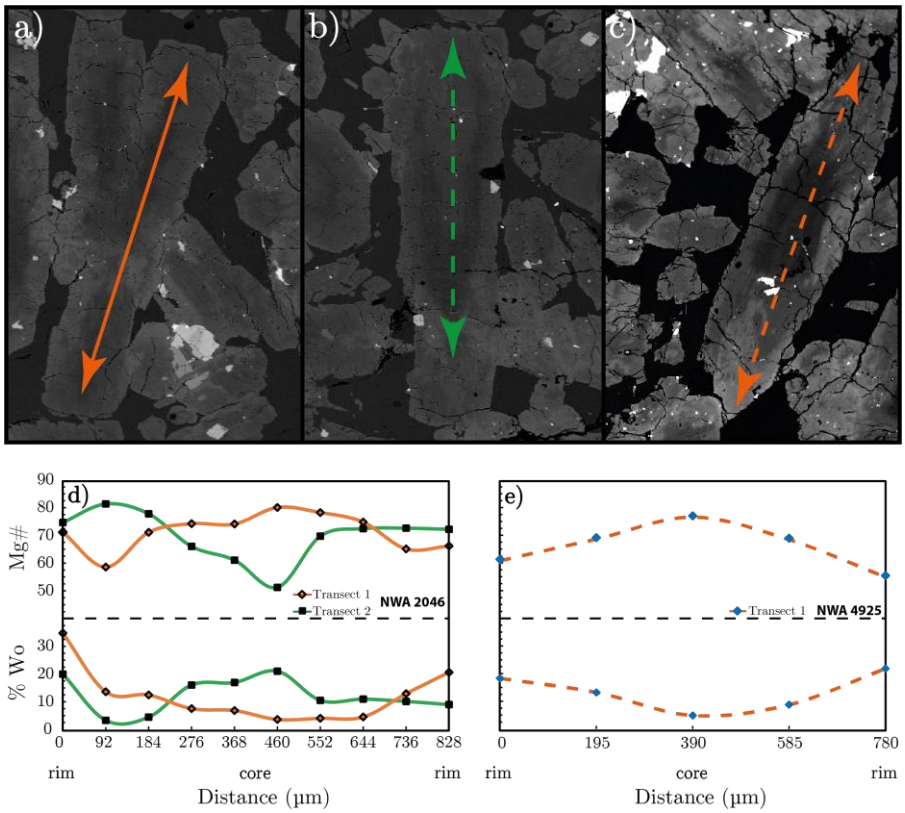

Supplementary Figure 3: Chemical zoning profile across pyroxene phenocrysts (rim to rim) in NWA 2046 (a) and NWA 4925 (b). Transect 1 and 2 of NWA 2046 highlight the type-I and type-II zoning profiles. Transverses are ~830 µm (or > 0.8 mm) in NWA 2046 and 780 µm (or < 0.8 mm) in NWA 4925.

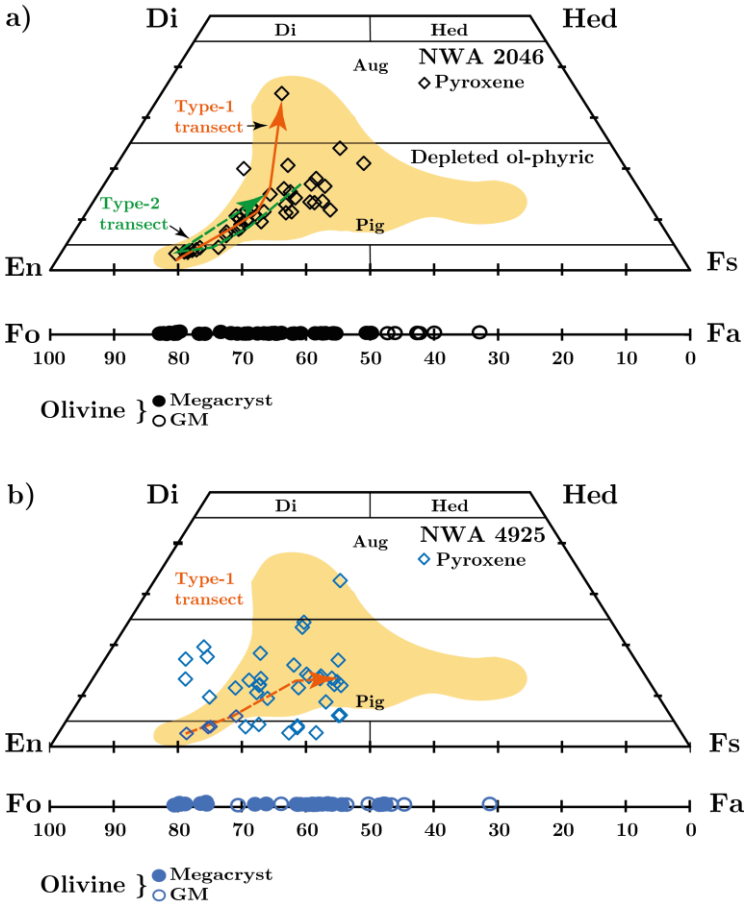

Supplementary Figure 4: Pyroxene quadrilateral and olivine compositions for (a) NWA 2046 and (b) NWA 4925. Solid and dashed, orange and green lines indicate transects for type-I and -II pyroxene phenocrysts from both samples (See Sup Fig. 3). Yellow fields show pyroxene compositional ranges from other depleted olivine-phyric shergottites (Wadhwa et al. 2001; Usui et al., 2008; Gross et al., 2013; Balta et al., 2015; Dunham et al., 2019).

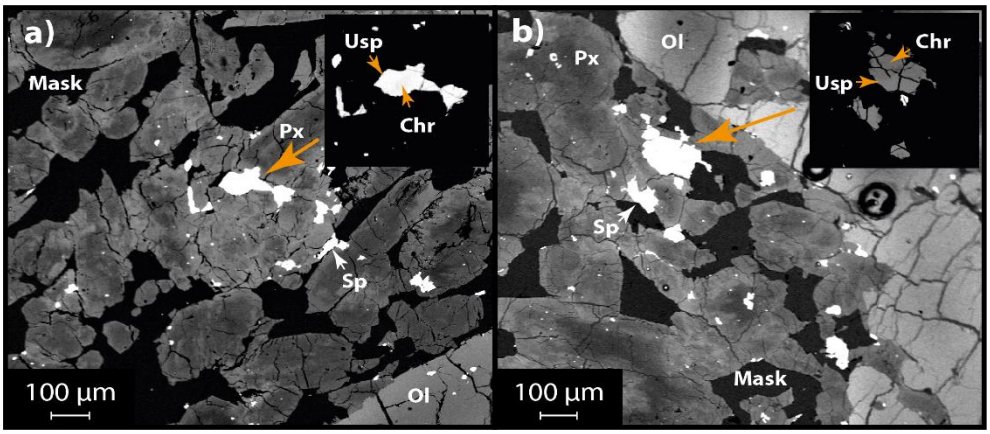

Supplementary Figure 5: BSE images showing intergrowths of chromite (Chr) and ulvöspinel (Usp) in (a) NWA 2046 and (b) NWA 4925.

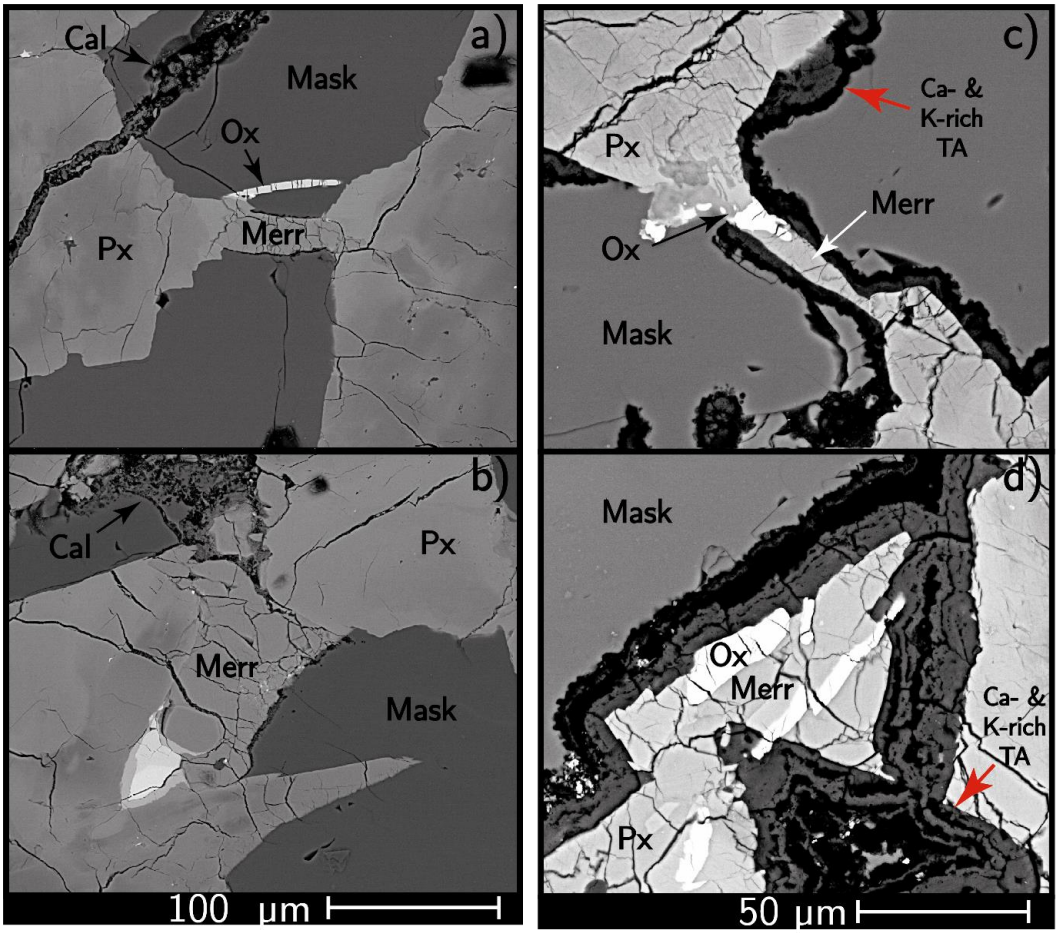

Supplementary Figure 6: BSE images of the merrillite (Merr) grains in NWA 2046 (a, b) and in NWA 4925 (c, d), typically found in association with pyroxene (Px) and maskelynite (Mask). Oxide phases in both samples are indicated as 'ox'. Evidence of calcite veining (Cal) and terrestrial alteration (Ca- & K-rich TA) can also be seen in the images of NWA 2046 and NWA 4925 respectively.

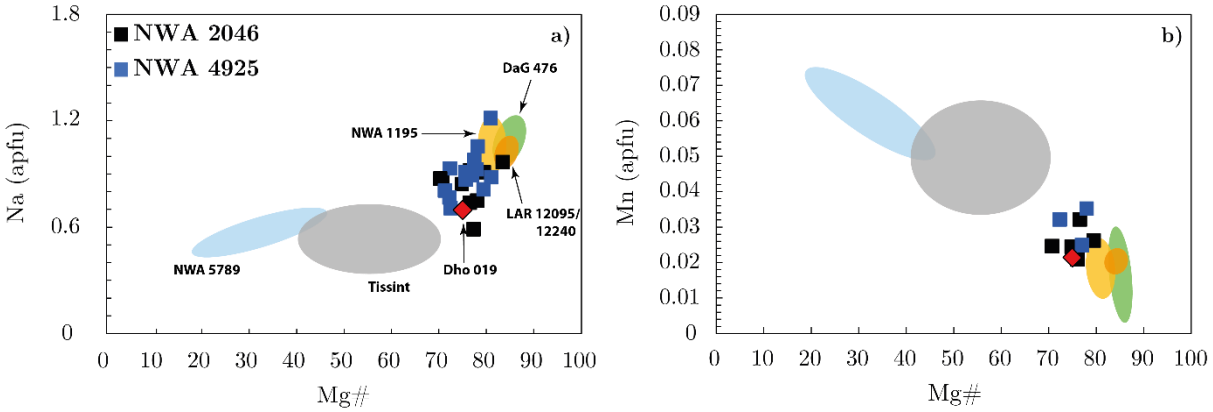

Supplementary Figure 7: Compositional variations of merrillite in NWA 2046 and NWA 4925, in comparison to other depleted olivine-phyric shergottites including DaG 476, NWA 1195, NWA 5789 (Shearer et al., 2015), LAR 12095/12240 (Dunham et al., 2019) and Tissint (Liu et al., 2016). Sodium (Na, a) and Mn (b) are expressed as number of atoms per formula unit (apfu), calculated on a basis of 56 oxygen, as outlined in Shearer et al. (2015).

8 Appendices

SUPPLEMENTARY DATA FOR CHAPTER TWO

Appendix A-1: Mineral major element standards, and LA-ICP-MS standards

Appendix A-2: NWA 2046 and NWA 4925 olivine, pyroxene, maskelynite, merrillite, and oxide major element data.

Appendix A-3: NWA 2046 and NWA 4925 olivine, pyroxene, maskelynite, merrillite, and oxide trace element data.

Appendix A-4: NWA 2046 and NWA 4925 bulk-rock major and trace element data.

Appendix A-5: Sr isotope data for maskelynite and pyroxene grains from NWA 2046 and NWA 4925.

SUPPLEMENTARY DATA FOR CHAPTER THREE

Appendix B-1: LA-ICP-MS trace element composition on standards SCOL1, 1-355OL, SH11-2, MOnGOL, BO2OL01, ALM1, BCR2G, N612, and N610.

Appendix B-2**:** Olivine trace and ultra-trace element data from the martian meteorites analysed in this chapter.

SUPPLEMENTARY DATA FOR CHAPTER FOUR

Appendix C-1: Major element compositions for glass and apatite standards. LA-ICP-MS trace element composition on standards BCR-2G and BHVO-2G.

Appendix C-2: Major and trace element compositions for olivine-hosted MI glasses analysed from the shergottite meteorites.

Appendix C-3: Major and trace element compositions for merrillite grains analysed from the shergottite meteorites.

SUPPLEMENTARY DATA FOR CHAPTER FOUR

Appendix D-1: Chassignite and nakhlite olivine trace element

A-1

Table 1: Mineral major element standards

	SiO_2	TiO_2	Al_2O_3	Cr_2O_3	FeO (tot)	MnO	MgO	CaO	NiO	Na_2O	K_2O	Total
Alma_PH1	37.43	0.03	21.00	-	35.68	0.21	2.40	3.65	0.03	0.01	0.02	100.46
Alma_PH1	37.44	0.09	21.02	0.01	35.39	0.18	2.41	4.00	0.03	-	0.02	100.59
Alma_PH1	37.37	0.06	20.84	0.02	35.67	0.21	2.32	3.72	-	-	0.01	100.21
Alma_PH1	37.39	0.09	20.97	-	35.40	0.22	2.33	3.93	-	0.01	-	100.35
Alma_PH1	37.04	0.07	20.97	-	35.37	0.17	2.35	4.03	0.02	-	0.01	100.02
Alma_PH1	37.35	0.06	20.92	0.01	35.18	0.19	2.32	4.08	0.01	-	0.01	100.13
Alma_PH1	37.14	0.05	20.84	0.01	35.33	0.21	2.36	3.65	-	-	-	99.58
Alma_PH1	37.36	0.06	21.01	-	35.21	0.22	2.33	4.07	0.01	0.01	0.01	100.29
Alma_PH1	37.22	0.07	21.07	0.04	35.60	0.21	2.37	3.69	0.01	-	0.02	100.29
Alma_PH1	37.37	0.07	20.89	0.03	35.16	0.22	2.31	4.13	0.01	0.01	0.01	100.20
Alma_PH1	37.63	0.07	21.03	-	35.42	0.20	2.36	3.77	-	-	-	100.47
Alma_PH1	37.64	0.07	21.15	0.03	35.27	0.22	2.33	4.27	-	-	0.01	100.99
Alma_PH1	37.67	0.07	21.23	0.01	35.98	0.20	2.45	3.63	0.02	0.01	0.02	101.27
Alma_PH1	37.53	0.05	21.11	-	35.91	0.21	2.37	3.96	-	-	0.02	101.15
CrO_PH1	0.05	-	0.02	99.49	0.01	0.03	-	-	0.03	-	0.02	99.64
CrO_PH1	0.04	0.02	0.01	99.72	0.02	-	-	-	-	0.01	-	99.81
CrO_PH1	0.01	0.01	0.01	99.65	0.03	0.03	0.01	-	0.01	0.02	0.01	99.80
CrO_PH1	0.03	-	0.01	100.05	0.03	0.18	-	-	-	-	0.01	100.31
CrO_PH1	0.04	-	0.01	100.27	0.01	0.18	-	-	-	-	-	100.52

CrO_PH1	0.02	0.01	0.01	100.03	-	0.23	0.01	-	-	-	-	100.32
CrO_PH1	0.04	-	0.01	100.15	-	0.21	0.01	0.01	-	-	-	100.44
CrO_PH1	0.04	-	0.02	100.00	0.01	0.01	0.01	-	0.02	-	-	100.10
CrO_PH1	0.03	0.01	0.01	99.91	0.01	0.03	-	0.03	0.01	-	-	100.04
Diop_PH1	55.16	0.05	0.04	0.01	0.80	0.08	18.10	25.92	-	-	0.04	100.21
Diop_PH1	55.33	0.05	0.03	-	0.80	0.08	18.20	26.11	0.01	-	0.04	100.65
Diop_PH1	55.24	0.04	0.03	-	0.81	0.07	18.22	26.14	-	-	0.05	100.59
Diop_PH1	55.07	0.06	0.04	-	0.85	0.09	18.25	25.73	0.02	-	0.06	100.16
Diop_PH1	55.11	0.05	0.03	0.01	0.84	0.10	18.26	25.95	-	-	0.05	100.39
Diop_PH1	55.01	0.04	0.05	-	0.83	0.08	18.14	25.78	-	-	0.04	99.98
Diop_PH1	55.01	0.04	0.04	-	0.81	0.09	18.12	25.93	-	0.01	0.06	100.10
Diop_PH1	54.75	0.04	0.04	0.01	0.81	0.10	18.07	25.93	-	-	0.07	99.83
Diop_PH1	54.89	0.06	0.04	0.01	0.83	0.07	18.12	25.94	0.01	-	0.06	100.03
Diop_PH1	54.79	0.06	0.04	-	0.84	0.09	18.14	25.82	-	-	0.05	99.82
Diop_PH1	55.41	0.06	0.03	-	0.81	0.10	18.14	25.76	0.01	-	0.05	100.36
Diop_PH1	55.52	0.07	0.04	-	0.83	0.10	18.17	25.83	0.01	-	0.06	100.64
Diop_PH1	55.59	0.03	0.05	0.01	0.82	0.09	18.21	25.67	0.01	-	0.07	100.55
Diop_PH1	55.59	0.02	0.04	-	0.85	0.08	18.10	25.86	-	-	0.06	100.58
Hema_PH1	0.03	0.02	-	-		-	0.01	0.01	-	-	-	99.45
Hema_PH1	0.04	0.01	-	-		0.01	-	-	-	-	0.02	99.61
Hema_PH1	0.03	0.01	0.01	-		0.02	-	0.01	-	0.01	-	100.44
Hema_PH1	0.03	-	0.01	-		-	0.01	-	-	-	0.02	100.30
TiO_PH1	0.03	99.73	-	0.02	0.01	-	-	0.01	-	-	-	99.80

TiO_PH1	0.03	100.08	-	-	0.01	0.01	0.01	-	-	-	-	100.15
TiO_PH1	0.06	99.94	-	0.01	-	-	0.01	0.01	0.01	-	0.01	100.05
TiO_PH1	0.05	99.76	-	0.02	-	0.01	-	-	0.02	0.01	0.01	99.86
TiO_PH1	0.07	99.27	0.01	-	-	-	0.01	-	-	0.01	-	99.36
TiO_PH1	0.04	99.74	-	-	-	0.01	-	0.01	0.02	-	-	99.81
TiO_PH1	0.02	99.83	0.01	-	-	-	-	-	-	-	0.01	99.87
TiO_PH1	0.05	99.60	-	-	-	0.02	0.01	-	-	-	-	99.67

*Oxide detection limit of 0.01 wt. %

Table 2: Trace element standards

	BCR-2G certified	BCR-2G 11um - 1	BCR-2G 11um - 2	BCR-2G 11um - 3	BCR-2G 11um - 4	BCR-2G 11um - 5	BHVO-2G certified	BHVO-2G 11um - 1	BHVO-2G 11um - 2	BHVO-2G 11um - 3	BHVO-2G 11um - 4
^{7}Li		557987	603385	515225	603969	689152		650644	653353	649381	643005
^{23}Na		147.55	bdl	bdl	bdl	81.76		bdl	bdl	bdl	bdl
^{24}Mg	23962	26051	27559	23876	26588	32095	17804	22833	21972	22210	22222
^{27}Al	21470	17838	22002	18163	20654	20019	42999	45779	44122	43676	43298
^{29}Si	70916	66317	69293	59617	68310	73457	71975	74089	72910	71398	71199
^{43}Ca	254301	307616	314959	273232	329666	404141	230460	320350	327523	323788	317474
^{45}Sc	50457	50457	50457	50457	50457	50457	81475	81475	81475	81475	81475
^{49}Ti	33	28.91	37.65	29.84	32.68	32.40	33	34.75	32.63	33.42	31.26
^{51}V	13605	12636	14812	12412	17277	14466	16300	16270	16082	15884	16609
^{53}Cr	425	420.61	482.55	459.07	485.79	504.17	308	366.81	357.99	345.12	361.35
^{55}Mn	17	17.92	26.76	8.75	18.86	26.71	293	351.42	355.91	344.71	334.51

^{57}Fe	1550	1554	1711	1455	1654	1839	1307	1612	1552	1572	1523
^{59}Co	97222	72995	100084	73838	86730	90112	87836	85993	85547	87251	87041
^{60}Ni	38	42.32	60.52	44.97	46.92	52.23	44	62.76	61.14	62.09	58.57
^{63}Cu	13	58.93	26.16	12.28	18.78	35.14	116	180.51	173.61	172.53	175.95
^{66}Zn	21	44.12	77.49	23.20	38.76	27.82	127	190.46	170.93	170.23	168.84
^{85}Rb	125	267.59	251.46	228.94	430.75	192.64	102	168.33	164.81	154.58	159.71
^{88}Sr	47	57.90	57.09	57.73	57.35	78.76	9.2	14.00	13.33	11.37	12.55
^{89}Y	342	322.33	337.38	294.59	384.02	377.77	396	411.31	385.82	387.95	397.80
^{90}Zr	35	31.75	33.58	30.65	32.67	31.81	26	22.99	22.09	23.38	22.51
^{93}Nb	184	163.67	174.44	183.85	166.18	192.56	170	168.79	162.49	155.58	159.11
^{137}Ba	12.5	17.45	17.01	17.83	12.31	14.54	18.3	18.10	18.21	17.27	18.47
^{139}La	683	665.90	728.29	574.69	656.28	689.12	131	134.37	135.02	133.34	152.86
^{140}Ce	24.7	24.29	24.33	23.08	25.88	35.09	15.2	15.29	14.55	14.40	15.66
^{141}Pr	53.3	55.89	54.25	59.60	74.84	57.82	37.6	38.34	38.08	36.54	36.99
^{146}Nd	6.7	8.83	6.89	6.67	9.60	28.69	5.35	5.40	4.95	5.25	5.20
^{147}Sm	28.9	30.90	29.81	23.19	25.96	27.98	24.5	23.86	23.32	25.11	19.38
^{153}Eu	6.59	11.38	7.03	6.98	6.37	7.40	6.1	5.98	5.62	6.30	5.93
^{157}Gd	1.97	4.80	6.46	3.07	12.34	3.00	2.07	2.01	1.65	2.34	2.43
^{159}Tb	6.71	13.02	7.69	7.76	10.80	7.07	6.16	6.30	6.18	6.43	4.58
^{163}Dy	1.02	2.89	1.60	1.39	2.24	1.81	0.92	0.71	0.78	0.91	0.85
^{165}Ho	6.44	10.27	7.32	7.06	7.08	7.60	5.28	4.49	5.22	4.64	4.87
^{166}Er	1.27	7.74	2.43	12.15	1.71	2.08	0.98	1.05	0.86	1.00	0.83
^{169}Tm	3.7	4.09	3.14	3.83	9.94	5.03	2.56	3.07	2.16	2.19	3.27

^{172}Yb	0.51	2.29	3.48	6.17	1.05	2.95	0.34	0.35	0.28	0.32	0.22
^{175}Lu	3.39	5.11	9.86	7.18	4.05	4.56	2.01	2.26	1.81	2.11	2.20
^{178}Hf	0.50	2.16	0.75	4.42	1.41	0.75	0.28	0.20	0.19	0.22	0.34
^{181}Ta	4.84	8.99	7.11	7.71	4.59	6.48	4.32	4.38	4.75	3.69	4.39
^{208}Pb	11	28.43	14.39	14.12	25.40	16.81	1.70	2.73	3.17	1.98	1.10
^{232}Th	5.9	9.84	7.59	7.47	10.41	8.02	1.22	1.48	1.09	1.08	1.27
^{238}U	1.69	4.32	3.36	6.60	16.96	3.53	0.40	0.41	0.48	0.42	0.48

*Trace element detection limit of 0.01 ppm

A-2

Table 1: NWA 2046 and NWA 4925 olivine megacryst and groundmass major element data

	SiO_2	TiO_2	Al_2O_3	Cr_2O_3	FeO (tot)	MnO	MgO	CaO	NiO	Na_2O	K_2O	Total	**Distance**
NWA 2046 megacrysts (> 500µm)													
Ol 1, 1	35.93	-	0.23	0.12	22.97	0.42	35.32	0.40	0.09	-	-	95.50	0
Ol 1, 2	38.69	0.01	0.04	0.16	17.09	0.36	42.73	0.14	0.12	0.01	0.02	99.37	112
Ol 1, 3	38.69	-	0.04	0.10	16.41	0.38	43.39	0.21	0.11	0.01	-	99.34	224
Ol 1, 4	38.68	-	0.13	0.11	17.12	0.34	41.70	0.30	0.08	0.01	-	98.47	336
Ol 1, 5	38.05	-	0.17	0.14	18.09	0.38	41.66	0.21	0.08	-	0.01	98.80	448
Ol 1, 6	38.32	0.01	0.05	0.08	18.30	0.39	41.50	0.18	0.09	0.01	-	98.93	560
Ol 1, 7	38.15	-	0.12	0.11	17.75	0.39	41.50	0.26	0.08	0.01	-	98.36	672
Ol 1, 8	37.51	0.01	0.29	0.12	18.00	0.35	39.79	0.46	0.08	0.01	0.01	96.62	784
Ol 1, 9	37.53	-	0.30	0.09	17.73	0.37	40.37	0.40	0.08	0.01	0.02	96.91	896

Ol 1, 10	36.79	0.01	0.02	0.10	27.63	0.46	34.24	0.19	0.04	0.01	-	99.50	1008
Ol 2, 1	37.11	-	0.02	0.23	27.21	0.52	34.57	0.18	0.10	0.01	-	99.95	
Ol 2, 2	36.52	0.03	0.01	0.34	29.35	0.55	32.55	0.22	0.05	0.01	-	99.63	
Ol 3, 1	34.67	0.01	-	0.04	37.60	0.69	26.29	0.22	0.04	0.01	-	99.57	
Ol 3, 2	36.37	0.01	0.02	0.08	32.97	0.59	30.07	0.17	0.04	0.01	-	100.33	
Ol 3, 3	35.11	0.02	0.01	0.05	36.43	0.68	27.29	0.19	0.02	0.02	-	99.82	
Ol 4, 1	36.42	0.02	0.03	0.10	27.81	0.50	34.62	0.19	0.06	0.01	-	99.76	
Ol 4, 2	36.17	-	0.01	0.06	30.67	0.58	32.11	0.25	0.05	0.02	-	99.94	
Ol 4, 3	37.05	0.02	0.02	0.07	25.63	0.50	36.25	0.23	0.08	0.01	-	99.85	
Ol 5 - 1	35.63	0.02	0.05	0.05	30.83	0.62	31.75	0.27	0.06	0.01	-	99.29	
Ol 5 - 2	35.77	0.01	0.03	0.05	31.63	0.61	31.10	0.26	0.03	0.01	-	99.51	
Ol 5 - 3	36.30	0.02	0.02	0.09	28.77	0.52	33.43	0.20	0.05	-	0.01	99.41	
Ol 5 - 4	33.98	0.01	0.02	0.01	41.02	0.73	23.28	0.25	0.01	-	0.01	99.32	
Ol 5 - 5	34.70	0.03	0.01	0.05	36.68	0.62	27.01	0.23	0.05	0.01	-	99.38	
Ol 5 - 6	33.55	0.02	-	0.05	41.50	0.76	22.89	0.25	0.03	0.01	-	99.04	
Ol 6, 1	35.78	0.03	0.02	0.08	37.82	0.65	26.09	0.19	0.01	-	-	100.66	
Ol 6, 2	36.27	-	0.02	0.08	33.97	0.63	29.38	0.22	0.02	0.01	-	100.61	
Ol 6, 3	36.36	0.06	0.02	0.12	30.23	0.51	32.56	0.17	0.05	0.01	-	100.10	
Ol 7, 1	35.81	-	0.03	0.08	30.96	0.54	31.53	0.18	0.06	0.02	-	99.21	0
Ol 7, 2	38.03	-	0.04	0.07	22.21	0.43	38.77	0.16	0.07	0.02	-	99.80	112
Ol 7, 3	38.33	-	0.04	0.11	18.28	0.37	41.80	0.28	0.11	0.02	-	99.33	224
Ol 7, 4	38.45	0.02	0.07	0.12	17.02	0.35	43.09	0.18	0.11	0.02	0.02	99.43	336
Ol 7, 5	38.67	0.02	0.06	0.07	16.71	0.36	42.97	0.20	0.11	0.02	0.01	99.20	448

Ol 7, 6	38.79	0.01	0.03	0.11	16.17	0.34	43.63	0.19	0.06	-	-	99.34	560
Ol 7, 7	38.71	0.02	0.13	0.13	16.18	0.34	43.14	0.22	0.09	0.03	-	98.98	672
Ol 7, 8	38.58	-	0.06	0.12	16.49	0.35	42.76	0.24	0.09	0.04	-	98.74	784
Ol 7, 9	38.52	-	0.07	0.15	18.09	0.35	41.92	0.17	0.08	0.01	-	99.37	896
Ol 7, 10	37.94	0.01	0.01	0.10	21.51	0.42	39.34	0.16	0.09	0.01	-	99.60	1008
Ol 7, 11	36.83	-	0.03	0.05	26.15	0.49	35.21	0.18	0.07	0.01	0.01	99.04	1120
Ol 8, 1	34.67	0.02	0.01	0.24	37.37	0.65	26.28	0.21	0.04	0.01	-	99.50	
Ol 8, 2	35.60	0.03	0.01	0.43	33.14	0.57	29.88	0.18	0.10	-	-	99.94	
Ol 8, 3	35.14	0.03	0.02	0.09	35.57	0.63	27.95	0.20	0.05	-	-	99.67	
Ol 8, 4	34.88	-	0.02	0.27	36.14	0.60	27.35	0.22	0.05	0.04	0.01	99.58	
Ol 8, 5	34.75	0.01	0.03	0.24	36.47	0.63	26.87	0.22	0.02	0.02	-	99.28	
Ol 9, 1	36.14	-	0.02	0.07	31.09	0.54	31.66	0.16	0.03	0.03	-	99.74	
Ol 9, 2	35.85	-	0.02	0.08	31.17	0.50	31.55	0.17	0.06	-	-	99.41	
Ol 9, 3	34.29	0.01	0.02	0.06	37.60	0.67	26.38	0.21	0.06	0.03	-	99.32	
NWA 2046 – groundmass olivine (< 500µm)													
Ol 1	33.11	0.11	0.01	0.02	47.49	0.84	17.49	0.27	0.06	0.01	-	99.42	Ol 1
Ol 2	33.71	0.04	0.02	0.02	43.61	0.79	20.68	0.23	0.02	-	-	99.12	Ol 2
Ol 3	33.48	0.02	0.02	0.05	45.69	0.80	18.79	0.25	0.01	0.01	0.01	99.12	Ol 3
Ol 4	34.21	0.03	0.02	0.04	42.93	0.71	21.33	0.21	0.04	0.02	-	99.53	Ol 4
Ol 5	36.09	0.01	-	0.06	33.54	0.60	29.01	0.22	0.03	0.01	-	99.57	Ol 5
Ol 6	34.56	0.02	-	0.05	41.18	0.74	22.94	0.25	0.03	0.01	-	99.79	Ol 6
Ol 7	36.66	0.01	0.02	0.04	29.81	0.58	32.07	0.17	0.03	0.01	-	99.40	Ol 7

Ol 8	36.80	0.02	0.01	0.08	29.75	0.57	31.77	0.13	0.04	0.01	0.02	99.19	Ol 8
Ol 9	33.57	0.04	0.01	0.03	45.39	0.82	18.70	0.21	0.04	-	-	98.79	Ol 9
Ol 10	33.39	0.10	-	0.02	45.83	0.79	18.56	0.22	0.05	0.02	0.01	98.98	Ol 10
Ol 11	32.36	0.11	0.03	0.02	51.38	0.87	13.87	0.30	0.05	0.01	-	98.99	Ol 11
NWA 2046 – weathering rind olivine													
Ol 1, c	39.09	-	-	-	25.89	0.60	34.17	0.26				100.01	
Ol 1, r	37.18	-	-	-	34.40	0.76	27.43	0.23				100.00	
Ol 2, c	40.64	-	-	0.31	17.01	-	41.82	0.22				100.00	
Ol 2, r	38.31	-	-	0.48	31.39	0.63	28.99	0.21				100.01	
Ol 3, c	38.69	-	-	-	26.64	0.40	33.98	0.29				100.00	
Ol 3, r	37.03	-	-	0.45	36.43	0.61	25.29	0.20				100.01	
NWA 4925													
Ol 1, 1	36.40	-	0.06	0.07	33.90	0.57	28.48	0.25	0.05	0.02	0.01	99.81	
Ol 1, 2	35.96	0.02	0.31	0.08	35.40	0.67	25.93	0.31	0.04	0.03	0.04	98.79	
Ol 1, 3	35.32	0.02	0.01	0.04	38.01	0.68	25.40	0.24	0.01	0.01	-	99.74	
Ol 2, 1	36.08	-	0.04	0.11	34.58	0.61	27.93	0.28	0.03	-	0.01	99.67	
Ol 2, 2	36.23	-	0.04	0.10	35.08	0.59	27.65	0.27	0.02	-	-	99.98	
Ol 3, 1	34.49	0.04	0.01	0.03	42.33	0.75	21.49	0.28	0.02	-	-	99.44	
Ol 3, 2	35.15	0.02	0.05	0.02	41.74	0.74	21.39	0.31	0.01	-	-	99.43	
Ol 4, 1	37.58	0.02	0.04	0.05	34.26	0.61	26.86	0.23	0.02	0.03	0.01	99.71	0
Ol 4, 2	38.54	-	0.27	0.10	21.64	0.46	37.54	0.30	0.07	0.02	0.03	98.97	380

Ol 4, 3	37.48	0.02	0.14	0.12	19.98	0.44	42.08	0.35	0.09	0.02	0.04	100.76	760
Ol 4, 4	37.73	0.01	0.18	0.12	18.91	0.38	41.76	0.29	0.07	0.02	0.20	99.68	1140
Ol 4, 5	37.92	0.01	0.05	0.06	27.13	0.50	32.33	0.28	0.02	0.01	0.01	98.32	1520
Ol 5, 1	37.50	0.02	0.02	0.06	35.65	0.63	25.99	0.28	0.03	0.02	-	100.20	0
Ol 5, 2	37.30	0.02	0.29	0.08	21.20	0.42	38.80	0.39	0.07	0.01	0.03	98.61	380
Ol 5, 3	38.26	0.02	0.30	0.09	18.56	0.41	41.44	0.44	0.09	0.02	0.04	99.67	760
Ol 5, 4	37.54	0.01	0.37	0.07	21.77	0.48	38.23	0.58	0.12	0.02	0.02	99.21	1140
Ol 5, 5	37.40	-	0.04	0.07	29.02	0.52	31.96	0.32	0.06	0.01	0.01	99.41	1520
Ol 6, 1	35.57	0.01	0.03	0.05	33.94	0.59	27.17	0.21	0.02	0.01	-	97.60	
Ol 6, 2	35.28	0.02	0.02	0.07	34.82	0.63	26.38	0.27	0.02	0.01	-	97.52	
Ol 6, 3	35.79	0.05	0.01	0.07	33.54	0.60	27.05	0.31	0.02	0.02	-	97.46	
Ol 6, 4	36.52	-	0.05	0.07	33.10	0.61	29.43	0.25	0.04	0.01	-	100.08	
Ol 6, 5	35.89	-	0.18	0.58	36.07	0.60	26.38	0.37	0.03	0.01	-	100.11	
Ol 9, 1	34.96	0.02	-	0.06	35.97	0.66	25.59	0.25	0.02	0.01	0.01	97.55	
Ol 9, 2	35.69	0.01	0.03	0.08	33.50	0.57	27.62	0.24	0.04	0.02	-	97.80	
Ol 9, 3	34.98	0.01	-	0.05	35.97	0.68	25.50	0.28	0.03	0.01	-	97.51	
NWA 4925 – weathering rind													
Ol 1	32.48	0.07	0.01	0.04	51.86	0.91	13.14	0.28	0.02	0.02	-	98.84	
Ol 2	34.13	0.03	0.02	0.02	42.61	0.75	20.84	0.23	0.03	0.01	0.01	98.67	
Ol 3	35.91	0.04	0.09	0.06	35.06	0.67	27.09	0.32	-	0.01	0.01	99.27	
Ol 4	36.64	0.03	0.07	0.08	30.63	0.61	30.39	0.32	0.05	0.01	0.02	98.84	
Ol 5	35.71	0.06	0.04	0.04	38.48	0.70	24.93	0.23	0.02	0.01	-	100.21	

Ol 6	37.89	-	0.05	0.07	25.98	0.52	35.01	0.16	0.04	0.01	-	99.74	
Ol 7	34.44	0.05	0.01	0.04	44.93	0.78	20.25	0.24	0.03	0.01	-	100.77	
Ol 8, 1	34.84	0.10	0.01	-	41.83	0.76	22.06	0.21	0.05	0.01	0.01	99.88	
Ol 8, 2	34.78	0.17	0.02	0.08	42.07	0.73	21.77	0.23	0.01	0.01	0.01	99.88	
Ol 9	35.39	0.02	0.08	0.04	40.79	0.72	23.03	0.31	0.01	-	-	100.39	
Ol 10, 1	36.00	0.01	0.02	0.14	34.73	0.57	27.98	0.23	0.05	0.02	-	99.75	
Ol 10, 2	35.60	-	0.11	0.12	31.68	0.54	28.33	0.28	0.03	0.02	0.01	96.72	
Ol 10, 3	35.72	0.01	0.03	0.15	32.38	0.58	28.23	0.26	0.04	0.02	0.01	97.43	
NWA 4925 – weathering rind olivine													
Ol 1, c	20.88	-	5.88	0.54	58.10	2.01	2.33	9.76			0.49	99.99	
Ol 1, r	38.11	-	0.72	-	35.21	0.79	24.39	0.78			-	100.00	
Ol 2, c	37.80	-	0.39	-	34.31	0.72	26.41	0.36			-	99.99	
Ol 2, r	39.36	-	0.49	-	28.66	0.63	30.33	0.53			-	100.00	
Ol 3, c	29.85	-	10.03	0.78	52.85	-	1.88	4.11			0.51	100.01	
Ol 3, r	30.65	-	11.18	0.94	52.13	-	1.82	2.87			0.41	100.00	
Ol 4, c	29.86	-	11.40	0.71	52.25	0.60	1.59	3.18			0.41	100.00	
Ol 4, r	39.37	-	-	-	33.09	0.59	26.42	0.52			-	99.99	

* Oxide detection limit of 0.01 wt. %

Table 2: NWA 2046 and NWA 4925 pyroxene major element data

	SiO_2	TiO_2	Al_2O_3	Cr_2O_3	FeO (tot)	MnO	MgO	CaO	NiO	Na_2O	K_2O	Total	**Distance**
NWA 2046													
Px 1, 1	53.07	0.10	0.76	0.46	16.07	0.54	22.95	5.84	0.03	0.07	0.01	99.90	
Px 1, 2	54.36	0.05	0.46	0.50	13.44	0.42	28.24	2.01	0.01	0.05	-	99.54	
Px 1, 3	51.67	0.21	1.90	0.68	13.03	0.46	21.55	10.03	-	0.14	0.04	99.71	0.00
Px 1, 4	54.58	0.05	0.40	0.60	11.91	0.38	29.19	1.70	0.01	0.04	-	98.86	92.00
Px 1, 5	54.37	0.05	0.49	0.52	14.04	0.44	27.62	2.30	-	0.03	0.01	99.87	184.00
Px 1, 6	51.80	0.19	0.80	0.41	18.78	0.63	20.49	8.24	0.03	0.07	0.01	101.45	276.00
Px 1, 7	51.06	0.32	0.97	0.48	20.94	0.63	18.43	8.58	0.02	0.07	0.01	101.51	368.00
Px 1, 8	49.90	0.57	0.76	0.26	24.68	0.73	14.55	10.52	-	0.09	-	102.06	460.00
Px 1, 9	52.79	0.09	0.68	0.38	17.80	0.59	23.00	5.38	-	0.05	-	100.76	552.00
Px 1, 10	52.73	0.09	0.68	0.54	16.20	0.58	23.90	5.64	0.01	0.08	-	100.45	644.00
Px 1, 11	51.65	0.10	0.80	0.43	16.45	0.55	24.47	5.27	0.01	0.08	0.02	99.83	736.00
Px 1, 12	53.26	0.11	0.70	0.48	16.61	0.56	24.21	4.61	-	0.05	-	100.59	828.00
Px 2, 1	52.07	0.15	0.64	0.33	19.68	0.63	20.35	5.57	-	0.06	-	99.48	
Px 2, 2	51.38	0.21	1.25	0.58	18.80	0.63	19.34	7.58	0.04	0.06	0.01	99.88	
Px 2, 3	51.57	0.23	1.12	0.52	19.57	0.60	19.20	6.97	-	0.08	0.01	99.87	
Px 3, 1	52.82	0.11	0.80	0.51	16.60	0.59	23.24	4.92	0.02	0.07	-	99.68	
Px 3, 2	50.67	0.38	0.93	0.40	23.35	0.64	17.41	5.71	-	0.07	-	99.56	
Px 3, 3	48.57	0.34	0.99	0.40	22.11	0.68	17.45	8.22	0.01	0.06	-	98.83	
Px 4, 1	51.24	0.25	1.72	0.84	13.02	0.51	18.01	18.77	0.02	0.13	-	102.81	0.00

Px 4, 2	50.40	0.40	2.37	0.21	22.60	0.61	17.93	6.71	-	0.09	0.01	101.33	92.00
Px 4, 3	52.27	0.13	0.96	0.49	16.20	0.54	22.38	6.22	0.01	0.06	0.01	99.27	184.00
Px 4, 4	53.56	0.09	0.63	0.52	15.66	0.52	25.33	3.86	0.07	0.05	0.01	100.30	276.00
Px 4, 5	53.83	0.03	0.54	0.47	15.88	0.52	25.53	3.51	0.02	0.04	-	100.37	368.00
Px 4, 6	54.48	0.07	0.49	0.72	12.74	0.41	28.76	1.87	-	0.04	-	99.58	460.00
Px 4, 7	54.53	0.04	0.48	0.59	13.78	0.44	27.83	2.07	0.05	0.04	0.01	99.86	552.00
Px 4, 8	53.95	0.06	0.50	0.48	15.68	0.46	26.13	2.29	-	0.08	-	99.63	644.00
Px 4, 9	51.95	0.30	0.79	0.44	19.72	0.61	20.67	6.54	0.01	0.07	0.01	101.11	736.00
Px 4, 10	51.26	0.21	1.30	0.57	17.67	0.56	19.40	10.61	0.01	0.10	0.01	101.70	828.00
Px 5, 1	52.72	0.10	0.70	0.66	15.36	0.57	23.80	5.39	0.04	0.04	-	99.38	
Px 5, 2	52.89	0.08	0.59	0.47	16.53	0.59	24.27	4.10	0.02	0.06	-	99.60	
Px 5, 3	52.03	0.14	0.89	0.44	17.62	0.57	21.72	5.73	-	0.06	-	99.20	
Px 6, 1	53.09	0.14	1.01	0.56	16.51	0.58	22.42	6.00	-	0.07	-	100.38	
Px 6, 2	53.06	0.13	0.80	0.62	16.63	0.58	23.22	4.99	-	0.06	0.01	100.10	
Px 6, 3	51.77	0.24	1.13	0.52	19.97	0.63	19.79	5.61	-	0.07	-	99.73	
Px 7, 1	50.45	0.32	1.16	0.73	20.15	0.62	17.16	8.73	-	0.11	-	99.43	
Px 7, 2	50.86	0.27	0.99	0.70	21.41	0.64	18.03	6.41	0.03	0.08	0.04	99.46	
Px 7, 3	49.75	0.61	1.16	1.05	20.42	0.59	14.68	11.47	0.01	0.13	-	99.87	
Px 7, 4	52.37	0.15	0.94	1.03	17.93	0.50	22.19	4.74	0.01	0.06	0.01	99.93	
Px 7, 5	50.77	0.29	1.09	0.69	21.03	0.68	18.34	6.51	0.02	0.06	0.01	99.49	
Px 9, 1	51.77	0.17	1.32	0.63	17.09	0.61	20.70	7.41	0.02	0.08	0.01	99.81	
Px 9, 2	53.13	0.08	0.67	0.48	16.40	0.58	23.75	4.18	0.02	0.06	-	99.35	
Px 9, 3	52.85	0.12	0.71	0.50	16.28	0.54	23.69	4.22	-	0.06	-	98.97	

Px 10, 1	52.54	0.15	0.95	0.53	17.84	0.57	21.04	5.37	-	0.06	-	99.04	
Px 10, 2	53.90	0.10	0.91	0.54	15.25	0.52	25.07	3.15	0.01	0.05	0.01	99.51	
Px 10, 3	54.24	0.06	0.56	0.46	15.31	0.52	25.47	2.83	0.01	0.06	0.01	99.51	
Px 10, 4	54.83	0.06	0.62	0.72	13.76	0.44	27.61	1.41	0.02	0.03	-	99.48	
Px 10, 5	51.30	0.45	0.83	0.36	22.34	0.70	17.80	5.58	0.01	0.08	-	99.44	
Px 11, 1	55.32	0.02	0.42	0.58	12.50	0.40	28.70	1.27	0.01	0.03	-	99.27	
Px 11, 2	55.43	0.04	0.46	0.69	12.08	0.42	28.99	1.22	0.04	0.03	-	99.40	
Px 11, 3	54.22	0.10	0.80	0.61	14.08	0.49	24.95	3.93	0.04	0.06	-	99.29	
Px 11, 4	53.21	0.12	0.69	0.42	17.95	0.57	22.19	4.06	-	0.05	-	99.27	
Px 11, 5	53.22	0.10	0.79	0.48	16.15	0.54	21.93	5.61	0.01	0.08	0.01	98.90	
Px 12, 1	55.72	0.05	0.41	0.55	12.51	0.43	28.76	1.27	0.03	0.02	-	99.75	
NWA 2046 – weathering rind													
Px 1	53.33	0.27	1.87	0.73	17.74	0.48	21.83	3.74			-	99.99	
Px 2	54.00		1.29	0.56	17.61	0.69	18.82	7.02			-	99.99	
Px 3	55.99		0.37	0.55	14.50	0.59	24.92	3.09			-	100.01	
Px 4	53.64	0.55	1.64	-	21.19	0.59	16.46	5.92			-	99.99	
Px 5	56.26		0.88	0.54	13.88	0.47	24.72	3.24			-	99.99	
Px 6	56.62		0.87	0.61	13.45	0.57	25.68	2.20			-	100.00	
Px 7	55.02		1.13	0.39	17.30	0.55	20.31	5.31			-	100.01	
Px 8	56.01		0.75	0.46	13.99	0.54	24.93	3.31			-	99.99	
NWA 4925													

Px 1, 1	51.52	0.28	1.08	0.44	21.16	0.63	18.80	5.86	-	0.09	0.03	99.88	0.00
Px 1, 2	53.21	0.14	1.04	0.50	17.41	0.57	21.86	4.62	-	0.13	0.23	99.70	195.00
Px 1, 3	53.63	0.10	1.20	0.95	13.88	0.45	26.10	1.85	0.02	0.04	0.04	98.26	390.00
Px 1, 4	52.48	0.15	1.41	0.40	18.24	0.58	22.68	3.03	0.02	0.04	0.04	99.07	585.00
Px 1, 5	50.31	0.39	1.12	0.42	23.36	0.68	16.29	6.32	0.01	0.08	0.01	99.00	780.00
Px 2, 1	52.69	0.18	1.62	0.79	13.49	0.51	18.53	11.17	-	0.11	0.04	99.13	
Px 2, 2	53.29	0.16	1.54	0.83	14.44	0.49	19.77	7.98	-	0.08	0.03	98.61	
Px 2, 3	52.20	0.23	1.37	0.62	19.51	0.59	18.59	5.63	0.01	0.08	0.02	98.85	
Px 3, 1	51.01	0.42	1.02	0.45	22.93	0.63	16.00	6.44	-	0.09	0.01	99.00	
Px 3, 2	52.58	0.29	0.95	0.44	21.26	0.64	17.17	6.11	0.02	0.08	0.01	99.54	
Px 3, 3	50.62	0.52	1.14	0.57	22.71	0.64	15.45	5.76	-	0.09	0.05	97.55	
Px 3, 4	52.02	0.23	1.41	1.01	19.65	0.60	18.59	5.74	-	0.08	0.04	99.37	
Px 4, 1	50.93	0.27	1.22	0.45	20.11	0.60	19.63	5.65	-	0.24	0.22	99.33	0.00
Px 4, 2	53.28	0.10	1.10	0.86	14.22	0.43	25.52	1.99	0.02	0.44	0.43	98.37	195.00
Px 4, 3	55.74	0.06	0.60	0.71	12.93	0.41	28.44	1.40	0.03	0.10	0.04	100.45	390.00
Px 4, 4	54.04	0.08	0.88	0.75	14.44	0.48	26.38	1.96	0.06	0.28	0.24	99.59	585.00
Px 4, 5	52.44	0.13	1.13	0.54	17.52	0.54	21.63	4.24	0.01	0.14	0.12	98.45	780.00
Px 5, 1	54.68	0.16	1.63	0.48	19.12	0.52	17.47	6.12	-	0.10	0.07	100.35	0.00
Px 5, 2	55.01	0.10	1.69	0.58	18.42	0.42	21.92	2.06	0.01	0.06	0.13	100.40	195.00
Px 5, 3	54.89	0.06	0.58	0.65	12.86	0.41	28.27	1.41	0.03	0.02	0.01	99.19	390.00
Px 5, 4	53.76	0.08	0.87	0.49	16.43	0.54	24.24	3.05	-	0.04	0.03	99.52	585.00
Px 5, 5	53.28	0.27	1.24	0.43	22.06	0.61	16.08	6.40	0.03	0.08	0.02	100.50	780.00
Px 6, 1	51.29	0.56	1.69	0.68	16.34	0.49	13.92	15.60	-	0.17	0.01	100.75	

Px 6, 2	50.57	0.59	1.69	0.70	17.01	0.53	14.08	15.51	-	0.16	0.02	100.86	
Px 6, 3	51.92	0.49	1.62	0.44	21.33	0.64	15.95	7.44	0.02	0.11	0.02	99.98	
Px 6, 4	54.01	0.12	1.59	0.52	16.63	0.54	21.05	4.58	0.03	0.06	0.06	99.19	
Px 7, 1	52.24	0.32	1.25	0.43	20.99	0.59	17.49	6.26	0.01	0.07	0.03	99.68	
Px 7, 2	51.82	0.52	0.97	0.36	22.08	0.65	15.78	8.43	0.02	0.08	-	100.70	
Px 7, 3	52.57	0.25	0.74	0.36	21.86	0.65	17.58	6.44	-	0.07	-	100.51	
Px 8, 1	52.23	0.32	1.66	0.64	18.48	0.58	17.63	8.62	0.02	0.09	0.02	100.29	
Px 8, 2	51.16	0.65	1.53	0.64	19.90	0.59	14.58	11.62	-	0.15	0.01	100.82	
Px 8, 3	50.85	0.53	1.44	0.51	21.78	0.55	15.31	8.62	0.02	0.11	0.02	99.74	
Px 9, 1	51.60	0.32	1.24	0.51	19.14	0.57	17.20	8.11	-	0.10	-	98.79	
Px 9, 2	53.55	0.09	0.82	0.44	15.52	0.54	21.74	5.53	0.04	0.05	0.01	98.33	
Px 9, 3	51.45	0.33	0.61	0.23	22.99	0.66	16.35	5.68	0.01	0.08	-	98.39	
Px 10	52.58	0.13	1.30	0.59	16.63	0.54	20.89	5.68	0.02	0.06	0.03	98.45	
Px 12, 1	52.17	0.25	1.53	0.68	18.76	0.56	18.14	6.64	0.01	0.07	0.01	98.82	
Px 12, 2	52.55	0.31	1.59	0.76	17.07	0.58	18.45	9.53	0.02	0.10	0.02	100.97	
Px 12, 3	53.58	0.10	0.69	0.41	15.62	0.54	22.32	5.16	-	0.06	0.01	98.49	
Px 13, 1	52.18	0.15	1.03	0.48	19.84	0.55	19.46	4.80	-	0.06	0.02	98.57	
Px 13, 2	53.59	0.09	0.87	0.52	16.67	0.54	22.71	3.87	-	0.04	0.02	98.91	
Px 13, 3	55.12	0.10	0.84	0.85	13.96	0.44	27.31	1.52	0.02	0.05	-	100.19	
Px 13, 4	54.53	0.09	0.97	0.85	13.07	0.41	26.82	1.61	0.03	0.03	0.04	98.44	
Px 13, 5	55.29	0.07	0.76	0.73	12.34	0.42	27.66	1.46	0.03	0.02	0.01	98.79	
Px 13, 6	53.45	0.12	1.06	0.53	15.00	0.51	22.14	5.81	-	0.07	0.03	98.73	
Px 13, 7	52.75	0.24	1.26	0.58	18.15	0.59	20.91	4.88	0.02	0.05	0.01	99.42	

Px 14, 1	55.88	0.06	0.70	0.69	12.77	0.39	27.65	1.34	0.02	0.03	0.01	99.53	
Px 14, 2	55.14	0.08	0.85	0.85	13.88	0.46	26.59	1.83	0.03	0.04	0.01	99.77	
Px 14, 3	54.07	0.09	0.86	0.55	15.47	0.56	22.08	5.47	0.01	0.06	-	99.22	
Px 14, 4	51.93	0.32	1.25	0.52	20.31	0.59	17.42	7.42	-	0.08	-	99.84	
Px 14, 5	52.16	0.31	1.22	0.45	20.25	0.61	18.98	5.44	-	0.06	-	99.48	
NWA 4925 – weathering rind													
Px 1, 1	54.99	-	2.90	0.53	15.29	0.38	22.05	3.86			-	100.00	
Px 1, 2	55.97		1.36	0.56	15.98	0.74	20.38	4.99			-	99.98	
Px 2, 1	53.63	0.41	2.23	0.41	18.58	0.61	17.40	6.73			-	100.00	
Px 2, 2	54.17	-	5.62	0.69	17.92	0.36	15.96	4.15			1.13	100.00	
Px 3	53.72	-	1.45	0.68	20.13	0.59	16.93	6.50			-	100.00	
Px 4	56.36	-	1.00	0.65	12.56	0.60	26.98	1.85			-	100.00	
Px 5	53.01	0.48	1.13	0.37	19.93	0.79	16.76	7.53			-	100.00	
Px 6, 1	54.79	-	1.46	0.65	14.77	0.61	20.14	7.57			-	99.99	
Px 6, 2	53.87	0.37	2.01	0.73	14.65	0.34	16.84	11.03			0.16	100.00	
Px 7	54.98	-	1.45	0.63	16.98	0.44	20.49	5.03			-	100.00	

* Oxide detection limit of 0.01 wt. %

Table 3: NWA 2046 and NWA 4925 maskelynite major element data

	SiO_2	TiO_2	Al_2O_3	Cr_2O_3	FeO (tot)	MnO	MgO	CaO	NiO	Na_2O	K_2O	Total	Or	An	Ab
NWA 2046															

Mask 1, 1	52.59	0.05	28.73	0.01	0.38	0.01	0.15	12.79	-	4.32	0.05	99.07	0.50	70.96	28.54
Mask 1, 2	52.64	0.05	28.65	-	0.60	0.01	0.12	12.51	0.02	4.42	0.12	99.12	1.20	69.53	29.27
Mask 2, 1	51.98	0.02	29.22	-	0.57	0.01	0.15	13.16	-	4.07	0.05	99.22	0.48	72.75	26.77
Mask 2, 2	52.33	0.05	28.92	-	0.48	0.01	0.18	13.03	-	4.19	0.03	99.21	0.25	72.16	27.59
Mask 3, 1	53.10	0.04	28.18	-	0.40	0.01	0.11	11.98	-	4.43	0.06	98.31	0.59	69.03	30.37
Mask 3, 2	53.48	0.05	27.84	-	0.41	0.01	0.12	11.73	-	4.50	0.08	98.22	0.86	68.04	31.10
Mask 3, 3	52.47	0.04	28.60	-	0.43	0.01	0.14	12.74	0.02	4.33	0.04	98.83	0.38	70.94	28.68
Mask 3, 4	53.60	0.05	27.90	-	0.40	0.02	0.12	11.76	0.02	4.83	0.06	98.76	0.66	66.73	32.62
Mask 3, 5	51.87	0.03	28.95	0.02	0.62	0.02	0.15	13.15	0.02	4.04	0.06	98.92	0.55	72.84	26.61
Mask 4, 1	52.29	0.05	29.01	-	0.57	0.01	0.17	13.20	0.01	4.05	0.03	99.40	0.33	72.99	26.68
Mask 4, 2	51.06	0.04	29.58	-	0.42	0.01	0.20	13.86	-	3.75	0.03	98.94	0.27	75.42	24.31
Mask 5, 1	54.37	0.09	27.81	0.02	0.38	0.02	0.13	11.42	-	5.00	0.11	99.35	1.08	65.00	33.92
Mask 5, 2	54.79	0.10	27.67	-	0.59	0.01	0.08	10.98	-	5.11	0.17	99.51	1.74	63.24	35.01
Mask 6, 1	51.71	0.01	29.32	-	0.40	-	0.19	13.47	0.01	4.03	0.02	99.16	0.19	73.58	26.23
Mask 6, 2	51.54	0.03	29.34	-	0.51	0.02	0.18	13.66	-	3.89	0.03	99.20	0.25	74.48	25.27
Mask 7, 1	51.61	0.04	29.18	-	0.47	-	0.20	13.35	0.01	4.00	0.04	98.89	0.39	73.44	26.17
Mask 7, 2	51.74	0.04	29.10	0.03	0.56	-	0.17	13.14	-	4.09	0.06	98.92	0.55	72.56	26.89
Mask 8, 1	52.06	0.02	29.09	0.02	0.41	-	0.16	13.11	0.01	4.14	0.04	99.06	0.40	72.39	27.21
Mask 8, 2	54.15	0.07	27.75	0.02	0.52	0.03	0.12	11.22	0.02	4.97	0.14	99.00	1.43	64.52	34.06
Mask 9, 1	51.85	0.03	29.07	-	0.44	0.02	0.16	13.36	0.03	4.02	0.05	99.01	0.46	73.30	26.25
Mask 9, 2	52.15	0.03	28.84	0.01	0.62	-	0.13	12.77	-	4.31	0.09	98.95	0.94	70.68	28.38
Mask 10, 1	51.64	0.03	29.46	-	0.36	-	0.18	13.54	0.02	3.87	0.02	99.10	0.15	74.52	25.33
Mask 10, 2	51.39	0.05	29.41	-	0.53	-	0.15	13.48	-	3.88	0.06	98.93	0.64	74.02	25.34

Mask 11, 1	51.70	0.04	29.18	-	0.44	-	0.22	13.40	-	3.98	0.01	98.96	0.11	73.78	26.11
Mask 11, 2	51.22	0.04	29.13	-	0.48	-	0.16	13.43	0.03	4.01	0.07	98.56	0.64	73.32	26.04
Mask 12, 1	52.69	0.05	28.65	-	0.44	0.02	0.14	12.58	0.01	4.40	0.04	99.00	0.37	70.33	29.30
Mask 12, 2	54.60	0.10	27.40	-	0.42	0.01	0.11	11.16	-	5.09	0.13	99.03	1.34	63.93	34.73
Mask 12, 3	51.73	0.04	29.14	-	0.49	0.02	0.17	13.18	-	4.02	0.03	98.81	0.27	73.16	26.57
Mask 12, 4	53.73	0.06	27.78	0.01	0.58	0.02	0.12	11.58	0.01	4.88	0.11	98.88	1.13	65.83	33.04
Mask 13, 1	53.93	0.11	27.89	-	0.63	0.02	0.11	11.64	-	4.96	0.13	99.43	1.30	65.47	33.23
Mask 13, 2	54.38	0.07	27.56	0.01	0.79	-	0.07	10.88	-	5.11	0.28	99.16	2.93	62.27	34.80
Mask 14, 1	51.50	0.04	29.32	-	0.39	0.03	0.17	13.63	0.01	3.84	0.02	98.94	0.22	74.74	25.04
Mask 14, 2	51.45	0.03	29.32	0.01	0.53	0.01	0.17	13.53	-	3.96	0.06	99.05	0.57	73.73	25.70
Mask 15, 1	52.01	0.04	29.05	0.01	0.39	-	0.19	13.28	-	4.06	0.03	99.07	0.26	73.13	26.61
Mask 15, 2	51.35	0.02	29.21	-	0.52	-	0.17	13.49	0.01	3.96	0.04	98.76	0.37	73.86	25.77
NWA 2046 – weathering rind															
Mask 1	55.80	-	29.75	-	0.41	-	0.42	13.62			-	100.00			
Mask 2	56.56	-	29.44	-	0.38	-	0.26	13.18			0.17	99.99			
Mask 3	58.25	-	28.68	-	0.47	-	-	12.60			-	100.00			
Mask 4	56.60	-	29.73	-	0.50	-	-	13.17			-	100.00			
Mask 5	56.13	-	29.50	-	0.80	-	-	13.57			-	100.00			
NWA 4925															
Mask 1, 1	53.15	0.05	28.37	-	0.47	0.03	0.11	12.15	0.02	4.68	0.12	99.14	0.01	67.75	31.04
Mask 1, 2	53.00	-	28.30	-	0.40	-	0.10	12.40	-	4.60	0.10	98.90	0.01	68.67	30.33

Mask 2, 1	53.40	-	28.00	-	0.40	-	0.10	11.90	-	4.70	0.10	98.60	0.01	67.32	31.66
Mask 2, 2	54.09	0.08	28.05	-	0.68	0.01	0.12	11.69	-	4.81	0.19	99.72	0.02	65.83	32.21
Mask 3, 1	53.89	0.09	28.06	-	0.66	0.01	0.11	11.63	0.01	4.83	0.11	99.40	0.01	66.16	32.69
Mask 3, 2	53.80	0.10	27.90	-	0.40	-	0.10	11.80	-	4.80	0.10	99.10	0.01	66.68	32.30
Mask 4, 1	51.40	-	29.30	-	0.50	-	0.10	13.40	-	3.90	-	98.70	-	74.26	25.74
Mask 4, 2	52.17	0.03	28.78	0.01	0.55	0.02	0.11	12.76	0.01	4.30	0.07	98.80	0.01	70.89	28.45
Mask 5, 1	52.05	0.05	29.04	-	0.49	-	0.16	13.10	0.02	4.09	0.04	99.04	-	72.66	26.98
Mask 5, 2	52.10	-	28.90	-	0.50	-	0.20	13.10	-	4.00	-	98.80	-	73.34	26.66
Mask 6, 1	51.70	-	29.20	-	0.50	-	0.10	13.10	-	4.10	0.10	98.80	0.01	72.13	26.88
Mask 6, 2	50.82	0.03	29.09	0.01	0.60	0.02	0.14	13.37	0.02	3.90	0.04	98.02	-	73.91	25.68
Mask 7, 1	52.10	-	28.90	-	0.60	-	0.10	13.10	-	4.20	0.10	99.00	0.01	71.66	27.35
Mask 7, 2	53.74	0.05	28.03	-	0.56	-	0.11	11.77	0.04	4.80	0.10	99.19	0.01	66.62	32.35
Mask 8, 1	51.40	-	29.40	-	0.40	-	0.20	13.60	-	3.80	-	99.00	-	75.04	24.96
Mask 8, 2	53.04	0.07	28.54	-	0.56	0.01	0.11	12.31	-	4.51	0.12	99.27	0.01	68.78	29.98
Mask 9, 1	51.20	-	29.50	-	0.50	-	0.20	13.60	-	3.70	0.10	98.80	0.01	74.78	24.22
Mask 9, 2	51.77	0.03	29.07	-	0.60	-	0.19	13.30	-	4.00	0.06	99.01	0.01	73.24	26.21
Mask 10, 1	54.60	0.10	27.50	-	0.50	-	0.10	11.10	-	5.10	0.10	98.90	0.01	63.96	34.99
Mask 10, 2	51.65	0.03	29.29	0.01	0.67	0.03	0.14	13.48	-	3.89	0.07	99.24	0.01	73.94	25.37
Mask 10, 3	54.71	0.09	27.53	0.01	0.59	0.01	0.09	11.18	-	5.05	0.16	99.42	0.02	63.99	34.40
Mask 10, 4	51.60	-	29.20	-	0.70	-	0.20	13.40	-	4.00	-	99.10	-	73.78	26.22
Mask 11, 1	53.47	0.06	28.01	0.02	0.52	-	0.14	11.87	0.01	4.79	0.07	98.96	0.01	67.04	32.24
Mask 11, 2	51.70	-	29.30	-	0.40	-	0.20	13.50	-	3.90	-	99.00	-	74.41	25.59
Mask 12, 1	54.41	0.08	28.23	-	0.50	0.01	0.11	11.64	-	4.65	0.13	99.75	0.01	66.83	31.81

Mask 12, 2	54.18	0.11	28.33	-	0.60	0.01	0.13	11.72	-	4.31	0.11	99.51	0.01	68.73	30.12
Mask 13, 1	54.43	0.04	28.20	0.03	0.47	0.01	0.13	11.92	-	4.66	0.06	99.92	0.01	67.84	31.56
Mask 13, 2	53.99	0.06	28.37	0.01	0.61	0.01	0.13	11.99	-	4.12	0.05	99.33	-	70.61	28.90
Mask 14, 1	54.59	0.07	28.67	-	0.45	0.02	0.13	11.75	-	4.77	0.12	100.56	0.01	66.60	32.21
Mask 14, 2	55.04	0.09	28.57	-	0.53	0.02	0.11	11.53	-	4.14	0.13	100.16	0.01	69.10	29.54
Mask 15, 1	52.56	0.04	29.31	-	0.50	0.02	0.18	13.45	0.01	3.93	0.03	100.02	-	73.98	25.72
Mask 15, 2	52.41	0.05	29.68	-	0.52	0.01	0.15	13.28	0.02	3.70	0.06	99.86	0.01	74.67	24.76
Mask 16, 1	53.08	0.06	29.15	0.01	0.47	-	0.14	12.69	0.03	4.04	0.06	99.71	0.01	72.09	27.34
Mask 16, 2	52.64	0.04	29.41	-	0.47	0.01	0.15	13.36	-	3.95	0.05	100.06	-	73.65	25.90
Mask 17, 1	53.42	0.04	28.99	0.01	0.41	0.04	0.16	12.77	0.02	4.34	0.03	100.22	-	70.96	28.73
Mask 17, 2	52.96	0.02	29.42	0.01	0.63	-	0.15	13.05	-	3.80	0.04	100.08	-	73.93	25.63
Mask 18, 1	52.48	0.06	29.56	0.01	0.53	-	0.18	13.15	0.01	3.84	0.02	99.84	-	74.07	25.76
Mask 18, 2	51.45	0.01	30.00	-	0.38	-	0.18	14.14	0.01	3.53	0.02	99.71	-	76.93	22.86
NWA 4925 – weathering rind															
Mask 1	60.22	-	28.17	-	-	-	0.32	11.29				100.00	Mask 1	60.22	
Mask 2	55.58	-	29.83	-	0.55	-	0.30	13.74				100.00	Mask 2	55.58	
Mask 3	56.13	-	29.48	-	0.36	-	0.33	13.70				100.00	Mask 3	56.13	
Mask 4	55.99	-	29.60	-	0.46	-	0.32	13.63				100.00	Mask 4	55.99	
Mask 5	56.15	-	29.56	-	0.58	-	0.43	13.28				100.00	Mask 5	56.15	

* Oxide detection limit of 0.01 wt. %

Table 4: NWA 2046 and NWA 4925 merrillite major element data

	SiO_2	TiO_2	Al_2O_3	Cr_2O_3	FeO (tot)	MnO	MgO	CaO	P_2O_5	Na_2O	K_2O	Total	Mg#	Ca#
NWA 2046														
Merr 1	0.10	-	0.02	-	1.66	0.09	3.00	47.54	46.08	1.30	0.02	99.79	76.35	91.94
Merr 2	0.68	-	0.52	-	1.96	-	2.60	43.51	49.44	1.29	-	99.79	70.28	92.32
Merr 3, 1	0.14	0.26	0.02	-	1.68	0.07	2.98	47.64	45.13	1.28	0.04	99.24	76.04	91.99
Merr 3, 2	-	-	-	-	1.45	-	2.89	43.88	50.67	1.11	-	99.79	78.04	91.60
Merr 3, 1	0.93	0.02	0.52	-	1.71	0.08	2.86	46.56	44.14	1.19	0.03	98.02	74.82	92.14
Merr 3, 2	1.40	-	0.85	-	1.63	-	2.98	44.65	47.18	1.08	0.22	99.79	76.52	91.50
Merr 3, 3	1.45	-	0.80	-	1.44	0.32	2.75	43.67	48.71	0.87	-	99.79	77.30	91.94
Merr 4	-	-	-	-	1.17	-	3.30	43.72	50.38	1.43	-	99.79	83.41	90.49
Merr 5	0.43	0.03	0.14	0.04	1.57	0.10	2.88	47.08	44.79	1.30	0.04	98.41	76.56	92.15
Merr 6	0.09	-	0.02	-	2.01	0.08	2.72	47.67	45.21	1.24	0.03	99.08	70.71	92.63
NWA 4925														
Merr 1, 1	0.41	-	0.36	-	1.69	-	2.46	44.47	49.48	1.13	-	99.79	72.18	92.85
Merr 1, 3	0.78	-	0.59	-	1.61	-	2.80	42.94	49.94	1.35	-	99.79	75.61	91.68
Merr 2	-	-	-	-	1.53	-	3.07	43.35	50.49	1.56	-	99.79	78.15	91.03
Merr 3	-	-	-	-	1.40	-	3.02	44.08	50.29	1.20	-	99.79	79.36	91.30
Merr 4, 1	-	-	-	-	1.70	-	2.96	43.81	50.25	1.28	-	99.79	75.63	91.41
Merr 4, 2	0.81	-	0.30	-	1.99	-	2.94	42.59	50.31	1.05	-	99.79	72.48	91.24
Merr 4, 3	1.63	-	-	-	2.43	-	3.38	45.17	46.23	1.17	-	99.79	71.26	90.57

Merr 5	0.41	0.04	0.04	0.03	1.70	0.08	3.19	47.28	44.94	1.27	0.02	99.00	77.02	91.41
Merr 6	1.28	0.53	0.63	-	1.42	-	3.40	44.58	46.86	1.29	-	99.79	81.02	90.41
Merr 7	0.58	-	-	-	1.63	0.34	3.14	43.63	49.25	1.44	-	99.79	77.45	90.90

* Oxide detection limit of 0.01 wt. %

Table 5: NWA 2046 and NWA 4925 oxides major element data

	SiO_2	TiO_2	Al_2O_3	Cr_2O_3	FeO (tot)	MnO	MgO	CaO	NiO	Na_2O	K_2O	Total
NWA 2046												
Chr 1, 1	0.17	0.48	6.10	59.77	27.47	0.44	4.51	0.07	0.01	-	-	99.02
Chr 1, 2	0.18	0.73	7.99	57.51	27.22	0.42	5.18	0.03	0.04	0.01	-	99.31
Chr 2, 1	0.14	0.91	6.28	57.71	31.07	0.42	1.86	0.02	-	0.01	0.01	98.42
Chr 2, 2	0.11	0.69	6.31	58.33	31.34	0.39	1.85	0.05	0.01	-	-	99.10
Chr 3	0.13	0.89	5.97	58.50	31.23	0.44	1.47	-	0.01	-	-	98.63
Chr 4, 1	0.13	0.43	5.68	60.60	27.28	0.43	4.74	0.11	0.01	-	0.01	99.42
Chr 4, 2	0.14	0.44	5.76	60.50	27.89	0.38	4.10	0.07	0.01	0.01	-	99.30
Chr 4, 3	0.12	0.50	5.72	60.16	27.99	0.42	3.85	0.25	0.01	0.01	-	99.03
Chr 5	0.16	0.63	7.27	59.83	22.34	0.38	7.20	0.08	-	0.03	0.16	98.08
Chr 6	0.14	0.77	7.29	54.50	33.29	0.46	1.66	0.02	0.01	-	0.01	98.14
Chr 7, 1	0.13	0.44	5.78	59.88	29.35	0.41	3.05	0.02	0.01	0.01	-	98.64
Chr 7, 2	0.13	0.48	5.71	59.50	29.46	0.44	3.11	0.05	0.01	0.01	-	98.90
Chr 7, 3	0.12	0.53	5.84	59.61	29.56	0.42	2.98	0.01	-	0.02	0.01	99.10
Chr 8, 1	0.15	0.49	5.69	58.08	30.30	0.45	3.25	0.03	-	0.01	0.01	98.46

Chr 8, 2	0.16	0.74	6.75	58.09	28.49	0.41	4.19	0.02	0.03	0.04	-	98.92
Chr 9, 1	0.22	2.12	5.34	54.16	32.28	0.43	2.71	0.49	0.01	0.02	0.01	97.79
Chr 9, 2	0.12	0.46	5.70	59.33	29.68	0.42	3.07	0.22	-	0.03	-	99.03
Chr 9, 3	0.02	13.44	6.75	35.65	39.39	0.52	3.75	0.07	0.03	0.02	0.01	99.65
Chr 10, 1	0.04	21.23	5.27	23.59	45.98	0.55	3.28	0.14	0.02	0.01	-	100.11
Chr 10, 2	0.55	16.52	6.59	29.01	42.39	0.53	3.39	0.21	-	-	0.02	99.21
Chr 11	0.12	0.61	6.91	60.44	23.22	0.42	7.12	0.02	0.03	-	0.02	98.90
Chr 12	0.14	0.58	6.79	59.36	25.05	0.38	6.04	0.09	-	-	-	98.43
Chr 13	0.13	0.65	7.09	58.75	25.04	0.39	5.99	0.10	0.01	-	-	98.16
Ox 3	0.05	23.93	2.82	16.72	52.39	0.52	1.56	0.04	-	0.01	-	98.02
Ox 4, 1	0.02	22.71	3.06	19.01	51.16	0.54	1.70	0.01	0.02	-	0.01	98.24
Ox 4, 2	0.03	19.49	3.62	24.53	48.46	0.52	1.62	0.04	-	-	-	98.31
Ox 5	0.07	29.12	2.28	1.50	61.51	0.68	1.91	0.20	0.03	0.01	0.03	97.34
Ox 6, 1	0.05	27.14	2.80	7.30	58.29	0.60	1.37	0.07	0.02	-	0.01	97.62
Ox 6, 2	0.04	27.08	2.86	7.43	58.14	0.61	1.34	0.05	0.02	-	-	97.56
Ox 7, 1	0.04	26.93	2.29	3.59	62.26	0.59	1.35	0.03	0.01	-	-	97.09
Ox 7, 2	0.06	27.24	2.12	3.57	61.84	0.61	1.40	0.12	0.02	0.01	0.01	97.00
Ox 8, 1	0.05	26.76	2.81	9.32	55.28	0.59	1.91	0.21	0.03	-	-	96.97
Ox 8, 2	0.04	26.18	2.69	9.04	56.53	0.58	1.92	0.21	0.01	0.01	0.01	97.21
Ox 9	0.05	19.00	4.17	23.35	49.60	0.51	1.79	0.05	-	-	-	98.51
Ox 10, 1	0.03	22.86	3.83	15.21	54.67	0.60	1.10	0.10	0.02	-	-	98.43
Ox 10, 2	0.05	23.33	3.53	13.72	55.01	0.56	1.14	0.29	0.01	-	-	97.64

Ox 11, 1	0.01	52.44	0.03	0.66	42.52	0.67	1.86	0.11	0.02	0.01	-	98.32
Ox 11, 2	0.04	52.27	0.04	0.61	42.86	0.69	1.87	0.15	0.04	-	-	98.56
Ox 12	0.03	52.14	0.08	0.47	42.66	0.64	1.94	0.17	-	0.01	0.02	98.16
Ox 13	0.02	52.56	0.06	0.29	43.20	0.70	1.60	0.07	0.04	0.02	0.02	98.58
Ox 14	0.02	52.48	0.05	0.31	43.30	0.66	1.57	0.05	-	-	-	98.44
Ox 15	0.06	51.43	0.17	0.43	43.40	0.68	1.51	0.72	0.03	0.01	-	98.43
Ox 16	0.06	51.87	0.04	0.36	43.39	0.68	1.52	0.80	0.02	0.01	0.02	98.76
Ox 17, 1	0.02	52.75	0.03	0.50	40.71	0.66	3.32	0.38	-	-	-	98.37
Ox 17, 2	0.07	52.40	0.31	0.75	41.04	0.65	3.21	0.14	0.02	-	0.01	98.59
Ox 18, 1	0.02	51.69	0.07	0.47	43.24	0.66	1.49	0.39	-	-	-	98.02
Ox 18, 2	0.03	51.76	0.07	0.41	43.02	0.67	1.54	0.47	0.04	0.02	0.01	98.04
NWA 4925												
Chr 1, 1	0.13	0.53	6.20	60.53	29.46	0.41	2.64	0.04	0.02	0.01	-	99.97
Chr 1, 2	0.13	0.73	6.55	59.25	29.61	0.40	2.57	0.06	-	0.02	-	99.32
Chr 2, 1	0.14	0.48	6.21	60.29	29.60	0.41	2.48	0.08	-	-	-	99.69
Chr 2, 2	0.13	0.49	6.07	60.72	29.15	0.39	2.93	0.05	-	-	-	99.93
Chr 3, 1	0.17	0.53	6.15	60.48	30.02	0.44	2.39	0.05	-	0.01	-	100.24
Chr 3, 2	0.13	0.61	6.11	60.03	29.82	0.42	2.47	0.05	-	0.14	0.01	99.79
Chr 4	0.97	0.75	7.67	55.36	28.56	0.41	3.74	0.23	0.02	-	-	97.72
Chr 5	0.15	0.47	9.26	56.44	29.65	0.40	2.94	0.05	-	-	0.01	99.37
Chr 6	0.13	0.73	6.18	57.06	32.41	0.44	1.52	0.11	0.01	0.02	0.01	98.60

Chr 7, 1	0.14	0.56	6.03	59.95	29.08	0.42	2.79	0.08	0.01	0.02	-	99.08
Chr 7, 2	0.12	0.59	6.23	60.21	28.62	0.40	3.35	0.12	-	-	-	99.64
Chr 8, 1	0.14	0.49	6.40	59.08	28.22	0.44	3.62	0.01	0.02	-	-	98.41
Chr 8, 2	0.12	0.68	7.64	57.46	30.50	0.42	2.69	0.09	0.01	-	-	99.61
Chr 9	0.13	0.59	6.52	58.51	30.46	0.43	2.06	-	-	-	0.02	98.73
Chr 10	0.14	0.56	6.86	58.01	29.43	0.42	3.21	-	0.02	-	-	98.64
Chr 11	0.12	0.58	6.32	58.95	29.97	0.40	2.26	0.03	0.02	-	0.01	98.66
Chr 12, 1	0.05	2.21	10.57	50.79	31.22	0.42	3.71	0.03	0.04	0.02	-	99.06
Chr 12, 2	0.12	0.58	6.78	59.17	29.08	0.43	3.10	0.12	-	-	0.01	99.39
Chr 13, 1	0.14	0.45	6.22	59.68	27.36	0.41	4.00	0.03	0.01	-	-	98.30
Chr 13, 2	0.14	0.47	6.48	59.45	27.62	0.42	3.91	0.08	0.01	-	0.02	98.59
Chr 14, 1	0.12	0.77	7.48	57.46	30.63	0.43	2.42	0.06	-	-	-	99.39
Chr 14, 2	0.12	0.72	6.55	57.51	30.88	0.41	2.36	0.09	-	-	0.01	98.65
Chr 15	0.16	0.97	10.80	54.77	25.60	0.40	5.72	0.04	0.03	-	-	98.48
Ox 5	0.05	14.76	5.96	30.88	42.11	0.45	3.12	0.12	0.01	0.04	-	97.50
Ox 6	0.04	8.71	6.47	40.48	40.62	0.45	1.45	0.07	-	0.01	0.01	98.31
Ox 7, 1	0.04	11.65	5.91	35.52	40.74	0.47	2.38	0.11	-	0.01	-	96.83
Ox 7, 2	0.05	20.77	3.63	22.17	47.82	0.57	2.33	0.07	0.05	-	0.01	97.47
Ox 8, 1	0.06	19.08	5.52	22.69	47.04	0.57	2.09	0.07	-	-	-	97.12
Ox 8, 2	0.06	19.43	5.42	22.45	47.17	0.55	2.05	0.07	0.01	0.01	-	97.22
Ox 9, 1	0.05	9.11	7.16	41.30	36.73	0.44	3.51	0.14	0.05	0.01	-	98.50
Ox 9, 2	0.07	9.08	6.58	41.10	39.02	0.46	2.31	0.09	0.02	-	-	98.72

Ox 10	0.05	10.32	6.53	38.22	39.53	0.44	2.61	0.11	0.03	0.01	-	97.86
Ox 11	0.03	16.63	4.31	29.00	45.46	0.54	2.30	0.08	0.02	-	0.01	98.38
Ox 12	0.03	24.50	4.10	13.79	52.15	0.62	3.05	0.10	0.02	0.01	-	98.35
Ox 13	0.06	23.52	4.20	14.06	52.24	0.61	2.99	0.15	0.02	-	0.01	97.89
Ox 14	0.04	23.68	3.90	13.71	53.49	0.59	2.37	0.17	0.03	-	0.02	97.99
Ox 15	0.03	21.89	4.62	17.78	50.57	0.60	2.38	0.13	-	-	0.02	98.01
Ox 16	0.01	52.87	0.04	0.48	42.38	0.72	2.30	0.21	0.02	-	0.01	99.03
Ox 17	0.02	52.63	0.06	0.60	41.09	0.70	2.56	0.45	-	-	0.01	98.12
Ox 18	0.08	52.20	0.04	0.47	41.47	0.72	2.92	0.59	-	0.01	-	98.48
Ox 19	0.34	47.48	0.49	1.09	44.52	0.70	1.61	0.55	0.02	0.02	-	96.82
Ox 20	0.03	52.85	0.07	0.50	41.63	0.72	2.82	0.21	0.02	-	-	98.83
Ox 21	0.03	52.80	0.05	0.49	41.04	0.70	3.15	0.41	-	-	-	98.68
Ox 22	0.04	51.75	0.02	0.26	43.16	0.78	1.69	0.42	0.01	0.01	-	98.12

* Oxide detection limit of 0.01 wt. %

A-3

Table 1: NWA 2046 and NWA 4925 olivine trace element data

	NWA 2046 megacrysts (> 500µm)								
^{7}Li	Ol 1, 1	Ol 1, 2	Ol 1, 3	Ol 2	Ol 3, 1	Ol 3, 2	Ol 3, 3	Ol 4, 1	Ol 4, 2
^{23}Na	27.08	bdl	bdl	17.56	bdl	bdl	bdl	6.18	3.32
^{27}Al	189.56	92.68	44.69	126.39	106.69	61.93	25.03	74.49	41.86

^{43}Ca	1950.51	701.39	503.02	974.32	619.21	364.75	76.18	415.00	253.71
^{45}Sc	4088.02	2554.33	2674.80	2302.64	3323.99	2178.50	1618.62	4367.11	1222.91
^{47}Ti	6.74	6.20	8.16	6.24	6.35	6.38	8.37	5.73	6.71
^{51}V	33.44	29.03	34.80	29.61	32.13	25.88	110.67	23.98	21.73
^{53}Cr	94.29	39.97	30.52	55.57	46.81	40.58	12.55	44.18	30.75
^{55}Mn	3827.61	2597.53	1905.60	2646.57	4075.04	3089.84	290.75	3889.60	1884.94
^{59}Co	2894.60	2492.63	4188.20	2905.22	2554.06	2797.62	4948.77	2447.62	3334.91
^{60}Ni	99.48	88.19	99.59	91.99	89.15	90.07	96.88	83.17	87.57
^{65}Cu	692.45	673.94	414.48	588.36	694.44	608.76	250.83	630.09	464.00
^{66}Zn	8.02	1.53	0.59	3.08	1.04	0.81	0.21	1.15	0.34
^{90}Zr	77.70	59.29	125.47	76.64	61.55	96.79	164.89	69.86	116.43
^{93}Nb	0.53	0.07	0.08	0.12	0.08	0.03	0.08	0.04	0.02
	NWA 2046 weathering rind olivine								
	Ol 2, c	Ol 2, r	Ol 3, c	Ol 3, r					
^{7}Li	bdl	bdl	bdl	bdl					
^{23}Na	29.73	45.21	45.58	13.39					
^{27}Al	338.07	760.71	597.64	99.80					
^{43}Ca	1529.83	1877.30	2023.94	2089.00					
^{45}Sc	9.25	8.63	11.33	10.92					
^{47}Ti	79.42	42.23	47.22	145.05					
^{51}V	18.49	60.08	66.64	14.42					
^{53}Cr	308.69	3249.52	3173.75	198.00					

^{55}Mn	4142.83	3644.33	3736.23	4747.61					
^{59}Co	98.87	95.14	97.40	96.64					
^{60}Ni	250.31	404.83	288.43	152.37					
^{65}Cu	0.73	0.25	0.24	0.37					
^{66}Zn	114.72	152.35	109.80	140.99					
^{90}Zr	0.23	0.09	0.02	0.14					
^{93}Nb	Ol 2, c	Ol 2, r	Ol 3, c	Ol 3, r					
	NWA 4925 megacrysts (> 500µm)								
	Ol 1, 1	Ol 1, 2	Ol 1, 3	Ol 2, 1	Ol 2, 2	Ol 2, 3	Ol 3		
^{7}Li	1.91	9.35	bdl	16.70	bdl	bdl	bdl		
^{23}Na	63.30	64.61	43.82	97.43	46.19	36.83	50.15		
^{27}Al	1048.82	867.59	678.17	1645.01	964.22	763.43	750.29		
^{43}Ca	2061.33	2387.69	1856.43	3670.91	3390.59	2964.20	8429.41		
^{45}Sc	8.33	7.05	8.70	8.18	11.84	9.82	8.89		
^{47}Ti	40.04	42.83	50.74	26.10	168.89	169.90	101.64		
^{51}V	29.04	33.51	22.36	51.47	51.11	38.62	14.29		
^{53}Cr	977.58	1060.90	520.11	2546.44	2496.11	1600.98	280.31		
^{55}Mn	3774.61	3091.28	4555.67	3211.84	4594.34	4380.10	4567.19		
^{59}Co	103.61	91.10	106.00	83.62	107.46	104.09	100.45		
^{60}Ni	425.77	542.54	360.31	471.63	277.14	228.43	204.63		
^{65}Cu	7.07	7.42	5.31	8.15	1.65	2.37	3.82		
^{66}Zn	108.39	69.13	140.43	91.02	125.81	117.39	117.29		

^{90}Zr	0.07	0.13	0.04	0.03	0.20	0.05	0.25		
^{93}Nb	bdl	bdl	bdl	bdl	0.01	bdl	bdl		
	NWA 4925 weathering rind olivine								
	Ol 1, c	Ol 1, r	Ol 2, c	Ol 2, r	Ol 3, c	Ol 3, r	Ol 4, c	Ol 4, r	
^{7}Li	11.99	35.98	28.37	bdl	52.06	26.12	25.67	26.58	
^{23}Na	708.35	151.47	540.46	38.43	675.81	86.96	587.88	137.31	
^{27}Al	19733.30	5120.72	17109.72	386.82	43908.79	1607.46	35776.66	3342.12	
^{43}Ca	56632.38	5295.13	67383.56	1923.92	18437.50	3775.86	17013.12	4494.43	
^{45}Sc	23.21	12.38	24.56	11.37	16.56	10.63	23.00	10.60	
^{47}Ti	108.03	55.24	183.92	111.13	82.31	85.64	295.09	60.58	
^{51}V	373.16	190.01	395.31	32.31	204.00	81.49	216.05	60.74	
^{53}Cr	3963.43	325.80	6277.29	180.89	4210.18	395.86	1695.74	396.02	
^{55}Mn	7052.27	5319.73	4137.13	4694.55	4202.15	4252.82	2071.34	3461.61	
^{59}Co	145.28	91.05	66.54	92.49	64.06	91.16	27.47	95.29	
^{60}Ni	986.45	330.63	854.90	227.98	627.63	318.24	601.52	385.79	
^{65}Cu	290.12	47.14	252.69	5.06	86.61	8.55	100.12	7.64	
^{66}Zn	316.29	200.57	756.06	155.48	271.13	202.52	292.36	163.59	
^{90}Zr	46.23	0.16	43.91	0.22	2.37	0.04	4.29	0.09	
^{93}Nb	0.54	bdl	0.57	bdl	0.03	bdl	0.03	bdl	

*Trace element detection limit of 0.01 ppm

Table 2: NWA 2046 and NWA 4925 pyroxene trace element data

NWA 2046 pyroxene (sample interior)													
	Px 1, 1	Px 1, 2	Px 2, 1	Px 2, 2	Px 3	Px 4	Px 5, 1	Px 5, 2	Px 6	Px 7			
^{7}Li	bdl	bdl	2.52	2.18	5.70	2.47	bdl	bdl	bdl	bdl			
^{23}Na	684.85	1022.73	235.75	611.45	262.20	387.61	739.37	468.83	1700.05	711.00			
^{24}Mg	104896.23	109513.24	144050.55	112291.79	137508.00	114908.77	112935.02	104178.82	156924.75	128637.52			
^{27}Al	6111.42	7164.17	3751.30	5335.71	3719.14	5044.53	6870.09	4815.76	2520.74	6457.03			
^{29}Si	254200.00	249000.00	251600.00	239600.00	248200.00	236900.00	247200.00	243200.00	247100.00	250700.00			
^{43}Ca	44316.67	47638.20	10466.48	39567.50	12444.55	34192.74	41805.02	43596.19	113029.29	22486.09			
^{45}Sc	46.70	44.95	20.68	37.45	23.27	41.17	42.38	45.97	45.66	27.32			
^{49}Ti	1304.77	1191.21	408.63	688.39	453.61	731.46	1055.25	888.77	2392.17	706.24			
^{51}V	221.16	254.68	146.24	229.34	169.15	245.64	249.42	212.78	67.45	167.86			
^{53}Cr	3027.39	3305.32	4560.51	3156.71	4589.78	3157.74	3576.57	2830.37	1083.37	3674.01			
^{55}Mn	4637.24	4148.93	3082.38	3869.93	3271.66	4117.69	4016.79	4441.65	7431.86	3692.66			
^{57}Fe	132193.14	109290.41	83669.96	98936.60	87512.52	105871.07	106486.83	118680.58	327099.07	97704.95			
^{59}Co	47.7790	46.5654	48.1101	44.7974	48.5141	46.0976	46.7357	47.5473	122.7073	48.4934			
^{60}Ni	46.8640	53.5803	181.6102	53.9074	170.6738	47.8939	73.6730	44.9256	240.4926	112.8307			
^{63}Cu	1.5910	1.5113	0.7669	0.7158	1.4457	0.7917	1.9105	0.6106	3.6866	1.3298			
^{66}Zn	89.4580	65.1251	54.9916	54.4655	51.2208	58.4440	62.3717	66.6705	157.8929	54.0110			
^{85}Rb	0.1123	0.3032	0.0640	0.1133	0.0707	0.0705	0.1447	0.0278	0.2342	0.7721			
^{88}Sr	10.7628	7.3697	5.4300	18.2799	2.8754	4.1663	8.7628	2.9131	59.8663	5.0036			
^{89}Y	3.5692	3.9353	0.5723	1.9089	0.6630	1.8872	3.5795	2.6449	164.4549	1.6235			
^{90}Zr	4.7846	3.0393	0.6255	0.7033	0.4887	0.3149	2.1407	0.7491	12.6914	1.3314			

^{93}Nb	0.0418	0.0359	0.0058	0.0104	0.0072	0.0014	0.0179	0.0034	0.0612	0.0183			
^{137}Ba	22.2844	13.7558	56.6740	94.8592	23.6126	8.1546	16.1176	6.0760	116.6814	19.9979			
^{139}La	0.0045	0.0294	0.0091	0.0057	0.0019	0.0037	0.0252	0.0013	2.7519	0.0147			
^{140}Ce	0.0228	0.0825	0.0095	0.0254	0.0090	0.0070	0.0916	0.0112	8.3411	0.0647			
^{141}Pr	0.0051	0.0183	0.0024	0.0042	0.0010	0.0025	0.0190	0.0028	1.7459	0.0103			
^{146}Nd	0.0480	0.1366	0.0147	0.0408	0.0107	0.0230	0.1483	0.0397	12.1443	0.0681			
^{147}Sm	0.0653	0.1196	0.0073	0.0452	0.0116	0.0343	0.1032	0.0594	10.2698	0.0471			
^{153}Eu	0.0272	0.0527	0.0055	0.0187	0.0036	0.0187	0.0458	0.0223	3.0709	0.0233			
^{157}Gd	0.2774	0.3291	0.0307	0.1719	0.0418	0.1101	0.3419	0.1798	22.0093	0.1522			
^{159}Tb	0.0670	0.0850	0.0089	0.0359	0.0098	0.0396	0.0715	0.0429	4.2385	0.0317			
^{163}Dy	0.5517	0.6412	0.0786	0.3200	0.0740	0.2624	0.6443	0.4291	30.1929	0.2590			
^{165}Ho	0.1373	0.1506	0.0173	0.0764	0.0247	0.0674	0.1424	0.1008	6.3327	0.0676			
^{166}Er	0.4340	0.4552	0.0695	0.2487	0.0876	0.2085	0.4055	0.3402	17.7125	0.2121			
^{169}Tm	0.0711	0.0694	0.0104	0.0354	0.0202	0.0389	0.0593	0.0558	2.2566	0.0269			
^{172}Yb	0.4886	0.5065	0.1121	0.2352	0.0985	0.2971	0.4497	0.4095	14.9225	0.2373			
^{175}Lu	0.0788	0.0755	0.0169	0.0435	0.0190	0.0474	0.0674	0.0615	1.9475	0.0394			
^{178}Hf	0.1913	0.1407	0.0222	0.0289	0.0186	0.0271	0.0972	0.0446	0.4347	0.0621			
^{208}Pb	0.1005	0.1101	0.0692	0.0816	0.0584	0.0764	0.0578	0.0437	0.2158	0.1642			
^{232}Th	0.0022	0.0037	0.0009	0.0016	bdl	bdl	0.0024	bdl	0.2710	0.0016			
^{238}U	0.0040	0.0057	bdl	0.0052	bdl	0.0043	0.0061	bdl	0.0680	bdl			
	NWA 2046 weathering rind pyroxene												
	Px 1, 1	Px 1, 2	Px 2	Px 3	Px 4	Px 5, 1	Px 5, 2	Px 5, 1	Px 6, 2	Px 7, 1	Px 7, 2	Px 7, 3	Px 7, 4

^{7}Li	bdl	2.96	bdl	bdl	bdl	bdl	bdl	bdl	bdl	bdl	bdl	bdl	bdl
^{23}Na	328.20	438.73	412.93	503.89	499.27	411.86	336.70	355.40	466.90	384.43	466.81	270.63	615.39
^{24}Mg	153909.28	145838.70	130755.40	132906.69	119883.23	149354.00	137944.28	138124.86	133843.48	128060.46	140055.12	149274.70	122672.54
^{27}Al	3260.28	4190.82	5108.28	4790.67	6154.14	4710.08	4247.34	4383.06	4767.49	5829.57	5508.45	3755.85	5312.98
^{29}Si	265784.74	261946.67	251108.08	251864.97	245711.24	261959.42	257700.09	258161.95	257124.64	252576.64	254956.82	260670.59	250063.36
^{43}Ca	13304.72	15637.49	27717.25	25464.72	36137.35	17160.62	23126.24	21681.62	25247.93	26458.00	19335.62	15499.13	31050.54
^{45}Sc	18.90	24.84	35.80	33.34	50.61	22.04	29.54	33.09	33.59	44.65	29.21	25.80	37.76
^{49}Ti	434.33	795.71	666.13	700.47	856.29	505.11	524.06	571.63	613.41	737.59	693.53	471.37	834.66
^{51}V	107.17	137.28	218.25	192.79	271.23	137.67	179.69	208.15	208.61	287.45	240.36	163.69	207.20
^{53}Cr	3463.83	3769.89	3566.46	3379.22	3476.25	3834.20	3579.94	3730.72	3498.80	4212.07	10320.96	3930.41	2996.47
^{55}Mn	3345.08	3452.22	3908.23	3929.10	4262.24	3395.42	3826.93	3843.51	3921.06	4111.90	3550.77	3574.23	4134.79
^{57}Fe	115768.87	123478.30	134768.26	135848.57	142519.68	117929.86	128215.38	128678.34	130058.09	137105.59	124518.76	122116.37	141895.97
^{59}Co	49.6817	49.2597	55.2869	52.3253	46.9042	51.3471	49.5343	50.2259	49.2737	49.6566	51.4303	49.7633	47.8342
^{60}Ni	162.4946	160.5690	560.2496	240.0917	52.8593	211.1040	111.6130	115.7277	99.2925	73.6806	161.0799	135.3725	53.2683
^{63}Cu	0.5025	1.1475	62.7346	22.1341	0.4605	3.1227	1.6841	0.4599	0.5662	0.4234	1.7712	0.6497	0.6589
^{66}Zn	56.4089	63.1519	60.2603	64.5205	66.3096	59.0014	60.9192	58.3578	58.5657	63.3266	65.7449	58.5954	67.2537
^{85}Rb	0.0102	0.0413	0.1859	0.1532	0.0613	0.3220	0.0828	bdl	0.0133	0.0074	0.2306	0.0429	0.0481
^{88}Sr	0.9644	1.7062	36.4809	1.2117	2.1155	8.4114	6.1683	0.3809	1.1324	0.5160	8.3871	0.3909	1.7694
^{89}Y	0.9824	2.3717	1.7034	1.8906	2.3684	1.2540	1.1461	1.1962	1.4042	1.8123	1.6930	0.7966	2.4487
^{90}Zr	0.7517	2.4059	0.7456	1.2357	0.5718	1.2121	0.3460	0.4434	0.6513	0.6196	1.2552	0.3333	1.3229
^{93}Nb	0.0181	0.0350	0.0110	0.0127	0.0035	0.0179	0.0029	0.0100	0.0098	0.0059	0.0255	0.0095	0.0175
^{137}Ba	2.0438	3.4924	955.8168	0.4662	4.7731	242.7249	57.3050	bdl	3.9708	0.2385	30.3490	0.4604	1.7970

^{139}La	0.0109	0.0347	0.0214	0.0092	0.0208	0.0321	0.0084	0.0018	0.0027	bdl	0.0149	0.0025	0.0082
^{140}Ce	0.0184	0.0878	0.0427	0.0385	0.0627	0.0697	0.0281	0.0085	0.0293	0.0058	0.0542	bdl	0.0305
^{141}Pr	0.0063	0.0158	0.0170	0.0085	0.0169	0.0127	0.0041	0.0017	0.0039	bdl	0.0107	0.0025	0.0151
^{146}Nd	0.0308	0.1313	0.0358	0.0590	0.0778	0.0969	0.0185	0.0251	0.0306	0.0173	0.0709	0.0154	0.0615
^{147}Sm	0.0338	0.1655	0.0451	0.0746	0.0804	0.0585	0.0230	0.0129	0.0213	0.0443	0.0708	bdl	0.0587
^{153}Eu	0.0189	0.0475	0.0236	0.0296	0.0213	0.0246	0.0017	0.0133	0.0140	0.0174	0.0223	0.0105	0.0324
^{157}Gd	0.1024	0.2679	0.1479	0.1340	0.1844	0.1001	0.1019	0.0653	0.1113	0.1488	0.1371	0.0626	0.1842
^{159}Tb	0.0205	0.0567	0.0327	0.0414	0.0440	0.0318	0.0179	0.0236	0.0259	0.0272	0.0371	0.0167	0.0521
^{163}Dy	0.1736	0.4731	0.2908	0.3210	0.3689	0.2167	0.2107	0.1931	0.2685	0.3115	0.3123	0.1448	0.4607
^{165}Ho	0.0440	0.0908	0.0751	0.0769	0.1105	0.0578	0.0584	0.0508	0.0693	0.0733	0.0745	0.0349	0.1121
^{166}Er	0.1239	0.3122	0.2497	0.2472	0.3360	0.1868	0.1657	0.1920	0.2085	0.2807	0.2780	0.1369	0.3169
^{169}Tm	0.0220	0.0505	0.0343	0.0399	0.0444	0.0314	0.0245	0.0282	0.0297	0.0451	0.0311	0.0154	0.0551
^{172}Yb	0.1176	0.3006	0.2758	0.3405	0.3850	0.1418	0.1950	0.1996	0.2158	0.2934	0.2702	0.1520	0.4021
^{175}Lu	0.0241	0.0509	0.0449	0.0491	0.0607	0.0262	0.0350	0.0344	0.0372	0.0450	0.0347	0.0266	0.0602
^{178}Hf	0.0244	0.1049	0.0335	0.0463	0.0269	0.0555	0.0228	0.0342	0.0379	0.0452	0.0702	0.0153	0.0585
^{208}Pb	bdl	0.0223	0.0880	0.0252	0.1682	0.0350	0.1407	bdl	bdl	0.0317	0.1580	0.1772	0.0313
^{232}Th	bdl	bdl	bdl	bdl	bdl	0.0118	0.0057	bdl	bdl	bdl	bdl	bdl	bdl
^{238}U	bdl	bdl	bdl	bdl	bdl	0.0026	0.0023	bdl	0.0018	bdl	0.0047	bdl	bdl
	NWA 4925 pyroxene (sample interior)												
	Px 1, 1	Px 1, 2	Px 1, 3	Px 2, 3	Px 2, 4	Px 3, 1	Px 3, 2	Px 4, 1	Px 4, 2	Px 5			
^{7}Li	5.65	13.24	11.40	7.04	5.90	2.87	7.32	bdl	bdl	bdl			
^{23}Na	631.63	468.73	610.38	265.69	524.25	859.33	515.36	728.00	674.97	1099.14			

^{24}Mg	92393.39	121548.32	109926.40	144517.60	109827.86	97047.78	120069.85	99238.63	88152.54	110297.65			
^{27}Al	8324.98	10350.36	10260.82	4525.67	7461.53	9597.35	7393.53	8053.74	5774.87	10664.41			
^{29}Si	240800.00	250700.00	245300.00	260600.00	245100.00	257200.00	256600.00	241200.00	250300.00	245600.00			
^{43}Ca	44674.27	18160.46	30691.75	11871.35	44289.00	58654.45	31245.01	77187.39	65774.21	39418.76			
^{45}Sc	58.28	27.25	35.45	24.03	45.17	62.70	36.10	61.16	63.18	39.26			
^{49}Ti	1773.71	798.80	949.27	427.64	816.52	2484.20	893.91	1316.78	2976.84	813.89			
^{51}V	214.94	172.32	194.61	164.12	252.26	263.00	199.79	301.07	148.70	218.94			
^{53}Cr	2940.90	6556.65	3393.97	4763.64	3373.81	3263.69	3402.72	3732.38	1920.07	2981.90			
^{55}Mn	4649.91	3614.25	3845.52	3356.31	4113.19	4746.58	3903.38	3956.73	5086.53	4052.41			
^{57}Fe	135307.55	99034.52	104216.78	87339.84	105015.16	132304.46	109115.25	104455.20	155159.49	106930.03			
^{59}Co	48.4106	51.7317	46.6084	50.5417	47.4520	47.9261	47.8497	41.5810	47.6866	45.5841			
^{60}Ni	43.1934	158.2017	103.4507	194.8059	60.9368	56.2593	95.8252	49.7353	45.0525	55.0361			
^{63}Cu	4.5873	9.5093	7.2275	5.1297	5.3468	4.5409	4.8441	4.4095	3.4127	3.0074			
^{66}Zn	85.9159	65.9021	70.2165	55.5286	65.6803	89.8811	65.7215	59.9917	110.5332	62.4405			
^{85}Rb	0.4422	1.4815	0.7320	0.2577	0.4706	0.6361	0.6717	0.5263	0.4474	0.4839			
^{88}Sr	76.9555	89.0563	97.4787	23.5587	40.4370	75.5182	49.4129	26.3742	34.8221	29.3783			
^{89}Y	5.2153	3.0618	3.2660	0.6102	2.3089	6.8208	2.5148	4.4843	8.0617	2.4279			
^{90}Zr	1.9863	1.7847	2.5182	0.1452	0.8232	28.2885	1.5339	2.3039	5.1041	1.3636			
^{93}Nb	0.0253	0.0244	0.0339	0.0037	0.0097	0.4685	0.0251	0.0108	0.0070	0.0094			
^{137}Ba	1458.0232	367.3965	1506.2120	98.8600	163.0336	1938.1544	184.0546	51.9476	86.6518	231.2978			
^{139}La	0.3327	1.2005	0.6021	0.0044	0.0170	0.0703	0.0390	0.0148	0.0119	0.0117			
^{140}Ce	0.0925	0.1843	0.1191	0.0025	0.0351	0.1392	0.0804	0.0381	0.0368	0.0276			
^{141}Pr	0.0500	0.1826	0.0908	0.0024	0.0107	0.0291	0.0159	0.0107	0.0167	0.0054			

^{146}Nd	0.2770	0.9407	0.4303	0.0136	0.0600	0.2507	0.1085	0.0693	0.1630	0.0607			
^{147}Sm	0.1807	0.2159	0.1448	0.0101	0.0493	0.2275	0.0895	0.1104	0.1800	0.0593			
^{153}Eu	0.0819	0.1343	0.0989	0.0061	0.0225	0.1083	0.0398	0.0491	0.0628	0.0408			
^{157}Gd	0.3963	0.3895	0.3831	0.0293	0.1726	0.5948	0.2480	0.4380	0.6608	0.1867			
^{159}Tb	0.0997	0.0622	0.0717	0.0081	0.0425	0.1403	0.0481	0.0979	0.1678	0.0412			
^{163}Dy	0.8550	0.3993	0.5413	0.0971	0.3507	1.0963	0.4295	0.8242	1.3617	0.3484			
^{165}Ho	0.2082	0.0959	0.1190	0.0224	0.0930	0.2743	0.1002	0.1919	0.3059	0.0825			
^{166}Er	0.6413	0.2883	0.3615	0.0744	0.2874	0.8435	0.3145	0.5671	0.9166	0.2887			
^{169}Tm	0.0971	0.0423	0.0496	0.0105	0.0394	0.1367	0.0462	0.0861	0.1586	0.0405			
^{172}Yb	0.6985	0.3077	0.3595	0.1125	0.3622	1.0489	0.3871	0.5572	1.2374	0.3089			
^{175}Lu	0.1158	0.0439	0.0554	0.0165	0.0531	0.1556	0.0524	0.0946	0.1758	0.0565			
^{178}Hf	0.1092	0.0713	0.1059	0.0103	0.0421	1.1535	0.0646	0.1138	0.2867	0.0644			
^{208}Pb	0.1042	0.0709	0.1128	0.0224	0.0512	0.0934	0.0540	0.0705	0.0446	0.0602			
^{232}Th	0.0022	0.0042	0.0040	bdl	0.0011	0.0181	0.0039	0.0014	0.0041	0.0023			
^{238}U	bdl	0.0144	0.0075	0.0071	0.0067	0.0123	0.0073	0.0114	0.0069	0.0061			
	NWA 4925 weathering rind												
	Px 1, 1	Px 1, 2	Px 2	Px 3	Px 4	Px 5, 1	Px 5, 2	Px 6	Px 7	Px 8	Px 9	Px 10	Px 11
^{7}Li	3.71	2.81	bdl	bdl	bdl	bdl	5.81	bdl	bdl	29.17	7.81	5.30	bdl
^{23}Na	470.02	355.27	757.14	386.46	499.59	623.33	534.86	836.69	546.94	148.17	694.44	700.64	1043.68
^{24}Mg	132296.21	143697.43	104282.94	99156.39	117744.92	114508.16	121380.66	97222.83	117606.68	171715.27	104788.54	93046.65	81739.98
^{27}Al	8872.41	6649.20	8241.36	5538.70	7781.75	7898.55	6898.52	9110.09	7295.97	4254.14	10951.96	8911.02	10730.33
^{29}Si	256955.11	263038.77	242752.29	182796.35	250277.31	249936.57	252768.22	236706.15	251424.96	168057.29	246373.66	234910.60	231952.26

^{43}Ca	23392.23	15852.80	38776.34	24438.85	35431.13	34112.50	28213.64	81488.35	29382.45	4610.67	34283.45	39202.25	79758.91
^{45}Sc	35.04	26.52	44.55	34.21	46.97	40.74	41.66	58.64	36.91	10.02	42.80	50.30	80.82
^{49}Ti	706.37	457.21	1466.36	1502.03	834.46	1249.82	696.63	1113.47	1000.32	52.63	1416.83	1857.25	2572.70
^{51}V	187.75	144.09	205.28	139.55	247.28	185.36	242.71	315.18	189.95	77.81	198.56	184.55	309.54
^{53}Cr	3983.06	3866.85	2679.00	2279.51	3354.97	3252.27	3649.48	3933.39	3205.45	2328.61	2814.61	2494.59	3720.74
^{55}Mn	3860.83	3503.69	4017.15	4546.27	4025.47	3931.22	4010.67	3557.87	4051.54	3189.38	4211.96	4404.73	3702.27
^{57}Fe	128479.77	121718.47	155531.62	238683.64	139374.27	143726.80	140964.12	124926.93	144358.42	204277.63	153552.52	173268.46	144011.60
^{59}Co	52.8227	50.3120	41.2068	75.4556	45.3989	46.4963	47.3896	36.5159	48.6427	85.9639	48.4401	67.3811	35.0772
^{60}Ni	144.7127	150.8896	40.5856	115.0375	52.5109	89.7315	83.4220	48.6367	78.8131	474.8943	83.0030	461.3913	36.1919
^{63}Cu	6.4038	7.1183	5.5399	6.2062	3.5776	5.1947	4.8658	4.1965	5.6587	9.1593	10.6170	44.5603	5.6115
^{66}Zn	64.5411	63.3045	82.5574	103.9905	66.4653	73.7758	69.4599	64.8370	78.8006	133.7465	92.5872	96.8301	79.4066
^{85}Rb	0.6162	0.6645	0.6134	0.4571	0.5443	0.9009	0.7069	0.5730	0.7510	1.0154	1.8462	1.1302	1.6228
^{88}Sr	44.1541	42.1553	56.7140	30.1300	37.2894	51.7815	63.8262	75.7323	47.9028	60.1983	48.2010	43.6819	37.7639
^{89}Y	3.6759	3.0615	9.1253	6.4703	2.4175	3.5250	1.7217	4.7071	2.9293	2.1660	6.8699	8.2583	9.6777
^{90}Zr	1.2270	0.4831	8.9206	4.2411	1.0319	5.1908	0.6910	5.0784	6.0801	0.1762	8.1613	6.6055	19.9391
^{93}Nb	0.0184	0.0139	0.1186	0.1441	0.0245	0.1282	0.0076	0.0501	0.0740	0.0030	0.0711	0.0467	0.1902
^{137}Ba	431.4756	360.7915	987.1127	142.2086	170.3209	254.6200	319.5540	486.0370	628.0816	477.7410	355.4590	224.9487	142.4514
^{139}La	2.1194	2.3832	2.8947	4.0339	0.3013	0.0565	0.0308	0.0590	0.0371	1.4066	1.2339	1.5524	0.5272
^{140}Ce	0.2818	0.2477	0.3924	0.1841	0.0554	0.0809	0.0212	0.1132	0.0876	0.1073	0.2303	0.1682	0.1635
^{141}Pr	0.4462	0.5518	0.5198	0.7483	0.0423	0.0204	0.0097	0.0289	0.0199	0.1862	0.1810	0.2037	0.1009
^{146}Nd	2.0752	2.4082	2.4058	3.4643	0.1832	0.1467	0.0385	0.1851	0.1017	1.0392	0.8772	0.9618	0.6658
^{147}Sm	0.4698	0.3811	0.7653	0.6721	0.0716	0.1291	0.0456	0.1708	0.0886	0.1722	0.3615	0.3589	0.3522
^{153}Eu	0.1653	0.1627	0.2680	0.2218	0.0463	0.0631	0.0365	0.0999	0.0625	0.1020	0.1335	0.1321	0.1464

^{157}Gd	0.6098	0.5864	1.2830	0.8962	0.2146	0.4019	0.1222	0.4671	0.2655	0.3442	0.7916	0.9154	1.1748
^{159}Tb	0.0802	0.0817	0.2544	0.1523	0.0542	0.0761	0.0304	0.1091	0.0704	0.0332	0.1639	0.1810	0.2273
^{163}Dy	0.5685	0.5133	1.6854	1.0262	0.3788	0.6164	0.3016	0.9087	0.5504	0.2293	1.1696	1.3503	1.9904
^{165}Ho	0.1354	0.0972	0.3496	0.2337	0.1070	0.1729	0.0670	0.2111	0.1164	0.0509	0.2598	0.3374	0.4050
^{166}Er	0.3657	0.3014	0.9936	0.7234	0.3101	0.4875	0.2328	0.6080	0.4051	0.1827	0.8201	0.9980	1.3077
^{169}Tm	0.0519	0.0333	0.1617	0.1090	0.0459	0.0867	0.0349	0.0827	0.0588	0.0223	0.1086	0.1299	0.1567
^{172}Yb	0.3340	0.2615	0.9505	0.7816	0.3644	0.5844	0.2586	0.6718	0.4448	0.1378	0.8180	0.8952	1.1148
^{175}Lu	0.0493	0.0362	0.1391	0.1168	0.0514	0.0813	0.0525	0.0954	0.0664	0.0245	0.1187	0.1518	0.1919
^{178}Hf	0.0489	0.0222	0.3705	0.1971	0.0354	0.1737	0.0323	0.1668	0.1790	bdl	0.2732	0.2951	0.7682
^{208}Pb	0.0605	0.0710	0.0934	0.0621	0.0470	0.0375	0.0381	0.0407	0.1031	bdl	0.0826	0.1772	0.1018
^{232}Th	0.0040	0.0021	0.0169	0.0051	0.0030	0.0055	bdl	0.0058	0.0085	bdl	0.0129	0.0070	bdl
^{238}U	0.0033	bdl	0.0047	0.0124	0.0032	0.0090	0.0173	0.0295	0.0054	0.0554	0.0098	0.0101	0.0057

*Trace element detection limit of 0.01 ppm

Table 2: NWA 2046 and NWA 4925 maskleynite trace element data

NWA 2046 mask (sample interior)											
	Mask 1, 1	Mask 2, 1	Mask 2, 2	Mask 3, 1	Mask 4, 1	Mask 4, 2	Mask 5, 1	Mask 5, 2			
^{7}Li	bdl	bdl	9.10	12.38	bdl	bdl	8.06	bdl			
^{23}Na	29552.13	34222.98	33012.18	30482.97	28331.92	27728.92	24540.67	27870.26			
^{24}Mg	894.82	459.74	557.61	709.13	850.36	1165.70	16537.45	1241.29			
^{27}Al	171452.64	127219.21	130131.27	133749.87	152049.37	146969.10	123683.55	160904.55			
^{29}Si	251500.00	243300.00	243500.00	241200.00	240700.00	240500.00	254300.00	253300.00			
^{43}Ca	96124.96	64670.23	66271.85	70540.27	86020.37	84999.95	77519.08	89722.76			

^{45}Sc	2.11	2.04	2.09	2.17	2.17	2.44	11.82	2.45			
^{49}Ti	286.32	343.99	287.77	226.37	162.44	166.85	369.95	233.14			
^{51}V	3.12	1.33	1.82	2.38	3.73	4.84	47.14	4.06			
^{53}Cr	9.10	1.03	0.71	0.82	1.98	13.81	570.63	13.14			
^{55}Mn	61.53	43.60	48.11	51.63	56.13	75.31	845.22	71.14			
^{57}Fe	2588.59	1933.17	2011.65	2211.61	2345.43	2375.35	23851.43	2905.84			
^{59}Co	0.4441	0.3883	0.3709	0.5962	0.6756	0.7148	9.2164	1.0059			
^{60}Ni	bdl	bdl	bdl	bdl	bdl	bdl	10.4348	bdl			
^{63}Cu	bdl	0.9454	0.7860	0.4679	1.3444	0.6714	0.9984	0.8219			
^{66}Zn	6.8458	4.7223	4.2953	4.2208	5.0777	4.2934	15.5370	4.6229			
^{85}Rb	0.2847	0.1152	0.0849	0.1530	0.0924	0.0306	0.1275	0.1124			
^{88}Sr	105.7802	101.0493	92.7377	83.9558	77.6728	73.0268	69.2660	92.3672			
^{89}Y	0.0996	0.1253	0.1030	0.1012	0.1234	0.0955	0.7929	0.1926			
^{90}Zr	bdl	bdl	bdl	bdl	0.0255	0.0142	0.3679	0.0835			
^{93}Nb	bdl	bdl	bdl	bdl	bdl	bdl	0.0050	bdl			
^{137}Ba	1.6326	4.2584	2.8450	2.2326	3.4175	3.2655	6.9820	2.1458			
^{139}La	bdl	0.0161	0.0224	0.0131	0.0121	0.0109	0.0135	0.0402			
^{140}Ce	0.0282	0.0393	0.0378	0.0306	0.0269	0.0301	0.0290	0.0306			
^{141}Pr	0.0174	0.0030	0.0063	0.0055	bdl	0.0040	0.0060	0.0061			
^{146}Nd	bdl	0.0217	0.0521	0.0333	0.0428	0.0723	0.0474	bdl			
^{147}Sm	bdl	0.0361	0.0144	0.0322	0.0306	0.0081	0.0387	0.0683			
^{153}Eu	0.7888	0.8793	0.7982	0.6338	0.4562	0.4405	0.4591	0.5613			
^{157}Gd	0.0857	0.0142	0.0152	0.0287	0.0327	0.0333	0.0779	bdl			

^{159}Tb	bdl	0.0051	0.0043	0.0050	0.0022	0.0022	0.0178	0.0055			
^{163}Dy	bdl	0.0348	0.0157	0.0320	bdl	0.0241	0.1230	0.0203			
^{165}Ho	bdl	0.0021	0.0045	0.0078	0.0023	0.0020	0.0341	0.0056			
^{166}Er	bdl	0.0064	0.0079	0.0085	0.0190	0.0114	0.1001	bdl			
^{169}Tm	bdl	bdl	bdl	bdl	bdl	bdl	0.0146	bdl			
^{172}Yb	0.1206	0.0153	0.0073	bdl	0.0103	bdl	0.1276	bdl			
^{175}Lu	bdl	bdl	bdl	bdl	bdl	0.0018	0.0149	bdl			
^{178}Hf	bdl	bdl	bdl	bdl	bdl	bdl	0.0216	bdl			
^{208}Pb	bdl	0.0796	bdl	bdl	0.0821	bdl	0.1622	bdl			
^{232}Th	bdl	bdl	bdl	bdl	bdl	bdl	bdl	bdl			
^{238}U	bdl	0.0043	bdl	bdl	bdl	bdl	bdl	bdl			
	NWA 2046 weathering rind mask										
	Mask 1	Mask 2	Mask 3	Mask 4	Mask 5						
^{7}Li	bdl	bdl	bdl	bdl	bdl						
^{23}Na	30107.18	31407.54	37346.06	31739.40	32452.20						
^{24}Mg	943.69	867.68	691.54	983.30	903.41						
^{27}Al	150404.74	147023.93	143500.70	147184.93	150802.20						
^{29}Si	257026.02	263546.29	268547.33	261697.88	258688.48						
^{43}Ca	87953.70	83828.92	76419.63	85005.92	83530.08						
^{45}Sc	3.27	3.46	3.38	3.09	3.27						
^{49}Ti	176.93	180.22	287.17	184.64	215.87						
^{51}V	4.20	3.73	2.12	3.30	3.19						

^{53}Cr	bdl	0.89	bdl	5.22	2.80						
^{55}Mn	58.43	53.08	48.50	63.14	65.41						
^{57}Fe	3233.25	2999.13	3042.69	3041.47	3237.62						
^{59}Co	0.8281	0.6612	0.5422	0.6377	0.6255						
^{60}Ni	bdl	bdl	bdl	bdl	0.6940						
^{63}Cu	1.1565	1.0460	1.6696	0.9496	0.9850						
^{66}Zn	6.6269	4.8335	5.5994	5.1999	6.3583						
^{85}Rb	0.0730	0.0202	0.0460	0.0135	0.1364						
^{88}Sr	76.6495	76.3027	97.9800	78.6661	83.7741						
^{89}Y	0.0701	0.0903	0.1211	0.0820	0.1288						
^{90}Zr	0.2307	0.0154	0.0156	0.0204	0.0756						
^{93}Nb	0.0037	bdl	bdl	bdl	bdl						
^{137}Ba	2.2383	1.3526	3.8132	1.3125	1.7895						
^{139}La	0.0124	0.0053	0.0294	0.0130	0.0118						
^{140}Ce	0.0371	0.0407	0.0384	0.0251	0.0268						
^{141}Pr	bdl	0.0073	0.0045	0.0060	bdl						
^{146}Nd	bdl	0.0282	0.0346	0.0279	0.0282						
^{147}Sm	0.0146	0.0213	0.0154	0.0173	0.0475						
^{153}Eu	0.5336	0.6176	0.8572	0.6314	0.6704						
^{157}Gd	bdl	0.0177	0.0376	0.0388	0.0446						
^{159}Tb	0.0062	0.0086	0.0061	0.0101	0.0062						
^{163}Dy	0.0388	0.0142	0.0531	0.0297	bdl						
^{165}Ho	0.0037	0.0056	0.0068	0.0023	0.0042						

^{166}Er	0.0141	0.0082	bdl	0.0210	0.0153						
^{169}Tm	bdl	bdl	bdl	bdl	bdl						
^{172}Yb	bdl	0.0195	0.0297	bdl	0.0136						
^{175}Lu	bdl	bdl	bdl	bdl	bdl						
^{178}Hf	0.0180	bdl	bdl	bdl	0.0093						
^{208}Pb	0.0393	bdl	bdl	bdl	bdl						
^{232}Th	bdl	bdl	bdl	bdl	bdl						
^{238}U	bdl	bdl	bdl	bdl	bdl						
	NWA 4925 mask (sample interior)										
	Mask 1, 1	Mask 1, 2	Mask 2, 1	Mask 3, 1	Mask 4, 1	Mask 5, 1	Mask 6, 1	Mask 7, 1	Mask 7, 2	Mask 8, 1	Mask 8, 2
^{7}Li	5.87	bdl	7.65	bdl	bdl	bdl	9.81	bdl	bdl	bdl	6.82
^{23}Na	28867.72	28941.31	30074.92	29766.66	29300.22	28991.89	35171.99	32415.35	30024.25	30382.21	28364.84
^{24}Mg	835.11	988.31	871.43	1080.21	900.00	961.11	976.57	765.54	953.41	1138.80	912.94
^{27}Al	139136.09	133322.26	143894.28	146151.02	136775.65	142048.92	123217.17	134541.58	144017.18	139390.89	141102.29
^{29}Si	244500.00	238700.00	251000.00	251000.00	242400.00	243800.00	241400.00	245700.00	245000.00	245300.00	240500.00
^{43}Ca	81568.23	76837.82	83244.79	83327.68	79908.29	83639.31	64621.10	74439.31	82826.40	78603.41	81036.55
^{45}Sc	2.77	2.56	2.49	2.77	2.43	2.63	2.49	2.39	2.38	2.38	2.44
^{49}Ti	182.60	170.37	184.33	175.49	169.74	168.84	413.96	246.38	182.92	183.81	173.80
^{51}V	3.13	3.78	3.42	4.26	3.52	3.63	1.86	2.47	3.31	4.20	3.56
^{53}Cr	1.40	2.70	2.55	3.41	1.10	1.19	33.35	0.99	1.05	2.07	1.60
^{55}Mn	56.49	58.38	62.11	66.44	60.33	61.89	96.97	52.80	60.34	57.21	54.40
^{57}Fe	2269.59	2127.39	2241.89	2278.42	2221.37	2165.15	3026.15	2082.43	2141.99	2101.84	1896.75

^{59}Co	0.8066	0.5814	0.7030	0.7751	0.5753	0.5366	1.4325	0.6507	0.7442	0.6739	0.5827
^{60}Ni	bdl	bdl	0.8072	0.8225	bdl	bdl	1.6477	bdl	bdl	bdl	bdl
^{63}Cu	bdl	bdl	bdl	0.7730	bdl	bdl	0.1936	bdl	bdl	bdl	bdl
^{66}Zn	4.6384	4.3962	4.8169	7.5475	4.1087	3.8353	5.1797	4.4135	4.6991	3.8094	3.8373
^{85}Rb	0.0827	0.0531	0.0526	0.0983	0.1086	0.0455	0.7696	0.0545	0.0297	0.0336	bdl
^{88}Sr	79.1655	76.3345	80.9126	80.8243	76.4647	77.6325	119.3681	92.1463	82.6519	76.7530	75.5351
^{89}Y	0.1010	0.0873	0.0942	0.0917	0.1051	0.0874	0.1566	0.1069	0.1052	0.1167	0.1077
^{90}Zr	0.0182	0.0116	0.0303	0.0843	bdl	bdl	0.1041	bdl	0.0131	bdl	0.0197
^{93}Nb	bdl	0.0025	bdl	0.0034	bdl	bdl	0.0041	bdl	0.0027	bdl	bdl
^{137}Ba	1.2919	2.3040	1.8579	2.9737	1.5631	1.2442	190.8706	2.1930	2.2292	1.2953	1.0204
^{139}La	0.0083	0.0128	0.0138	0.0344	0.0121	0.0106	0.0248	0.0232	0.0130	0.0175	0.0121
^{140}Ce	0.0347	0.0272	0.0444	0.0646	0.0222	0.0349	0.0577	0.0363	0.0308	0.0267	0.0271
^{141}Pr	0.0047	0.0036	0.0050	0.0053	0.0043	0.0051	0.0079	0.0061	0.0048	0.0039	bdl
^{146}Nd	0.0124	0.0423	0.0333	0.0298	0.0320	0.0466	0.0620	0.0504	0.0182	0.0272	0.0457
^{147}Sm	0.0206	bdl	0.0223	bdl	bdl	bdl	0.0629	0.0324	0.0184	0.0237	0.0163
^{153}Eu	0.5423	0.5314	0.5096	0.4985	0.4677	0.4584	0.9872	0.6698	0.5329	0.4538	0.5091
^{157}Gd	0.0194	0.0265	0.0351	0.0145	0.0284	0.0275	0.0225	0.0168	0.0319	bdl	0.0186
^{159}Tb	0.0049	0.0074	0.0031	0.0024	bdl	0.0052	bdl	bdl	0.0043	bdl	0.0031
^{163}Dy	0.0194	0.0144	0.0330	0.0262	0.0344	0.0200	0.0395	0.0237	0.0409	bdl	0.0226
^{165}Ho	0.0043	0.0053	0.0046	0.0062	0.0052	0.0034	0.0025	0.0090	0.0056	0.0049	0.0025
^{166}Er	0.0152	0.0151	0.0070	0.0074	0.0111	bdl	0.0226	0.0072	bdl	bdl	0.0129
^{169}Tm	bdl	bdl	bdl	bdl	bdl	bdl	0.0022	bdl	0.0045	bdl	0.0037
^{172}Yb	0.0164	0.0148	bdl	bdl	bdl	0.0079	0.0379	bdl	bdl	bdl	bdl

^{175}Lu	bdl	bdl	bdl	bdl	bdl	bdl	bdl	bdl	bdl	bdl	bdl
^{178}Hf	bdl	bdl	bdl	bdl	bdl	bdl	bdl	bdl	bdl	bdl	bdl
^{208}Pb	0.0776	0.0528	0.0568	0.2199	0.0722	bdl	0.1224	bdl	0.1213	bdl	bdl
^{232}Th	bdl	bdl	bdl	bdl	bdl	bdl	bdl	bdl	bdl	bdl	bdl
^{238}U	bdl	bdl	bdl	bdl	bdl	bdl	0.0031	bdl	bdl	bdl	bdl
	NWA 4925 weathering rind mask										
	Mask 1	Mask 2	Mask 3	Mask 4	Mask 5						
^{7}Li	7.57	9.04	bdl	8.68	8.14						
^{23}Na	40584.87	30594.80	30421.67	29804.50	37567.55						
^{24}Mg	594.00	918.58	987.49	911.88	663.46						
^{27}Al	139671.97	147990.43	148459.45	149179.33	145891.10						
^{29}Si	274654.45	261821.93	261119.80	259558.47	264863.06						
^{43}Ca	70857.72	85155.96	85336.35	86910.37	77446.63						
^{45}Sc	4.87	4.77	4.84	4.65	4.39						
^{49}Ti	398.02	165.27	196.25	162.78	322.49						
^{51}V	1.72	3.84	4.58	4.18	2.19						
^{53}Cr	bdl	bdl	1.94	1.06	bdl						
^{55}Mn	46.12	68.43	69.73	60.78	52.97						
^{57}Fe	3045.04	3181.75	3309.84	3306.63	3060.95						
^{59}Co	0.5229	0.5827	0.8564	0.6975	0.4897						
^{60}Ni	bdl	bdl	2.0666	bdl	bdl						
^{63}Cu	bdl	bdl	bdl	bdl	bdl						

^{66}Zn	5.9172	5.0535	4.8323	6.1660	5.5485						
^{85}Rb	0.2226	0.0941	0.0799	0.0277	0.0770						
^{88}Sr	118.2061	77.6830	76.0947	77.5550	104.9663						
^{89}Y	0.1599	0.0874	0.2702	0.0806	0.1379						
^{90}Zr	0.0248	0.0322	0.9468	0.0091	bdl						
^{93}Nb	bdl	bdl	0.0305	0.0051	bdl						
^{137}Ba	7.0505	0.9284	1.9604	1.2543	4.7029						
^{139}La	0.0288	0.0143	0.0449	0.0154	0.0278						
^{140}Ce	0.0702	0.0384	0.0264	0.0318	0.0437						
^{141}Pr	0.0065	0.0082	0.0089	0.0096	0.0098						
^{146}Nd	0.0774	0.0101	0.1019	0.0850	0.0306						
^{147}Sm	0.0350	0.0110	0.0361	0.0139	0.0130						
^{153}Eu	1.1325	0.5476	0.4982	0.5969	0.9130						
^{157}Gd	0.0561	0.0373	0.0611	0.0242	0.0361						
^{159}Tb	0.0082	0.0038	0.0115	0.0038	bdl						
^{163}Dy	0.0254	0.0277	0.0387	bdl	0.0187						
^{165}Ho	0.0054	0.0065	0.0076	0.0087	0.0057						
^{166}Er	bdl	bdl	0.0317	0.0134	bdl						
^{169}Tm	bdl	bdl	0.0026	bdl	0.0073						
^{172}Yb	bdl	bdl	0.0207	0.0127	bdl						
^{175}Lu	0.0047	0.0057	0.0024	bdl	0.0035						
^{178}Hf	bdl	bdl	0.0128	bdl	0.0102						
^{208}Pb	0.0471	0.0424	bdl	0.0661	0.0371						

^{232}Th	bdl	bdl	bdl	bdl	bdl						
^{238}U	bdl	bdl	bdl	bdl	bdl						

*Trace element detection limit of 0.01 ppm

Table 2: NWA 2046 and NWA 4925 merrillite trace element data

NWA 2046 merrillite													
	Phos 2, 1	Phos 2, 2	Phos 3, 1	Phos 3, 2	Phos 3, 3	Phos 4, 1	Phos 4, 2	Phos 5, 1	Phos 5, 2	Phos 6, 2	Phos 6, 3		
^{7}Li	bdl	bdl	bdl	bdl	bdl	bdl	bdl	bdl	bdl	bdl	bdl		
^{23}Na	6063.45	5819.00	10935.58	8053.82	7419.00	15099.00	15293.46	15426.61	15560.90	11265.09	22345.41		
^{24}Mg	13557.55	12497.77	21695.24	13415.48	17533.26	21898.68	20693.32	24602.57	22069.55	19883.27	13136.25		
^{27}Al	1597.70	2832.56	1287.53	2578.87	7083.73	1640.45	2560.56	2201.10	2633.42	1434.33	79606.50		
^{29}Si	11070.54	9149.52	9518.59	9213.251	26864.71	2743.16	3530.195	12095.65	6074.18	10380.995	116236.81		
^{43}Ca	339800	339800	503098	527443	476663	512586	515222	490422	458376	517425	334356		
^{45}Sc	44.43	42.30	89.32	67.40	56.62	95.38	93.27	85.58	84.56	96.02	47.36		
^{49}Ti	52.91	32.44	92.52	65.12	573.62	61.45	52.96	202.13	28255.27	48.41	323.92		
^{51}V	4.47	4.03	10.82	5.94	9.09	9.76	9.69	14.13	42.42	9.30	6.63		
^{53}Cr	46.90	36.09	58.37	53.04	129.32	25.61	26.61	79.02	253.23	14.49	24.37		
^{55}Mn	854.79	527.64	1173.80	1235.05	1500.89	1028.12	1061.16	1104.36	1162.01	1128.95	440.99		
^{57}Fe	439398.61	8650.34	26989.29	22183.02	37730.91	19216.87	19506.68	28428.03	40363.75	23422.03	10063.32		
^{59}Co	1150.5233	4.5366	4.5329	3.2261	9.4304	3.4794	3.7181	8.7874	6.9760	3.9378	3.1288		
^{60}Ni	9302.8606	167.6884	5.8808	6.6773	12.6469	7.7759	6.9983	71.1181	13.7136	7.3567	6.3037		
^{63}Cu	1902.3748	6.0108	3.1136	3.4945	8.2855	1.9690	2.1614	5.7824	2.5170	3.8824	3.5660		
^{66}Zn	35.6105	14.9092	20.7848	12.6961	28.1673	9.6800	11.7211	20.3126	24.5582	9.8493	18.1810		

^{85}Rb	0.3185	4.3264	2.0795	1.2939	2.0292	1.6787	1.9374	2.1330	1.2779	2.8164	3.5992		
^{88}Sr	196.6376	204.3851	266.8894	300.7637	271.7352	208.4808	249.4977	262.0956	217.7481	261.3255	162.7556		
^{89}Y	417.6817	402.0060	1439.2821	1122.1395	680.3885	1718.0167	1626.0331	1503.3649	1426.0086	1551.9547	618.2876		
^{90}Zr	106.2641	99.3436	62.3616	267.6391	527.2612	107.0858	119.6651	38.8787	183.7817	85.5656	37.1757		
^{93}Nb	0.0739	bdl	bdl	0.2404	0.2113	bdl	bdl	bdl	3.6214	0.1266	0.1283		
^{137}Ba	109.6900	79.9624	38.2976	272.0572	204.7030	68.1726	68.1917	135.5741	31.1340	50.8722	60.4249		
^{139}La	4.5518	5.6031	24.3093	16.2988	11.7456	28.6901	27.4339	24.7403	24.7549	24.6829	9.2269		
^{140}Ce	15.5358	13.6394	70.2500	51.4144	35.1489	86.6182	83.2183	76.9259	71.3862	71.1027	25.4679		
^{141}Pr	3.0662	2.6714	13.1536	10.0629	8.1647	17.1398	16.4680	15.3544	14.6506	14.1861	4.9279		
^{146}Nd	18.1075	18.6211	105.3550	74.8030	53.3239	133.7923	124.9337	115.0613	106.2217	107.2108	38.6458		
^{147}Sm	14.9443	14.3131	82.4811	65.3910	45.1387	102.9203	99.7479	88.8818	88.5466	87.7844	34.6967		
^{153}Eu	6.8697	6.6460	25.1809	18.9616	15.1743	32.6744	30.9944	26.9793	24.5132	24.8111	12.9861		
^{157}Gd	42.3922	41.3663	188.0546	146.8890	105.4110	239.4059	224.8470	210.9151	194.6417	203.8864	77.8350		
^{159}Tb	9.2202	8.3584	35.8740	27.8064	22.3860	45.7953	43.5388	39.4577	37.0395	39.5360	14.9939		
^{163}Dy	69.6247	67.1579	260.8501	198.7876	141.6887	326.9901	305.1791	285.6317	268.6070	279.7992	111.8128		
^{165}Ho	15.1208	16.0034	56.4778	41.7875	30.9031	65.9405	61.5647	57.3633	55.4919	59.6728	22.7979		
^{166}Er	50.5322	55.5993	159.1188	117.2902	90.9709	189.3425	176.8079	167.8910	156.7694	173.2114	71.2512		
^{169}Tm	7.2955	8.9339	20.3210	15.7417	9.2685	24.1780	22.8440	20.8476	20.0979	21.5596	9.3194		
^{172}Yb	56.5169	60.2456	130.6293	100.7466	72.6211	150.5440	145.7395	135.5597	128.2632	149.4249	60.4993		
^{175}Lu	9.8085	9.5045	18.8070	14.0658	9.5060	20.8263	19.3392	19.1268	18.1489	19.7899	9.0210		
^{178}Hf	0.9879	1.9168	1.6358	4.5590	12.3461	3.5693	4.0155	1.3403	5.5377	2.5470	0.2818		
^{208}Pb	1.0369	1.8767	2.3717	2.2444	4.8396	2.4325	2.2179	1.5265	2.2127	1.4977	1.8631		
^{232}Th	1.3831	2.0360	2.1769	3.1490	1.0285	2.2070	2.4874	2.3215	2.0751	3.2832	1.1169		

^{238}U	0.9134	0.7792	0.4830	1.0426	1.0389	0.4914	0.6403	0.4039	0.4484	0.7997	0.4849		
	NWA 4925 merrillite												
	Phos 1, 1	Phos 1, 2	Phos 2	Phos 3	Phos 4, 1	Phos 4, 2							
^{7}Li	213.46	72.78	30.129	280.639	112.494	162.461							
^{23}Na	13334.95	9830.47	7014.32	4946.09	33061.63	6350.22							
^{24}Mg	16353.52	30516.23	54497.37	445675.08	13925.77	129255.20							
^{27}Al	59839.55	23218.70	4835.25	34062.71	89783.50	19876.82							
^{29}Si	113232.02	95864.92	138261.99	1115089.26	182345.98	392647.54							
^{43}Ca	352181.15	365802.96	259775.66	338000.00	334100.00	334100.00							
^{45}Sc	73.42	76.00	76.64	326.56	37.62	187.60							
^{49}Ti	365.25	749.54	1967.75	12509.42	271.84	24630.57							
^{51}V	15.44	25.67	58.09	838.05	5.26	463.84							
^{53}Cr	43.42	126.56	554.50	12112.17	36.75	15351.60							
^{55}Mn	2809.28	2049.22	3271.49	24543.51	870.33	9673.78							
^{57}Fe	16504.85	47107.51	106114.63	661306.40	10249.39	320073.33							
^{59}Co	30.7367	17.8041	26.0836	231.9544	5.8733	172.4969							
^{60}Ni	73.5257	54.6091	45.1050	227.2098	13.5852	874.7314							
^{63}Cu	25.5472	9.0242	4.0721	13.5959	bdl	131.0412							
^{66}Zn	37.6585	41.2310	89.4452	589.5960	18.2384	400.8072							
^{85}Rb	9.0616	2.5565	1.1245	3.8054	4.1920	1.8482							
^{88}Sr	377.5013	182.2777	113.3611	139.5135	298.0575	136.0972							
^{89}Y	547.5815	944.1759	659.5340	216.3681	688.4025	527.9544							

^{90}Zr	35.7269	21.2757	29.5953	50.6410	23.8410	403.1572							
^{93}Nb	0.1552	0.0622	bdl	bdl	bdl	9.8876							
^{137}Ba	1406.5592	457.2980	42.0212	441.5395	388.7432	182.1961							
^{139}La	15.7067	23.7636	11.7042	4.1064	13.1215	9.7103							
^{140}Ce	17.9699	49.3188	35.0372	9.8276	38.4786	28.4798							
^{141}Pr	4.7854	11.5881	6.9019	2.6186	7.0680	5.1933							
^{146}Nd	29.2949	75.8091	48.8166	13.4757	50.5079	36.2906							
^{147}Sm	19.4904	60.1459	41.2465	12.4821	41.2641	34.8633							
^{153}Eu	17.2046	17.3447	11.8847	3.8673	11.5673	9.7277							
^{157}Gd	43.7279	125.0242	94.7562	25.8577	83.0267	58.1212							
^{159}Tb	10.6826	25.0251	17.9554	7.3319	18.2161	13.5692							
^{163}Dy	93.1394	178.5904	121.4195	35.9985	128.7420	95.4644							
^{165}Ho	20.1480	36.7134	25.1793	7.5666	26.4059	21.1227							
^{166}Er	79.4053	108.1936	69.7487	20.3948	73.4853	54.1590							
^{169}Tm	12.9123	14.3354	9.4281	3.5909	10.0680	8.5501							
^{172}Yb	100.3209	90.3445	56.1309	23.7323	65.9576	60.5482							
^{175}Lu	16.5493	12.1001	7.5214	2.4030	8.6615	7.0103							
^{178}Hf	0.8183	1.1813	1.6439	2.5339	0.9649	34.7389							
^{208}Pb	2.6101	1.8828	0.2808	bdl	1.5752	bdl							
^{232}Th	4.2282	2.0922	0.9275	0.4728	1.5885	1.7453							
^{238}U	0.9286	0.3060	0.0749	bdl	0.2068	bdl							

*Trace element detection limit of 0.01 ppm

A-4

Table 1: NWA 2046 and NWA 4925 bulk-rock major and trace element data

	NWA 2046		**NWA 4925**
SiO_2	49.9		49.2
TiO_2	0.48		0.46
Al_2O_3	5.66		5.23
FeO	18.5		20.0
MnO	0.53		0.56
CaO	16.4		15.50
MgO	7.41		8.07
Na_2O	0.75		0.58
K_2O	0.02		0.11
P_2O_5	0.34		0.34
Total	100.00		100.00
Mg#			
^{7}Li	2.34		9.71
^{23}Na	0.04		0.11
^{24}Mg	0.05		3.63
^{27}Al	34.90		35.61
^{29}Si	3005		3045
^{43}Ca	176		177
^{45}Sc	4911		5233

^{49}Ti	3308		3477
^{51}V	46.8		52.8
^{53}Cr	148		160
^{55}Mn	29		15
^{57}Fe	48		51
^{59}Co	11.52		10.63
^{60}Ni	1.49		1.59
^{63}Cu	0.45		1.24
^{66}Zn	32		80
^{85}Rb	11.55		13.24
^{88}Sr	13		13
^{89}Y	0.24		0.25
^{90}Zr	0.11		0.12
^{93}Nb	2.05		0.58
^{137}Ba	0.02		0.04
^{139}La	87		700
^{140}Ce	0.58		2.07
^{141}Pr	1.30		1.63
^{146}Nd	0.22		0.47
^{147}Sm	1.18		2.40
^{153}Eu	0.67		0.92
^{157}Gd	0.34		0.49
^{159}Tb	1.31		1.61

^{163}Dy	0.28		0.31
^{165}Ho	2.08		2.25
^{166}Er	0.44		0.48
^{169}Tm	1.26		1.32
^{172}Yb	0.18		0.18
^{175}Lu	1.16		1.20
^{178}Hf	0.17		0.17
^{181}Ta	0.60		0.58
^{208}Pb	0.02		0.02
^{232}Th	0.04		0.04
^{238}U	0.05		0.02

* Oxide detection limit of 0.01 wt. %; Trace element detection limit of 0.01 ppm

A-5

Table 1: Sr isotope data for maskelynite and pyroxene grains from NWA 2046 and NWA 4925

	NWA 2046						
	Line number	$^{87}Sr/^{86}Sr$	1 std		^{87}Rb	^{86}Sr	$(Rb/Sr)_m$
Mask 2	1	-	-		0.033	7.969	0.004
	2	0.701289	0.00038				
	3	0.701513	0.00032				
Mask 3	1	-	-		0.017	7.429	0.002
	2	0.701289	0.00032				
	3	0.701513	0.00036				

	4	-	-				
Mask 4	1	0.701452	0.00034		0.043	8.278	0.005
	2	0.700971	0.00033				
	3		0.00041				
	4	0.701187	0.0005				
Mask 5-6	1	-	-		0.028	9.554	0.003
	2	0.701691	0.00042				
	3		0.00032				
	4	0.701425	0.00029				
	5		0.00034				
	6	0.701573	0.00029				
	7	0.701295	0.00025				
	8	0.701198	0.00031				
Mask 7	1	0.70143	0.00065				
	2	0.701214	0.0013				
Mask 8	1	-	-				
	2	0.701105	0.00047				
	3	0.701221	0.00087				
	4	0.701345	0.00076				
Px 1	1	0.70489	0.00004		0.058	0.894	0.065
	2	0.704275	0.00086				

	NWA 2046 weathering rind						
Mask 1	1	0.702497	0.00052				
	2	0.702149	0.001				
	3	0.70219	0.00079				
	4	0.701735	0.00094				
	NWA 4925						
Mask 2	1	0.702037	0.00033		0.012	8.618	0.001
	2	0.701533	0.00044				
	3	0.701949	0.00031				
Mask 3	1	0.701167	0.00064		0.027	11.770	0.002
	2	0.701337	0.00067				
	3	0.701457	0.00035				
	4	0.701285	0.00028				
Mask 4	1	0.701244	0.00052		0.030	8.149	0.004
Px 1	1	0.710089	0.00036		0.163	8.600	0.019
	2	0.709451	0.00040				
	3	0.710256	0.00024				
Px 4	1	0.71105	0.00067		0.101	3.155	0.032
	2	0.710678	0.00066				
	3	0.71021	0.00035				
Px 5	1	0.709593	0.00051		0.182	6.159	0.030

	2	0.709994	0.00056				
	3	0.710877	0.00037				
	NWA 4925 weathering rind						
Mask 1	1	0.70214	0.0012				
	2	0.701978	0.0011				
Mask 2	1	0.702269	0.00085				
	2	0.701918	0.0014				
Mask 3	1	0.703419	0.00061				
	2	0.702827	0.0013				
	3	0.703166	0.001				
Mask 4	1	0.703415	0.0012				
	2	0.703013	0.0022				
Mask 5	1	0.702405	0.001				
	2	0.702876	0.001				
	3	0.702892	0.00084				
	4	0.702469	0.00056				
	5	0.701628	0.00094				
	6	0.701955	0.000011				
Mask 6	1	0.702037	0.00033				
	2	0.701533	0.00044				
	3	0.701949	0.00031				

B-1

Table 1: SCOL1 standard trace element data

	SCOL1-01	SCOL1-02	SCOL1-03	SCOL1-04	SCOL1-05	SCOL1-06	SCOL1-07	SCOL1-08
^{7}Li	1.79	1.77	1.85	1.84	1.82	1.76	1.80	1.78
^{12}C	bdl	bdl	bdl	bdl	bdl	bdl	bdl	bdl
^{19}F	bdl	65.53	84.17	102.98	bdl	bdl	72.57	54.46
^{23}Na	85.96	84.60	99.75	87.91	85.67	85.21	87.15	85.70
^{24}Mg	339251.00	336786.00	341373.44	346627.97	339377.13	334420.06	337516.28	338258.31
^{25}Mg	350829.94	351823.78	352011.88	348751.94	337101.78	320072.59	310316.19	303610.00
^{27}Al	99.45	99.73	96.76	97.02	100.43	103.34	101.99	100.90
^{28}Si	190715.28	190715.28	190715.28	190715.28	190715.28	190715.28	190715.28	190715.28
^{29}Si	191942.39	190770.84	190680.17	190309.67	190659.44	194897.31	193259.69	192059.03
^{31}P	24.92	20.75	16.80	17.67	21.68	21.45	19.70	19.21
^{35}Cl	154.30	123.38	132.81	133.62	135.36	161.81	129.73	141.28
^{39}K	46.24	4.27	bdl	bdl	34.84	37.57	27.47	7.39
^{43}Ca	433.05	423.51	394.30	391.18	426.70	428.78	440.86	447.14
^{44}Ca	828.30	826.18	867.84	865.38	831.57	808.24	823.54	824.08
^{45}Sc	5.10	5.07	4.94	4.91	5.01	4.84	4.67	4.73
^{47}Ti	7.33	7.40	6.89	6.98	6.97	7.06	7.01	6.98
^{51}V	3.15	3.18	3.22	3.22	3.18	3.15	3.18	3.17
^{52}Cr	139.48	137.51	142.31	142.80	136.57	134.31	134.75	134.41
^{53}Cr	140.75	141.68	147.55	142.69	142.39	142.57	144.60	145.42

^{55}Mn	1004.26	990.82	1018.65	1020.69	991.60	973.03	997.35	979.67
^{56}Fe	97548.27	96294.47	96921.55	96370.42	82462.01	70326.25	62232.64	61752.71
^{59}Co	159.41	157.30	163.54	161.64	152.80	154.10	153.46	152.27
^{60}Ni	3213.68	3186.61	3258.88	3223.89	3187.07	3171.12	3176.46	3173.81
^{62}Ni	3184.95	3161.59	3293.25	3296.70	3196.42	3228.21	3187.22	3147.26
^{63}Cu	0.8820	0.8880	0.8980	0.8620	0.8990	0.9090	0.8950	0.8380
^{65}Cu	1.1500	1.1700	1.1500	1.1700	1.2400	1.4100	1.5600	1.6100
^{66}Zn	57.3700	57.9600	53.7000	53.0900	58.3700	58.7300	58.0100	57.0500
^{69}Ga	0.0670	0.0731	0.0765	0.0713	0.0745	0.0712	0.0723	0.0653
^{71}Ga	0.0269	0.0266	0.0278	0.0303	0.0232	0.0269	0.0315	0.0293
^{72}Ge	0.5900	0.5700	0.6000	0.6500	0.6700	0.7600	0.7900	0.8500
^{73}Ge	0.5600	0.5400	0.5500	0.5300	0.5500	0.6600	0.7200	0.7500
^{74}Ge	0.5600	0.5400	0.5500	0.5700	0.6000	0.6400	0.7200	0.7400
^{75}As	0.0710	0.0420	0.0480	0.0590	0.0490	0.0500	0.0400	0.0400
^{79}Br	bdl	bdl	bdl	bdl	bdl	bdl	bdl	bdl
^{85}Rb	0.0002	0.0013	0.0007	bdl	0.0035	0.0026	0.0005	0.0014
^{86}Sr	0.1580	bdl	bdl	bdl	0.0790	0.0510	bdl	bdl
^{88}Sr	0.0005	0.0009	0.0006	0.0004	0.0004	0.0003	0.0010	0.0013
^{89}Y	0.0320	0.0323	0.0317	0.0320	0.0325	0.0327	0.0343	0.0338
^{90}Zr	0.0650	0.0666	0.0593	0.0583	0.0704	0.0718	0.0693	0.0737
^{93}Nb	0.0019	0.0038	0.0024	0.0024	0.0018	0.0025	0.0022	0.0091
^{95}Mo	0.0160	0.0180	0.0180	0.0210	0.0220	0.0200	0.0200	0.0220
^{98}Mo	0.3000	0.2900	0.3000	0.2900	0.3200	0.3600	0.4200	0.4100

^{107}Ag	bdl	bdl	0.0004	bdl	0.0280	0.0002	0.0007	0.0002
^{109}Ag	bdl	bdl	0.0004	0.0027	0.0003	0.0003	0.0001	bdl
^{111}Cd	0.0160	0.0120	0.0150	0.0110	0.0220	0.0130	0.0190	0.0180
^{112}Cd	0.0310	0.0210	0.0250	0.0230	0.0240	0.0260	0.0260	0.0310
^{114}Cd	0.0220	0.0190	0.0220	0.0220	0.0250	0.0190	0.0180	0.0220
^{115}In	0.0025	0.0025	0.0023	0.0031	0.0028	0.0042	0.0040	0.0040
^{118}Sn	0.2300	0.1900	0.1900	0.1700	0.1900	0.2100	0.2200	0.2000
^{120}Sn	0.2200	0.2000	0.1800	0.1800	0.2000	0.2100	0.2300	0.2000
^{121}Sb	0.0200	0.0100	0.0130	0.0100	0.0054	0.0040	0.0027	0.0040
^{123}Sb	0.0150	0.0100	0.0130	0.0100	0.0080	0.0040	0.0800	0.0026
^{127}I	bdl	bdl	bdl	bdl	bdl	bdl	bdl	bdl
^{133}Cs	0.0002	0.0014	bdl	bdl	bdl	0.0013	bdl	bdl
^{137}Ba	bdl	0.0018	0.0012	0.0027	0.0005	bdl	0.0054	0.0042
^{138}Ba	0.0001	0.0042	0.0025	0.0003	bdl	0.0006	0.0033	0.0009
^{139}La	bdl	bdl	bdl	bdl	bdl	bdl	0.0001	0.0002
^{140}Ce	0.0003	0.0005	0.0002	bdl	0.0003	bdl	0.0008	0.0006
^{141}Pr	bdl	bdl	0.0001	bdl	bdl	0.0001	bdl	bdl
^{146}Nd	bdl	0.0004	bdl	0.0003	0.0001	bdl	0.0005	0.0005
^{147}Sm	bdl	0.0001	bdl	0.0002	bdl	0.0002	bdl	bdl
^{153}Eu	bdl	0.0001	0.0001	bdl	bdl	0.0001	0.0003	0.0001
^{157}Gd	0.0018	0.0009	0.0005	0.0006	0.0006	0.0004	0.0004	0.0016
^{159}Tb	0.0003	0.0002	0.0002	0.0002	0.0002	0.0002	0.0004	0.0001
^{163}Dy	0.0029	0.0031	0.0018	0.0029	0.0015	0.0035	0.0036	0.0028

^{165}Ho	0.0008	0.0014	0.0008	0.0011	0.0012	0.0006	0.0012	0.0011
^{166}Er	0.0043	0.0057	0.0051	0.0039	0.0072	0.0060	0.0046	0.0047
^{169}Tm	0.0015	0.0013	0.0009	0.0014	0.0006	0.0012	0.0013	0.0013
^{172}Yb	0.0137	0.0110	0.0112	0.0110	0.0107	0.0168	0.0138	0.0107
^{175}Lu	0.0038	0.0033	0.0030	0.0028	0.0026	0.0040	0.0035	0.0027
^{178}Hf	0.0007	0.0003	0.0015	0.0017	0.0011	0.0008	0.0008	0.0023
^{181}Ta	bdl	0.0002	0.0001	0.0001	0.0002	0.0001	bdl	0.0011
^{182}W	0.0001	0.0002	0.0002	0.0001	bdl	0.0003	0.0006	0.0001
^{183}W	0.0001	bdl	0.0002	0.0002	0.0001	bdl	0.0004	bdl
^{184}W	0.0001	0.0002	0.0003	bdl	bdl	bdl	0.0007	bdl
^{185}Re	0.0001	bdl	bdl	0.0003	0.0002	0.0002	bdl	0.0001
^{187}Re	0.0012	bdl	0.0001	bdl	0.0014	0.0003	0.0001	0.0002
^{205}Tl	bdl	bdl	0.0002	bdl	bdl	bdl	0.0001	bdl
^{208}Pb	0.0062	0.0076	0.0024	0.0019	0.0012	0.0014	0.0044	0.0018
^{209}Bi	bdl	bdl	0.0003	bdl	0.0005	0.0006	bdl	bdl
^{232}Th	bdl	bdl	0.0002	0.0001	0.0003	bdl	bdl	0.0014
^{238}U	bdl	0.0001	0.0001	bdl	0.0001	0.0004	bdl	0.0007

*Trace element detection limit of 0.0001 ppm

Table 2: 1-355OL standard trace element data

	1-355OL501	1-355OL502	1-355OL503	1-355OL504	1-355OL505	1-355OL506	1-355OL507	1-355OL508
^{7}Li	1.06	1.05	1.04	1.03	1.03	1.06	1.05	0.98

^{12}C	bdl	bdl	bdl	bdl	bdl	bdl	bdl	bdl
^{19}F	134.58	102.85	56.39	49.69	bdl	29.19	3.71	29.17
^{23}Na	98.17	106.90	135.68	133.11	135.00	132.21	158.61	131.07
^{24}Mg	332969.75	333785.94	340885.16	348363.63	346208.94	358006.22	350040.75	336761.56
^{25}Mg	366097.38	374589.59	306474.75	359519.31	355143.44	358390.25	356776.81	299349.31
^{27}Al	61.09	64.54	70.58	69.77	69.15	66.44	67.35	68.94
^{28}Si	190798.67	191885.34	190715.28	192131.61	190715.28	190715.30	186948.06	190715.28
^{29}Si	190715.30	190715.31	192225.73	190715.27	191197.23	190241.11	190715.27	186637.66
^{31}P	59.38	61.08	50.25	54.74	50.48	49.19	55.16	47.52
^{35}Cl	122.71	131.76	160.48	166.74	216.39	167.94	243.37	224.57
^{39}K	20.66	15.66	2.12	9.23	bdl	bdl	bdl	5.19
^{43}Ca	119.68	124.16	134.25	140.20	146.09	119.77	125.49	141.10
^{44}Ca	578.79	536.80	534.66	480.33	543.27	595.23	459.98	534.24
^{45}Sc	2.88	2.89	2.14	2.25	2.49	2.57	2.13	2.16
^{47}Ti	10.59	11.46	11.59	9.98	11.78	10.60	9.72	11.03
^{51}V	5.94	5.87	5.63	5.93	5.75	5.79	5.72	5.64
^{52}Cr	224.22	223.23	199.97	212.49	211.25	215.89	207.26	198.48
^{53}Cr	225.04	218.26	214.56	218.02	218.44	220.72	213.45	211.81
^{55}Mn	646.68	634.33	593.95	618.35	615.67	625.13	607.26	589.18
^{56}Fe	66183.77	65145.23	42841.84	54659.30	64109.62	64502.11	54783.71	41738.62
^{59}Co	141.34	139.58	128.51	132.00	129.74	136.60	131.56	124.72
^{60}Ni	3098.04	3052.94	2963.28	3066.18	2945.81	2998.17	3055.39	2826.44
^{62}Ni	3165.17	3155.86	2965.47	3039.23	2945.19	3048.83	3028.05	2882.87

^{63}Cu	0.7870	0.7910	0.8020	0.8630	0.8150	0.7850	0.8490	0.7930
^{65}Cu	1.1100	1.1400	1.5500	1.6000	1.6600	1.7200	2.0500	2.0300
^{66}Zn	48.8700	48.3900	48.8800	49.5500	49.6200	48.7800	48.6500	46.6400
^{69}Ga	0.0756	0.0753	0.0691	0.0795	0.0681	0.0741	0.0740	0.0700
^{71}Ga	0.0374	0.0276	0.0376	0.0335	0.0325	0.0356	0.0358	0.0304
^{72}Ge	0.4100	0.4400	0.5700	0.5500	0.5900	1.5400	2.1800	2.3200
^{73}Ge	0.3600	0.3700	0.4600	0.4700	0.5100	0.5500	1.9000	1.9400
^{74}Ge	0.3400	0.3500	0.2600	0.4600	0.5700	0.5300	2.4000	2.3800
^{75}As	0.0480	0.0510	0.0600	0.0600	0.0810	0.0870	0.9500	0.7800
^{79}Br	bdl	bdl	bdl	bdl	bdl	bdl	bdl	bdl
^{85}Rb	bdl	bdl	0.0010	bdl	0.0025	0.0014	0.0002	0.0008
^{86}Sr	0.0030	0.0020	bdl	bdl	bdl	0.0140	0.0290	bdl
^{88}Sr	0.0023	0.0040	0.0037	0.0007	0.0028	0.0045	0.0013	0.0027
^{89}Y	0.0008	0.0007	0.0002	0.0006	0.0006	0.0007	0.0001	0.0005
^{90}Zr	0.0962	0.0933	0.0982	0.1065	0.1051	0.0893	0.0950	0.1063
^{93}Nb	0.5310	0.5490	0.5590	0.3390	0.4810	0.2910	0.3280	0.5090
^{95}Mo	0.0120	0.0110	0.0190	0.0190	0.0150	0.0130	0.0100	0.0100
^{98}Mo	0.2900	0.2900	0.4000	0.3900	0.3300	0.3400	0.2500	0.2700
^{107}Ag	bdl	bdl	bdl	0.0001	0.0010	0.0006	bdl	0.0700
^{109}Ag	0.0001	0.0009	bdl	bdl	bdl	0.0007	bdl	bdl
^{111}Cd	0.0080	0.0080	0.0110	0.0100	0.0107	0.0050	0.1700	0.1200
^{112}Cd	0.0170	0.0190	0.0250	0.0190	0.9700	0.0390	0.3500	0.3200
^{114}Cd	0.0140	0.0150	0.0130	0.0210	0.0240	0.0180	0.2100	0.1300

^{115}In	0.0010	0.0012	0.0015	0.0017	0.0017	0.0025	0.0290	0.0200
^{118}Sn	0.1900	0.1700	0.2200	0.2600	0.3200	0.2600	1.6300	1.7000
^{120}Sn	0.2000	0.1700	0.2200	0.2400	0.3000	0.2600	1.5300	1.5600
^{121}Sb	0.0060	0.0070	0.0030	0.0040	0.0062	bdl	0.3100	0.3900
^{123}Sb	0.0110	0.0100	0.0012	0.0030	0.0140	bdl	0.0800	0.3400
^{127}I	bdl	bdl	bdl	bdl	bdl	bdl	bdl	bdl
^{133}Cs	bdl	bdl	0.0020	0.0007	0.0024	0.0004	bdl	bdl
^{137}Ba	0.0017	bdl	bdl	0.0054	0.0015	0.0055	bdl	0.0030
^{138}Ba	0.0001	0.0016	0.0008	0.0003	0.0015	0.0046	0.0002	0.0016
^{139}La	0.0002	0.0002	0.0003	0.0001	0.0005	0.0009	bdl	bdl
^{140}Ce	0.0002	0.0012	0.0008	0.0001	0.0012	0.0032	0.0001	0.2550
^{141}Pr	0.0001	0.0002	0.0002	bdl	0.0001	0.0004	bdl	0.0001
^{146}Nd	0.0003	0.0013	0.0007	bdl	0.0008	0.0022	0.0003	bdl
^{147}Sm	0.0002	bdl	0.0004	0.0004	bdl	0.0004	bdl	bdl
^{153}Eu	0.0001	bdl	0.0001	0.0002	0.0004	bdl	bdl	0.0011
^{157}Gd	0.0004	bdl	0.0003	0.0003	bdl	0.0002	bdl	0.0013
^{159}Tb	bdl	bdl	bdl	bdl	bdl	bdl	bdl	bdl
^{163}Dy	bdl	bdl	bdl	0.0001	bdl	0.0003	0.0002	0.0011
^{165}Ho	bdl	bdl	bdl	bdl	bdl	0.0001	0.0002	0.0005
^{166}Er	bdl	bdl	bdl	bdl	bdl	bdl	bdl	bdl
^{169}Tm	bdl	bdl	bdl	bdl	bdl	0.0001	bdl	0.0003
^{172}Yb	0.0004	bdl	0.0002	bdl	0.0002	bdl	bdl	0.0012
^{175}Lu	bdl	0.0001	bdl	0.0002	bdl	bdl	0.0001	bdl

^{178}Hf	0.0030	0.0019	0.0020	0.0039	0.0046	0.0021	0.0025	0.0036
^{181}Ta	0.0290	0.0341	0.0338	0.0222	0.0323	0.0216	0.0245	0.0315
^{182}W	0.0014	0.0001	0.0004	bdl	bdl	bdl	bdl	bdl
^{183}W	0.0013	0.0001	bdl	0.0005	bdl	bdl	0.0038	0.0030
^{184}W	bdl	0.0001	bdl	0.0001	0.0001	bdl	0.3000	bdl
^{185}Re	0.0003	0.0003	0.0002	0.0001	0.0003	0.0012	0.0004	0.0026
^{187}Re	bdl	0.0001	bdl	bdl	0.0003	0.0003	0.0080	bdl
^{205}Tl	0.0003	0.0001	bdl	bdl	bdl	bdl	bdl	bdl
^{208}Pb	0.0010	0.0019	0.0014	0.0023	0.0026	0.0025	0.0027	0.1111
^{209}Bi	bdl	0.0005	bdl	0.0006	0.0003	0.0004	bdl	bdl
^{232}Th	bdl	bdl	bdl	bdl	bdl	0.0003	bdl	bdl
^{238}U	bdl	0.0001	0.0001	0.0001	0.0001	0.0003	bdl	bdl

*Trace element detection limit of 0.0001 ppm

Table 3: SH11-2 standard trace element data

	SH11-2-101	SH11-2-102	SH11-2-103	SH11-2-104	1-SH112-105	1-SH112-106	1-SH112-107	1-SH112-108
^{7}Li	2.14	2.19	2.10	2.07	2.16	2.17	2.15	2.16
^{12}C	bdl	bdl	bdl	bdl	bdl	bdl	bdl	bdl
^{19}F	81.89	100.72	48.06	47.30	26.18	36.29	56.99	52.10
^{23}Na	159.01	160.21	157.91	158.90	145.30	90.75	148.14	146.60
^{24}Mg	333393.78	332497.84	329092.34	325190.84	316042.03	313386.50	331003.00	332411.69

^{25}Mg	247896.44	247334.13	339319.72	346488.03	293686.75	296761.25	201507.14	204233.56
^{27}Al	241.78	248.73	257.77	257.68	252.99	256.99	231.35	239.66
^{28}Si	190762.02	190762.02	190762.02	190762.02	189801.88	192991.81	190148.42	192975.19
^{29}Si	190761.98	190761.97	190762.00	190762.00	190715.28	190715.28	190715.31	190715.33
^{31}P	58.12	52.54	56.15	56.60	74.04	71.98	59.60	58.66
^{35}Cl	141.97	144.41	144.61	159.01	171.83	193.57	173.35	205.63
^{39}K	bdl	bdl	0.39	bdl	0.41	58.02	40.69	49.63
^{43}Ca	553.20	559.21	582.37	601.05	602.56	612.15	671.73	668.41
^{44}Ca	1012.92	1025.46	1018.45	1034.78	980.88	950.70	1085.78	1055.29
^{45}Sc	4.97	4.68	4.55	4.51	5.12	5.11	4.40	4.41
^{47}Ti	38.31	35.80	39.64	38.18	36.71	36.11	39.59	39.02
^{51}V	4.34	4.39	5.84	5.87	5.14	5.02	3.40	3.33
^{52}Cr	128.64	126.09	118.92	120.63	130.45	130.23	125.11	125.73
^{53}Cr	132.95	132.80	129.24	131.41	131.69	133.30	129.67	130.99
^{55}Mn	1200.75	1209.62	1140.11	1153.20	1213.74	1239.78	1174.67	1186.83
^{56}Fe	111523.66	111898.05	71992.75	71913.59	108844.70	109105.16	90637.96	90820.93
^{59}Co	172.40	172.18	160.84	163.46	174.72	177.32	169.83	171.44
^{60}Ni	3003.91	3031.25	2893.80	2953.88	3097.34	3145.73	3049.19	3061.58
^{62}Ni	3011.51	3082.22	2928.34	2960.62	3161.45	3248.70	3007.77	3063.32
^{63}Cu	0.9200	0.9300	1.2400	1.2400	1.2400	1.2300	1.5300	1.4200
^{65}Cu	1.3900	1.4500	1.9400	1.9400	2.0400	1.9700	2.6000	2.4100
^{66}Zn	68.4300	67.6400	65.6300	67.1200	67.6500	66.0000	65.7200	67.1100
^{69}Ga	0.1000	0.1000	0.1400	0.1300	0.1200	0.1400	0.0960	0.0180

^{71}Ga	0.0700	0.0700	0.1000	0.1000	0.1070	0.1070	0.1130	bdl
^{72}Ge	0.6600	0.6400	0.8200	0.8300	0.9400	0.9000	3.0100	bdl
^{73}Ge	0.5700	0.5600	0.7000	0.7200	0.8600	0.8300	2.6400	2.6500
^{74}Ge	0.5400	0.5500	0.7300	0.7400	0.8600	0.8500	3.3200	3.1800
^{75}As	0.0600	0.0600	0.0500	0.0600	0.0850	0.0900	0.3900	0.6200
^{79}Br	bdl	bdl	bdl	bdl	bdl	bdl	bdl	bdl
^{85}Rb	0.0004	0.0017	0.0004	bdl	bdl	bdl	bdl	bdl
^{86}Sr	0.0310	bdl	0.0450	bdl	bdl	bdl	bdl	bdl
^{88}Sr	0.0062	0.0059	0.0088	0.0069	0.0062	0.0048	0.0058	0.0064
^{89}Y	0.0460	0.0470	0.0700	0.0600	0.0579	0.0602	0.0646	0.0649
^{90}Zr	0.0328	0.0358	0.0379	0.0401	0.0365	0.0385	0.0385	0.0398
^{93}Nb	0.0018	0.0031	0.0025	0.0028	0.0021	0.0022	0.0051	0.0041
^{95}Mo	0.0200	0.0200	0.0270	0.0400	0.0230	0.0310	0.0230	0.0230
^{98}Mo	0.2900	0.3100	0.3800	0.4000	0.3400	0.3400	0.2400	0.2600
^{107}Ag	bdl	0.0004	bdl	bdl	bdl	bdl	bdl	bdl
^{109}Ag	bdl	0.0004	bdl	bdl	0.0001	bdl	bdl	bdl
^{111}Cd	0.0170	0.0230	0.0270	0.0210	0.0260	0.0200	0.2100	0.1700
^{112}Cd	0.0290	0.0300	0.0270	0.0260	0.0420	0.0340	0.4200	0.3200
^{114}Cd	0.0210	0.0220	0.0270	0.0240	0.0270	0.0320	0.3000	0.2700
^{115}In	0.0059	0.0053	0.0060	0.0070	0.0090	0.0087	0.0900	0.0760
^{118}Sn	0.1800	0.2000	0.2000	0.2100	0.2400	0.2800	1.2100	1.3400
^{120}Sn	0.1800	0.2000	0.2000	0.2200	0.2600	0.2800	1.2500	1.3000
^{121}Sb	0.0130	0.6500	0.0060	0.0080	0.0004	0.0040	0.1800	0.2300

^{123}Sb	0.0100	0.0120	0.0040	0.0040	0.0059	0.0022	0.1600	0.1000
^{127}I	bdl	bdl	bdl	bdl	bdl	bdl	bdl	bdl
^{133}Cs	bdl	0.0001	0.0008	0.0011	0.0001	0.0002	bdl	bdl
^{137}Ba	bdl	0.0028	bdl	bdl	bdl	bdl	0.0008	bdl
^{138}Ba	0.0003	0.0377	0.0004	0.0009	0.0017	0.0017	0.0002	bdl
^{139}La	0.0001	bdl	0.0004	0.0002	0.0002	0.0012	bdl	bdl
^{140}Ce	0.0003	0.0001	0.0004	0.0002	0.0002	0.0002	0.0002	0.0002
^{141}Pr	bdl	0.0001	bdl	0.0001	bdl	bdl	bdl	bdl
^{146}Nd	0.0002	0.0005	0.0002	bdl	0.0007	0.0005	0.0006	0.0004
^{147}Sm	0.0010	0.0004	bdl	0.0001	0.0005	bdl	0.0002	bdl
^{153}Eu	0.0002	0.0004	0.0004	0.0003	0.0003	0.0002	0.0010	bdl
^{157}Gd	0.0014	0.0007	0.0021	0.0008	0.0014	0.0016	0.0040	0.0014
^{159}Tb	0.0003	0.0006	0.0002	0.0007	0.0003	0.0005	0.0006	0.0005
^{163}Dy	0.0055	0.0046	0.0053	0.0053	0.0061	0.0052	0.0043	0.0066
^{165}Ho	0.0010	0.0018	0.0021	0.0015	0.0021	0.0023	0.0023	0.0021
^{166}Er	0.0114	0.0082	0.0103	0.0108	0.0115	0.0097	0.0085	0.0093
^{169}Tm	0.0019	0.0019	0.0029	0.0024	0.0026	0.0023	0.0015	0.0019
^{172}Yb	0.0160	0.0240	0.0260	0.0240	0.0260	0.0280	0.1000	0.0870
^{175}Lu	0.0058	0.0051	0.0063	0.0059	0.0064	0.0048	0.0063	0.0060
^{178}Hf	0.0005	0.0013	0.0009	0.0004	0.0014	0.0010	0.0062	0.0040
^{181}Ta	bdl	bdl	bdl	bdl	bdl	bdl	bdl	bdl
^{182}W	0.0023	0.0001	0.0002	0.0004	bdl	bdl	bdl	bdl
^{183}W	0.0040	bdl	0.0001	0.0002	bdl	bdl	bdl	bdl

^{184}W	bdl	bdl	0.0002	bdl	bdl	bdl	bdl	bdl
^{185}Re	0.0002	0.0003	0.0001	0.0004	0.0001	bdl	0.0009	0.0035
^{187}Re	bdl	bdl	0.0003	0.0003	0.0003	0.0003	0.0006	bdl
^{205}Tl	bdl	bdl	0.0006	bdl	bdl	0.0004	0.0046	bdl
^{208}Pb	0.0008	0.0003	0.0026	0.0015	0.0021	0.0017	0.0028	0.0031
^{209}Bi	bdl	bdl	0.0005	bdl	0.0003	0.0004	0.0150	0.0070
^{232}Th	bdl	bdl	0.0001	bdl	bdl	bdl	bdl	bdl
^{238}U	bdl	bdl	bdl	bdl	0.0001	bdl	bdl	0.0001

*Trace element detection limit of 0.0001 ppm

Table 4: MOnGOL standard trace element data

	MOnGOL-01	MOnGOL-02	MOnGOL-03	MOnGOL-04	MOnGOL-05	MOnGOL-06
^{7}Li	2.13	2.11	2.12	2.06	2.02	2.05
^{12}C	bdl	bdl	bdl	bdl	bdl	bdl
^{19}F	65.17	62.79	43.86	41.89	196.99	585.83
^{23}Na	163.61	164.25	167.32	165.67	173.40	175.41
^{24}Mg	331072.25	332900.13	350226.84	342392.06	262992.16	260085.11
^{25}Mg	340408.00	345140.66	357734.63	351326.44	287603.72	280298.63
^{27}Al	254.36	259.41	263.69	260.81	258.63	245.91
^{28}Si	190434.81	190434.81	190434.81	190434.81	190434.81	190434.81
^{29}Si	189478.81	189698.61	192181.53	190400.27	188177.66	189045.88
^{31}P	56.25	59.86	57.03	56.62	70.02	68.96

^{35}Cl	148.03	156.25	172.11	149.52	246.38	210.01
^{39}K	bdl	bdl	bdl	bdl	bdl	bdl
^{43}Ca	570.07	565.17	594.66	563.78	548.64	535.17
^{44}Ca	943.73	936.12	941.45	910.28	895.61	895.78
^{45}Sc	4.69	4.74	4.45	4.42	4.12	4.07
^{47}Ti	36.49	36.69	37.71	38.06	33.09	32.49
^{51}V	5.68	5.64	5.94	5.63	5.42	5.29
^{52}Cr	127.03	124.56	126.63	125.57	123.34	125.57
^{53}Cr	132.53	133.34	138.69	137.54	134.93	134.01
^{55}Mn	1187.05	1178.74	1221.88	1210.59	1154.42	1165.66
^{56}Fe	81392.22	80855.87	86618.32	85749.02	78382.99	80602.78
^{59}Co	168.15	163.01	161.83	158.86	152.59	153.66
^{60}Ni	3106.04	3074.09	3233.41	3190.65	3177.48	3183.63
^{62}Ni	2977.41	2935.97	3125.11	3073.89	3114.14	3117.42
^{63}Cu	1.1190	1.1350	1.1230	1.1380	1.2700	1.2720
^{65}Cu	1.9150	1.8310	1.7400	1.9200	1.9620	1.9280
^{66}Zn	67.5800	65.8600	67.1300	66.3900	69.4800	70.5000
^{69}Ga	0.1290	0.1256	0.1262	0.1399	0.1411	0.1421
^{71}Ga	0.0977	0.0949	0.1021	0.0913	0.0969	0.1017
^{72}Ge	0.7020	0.6890	0.6390	0.7140	0.8140	0.9660
^{73}Ge	0.6660	0.6200	0.6870	0.6570	0.7420	0.7910
^{74}Ge	0.6450	0.6510	0.6290	0.6350	0.7630	0.8030
^{75}As	0.0799	0.0728	0.0787	0.0672	0.0728	0.0625

^{79}Br	bdl	bdl	bdl	bdl	65.7900	57.6200
^{85}Rb	0.0019	0.0010	0.0014	bdl	0.0054	bdl
^{86}Sr	bdl	bdl	0.1240	0.1480	0.0390	0.0830
^{88}Sr	0.0066	0.0055	0.0052	0.0061	0.0073	0.0040
^{89}Y	0.0637	0.0590	0.0556	0.0590	0.0597	0.0556
^{90}Zr	0.0339	0.0358	0.0342	0.0433	0.0538	0.0332
^{93}Nb	0.0030	0.0022	0.0033	0.0036	0.0042	0.0029
^{95}Mo	0.0294	0.0284	0.0196	0.0976	0.0330	0.0286
^{98}Mo	0.3370	0.3340	0.3390	0.3470	0.3570	0.3540
^{107}Ag	0.0007	0.0001	0.0002	0.0006	0.0011	0.0006
^{109}Ag	0.0002	bdl	0.0001	0.0044	0.0013	bdl
^{111}Cd	0.0134	0.0160	0.0112	0.0188	0.0228	0.0264
^{112}Cd	0.0289	0.0355	0.0351	0.0286	0.0274	0.0311
^{114}Cd	0.0301	0.0346	0.0235	0.0243	0.0310	0.0415
^{115}In	0.0057	0.0078	0.0066	0.0061	0.0069	0.0069
^{118}Sn	0.2040	0.1953	0.2220	0.2030	0.2040	0.1670
^{120}Sn	0.1915	0.1894	0.2470	0.2080	0.1860	0.1674
^{121}Sb	0.0013	bdl	bdl	0.0020	0.0026	bdl
^{123}Sb	0.0002	bdl	0.0015	0.0026	0.0014	0.0023
^{127}I	bdl	bdl	bdl	bdl	0.0085	0.0072
^{133}Cs	0.0009	bdl	0.0009	bdl	0.0027	bdl
^{137}Ba	0.0090	0.0018	0.0839	bdl	0.0037	0.0003
^{138}Ba	0.0068	0.0001	bdl	bdl	0.0030	bdl

^{139}La	0.0002	bdl	bdl	0.0001	0.0002	bdl
^{140}Ce	0.0005	0.0003	0.0003	0.0002	0.0021	0.0003
^{141}Pr	0.0001	bdl	0.0001	bdl	0.0019	bdl
^{146}Nd	0.0002	0.0001	0.0005	0.0003	0.0015	0.0005
^{147}Sm	0.0002	0.0002	0.0007	bdl	0.0016	bdl
^{153}Eu	0.0005	bdl	0.0003	0.0001	0.0013	0.0002
^{157}Gd	0.0022	0.0006	0.0030	0.0024	bdl	bdl
^{159}Tb	0.0006	0.0005	0.0004	0.0006	0.0017	0.0003
^{163}Dy	0.0027	0.0034	0.0068	0.0065	0.0060	0.0037
^{165}Ho	0.0021	0.0018	0.0022	0.0017	0.0037	0.0018
^{166}Er	0.0125	0.0097	0.0073	0.0099	0.0075	0.0089
^{169}Tm	0.0034	0.0027	0.0025	0.0024	0.0034	0.0022
^{172}Yb	0.0294	0.0253	0.0252	0.0236	0.0234	0.0217
^{175}Lu	0.0048	0.0059	0.0063	0.0057	0.0064	0.0056
^{178}Hf	0.0038	bdl	0.0005	0.0022	0.0035	0.0006
^{181}Ta	0.0005	bdl	bdl	bdl	0.0020	bdl
^{182}W	bdl	bdl	bdl	0.0002	bdl	bdl
^{183}W	0.0003	0.0002	bdl	0.0023	0.0071	bdl
^{184}W	0.0001	bdl	0.0002	0.0002	0.0025	0.0001
^{185}Re	0.0003	0.0003	bdl	bdl	0.0001	0.0001
^{187}Re	0.0002	0.0001	0.0001	0.0049	bdl	bdl
^{205}Tl	0.0002	0.0002	bdl	0.0015	0.0004	bdl
^{208}Pb	0.0032	0.0023	0.0019	0.0019	0.0054	0.0020

^{209}Bi	0.0001	0.0002	bdl	0.0002	0.0006	0.0009
^{232}Th	0.0003	bdl	bdl	bdl	0.0020	bdl
^{238}U	0.0002	bdl	bdl	0.0001	0.0017	0.0001

*Trace element detection limit of 0.0001 ppm

Table 5: BO2OL01 standard trace element data

	BO2OL01-1	BO2OL01-2	BO2OL01-3	BO2OL01-4	BO2OL01-5	BO2OL01-6	BO2OL01-7	BO2OL01-8	BO2OL01-9
^{7}Li	1.77	1.75	1.69	1.67	1.69	1.74	1.66	1.61	1.71
^{12}C	bdl	bdl	bdl	bdl	bdl	bdl	bdl	bdl	bdl
^{19}F	417.51	440.49	419.02	410.16	70.48	45.73	46.18	66.42	76.66
^{23}Na	29.23	48.29	60.73	76.33	62.14	73.97	69.81	88.91	89.67
^{24}Mg	315142.66	312886.28	336945.91	334965.94	328342.09	325858.66	328677.56	344339.56	343207.34
^{25}Mg	352887.84	356699.41	340568.97	340144.66	333216.81	328895.38	334433.94	352620.28	358143.44
^{27}Al	110.73	113.08	113.61	114.99	123.56	116.99	125.11	97.88	100.42
^{28}Si	190561.61	189632.14	191214.03	190651.08	190704.70	189474.48	192176.56	186975.75	186975.75
^{29}Si	190715.31	190715.33	190715.27	190715.27	190715.27	190715.25	190715.27	186952.28	186823.98
^{31}P	66.11	64.23	58.22	58.66	58.37	60.46	59.87	19.40	22.03
^{35}Cl	164.78	220.36	197.41	261.27	171.06	182.79	199.62	202.73	170.25
^{39}K	35.90	20.01	108.17	bdl	1489.79	197.70	422.74	bdl	bdl
^{43}Ca	360.77	365.16	404.11	420.08	437.79	412.55	398.81	378.54	364.12
^{44}Ca	800.52	814.25	730.86	738.17	733.86	740.65	748.40	723.20	719.20
^{45}Sc	4.57	4.58	3.89	3.97	3.95	3.77	3.87	3.49	3.54

^{47}Ti	7.29	7.72	7.63	7.84	8.23	7.69	7.92	9.08	8.83
^{51}V	3.31	3.39	3.32	3.36	3.34	3.34	3.42	2.73	2.53
^{52}Cr	85.97	86.87	81.54	80.60	82.10	81.41	81.66	76.90	77.24
^{53}Cr	85.93	87.54	86.73	86.56	88.16	89.25	88.07	83.88	84.98
^{55}Mn	1103.28	1115.70	1064.80	1059.19	1018.23	1044.34	1033.04	1078.61	1080.01
^{56}Fe	92852.60	92342.24	77851.02	76876.08	57099.09	56834.30	56682.46	71735.52	72476.64
^{59}Co	170.21	167.68	164.66	162.51	153.08	154.85	154.78	151.77	151.86
^{60}Ni	3399.00	3475.05	3314.26	3298.29	3210.26	3263.02	3250.10	3290.33	3302.43
^{62}Ni	3482.50	3503.36	3334.77	3248.95	3194.01	3268.80	3240.18	3107.68	3199.06
^{63}Cu	2.0930	2.0940	2.1020	2.0450	2.0040	2.1340	2.0440	1.3170	1.3090
^{65}Cu	2.7420	2.8020	2.8100	2.7200	3.0300	3.1100	3.0100	3.4800	3.4900
^{66}Zn	55.4700	58.1000	55.9500	54.2300	53.1600	56.1600	55.8300	51.8500	51.7800
^{69}Ga	0.0739	0.0775	0.0782	0.0727	0.0647	0.0758	0.0706	0.0675	0.0745
^{71}Ga	0.0293	0.0317	0.0286	0.0338	0.0305	0.0309	0.0324	0.0260	0.0271
^{72}Ge	0.7260	0.7470	0.8980	0.7220	0.9000	0.9200	0.8400	2.5800	2.5500
^{73}Ge	0.7190	0.6890	0.7100	0.6930	0.8000	0.8500	0.8000	2.2200	2.2200
^{74}Ge	0.6560	0.7220	0.7730	0.7060	0.8500	0.8600	0.8000	2.7400	2.7900
^{75}As	0.1299	0.1309	0.0990	0.0959	0.1050	0.1190	0.1090	0.6100	0.5200
^{79}Br	65.5700	69.6500	53.4700	68.2200	bdl	bdl	bdl	bdl	bdl
^{85}Rb	bdl	bdl	bdl	bdl	bdl	0.0053	0.0028	bdl	0.0005
^{86}Sr	bdl	0.0730	bdl	bdl	bdl	0.0890	bdl	bdl	0.0650
^{88}Sr	0.0041	0.0385	0.0056	0.0053	0.0034	0.0054	0.0053	0.0024	0.0021
^{89}Y	0.0243	0.0341	0.0246	0.0272	0.0270	0.0265	0.0275	0.0209	0.0194

^{90}Zr	0.0051	0.0079	0.0075	0.0052	0.0082	0.0107	0.0088	0.0058	0.0038
^{93}Nb	0.0293	0.0436	0.0271	0.0222	0.0255	0.0255	0.0251	0.0002	bdl
^{95}Mo	0.0273	0.0228	0.0270	0.0256	0.0290	0.0270	0.0260	0.0150	0.0220
^{98}Mo	0.3100	0.3230	0.3940	0.3610	0.3300	0.3500	0.3400	0.2700	0.2800
^{107}Ag	bdl	bdl	0.0002	bdl	bdl	0.0002	bdl	bdl	bdl
^{109}Ag	bdl	bdl	0.0012	0.0001	0.0008	bdl	0.0005	bdl	bdl
^{111}Cd	0.0255	0.0349	0.0143	0.0186	0.0270	0.0250	0.0250	0.1900	0.1500
^{112}Cd	0.0370	0.0334	0.0281	0.0334	0.0350	0.0190	0.0350	0.2600	0.2200
^{114}Cd	0.0365	0.0320	0.0262	0.0341	0.0290	0.0240	0.0310	0.2300	0.2000
^{115}In	0.0046	0.0032	0.0034	0.0026	0.0056	0.0036	0.0055	0.0410	0.0360
^{118}Sn	0.2150	0.1990	0.1610	0.2050	0.2800	0.2800	0.3400	1.2800	1.0500
^{120}Sn	0.2100	0.2110	0.1730	0.2030	0.3000	0.2900	0.3000	1.2200	1.0900
^{121}Sb	0.0264	0.0255	0.0019	bdl	0.0025	0.0063	0.0059	0.0800	0.1300
^{123}Sb	0.0130	0.0289	0.0048	bdl	0.0069	0.0070	0.0099	0.0400	0.0700
^{127}I	0.0081	0.0085	0.0069	0.0088	bdl	bdl	bdl	bdl	bdl
^{133}Cs	bdl	0.0512	0.0001	0.0008	0.0010	0.0010	bdl	0.0004	0.0004
^{137}Ba	0.0036	0.0470	0.0067	bdl	bdl	0.0025	0.0020	bdl	bdl
^{138}Ba	0.0020	0.0367	0.0024	0.0006	0.0029	0.0007	0.0002	0.0002	bdl
^{139}La	0.0002	0.0100	0.0009	0.0004	0.0003	0.0002	bdl	bdl	bdl
^{140}Ce	0.0008	0.0054	0.0009	0.0010	0.0002	0.0009	0.0005	0.0002	bdl
^{141}Pr	0.0002	0.0019	0.0001	bdl	0.0001	0.0001	0.0001	bdl	bdl
^{146}Nd	0.0010	0.0054	0.0004	0.0002	0.0007	bdl	0.0007	bdl	0.0003
^{147}Sm	0.0002	0.0019	0.0001	0.0001	0.0006	0.0003	bdl	0.0002	0.0008

^{153}Eu	0.0001	0.0003	0.0002	0.0001	bdl	0.0001	0.0001	0.0001	bdl
^{157}Gd	0.0018	0.0029	0.0009	0.0003	0.0005	0.0005	0.0014	0.0003	0.0005
^{159}Tb	0.0001	0.0004	0.0001	0.0003	0.0001	0.0002	0.0003	0.0002	0.0001
^{163}Dy	0.0018	0.0032	0.0012	0.0026	0.0017	0.0018	0.0034	0.0013	0.0024
^{165}Ho	0.0007	0.0007	0.0006	0.0008	0.0007	0.0005	0.0011	0.0005	0.0009
^{166}Er	0.0040	0.0047	0.0042	0.0039	0.0030	0.0023	0.0040	0.0030	0.0053
^{169}Tm	0.0010	0.0010	0.0012	0.0012	0.0011	0.0013	0.0009	0.0008	0.0007
^{172}Yb	0.0109	0.0130	0.0145	0.0134	0.0092	0.0128	0.0115	0.0109	0.0097
^{175}Lu	0.0027	0.0031	0.0020	0.0034	0.0037	0.0032	0.0033	0.0026	0.0026
^{178}Hf	bdl	0.0515	bdl	0.0002	0.0004	bdl	bdl	0.0005	bdl
^{181}Ta	0.0005	0.0004	0.0003	0.0002	0.0002	0.0005	0.0006	bdl	bdl
^{182}W	0.0002	0.0001	0.0080	bdl	0.0005	0.0006	0.0008	bdl	0.0014
^{183}W	0.0116	bdl	0.0214	bdl	0.0004	bdl	0.0007	bdl	bdl
^{184}W	0.0026	0.0002	0.0162	0.0003	0.0004	0.0001	bdl	bdl	0.0067
^{185}Re	0.0001	bdl	bdl	bdl	0.0005	bdl	bdl	0.0007	0.0009
^{187}Re	bdl	bdl	0.0001	0.0001	bdl	0.0003	0.0003	0.0070	bdl
^{205}Tl	bdl	0.0003	bdl	bdl	bdl	0.0003	0.0009	bdl	bdl
^{208}Pb	0.0018	0.0025	0.0015	0.0016	0.0006	0.0015	0.0019	0.0022	0.0012
^{209}Bi	bdl	bdl	0.0002	0.0009	0.0005	0.0005	0.0012	bdl	bdl
^{232}Th	0.0004	0.0045	0.0004	bdl	0.0001	0.0002	0.0003	bdl	0.0002
^{238}U	0.0004	0.0021	0.0003	0.0001	bdl	0.0002	0.0001	0.0003	0.0002

*Trace element detection limit of 0.0001 ppm

Table 6: ALM1 standard trace element data

	ALM1-01	ALM1-02	ALM1-03
^{7}Li	2.85	2.97	3.03
^{12}C	bdl	bdl	bdl
^{19}F	67.40	59.98	49.57
^{23}Na	49.68	49.00	52.29
^{24}Mg	342659.38	343201.97	356029.50
^{25}Mg	353694.72	355034.25	369343.25
^{27}Al	23.68	23.88	24.87
^{28}Si	189172.72	189172.72	189172.73
^{29}Si	187037.23	188124.06	188841.25
^{31}P	59.86	55.43	60.09
^{35}Cl	154.30	153.21	163.03
^{39}K	bdl	bdl	bdl
^{43}Ca	40.87	35.87	44.71
^{44}Ca	397.90	411.40	428.32
^{45}Sc	11.92	12.10	10.61
^{47}Ti	8.94	8.53	8.76
^{51}V	0.49	0.61	0.56
^{52}Cr	13.44	13.99	13.92
^{53}Cr	16.83	16.59	17.15
^{55}Mn	834.09	836.98	882.15

^{56}Fe	55316.87	55919.30	60249.60
^{59}Co	133.47	132.72	137.85
^{60}Ni	3034.50	3055.19	3178.11
^{62}Ni	2898.99	2920.43	3094.67
^{63}Cu	0.0292	0.0341	0.0561
^{65}Cu	0.8140	0.7820	0.7360
^{66}Zn	39.4100	39.0800	41.9700
^{69}Ga	0.0524	0.0491	0.0483
^{71}Ga	0.0034	0.0006	0.0018
^{72}Ge	0.5940	0.6140	0.5780
^{73}Ge	0.5640	0.6440	0.5790
^{74}Ge	0.5730	0.5950	0.5700
^{75}As	0.1066	0.1101	0.0891
^{79}Br	bdl	bdl	bdl
^{85}Rb	0.0010	0.0007	0.0026
^{86}Sr	bdl	bdl	0.1540
^{88}Sr	bdl	0.0001	0.0013
^{89}Y	0.0266	0.0250	0.0276
^{90}Zr	0.0098	0.0094	0.0079
^{93}Nb	0.0621	0.0544	0.0557
^{95}Mo	0.0135	0.0164	0.0166
^{98}Mo	0.3530	0.3660	0.3410
^{107}Ag	bdl	0.0002	0.0007

^{109}Ag	0.0008	bdl	0.0004
^{111}Cd	0.0051	0.0036	0.0049
^{112}Cd	0.0183	0.0158	0.0184
^{114}Cd	0.0138	0.0153	0.0132
^{115}In	0.0024	0.0020	0.0027
^{118}Sn	0.1790	0.1809	0.2220
^{120}Sn	0.1735	0.1929	0.2290
^{121}Sb	bdl	0.0011	0.0050
^{123}Sb	bdl	0.0002	0.0025
^{127}I	bdl	bdl	bdl
^{133}Cs	0.0001	bdl	bdl
^{137}Ba	0.0020	bdl	0.0384
^{138}Ba	0.0004	0.0002	0.0261
^{139}La	bdl	bdl	0.0166
^{140}Ce	0.0001	0.0040	0.0421
^{141}Pr	bdl	0.0055	0.0044
^{146}Nd	bdl	bdl	0.0173
^{147}Sm	bdl	0.0013	0.0013
^{153}Eu	bdl	0.0001	0.0006
^{157}Gd	0.0014	bdl	0.0015
^{159}Tb	bdl	bdl	0.0001
^{163}Dy	0.0019	0.0012	0.0028
^{165}Ho	0.0005	0.0008	0.0012

^{166}Er	0.0079	0.0053	0.0073
^{169}Tm	0.0017	0.0024	0.0021
^{172}Yb	0.0338	0.0323	0.0313
^{175}Lu	0.0136	0.0141	0.0115
^{178}Hf	bdl	bdl	0.0008
^{181}Ta	0.0005	0.0015	0.0006
^{182}W	0.0003	0.0002	bdl
^{183}W	bdl	bdl	0.0003
^{184}W	bdl	bdl	bdl
^{185}Re	bdl	0.0001	0.0001
^{187}Re	0.0002	0.0001	0.0003
^{205}Tl	bdl	bdl	bdl
^{208}Pb	0.0018	0.0011	0.0354
^{209}Bi	bdl	bdl	0.0007
^{232}Th	bdl	bdl	0.0002
^{238}U	bdl	0.0002	0.0001

*Trace element detection limit of 0.0001 ppm

Table 7: BCR2G standard trace element data

	BCR2G-01	BCR2G-02	BCR2G-03	BCR2G-04	BCR2G-05	BCR2G-06	BCR2G-07	BCR2G-08
^{7}Li	9.31	9.41	9.49	9.20	9.37	8.66	9.21	9.10
^{12}C	bdl	bdl	bdl	bdl	bdl	bdl	bdl	bdl

^{19}F	41.27	55.62	27.32	32.56	11.93	7.46	bdl	31.79
^{23}Na	22801.00	22707.90	23266.50	22653.22	23224.67	21666.40	22827.26	22868.98
^{24}Mg	22625.92	22797.52	22709.04	22161.52	22373.86	22449.38	21939.54	18177.45
^{25}Mg	13897.84	31.24	14514.00	15691.12	17368.94	20200.87	23447.92	23184.61
^{27}Al	62387.65	7066.87	63486.47	66147.38	67715.70	71061.52	73447.62	73443.55
^{28}Si	255237.22	255369.03	257547.47	257710.48	253047.06	254300.13	254336.44	254300.11
^{29}Si	254300.20	254300.19	254300.17	254300.17	254300.16	254300.14	254300.13	254300.13
^{31}P	1238.77	1238.28	1241.17	1193.92	1214.79	1016.45	1182.76	1448.04
^{35}Cl	161.77	84.59	198.95	175.63	183.62	172.77	185.07	154.91
^{39}K	bdl	bdl	bdl	bdl	bdl	8280.13	277798.28	14436.34
^{43}Ca	54384.38	73807.12	53423.31	53086.70	53218.52	51701.47	49306.18	49427.30
^{44}Ca	55644.65	74274.91	53756.58	53329.43	52898.24	51165.72	48335.35	48244.74
^{45}Sc	31.89	32.40	31.42	31.13	30.87	33.67	30.87	30.36
^{47}Ti	14598.05	14752.36	14374.49	14037.56	13840.27	14381.47	13827.62	13545.51
^{51}V	251.88	17.13	264.09	280.99	313.96	363.52	422.26	429.69
^{52}Cr	16.76	16.63	16.47	16.15	16.64	16.25	16.58	15.60
^{53}Cr	21.33	21.20	21.33	20.91	21.67	21.66	21.64	21.64
^{55}Mn	1524.31	1541.13	1556.43	1496.19	1532.49	1480.24	1507.31	1504.96
^{56}Fe	103740.41	105960.63	100264.55	88741.20	84123.02	77969.16	72089.26	88164.23
^{59}Co	37.70	38.32	38.04	36.93	38.26	36.91	38.00	35.42
^{60}Ni	11.87	12.05	12.55	12.02	12.22	11.44	12.01	12.01
^{62}Ni	14.50	12.98	14.68	13.15	13.60	12.79	14.52	14.24
^{63}Cu	22.6000	36.2300	20.7600	19.7600	19.9200	18.2200	17.4300	16.7600

^{65}Cu	23.2000	35.4400	21.5100	20.3800	20.7300	19.0300	18.0600	17.5900
^{66}Zn	137.9500	139.8400	140.7700	134.6900	140.8800	134.6400	140.6600	146.9600
^{69}Ga	59.8200	19.0500	58.3300	63.5100	70.0600	81.1500	85.0500	84.2200
^{71}Ga	24.5900	31.5300	23.5800	23.0600	23.2200	22.2400	21.4400	21.0000
^{72}Ge	10.6500	133.5200	6.1300	4.0200	3.2100	2.3000	1.8700	1.8300
^{73}Ge	11.3400	118.7200	7.0800	4.9900	4.0200	3.0400	2.4000	2.3700
^{74}Ge	9.2700	160.3600	5.0000	3.1200	2.5300	1.8200	1.4100	1.3700
^{75}As	7.6500	192.1000	3.5000	2.0200	1.5900	1.1500	0.8600	0.9200
^{79}Br	bdl	bdl	bdl	bdl	bdl	bdl	bdl	bdl
^{85}Rb	46.2100	46.5100	47.9600	46.7700	47.1000	45.2000	46.8000	45.3500
^{86}Sr	321.5300	326.6500	324.2200	318.1400	317.1700	330.1300	313.9900	323.1100
^{88}Sr	327.0800	329.5600	326.9300	321.5300	317.1500	327.8100	310.9300	325.3100
^{89}Y	29.1200	29.0100	29.7200	30.5400	30.2100	30.4400	29.7000	29.8700
^{90}Zr	161.8300	164.7600	162.9600	161.1000	158.3900	174.7900	157.6500	158.3900
^{93}Nb	19.6800	49.1400	18.1100	16.5900	15.1600	13.2500	11.8200	11.8500
^{95}Mo	153.2800	16.8700	161.9300	176.8700	197.6400	226.3300	255.2700	256.8100
^{98}Mo	154.3000	17.0700	163.7900	178.3400	198.2900	226.6400	255.7000	257.1900
^{107}Ag	5.3500	304.7900	1.0700	0.4900	0.4200	0.2700	0.2100	0.1800
^{109}Ag	5.0200	306.3500	0.9800	0.4800	0.4000	0.2500	0.2000	0.1800
^{111}Cd	6.8500	358.9000	1.5300	0.6000	0.6000	0.3800	0.2900	0.2800
^{112}Cd	7.7300	319.5200	1.9800	0.8200	0.8200	0.5000	0.3500	0.3900
^{114}Cd	7.6700	341.8300	1.7800	0.7000	0.7100	0.4600	0.3100	0.3400
^{115}In	5.2100	822.0100	0.6300	0.2400	0.2100	0.1340	0.1040	0.1030

^{118}Sn	13.4800	165.0600	7.6900	4.9800	3.8800	2.7000	2.2100	2.1400
^{120}Sn	13.2600	161.3300	7.3600	4.9400	3.8600	2.7800	2.2000	2.1400
^{121}Sb	5.3200	351.1800	1.3200	0.6700	0.5400	0.3600	0.2600	0.2800
^{123}Sb	4.9800	362.0300	1.2900	0.6900	0.5500	0.3500	0.2600	0.2800
^{127}I	bdl	bdl	bdl	bdl	bdl	bdl	bdl	bdl
^{133}Cs	1.1230	1.1190	1.1590	1.1450	1.1430	1.1160	1.1240	1.1070
^{137}Ba	651.2500	658.7100	667.8700	651.2300	647.2600	640.4600	645.4300	675.7300
^{138}Ba	648.8400	654.0300	663.4900	648.0300	638.5100	646.4700	630.2800	672.9100
^{139}La	23.1400	23.2400	23.5200	23.0900	22.8400	24.4700	22.5400	23.3800
^{140}Ce	41.0100	23.7800	42.5900	45.1200	47.6700	50.0600	50.5100	50.7100
^{141}Pr	6.2100	6.2800	6.2900	6.1900	6.1700	6.4100	6.1500	6.3300
^{146}Nd	26.2400	26.5500	26.6300	26.3600	26.1600	27.7400	25.5900	27.5100
^{147}Sm	6.0300	6.1000	6.1000	6.0100	5.9700	6.4100	6.0000	6.3400
^{153}Eu	12.4100	169.6500	6.4200	4.2200	3.2600	2.3200	1.8500	1.7900
^{157}Gd	5.7700	5.9000	6.0200	5.8000	5.6800	6.2000	5.7500	6.1500
^{159}Tb	0.9180	0.9290	0.9250	0.9200	0.9160	0.9890	0.8850	0.9080
^{163}Dy	5.6800	5.6800	5.6200	5.6600	5.5200	6.1100	5.4900	6.0200
^{165}Ho	1.1510	1.1650	1.1710	1.1590	1.1540	1.2430	1.1240	1.1520
^{166}Er	3.2300	3.2500	3.2300	3.1900	3.1400	3.5300	3.1700	3.4000
^{169}Tm	0.4510	0.4480	0.4380	0.4460	0.4480	0.4830	0.4390	0.4570
^{172}Yb	14.7200	135.5500	9.1300	6.7300	5.2200	3.8100	3.0700	3.1200
^{175}Lu	0.4460	0.4500	0.4440	0.4490	0.4390	0.4750	0.4330	0.4430
^{178}Hf	14.7800	92.9100	10.9500	8.4300	6.8300	5.2800	4.4000	4.3600

^{181}Ta	0.6760	0.7060	0.6880	0.6880	0.6830	0.7460	0.6780	0.7000
^{182}W	10.2200	453.1100	2.4600	1.3100	0.9300	0.6400	0.4600	0.4900
^{183}W	9.4100	446.2400	2.3300	1.2900	0.9100	0.6200	0.4600	0.4700
^{184}W	9.7200	446.6600	2.4100	1.3600	0.9200	0.6500	0.4700	0.4800
^{185}Re	0.8400	147.3600	0.1240	0.0109	0.0270	0.0230	0.0135	0.0210
^{187}Re	0.8700	142.1800	0.1030	0.0150	0.0280	0.0200	0.0137	0.0200
^{205}Tl	4.7500	149.3700	1.3600	0.5400	0.5500	0.3600	0.2800	0.2700
^{208}Pb	19.2900	52.6700	16.4600	14.5200	14.4300	12.0800	10.4600	10.0600
^{209}Bi	2.0900	635.1100	0.2800	0.1070	0.0960	0.0580	0.0440	0.0560
^{232}Th	5.4000	5.4800	5.4700	5.4500	5.3500	5.6900	5.3400	5.4900
^{238}U	13.5100	203.0400	6.3400	3.9700	3.0200	2.1200	1.6300	1.6200

*Trace element detection limit of 0.0001 ppm

Table 8: N612 standard trace element data

	N612-01	N612-02	N612-03	N612-04	N612-05	N612-06	N612-07
^{7}Li	40.18	39.94	40.93	39.73	40.23	40.00	40.31
^{12}C	bdl	bdl	bdl	bdl	bdl	bdl	bdl
^{19}F	90.33	64.20	137.46	97.32	114.55	86.82	92.44
^{23}Na	100672.52	100172.23	102762.70	103085.80	101484.91	101303.66	101076.66
^{24}Mg	63.89	63.76	74.17	71.61	68.12	65.52	66.96
^{25}Mg	40.89	18280.86	41.87	46.50	49.67	53.61	57.36
^{27}Al	9287.92	83029.52	9560.10	9590.92	9904.23	10198.97	10458.22

^{28}Si	334460.28	336625.22	339785.03	338111.53	335522.47	336850.66	336818.97
^{29}Si	337042.13	337042.09	337042.09	337042.09	337042.06	337042.06	337042.03
^{31}P	66.48	46.30	41.55	42.83	45.53	45.86	50.66
^{35}Cl	113.59	182.54	119.54	170.54	140.04	157.51	138.12
^{39}K	78.95	68.61	59.84	46.15	55.83	354.05	bdl
^{43}Ca	97380.98	74663.47	95761.54	92715.06	90633.81	89729.37	88726.48
^{44}Ca	97450.73	75120.42	95629.70	93797.26	90406.03	90009.12	88870.43
^{45}Sc	40.94	40.66	38.60	39.64	39.60	40.27	40.36
^{47}Ti	44.57	44.37	43.43	43.89	43.57	43.95	44.60
^{51}V	22.24	329.68	23.85	26.06	28.19	30.23	32.81
^{52}Cr	36.15	36.54	36.38	36.73	36.04	36.41	36.51
^{53}Cr	35.42	36.36	36.70	37.33	36.16	36.24	36.24
^{55}Mn	38.75	38.41	38.87	39.03	38.23	38.60	38.93
^{56}Fe	48.81	54.15	51.14	49.94	51.78	50.02	51.77
^{59}Co	35.57	35.31	35.55	35.77	35.14	35.66	35.46
^{60}Ni	38.90	38.18	39.07	39.31	38.38	38.41	39.17
^{62}Ni	39.17	37.87	38.66	39.49	38.91	38.63	38.68
^{63}Cu	48.4600	30.4100	45.9300	44.3500	42.6100	41.9300	39.8900
^{65}Cu	47.5600	30.8100	45.3500	44.1500	42.5300	41.0700	39.7700
^{66}Zn	39.3500	38.4900	38.9200	39.9300	38.6600	39.2000	39.0500
^{69}Ga	24.7900	82.1300	26.1200	27.9000	29.8900	31.5300	33.1000
^{71}Ga	42.0900	32.4800	41.1500	40.5900	39.8600	39.5900	38.2500
^{72}Ge	208.3100	13.2200	119.7900	82.0400	62.9400	53.2800	44.8900

^{73}Ge	177.7700	15.6100	110.8800	78.6400	60.6900	53.0300	44.8500
^{74}Ge	263.7000	12.0400	132.7500	85.4500	64.4900	54.2600	45.2500
^{75}As	343.4000	9.1800	143.7600	88.4900	65.9900	54.7100	45.0300
^{79}Br	bdl	bdl	bdl	bdl	bdl	bdl	bdl
^{85}Rb	31.3000	31.0800	31.6900	31.6900	31.1400	31.2800	31.4700
^{86}Sr	78.6000	78.9900	77.4000	78.6900	78.4200	78.2500	78.7700
^{88}Sr	77.7400	77.8400	78.2400	79.6300	78.8600	78.2500	77.8100
^{89}Y	37.6900	38.9900	38.9400	38.1500	38.3200	38.8400	38.9000
^{90}Zr	38.7300	38.8300	36.7000	37.6600	37.4500	38.2700	38.4100
^{93}Nb	66.6400	26.7100	60.5900	54.4200	49.1900	46.5400	43.6100
^{95}Mo	21.8100	196.4100	24.0300	26.3900	28.6700	30.5800	32.6800
^{98}Mo	21.9300	197.3100	24.0200	26.3000	28.4300	30.6000	32.6100
^{107}Ag	1705.1600	10.1400	124.3300	63.2300	43.4100	35.3500	28.6800
^{109}Ag	1767.0800	10.1000	124.2900	62.8800	43.6800	35.2700	28.4500
^{111}Cd	1666.9000	12.7900	150.5600	81.8800	56.5400	46.3000	37.0100
^{112}Cd	1076.0900	12.9800	146.0700	80.4300	55.5900	45.7700	36.8500
^{114}Cd	1358.0000	12.8400	148.5500	81.1800	55.8900	45.9700	36.9700
^{115}In	bdl	18.3800	241.9200	116.6100	78.4900	62.8800	50.6100
^{118}Sn	270.3600	19.3100	136.1100	90.3900	67.9200	57.5500	48.2000
^{120}Sn	269.0300	19.3300	135.1200	89.3400	67.7600	57.3200	48.3200
^{121}Sb	1081.7500	7.6600	177.7300	96.1500	67.6200	54.9100	44.8200
^{123}Sb	1182.0400	7.0300	179.7100	95.1500	67.1400	54.5900	44.0800
^{127}I	bdl	bdl	bdl	bdl	bdl	bdl	bdl

^{133}Cs	42.4900	42.0100	43.5000	42.8800	42.6000	42.4900	42.6200
^{137}Ba	38.8400	39.1600	39.4900	39.8400	39.1800	39.0300	39.3600
^{138}Ba	39.1800	39.0200	39.6300	39.3500	39.3400	39.1700	39.2600
^{139}La	36.3200	36.4500	35.7100	35.6500	35.7600	36.1100	36.3100
^{140}Ce	30.5500	53.9800	32.8700	34.5100	35.6300	36.8900	37.2500
^{141}Pr	38.0400	37.8200	37.9500	37.9000	37.6900	37.8200	38.1000
^{146}Nd	35.8600	35.7300	35.1800	35.3700	35.2200	35.7200	35.6500
^{147}Sm	37.9700	38.3200	37.1600	37.4700	37.5000	37.9700	37.8700
^{153}Eu	293.9800	18.2000	133.2800	85.3000	63.1400	53.4800	45.1600
^{157}Gd	37.7200	37.9300	36.7100	37.1000	36.8500	37.4600	37.7500
^{159}Tb	38.2100	38.1300	36.9400	37.2900	37.3200	37.8300	37.9400
^{163}Dy	36.0600	36.3400	34.7400	35.1500	35.0300	35.7600	36.0000
^{165}Ho	38.9200	39.0300	37.6600	37.8300	37.9000	38.6500	38.6700
^{166}Er	38.6900	38.6900	37.2000	37.6400	37.6500	38.2800	38.4200
^{169}Tm	37.5200	37.4300	36.2300	36.2300	36.4300	37.1100	37.2000
^{172}Yb	214.5200	20.6500	125.6500	85.0300	66.4400	57.2100	49.0500
^{175}Lu	37.6600	37.7600	36.4600	36.3500	36.6200	37.2500	37.5000
^{178}Hf	137.5500	20.3300	97.6000	72.4700	58.3200	51.7700	45.0000
^{181}Ta	38.2000	38.2600	37.1700	36.9700	37.2400	37.8500	38.0200
^{182}W	1977.4300	18.3300	201.4800	108.5900	74.0800	60.5300	49.2000
^{183}W	1789.0300	18.3100	202.0400	108.9700	74.7100	60.2900	49.1800
^{184}W	1900.9300	18.3500	201.7700	108.3600	73.7700	60.5300	49.4600
^{185}Re	bdl	3.1200	41.0000	20.0100	13.3900	10.7600	8.7700

^{187}Re	bdl	3.0900	40.5400	19.8900	13.2600	10.7200	8.6200
^{205}Tl	458.1500	7.1600	74.8500	41.2200	29.1200	23.7500	19.1700
^{208}Pb	71.2100	25.6800	64.4200	57.7300	52.5100	48.7700	44.0300
^{209}Bi	bdl	9.2500	186.5900	91.1100	61.8100	49.3100	39.6900
^{232}Th	38.5400	38.3600	37.2600	37.0500	37.7100	38.1700	37.9900
^{238}U	360.7300	18.9900	149.0400	94.9500	68.7500	56.9100	47.7700

*Trace element detection limit of 0.0001 ppm

Table 9: N610 standard trace element data

	N610-01	N610-02	N610-03	N610-04	N610-05
^{7}Li	484.87	487.33	445.87	449.05	41.13
^{12}C	bdl	bdl	bdl	bdl	bdl
^{19}F	145.58	17.14	bdl	17.32	112.05
^{23}Na	100835.47	99899.72	96482.10	98922.11	102410.15
^{24}Mg	524.28	525.11	524.47	527.54	69.48
^{25}Mg	382.19	400.11	596.70	602.04	67.36
^{27}Al	10237.32	10636.64	10445.23	10386.78	10678.43
^{28}Si	325451.59	324781.88	325800.13	325800.13	337042.00
^{29}Si	325800.06	337041.84	325800.09	325800.09	337041.97
^{31}P	373.39	383.81	307.49	310.46	46.78
^{35}Cl	155.41	179.64	204.14	168.29	122.24
^{39}K	21.59	1.44	261.86	259.56	70.65

^{43}Ca	81620.91	83460.83	80411.06	81220.23	85134.65
^{44}Ca	81028.36	84133.00	81967.78	82059.93	85090.67
^{45}Sc	446.75	441.98	441.61	435.51	39.90
^{47}Ti	471.92	464.67	479.01	468.94	44.80
^{51}V	316.88	333.32	483.22	480.48	39.07
^{52}Cr	421.70	421.02	384.14	388.18	37.00
^{53}Cr	421.96	419.97	408.04	414.64	37.05
^{55}Mn	464.62	465.76	439.85	439.32	39.23
^{56}Fe	639.22	629.82	387.46	390.05	48.39
^{59}Co	431.22	431.50	406.88	411.49	36.24
^{60}Ni	463.42	458.35	450.14	444.22	39.35
^{62}Ni	467.19	456.77	448.22	450.40	38.77
^{63}Cu	302.8000	318.2200	460.9200	457.4400	38.5200
^{65}Cu	315.0700	334.3300	490.7700	485.0600	38.3400
^{66}Zn	485.8700	481.1000	451.6300	452.6200	38.9500
^{69}Ga	305.8700	322.7400	456.8300	452.2300	37.2100
^{71}Ga	309.8300	320.0900	455.4700	454.4700	36.9400
^{72}Ge	286.6500	297.4600	436.7800	430.2000	36.4500
^{73}Ge	289.2000	301.3700	447.9700	441.9400	36.3500
^{74}Ge	284.9400	296.3700	419.1500	417.4800	36.6700
^{75}As	243.2200	252.9800	354.4900	348.1600	35.9200
^{79}Br	bdl	bdl	bdl	bdl	bdl
^{85}Rb	436.6500	435.6500	406.9200	412.8300	31.4800

^{86}Sr	512.7600	509.1400	502.4600	500.3100	78.0700
^{88}Sr	516.2700	518.1400	499.0200	494.7700	78.0500
^{89}Y	335.1600	348.8500	496.7300	495.9900	37.7200
^{90}Zr	452.0700	448.9000	432.0400	426.4700	37.7000
^{93}Nb	340.2400	355.9800	503.7300	500.0500	38.4400
^{95}Mo	308.0400	326.0800	473.8600	472.0700	37.7200
^{98}Mo	308.3200	323.4500	469.6800	468.1800	37.6000
^{107}Ag	176.0800	183.5700	256.7700	256.2500	22.1000
^{109}Ag	175.5100	183.4300	257.8100	256.2500	22.1300
^{111}Cd	181.1700	188.5900	274.4600	272.0600	27.9900
^{112}Cd	184.8700	193.8800	278.7000	278.0800	28.0800
^{114}Cd	182.7600	191.2100	277.7000	275.6300	28.0200
^{115}In	333.8200	347.6300	461.0300	458.1800	39.0400
^{118}Sn	312.1700	326.3100	468.5100	462.6200	38.7800
^{120}Sn	311.9300	326.9000	457.3100	453.5900	38.6400
^{121}Sb	295.1300	308.2200	422.1100	419.2200	34.9200
^{123}Sb	289.7900	303.7400	419.4100	418.0900	34.7500
^{127}I	bdl	bdl	bdl	bdl	bdl
^{133}Cs	383.1900	386.3300	352.5200	360.5000	42.7600
^{137}Ba	444.6400	442.3800	415.4700	417.8200	39.0800
^{138}Ba	447.2800	448.9900	422.1900	425.8800	39.0400
^{139}La	442.0300	442.9800	417.0800	418.7900	35.6400
^{140}Ce	335.3100	352.6400	475.7300	470.4500	37.9200

^{141}Pr	452.0900	453.2400	424.9500	426.6400	37.4600
^{146}Nd	425.0200	422.9400	411.2900	410.1200	35.1300
^{147}Sm	442.8600	439.9500	435.6900	433.5900	37.1800
^{153}Eu	328.1700	341.5100	475.0100	471.8000	34.9000
^{157}Gd	436.6300	434.4600	423.4000	422.4900	36.6700
^{159}Tb	449.5400	449.8500	426.4900	425.5000	37.1800
^{163}Dy	434.4700	433.4200	421.7500	421.1200	34.9400
^{165}Ho	457.1800	459.1700	436.2400	436.7300	37.7400
^{166}Er	455.0000	455.7200	434.0000	432.7000	37.5500
^{169}Tm	438.2000	441.1000	419.4500	419.0000	36.3600
^{172}Yb	336.7600	348.0700	518.0600	509.0300	38.5200
^{175}Lu	446.6500	448.9700	424.9200	424.0700	36.5600
^{178}Hf	316.0600	327.0200	475.2600	472.8700	36.0100
^{181}Ta	451.6400	458.0100	430.5300	429.5700	37.1900
^{182}W	329.2800	344.9200	486.0700	478.9000	37.5900
^{183}W	325.0200	342.1400	491.4300	485.5500	37.4400
^{184}W	329.3100	345.4900	481.6700	475.1300	37.4900
^{185}Re	36.6100	38.5000	54.4900	53.5400	6.5600
^{187}Re	36.7300	38.3200	54.3100	53.3100	6.5500
^{205}Tl	44.9900	47.8200	64.0800	63.3000	14.8800
^{208}Pb	314.5200	328.6700	447.3900	446.1900	38.4700
^{209}Bi	252.8600	264.6400	350.8200	349.7900	30.1200
^{232}Th	458.1900	464.6700	438.6500	432.1700	37.4900

^{238}U	343.2100	362.6100	491.8700	486.9400	37.5000

*Trace element detection limit of 0.0001 ppm

B-2

Legend
"Standard" silicates
"Transitional" silicates
Filtered for terrestrial alteration
Filtered for Cr-spinel contamination

Table 1: Olivine trace element data for DaG 1037

	Ol_01-core	**Ol_02-core**	**Ol_02-rim**	**Ol_03-core**	**Ol_03-rim**	**Ol_04-core**	**Ol_04-rim**	**Ol_05-core**	**Ol_05-rim**	**Ol_08-core**	**Ol_09-core**	**Ol_09-rim**
^{7}Li	3.77	3.28	3.50	3.75	4.02	3.71	3.52	5.52	4.27	7.44	6.00	4.10
^{12}C	bdl	bdl	bdl	bdl	bdl	bdl	bdl	bdl	bdl	bdl	bdl	bdl
^{19}F	39.36	25.10	31.02	51.64	29.17	28.84	44.55	42.13	34.88	bdl	33.04	18.64
^{23}Na	72.30	85.09	57.76	105.60	79.80	74.28	60.57	92.09	85.80	60.45	89.34	46.64
^{24}Mg	238231.20	230839.75	216630.83	247663.38	201796.25	229965.98	199325.63	240955.13	197418.03	248484.03	246849.22	193982.50
^{25}Mg	248192.88	236286.25	222105.86	254584.75	207531.55	235331.30	206272.77	246214.88	200815.66	254162.20	255230.72	200176.58
^{27}Al	570.49	839.34	592.60	899.23	404.96	502.74	161.75	538.75	356.24	740.98	616.88	209.50
^{28}Si	177131.53	173521.20	169140.55	179357.91	170554.77	173646.30	168857.23	175921.81	167981.14	177481.47	174466.84	168610.38
^{29}Si	176692.08	174354.89	170007.70	177907.42	170895.83	173326.53	169820.73	176131.16	168137.94	178094.41	173326.53	169587.00
^{31}P	123.13	167.71	119.07	146.95	192.15	76.63	141.19	87.13	229.13	133.72	170.66	96.08
^{35}Cl	168.99	178.90	193.83	157.25	173.24	181.75	159.70	182.93	187.13	199.12	154.44	154.85

^{39}K	51.99	bdl	266.21	bdl	14.54	bdl	123.67	bdl	bdl	173.86	bdl	546.02
^{43}Ca	1359.48	1611.92	1615.05	1580.87	2288.65	1577.94	1717.86	1496.42	1961.93	1365.37	1381.57	1895.04
^{44}Ca	1605.07	1854.77	1849.71	1849.78	2530.91	1828.48	1955.02	1785.50	2179.22	1615.61	1570.67	2081.48
^{45}Sc	8.33	9.25	8.82	8.17	10.54	7.84	10.53	8.28	11.07	7.72	7.34	10.23
^{47}Ti	23.56	36.64	31.32	34.98	139.98	36.16	132.54	46.27	87.23	32.45	26.72	114.61
^{51}V	26.09	24.15	26.60	43.92	18.50	26.83	23.07	32.80	33.24	37.15	36.78	20.25
^{52}Cr	569.97	514.34	549.67	1774.98	323.43	542.54	392.39	629.82	949.89	1202.17	1379.58	336.94
^{53}Cr	603.93	550.65	584.33	1870.50	361.21	580.42	425.43	677.12	1024.53	1278.71	1463.67	367.33
^{55}Mn	3749.81	3870.86	3991.42	3623.13	4837.64	3831.79	4626.17	3625.96	4593.92	3434.54	3309.38	4739.76
^{56}Fe	184957.14	188614.30	193961.23	170110.61	233182.25	179129.30	221192.63	172310.91	221460.63	156573.11	147263.28	220654.69
^{59}Co	103.35	105.66	105.62	100.89	134.13	98.90	121.65	100.42	116.24	99.33	95.50	111.86
^{60}Ni	536.51	465.75	380.79	564.50	210.18	497.31	238.63	499.85	266.58	578.89	592.95	210.52
^{62}Ni	539.73	457.61	384.70	566.58	207.52	487.13	236.93	499.75	265.15	581.80	590.34	208.54
^{63}Cu	0.68600	1.96600	1.18300	1.85000	1.17900	0.83300	0.23900	0.89200	0.33400	0.98400	0.82400	0.62700
^{65}Cu	1.63000	2.38000	3.20000	2.54000	2.75000	2.04000	1.59000	1.14000	0.68000	1.38000	1.89000	1.42000
^{66}Zn	89.48000	89.58000	92.13000	83.02000	98.83000	84.32000	101.44000	84.21000	105.57000	79.55000	76.73000	103.89000
^{69}Ga	0.92100	0.83400	0.84800	1.14800	0.83500	0.80400	0.67000	0.95700	0.98600	1.17000	0.81400	0.64100
^{71}Ga	0.59300	0.56700	0.57600	0.86300	0.52200	0.57500	0.40400	0.53600	0.73800	0.66500	0.58800	0.36800
^{72}Ge	1.32000	1.32000	1.24000	1.32000	1.55000	1.14000	1.38000	1.16000	1.58000	1.13000	1.07000	1.36000
^{73}Ge	1.07000	1.22000	1.10000	1.13000	1.37000	1.06000	1.17000	1.01000	1.29000	0.88000	0.92000	1.09000
^{74}Ge	1.11000	1.11000	1.08000	1.11000	1.16000	0.95000	1.13000	1.00000	1.25000	0.94000	0.89000	1.09000
^{75}As	0.70000	0.61000	0.60000	0.96000	0.49000	0.88000	0.47000	1.32000	0.45000	1.06000	1.31000	0.65000
^{79}Br	bdl	bdl	bdl	bdl	bdl	bdl	bdl	bdl	bdl	bdl	bdl	bdl

^{85}Rb	0.15190	0.25300	0.19010	0.28100	0.18230	0.21560	0.09510	0.40500	0.11190	0.55800	0.41000	0.10980
^{86}Sr	5.99000	5.46000	5.30000	7.65000	6.51000	5.49000	4.15000	10.19000	5.97000	9.29000	7.30000	6.63000
^{88}Sr	5.99000	5.49000	5.29000	7.82000	6.71000	5.64000	4.12000	10.35000	6.02000	9.27000	7.36000	6.90000
^{89}Y	0.17380	0.18190	0.25700	0.18780	0.29200	0.16040	0.31700	0.17300	0.35000	0.14330	0.15710	0.25600
^{90}Zr	0.05500	0.13280	0.11120	0.06420	0.26200	0.03220	0.11050	0.08930	0.02380	0.06640	0.04160	0.12840
^{93}Nb	0.00216	0.00266	0.00214	0.00386	0.00034	0.00260	0.00126	0.00270	0.00167	0.00302	0.00314	0.00047
^{95}Mo	0.07000	0.10000	0.09000	0.08000	0.13000	0.08000	0.10000	0.08000	0.11000	0.08000	0.09000	0.12000
^{98}Mo	0.06000	0.04900	0.04500	0.06000	0.02200	0.06000	0.03900	0.07000	0.03200	0.07000	0.08000	0.03000
^{107}Ag	0.01800	0.03400	0.05000	0.02900	0.02100	0.02500	0.01600	0.00880	0.00240	0.00300	bdl	0.00210
^{109}Ag	0.01600	0.04100	0.05100	0.03600	bdl	0.02800	0.01400	0.00720	0.00110	0.00280	0.01400	0.00180
^{111}Cd	0.08500	0.05300	0.07800	0.06800	0.06700	0.09200	0.06400	0.15000	0.04300	0.09700	0.12000	0.05400
^{112}Cd	0.11300	0.10300	0.11300	0.09900	0.10900	0.10200	0.11800	0.16000	0.07900	0.11500	0.11500	0.06300
^{114}Cd	0.11000	0.10800	0.10000	0.08700	0.02100	0.09700	0.08900	0.14000	0.06600	0.11900	0.11200	0.08200
^{115}In	0.01600	0.02800	0.02900	0.01150	0.01500	0.01240	0.03100	0.01270	0.05500	0.00540	0.00700	0.03300
^{118}Sn	0.49000	0.45000	0.53000	0.42000	0.48000	0.45000	0.42000	0.44000	0.42000	0.43000	0.40000	0.35000
^{120}Sn	0.47000	0.48000	0.53000	0.42000	0.47000	0.44000	0.41000	0.45000	0.40000	0.44000	0.35000	1.92000
^{121}Sb	0.02000	0.05300	0.03100	0.03400	0.02700	0.03600	0.02400	0.03300	0.20000	0.02400	0.02400	0.02400
^{123}Sb	0.04100	0.02100	0.04600	0.04100	bdl	0.03200	0.00990	0.03600	0.03800	0.01700	0.04600	0.01900
^{127}I	bdl	bdl	bdl	bdl	bdl	bdl	bdl	bdl	bdl	bdl	bdl	bdl
^{133}Cs	bdl	0.00552	0.00188	0.00600	0.00199	0.00704	0.00344	0.00840	0.00213	0.01190	0.00660	0.00224
^{137}Ba	3.66000	2.74000	3.02000	3.79000	3.14000	1.80700	2.73000	4.18000	2.92000	5.80000	2.88000	2.82000
^{138}Ba	3.77000	2.68100	2.99000	3.69000	3.11000	2.42200	2.68800	4.20000	2.89000	5.71000	2.92000	2.81000
^{139}La	bdl	0.00073	0.00033	0.00074	0.00108	0.00030	0.00007	0.00092	0.00101	0.00065	0.00083	0.00085

^{140}Ce	0.00041	0.00116	0.00115	0.00148	0.00094	0.00039	0.00028	0.00149	0.00024	0.00089	0.00058	0.00169
^{141}Pr	0.00032	0.00024	bdl	0.00035	0.00014	0.00008	0.00013	0.00034	0.00005	bdl	0.00006	0.00019
^{146}Nd	0.00269	0.00118	0.00167	0.00113	0.00193	0.00118	0.00083	0.00185	0.00070	0.00186	0.00262	0.00164
^{147}Sm	0.00253	0.00131	0.00200	0.00109	bdl	0.00310	0.00054	0.00180	0.00330	0.00081	0.00160	0.00280
^{153}Eu	0.00116	0.00044	0.00069	0.00153	0.00144	0.00046	0.00117	0.00142	0.00260	0.00094	0.00079	0.00195
^{157}Gd	0.00270	0.00460	0.00470	0.00580	0.00470	0.00810	0.00470	0.00630	0.00860	0.00760	0.00640	0.00500
^{159}Tb	0.00134	0.00141	0.00194	0.00218	0.00205	0.00178	0.00158	0.00211	0.00286	0.00208	0.00223	0.00269
^{163}Dy	0.01800	0.02270	0.01950	0.02090	0.02870	0.01460	0.02650	0.02170	0.03720	0.01970	0.01810	0.01850
^{165}Ho	0.00604	0.00741	0.00962	0.00611	0.00819	0.00492	0.01197	0.00656	0.01106	0.00631	0.00515	0.00888
^{166}Er	0.02500	0.02710	0.04250	0.01820	0.05300	0.02330	0.05200	0.02200	0.05530	0.01600	0.01990	0.03990
^{169}Tm	0.00483	0.00528	0.00849	0.00363	0.01054	0.00200	0.01530	0.00363	0.01057	0.00303	0.00352	0.01123
^{172}Yb	0.04460	0.04060	0.06980	0.03230	0.11890	0.03310	0.13070	0.03930	0.12170	0.03020	0.03020	0.10650
^{175}Lu	0.00678	0.00775	0.01540	0.00626	0.02370	0.00535	0.02800	0.00729	0.02310	0.00457	0.00594	0.02240
^{178}Hf	0.00044	0.00249	0.00021	0.00149	0.00490	0.00059	0.00156	0.00264	0.00025	0.00143	0.00129	0.00204
^{181}Ta	bdl	0.00007	0.00004	bdl	bdl	bdl	bdl	0.00003	bdl	bdl	bdl	bdl
^{182}W	0.00960	0.00360	0.00560	0.00220	bdl	0.00640	0.00500	0.03000	0.00340	0.01040	0.01140	0.00470
^{183}W	0.00460	0.00450	0.00780	0.00380	bdl	0.00510	0.00380	0.03700	0.00700	0.00480	0.01800	bdl
^{184}W	0.00860	0.00390	0.00710	0.00290	bdl	0.00540	0.00550	0.03300	0.00560	0.01130	0.01340	0.00320
^{185}Re	bdl	0.00043	0.00070	0.00106	bdl	0.00063	0.00084	0.00014	0.00016	bdl	0.00049	bdl
^{187}Re	0.00068	0.00104	0.00103	0.00002	bdl	bdl	0.00014	bdl	0.00047	0.00004	bdl	bdl
^{205}Tl	0.01500	0.01110	0.01700	0.01220	bdl	0.01500	0.01100	0.01160	0.00280	0.01150	0.01370	0.00620
^{208}Pb	0.02300	0.07590	0.00706	0.01210	0.01040	bdl	0.00691	0.00860	0.00156	0.00770	0.00228	0.00940
^{209}Bi	0.00230	bdl	0.00050	0.00130	bdl	0.00020	bdl	bdl	0.00190	bdl	0.00220	bdl

^{232}Th	bdl	0.00007	bdl	bdl	bdl	bdl	bdl	bdl	0.00008	bdl	bdl	bdl
^{238}U	0.00476	0.00717	0.00766	0.03230	0.01270	0.02120	0.00627	0.09620	0.02490	0.09030	0.07190	0.06290

*Trace element detection limit of 0.0001 ppm

Table 2: Olivine trace element data for Dho 019

	Ol_01-core	**Ol_01-rim**	**Ol_02-core**	**Ol_03-core**
^{7}Li	4.21	4.67	4.71	3.70
^{12}C	bdl	bdl	bdl	bdl
^{19}F	46.25	30.26	8.13	45.65
^{23}Na	75.26	88.01	81.57	59.77
^{24}Mg	165113.30	153896.78	171114.97	173050.06
^{25}Mg	170276.73	158689.22	174941.61	177982.16
^{27}Al	1106.52	1036.06	693.10	661.66
^{28}Si	179550.70	177192.78	177914.66	177880.66
^{29}Si	177626.95	177626.95	177626.95	177626.95
^{31}P	135.09	130.14	284.15	140.61
^{35}Cl	177.78	208.27	197.74	176.6
^{39}K	157.66	bdl	49.35	286.10
^{43}Ca	3889.52	4328.11	3071.95	9260.79
^{44}Ca	4117.58	4583.91	3233.42	9463.69
^{45}Sc	12.65	12.05	12.82	13.15
^{47}Ti	131.59	179.12	147.13	151.16
^{51}V	26.72	20.56	18.71	19.23

^{52}Cr	493.55	349.34	488.82	518.96
^{53}Cr	528.76	381.60	526.80	559.97
^{55}Mn	6124.22	6493.65	5919.72	5988.07
^{56}Fe	344842.81	360998.53	314651.91	332758.44
^{59}Co	158.46	159.39	147.42	152.50
^{60}Ni	75.65	70.06	82.34	79.71
^{62}Ni	74.53	69.58	80.19	80.60
^{63}Cu	1.58300	1.44600	0.87000	0.78600
^{65}Cu	3.90000	3.62000	1.84000	2.75000
^{66}Zn	161.06000	169.39000	149.68000	168.84000
^{69}Ga	2.01400	1.85100	1.55200	0.85300
^{71}Ga	1.27500	0.97500	0.55900	0.74000
^{72}Ge	2.78000	2.13000	2.06000	2.16000
^{73}Ge	2.22000	1.69000	1.75000	1.59000
^{74}Ge	2.21000	1.68000	1.57000	1.51000
^{75}As	3.60000	2.54000	0.75000	3.39000
^{79}Br	bdl	bdl	bdl	bdl
^{85}Rb	0.25400	0.25300	0.13170	0.14120
^{86}Sr	51.05000	62.04000	64.22000	42.89000
^{88}Sr	52.15000	61.71000	64.00000	43.08000
^{89}Y	0.42300	0.37200	0.40900	0.45500
^{90}Zr	0.14760	0.81700	0.17700	0.03490
^{93}Nb	0.00253	0.00593	0.00378	0.00109

^{95}Mo	0.37000	0.52000	0.17000	0.15000
^{98}Mo	0.28000	0.43000	0.07000	0.06100
^{107}Ag	0.01300	0.09100	0.00530	0.01400
^{109}Ag	0.01700	0.09800	0.00590	0.01600
^{111}Cd	0.17000	0.25000	0.08900	0.13000
^{112}Cd	0.26000	0.21000	0.11000	0.14000
^{114}Cd	0.25000	0.27000	0.11400	0.13000
^{115}In	0.11600	0.12600	0.03200	0.03400
^{118}Sn	0.76000	0.71000	0.56000	0.57000
^{120}Sn	0.72000	0.66000	0.53000	0.54000
^{121}Sb	0.27000	0.23000	0.06300	0.18000
^{123}Sb	0.30000	0.23000	0.04200	0.19000
^{127}I	bdl	bdl	bdl	bdl
^{133}Cs	bdl	0.00850	0.00236	0.00280
^{137}Ba	8.62000	9.13000	10.25000	1.21700
^{138}Ba	8.93000	9.51000	10.16000	1.25900
^{139}La	0.00050	0.00108	0.00017	0.00037
^{140}Ce	0.00399	0.00700	0.00272	0.00255
^{141}Pr	0.00015	0.00059	0.00006	0.00010
^{146}Nd	0.00237	0.00264	0.00214	0.00129
^{147}Sm	0.00252	0.00279	0.00086	0.00090
^{153}Eu	0.00252	0.00310	0.00067	0.00073
^{157}Gd	0.00580	0.00600	0.00510	0.00550

^{159}Tb	0.00304	0.00223	0.00315	0.00323
^{163}Dy	0.03930	0.02690	0.04050	0.04800
^{165}Ho	0.01488	0.00824	0.01490	0.01510
^{166}Er	0.06540	0.05510	0.07630	0.08070
^{169}Tm	0.01452	0.01418	0.01170	0.01170
^{172}Yb	0.13420	0.12810	0.13700	0.11370
^{175}Lu	0.02930	0.02890	0.02490	0.02300
^{178}Hf	0.00312	0.02170	0.00810	0.00039
^{181}Ta	bdl	0.00014	0.00009	bdl
^{182}W	0.09800	0.08100	0.01250	0.03000
^{183}W	0.09900	0.06700	0.01090	0.02800
^{184}W	0.11100	0.08200	0.01600	0.03300
^{185}Re	bdl	0.00100	bdl	0.00067
^{187}Re	0.00083	0.00150	0.00058	0.00100
^{205}Tl	0.02000	0.02100	0.00630	0.00640
^{208}Pb	0.98200	1.49700	0.41400	0.40800
^{209}Bi	bdl	bdl	bdl	bdl
^{232}Th	bdl	bdl	0.00046	bdl
^{238}U	0.04910	0.05900	0.01880	0.06090

*Trace element detection limit of 0.0001 ppm

Table 3: Olivine trace element data for NWA 2046

	Ol_01-core	**Ol_01-rim**	**Ol_02-core**	**Ol_02-rim**	**Ol_03-core**	**Ol_03-rim**	**Ol_04-core**

^{7}Li	5.59	1.66	4.51	2.03	1.24	2.99	2.30
^{12}C	bdl	bdl	bdl	bdl	bdl	bdl	bdl
^{19}F	52.30	53.13	55.77	74.85	70.15	bdl	53.88
^{23}Na	107.87	84.59	111.02	69.76	111.94	51.63	127.40
^{24}Mg	267820.78	236195.45	268560.63	222318.34	286300.50	179418.84	290477.31
^{25}Mg	253547.55	223149.48	251093.83	204538.34	271094.06	158163.88	266953.44
^{27}Al	668.38	160.75	646.08	199.57	447.32	119.03	545.93
^{28}Si	179122.78	180852.31	175336.52	186975.77	186975.77	182301.38	186975.77
^{29}Si	180180.06	182745.56	175731.91	186971.41	187135.33	184883.28	187584.58
^{31}P	126.59	86.23	136.59	108.21	99.84	112.17	112.62
^{35}Cl	236.87	127.76	173.86	128.76	181.90	182.77	184.66
^{39}K	40.32	5.98	37.16	bdl	36.24	bdl	39.91
^{43}Ca	1715.88	1845.25	1898.12	1517.57	3105.28	1530.14	2957.07
^{44}Ca	2030.29	2142.14	2210.67	1834.14	3541.28	1827.83	3375.49
^{45}Sc	6.87	9.26	6.77	10.10	5.94	10.06	6.42
^{47}Ti	32.11	61.61	34.87	105.96	39.26	97.35	23.50
^{51}V	37.61	19.82	39.80	18.62	20.75	17.49	37.11
^{52}Cr	1875.71	789.70	2261.79	593.35	859.83	365.30	2494.84
^{53}Cr	2023.29	849.24	2415.92	646.30	928.76	414.15	2676.08
^{55}Mn	3024.07	4120.16	2763.28	4906.78	2842.55	5945.96	2906.69
^{56}Fe	141416.53	226989.33	127729.09	251407.83	122703.05	295990.03	127311.77
^{59}Co	98.12	117.34	92.35	122.88	96.35	162.63	97.47
^{60}Ni	674.60	409.17	672.37	403.84	718.68	350.36	726.95

^{62}Ni	683.01	414.69	680.42	403.61	724.69	352.17	730.21
^{63}Cu	1.04100	0.58000	1.07700	0.36600	0.71400	0.29400	0.70500
^{65}Cu	9.2400	0.6500	1.6000	0.7500	1.2700	1.2500	1.4600
^{66}Zn	66.27000	97.06000	60.85000	112.24000	55.90000	156.98000	64.65000
^{69}Ga	9.88000	0.89600	6.62000	0.70900	4.41000	0.72600	5.82000
^{71}Ga	0.48400	0.43600	0.42100	0.58300	0.19700	0.75800	0.36400
^{72}Ge	0.7000	0.9000	0.6900	0.9200	0.7100	0.9600	0.8600
^{73}Ge	0.5500	0.7000	0.5200	0.7300	0.5600	0.6700	0.7100
^{74}Ge	0.5300	0.6100	0.5400	0.6500	0.5600	0.6200	0.6700
^{75}As	11.6600	0.0500	1.0600	0.0500	0.5000	1.3700	0.5200
^{79}Br	bdl	bdl	bdl	bdl	bdl	bdl	bdl
^{85}Rb	0.09020	0.00840	0.07590	0.00620	0.07100	bdl	0.09090
^{86}Sr	13.23000	1.53800	8.96000	0.57300	6.82000	0.06200	8.93000
^{88}Sr	13.48000	1.52600	9.28000	0.73400	6.91000	0.01290	8.74000
^{89}Y	0.10070	0.14330	0.10400	0.16970	0.07450	0.17770	0.08760
^{90}Zr	0.08110	0.02250	0.11540	0.19900	0.06290	0.06140	0.04840
^{93}Nb	0.00496	0.00206	0.00517	0.00136	0.00500	0.00099	0.00678
^{95}Mo	0.08000	0.11000	0.06000	0.12000	0.08000	0.10000	0.08000
^{98}Mo	0.10000	0.05000	0.09000	0.07000	0.08000	0.08000	0.10000
^{107}Ag	0.00250	0.00700	0.00090	0.00400	bdl	0.00700	0.00280
^{109}Ag	0.00230	0.00800	0.41000	0.00400	0.00160	0.00400	0.00270
^{111}Cd	0.05000	0.01400	0.01800	0.01000	0.03100	0.02200	0.02600
^{112}Cd	0.05000	0.02600	0.03000	0.02900	0.03900	0.04000	0.03700

^{114}Cd	0.04300	0.02300	0.02100	0.02000	0.02900	0.03200	0.03000
^{115}In	0.00600	0.01000	0.00500	0.02100	0.00370	0.02300	0.00600
^{118}Sn	0.19000	0.21000	0.21000	0.25000	0.22000	0.24000	0.28000
^{120}Sn	0.20000	0.20000	0.20000	0.24000	0.23000	0.25000	0.28000
^{121}Sb	0.06000	0.00700	0.01100	0.00900	0.01200	0.01600	0.02200
^{123}Sb	0.06000	0.00900	0.01000	0.00900	0.01300	0.02200	0.01400
^{127}I	bdl	bdl	bdl	bdl	bdl	bdl	bdl
^{133}Cs	0.00357	bdl	0.00167	bdl	0.00180	0.00108	bdl
^{137}Ba	94.30000	4.62000	61.85000	1.58000	41.63000	0.06010	55.19000
^{138}Ba	95.97000	4.70000	62.78000	1.59100	42.47000	0.06000	55.78000
^{139}La	0.00269	bdl	0.00191	bdl	0.00164	0.00006	0.00177
^{140}Ce	0.00566	0.00008	0.00683	0.00010	0.00490	0.00010	0.00788
^{141}Pr	0.00063	0.00004	0.00045	0.00006	0.00039	0.00003	0.00067
^{146}Nd	0.00132	0.00022	0.00152	0.00033	0.00370	bdl	0.00341
^{147}Sm	0.00114	0.00063	0.00082	0.00062	0.00056	0.00056	0.00086
^{153}Eu	0.00218	0.00014	0.00228	0.00016	0.00131	0.00016	0.00284
^{157}Gd	0.00490	0.00188	0.00320	0.00510	0.00360	0.00048	0.00490
^{159}Tb	0.00088	0.00127	0.00104	0.00175	0.00022	0.00108	0.00123
^{163}Dy	0.01220	0.01220	0.00690	0.01940	0.00320	0.01750	0.01100
^{165}Ho	0.00371	0.00595	0.00409	0.00611	0.00309	0.00665	0.00341
^{166}Er	0.01610	0.02680	0.01400	0.02520	0.00940	0.03270	0.01180
^{169}Tm	0.00260	0.00423	0.00263	0.00592	0.00164	0.00818	0.00211
^{172}Yb	0.02210	0.04690	0.02540	0.07090	0.02070	0.10110	0.01830

^{175}Lu	0.00554	0.00934	0.00460	0.01810	0.00366	0.02060	0.00388
^{178}Hf	0.00156	0.00091	0.00290	0.00780	0.00270	0.00052	0.00099
^{181}Ta	bdl	0.00009	bdl	0.00004	0.00007	0.00003	bdl
^{182}W	0.01300	0.00110	0.00100	0.00140	0.00130	0.00700	0.00200
^{183}W	0.01000	0.00070	0.00070	0.00190	0.00220	0.00500	0.00260
^{184}W	0.01100	0.00100	0.00110	0.00160	0.00080	0.00700	0.00250
^{185}Re	0.00015	0.00022	bdl	bdl	bdl	bdl	bdl
^{187}Re	bdl	0.00027	bdl	bdl	bdl	bdl	bdl
^{205}Tl	0.01100	bdl	0.00190	bdl	0.00150	0.00270	0.00150
^{208}Pb	0.07330	0.05290	0.04170	0.05160	0.16840	0.03760	0.07320
^{209}Bi	bdl	bdl	bdl	0.00080	bdl	bdl	bdl
^{232}Th	0.00067	0.00007	0.00075	0.00020	0.00097	0.00005	0.00020
^{238}U	0.00765	0.00048	0.00981	0.00006	0.00612	0.00004	0.00499

*Trace element detection limit of 0.0001 ppm

Table 4: Olivine trace element data for NWA 4925

	Ol_01-core	**Ol_01-rim**	**Ol_02-core**	**Ol_03-core**	**Ol_04-core**	**Ol_05-core**	**Ol_05-rim**	**Ol_06-core**	**Ol_07-core**	**Ol_08-core**	**Ol_09-core**
^{7}Li	17.81	3.43	18.45	19.66	15.82	11.22	6.00	16.42	14.95	11.05	10.16
^{12}C	bdl	bdl	bdl	bdl	bdl	bdl	bdl	bdl	bdl	bdl	bdl
^{19}F	78.48	69.45	84.78	87.16	113.90	31.44	43.68	63.94	48.98	85.91	67.03
^{23}Na	131.96	56.13	129.57	128.71	158.93	109.05	68.98	146.89	86.78	90.86	95.48
^{24}Mg	261412.89	178395.56	253430.44	242161.13	226882.72	255952.33	205671.22	244504.88	216224.73	240623.55	235105.92
^{25}Mg	262326.00	178035.06	255954.48	244601.69	230558.67	254277.91	204941.23	244025.84	211756.72	237071.88	231122.63

^{27}Al	2122.73	414.06	2341.94	1625.62	2126.08	990.62	354.03	1179.99	695.39	1595.25	2042.43
^{28}Si	187116.00	165613.78	187116.00	183376.48	183376.47	185339.72	164304.95	185339.72	164304.95	179870.67	179870.69
^{29}Si	187467.70	166532.36	189073.42	181693.47	183053.38	186093.22	164409.53	186287.30	164504.47	182502.94	181303.72
^{31}P	136.37	109.45	143.96	125.19	136.79	225.07	99.57	125.07	114.81	124.67	112.27
^{35}Cl	134.59	118.20	147.47	140.05	114.17	129.50	133.41	138.51	129.91	124.10	135.59
^{39}K	1532.13	94.98	1638.41	1964.48	4010.21	901.19	107.74	2199.31	267.95	171.12	205.85
^{43}Ca	2961.44	1521.32	3356.82	4990.27	3792.97	2530.37	1711.06	2670.73	2008.49	2056.98	4668.02
^{44}Ca	3380.64	1784.73	3675.05	5277.48	4058.44	2876.26	1939.97	2994.79	2245.67	2337.44	4969.54
^{45}Sc	7.41	10.12	7.80	7.43	7.13	8.60	8.29	7.64	6.99	7.55	7.89
^{47}Ti	33.83	114.67	33.75	34.97	31.83	50.55	43.57	38.55	24.52	26.05	30.04
^{51}V	48.56	16.18	52.34	48.12	44.84	36.45	22.82	41.81	47.62	30.31	34.57
^{52}Cr	2497.02	270.41	2888.22	2993.43	2794.17	829.56	492.19	1543.78	2435.96	1220.37	1528.53
^{53}Cr	2623.78	295.30	3034.11	3124.72	2972.60	879.75	528.97	1639.00	2599.87	1296.57	1630.58
^{55}Mn	3361.50	5204.48	3171.73	3127.85	2666.62	3650.98	3713.53	2799.50	3098.67	3488.88	3669.86
^{56}Fe	197034.63	356114.63	197043.78	207524.05	179893.52	188311.88	234973.92	175973.39	195060.38	205036.81	212866.33
^{59}Co	119.86	143.64	95.73	112.10	82.99	120.61	109.03	88.09	89.00	104.98	111.41
^{60}Ni	685.95	294.91	653.92	682.64	656.15	614.74	368.76	640.81	509.87	562.62	531.70
^{62}Ni	671.40	293.84	644.11	672.95	648.66	611.10	371.83	630.93	506.79	562.79	533.63
^{63}Cu	8.76000	1.91300	8.71000	6.98000	9.36000	10.02000	2.87000	12.09000	6.31000	3.45000	3.91000
^{65}Cu	7.58000	5.38000	8.00000	5.86000	9.29000	11.00000	5.75000	9.61000	3.11000	5.18000	4.65000
^{66}Zn	76.65000	127.94000	86.74000	85.66000	75.31000	70.63000	97.65000	70.94000	100.48000	100.75000	104.55000
^{69}Ga	21.58000	3.15700	22.51000	21.20000	21.46000	17.90000	6.61000	15.04000	15.70000	16.51000	14.11000
^{71}Ga	1.83000	0.78400	2.15200	2.10000	3.62000	1.17400	0.56100	2.76900	1.15200	1.12100	1.20200

^{72}Ge	0.57000	0.61000	0.55000	0.60000	0.57000	0.76000	0.69000	0.71000	0.81000	0.70000	0.64000
^{73}Ge	0.47000	0.48000	0.46000	0.47000	0.47000	0.63000	0.51000	0.65000	0.61000	0.53000	0.55000
^{74}Ge	0.46000	0.42000	0.45000	0.46000	0.46000	0.58000	0.50000	0.59000	0.59000	0.54000	0.54000
^{75}As	0.67000	0.47000	0.66000	0.53000	0.62000	0.92000	1.00000	1.12000	0.16000	0.29000	0.22000
^{79}Br	bdl	bdl	bdl	bdl	bdl	bdl	bdl	bdl	bdl	bdl	bdl
^{85}Rb	2.44600	0.15100	2.72100	3.61000	8.02000	1.94400	0.25940	5.10000	0.58100	0.25940	0.30900
^{86}Sr	26.23000	2.97000	27.97000	30.54000	25.17000	14.66000	6.51000	15.83000	15.77000	16.09000	17.08000
^{88}Sr	25.92000	3.04000	27.82000	30.57000	25.45000	14.70000	6.61000	16.04000	15.54000	16.55000	17.11000
^{89}Y	0.14070	0.13860	0.13030	0.14640	0.12580	0.15090	0.14890	0.11260	0.10030	0.09410	0.11420
^{90}Zr	0.17450	0.23390	0.25800	0.17500	0.19240	0.22800	0.09090	0.62000	0.26700	0.18960	0.23300
^{93}Nb	0.00844	0.00058	0.00837	0.00908	0.00960	0.00528	0.00159	0.00629	0.00731	0.00493	0.00782
^{95}Mo	0.06100	0.08000	0.07000	0.05500	0.05100	0.08000	0.06000	0.08000	0.10000	0.08000	0.09000
^{98}Mo	0.07000	0.06000	0.09000	0.12000	0.06000	0.07000	0.06000	0.08000	0.05000	0.07000	0.07000
^{107}Ag	0.00320	0.00160	0.00310	0.00310	0.00500	0.00600	0.00180	0.00430	0.00230	0.00120	0.00130
^{109}Ag	0.00360	0.00130	0.00300	0.00460	0.00490	0.00480	0.00200	0.00260	0.00110	0.00090	0.00090
^{111}Cd	0.04000	0.04000	0.03400	0.02700	0.02900	0.02400	0.02100	0.02600	0.01400	0.04200	0.04300
^{112}Cd	0.04300	0.04100	0.04000	0.03800	0.02700	0.02600	0.01600	0.03100	0.02500	0.05000	0.04100
^{114}Cd	0.04000	0.04300	0.04000	0.03100	0.03600	0.02400	0.02100	0.02400	0.02100	0.03800	0.03800
^{115}In	0.00260	0.00700	0.00320	0.00300	0.00220	0.00280	0.00460	0.00210	0.02000	0.00380	0.00540
^{118}Sn	0.17000	0.15000	0.20000	0.21000	0.18000	0.17000	0.17000	0.18000	0.19000	0.18000	0.19000
^{120}Sn	0.18000	0.16000	0.20000	0.20000	0.17000	0.17000	0.18000	0.18000	0.21000	0.17000	0.17000
^{121}Sb	0.02100	0.03800	0.03800	0.01900	0.02400	0.02600	0.02200	0.02500	0.00490	0.01400	0.12000
^{123}Sb	0.01400	0.04400	0.03400	0.02200	0.01900	0.02400	0.02800	0.02900	0.01000	0.00800	0.12000

^{127}I	bdl	bdl	bdl	bdl	bdl	bdl	bdl	bdl	bdl	bdl	bdl
^{133}Cs	0.09250	0.00596	0.10230	0.14980	0.33500	0.07710	0.00770	0.20920	0.01970	0.00720	0.00710
^{137}Ba	203.27000	25.09000	203.97000	195.18000	181.90000	166.83000	61.03000	125.97000	147.42000	155.50000	130.63000
^{138}Ba	202.90000	25.34000	202.39000	194.37000	181.08000	167.12000	61.36000	126.27000	146.79000	156.31000	132.49000
^{139}La	0.01043	0.00142	0.00906	0.00873	0.00819	0.00390	0.00185	0.00358	0.00341	0.00620	0.00499
^{140}Ce	0.02090	0.00398	0.01540	0.01660	0.01680	0.01510	0.00245	0.00860	0.00677	0.03020	0.03210
^{141}Pr	0.00263	0.00045	0.00235	0.00169	0.00136	0.00080	0.00460	0.00103	0.00046	0.00092	0.00139
^{146}Nd	0.01400	0.00152	0.01640	0.00970	0.00780	0.00570	0.00197	0.00570	0.00500	0.00770	0.00820
^{147}Sm	0.00501	0.00055	0.00540	0.00129	0.00186	0.00243	0.00192	0.00199	0.00117	0.00267	0.00267
^{153}Eu	0.00870	0.00112	0.00609	0.00609	0.00789	0.00674	0.00230	0.00326	0.00410	0.00492	0.00408
^{157}Gd	0.01080	0.00213	0.00740	0.00448	0.00670	0.00800	0.00360	0.00650	0.00278	0.00470	0.00600
^{159}Tb	0.00175	0.00099	0.00216	0.00197	0.00175	0.00162	0.00145	0.00120	0.00106	0.00105	0.00132
^{163}Dy	0.01920	0.01110	0.01680	0.01350	0.01340	0.01460	0.01380	0.01350	0.00840	0.00790	0.01510
^{165}Ho	0.00443	0.00466	0.00536	0.00421	0.00437	0.00489	0.00529	0.00516	0.00333	0.00237	0.00413
^{166}Er	0.01820	0.02570	0.01760	0.01820	0.01350	0.02060	0.02520	0.01620	0.01290	0.01380	0.01220
^{169}Tm	0.00357	0.00604	0.00328	0.00250	0.00285	0.00497	0.00493	0.00416	0.00237	0.00234	0.00363
^{172}Yb	0.02900	0.07350	0.02740	0.02210	0.01940	0.03660	0.04740	0.03160	0.02080	0.01700	0.03020
^{175}Lu	0.00539	0.01540	0.00658	0.00421	0.00446	0.00789	0.01065	0.00569	0.00426	0.00389	0.00570
^{178}Hf	0.00131	0.00260	0.00179	0.00142	0.00150	0.00500	0.00180	0.00220	0.00180	0.00300	0.00290
^{181}Ta	bdl	0.00000	bdl	bdl	0.00005	0.00004	0.00002	bdl	0.00003	0.00016	0.00006
^{182}W	0.00180	0.00110	0.00350	0.00300	0.00460	0.00800	0.00510	0.00900	0.00200	0.00240	0.00350
^{183}W	0.00190	0.00100	0.00380	0.00170	0.00380	0.00700	bdl	0.01100	0.00330	0.00150	0.00310
^{184}W	0.00300	0.00090	0.00380	0.00200	0.00410	0.00800	0.00460	0.00800	0.00270	0.00210	0.00300

^{185}Re	0.00019	bdl	0.00006	0.00031	0.00023	bdl	bdl	0.00018	0.00006	bdl	0.00032
^{187}Re	0.00016	bdl	bdl	0.00025	bdl	0.00030	bdl	0.00009	0.00032	0.00022	0.00024
^{205}Tl	0.01030	0.00700	0.01400	0.01220	0.02900	0.01200	0.00490	0.01800	0.00160	0.01010	0.00640
^{208}Pb	0.00819	0.01260	0.01190	0.01076	0.01280	0.03890	0.01000	0.02370	0.01260	0.01150	0.02630
^{209}Bi	bdl	bdl	bdl	0.00090	bdl	bdl	bdl	0.00025	0.00030	0.00052	0.00090
^{232}Th	0.00088	0.00000	0.00137	0.00068	0.00204	0.00109	0.00048	0.00257	0.00135	0.00115	0.00191
^{238}U	0.00832	0.00131	0.00885	0.00631	0.00874	0.05020	0.01410	0.13490	0.03760	0.00114	0.00378

*Trace element detection limit of 0.0001 ppm

Table 5: Olivine trace element data for SaU 005

	Ol_01-core	**Ol_01-rim**	**Ol_02-rim**	**Ol_03-core**	**Ol_04-core**
^{7}Li	3.93	4.01	4.20	2.95	3.62
^{12}C	bdl	bdl	bdl	bdl	bdl
^{19}F	6.33	18.03	21.36	27.46	20.60
^{23}Na	107.79	90.77	93.76	92.93	103.62
^{24}Mg	239066.36	225475.72	225860.66	236890.53	240602.17
^{25}Mg	248290.09	233900.91	235303.20	246545.67	243099.75
^{27}Al	583.53	252.15	283.01	438.21	544.33
^{28}Si	175289.77	175289.77	175289.77	175289.77	175289.77
^{29}Si	174763.17	172043.31	174411.20	175324.31	175583.52
^{31}P	218.22	129.62	138.57	146.06	92.20
^{35}Cl	127.43	132.52	142.35	152.82	135.21
^{39}K	45.37	14.05	18.90	21.37	27.65

^{43}Ca	2025.63	2125.92	2246.75	2412.19	2037.11
^{44}Ca	2214.04	2340.40	2406.63	2632.74	2235.31
^{45}Sc	9.62	9.23	9.52	8.97	8.43
^{47}Ti	45.68	51.17	75.58	43.38	52.58
^{51}V	42.08	31.29	31.18	31.70	31.20
^{52}Cr	966.77	598.44	637.27	674.89	604.76
^{53}Cr	1001.95	619.96	655.97	694.82	630.20
^{55}Mn	4124.40	4396.35	4511.62	4255.77	4293.68
^{56}Fe	199181.66	226306.59	227757.39	212584.00	210800.45
^{59}Co	108.48	113.12	116.48	109.26	109.72
^{60}Ni	460.95	360.58	366.39	429.56	442.59
^{62}Ni	470.81	367.88	366.95	444.22	454.94
^{63}Cu	0.99000	0.51100	0.54800	0.81000	1.04300
^{65}Cu	1.47900	1.16500	1.26100	1.28600	1.37300
^{66}Zn	74.49000	90.98000	89.06000	88.98000	85.50000
^{69}Ga	1.17900	0.91500	0.94100	0.99900	0.98100
^{71}Ga	0.79900	0.57500	0.56800	0.65100	0.66100
^{72}Ge	0.66600	0.85400	0.81800	0.70400	0.88300
^{73}Ge	0.53300	0.73700	0.62400	0.63900	0.69300
^{74}Ge	0.53300	0.66000	0.55500	0.57400	0.59700
^{75}As	0.63500	0.58700	0.47300	0.86700	0.58400
^{79}Br	bdl	bdl	bdl	bdl	bdl
^{85}Rb	0.06830	0.03990	0.04090	0.07530	0.08100

^{86}Sr	17.25000	12.81000	14.67000	16.50000	13.20000
^{88}Sr	17.26000	12.99000	14.49000	16.54000	13.28000
^{89}Y	0.10964	0.21909	0.21455	0.20273	0.15545
^{90}Zr	0.07740	0.02080	0.02620	0.03870	0.05650
^{93}Nb	0.00185	0.00040	0.00054	0.00120	0.00121
^{95}Mo	0.11390	0.10270	0.12110	0.13390	0.10300
^{98}Mo	0.06570	0.05640	0.06480	0.06850	0.07400
^{107}Ag	bdl	bdl	0.00163	0.00270	0.00193
^{109}Ag	0.00091	bdl	0.00116	0.00190	0.00089
^{111}Cd	0.02080	0.02270	0.02110	0.03610	0.03070
^{112}Cd	0.04130	0.03200	0.03250	0.05000	0.03190
^{114}Cd	0.02800	0.03600	0.02860	0.03780	0.04220
^{115}In	0.00477	0.00918	0.00876	0.00774	0.00620
^{118}Sn	0.17230	0.17590	0.17470	0.18800	0.18700
^{120}Sn	0.16960	0.16570	0.15370	0.19800	0.16100
^{121}Sb	0.01320	0.01910	0.01340	0.02890	0.01860
^{123}Sb	0.01590	0.01230	0.01210	0.03110	0.01930
^{127}I	bdl	bdl	bdl	bdl	bdl
^{133}Cs	0.00108	0.00125	bdl	0.00284	0.00266
^{137}Ba	4.98000	4.17000	4.91000	4.02000	4.12000
^{138}Ba	4.90000	4.25000	4.85000	3.87000	3.98000
^{139}La	0.00009	0.00007	bdl	0.00007	0.00030
^{140}Ce	0.00025	0.00020	0.00063	bdl	0.00103

^{141}Pr	0.00005	0.00004	0.00008	0.00005	0.00018
^{146}Nd	0.00042	0.00070	0.00031	0.00048	0.00106
^{147}Sm	0.00039	0.00078	0.00036	0.00035	0.00046
^{153}Eu	0.00018	0.00030	0.00059	0.00038	0.00049
^{157}Gd	0.00200	0.00450	0.00297	0.00162	0.00188
^{159}Tb	0.00118	0.00101	0.00149	0.00071	0.00094
^{163}Dy	0.00936	0.01200	0.01800	0.01055	0.00945
^{165}Ho	0.00517	0.00716	0.00775	0.00392	0.00494
^{166}Er	0.01930	0.02970	0.03460	0.01790	0.01790
^{169}Tm	0.00352	0.00484	0.00562	0.00430	0.00337
^{172}Yb	0.03080	0.04400	0.06370	0.03240	0.03300
^{175}Lu	0.00768	0.01020	0.01320	0.00682	0.00694
^{178}Hf	0.00340	0.00051	0.00079	0.00129	0.00225
^{181}Ta	bdl	bdl	bdl	bdl	bdl
^{182}W	0.00100	0.00197	0.00101	0.00175	0.00051
^{183}W	0.00114	0.00204	0.00105	0.00199	0.00087
^{184}W	0.00238	0.00186	0.00198	0.00191	0.00128
^{185}Re	0.00008	0.00018	bdl	0.00027	0.00015
^{187}Re	0.00020	bdl	0.00005	0.00012	0.00018
^{205}Tl	0.00156	0.00108	0.00181	0.00446	0.00093
^{208}Pb	0.10260	0.07430	0.06900	0.08110	0.10830
^{209}Bi	0.00036	bdl	0.00051	0.00036	0.00057
^{232}Th	bdl	bdl	bdl	0.00007	bdl

^{238}U	0.10100	0.05780	0.04960	0.04880	0.05480

*Trace element detection limit of 0.0001 ppm

Table 6: Olivine trace element data for Tissint

	Ol_01-core	**Ol_01-rim**	**Ol_02-rim**	**Ol_03-core**	**Ol_04-core**
^{7}Li	1.00	1.57	0.84	1.02	1.07
^{12}C	bdl	bdl	bdl	bdl	bdl
^{19}F	bdl	30.49	51.17	48.23	65.26
^{23}Na	89.53	73.91	112.28	92.26	80.92
^{24}Mg	262527.34	214931.34	274370.06	262867.59	269608.94
^{25}Mg	271444.06	219318.53	284995.63	274512.16	277923.28
^{27}Al	274.18	173.07	265.97	246.19	268.09
^{28}Si	179964.16	179964.16	179964.16	179964.16	179964.16
^{29}Si	180868.83	180886.97	178881.50	179413.19	176244.09
^{31}P	111.62	706.47	195.78	199.95	14.35
^{35}Cl	162.21	135.76	141.05	161.00	132.25
^{39}K	bdl	bdl	bdl	bdl	bdl
^{43}Ca	1450.12	1722.17	1305.31	1352.68	1384.86
^{44}Ca	1699.72	1970.52	1601.15	1638.24	1684.61
^{45}Sc	7.93	13.47	7.10	7.61	7.21
^{47}Ti	41.69	49.55	32.75	33.98	48.93
^{51}V	42.25	40.32	40.57	38.71	38.92
^{52}Cr	2336.84	836.24	3503.35	2402.73	2299.00

^{53}Cr	2438.59	859.00	3744.70	2546.70	2437.21
^{55}Mn	3661.62	5353.04	3251.50	3655.48	3355.99
^{56}Fe	172388.98	281938.59	149569.73	169434.05	153054.56
^{59}Co	106.05	143.88	104.70	105.66	103.02
^{60}Ni	826.08	436.02	938.08	901.70	865.72
^{62}Ni	806.06	442.87	905.46	863.64	844.55
^{63}Cu	0.34700	0.14060	0.50800	0.37700	0.18900
^{65}Cu	1.03200	0.58700	1.03200	0.90200	0.89000
^{66}Zn	77.58000	134.38000	64.45000	76.65000	63.33000
^{69}Ga	0.32900	0.43500	0.29300	0.26500	0.29200
^{71}Ga	0.33600	0.44900	0.28900	0.25500	0.29200
^{72}Ge	0.86600	1.20400	0.80900	0.97700	0.40900
^{73}Ge	0.68900	0.90600	0.72400	0.79700	0.37700
^{74}Ge	0.66300	0.81100	0.72500	0.73300	0.34600
^{75}As	0.07180	0.07110	0.07330	0.07530	0.08600
^{79}Br	bdl	bdl	bdl	bdl	bdl
^{85}Rb	0.00110	bdl	0.00150	0.00220	0.00130
^{86}Sr	0.04100	0.04200	bdl	bdl	0.04200
^{88}Sr	0.03550	0.03400	0.05790	0.02410	0.06690
^{89}Y	0.09150	0.17900	0.08200	0.08660	0.07780
^{90}Zr	0.02160	0.03150	0.02300	0.01580	0.02040
^{93}Nb	0.00141	0.00173	0.00436	0.00276	0.00313
^{95}Mo	0.12230	0.12920	0.07920	0.09190	0.06650

^{98}Mo	0.09890	0.07900	0.10270	0.10220	0.10290
^{107}Ag	0.00064	0.00018	bdl	0.00008	bdl
^{109}Ag	0.00007	bdl	0.00117	0.00007	0.00025
^{111}Cd	0.00720	0.00960	0.01470	0.04830	0.01550
^{112}Cd	0.02270	0.02000	0.03010	0.02580	0.02780
^{114}Cd	0.02440	0.01680	0.02150	0.02490	0.02200
^{115}In	0.00567	0.00635	0.00349	0.00356	0.00357
^{118}Sn	0.20700	0.16750	0.16000	0.21400	0.18200
^{120}Sn	0.20700	0.17270	0.16320	0.19800	0.17700
^{121}Sb	0.00560	bdl	0.00100	0.00070	bdl
^{123}Sb	bdl	0.00210	0.00570	0.00560	bdl
^{127}I	bdl	bdl	bdl	bdl	bdl
^{133}Cs	bdl	bdl	0.00120	0.00076	0.00237
^{137}Ba	0.00490	0.01210	0.01450	0.00940	0.00450
^{138}Ba	0.00241	0.00682	0.00759	0.00342	0.00211
^{139}La	0.00006	0.00012	0.00016	0.00007	0.00004
^{140}Ce	0.00037	0.00011	0.00032	0.00015	0.00007
^{141}Pr	0.00008	0.00007	0.00007	0.00007	0.00004
^{146}Nd	0.00048	0.00047	0.00057	0.00092	0.00060
^{147}Sm	0.00044	0.00026	0.00024	0.00027	0.00047
^{153}Eu	0.00014	0.00016	0.00015	0.00020	0.00014
^{157}Gd	0.00247	0.00096	0.00082	0.00108	0.00204
^{159}Tb	0.00131	0.00103	0.00069	0.00109	0.00056

^{163}Dy	0.00940	0.01510	0.00570	0.00799	0.00980
^{165}Ho	0.00203	0.00681	0.00428	0.00365	0.00310
^{166}Er	0.01400	0.02250	0.01190	0.01300	0.01380
^{169}Tm	0.00236	0.00505	0.00217	0.00289	0.00216
^{172}Yb	0.02870	0.04664	0.02010	0.02160	0.02180
^{175}Lu	0.00440	0.00927	0.00343	0.00429	0.00507
^{178}Hf	0.00046	0.00081	0.00048	0.00176	0.00127
^{181}Ta	0.00007	bdl	bdl	bdl	0.00018
^{182}W	0.00354	0.00058	0.00030	0.00263	0.00089
^{183}W	0.00169	0.00099	0.00105	0.00161	0.00054
^{184}W	0.00282	0.00124	0.00077	0.10390	0.00016
^{185}Re	0.00008	0.00039	bdl	bdl	0.00006
^{187}Re	bdl	bdl	0.00016	bdl	0.00023
^{205}Tl	0.00501	0.00449	0.00123	0.00046	0.00093
^{208}Pb	0.00478	0.00176	0.16800	0.12300	0.00250
^{209}Bi	bdl	bdl	0.00192	0.00127	0.00043
^{232}Th	0.00000	0.00026	0.00031	0.00015	0.00014
^{238}U	0.00018	0.00014	0.00020	0.00012	0.00017

*Trace element detection limit of 0.0001 ppm

Table 7: Olivine trace element data for NWA 6234

	Ol_01-core	**Ol_02- core**	**Ol_03-core**	**Ol_04-core**	**Ol_05-rim**
^{7}Li	2.25	2.29	2.87	2.08	3.12

^{12}C	bdl	bdl	bdl	bdl	bdl
^{19}F	34.59	51.55	75.15	34.07	46.65
^{23}Na	71.21	80.83	65.93	62.72	70.63
^{24}Mg	254238.13	250497.13	246101.73	249501.03	216569.95
^{25}Mg	257925.77	257574.19	251643.89	255138.88	222896.17
^{27}Al	716.99	680.84	478.36	633.55	842.07
^{28}Si	180444.80	182079.44	178843.59	179335.08	179433.03
^{29}Si	179029.28	180151.13	177580.23	177813.94	180151.13
^{31}P	186.75	182.61	492.25	222.80	179.06
^{35}Cl	188.37	158.23	162.86	167.80	232.69
^{39}K	11.49	bdl	202.24	129.25	92.87
^{43}Ca	1926.32	2075.19	1579.65	1691.56	2043.96
^{44}Ca	2167.19	2254.33	1832.42	1930.09	2303.39
^{45}Sc	7.52	7.93	9.04	7.91	9.14
^{47}Ti	45.64	44.61	48.51	49.64	58.09
^{51}V	30.38	29.33	21.19	22.01	21.44
^{52}Cr	1895.06	2098.00	1693.53	1834.44	1606.51
^{53}Cr	2008.08	2254.40	1791.07	1951.58	1706.09
^{55}Mn	3728.85	3856.73	3813.63	3825.05	4633.79
^{56}Fe	185733.16	194927.03	203704.42	198637.64	241540.34
^{59}Co	108.61	111.66	120.15	109.43	125.25
^{60}Ni	674.37	653.71	593.27	632.18	548.90
^{62}Ni	668.95	662.25	600.95	633.51	546.55

^{63}Cu	2.74300	2.46100	1.65900	2.03900	3.47000
^{65}Cu	3.45000	3.75000	3.34000	3.52000	3.43000
^{66}Zn	76.57000	80.11000	75.83000	84.94000	107.94000
^{69}Ga	6.63000	7.04000	4.25000	6.79000	9.95000
^{71}Ga	1.57700	1.58300	0.69000	0.98400	1.52100
^{72}Ge	1.38000	1.41000	1.52000	1.34000	1.37000
^{73}Ge	1.07000	1.17000	1.02000	1.01000	1.00000
^{74}Ge	1.06000	1.11000	1.12000	1.05000	0.97000
^{75}As	5.90000	4.20000	0.97000	0.95000	0.71000
^{79}Br	bdl	bdl	bdl	bdl	bdl
^{85}Rb	0.12310	0.10960	0.06390	0.08570	0.14470
^{86}Sr	43.06000	52.48000	16.83000	24.36000	36.57000
^{88}Sr	42.61000	52.04000	16.48000	24.39000	36.40000
^{89}Y	0.12060	0.12530	0.11490	0.12920	0.14380
^{90}Zr	0.08000	0.10110	0.06830	0.10050	0.23600
^{93}Nb	0.01040	0.00760	0.00870	0.01370	0.01290
^{95}Mo	0.08000	0.09000	0.07000	0.08000	0.08000
^{98}Mo	0.06100	0.05300	0.05900	0.05500	0.05900
^{107}Ag	bdl	bdl	0.04900	bdl	0.01400
^{109}Ag	bdl	bdl	0.14000	bdl	0.01900
^{111}Cd	0.04400	0.13000	0.09500	0.13000	0.07400
^{112}Cd	0.13000	0.16000	0.15000	0.11000	0.14000
^{114}Cd	0.09000	0.14000	0.12000	0.14000	0.15000

^{115}In	0.03800	0.08900	0.06100	0.05400	0.05900
^{118}Sn	0.81000	0.74000	1.00000	0.77000	0.69000
^{120}Sn	0.81000	0.68000	1.00000	0.75000	0.75000
^{121}Sb	0.17000	0.13000	0.03800	0.04400	0.06100
^{123}Sb	0.17000	0.11000	0.09000	0.05700	1.25000
^{127}I	bdl	bdl	bdl	bdl	bdl
^{133}Cs	0.00419	0.00303	0.00230	0.00480	0.00600
^{137}Ba	53.22000	56.74000	36.70000	60.20000	87.95000
^{138}Ba	52.27000	56.54000	36.52000	59.68000	87.92000
^{139}La	0.00093	0.00083	0.00046	0.00139	0.00233
^{140}Ce	0.00095	0.00084	0.00051	0.00248	0.00246
^{141}Pr	0.00024	0.00019	0.00007	0.00005	0.00042
^{146}Nd	0.00128	0.00094	0.00080	0.00069	0.00243
^{147}Sm	0.00037	0.00174	0.00064	0.00091	0.00155
^{153}Eu	0.00149	0.00197	0.00111	0.00179	0.00206
^{157}Gd	0.00570	0.00460	0.00231	0.00430	0.00490
^{159}Tb	0.00116	0.00151	0.00120	0.00150	0.00150
^{163}Dy	0.01630	0.01050	0.01440	0.01340	0.01160
^{165}Ho	0.00371	0.00411	0.00389	0.00377	0.00470
^{166}Er	0.01660	0.01830	0.01960	0.01660	0.02000
^{169}Tm	0.00306	0.00217	0.00339	0.00415	0.00440
^{172}Yb	0.03470	0.03350	0.03590	0.03720	0.03850
^{175}Lu	0.00563	0.00532	0.00685	0.00595	0.00989

^{178}Hf	0.00245	0.00200	0.00319	0.00317	0.00500
^{181}Ta	0.00034	bdl	bdl	0.00006	0.00015
^{182}W	0.06600	0.10400	0.10000	0.08300	0.06200
^{183}W	0.05200	0.09900	0.10000	0.05600	0.05200
^{184}W	0.05400	0.09500	0.12000	0.07600	0.05100
^{185}Re	0.00140	bdl	bdl	bdl	0.00160
^{187}Re	0.00300	bdl	bdl	bdl	bdl
^{205}Tl	0.00760	0.00840	0.01000	0.03100	0.02400
^{208}Pb	0.04530	0.03010	0.08070	0.07010	0.07340
^{209}Bi	bdl	0.00840	bdl	bdl	bdl
^{232}Th	0.00008	bdl	bdl	0.00035	0.00023
^{238}U	0.09670	0.22200	0.01348	0.04140	0.05490

*Trace element detection limit of 0.0001 ppm

Table 8: Olivine trace element data for NWA 10170

	Ol_01-core	**Ol_02-core**	**Ol_02-rim**	**Ol_03-core**	**Ol_03-rim**	**Ol_04-core**	**Ol_05-core**
^{7}Li	1.98	3.64	3.24	1.78	4.01	3.65	2.01
^{12}C	bdl	bdl	bdl	bdl	bdl	bdl	bdl
^{19}F	245.39	372.29	bdl	304.35	310.14	125.02	309.93
^{23}Na	164.20	117.35	141.60	163.72	138.44	134.69	144.48
^{24}Mg	191832.72	175233.45	175466.77	198190.84	169570.38	180837.63	189792.88
^{25}Mg	206540.22	188415.02	188059.67	214672.03	183066.13	195604.47	204731.56
^{27}Al	518.90	493.20	510.98	543.81	440.83	438.86	489.70

^{28}Si	174869.06	174869.06	174869.06	174869.06	174869.06	174869.06	174869.06
^{29}Si	170899.97	176346.28	175462.63	175304.16	175164.98	175477.20	174316.67
^{31}P	290.71	384.00	390.92	642.26	622.59	810.01	202.39
^{35}Cl	228.39	232.78	245.04	235.31	239.48	251.10	209.21
^{39}K	55.36	30.60	69.92	58.10	46.60	35.46	41.19
^{43}Ca	1570.44	1581.53	1538.01	1760.92	1456.72	1405.97	1392.25
^{44}Ca	1864.37	1866.78	1718.85	2044.58	1682.41	1647.94	1678.23
^{45}Sc	7.19	9.11	8.61	7.74	9.19	9.71	7.35
^{47}Ti	64.99	63.87	45.77	51.10	41.66	48.58	41.60
^{51}V	36.92	35.38	29.42	34.01	31.53	30.80	29.81
^{52}Cr	2501.58	1677.33	1384.87	1906.68	1595.10	1306.10	1605.08
^{53}Cr	2618.91	1754.89	1454.79	2014.78	1702.37	1342.66	1714.52
^{55}Mn	3486.75	4433.38	4313.30	3613.60	4393.79	4224.49	3745.56
^{56}Fe	173139.25	226103.23	226370.73	175706.64	234275.63	218749.33	184473.61
^{59}Co	96.98	105.40	101.91	100.44	105.76	103.21	97.80
^{60}Ni	612.31	563.93	541.25	623.36	557.17	561.38	591.28
^{62}Ni	602.52	564.24	541.25	621.39	554.19	564.97	579.28
^{63}Cu	3.39000	0.99300	1.62400	2.10200	1.62000	1.21900	2.15700
^{65}Cu	3.20000	2.47700	2.24800	2.23500	2.20400	1.96200	2.47900
^{66}Zn	85.88000	109.83000	112.08000	72.00000	112.37000	108.16000	89.69000
^{69}Ga	1.51800	2.14400	1.78500	1.33100	1.37600	1.28500	1.28800
^{71}Ga	0.71500	1.01100	1.00000	0.53100	1.00200	0.78000	0.67800
^{72}Ge	0.50000	0.47300	0.50200	0.61500	0.52900	0.64000	0.59300

^{73}Ge	0.43000	0.45600	0.40600	0.52000	0.45600	0.49500	0.46700
^{74}Ge	0.35700	0.37100	0.35700	0.45200	0.37900	0.47100	0.42900
^{75}As	0.14710	0.32600	0.20300	0.19800	0.13930	0.15940	0.15700
^{79}Br	51.21000	59.24000	48.12000	52.35000	62.61000	76.33000	62.43000
^{85}Rb	0.09920	0.09980	0.11130	0.10150	0.07950	0.06700	0.07800
^{86}Sr	10.95000	14.86000	12.07000	13.83000	8.35000	7.58000	10.28000
^{88}Sr	11.25000	14.60000	11.90000	13.59000	7.94000	7.35000	10.20000
^{89}Y	0.17200	0.16550	0.14370	0.15200	0.12790	0.13350	0.11100
^{90}Zr	0.48600	0.21500	0.16910	0.14180	0.13550	0.15530	0.10120
^{93}Nb	0.02090	0.01650	0.01760	0.01750	0.01560	0.01440	0.01610
^{95}Mo	0.09950	0.10920	0.11900	0.09020	0.09790	0.10900	0.10470
^{98}Mo	0.06890	0.07720	0.07030	0.08420	0.07380	0.06600	0.07900
^{107}Ag	0.07140	0.04760	0.03140	0.09530	0.25500	0.01920	0.06170
^{109}Ag	0.07180	0.04570	0.02880	0.09220	0.25600	0.01900	0.06040
^{111}Cd	0.02740	0.06290	0.05620	0.04660	0.03050	0.04550	0.03050
^{112}Cd	0.04320	0.06920	0.05590	0.05930	0.06190	0.05280	0.03820
^{114}Cd	0.03530	0.07200	0.04550	0.05280	0.04450	0.04130	0.03240
^{115}In	0.01680	0.02020	0.02880	0.00487	0.01450	0.01770	0.01460
^{118}Sn	0.23400	0.22400	0.23200	0.21200	0.23300	0.21500	0.18390
^{120}Sn	0.23100	0.22100	0.22800	0.20100	0.24300	0.21300	0.19100
^{121}Sb	0.02010	0.01430	0.06200	0.00500	0.02590	0.01650	0.01690
^{123}Sb	0.01750	0.01320	0.06400	0.01810	0.03070	0.01630	0.01970
^{127}I	0.00799	0.00759	0.00789	0.00756	0.00832	0.00838	0.00701

^{133}Cs	0.02410	0.00354	0.00596	0.00990	0.00670	0.00395	0.01310
^{137}Ba	9.05000	13.51000	9.27000	8.98000	5.18000	5.87000	6.65000
^{138}Ba	8.82000	12.84000	9.11000	8.90000	5.10000	5.76000	6.72000
^{139}La	0.00700	0.00524	0.01075	0.00692	0.00169	0.00155	0.00132
^{140}Ce	0.02490	0.01910	0.02300	0.01380	0.00705	0.00712	0.00481
^{141}Pr	0.00314	0.00183	0.00304	0.00213	0.00044	0.00064	0.00066
^{146}Nd	0.01410	0.00670	0.01560	0.00890	0.00203	0.00294	0.00310
^{147}Sm	0.00580	0.00280	0.00433	0.00368	0.00072	0.00122	0.00106
^{153}Eu	0.00301	0.00149	0.00175	0.00185	0.00046	0.00073	0.00042
^{157}Gd	0.01350	0.00810	0.00710	0.00880	0.00290	0.00420	0.00191
^{159}Tb	0.00310	0.00187	0.00178	0.00211	0.00097	0.00112	0.00061
^{163}Dy	0.02610	0.02040	0.02120	0.01860	0.01160	0.01310	0.00940
^{165}Ho	0.00850	0.00596	0.00784	0.00618	0.00518	0.00493	0.00449
^{166}Er	0.02760	0.02560	0.02510	0.02320	0.01960	0.02070	0.02060
^{169}Tm	0.00610	0.00499	0.00503	0.00431	0.00397	0.00449	0.00350
^{172}Yb	0.04820	0.03460	0.03930	0.03520	0.03650	0.04090	0.03080
^{175}Lu	0.01080	0.00683	0.00810	0.00760	0.00668	0.00823	0.00631
^{178}Hf	0.01480	0.00660	0.00560	0.00540	0.00212	0.00316	0.00180
^{181}Ta	0.00137	0.00036	0.00087	0.00047	0.00013	0.00032	0.00052
^{182}W	0.00700	0.00900	0.00880	0.01800	0.00760	0.00171	0.00626
^{183}W	0.00470	0.00610	0.00640	0.02030	0.00970	0.00228	0.00540
^{184}W	0.00820	0.00770	0.00910	0.02080	0.00970	0.00280	0.00741
^{185}Re	0.00016	bdl	0.00059	0.00013	bdl	0.00012	0.00018

^{187}Re	0.00000	0.00004	0.00002	0.00015	bdl	0.00018	bdl
^{205}Tl	0.00293	0.06560	0.02400	0.00982	0.00478	0.01430	0.00279
^{208}Pb	1.72100	0.30500	0.76500	1.14900	2.44000	0.79100	2.25100
^{209}Bi	0.00191	0.00075	0.00184	0.00152	0.00199	0.00165	0.00049
^{232}Th	0.00410	0.00077	0.00318	0.00032	0.00036	0.00026	0.00020
^{238}U	0.01510	0.02990	0.01790	0.02900	0.01140	0.01200	0.01250

*Trace element detection limit of 0.0001 ppm

Table 9: Olivine trace element data for NWA 1068

	Ol_01-core	**Ol_01-rim**	**Ol_02-rim**	**Ol_03-core**	**Ol_04-core**	**Ol_05-core**	**Ol_06-core**
^{7}Li	5.94	6.03	5.76	2.74	3.45	3.34	3.86
^{12}C	bdl	bdl	bdl	bdl	bdl	bdl	bdl
^{19}F	49.31	44.54	55.47	62.95	73.88	43.93	52.16
^{23}Na	81.05	35.30	70.43	8.95	76.21	52.41	54.16
^{24}Mg	203657.63	208546.56	166136.95	202143.95	204649.28	222027.50	196217.72
^{25}Mg	243971.31	250836.42	202145.13	234759.97	245872.56	254790.66	229418.88
^{27}Al	1199.51	1309.68	526.70	573.25	902.81	717.02	548.19
^{28}Si	175384.59	175700.06	174552.75	172137.20	175408.08	174242.20	172359.97
^{29}Si	174354.94	175149.58	174495.19	170755.64	174635.39	172344.95	175009.36
^{31}P	287.14	342.87	212.65	143.99	165.62	176.47	297.08
^{35}Cl	163.07	181.55	149.47	143.54	143.85	154.2	161.19
^{39}K	bdl	54.81	bdl	104.90	bdl	23.43	25.61
^{43}Ca	4875.07	4670.81	3667.46	2553.17	5516.70	8533.08	4238.38

^{44}Ca	5411.90	5138.42	4023.27	3020.10	6055.77	9270.74	4804.47
^{45}Sc	9.23	9.48	10.37	9.08	8.46	8.48	9.43
^{47}Ti	67.18	56.27	538.16	51.09	48.88	42.67	50.21
^{51}V	39.32	38.24	29.60	24.86	25.82	26.86	24.56
^{52}Cr	2163.27	1944.96	436.41	705.43	904.43	986.50	931.45
^{53}Cr	2279.76	2054.08	465.18	747.00	957.93	1045.04	976.19
^{55}Mn	4423.67	4163.01	5684.29	4419.35	4367.72	4338.45	4887.99
^{56}Fe	261500.97	240333.11	333530.50	261653.89	237826.81	246608.30	299546.34
^{59}Co	144.38	137.67	168.62	146.15	145.37	141.01	155.96
^{60}Ni	649.56	651.24	553.20	656.84	703.85	724.73	629.84
^{62}Ni	620.85	634.41	535.74	618.66	680.35	693.14	616.52
^{63}Cu	1.56200	2.22300	1.35800	0.52200	1.99300	1.09300	0.63400
^{65}Cu	1.17000	2.12000	1.10000	1.64000	1.58000	1.56000	1.99000
^{66}Zn	111.34000	107.69000	117.78000	88.32000	91.88000	80.78000	110.11000
^{69}Ga	3.47000	4.50000	1.99700	1.78000	1.88300	1.07300	1.17400
^{71}Ga	1.20400	1.05200	1.25400	0.35900	0.69100	0.44000	0.59200
^{72}Ge	0.74000	0.82000	0.78000	0.77000	0.91000	1.04000	0.72000
^{73}Ge	0.66000	0.67000	0.73000	0.66000	0.81000	0.93000	0.63000
^{74}Ge	0.60000	2.11000	0.72000	0.64000	0.75000	0.88000	0.59000
^{75}As	0.13600	0.45000	0.14000	0.34000	0.33000	0.17000	0.47000
^{79}Br	bdl	bdl	bdl	bdl	bdl	bdl	bdl
^{85}Rb	0.18310	0.24500	0.10520	0.03690	0.17470	0.11560	0.08060
^{86}Sr	12.59000	15.13000	6.13000	4.76000	9.94000	10.31000	5.07000

^{88}Sr	12.19000	14.63000	5.82000	4.67000	9.79000	10.22000	5.11000
^{89}Y	0.16100	0.17400	0.22100	0.13980	0.14200	0.12600	0.14770
^{90}Zr	0.63900	0.72400	5.93000	0.15700	0.18300	0.22400	0.16000
^{93}Nb	0.03600	0.05690	0.21200	0.01440	0.01200	0.01650	0.02700
^{95}Mo	0.11000	0.12000	0.13000	0.11000	0.12000	0.10000	0.12000
^{98}Mo	0.08000	0.08000	0.08000	0.08000	0.09000	0.08000	0.10000
^{107}Ag	bdl	bdl	0.00130	0.00068	bdl	bdl	bdl
^{109}Ag	bdl	bdl	0.00092	bdl	0.00084	bdl	0.00108
^{111}Cd	0.03700	0.08200	0.07100	0.07500	0.09600	0.04900	0.10000
^{112}Cd	0.03700	0.09600	0.07400	0.08100	0.10300	0.05000	0.10800
^{114}Cd	0.04700	0.08700	0.06600	0.07600	0.08900	0.04800	0.09600
^{115}In	0.00710	0.01280	0.00910	0.01060	0.01600	0.00640	0.01260
^{118}Sn	0.22000	0.36000	0.22000	0.22000	0.21000	0.22000	0.25000
^{120}Sn	0.23000	0.35000	0.19000	0.21000	0.21000	0.23000	0.22000
^{121}Sb	0.00610	0.00890	0.00360	0.00740	0.00550	bdl	0.01010
^{123}Sb	bdl	0.01200	bdl	bdl	0.00800	0.01250	0.00900
^{127}I	bdl	bdl	bdl	bdl	bdl	bdl	bdl
^{133}Cs	0.01069	0.00958	0.00680	0.00175	0.00799	0.00634	0.00359
^{137}Ba	24.01000	37.13000	9.23000	14.77000	13.03000	6.92000	6.78000
^{138}Ba	23.99000	37.70000	9.04000	14.85000	13.01000	6.81000	6.73000
^{139}La	0.00312	0.00418	0.00099	0.00062	0.00446	0.00168	0.00080
^{140}Ce	0.00878	0.01351	0.00308	0.00268	0.01118	0.00292	0.00119
^{141}Pr	0.00111	0.00104	0.00052	0.00004	0.00103	0.00050	0.00031

^{146}Nd	0.00440	0.00870	0.00286	0.00121	0.00730	0.00293	0.00224
^{147}Sm	0.00182	0.00289	0.00166	0.00090	0.00178	0.00171	0.00089
^{153}Eu	0.00190	0.00235	0.00128	0.00073	0.00172	0.00102	0.00070
^{157}Gd	0.00543	0.00670	0.00680	0.00228	0.00550	0.00500	0.00280
^{159}Tb	0.00129	0.00185	0.00220	0.00096	0.00173	0.00147	0.00131
^{163}Dy	0.01620	0.01870	0.02490	0.01830	0.01660	0.01520	0.01730
^{165}Ho	0.00445	0.00558	0.00954	0.00477	0.00541	0.00521	0.00526
^{166}Er	0.02250	0.02490	0.03800	0.02060	0.02190	0.02020	0.02340
^{169}Tm	0.00438	0.00453	0.00600	0.00407	0.00385	0.00375	0.00435
^{172}Yb	0.04030	0.03970	0.07000	0.02850	0.03570	0.03440	0.03970
^{175}Lu	0.00834	0.01055	0.01350	0.00785	0.00721	0.00682	0.00883
^{178}Hf	0.01150	0.01400	0.16000	0.00302	0.00516	0.00478	0.00510
^{181}Ta	0.00031	0.00037	0.00670	bdl	0.00018	0.00029	0.00004
^{182}W	0.02300	0.16000	0.09500	0.06000	0.15000	0.02100	0.26000
^{183}W	0.01700	0.17000	0.10200	0.05600	0.14000	0.02000	0.26000
^{184}W	0.02200	0.17000	0.09200	0.06900	0.15000	0.01900	0.27000
^{185}Re	bdl	0.00032	0.00028	0.00027	bdl	bdl	0.00027
^{187}Re	bdl	0.00040	bdl	bdl	bdl	0.00046	bdl
^{205}Tl	0.00340	0.01150	0.00270	0.00460	0.00620	0.00260	0.00680
^{208}Pb	0.13180	0.16640	0.09490	0.02100	0.10860	0.03330	0.05810
^{209}Bi	bdl	bdl	0.00061	bdl	bdl	bdl	bdl
^{232}Th	0.00179	0.00192	0.00027	bdl	0.00080	0.00011	0.00009
^{238}U	0.00616	0.00740	0.00564	0.00204	0.00926	0.00581	0.00269

*Trace element detection limit of 0.0001 ppm

Table 10: Olivine trace element data for NWA 1183

	Ol_01-core	Ol_02-core	Ol_03-core	Ol_04-core	Ol_04-rim	Ol_05-core	Ol_05-rim
^{7}Li	9.92	5.49	3.22	10.76	7.69	3.79	5.29
^{12}C	bdl	bdl	bdl	bdl	bdl	bdl	bdl
^{19}F	bdl	42.44	32.73	34.48	47.63	42.63	42.30
^{23}Na	121.74	72.72	119.63	126.23	113.61	131.76	77.49
^{24}Mg	230435.63	221580.22	230405.78	251824.34	156763.45	244725.67	187733.44
^{25}Mg	233790.92	227089.95	234448.83	257491.78	159979.78	246252.16	190349.27
^{27}Al	808.41	761.64	1822.61	1024.18	776.16	1364.69	1124.92
^{28}Si	177279.97	176824.52	174084.02	180043.48	161583.28	179722.78	167010.44
^{29}Si	176458.36	177767.19	177767.19	180010.89	160331.70	178094.41	166268.19
^{31}P	153.73	478.08	236.19	235.38	290.90	129.80	167.73
^{35}Cl	203.90	164.36	200.81	188.79	154.38	191.42	180.97
^{39}K	bdl	1108.94	bdl	bdl	bdl	bdl	1227.97
^{43}Ca	1869.98	2110.22	1857.85	1718.35	3140.72	1912.17	1845.38
^{44}Ca	2170.58	2326.68	2148.22	1973.57	3389.19	2202.82	2055.08
^{45}Sc	8.19	10.44	9.12	7.37	11.13	7.11	8.80
^{47}Ti	38.62	55.95	65.69	38.32	142.95	58.49	50.91
^{51}V	27.31	23.89	38.73	26.89	20.79	25.19	21.54
^{52}Cr	1180.61	793.66	1269.19	1290.00	355.58	818.11	460.24
^{53}Cr	1273.72	853.74	1384.80	1373.98	394.75	875.83	495.12

^{55}Mn	4164.98	4444.23	4107.57	3615.92	5122.80	4140.73	4406.81
^{56}Fe	175875.86	185793.81	166755.31	153744.84	237608.31	159774.34	200029.41
^{59}Co	127.60	121.29	111.74	107.92	138.62	121.24	109.51
^{60}Ni	704.10	643.73	706.71	821.17	445.86	784.83	534.56
^{62}Ni	688.16	644.55	714.18	815.41	446.35	800.19	536.16
^{63}Cu	1.83200	1.18700	0.80100	1.23700	0.98600	0.90300	0.83100
^{65}Cu	2.51000	2.12000	1.62000	1.80000	1.78000	2.38000	1.46000
^{66}Zn	87.87000	101.35000	80.73000	80.48000	120.74000	81.68000	120.48000
^{69}Ga	7.67000	43.15000	38.08000	10.54000	46.46000	37.70000	7.64000
^{71}Ga	1.48100	1.01300	0.56800	1.10400	0.83100	0.48500	0.98100
^{72}Ge	1.19000	1.53000	1.35000	1.50000	0.79000	1.16000	1.20000
^{73}Ge	1.06000	1.43000	2.13000	1.36000	0.50000	1.11000	1.02000
^{74}Ge	0.99000	4.67000	1.23000	1.34000	0.63000	1.00000	1.03000
^{75}As	4.53000	3.06000	1.56000	2.72000	2.18000	1.94000	1.24000
^{79}Br	bdl	bdl	bdl	bdl	bdl	bdl	bdl
^{85}Rb	0.13920	0.10140	0.22800	0.14780	0.21800	0.25900	0.12880
^{86}Sr	9.87000	15.63000	15.58000	9.27000	17.40000	13.46000	7.14000
^{88}Sr	10.09000	16.15000	15.52000	9.42000	15.24000	13.37000	6.96000
^{89}Y	1.11100	1.08000	0.81700	1.47700	0.83000	1.46600	0.79100
^{90}Zr	0.07960	0.15980	0.42800	0.35600	1.40100	0.48000	0.31700
^{93}Nb	0.01260	0.01840	0.02740	0.01320	0.05160	0.01690	0.02400
^{95}Mo	0.10000	0.12000	0.10000	0.09000	0.09000	0.09000	0.10000
^{98}Mo	0.08000	0.15000	0.08000	0.08000	0.07000	0.09000	0.08000

^{107}Ag	0.00430	0.42000	0.00440	0.07400	0.00360	0.11800	0.07700
^{109}Ag	0.00360	0.00160	0.00450	0.08800	0.00550	0.00580	0.00260
^{111}Cd	0.53000	1.46000	0.33000	0.48000	0.34000	0.39000	0.19000
^{112}Cd	0.54000	0.59000	0.31000	0.50000	0.32000	0.41000	0.18000
^{114}Cd	0.52000	0.45000	0.33000	0.48000	0.33000	0.38000	0.19000
^{115}In	0.01200	0.47000	0.01900	0.01700	bdl	0.00960	0.01140
^{118}Sn	0.33000	0.36000	0.34000	0.36000	0.29000	0.31000	0.31000
^{120}Sn	0.33000	0.39000	0.32000	0.38000	0.30000	0.30000	0.33000
^{121}Sb	0.07300	0.57000	0.02200	0.03200	0.03100	0.01800	0.01900
^{123}Sb	0.06800	0.47000	0.02000	bdl	0.01700	0.02800	0.01800
^{127}I	bdl	bdl	bdl	bdl	bdl	bdl	bdl
^{133}Cs	0.00620	0.00328	0.01130	0.00480	0.01000	0.01090	0.00910
^{137}Ba	63.05000	425.78000	379.38000	92.40000	468.49000	381.72000	66.67000
^{138}Ba	63.41000	413.81000	372.91000	91.57000	473.70000	375.70000	66.82000
^{139}La	1.25300	1.33800	0.52300	1.71900	0.44100	0.85200	0.56600
^{140}Ce	0.31900	0.62000	0.52600	0.36000	1.21600	0.66400	0.20410
^{141}Pr	0.25600	0.27700	0.13970	0.41800	0.13160	0.28000	0.13070
^{146}Nd	1.25200	1.23300	0.64800	1.88800	0.55700	1.24700	0.60800
^{147}Sm	0.22900	0.22900	0.13530	0.35500	0.13150	0.30400	0.14600
^{153}Eu	0.07650	0.07160	0.04570	0.10140	0.04240	0.09760	0.03850
^{157}Gd	0.29500	0.26000	0.17300	0.43400	0.14800	0.37700	0.16700
^{159}Tb	0.03070	0.02860	0.02600	0.05010	0.02360	0.04630	0.02260
^{163}Dy	0.16680	0.15990	0.14730	0.24100	0.15110	0.26200	0.09570

^{165}Ho	0.03250	0.02910	0.02790	0.04750	0.03320	0.05590	0.02310
^{166}Er	0.08070	0.09290	0.07830	0.10840	0.10120	0.14320	0.06700
^{169}Tm	0.00950	0.01035	0.01128	0.01350	0.01580	0.01980	0.00990
^{172}Yb	0.06890	0.10600	0.07370	0.07800	0.09100	0.08200	0.07020
^{175}Lu	0.01170	0.01320	0.01260	0.01370	0.02260	0.01740	0.01200
^{178}Hf	0.00112	0.00450	0.01460	0.01130	0.04780	0.01550	0.00790
^{181}Ta	bdl	0.00014	0.00043	0.00032	0.00300	0.00071	bdl
^{182}W	0.03000	0.35000	0.02000	0.04700	bdl	0.03400	0.02200
^{183}W	0.02800	0.34000	0.02300	0.01700	0.01700	0.02400	0.03200
^{184}W	0.02700	0.35000	0.01700	0.04800	0.01500	0.02500	0.02300
^{185}Re	bdl	0.00700	0.00050	bdl	bdl	0.00680	0.00049
^{187}Re	bdl	0.00097	bdl	bdl	bdl	bdl	bdl
^{205}Tl	0.00560	0.04300	0.00670	bdl	0.00970	0.03200	0.00650
^{208}Pb	0.29000	0.47200	0.36400	0.34200	0.66700	0.52600	0.44800
^{209}Bi	bdl	0.23000	0.00220	bdl	0.00380	0.00240	bdl
^{232}Th	0.00060	0.00246	0.01480	0.00076	0.03840	0.02070	0.00880
^{238}U	0.01380	0.01110	0.00308	0.00890	0.00304	0.00207	0.00463

*Trace element detection limit of 0.0001 ppm

Table 11: Olivine trace element data for NWA 11013

	Ol_01-01	**Ol_01-02**	**Ol_01-03**	**Ol_01-04**	**Ol_01-05**	**Ol_01-06**
^{7}Li	12.70	5.45	5.52	7.19	7.09	11.00
^{12}C	bdl	bdl	bdl	bdl	bdl	bdl

^{19}F	132.70	30.98	180.90	167.83	155.90	41.71
^{23}Na	120.65	111.77	120.60	130.31	109.72	62.50
^{24}Mg	67080.93	97403.72	98231.53	96726.42	84274.28	61244.59
^{25}Mg	71846.34	105248.73	106183.70	104989.52	91530.41	66653.47
^{27}Al	127.16	115.93	112.92	114.38	125.40	100.41
^{28}Si	172017.69	172017.70	172017.69	172017.69	172017.69	172017.69
^{29}Si	173713.84	171764.63	173257.72	174378.03	172148.59	174040.03
^{31}P	316.44	189.95	178.21	240.34	172.36	181.12
^{35}Cl	234.65	208.09	202.14	212.30	303.39	274.95
^{39}K	bdl	1.23	bdl	bdl	bdl	bdl
^{43}Ca	4288.34	4302.00	3874.06	3937.12	3933.79	3406.77
^{44}Ca	4561.50	4520.45	4206.01	4185.94	4204.53	3727.72
^{45}Sc	9.47	10.10	9.46	9.61	9.38	8.76
^{47}Ti	217.13	122.77	117.72	113.89	153.76	227.47
^{51}V	10.03	14.90	13.34	12.44	11.83	7.24
^{52}Cr	19.82	73.44	84.27	81.64	60.42	19.86
^{53}Cr	52.46	102.89	113.53	113.48	90.89	55.30
^{55}Mn	10492.45	8324.45	8396.33	8690.33	9109.94	11262.01
^{56}Fe	490440.09	403366.00	408169.78	417843.72	446692.44	506589.72
^{59}Co	189.67	192.95	198.65	201.57	194.48	191.04
^{60}Ni	106.30	194.84	207.88	208.51	163.13	90.52
^{62}Ni	103.46	193.48	206.64	203.87	162.02	85.99
^{63}Cu	0.15790	0.28500	0.38600	0.22600	0.14700	0.15700

^{65}Cu	0.57700	0.60800	0.53400	0.47300	0.85600	0.40000
^{66}Zn	282.41000	187.34000	183.91000	191.34000	224.30000	256.86000
^{69}Ga	0.27100	0.18040	0.19240	0.17650	0.20730	0.30400
^{71}Ga	0.26400	0.15820	0.16140	0.15670	0.19370	0.30900
^{72}Ge	2.26900	2.10400	2.12200	2.26900	2.19600	2.57000
^{73}Ge	2.09900	1.85000	1.91100	1.82500	1.95700	2.31600
^{74}Ge	2.02700	1.79200	1.82000	1.72900	1.86500	2.17700
^{75}As	0.08150	0.07170	0.07190	0.08090	0.08410	0.08810
^{79}Br	57.24000	57.98000	55.29000	55.23000	57.69000	63.29000
^{85}Rb	0.00150	0.00150	0.00150	bdl	0.00190	0.00210
^{86}Sr	bdl	0.24000	0.14300	bdl	bdl	0.09000
^{88}Sr	0.08130	0.07740	0.13770	0.01940	0.03760	0.10480
^{89}Y	0.88100	0.31400	0.30200	0.29400	0.35200	1.40600
^{90}Zr	0.08190	0.04050	0.03900	0.04620	0.05240	0.08700
^{93}Nb	0.00168	0.00067	0.00082	0.00080	0.00107	0.00354
^{95}Mo	0.21900	0.20700	0.18100	0.21000	0.22700	0.26200
^{98}Mo	0.03180	0.03950	0.03140	0.03020	0.03080	0.02530
^{107}Ag	0.00042	bdl	0.00050	0.00031	0.00083	0.00503
^{109}Ag	0.00042	0.00026	0.00136	bdl	0.00118	0.00518
^{111}Cd	0.06970	0.05280	0.06380	0.07150	0.09060	0.10700
^{112}Cd	0.08570	0.07070	0.07120	0.06750	0.08310	0.13170
^{114}Cd	0.08270	0.07150	0.06050	0.05930	0.07350	0.13500
^{115}In	0.01510	0.00970	0.01300	0.01160	0.01308	0.02670

^{118}Sn	0.18130	0.20600	0.17200	0.15560	0.24700	0.19800
^{120}Sn	0.18090	0.17500	0.16330	0.16240	0.23500	0.21100
^{121}Sb	0.00690	0.00650	0.00330	0.00820	0.00890	0.00130
^{123}Sb	0.00730	bdl	0.00300	0.00790	0.01040	0.00770
^{127}I	0.00719	0.00736	0.00706	0.00696	0.00733	0.00813
^{133}Cs	bdl	0.00179	0.00064	0.00029	0.00042	0.00390
^{137}Ba	0.01550	0.04460	0.16000	0.00270	0.01730	0.05100
^{138}Ba	0.01010	0.05600	0.16070	0.00035	0.01320	0.04450
^{139}La	0.00285	0.00357	0.00657	0.00048	0.00029	0.00142
^{140}Ce	0.00748	0.00699	0.01051	0.00190	0.00283	0.00530
^{141}Pr	0.00182	0.00117	0.00147	0.00036	0.00081	0.00211
^{146}Nd	0.01660	0.00900	0.00770	0.00260	0.00630	0.02120
^{147}Sm	0.01160	0.00390	0.00420	0.00154	0.00310	0.01060
^{153}Eu	0.00311	0.00204	0.00224	0.00185	0.00170	0.00155
^{157}Gd	0.04880	0.01440	0.01320	0.01170	0.01640	0.04700
^{159}Tb	0.01290	0.00349	0.00410	0.00412	0.00444	0.01640
^{163}Dy	0.11200	0.04070	0.03580	0.03470	0.04280	0.16900
^{165}Ho	0.03580	0.01185	0.01264	0.01200	0.01500	0.05920
^{166}Er	0.13500	0.05460	0.05070	0.04510	0.04430	0.23500
^{169}Tm	0.02560	0.00992	0.00895	0.00860	0.01123	0.04990
^{172}Yb	0.13400	0.07720	0.09550	0.09370	0.11140	0.35700
^{175}Lu	0.03450	0.02070	0.01830	0.01930	0.02000	0.05830
^{178}Hf	0.00300	0.00185	0.00161	0.00104	0.00170	0.00310

^{181}Ta	bdl	bdl	bdl	bdl	0.00003	0.00004
^{182}W	0.00069	0.00043	bdl	0.00031	0.00182	0.09590
^{183}W	0.00095	0.00033	bdl	bdl	0.00091	0.09090
^{184}W	0.00058	bdl	bdl	0.00011	0.00105	0.09630
^{185}Re	0.00023	0.00031	0.00024	0.00008	bdl	bdl
^{187}Re	0.00017	0.00024	0.00022	bdl	0.00020	0.00000
^{205}Tl	0.00102	0.00011	bdl	bdl	0.00051	0.00143
^{208}Pb	0.00620	0.00383	0.03270	0.00037	0.00324	0.00250
^{209}Bi	0.00070	0.00220	0.00078	0.00115	0.00051	0.00142
^{232}Th	0.00075	0.00282	0.00186	bdl	0.00031	0.00225
^{238}U	0.00015	0.00124	0.00114	0.00105	0.00058	0.00059

*Trace element detection limit of 0.0001 ppm

Table 12: Olivine trace element data for Chassigny

	Ol_01-core	**Ol_02-core**	**Ol_03-core**	**Ol_04-core**	**Ol_05-core**
^{7}Li	2.88	2.15	2.41	2.00	2.97
^{12}C	bdl	bdl	bdl	bdl	bdl
^{19}F	308.30	174.05	238.74	215.48	174.96
^{23}Na	76.65	81.11	72.30	62.47	71.00
^{24}Mg	175498.67	171531.77	173709.23	174722.28	174962.28
^{25}Mg	184003.19	183496.91	186397.88	186632.84	184326.94
^{27}Al	94.61	85.67	97.73	88.28	94.13
^{28}Si	168932.61	168932.59	168932.61	168932.61	168932.61

^{29}Si	171010.25	169646.47	169304.50	170586.66	167131.42
^{31}P	130.64	57.68	99.70	58.39	136.99
^{35}Cl	165.39	168.47	183.18	130.72	217.16
^{39}K	16.07	9.53	bdl	1.44	bdl
^{43}Ca	1489.54	799.83	1237.98	847.46	1067.50
^{44}Ca	1743.85	1110.20	1583.03	1124.23	1337.76
^{45}Sc	5.35	5.89	5.82	5.59	6.08
^{47}Ti	98.57	148.91	85.99	136.63	113.42
^{51}V	4.64	5.37	4.78	4.35	5.15
^{52}Cr	124.79	150.94	149.85	134.62	152.08
^{53}Cr	138.22	165.09	160.62	145.39	168.22
^{55}Mn	4301.41	4204.06	4300.23	4262.37	4215.96
^{56}Fe	221113.41	217965.75	217251.72	220867.97	216085.27
^{59}Co	157.18	156.87	157.33	158.80	153.63
^{60}Ni	516.59	528.12	517.55	532.24	513.11
^{62}Ni	514.29	516.46	513.23	525.61	505.04
^{63}Cu	1.97600	2.28600	1.10500	1.45000	0.59600
^{65}Cu					
^{66}Zn	79.96000	84.72000	82.06000	80.30000	78.99000
^{69}Ga	0.12650	0.14170	0.12660	0.12520	0.12440
^{71}Ga	0.08520	0.09790	0.06710	0.09050	0.08780
^{72}Ge	1.48600	1.36000	1.37400	1.28400	1.44200
^{73}Ge	1.43900	1.20600	1.18000	1.13600	1.27900

^{74}Ge	1.31600	1.21100	1.21900	1.04000	1.22400
^{75}As	0.12900	0.17200	0.15600	0.15400	0.12020
^{79}Br	57.48000	53.09000	58.16000	50.54000	56.32000
^{85}Rb	0.02270	0.03300	bdl	0.01030	0.00780
^{86}Sr	bdl	0.08800	0.15100	0.13300	bdl
^{88}Sr	0.11120	0.15000	0.04930	0.06150	0.05520
^{89}Y	0.25500	0.25800	0.28000	0.27100	0.31700
^{90}Zr	0.04030	0.40800	0.08550	0.65600	0.40800
^{93}Nb	0.00117	0.00285	0.00014	0.01570	0.00181
^{95}Mo	0.09600	0.11400	0.10130	0.10470	0.09880
^{98}Mo	0.07010	0.07620	0.07480	0.06790	0.05860
^{107}Ag	0.02090	0.01240	0.00650	0.01840	0.00860
^{109}Ag	0.02560	0.01190	0.00840	0.02020	0.00730
^{111}Cd	0.02550	0.03820	0.02470	0.02430	0.05160
^{112}Cd	0.04490	0.05340	0.04530	0.05070	0.06280
^{114}Cd	0.03190	0.04300	0.03170	0.03400	0.05280
^{115}In	0.00374	0.00335	0.00378	0.00323	0.00453
^{118}Sn	0.20700	0.18200	0.19500	0.20500	0.20400
^{120}Sn	0.20300	0.19200	0.18700	0.18400	0.20200
^{121}Sb	0.02730	0.01200	0.01810	0.01900	0.01660
^{123}Sb	0.02030	0.00450	0.01030	0.01340	0.00610
^{127}I	0.00724	0.00671	0.00737	0.00624	0.00717
^{133}Cs	0.00191	0.00229	bdl	0.00234	0.00126

^{137}Ba	0.08610	0.16100	0.02920	0.09990	0.03420
^{138}Ba	0.10470	0.14510	0.04220	0.08860	0.04410
^{139}La	0.00048	0.00157	0.00012	0.00171	0.00083
^{140}Ce	0.00145	0.00271	0.00034	0.00357	0.00159
^{141}Pr	0.00028	0.00033	0.00011	0.00034	0.00027
^{146}Nd	0.00117	0.00118	0.00127	0.00153	0.00149
^{147}Sm	0.00089	0.00030	0.00087	0.00053	0.00092
^{153}Eu	0.00044	0.00070	0.00061	0.00026	0.00054
^{157}Gd	0.01100	0.00530	0.00960	0.00260	0.00970
^{159}Tb	0.00286	0.00265	0.00367	0.00329	0.00379
^{163}Dy	0.02960	0.03000	0.03370	0.03320	0.03580
^{165}Ho	0.00916	0.00913	0.01142	0.00941	0.01078
^{166}Er	0.03750	0.04950	0.03900	0.04150	0.04960
^{169}Tm	0.00606	0.00851	0.00623	0.00817	0.00844
^{172}Yb	0.04230	0.06410	0.05860	0.07120	0.06660
^{175}Lu	0.01000	0.01043	0.01091	0.01410	0.01240
^{178}Hf	0.00090	0.01600	0.00178	0.01950	0.02020
^{181}Ta	0.00004	0.00004	bdl	0.00014	0.00003
^{182}W	0.00760	0.01550	0.01090	0.01000	0.00670
^{183}W	0.00860	0.01110	0.01060	0.00930	0.00830
^{184}W	0.01100	0.01310	0.01170	0.00910	0.00403
^{185}Re	bdl	0.00147	0.00038	0.00023	0.00031
^{187}Re	bdl	0.00163	0.00045	0.00045	0.00068

^{205}Tl	0.00076	0.00002	0.00113	0.00054	0.00041
^{208}Pb	0.08940	0.19780	0.09650	0.06030	0.01800
^{209}Bi	0.00162	0.00146	0.00130	0.00048	bdl
^{232}Th	0.00162	0.00146	0.00130	0.00048	bdl
^{238}U	0.00027	0.00111	0.00013	0.00022	0.00063

*Trace element detection limit of 0.0001 ppm

C-1

Table 1: Glass standard major element data

	Glass_14_1	Glass_14_2	Glass_14_3	Glass_21_1	Glass_21_2		Glass_14_1	Glass_14_1	Glass_14_1		Glass_14_ reference	Glass_21_ reference
	Basalt_NMNH-113716-1						Basaltic glass Smithsonian (Indian Ocean)				NMNH-113716-1	NMNH-117218-3
SiO_2	51.50	51.38	51.40	55.31	55.30		52.07	51.69	52.16		51.52	55.24
TiO_2	1.33	1.32	1.37	0.38	0.39		1.29	1.22	1.26		1.30	0.38
Al_2O_3	15.01	15.12	15.10	5.10	5.09		15.36	15.55	15.27		15.39	5.30
FeO	9.42	9.19	9.28	0.46	0.44		9.04	8.79	8.73		8.12	
MnO	0.14	0.14	0.16	0.53	0.54		0.14	0.14	0.16		0.17	0.55
CaO	11.41	11.37	11.39	15.30	15.21		11.23	11.24	11.14		11.31	14.80
MgO	8.24	8.27	8.26	3.95	3.95		8.39	8.17	8.21		8.21	3.94
Na_2O	2.63	2.51	2.56	1.24	1.30		2.63	2.57	2.54		2.48	1.20
K_2O	0.08	0.10	0.08	11.88	11.88		0.08	0.07	0.10		0.09	11.30
Cr_2O_3	0.03	0.02	0.02	0.02	0.01		0.04	0.05	0.04			
P_2O_5	0.12	0.12	0.13	4.05	4.11		0.13	0.12	0.12		0.12	3.93
SO_3	0.32	0.31	0.29	0.29	0.29		0.31	0.29	0.32		0.30	0.30
Total	100.23	99.85	100.04	98.51	98.51		100.72	99.91	100.03		99.01	96.94

*Oxide element detection limit of 0.01 wt. %

Table 2: Apatite standard major element data

	Apatite_SPI_1	Apatite_SPI_2	Apatite_SPI_3

P_2O_5	42.30	42.53	42.34
SiO_2	0.12	0.11	0.12
MgO	0.02	0.00	0.01
CaO	55.63	55.61	55.42
FeO	0.01	0.00	0.01
Na_2O	0.20	0.15	0.15
F	3.25	3.07	3.42
Cl	0.01	0.00	0.12
Total	101.53	101.47	101.59

*Oxide element detection limit of 0.01 wt. %

Table 3: BCR-2G standard trace element data

	BCR-2G certified	BCR-2G - 1	BCR-2G - 2	BCR-2G - 3	BCR-2G - 4	BCR-2G - 5	BCR-2G - 6	BCR-2G - 7	BCR-2G - 8	BCR-2G - 9
11µm spot										
^{7}Li	9.00	bdl	bdl	bdl	bdl	bdl	42.16	bdl	bdl	bdl
^{23}Na	23962.00	26381.84	25861.30	24894.29	26525.60	28095.00	24058.75	26607.35	24807.23	23011.03
^{24}Mg	21469.51	20023.43	19696.17	18412.03	19934.92	21238.87	18801.92	20276.02	18834.18	18229.56
^{27}Al	70916.44	72571.75	66721.95	66363.92	72133.60	74414.93	64844.87	71119.34	63331.40	64269.21
^{29}Si	254301.21	282019.45	290076.24	296134.37	276723.55	266773.07	301879.39	290653.19	297909.54	302312.95
^{43}Ca	50457.35	48634.56	48105.25	42939.61	49142.42	50691.44	44693.38	48461.45	46537.98	42225.47

^{45}Sc	33.00	34.33	35.78	34.89	32.93	34.65	36.22	32.82	30.86	34.67
^{49}Ti	13605.22	12967.57	12202.85	12194.45	12410.10	12507.93	11287.21	11446.71	11071.43	11047.81
^{51}V	425.00	465.74	447.15	454.82	481.05	473.98	414.64	412.61	430.00	418.49
^{53}Cr	17.00	14.57	16.85	17.03	12.18	23.39	15.46	12.40	15.27	12.60
^{55}Mn	1550.00	1636.50	1607.78	1576.51	1679.21	1684.50	1505.97	1443.31	1495.34	1547.79
^{57}Fe	97221.67	85019.07	84888.42	86754.25	90591.56	93607.88	82249.50	79312.07	85262.38	86805.43
^{59}Co	38.00	47.07	47.69	44.33	48.12	47.12	43.10	42.47	41.55	43.38
^{60}Ni	13.00	12.66	8.27	12.53	15.70	16.40	16.02	12.49	13.73	17.23
^{63}Cu	21.00	19.93	21.92	17.81	17.10	21.65	19.32	19.29	17.63	17.50
^{66}Zn	125.00	199.10	216.49	212.90	216.20	207.50	206.59	196.87	205.77	201.27
^{85}Rb	47.00	52.23	57.17	56.23	56.72	60.64	53.24	51.97	52.36	48.68
^{88}Sr	342.00	312.44	328.99	310.51	332.92	331.69	294.07	294.76	308.00	272.05
^{89}Y	35.00	30.59	32.20	30.21	31.51	36.40	29.96	30.39	29.65	24.61
^{90}Zr	184.00	158.85	175.27	162.54	169.78	184.46	148.59	156.85	161.08	137.58
^{93}Nb	12.50	11.54	13.06	11.85	12.20	13.82	12.03	10.86	11.64	9.95
^{137}Ba	683.00	622.97	676.09	613.21	673.95	756.00	598.48	651.05	666.79	576.93
^{139}La	24.70	23.39	23.97	22.43	24.21	25.98	20.90	21.23	23.71	19.75
^{140}Ce	53.30	50.78	51.46	47.29	51.34	56.44	47.06	49.69	52.95	41.84
^{141}Pr	6.70	6.46	6.88	5.73	6.49	7.61	5.67	5.65	6.90	5.87
^{146}Nd	28.90	25.92	25.72	25.02	27.83	29.27	21.90	28.31	26.42	22.77
^{147}Sm	6.59	6.14	6.48	6.10	5.23	6.51	6.19	5.19	7.03	5.36
^{153}Eu	1.97	1.52	1.49	1.77	1.95	1.50	2.12	2.16	1.77	1.47
^{157}Gd	6.71	7.88	6.04	5.79	6.36	5.49	6.37	5.10	7.15	4.37

^{159}Tb	1.02	0.92	0.97	0.88	0.95	0.99	0.85	0.70	0.75	0.80
^{163}Dy	6.44	6.71	5.26	5.00	6.16	5.70	6.29	5.12	7.16	5.23
^{165}Ho	1.27	1.53	1.28	1.03	0.96	1.18	0.97	1.43	0.95	0.89
^{166}Er	3.70	3.64	3.40	3.46	2.78	4.70	3.11	2.95	3.42	2.49
^{169}Tm	0.51	0.39	0.54	0.36	0.32	0.69	0.42	0.37	0.35	0.39
^{172}Yb	3.39	2.28	2.81	2.63	1.71	3.86	2.75	3.06	2.41	2.18
^{175}Lu	0.50	0.51	0.53	0.55	0.35	0.44	0.40	0.34	0.55	0.45
^{178}Hf	4.84	5.09	4.24	4.28	3.45	5.79	4.55	4.70	5.01	4.18
^{181}Ta	0.78	0.67	0.68	0.66	0.65	0.71	0.77	0.68	0.75	0.61
^{208}Pb	11.00	12.76	13.47	11.49	11.50	14.06	11.55	11.89	12.17	10.79
^{232}Th	5.90	5.74	6.03	5.09	4.71	5.96	5.49	5.53	5.09	4.83
^{238}U	1.69	1.49	1.86	2.18	1.73	1.79	1.79	1.63	1.68	1.54

*Trace element detection limit of 0.01 ppm

Table 4: BHVO-2G standard trace element data

	BHVO-2G certified	BHVO-2G-1	BHVO-2G-2	BHVO-2G-3	BHVO-2G-4	BHVO-2G-5	BHVO-2G-6	BHVO-2G-7	BHVO-2G-8	BHVO-2G-9
11µm spot										
^{7}Li		bdl	bdl	bdl	bdl	bdl	bdl	bdl	bdl	bdl
^{23}Na	17804.45	20763.77	20308.97	19020.25	18824.94	22062.66	20089.74	21907.62	19617.21	20567.63
^{24}Mg	42999.33	43616.61	45112.69	41400.42	43875.76	46714.48	42573.08	46350.89	42657.30	44769.52
^{27}Al	71974.89	73268.28	74215.92	74126.83	73166.65	78196.58	71066.88	78436.59	72225.81	76027.21
^{29}Si	230460.48	339229.93	328707.68	306076.64	346339.67	311779.01	296113.98	310809.84	323718.98	261576.73

^{43}Ca	81475.04	81474.75	81474.75	81474.75	81474.75	81474.75	81474.75	81474.75	81474.75	81474.75
^{45}Sc	33.00	36.42	34.23	35.78	33.24	36.96	36.60	38.84	32.98	35.51
^{49}Ti	16300.00	15917.89	14675.50	15771.13	14955.04	16202.80	15754.52	16250.23	13932.88	15060.80
^{51}V	308.00	374.17	356.65	397.51	348.00	383.19	368.07	375.84	350.79	355.17
^{53}Cr	293.00	315.66	306.87	324.51	308.82	363.38	313.25	348.69	323.88	298.90
^{55}Mn	1307.00	1571.10	1494.07	1538.80	1425.29	1574.57	1514.81	1612.14	1413.20	1438.40
^{57}Fe	87836.46	91251.19	86325.87	92615.95	80131.49	93133.69	85137.25	91025.11	84504.11	84695.60
^{59}Co	44.00	67.32	59.64	65.60	57.65	66.71	59.70	67.16	57.96	59.80
^{60}Ni	116.00	171.86	157.72	172.14	145.68	183.92	162.39	183.14	164.59	167.92
^{63}Cu	127.00	185.15	155.04	178.16	157.92	189.99	167.01	184.68	169.70	165.73
^{66}Zn	102.00	185.97	182.04	195.56	169.92	192.86	172.19	206.07	188.96	154.10
^{85}Rb	9.20	13.20	10.50	12.24	9.69	12.56	11.55	14.53	13.09	11.86
^{88}Sr	396.00	413.15	347.56	431.25	369.04	420.39	399.86	439.66	394.88	366.01
^{89}Y	26.00	26.05	22.29	25.77	22.19	25.05	22.61	28.27	23.87	22.60
^{90}Zr	170.00	176.03	137.22	162.77	156.21	171.73	163.20	167.93	164.83	145.08
^{93}Nb	18.30	20.61	16.27	18.81	18.89	20.92	19.86	22.25	18.63	18.56
^{137}Ba	131.00	147.38	127.66	135.20	115.66	142.60	138.41	155.72	145.15	140.49
^{139}La	15.20	15.93	12.72	15.04	14.52	15.99	15.77	17.77	15.19	14.10
^{140}Ce	37.60	42.09	33.80	36.50	37.46	38.34	40.16	40.86	38.53	35.53
^{141}Pr	5.35	6.23	4.65	5.25	4.75	5.53	5.99	5.82	6.01	4.47
^{146}Nd	24.50	28.60	23.42	23.61	22.00	24.79	24.39	25.82	23.70	23.96
^{147}Sm	6.10	6.62	4.83	5.53	4.82	6.53	5.00	5.78	6.25	6.04
^{153}Eu	2.07	2.49	1.73	2.33	1.82	2.19	1.82	2.06	1.95	2.23

^{157}Gd	6.16	7.62	4.94	5.16	7.15	6.60	5.66	6.63	6.11	5.77
^{159}Tb	0.92	0.91	0.59	0.91	0.77	0.93	0.94	0.88	0.75	0.87
^{163}Dy	5.28	6.06	4.89	4.45	5.04	5.26	3.47	5.00	4.65	5.00
^{165}Ho	0.98	1.11	0.71	0.86	1.20	1.00	0.97	1.22	0.87	1.07
^{166}Er	2.56	3.29	2.01	2.20	1.96	2.93	2.84	1.96	2.17	2.45
^{169}Tm	0.34	0.42	0.19	0.23	0.24	0.48	0.32	0.30	0.41	0.32
^{172}Yb	2.01	2.62	1.80	1.27	1.81	2.81	2.12	2.14	1.40	1.84
^{175}Lu	0.28	0.26	0.21	0.23	0.44	0.46	0.23	0.42	0.24	0.20
^{178}Hf	4.32	4.33	4.18	4.10	4.57	4.44	4.26	4.92	4.49	4.25
^{181}Ta	1.15	1.20	0.85	1.24	1.11	1.14	1.22	1.11	0.84	0.97
^{208}Pb	1.70	1.94	2.24	2.50	2.15	3.33	3.60	2.18	1.79	2.21
^{232}Th	1.22	1.62	0.92	1.31	1.04	1.63	1.43	1.35	1.04	1.24
^{238}U	0.40	0.42	0.63	0.31	0.37	0.36	0.41	0.33	0.39	0.49

*Trace element detection limit of 0.01 ppm

Table 4 *continued*

	BHVO-2G-10	BHVO-2G-11	BHVO-2G-12	BHVO-2G-13	BHVO-2G-14	BHVO-2G-15	BHVO-2G-16	BHVO-2G-17
^{7}Li	bdl	bdl	bdl	bdl	bdl	bdl	bdl	bdl
^{23}Na	21296.44	20083.80	20691.81	21392.53	21186.38	20259.22	21738.46	20700.20
^{24}Mg	46475.39	43663.04	45247.32	46044.29	46231.85	43542.45	46411.89	48573.29
^{27}Al	79086.83	76338.44	74371.06	80167.99	78250.41	72804.68	79143.14	79500.47
^{29}Si	301294.07	333456.71	348312.09	215167.24	230984.72	287611.31	300679.64	335555.57

^{43}Ca	81474.75	81474.75	81474.75	81474.75	81474.75	81474.75	81474.75	81474.75
^{45}Sc	35.26	37.26	36.56	36.75	36.99	32.65	35.93	35.14
^{49}Ti	16067.22	16191.56	16283.64	16343.69	16523.09	13782.80	16168.14	15474.14
^{51}V	350.82	377.32	395.80	377.88	383.36	340.20	388.82	361.81
^{53}Cr	324.86	340.78	330.43	305.87	332.72	300.73	336.84	319.26
^{55}Mn	1472.42	1524.95	1643.84	1535.82	1608.05	1413.50	1599.17	1498.79
^{57}Fe	81050.17	90375.14	97326.99	88852.65	91436.80	81294.92	90272.27	83773.08
^{59}Co	63.09	64.62	64.99	62.14	62.75	58.97	62.02	60.65
^{60}Ni	170.65	174.78	172.85	176.28	174.32	163.38	172.55	173.97
^{63}Cu	177.05	176.17	175.33	181.18	177.10	157.77	181.98	177.94
^{66}Zn	184.21	168.37	185.78	316.38	173.25	168.42	163.14	189.43
^{85}Rb	12.91	11.79	12.14	13.28	12.11	13.07	11.26	11.09
^{88}Sr	415.94	400.33	445.74	421.10	402.64	376.56	405.80	392.11
^{89}Y	24.27	25.98	27.22	26.29	24.00	22.55	25.33	23.50
^{90}Zr	172.05	159.26	181.09	156.84	144.13	156.96	169.68	149.03
^{93}Nb	20.76	18.00	20.19	18.33	18.78	18.97	19.88	19.38
^{137}Ba	139.47	146.82	169.23	130.21	135.65	136.76	137.04	140.68
^{139}La	16.88	15.87	16.65	16.13	15.34	14.92	16.86	15.40
^{140}Ce	39.27	41.04	40.23	39.19	38.15	37.80	40.29	37.87
^{141}Pr	5.67	5.59	6.02	5.93	5.19	5.37	5.23	5.88
^{146}Nd	24.64	23.91	26.59	24.16	21.81	21.29	21.77	24.87
^{147}Sm	7.06	6.68	4.69	5.95	6.73	6.55	4.97	5.59
^{153}Eu	2.19	2.30	2.29	2.49	2.26	1.89	2.11	1.74

^{157}Gd	5.69	6.66	6.60	8.92	7.30	5.87	7.39	9.26
^{159}Tb	0.67	0.62	1.05	0.78	0.84	0.73	0.86	1.01
^{163}Dy	5.80	5.69	5.84	4.78	6.17	4.72	5.27	5.48
^{165}Ho	1.11	0.95	1.06	0.96	0.96	0.92	0.99	0.80
^{166}Er	2.13	2.02	2.80	2.15	2.53	2.50	2.82	2.69
^{169}Tm	0.23	0.28	0.34	0.19	0.20	0.37	0.12	0.36
^{172}Yb	1.51	2.07	2.28	2.73	2.35	2.14	2.26	2.27
^{175}Lu	0.26	0.32	0.23	0.37	0.40	0.33	0.26	0.42
^{178}Hf	4.42	4.58	5.22	5.35	4.71	4.66	4.73	4.08
^{181}Ta	1.18	1.27	1.32	1.24	1.06	1.01	1.15	1.20
^{208}Pb	2.99	2.99	3.05	1.62	3.00	2.94	1.65	2.42
^{232}Th	1.11	1.03	1.52	1.57	1.13	1.30	1.17	1.03
^{238}U	0.52	0.51	0.52	0.51	0.45	0.38	0.40	0.33

*Trace element detection limit of 0.01 ppm

C-2

Table 5: DaG 1037 melt inclusion glass major and trace element data

	MI glass_1	**MI glass_2**	**2SD**	**MI glass_3**	**2SD**	**MI glass_4**	**2SD**
SiO_2	63.12	64.94	0.45	62.62	1.34	64.99	1.20
TiO_2	0.82	1.11	0.05	1.06	0.07	1.02	0.07
Al_2O_3	15.28	16.08	0.13	16.51	0.47	15.95	0.52
FeO	3.06	3.01	0.09	3.04	0.03	3.67	0.33
MnO	0.09	0.07	0.01	0.07	0.01	0.09	0.02

CaO	14.12	12.83	0.18	13.50	0.79	11.35	1.03
MgO	0.85	0.69	0.01	0.76	0.00	0.91	0.05
Na_2O	2.24	2.04	0.06	2.31	0.28	1.69	0.10
K_2O	0.03	0.04	0.01	0.04	0.01	0.36	0.03
Cr_2O_3	0.08	0.02	0.02	0.01	0.00	0.02	0.00
P_2O_5	0.70	0.77	0.01	0.68	0.00	1.09	0.54
SO_3	0.11	0.03	0.02	0.03	0.01	0.07	0.07
Total	100.49	101.63	0.26	100.63	0.44	101.20	0.51
Mg#	33.08	29.04		30.82		30.75	
CaO/Al_2O_3	0.92	0.80		0.82		0.71	
^{7}Li	bdl			bdl			
^{23}Na	14446.5989			21176.0186			
^{24}Mg	4049.9197			33914.2487			
^{27}Al	69528.7202			72900.4236			
^{29}Si	232393.4473			222612.7374			
^{43}Ca	120069.2078			54145.3073			
^{45}Sc	31.2957			24.9607			
^{49}Ti	5519.3974			6438.8387			
^{51}V	10.1103			15.9568			
^{53}Cr	105.2617			439.4718			
^{55}Mn	483.3327			1305.4573			
^{57}Fe	13174.6684			46663.5188			

^{59}Co	2.1235			27.1855			
^{60}Ni	bdl			74.5782			
^{63}Cu	bdl			19.2823			
^{66}Zn	32.8329			67.1751			
^{85}Rb	1.7621			1.7977			
^{88}Sr	56.8158			81.3067			
^{89}Y	42.2451			32.9310			
^{90}Zr	19.2085			22.9757			
^{93}Nb	0.4910			0.3658			
^{137}Ba	7.0708			10.3264			
^{139}La	0.2985			0.1839			
^{140}Ce	0.7129			1.1358			
^{141}Pr	0.2200			0.2503			
^{146}Nd	1.2544			1.3944			
^{147}Sm	0.5228			0.6242			
^{153}Eu	0.8309			0.8079			
^{157}Gd	2.9557			3.7018			
^{159}Tb	0.7136			0.5489			
^{163}Dy	6.5860			5.2127			
^{165}Ho	1.6749			0.8931			
^{166}Er	4.8697			3.0598			
^{169}Tm	0.6440			0.3552			
^{172}Yb	3.5077			2.6408			

^{175}Lu	0.4081			0.3124			
^{178}Hf	1.1763			0.6381			
^{181}Ta	0.0428			0.0492			
^{208}Pb	bdl			3.3271			
^{232}Th	0.0578			bdl			
^{238}U	0.1084			bdl			

*Oxide element detection limit of 0.01 wt. %; Trace element detection limit of 0.01 ppm

Table 6: Dho 019 melt inclusion pyroxene daughter crystal major and trace element data

	MI pyroxene_1	**2SD**	**MI pyroxene_2**	**2SD**	**MI pyroxene_3**	**2SD**
SiO_2	48.22	1.22	52.30	1.23	52.52	0.48
TiO_2	0.13	0.06	0.15	0.05	0.30	0.03
Al_2O_3	1.16	0.20	0.97	0.12	0.96	0.14
FeO	26.84	2.50	25.16	1.12	24.40	0.50
MnO	0.62	0.00	0.67	0.03	0.67	0.04
CaO	3.93	0.71	4.52	0.28	5.16	0.29
MgO	19.23	0.66	18.30	0.44	18.05	0.74
Na_2O	0.09	0.01	0.06	0.02	0.08	0.01
K_2O	0.03	0.02	0.00	0.00	0.02	0.03
Cr_2O_3	0.47	0.06	0.41	0.06	0.31	0.06
P_2O_5	0.02	0.00	0.02	0.02	0.01	0.00
SO_3	0.02	0.01	0.01	0.00	0.00	0.00
Total	100.78	2.54	102.59	0.21	102.49	0.39

Mg#	56.13		56.46		56.86	
CaO/Al_2O_3	3.48		4.69		5.41	
^{7}Li	74.5760		bdl		36.1204	
^{23}Na	8827.4360		1615.9521		8889.8390	
^{24}Mg	52991.9722		55970.8195		52841.2958	
^{27}Al	60041.2753		49803.8955		43775.1090	
^{29}Si	254400.0452		224655.2814		288089.4833	
^{43}Ca	97063.7796		74625.3213		50819.5489	
^{45}Sc	29.6523		27.1543		30.8458	
^{49}Ti	3227.2092		5260.1871		3648.5603	
^{51}V	69.3123		34.4458		40.1473	
^{53}Cr	3917.0143		675.5405		422.5349	
^{55}Mn	2579.8888		3054.6541		2346.3921	
^{57}Fe	75938.6522		143275.4099		108286.6328	
^{59}Co	28.3812		70.6036		50.5371	
^{60}Ni	87.3768		208.0046		77.5925	
^{63}Cu	4.3324		27.2858		9.1290	
^{66}Zn	220.9608		362.1862		130.9554	
^{85}Rb	105.1095		3.1766		3.3554	
^{88}Sr	261.7493		226.7197		424.8572	
^{89}Y	34.6616		26.2314		15.3789	
^{90}Zr	28.2601		27.3100		25.6678	

^{93}Nb	0.8330		0.3643		0.5469	
^{137}Ba	16.6181		27.9935		37.4729	
^{139}La	0.3899		0.1843		0.3159	
^{140}Ce	1.3355		0.8401		0.6566	
^{141}Pr	0.2194		0.2342		0.1839	
^{146}Nd	2.6560		1.1685		1.2398	
^{147}Sm	1.4834		1.4152		0.7873	
^{153}Eu	0.8745		0.3955		0.2390	
^{157}Gd	2.9284		2.2211		1.9582	
^{159}Tb	0.8630		0.5575		0.3892	
^{163}Dy	6.3033		3.9135		2.2655	
^{165}Ho	1.6134		1.0328		0.6624	
^{166}Er	4.0401		3.0179		1.6137	
^{169}Tm	0.4344		0.4252		0.2928	
^{172}Yb	2.5338		2.6004		2.1783	
^{175}Lu	0.4577		0.3892		0.2300	
^{178}Hf	1.5514		1.0472		1.2017	
^{181}Ta	0.0588		bdl		0.0384	
^{208}Pb	6.0939		1.6471		1.6269	
^{232}Th	0.1422		bdl		bdl	
^{238}U	0.1920		0.5832		0.1972	

*Oxide element detection limit of 0.01 wt. %; Trace element detection limit of 0.01 ppm

Table 7: SaU 005 melt inclusion glass major and trace element data

	MI glass_1	**MI glass_2**	**2SD**	**MI glass_3**
SiO_2	67.54	69.36	0.62	63.02
TiO_2	0.42	0.32	0.00	0.63
Al_2O_3	19.36	20.39	0.18	17.88
FeO	1.83	2.83	0.47	4.29
MnO	0.04	0.10	0.01	0.12
CaO	7.64	4.45	0.14	9.75
MgO	0.88	1.26	0.36	3.20
Na_2O	2.01	0.82	0.09	0.48
K_2O	0.01	0.11	0.02	0.06
Cr_2O_3	0.03	0.00	0.00	0.01
P_2O_5	2.17	0.94	0.01	0.76
SO_3	0.02	0.01	0.00	0.05
Total	101.93	100.73	0.20	101.04
Mg#	46.08	43.93		57.06
CaO/Al_2O_3	0.39	0.22		0.55
^{7}Li	bdl	bdl		bdl
^{23}Na	11399.7534	25999.0272		9210.7243
^{24}Mg	49489.3091	10877.2300		30496.9261
^{27}Al	48153.5466	70743.6210		50359.3342
^{29}Si	213001.7488	261049.6756		232125.2354

^{43}Ca	62887.3257	41878.9331		72747.5707
^{45}Sc	29.9493	19.2218		35.0901
^{49}Ti	5188.9289	3796.1861		3632.6255
^{51}V	66.0962	13.1428		59.1204
^{53}Cr	731.1047	147.9833		576.3321
^{55}Mn	1434.7518	584.0797		1111.5203
^{57}Fe	37128.2786	14722.4909		29449.7794
^{59}Co	21.9590	3.8466		13.9814
^{60}Ni	144.8734	9.4552		72.1670
^{63}Cu	5.7985	bdl		1.5858
^{66}Zn	40.6221	11.5457		36.6817
^{85}Rb	1.3463	bdl		bdl
^{88}Sr	174.1049	68.9516		25.1056
^{89}Y	26.4322	26.6985		18.9119
^{90}Zr	20.3906	20.4100		22.9407
^{93}Nb	0.3650	0.1217		0.1301
^{137}Ba	35.2566	10.2950		1.1055
^{139}La	0.0879	0.2642		0.0481
^{140}Ce	0.3707	0.5514		0.3373
^{141}Pr	0.0396	0.0800		0.0636
^{146}Nd	0.4794	1.0423		0.5711
^{147}Sm	0.2605	0.9712		0.9056
^{153}Eu	0.2351	0.5483		0.3912

^{157}Gd	2.2143	2.0368		1.4939
^{159}Tb	0.5088	0.5571		0.4443
^{163}Dy	5.1946	3.9330		3.7749
^{165}Ho	0.9041	0.9737		0.6937
^{166}Er	2.2071	2.9197		1.8106
^{169}Tm	0.5133	0.4826		0.3711
^{172}Yb	3.2707	1.7038		1.6983
^{175}Lu	0.2692	0.4530		0.2183
^{178}Hf	0.5372	0.5669		0.8839
^{181}Ta	0.0267	bdl		0.0453
^{208}Pb	0.8618	bdl		bdl
^{232}Th	bdl	bdl		0.0306
^{238}U	0.0773	bdl		0.0241

*Oxide element detection limit of 0.01 wt. %; Trace element detection limit of 0.01 ppm

Table 8: NWA 6234 melt inclusion glass major and trace element data

	MI glass_1	**2SD**	**MI glass_2**	**2SD**
SiO_2	56.88	0.21	57.96	0.50
TiO_2	0.06	0.02	0.07	0.01
Al_2O_3	27.80	0.17	27.40	0.21
FeO	1.41	0.06	1.05	0.05
MnO	0.02	0.01	0.01	0.01
CaO	11.04	0.10	10.49	0.27

MgO	0.20	0.02	0.17	0.01
Na_2O	4.85	0.08	5.20	0.18
K_2O	0.28	0.02	0.39	0.06
Cr_2O_3	0.02	0.01	0.00	0.01
P_2O_5	0.07	0.01	0.06	0.01
SO_3	0.00	0.00	0.00	0.00
Total	102.61	0.14	102.80	0.25
Mg#	20.01		22.34	
CaO/Al_2O_3	0.40		0.38	
^{7}Li	bdl		bdl	
^{23}Na	25628.7861		29422.0191	
^{24}Mg	3270.0657		635.4559	
^{27}Al	94043.7007		98587.2019	
^{29}Si	208903.1347		205476.0638	
^{43}Ca	45960.8062		47088.9860	
^{45}Sc	4.7909		2.9897	
^{49}Ti	277.5552		299.8153	
^{51}V	10.4693		3.3999	
^{53}Cr	46.9222		bdl	
^{55}Mn	173.9196		31.2173	
^{57}Fe	6559.0438		3343.1380	
^{59}Co	1.5854		0.4437	

^{60}Ni	bdl		bdl	
^{63}Cu	bdl		bdl	
^{66}Zn	10.6020		10.1869	
^{85}Rb	4.0970		2.3264	
^{88}Sr	84.3133		96.8223	
^{89}Y	0.2688		0.1509	
^{90}Zr	1.0358		0.5002	
^{93}Nb	0.0250		0.0251	
^{137}Ba	15.3450		12.3512	
^{139}La	0.0778		0.0635	
^{140}Ce	0.0881		0.1109	
^{141}Pr	bdl		0.0388	
^{146}Nd	bdl		0.1164	
^{147}Sm	bdl		0.3727	
^{153}Eu	0.1537		0.3623	
^{157}Gd	0.3079		0.1608	
^{159}Tb	0.0318		0.0340	
^{163}Dy	0.1967		0.0591	
^{165}Ho	bdl		bdl	
^{166}Er	0.0984		bdl	
^{169}Tm	bdl		bdl	
^{172}Yb	0.0711		bdl	
^{175}Lu	bdl		0.0242	

^{178}Hf	0.1081		0.1340	
^{181}Ta	0.0199		bdl	
^{208}Pb	2.7870		1.6513	
^{232}Th	bdl		bdl	
^{238}U	0.0438		0.0354	

*Oxide element detection limit of 0.01 wt. %; Trace element detection limit of 0.01 ppm

Table 9: NWA 10170 melt inclusion glass major and trace element data

	MI glass_1	**2SD**	**MI glass_2**	**2SD**
SiO_2	77.21	0.24	72.82	0.24
TiO_2	0.49	0.02	0.34	0.02
Al_2O_3	14.30	0.10	19.68	0.41
FeO	1.45	0.07	1.17	0.03
MnO	0.03	0.00	0.02	0.01
CaO	5.16	0.09	0.92	0.01
MgO	0.09	0.01	0.10	0.01
Na_2O	1.11	0.48	1.28	0.06
K_2O	0.17	0.01	4.11	1.22
Cr_2O_3	0.01	0.00	0.01	0.01
P_2O_5	0.26	0.02	0.28	0.01
SO_3	0.02	0.00	0.00	0.00
Total	100.31	0.23	100.74	0.74
Mg#	9.96		12.69	

CaO/Al_2O_3	0.36		0.92	
^{7}Li	bdl		bdl	
^{23}Na	16563.9532		28835.7283	
^{24}Mg	3717.9086		11044.1154	
^{27}Al	56235.4390		63025.3341	
^{29}Si	256954.7354		200689.6325	
^{43}Ca	40983.6174		64438.8998	
^{45}Sc	5.4901		12.1778	
^{49}Ti	2327.5511		2207.8013	
^{51}V	2.5955		48.5575	
^{53}Cr	92.8975		202.6866	
^{55}Mn	220.0525		565.2268	
^{57}Fe	7534.3088		13043.5194	
^{59}Co	8.4973		4.7303	
^{60}Ni	80.8667		17.0109	
^{63}Cu	7.2965		1.7508	
^{66}Zn	16.1762		10.3599	
^{85}Rb	4.1090		436.6468	
^{88}Sr	94.0755		151.1531	
^{89}Y	11.3663		61.9236	
^{90}Zr	78.3982		60.8309	
^{93}Nb	2.3271		4.2570	

^{137}Ba	42.8787		50.1600	
^{139}La	1.2437		4.7274	
^{140}Ce	4.3525		11.1791	
^{141}Pr	0.4033		2.2238	
^{146}Nd	2.8631		10.9330	
^{147}Sm	0.9489		6.4456	
^{153}Eu	0.6226		3.5645	
^{157}Gd	2.9009		8.8380	
^{159}Tb	0.4031		1.4417	
^{163}Dy	3.1730		13.6453	
^{165}Ho	0.5795		2.7131	
^{166}Er	1.4732		8.9841	
^{169}Tm	0.1732		1.1452	
^{172}Yb	1.3489		5.9769	
^{175}Lu	0.2005		0.8335	
^{178}Hf	3.2062		1.3362	
^{181}Ta	0.0339		0.1801	
^{208}Pb	1.8428		2.6294	
^{232}Th	0.3838		0.5224	
^{238}U	bdl		0.1780	

*Oxide element detection limit of 0.01 wt. %; Trace element detection limit of 0.01 ppm

Table 10: NWA 1068 melt inclusion glass major and trace element data

	MI glass_1	**2SD**	**MI glass_2**	**2SD**
SiO_2	66.05	0.75	70.58	0.45
TiO_2	0.46	0.04	0.51	0.01
Al_2O_3	18.62	0.13	19.78	0.48
FeO	0.99	0.16	1.98	0.02
MnO	0.01	0.01	0.02	0.01
CaO	3.91	0.18	5.42	0.31
MgO	0.14	0.04	0.10	0.01
Na_2O	1.78	0.04	1.29	0.05
K_2O	6.07	0.29	0.35	0.02
Cr_2O_3	0.00	0.01	0.00	0.00
P_2O_5	0.70	0.10	1.30	0.38
SO_3	0.01	0.01	0.04	0.00
Total	98.73	0.13	101.36	0.65
Mg#	19.39		8.40	
CaO/Al_2O_3	0.21		0.27	
^{7}Li	bdl		bdl	
^{23}Na	10193.3907		9584.3870	
^{24}Mg	11126.4433		14866.1201	
^{27}Al	58387.8301		44764.6537	

^{29}Si	233984.6208		190050.3040	
^{43}Ca	39944.7067		53917.8668	
^{45}Sc	14.8655		29.0819	
^{49}Ti	4107.1882		4367.9266	
^{51}V	33.1494		89.8201	
^{53}Cr	70.9256		204.0268	
^{55}Mn	551.8144		641.3476	
^{57}Fe	15220.7175		20308.9246	
^{59}Co	7.3195		9.4983	
^{60}Ni	45.9797		60.5063	
^{63}Cu	4.4936		8.3811	
^{66}Zn	16.3593		24.2463	
^{85}Rb	352.8747		91.4608	
^{88}Sr	123.3818		147.7365	
^{89}Y	19.4288		22.0773	
^{90}Zr	82.6571		61.4951	
^{93}Nb	5.2309		4.2210	
^{137}Ba	88.0546		44.9770	
^{139}La	2.5840		2.8298	
^{140}Ce	6.3910		7.5840	
^{141}Pr	0.9460		1.0844	
^{146}Nd	4.1035		5.2010	
^{147}Sm	1.5953		1.8025	

^{153}Eu	0.3958		0.7904	
^{157}Gd	2.7656		3.7474	
^{159}Tb	0.4838		0.7260	
^{163}Dy	3.4150		4.6006	
^{165}Ho	0.6961		0.9638	
^{166}Er	1.9189		2.4002	
^{169}Tm	0.3094		0.2914	
^{172}Yb	1.7528		1.9457	
^{175}Lu	0.2126		0.2808	
^{178}Hf	2.2768		1.7563	
^{181}Ta	0.2540		0.2351	
^{208}Pb	23.9130		2.5446	
^{232}Th	0.7301		0.3939	
^{238}U	0.2912		0.1555	

*Oxide element detection limit of 0.01 wt. %; Trace element detection limit of 0.01 ppm

Table 11: NWA 1183 melt inclusion glass major and trace element data

	MI glass_1	**2SD**	**MI glass_2**	**2SD**
SiO_2	66.24	0.34	65.46	0.46
TiO_2	0.44	0.05	0.46	0.02
Al_2O_3	17.82	0.13	18.15	0.15
FeO	1.11	0.06	1.48	0.17
MnO	0.03	0.01	0.04	0.03

CaO	1.87	0.17	3.03	0.36
MgO	0.27	0.04	0.30	0.06
Na_2O	1.55	0.17	1.80	0.14
K_2O	7.55	0.10	7.17	0.22
Cr_2O_3	0.01	0.01	0.01	0.01
P_2O_5	1.16	0.19	1.06	0.13
SO_3	0.02	0.02	0.03	0.04
Total	98.06	0.48	98.99	0.46
Mg#	29.82		26.26	
CaO/Al_2O_3	0.11		0.17	
^{7}Li			37.0306	
^{23}Na			13639.9451	
^{24}Mg			1974.0469	
^{27}Al			75788.4104	
^{29}Si			254311.0245	
^{43}Ca			26750.9274	
^{45}Sc			10.0889	
^{49}Ti			3850.6786	
^{51}V			33.4023	
^{53}Cr			70.7040	
^{55}Mn			261.5797	
^{57}Fe			6910.8032	

^{59}Co			3.5810	
^{60}Ni			26.4484	
^{63}Cu			10.5953	
^{66}Zn			38.1424	
^{85}Rb			484.8374	
^{88}Sr			176.9529	
^{89}Y			17.2244	
^{90}Zr			132.5603	
^{93}Nb			10.3178	
^{137}Ba			390.4488	
^{139}La			5.7016	
^{140}Ce			11.4674	
^{141}Pr			2.3472	
^{146}Nd			10.3887	
^{147}Sm			3.0869	
^{153}Eu			1.1431	
^{157}Gd			3.5545	
^{159}Tb			0.5115	
^{163}Dy			3.1595	
^{165}Ho			0.7351	
^{166}Er			1.5526	
^{169}Tm			0.3769	
^{172}Yb			1.7001	

^{175}Lu			0.2740	
^{178}Hf			3.9627	
^{181}Ta			0.5099	
^{208}Pb			31.2341	
^{232}Th			1.3857	
^{238}U			0.3825	

*Oxide element detection limit of 0.01 wt. %; Trace element detection limit of 0.01 ppm

Table 12: LAR 12011 melt inclusion glass major (SEM) and trace element data

	MI glass_1	**2SD**	**MI glass_2**	**2SD**	**MI glass_3**	**2SD**	**MI glass_4**	**2SD**	**MI glass_5**	**2SD**
SiO_2	71.74	0.30	71.28	1.92	70.01	5.81	58.63	1.37	66.29	7.82
TiO_2	0.13	0.25	0.25	0.24	0.00	0.00	0.08	0.15	0.05	0.10
Al_2O_3	15.51	0.17	14.61	0.18	13.66	1.59	19.11	1.29	17.34	4.14
FeO	1.56	0.40	1.29	0.28	2.58	0.63	1.78	-	1.16	0.43
MnO	0.00	0.00	0.00	0.00	0.00	0.00	0.00	0.00	0.00	0.00
CaO	2.52	0.44	1.89	1.21	4.43	1.95	7.45	1.65	7.00	2.37
MgO	0.00	0.00	0.00	0.00	1.74	1.08	0.36	-	0.00	0.00
Na_2O	7.29	0.37	7.37	0.57	5.97	0.57	5.33	0.16	5.84	1.01
K_2O	1.26	0.14	2.74	0.56	1.65	0.38	7.62	1.47	2.32	0.67
Cr_2O_3	0.00	0.00	0.00	0.00	0.00	0.00	0.00	0.00	0.00	0.00
P_2O_5	0.00	0.00	0.58	0.95	1.61	1.73	0.31	0.34	0.00	0.00
SO_3										
Total	100.00	0.01	100.00	0.01	99.06	0.79	98.74	0.33	100.09	0.18

Mg#										
CaO/Al_2O_3										
^{7}Li	bdl		bdl		bdl		bdl		bdl	
^{23}Na	59709.7096		60897.6809		37238.5014		37438.0967		45691.4739	
^{24}Mg	1171.1384		8580.4015		22225.9584		56949.2319		24835.6678	
^{27}Al	119289.9543		127031.0110		147899.9263		119921.3560		104580.5436	
^{29}Si	172938.0000		177612.0000		145828.8000		151126.0000		172938.0000	
^{43}Ca	19512.5651		30359.8142		55592.7426		47109.2114		36815.1963	
^{45}Sc	bdl		18.1700		10.9758		35.6524		24.7058	
^{49}Ti	2572.9069		3813.4428		2022.2358		2536.3547		4366.0802	
^{51}V	bdl		61.7471		48.0720		105.4580		93.0380	
^{53}Cr	bdl		254.0152		324.0634		3718.1277		460.0599	
^{55}Mn	299.2067		496.7990		1291.9170		1754.4694		874.3774	
^{57}Fe	5685.2268		10789.4019		36429.8454		49362.3628		23423.4844	
^{59}Co	bdl		4.3818		12.6894		46.7483		10.0392	
^{60}Ni	bdl		17.7365		37.3320		299.2007		68.7839	
^{63}Cu	bdl		bdl		10.3122		12.8074		9.6806	
^{66}Zn	bdl		bdl		58.6751		149.2503		43.8442	
^{85}Rb	26.6878		57.2057		126.7527		51.0551		44.1679	
^{88}Sr	270.8619		80.2086		157.5203		152.4652		279.9349	
^{89}Y	0.5661		2.1433		12.2138		5.9711		49.9097	
^{90}Zr	141.6300		247.4095		54.7984		92.5088		123.3683	

^{93}Nb	19.5911		18.6050		3.7139		2.3954		19.7790	
^{137}Ba	147.8483		240.4703		188.5972		110.7385		157.4920	
^{139}La	0.0412		0.2018		1.9193		0.2452		8.5996	
^{140}Ce	0.1708		0.7518		5.4924		0.6505		20.4322	
^{141}Pr	0.1079		0.3001		0.7936		0.2906		2.6632	
^{146}Nd	0.6797		1.5531		3.9847		1.1253		10.9893	
^{147}Sm	0.2931		0.8850		1.6353		0.7508		4.5873	
^{153}Eu	0.1317		bdl		0.5638		0.5513		1.3572	
^{157}Gd	bdl		bdl		2.2089		bdl		7.2300	
^{159}Tb	0.1280		0.2979		0.3841		0.3039		1.6728	
^{163}Dy	0.6920		2.2422		2.9244		2.3479		9.3565	
^{165}Ho	0.1121		0.3464		0.5905		0.3325		2.1713	
^{166}Er	0.3214		0.9299		1.5015		1.3372		5.8309	
^{169}Tm	0.0518		0.1739		0.3324		0.1739		0.7437	
^{172}Yb	0.3486		0.6687		1.4183		0.9543		3.6410	
^{175}Lu	bdl		0.1125		0.2020		0.1027		0.4736	
^{178}Hf	1.8880		4.1335		1.7764		1.8249		2.9160	
^{181}Ta	0.4993		0.7414		0.1171		0.2167		0.8643	
^{208}Pb	3.7602		7.8924		3.9152		1.6502		2.6352	
^{232}Th	0.1027		0.1012		0.2106		0.0968		1.9914	
^{238}U	0.2346		0.2157		0.1602		0.1047		0.2631	

* Trace element detection limit of 0.01 ppm

C-3

Table 1: DaG 1037 merrillite major and trace element data

	Merr_1	**SD**	**Merr_2**	**Merr_3**	**SD**	**Merr_4**	**SD**
P_2O_5	46.62	1.21	46.46	46.96	0.01	47.18	0.12
SiO_2	0.70	0.18	0.68	0.40	0.05	0.11	0.06
MgO	3.18	0.06	3.23	3.35	0.04	3.39	0.02
CaO	46.83	0.54	47.22	47.79	0.22	48.36	0.14
FeO	1.26	0.01	1.21	1.40	0.02	1.19	0.05
Na_2O	1.57	0.15	1.50	1.35	0.01	1.30	0.03
Total	100.14	0.38	100.74	101.23	0.24	101.53	0.16
Mg#	81.77		82.58	81.04		83.51	
^{7}Li	bdl		bdl	16.5342			
^{23}Na	13897.5262		13040.2855	8839.7954			
^{24}Mg	20174.3642		19137.6517	28072.2128			
^{27}Al	15979.5900		1225.3967	2388.1782			
^{29}Si	27280.0159		bdl	75890.7963			
^{43}Ca	303344.5090		347590.8503	289153.4904			
^{45}Sc	93.2612		73.5684	78.4480			
^{49}Ti	159.0939		40.9788	1357.8772			
^{51}V	9.9612		10.4939	41.1553			
^{53}Cr	69.9575		37.7954	539.2059			
^{55}Mn	345.6385		420.0642	1229.3275			

^{57}Fe	7309.3872		6605.3321	18893.7562			
^{59}Co	4.3854		2.7477	15.8841			
^{60}Ni	17.2701		13.1846	29.5973			
^{63}Cu	5.7711		1.3149	2.3748			
^{66}Zn	13.6305		9.0440	24.1166			
^{85}Rb	1.5478		1.5958	0.6692			
^{88}Sr	135.5740		172.4524	120.7963			
^{89}Y	625.7339		818.1579	647.9105			
^{90}Zr	23.5552		44.9280	27.0254			
^{93}Nb	bdl		0.0260	0.0245			
^{137}Ba	16.9299		6.9826	10.0791			
^{139}La	9.7767		13.2828	9.7026			
^{140}Ce	24.5473		40.2384	30.3619			
^{141}Pr	4.8303		8.1238	5.7362			
^{146}Nd	37.0519		61.1506	41.1653			
^{147}Sm	37.2028		50.5734	35.1813			
^{153}Eu	13.0020		15.6484	12.6225			
^{157}Gd	69.9946		116.6750	79.5798			
^{159}Tb	13.7939		24.0409	16.8920			
^{163}Dy	95.1146		166.2066	130.1185			
^{165}Ho	24.6039		37.5039	28.4497			
^{166}Er	66.1336		101.4496	82.4891			
^{169}Tm	11.2150		14.8016	12.1198			

^{172}Yb	68.9152		86.3171	74.4069			
^{175}Lu	11.2647		12.8539	11.9925			
^{178}Hf	0.5730		1.4332	1.5478			
^{181}Ta	0.0389		bdl	bdl			
^{208}Pb	1.5804		0.6459	0.7308			
^{232}Th	2.1185		1.7178	1.2846			
^{238}U	0.5400		0.5329	0.3942			

*Oxide element detection limit of 0.01 wt. %; Trace element detection limit of 0.01 ppm

Table 2: Dho 019 merrillite major and trace element data

	Merr_1	**SD**	**Merr_2**	**SD**
P_2O_5	45.59	1.10	46.18	0.06
SiO_2	0.94	1.02	0.33	0.19
MgO	3.22	0.26	3.09	0.14
CaO	47.13	1.29	47.83	0.05
FeO	2.85	0.42	2.24	0.14
Na_2O	1.06	0.01	1.01	0.07
Total	100.78	0.70	100.67	0.11
Mg#	66.87		71.07	
^{7}Li	bdl		16.8266	
^{23}Na	8432.2468		8817.8614	
^{24}Mg	17988.0395		22877.8569	

^{27}Al	671.5076		3387.6008	
^{29}Si	bdl		26163.7969	
^{43}Ca	348542.6046		318849.2640	
^{45}Sc	79.9579		65.0524	
^{49}Ti	61.7583		303.2647	
^{51}V	15.4626		15.1327	
^{53}Cr	90.7373		129.0343	
^{55}Mn	820.3220		827.1936	
^{57}Fe	10961.3072		13149.2141	
^{59}Co	3.2280		6.1851	
^{60}Ni	16.6348		27.1989	
^{63}Cu	3.5026		5.8210	
^{66}Zn	13.0534		14.9272	
^{85}Rb	0.9463		3.9986	
^{88}Sr	391.3929		367.1313	
^{89}Y	921.6497		702.5548	
^{90}Zr	77.9117		55.9248	
^{93}Nb	0.0607		0.1313	
^{137}Ba	8.4670		18.9130	
^{139}La	30.8338		25.4196	
^{140}Ce	94.0239		75.6415	
^{141}Pr	17.9979		15.1438	
^{146}Nd	125.2084		100.6051	

^{147}Sm	76.8503		59.2456	
^{153}Eu	16.7622		14.1282	
^{157}Gd	137.3190		110.0760	
^{159}Tb	22.9218		19.5344	
^{163}Dy	151.1222		130.3428	
^{165}Ho	28.3738		28.0498	
^{166}Er	91.7865		76.0924	
^{169}Tm	11.6964		10.2272	
^{172}Yb	75.5659		63.7497	
^{175}Lu	9.4015		9.5066	
^{178}Hf	2.1052		1.9270	
^{181}Ta	0.0534		0.0169	
^{208}Pb	3.1090		4.4798	
^{232}Th	3.5382		3.2361	
^{238}U	0.5752		0.7999	

*Oxide element detection limit of 0.01 wt. %; Trace element detection limit of 0.01 ppm

Table 3: SaU 005 melt inclusion glass major and trace element data

	Merr_1	**SD**	**Merr_2**	**SD**	**Merr_3**	**SD**
P_2O_5	46.92	0.39	47.31	0.23	47.31	0.27
SiO_2	0.25	0.13	0.10	0.00	0.06	0.01
MgO	3.57	0.05	3.45	0.03	3.39	0.00
CaO	47.98	0.09	48.11	0.04	48.10	0.33

FeO	1.15	0.03	1.17	0.02	1.14	0.03
Na_2O	1.39	0.02	1.38	0.04	1.41	0.01
Total	101.24	0.26	101.52	0.23	101.41	0.10
Mg#	84.68		84.09		84.14	
^{7}Li	bdl		bdl			
^{23}Na	12430.5207		10351.5104			
^{24}Mg	30324.7399		17306.3531			
^{27}Al	9790.0421		2364.3513			
^{29}Si	51173.5845		10563.1339			
^{43}Ca	262985.3959		263941.4011			
^{45}Sc	38.9293		36.1933			
^{49}Ti	383.4241		5515.4429			
^{51}V	22.3628		13.0100			
^{53}Cr	234.3361		69.8398			
^{55}Mn	775.1886		405.0861			
^{57}Fe	20099.8463		74643.9665			
^{59}Co	11.9172		156.4939			
^{60}Ni	114.5359		3039.6998			
^{63}Cu	10.7518		98.0484			
^{66}Zn	27.8868		22.7802			
^{85}Rb	bdl		0.9233			
^{88}Sr	146.3928		118.6826			

^{89}Y	763.2590		715.3982			
^{90}Zr	5.4763		27.6036			
^{93}Nb	bdl		1.1564			
^{137}Ba	6.8122		2.8554			
^{139}La	15.3784		13.2771			
^{140}Ce	43.9890		39.9421			
^{141}Pr	8.6151		7.8606			
^{146}Nd	61.7215		58.7833			
^{147}Sm	52.2952		48.0450			
^{153}Eu	12.7539		12.3505			
^{157}Gd	111.3618		98.5119			
^{159}Tb	20.5279		18.8100			
^{163}Dy	142.7006		127.8008			
^{165}Ho	29.2218		27.9001			
^{166}Er	80.8412		74.3023			
^{169}Tm	9.3677		10.1676			
^{172}Yb	54.9517		56.9161			
^{175}Lu	9.1088		7.9301			
^{178}Hf	0.4207		1.6885			
^{181}Ta	bdl		0.0612			
^{208}Pb	bdl		0.4120			
^{232}Th	1.0409		1.3504			
^{238}U	0.3017		0.1663			

*Oxide element detection limit of 0.01 wt. %; Trace element detection limit of 0.01 ppm

Table 4: NWA 6234 merrillite major and trace element data

	Merr_1	**SD**	**Merr_2**	**SD**	**Merr_3**	**SD**
P_2O_5	46.49	0.47	46.81	0.22	45.95	0.93
SiO_2	0.17	0.02	0.17	0.03	0.23	0.12
MgO	3.05	0.09	2.96	0.04	3.22	0.20
CaO	47.75	0.35	47.96	0.22	47.42	0.57
FeO	2.02	0.00	2.16	0.11	1.76	0.04
Na_2O	1.14	0.00	1.16	0.04	1.09	0.11
Total	100.61	0.89	101.20	0.14	99.78	1.85
Mg#	79.99		79.97		80.04	
^{7}Li	bdl		bdl			
^{23}Na	5874.3085		7131.1643			
^{24}Mg	37191.8223		14749.7937			
^{27}Al	2962.5659		406.8583			
^{29}Si	87641.2306		bdl			
^{43}Ca	199389.7983		357360.3585			
^{45}Sc	62.7276		40.3264			
^{49}Ti	1209.0217		31.4839			
^{51}V	68.9554		11.9197			
^{53}Cr	161.4533		12.1643			

^{55}Mn	2141.6228		688.8206			
^{57}Fe	51947.5035		7717.2299			
^{59}Co	16.4745		1.1953			
^{60}Ni	24.9608		bdl			
^{63}Cu	4.2934		2.8373			
^{66}Zn	60.5703		11.2132			
^{85}Rb	3.1614		3.2917			
^{88}Sr	312.8392		441.2933			
^{89}Y	371.4905		571.4942			
^{90}Zr	51.2587		74.7236			
^{93}Nb	0.2076		0.1186			
^{137}Ba	39.7184		38.3125			
^{139}La	29.8753		42.9849			
^{140}Ce	73.1605		105.4079			
^{141}Pr	10.8298		16.3561			
^{146}Nd	64.9948		94.1473			
^{147}Sm	37.9063		48.4907			
^{153}Eu	12.3439		20.1319			
^{157}Gd	58.0823		90.6356			
^{159}Tb	11.0560		16.7513			
^{163}Dy	62.1377		112.0464			
^{165}Ho	14.2470		23.1522			
^{166}Er	37.0915		60.5006			

^{169}Tm	5.2604		7.9426			
^{172}Yb	30.2404		45.4622			
^{175}Lu	4.5336		6.4986			
^{178}Hf	1.8916		0.6743			
^{181}Ta	0.0170		bdl			
^{208}Pb	4.2466		5.3747			
^{232}Th	4.3750		5.4869			
^{238}U	1.7253		3.3565			

*Oxide element detection limit of 0.01 wt. %; Trace element detection limit of 0.01 ppm

Table 5: NWA 10170 melt inclusion glass major and trace element data

	Merr_1	**SD**	**Merr_2**	**SD**	**Merr_3**	**SD**	**Merr_4**	**SD**
P_2O_5	46.26	0.01	46.43	0.75	46.96	0.37	46.36	1.00
SiO_2	0.48	0.17	0.45	0.20	0.22	0.04	0.32	0.06
MgO	3.15	0.04	3.46	0.01	3.54	0.08	3.41	0.01
CaO	47.73	0.04	47.35	0.81	48.43	0.62	47.03	0.77
FeO	1.75	0.06	1.68	0.06	1.63	0.12	1.39	0.06
Na_2O	1.30	0.04	1.07	0.09	1.11	0.05	1.22	0.07
Total	100.65	0.19	100.45	1.47	101.88	0.40	99.72	1.96
Mg#	76.26		78.56		79.53		81.37	
^{7}Li	bdl		bdl		bdl		bdl	bdl
^{23}Na	13124.4821		9699.6210		10155.9406		9871.7733	13124.4821

^{24}Mg	15485.1058		24030.8500		18892.9173		20670.9286	15485.1058
^{27}Al	9955.8823		578.9682		1060.4870		364.4454	9955.8823
^{29}Si	38256.5983		5551.2337				37182.5981	38256.5983
^{43}Ca	303108.0887		315518.5451		349400.6710		328524.6424	303108.0887
^{45}Sc	64.5247		40.1535		65.9573		52.5650	64.5247
^{49}Ti	42.6175		11075.2987		45.8057		83.7380	42.6175
^{51}V	12.0655		55.0251		11.9220		17.1279	12.0655
^{53}Cr	7.2969		276.3521		11.9857		24.4793	7.2969
^{55}Mn	495.1771		919.2816		592.2919		672.4359	495.1771
^{57}Fe	7393.8643		20070.8380		7466.1625		9588.5366	7393.8643
^{59}Co	1.0905		8.5949		1.3585		3.6459	1.0905
^{60}Ni	bdl		28.8072		bdl		10.7852	bdl
^{63}Cu	10.8173		9.8495		8.3422		4.0351	10.8173
^{66}Zn	23.1334		34.0986		14.4311		18.9494	23.1334
^{85}Rb	2.1522		6.2517		3.4923		0.9153	2.1522
^{88}Sr	317.9343		276.2214		371.6596		234.3876	317.9343
^{89}Y	662.9662		734.4888		848.1448		545.2613	662.9662
^{90}Zr	16.9355		74.1108		21.4994		24.6424	16.9355
^{93}Nb	bdl		15.1009		0.0724		0.0299	bdl
^{137}Ba	27.7651		21.6554		19.4080		17.0857	27.7651
^{139}La	59.5261		58.9407		65.6272		42.9838	59.5261
^{140}Ce	153.3609		145.3763		155.4467		102.7686	153.3609
^{141}Pr	22.8118		21.5438		24.3654		14.5471	22.8118

^{146}Nd	131.3159		125.6204		132.3768		85.3105	131.3159
^{147}Sm	68.9660		71.4676		71.3725		45.9008	68.9660
^{153}Eu	25.9895		27.5799		28.9654		20.5950	25.9895
^{157}Gd	126.9273		123.5272		133.8173		84.5054	126.9273
^{159}Tb	21.8673		22.4381		23.6540		15.4522	21.8673
^{163}Dy	149.9647		153.6056		156.6064		106.8519	149.9647
^{165}Ho	29.8168		31.9342		30.4230		21.8480	29.8168
^{166}Er	88.7936		83.4771		84.0496		60.1458	88.7936
^{169}Tm	11.8285		9.5675		11.2386		7.7119	11.8285
^{172}Yb	70.6552		62.4276		67.7651		47.8389	70.6552
^{175}Lu	10.4774		8.4725		10.3570		7.7818	10.4774
^{178}Hf	0.7269		3.5468		0.3308		0.4969	0.7269
^{181}Ta	bdl		0.5076		bdl		bdl	bdl
^{208}Pb	8.8799		15.0130		9.1945		9.2414	8.8799
^{232}Th	8.1790		7.7259		8.4164		7.8968	8.1790
^{238}U	1.4155		1.8819		1.5447		1.8063	1.4155

*Oxide element detection limit of 0.01 wt. %; Trace element detection limit of 0.01 ppm

Table 6: NWA 1068 melt inclusion glass major and trace element data

	Merr_1	**SD**	**Merr_2**	**Merr_3**
P_2O_5	45.40	1.18	45.80	44.95
SiO_2	1.41	0.67	0.39	0.84
MgO	2.82	0.14	2.41	2.16

CaO	46.39	0.86	48.37	48.45
FeO	2.13	0.08	1.94	2.15
Na_2O	1.50	0.09	1.24	1.14
Total	99.66	1.69	101.30	101.05
Mg#	70.22		68.89	64.17
^{7}Li	bdl			
^{23}Na	20546.4382			
^{24}Mg	9429.8829			
^{27}Al	36076.6285			
^{29}Si	103161.1132			
^{43}Ca	210342.8567			
^{45}Sc	40.2030			
^{49}Ti	178.7105			
^{51}V	11.7430			
^{53}Cr	14.2301			
^{55}Mn	334.6124			
^{57}Fe	7802.8345			
^{59}Co	2.7299			
^{60}Ni	9.6358			
^{63}Cu	7.8703			
^{66}Zn	14.2014			
^{85}Rb	5.3058			

^{88}Sr	180.1651			
^{89}Y	645.5185			
^{90}Zr	36.8787			
^{93}Nb	0.1630			
^{137}Ba	68.7027			
^{139}La	108.1690			
^{140}Ce	246.7317			
^{141}Pr	37.6269			
^{146}Nd	181.0294			
^{147}Sm	74.5546			
^{153}Eu	20.8604			
^{157}Gd	123.5402			
^{159}Tb	19.0506			
^{163}Dy	115.7876			
^{165}Ho	24.0655			
^{166}Er	64.1636			
^{169}Tm	7.5017			
^{172}Yb	50.6084			
^{175}Lu	6.4318			
^{178}Hf	0.6335			
^{181}Ta	0.0232			
^{208}Pb	5.3090			
^{232}Th	13.6850			

^{238}U	1.7340			

*Oxide element detection limit of 0.01 wt. %; Trace element detection limit of 0.01 ppm

Table 7: NWA 1183 melt inclusion glass major and trace element data

	Merr_1	**SD**	**Merr_2**	**SD**
P_2O_5	46.14	0.16	46.72	0.19
SiO_2	0.17	0.06	0.34	0.12
MgO	2.33	0.04	2.71	0.06
CaO	47.92	0.02	47.43	0.06
FeO	3.00	0.08	2.49	0.01
Na_2O	1.35	0.04	1.37	0.06
Total	100.90	0.11	101.06	0.03
Mg#	58.06		65.98	
^{7}Li	bdl			
^{23}Na	9426.2837			
^{24}Mg	15954.3278			
^{27}Al	2250.6806			
^{29}Si	13950.1681			
^{43}Ca	329888.6929			
^{45}Sc	69.4802			
^{49}Ti	74.1431			
^{51}V	13.9322			

^{53}Cr	9.4793			
^{55}Mn	802.1744			
^{57}Fe	15009.3822			
^{59}Co	3.6581			
^{60}Ni	9.4228			
^{63}Cu	9.6583			
^{66}Zn	7.8452			
^{85}Rb	6.7303			
^{88}Sr	193.3973			
^{89}Y	654.5258			
^{90}Zr	128.6011			
^{93}Nb	1.5339			
^{137}Ba	471.3989			
^{139}La	91.4656			
^{140}Ce	222.6738			
^{141}Pr	32.2020			
^{146}Nd	168.1870			
^{147}Sm	65.8277			
^{153}Eu	21.0591			
^{157}Gd	95.3920			
^{159}Tb	16.1946			
^{163}Dy	132.7534			
^{165}Ho	26.5160			

^{166}Er	76.6422			
^{169}Tm	10.8335			
^{172}Yb	60.4529			
^{175}Lu	9.1743			
^{178}Hf	3.0781			
^{181}Ta	0.1095			
^{208}Pb	4.6604			
^{232}Th	22.9958			
^{238}U	4.2658			

*Oxide element detection limit of 0.01 wt. %; Trace element detection limit of 0.01 ppm

D-1

8.1 Nakhlite and Chassignite olivine trace and ultra-trace elements

8.1.1 Olivine ultra-trace elements in chassignite and nakhlites indicate late-stage trace element enrichment?

Nakhlites and chassignite meteorites show near-identical ejection (i.e., 11 Ma; Cohen et al., 2017) and crystallisation ages (1340 ± 40 Ma) that, along with previously observed similarities bulk-rock trace element characteristics (e.g., McCubbin et al., 2013; Udry and Day, 2018), suggest that these rocks originate from the same magmatic system. Olivine from NWA 11013 and Chassigny have parallel trace element patterns (**Figure 3.6**, **Figure 3.7**) that suggest derivation from a similar parent melt. The CI-normalised REE patterns for melts in equilibrium with NWA 11013 and Chassigny olivine show LREE-depleted patterns that differ from the LREE-enriched REE patterns of nakhlite-chassignite bulk-rock and pyroxene equilibrium melts (Udry and Day, 2018), and olivine-hosted melt inclusions (Ostwald et al., 2024) (**Figure 8.1**). These findings, which indicate different parent magma compositions for NWA 11013 and Chassigny olivine and bulk-rock, suggest that these samples likely crystallised with open-system behaviour, possibly through assimilation of a LREE-enriched component or mixing with a LREE-enriched melt. If the REE patterns of NWA 11013 and Chassigny olivine reflect the parent melts of olivine, then the LREE enrichment observed in these meteorites must have occurred later. Assuming nakhlites and chassignites formed from the same mantle source, discrepancies in calculated parent melt compositions for NWA 11013 and Chassigny olivine (**Figure 8.1**) might imply that chassignite meteorites were derived from early fractional crystallisation of the LREE-depleted nakhlite-chassignite parental magma and nakhlites from later fractional crystallisation of a more evolved magma. This interpretation is consistent with the Fo contents of olivine in these samples, with more Mg-rich olivine in Chassigny (Fo_{69-68}) relative to NWA 11013 (Fo_{40-14}) (**Table 3.1**) (Udry and Day, 2018). Discrepancies in redox conditions between NWA 11013 and Chassigny are also inconsistent with both samples being derived from a common mantle source but have previously been interpreted to reflect late-stage reduction in nakhlites caused by S_2 degassing (i.e., Righter et al., 2014; Nicklas et al., 2021). Alternatively, these discrepancies may reflect a shift in redox conditions during incompatible element change i.e., crustal fluid alteration.

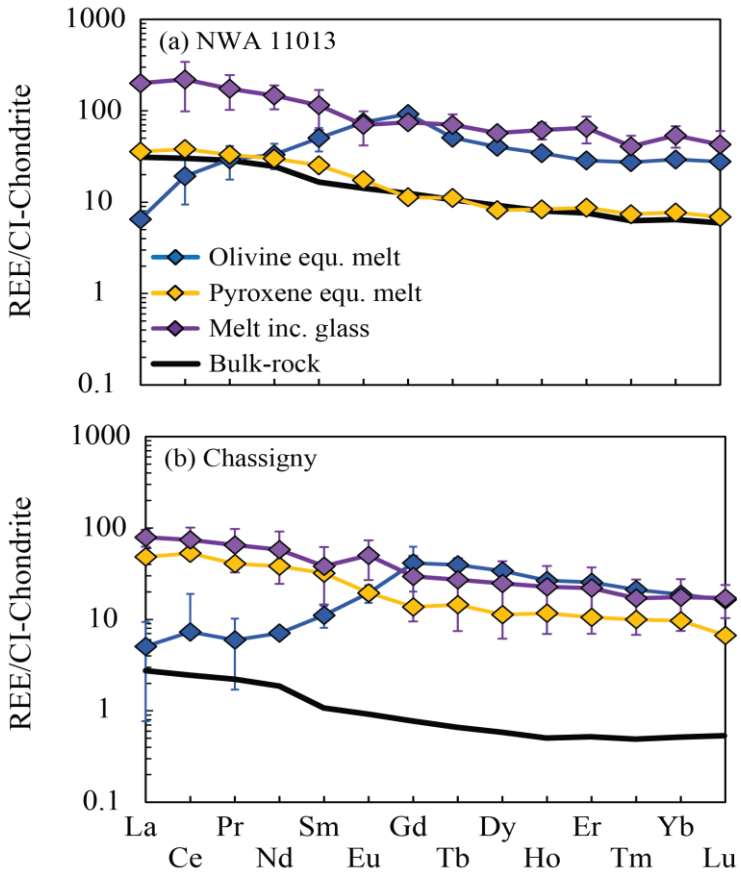

Figure 8.1: REE patterns for melts in equilibrium with NWA 11013 and Chassigny olivine in comparison with nakhlite-chassignite bulk-rock, olivine-hosted melt inclusion, and pyroxene equilibrium melt REE patterns. Literature nakhlite-chassignite bulk-rock, olivine-hosted melt inclusion, and pyroxene equilibrium melt REE data taken from Udry and Day (2018) and Ostwald et al. (2024).

In the traditional model for nakhlite-chassignite petrogenesis, these meteorites are postulated to represent low-degree partial melts of a long-lived and depleted mantle source that was metasomatized by LREE- and Cl-rich fluids (i.e., Harper et al. 1995; Borg et al., 2003; Treiman, 2005; McCubbin et al., 2013; Udry and Day, 2018). The timing of LREE- and Cl-enrichment in Chassigny has, however, been challenged by previous studies of apatite in olivine-hosted melt inclusions (i.e., McCubbin and Nekvasil, 2008; McCubbin et al., 2013, and Shearer et al., 2018), which were shown to preserve Cl isotopic characteristics that suggest the melt inclusions were trapped prior to a LREE- and Cl-rich crustal fluid having modified Chassigny. These findings, which reflect later addition of enriched crustal fluids after cumulate olivine in Chassigny had begun to crystallise, may account for the LREE-depleted REE patterns and positive Zr–Hf anomalies for Chassigny olivine (**Figure 3.6**, **Figure 3.7**), which contrast the LREE-enriched REE patterns and negative Zr–Hf anomalies observed for bulk-rock. In contrast, apatite and amphibole grains hosted in olivine and clinopyroxene melt inclusions from nakhlite meteorites were previously shown to preserve Cl-rich characteristics that suggest fluid infiltration before or during the

crystallisation of cumulate olivine (McCubbin et al., 2013). This proposed timing of fluid infiltration is consistent with the negative Zr–Hf anomalies observed in the ITE patterns for NWA 11013 olivine (**Figure 3.7**), which mirror bulk-rock, and thus, further highlight that NWA 11013 olivine grains and bulk-rock are genetically linked. Furthermore, the negative Zr–Hf anomalies observed for NWA 11013 olivine are less pronounced in more LREE-depleted olivine REE patterns, which in addition to the proposed timing of fluid infiltration for nakhlites, may suggest that olivine began to crystalise prior to or during the initial stages of fluid infiltration and continued to crystallise after the addition of the LREE- and Cl-rich fluid.

These findings suggest that olivine in NWA 11013 and Chassigny likely began to crystallise from initially LREE-depleted parent melt compositions before any mixing with more evolved or new magmas had occurred and prior to LREE- and Cl-rich crustal fluid infiltration. This model of mixing between compositionally dissimilar melt compositions for NWA 11013 and Chassigny, is not unlike that proposed for LAR 12011 and highlights the complex magmatic and post magmatic histories of these samples.

8.1.2 Summary

The CI-normalised REE patterns for melts in equilibrium with olivine from NWA 11013 and Chassigny are LREE-depleted and inconsistent with the LREE-enriched bulk-rock REE patterns of nakhlite-chassignite meteorites, indicating that these samples crystallised with open-system behaviour. These findings support a model of magma mixing between compositionally distinct melts and previous interpretations that cumulate olivine in nakhlite-chassignite meteorites began to crystalise prior to or during the early stages of LREE- and Cl-rich fluid infiltration. Variations in Zr-Hf anomalies in the olivine ITE pattern for NWA 11013 also suggest that olivine continued to crystallise after the Cl- and LREE-rich fluid infiltrated their parent magma. The V-in-olivine fO_2 estimates for NWA 11013 are more oxidized than estimates for the shergottite meteorites and more reduced than estimates for Chassigny, consistent with the findings of numerous other studies.

9 Publication arising from this thesis

Peel, C.J., Howarth, G.H., Day, J.M., le Roux, P. and Alard, O., 2023. Constraints on martian depleted shergottite volcanism from the petrogenesis of olivine-phyric shergottites NWA 2046 and NWA 4925. Journal of African Earth Sciences, 202, 104901. https://doi.org/10.1016/j.jafrearsci.2023.104901